
Long-Term Performance of Container Materials for High-Level Waste

Prepared by J. A. Beavers, N. G. Thompson, A. J. Markworth,
H. J. Cialone, B. S. Majumdar, J. K. McCoy

Battelle Columbus Division

**Prepared for
U.S. Nuclear Regulatory
Commission**

NOTICE

This report was prepared as an account of work sponsored by an agency of the United States Government. Neither the United States Government nor any agency thereof, or any of their employees, makes any warranty, expressed or implied, or assumes any legal liability of responsibility for any third party's use, or the results of such use, of any information, apparatus, product or process disclosed in this report, or represents that its use by such third party would not infringe privately owned rights.

NOTICE

Availability of Reference Materials Cited in NRC Publications

Most documents cited in NRC publications will be available from one of the following sources:

1. The NRC Public Document Room, 1717 H Street, N.W.
Washington, DC 20555
2. The Superintendent of Documents, U.S. Government Printing Office, Post Office Box 37082,
Washington, DC 20013-7082
3. The National Technical Information Service, Springfield, VA 22161

Although the listing that follows represents the majority of documents cited in NRC publications, it is not intended to be exhaustive.

Referenced documents available for inspection and copying for a fee from the NRC Public Document Room include NRC correspondence and internal NRC memoranda; NRC Office of Inspection and Enforcement bulletins, circulars, information notices, inspection and investigation notices; Licensee Event Reports; vendor reports and correspondence; Commission papers; and applicant and licensee documents and correspondence.

The following documents in the NUREG series are available for purchase from the GPO Sales Program: formal NRC staff and contractor reports, NRC-sponsored conference proceedings, and NRC booklets and brochures. Also available are Regulatory Guides, NRC regulations in the *Code of Federal Regulations*, and *Nuclear Regulatory Commission Issuances*.

Documents available from the National Technical Information Service include NUREG series reports and technical reports prepared by other federal agencies and reports prepared by the Atomic Energy Commission, forerunner agency to the Nuclear Regulatory Commission.

Documents available from public and special technical libraries include all open literature items, such as books, journal and periodical articles, and transactions. *Federal Register* notices, federal and state legislation, and congressional reports can usually be obtained from these libraries.

Documents such as theses, dissertations, foreign reports and translations, and non-NRC conference proceedings are available for purchase from the organization sponsoring the publication cited.

Single copies of NRC draft reports are available free, to the extent of supply, upon written request to the Division of Information Support Services, Distribution Section, U.S. Nuclear Regulatory Commission, Washington, DC 20555.

Copies of industry codes and standards used in a substantive manner in the NRC regulatory process are maintained at the NRC Library, 7920 Norfolk Avenue, Bethesda, Maryland, and are available there for reference use by the public. Codes and standards are usually copyrighted and may be purchased from the originating organization or, if they are American National Standards, from the American National Standards Institute, 1430 Broadway, New York, NY 10018.

Long-Term Performance of Container Materials for High-Level Waste

Manuscript Completed: September 1987
Date Published: November 1987

Prepared by
J. A. Beavers*, N. G. Thompson*, A. J. Markworth,
H. J. Cialone, B. S. Majumdar, and J. K. McCoy

Battelle Columbus Division
505 King Avenue
Columbus, OH 43201-2693

*Cortest Columbus, Inc.

Prepared for
Division of Engineering
Office of Nuclear Regulatory Research
U.S. Nuclear Regulatory Commission
Washington, DC 20555
NRC FIN B6764

PREVIOUS REPORTS IN SERIES

NUREG/CR-3405, Volume 1: "Long-Term Performance of Materials Used for High-Level Waste Packaging: Annual Report, March 1982-April 1983."

NUREG/CR-3427, Volume 1: "Long-Term Performance of Materials Used for High-Level Waste Packaging: Quarterly Report, April-June 1983."

NUREG/CR-3427, Volume 2: "Long-Term Performance of Materials Used for High-Level Waste Packaging: Quarterly Report, July-September 1983."

NUREG/CR-3427, Volume 3: "Long-Term Performance of Materials Used for High-Level Waste Packaging: Quarterly Report, October-December 1983."

NUREG/CR-3427, Volume 4: "Long-Term Performance of Materials Used for High-Level Waste Packaging: Annual Report, April 1983-April 1984."

NUREG/CR-3900, Volume 1: "Long-Term Performance of Materials Used for High-Level Waste Packaging: Quarterly Report, April-June 1984."

NUREG/CR-3900, Volume 2: "Long-Term Performance of Materials Used for High-Level Waste Packaging: Quarterly Report, July-September 1984."

NUREG/CR-3900, Volume 3: "Long-Term Performance of Materials Used for High-Level Waste Packaging: Quarterly Report, October-December 1984."

NUREG/CR-3900, Volume 4: "Long-Term Performance of Materials Used for High-Level Waste Packaging: Annual Report, April 1984-April 1985."

NUREG/CR-4379, Volume 1: "Long-Term Performance of Materials Used for High-Level Waste Packaging: Quarterly Report, April-June 1985."

NUREG/CR-4379, Volume 2: "Long-Term Performance of Materials Used for High-Level Waste Packaging: Quarterly Report, July-September 1985."

NUREG/CR-4379, Volume 3: "Long-Term Performance of Materials Used for High-Level Waste Packaging: Quarterly Report, October-December 1985."

NUREG/CR-4379, Volume 4: "Long-Term Performance of Materials Used for High-Level Waste Packaging: Annual Report, April 1985-March 1986."

NUREG/CR-4795: "Long-Term Performance of High-Level Glass Waste Forms: Topical Report, September 1987."

NUREG/CR-4956: "System Performance of High-Level Waste Package Components: Topical Report, September 1987."

NUREG/CR-4954: "Long-Term Performance of Spent Fuel Waste Forms: Topical Report, September 1987."

ABSTRACT

This report describes the results of experimental and analytical studies of high-level waste container degradation. Corrosion and hydrogen embrittlement tests were conducted on selected materials to identify environmental and metallurgical factors that promote material degradation, especially stress-corrosion cracking. A major emphasis on overpack materials focused on cast and wrought low-carbon steels.

Results of the corrosion work show that, to more completely identify potential failure modes, exposure environments must be further defined. Predictions of pitting rates based on models utilizing nonreactive walls may lead to rejection of carbon steel as a viable overpack material when, on the basis of performance, it may perform satisfactorily. Hydrogen embrittlement was shown to be promoted in regions of microstructural change such as the weld heat-affected zone. These findings show that hydrogen embrittlement is important to container integrity.

A small portion of this task was devoted to studying the possible internal corrosion of the canister. It was found that Type 304L stainless steel will likely contain high-level waste glass for the retrieval period and probably the thermal period. Modeling studies focused on general corrosion and pitting corrosion, with the models being extended to account for more realistic conditions. Results show that pit wall reactivity is an important consideration in predicting corrosion rates.

TABLE OF CONTENTS

	<u>Page</u>
EXECUTIVE SUMMARY	1
1. INTRODUCTION	1-1
1.1 Task Objectives	1-1
1.2 Report Organization	1-2
2. HYDROGEN EMBRITTLEMENT	2-1
2.1 Background	2-1
2.1.1 Sources of Hydrogen	2-1
2.1.2 Candidate Container Materials	2-2
2.1.3 Effects Considered	2-3
2.2 Objectives and Approach	2-6
2.2.1 Objectives	2-6
2.2.2 Approach	2-6
2.2.3 Materials Studied	2-10
2.3 Experimental Procedures	2-10
2.3.1 Material/Specimen Preparation	2-10
2.3.1.1 Battelle Steel Castings	2-10
2.3.1.2 Welded Steel Castings	2-18
2.3.1.3 Iron Castings	2-19
2.3.1.4 Test Specimens	2-24
2.3.2 Hydrogen-Embrittlement Experiments to Assess Role of Composition, Processing, and Dopants	2-26
2.3.3 Hydrogen Absorption Experiments	2-26
2.3.4 Experiments Involving High-Pressure Hydrogen at Moderately Elevated Temperatures	2-27
2.4 Results	2-30
2.4.1 Effects of Hydrogen on Tensile Properties	2-30
2.4.1.1 Battelle Cast Steel--Effects of Hydrogen on Tensile Properties	2-30
2.4.1.2 Welded Steel Castings	2-33
2.4.1.3 Commercial-Purity Iron	2-38
2.4.2 Effects of Hydrogen on Fracture Toughness	2-39
2.4.2.1 Battelle Cast Steel and Welded Steel Plates	2-39

TABLE OF CONTENTS
(Continued)

	<u>Page</u>
2.4.2.2 Commercial-Purity Iron	2-45
2.4.3 Hydrogen Absorption in Basalt-Repository Environment	2-47
2.4.4 Short-Term and Long-Term Effects of Hydrogen at Moderately Elevated Temperatures	2-51
2.4.4.1 Test Data	2-51
2.4.4.2 J-Integral Results	2-57
2.4.4.3 Short-Term Effects of Elevated Temperature Hydrogen	2-57
2.4.4.4 Long-Term Effects of Elevated- Temperature Hydrogen	2-59
2.4.4.5 Fractography	2-63
2.4.4.6 Microstructure	2-68
2.5 Discussion	2-73
2.5.1 Mechanical Degradation Analysis	2-73
2.5.2 Summary of Hydrogen Effects	2-76
2.5.2.1 Discussion on Short-Term and Long- Term Effects of High-Pressure Hydro- gen at Moderately Elevated Temperatures	2-77
2.5.3 Areas of Most Severe Degradation and Implica- tions for Long-Term Integrity of Waste Containers	2-88
2.6 Conclusions and Recommendations	2-88
2.7 References for Chapter 2.....	2-88
3. OVERPACK CORROSION	3-1
3.1 Titanium Grade 12-Salt System	3-1
3.1.1 Task Objective	3-1
3.1.2 Experimental Approach	3-2
3.1.2.1 Materials	3-2
3.1.2.2 Specimen Preparation and Examination	3-2
3.1.2.3 Solution Preparation	3-4
3.1.2.4 Autoclave Exposures	3-6
3.1.2.5 Deposit-Growth Studies	3-7
3.1.2.6 Slow Strain Rate Tests	3-8

TABLE OF CONTENTS
(Continued)

	<u>Page</u>
3.1.3 Results and Discussion	3-8
3.1.3.1 First Autoclave Exposure	3-8
3.1.3.2 Second Autoclave Exposure	3-12
3.1.3.3 Third Autoclave Exposure	3-19
3.1.3.4 Deposit-Growth Studies	3-21
3.1.3.5 Slow Strain Rate Studies	3-28
3.1.4 Conclusions	3-28
3.2 Carbon Steel-Basalt System	3-33
3.2.1 Potentiodynamic Polarization Studies	3-33
3.2.1.1 Objective	3-33
3.2.1.2 Experimental Approach	3-33
3.2.1.3 Results of Metallurgical Studies	3-37
3.2.1.4 Results of Preliminary Environ- mental Studies	3-43
3.2.1.5 Statistical Environmental Studies	3-47
3.2.1.6 Summary	3-79
3.2.2 Pit-Propagation Studies	3-80
3.2.2.1 Objectives	3-81
3.2.2.2 Experimental Approach	3-81
3.2.2.3 Pit-Propagation Results	3-85
3.2.2.4 Summary	3-118
3.2.3 Autoclave Studies	3-123
3.2.3.1 Objective	3-123
3.2.3.2 Approach	3-123
3.2.3.3 Results and Discussion	3-123
3.2.3.4 Summary	3-133
3.2.4 Literature Survey on Stress-Corrosion Crack- ing of Carbon Steels	3-135
3.2.5 Slow Strain Rate Studies	3-141
3.2.5.1 Objective	3-141
3.2.5.2 Approach	3-141
3.2.5.3 Preliminary SSR Experiments in Basalt Groundwater	3-142

TABLE OF CONTENTS
(Continued)

	<u>Page</u>
3.2.5.4 Slow Strain Rate Experiments in Solutions From the Statistical Design Matrix	3-143
3.2.5.5 SSR Experiments in Ferric Chloride Solutions	3-146
3.2.5.6 Slow Strain Rate Experiments in Nitrate Solutions	3-158
3.2.5.7 Summary	3-162
3.3 Stainless Steel-Tuff System	3-162
3.3.1 Introduction	3-162
3.3.2 Approach and Results	3-163
3.4 References for Chapter 3	3-166
4. INTERNAL CANISTER CORROSION	4-1
4.1 Background	4-1
4.1.1 Savannah River Laboratory (SRL) Data	4-1
4.1.2 Pacific Northwest Laboratory Data	4-4
4.1.3 Oak Ridge National Laboratory Data	4-6
4.1.4 Miscellaneous Data	4-6
4.2 Experimental Approach	4-6
4.2.1 Materials	4-7
4.2.2 Test Planning	4-9
4.2.3 Laboratory Procedure	4-9
4.3 Results and Discussion	4-11
4.3.1 Pit-Depth Measurements	4-11
4.3.2 Corrosion-Product Analysis	4-18
4.3.3 CF8 Alloy Exposure	4-21
4.4 Conclusions	4-22
4.5 References for Chapter 4	4-24
5. CORROSION MODELING STUDIES	5-1
5.1 Pitting-Corrosion Modeling	5-1
5.1.1 Pit-Generation Kinetics	5-1
5.1.1.1 Literature Review	5-1

TABLE OF CONTENTS
(Continued)

	<u>Page</u>
5.1.1.2 Relationship Between Pit-Generation Rate and Other Quantities	5-2
5.1.2 Pit-Growth Kinetics	5-3
5.1.2.1 Background and Review	5-3
5.1.2.2 Binary-Electrolyte Pit-Growth Model for an Inert-Wall Pit, With No Con- sideration of Electrode Kinetics at Pit Base	5-5
5.1.2.3 Inclusion of Electrode Kinetics at Pit Base	5-11
5.1.2.4 Inclusion of Chemically Active Pit Walls	5-16
5.1.3 Evolution of the Pit-Depth Distribution	5-22
5.1.4 Conclusions	5-22
5.2 General Corrosion Modeling	5-23
5.2.1 General Description of Model	5-23
5.2.1.1 Assumptions	5-23
5.2.1.2 Mass-Transport Formalism	5-24
5.2.1.3 Generation and Annihilation of Chem- ical Species	5-24
5.2.1.4 Film-Growth Kinetics	5-25
5.2.1.5 Initial Conditions and Boundary Conditions	5-26
5.2.2 Numerical-Integration Technique	5-28
5.2.3 Application to Specific Examples	5-28
5.2.3.1 One Chemical Species (Oxidizing) With Maximum-Rate Kinetics	5-29
5.2.3.2 Two Chemical Species (One Oxidizing and One Reducing) With Maximum-Rate Kinetics	5-32
5.2.3.3 One Chemical Species (Oxidizing) With Film-Growth Kinetics	5-34
5.2.4 Conclusions	5-41
5.3 References for Chapter 5	5-42

TABLE OF CONTENTS
(Continued)

	<u>Page</u>
6. CONCLUSIONS	6-1
6.1 Hydrogen Embrittlement	6-1
6.2 Overpack Corrosion	6-4
6.2.1 Titanium Grade 12-Salt System	6-4
6.2.2 Carbon Steel-Basalt System	6-4
6.2.2.1 Potentiodynamic Polarization	6-4
6.2.2.2 Pit Propagation	6-6
6.2.2.3 Autoclave Studies	6-7
6.2.2.4 Slow Strain Rate Studies	6-8
6.2.3 Stainless Steel-Tuff System	6-9
6.3 Internal Canister Corrosion	6-9
6.4 Corrosion Modeling Studies	6-10
6.4.1 Pitting Corrosion	6-10
6.4.2 General Corrosion	6-10
Appendix A. POTENTIODYNAMIC POLARIZATION DATA AND ANALYSES	A-1
Appendix B. POTENTIAL AND CURRENT DATA FOR ELECTROCHEMICAL PIT-PROPAGATION EXPERIMENTS	B-1
Appendix C. POTENTIODYNAMIC POLARIZATION CURVES FOR SELECTED SOLUTIONS FROM STATISTICAL MATRIX	C-1
Appendix D. POTENTIODYNAMIC POLARIZATION CURVES FOR NITRATE SOLUTIONS	D-1
Appendix E. CORROSION MODEL CODE DOCUMENTATION	E-1
Appendix F. QUALITY ASSURANCE PROCEDURES	F-1

LIST OF TABLES

	<u>Page</u>
Table 2.1. Specified composition for ASTM A216, Grade WCA, cast carbon steel	2-2
Table 2.2. Chemical compositions of steels cast by Battelle	2-14
Table 2.3. Chemical compositions of cast-steel sample plates provided by Colorado School of Mines	2-18
Table 2.4. Average chemical composition of iron ingots	2-22
Table 2.5. Test matrix involving high-pressure hydrogen and helium at elevated temperatures, for assessing short-term and long-term effects of pre-exposure	2-28
Table 2.6. Tensile properties of Battelle steels	2-31
Table 2.7. Tensile properties of welded cast-steel plates	2-36
Table 2.8. Tensile properties of iron ingots	2-38
Table 2.9. Room-temperature fracture-toughness data for cast steels	2-41
Table 2.10. Hydrogen absorbed during exposure to simulated basalt groundwater	2-48
Table 2.11. Results of fracture toughness experiments with high-pressure, elevated-temperature hydrogen or helium	2-52
Table 2.12. Short-term effects of elevated-temperature hydrogen	2-59
Table 2.13. Long-term effects of elevated-temperature hydrogen	2-60
Table 2.14. Rate of decrease of J_G at various temperatures, for specimens pre-exposed to hydrogen and subse- quently fracture tested at room temperature	2-81
Table 2.15. Activation energies of various processes rela- ted to hydrogen in iron and steels	2-86
Table 3.1. Certified chemical analyses for Titanium Grade 12 material	3-3

LIST OF TABLES
(Continued)

	<u>Page</u>
Table 3.2. Results of gravimetric measurements performed on Titanium Grade 12 specimens exposed 900 hours to deaerated Brine A at 250 C (first autoclave exposure)	3-9
Table 3.3. Results of EDS analyses of deposits found on one of the heated polarization-resistance specimens	3-14
Table 3.4. Results of XRD analyses of deposits found on one of the heated polarization-resistance specimens	3-14
Table 3.5. Results of ICAP analyses of test solution from the autoclave exposure of Titanium Grade 12 in Brine A where effect of heat transfer was studied	3-15
Table 3.6. Results of gravimetric measurements performed on Titanium Grade 12 specimens exposed 1,000 hours to deaerated Brine A at 250 C (second autoclave exposure)	3-17
Table 3.7. Results of gravimetric measurements performed on Titanium Grade 12 specimens exposed for 1,000 hours to deaerated Brine A at 250 C (third autoclave exposure)	3-23
Table 3.8. Chemical compositions and other data on steels used in the corrosion studies	3-38
Table 3.9. Nominal compositions of test solutions	3-39
Table 3.10. Summary of results of potentiodynamic polarization tests performed on cast and wrought steels in deaerated basalt groundwater at 90 C and a scan rate of 0.6 V/hr	3-40
Table 3.11. Summary of results of potentiodynamic polarization tests performed on doped cast BCL steel and clean wrought BCL steel in deaerated basalt groundwater at 90 C comparing fast scan rate and slow scan rate data	3-48
Table 3.12. High and low concentrations of species selected for evaluation in the electrochemical experiments	3-52

LIST OF TABLES
(Continued)

	<u>Page</u>
Table 3.13. Concentrations of species in basalt groundwater or in actual or simulated basalt repository environments	3-53
Table 3.14. Experimentally measured polarization parameters for solution 33 which represented the mid-point concentration of species defined in Table 3.12 (4 replicates, A to D)	3-55
Table 3.15. Results of statistical analysis indicating the effect of each chemical species on the polarization parameters measured by potentiodynamic polarization	3-56
Table 3.16. Summary of results of statistical analysis for the main effects of the chemical species based on a 90-percent or greater probability of significance	3-58
Table 3.17. Main effects and interactions selected from screening tests which were examined in main test matrix	3-59
Table 3.18. Experimental design developed utilizing COED for main matrix of experiments	3-60
Table 3.19. Measured range and median values of solution variables in main matrix of experiments	3-61
Table 3.20. Terms that had a high degree of correlation	3-62
Table 3.21. Effect of concentration range for each variable (with all other variables held at their median values) on the corrosion parameters	3-71
Table 3.22. Model predictions for corrosion parameters compared to measured values for several solutions used in examining two-factor interactions	3-73
Table 3.23. pH as a function of exposure time for simulated basalt groundwater solutions in contact with basalt rock and 1018 carbon steel specimens at 90 C	3-87

LIST OF TABLES
(Continued)

	<u>Page</u>
Table 3.24. Uncoupled potentials for pit and BES specimens as a function of exposure time and pH of packing paste for pit-propagation experiments in basalt groundwater at 75 C	3-100
Table 3.25. Experimental parameters for the electrochemical pit-propagation tests performed at 25 C; pit specimen area = 0.13 cm ² , BES specimen area = 24 cm ²	3-102
Table 3.26. Summary of electrochemical pit-propagation experiments for carbon steel in basalt groundwater at 25 C using simulated pits prepacked with 0.1 N HCl-Fe ₃ O ₄ paste	3-103
Table 3.27. Summary of electrochemical pit-propagation experiments for carbon steel with millscale in aerated basalt groundwater at 25 C using simulated pits prepacked with 0.1 N HCl-Fe ₃ O ₄ paste	3-111
Table 3.28. Summary of electrochemical pit-propagation experiments for carbon steel in aerated Solution No. 30 (#26) and aerated Solution No. 47 (#31) at 25 C using simulated pits prepacked with pH 1 Fe ₃ O ₄ paste	3-113
Table 3.29. Summary of electrochemical pit-propagation experiments for carbon steel in aerated Brine A (Experiment 27) and aerated Brine B (Experiment 28) at 25 C using simulated pits prepacked with pH 1 Fe ₃ O ₄ paste	3-120
Table 3.30. Corrosion rates calculated from weight loss and pit depths for cast specimens of clean 1018 steel exposed for 1000 hours to a deaerated simulated basalt groundwater at 250 C	3-125
Table 3.31. Corrosion rates calculated from weight loss and pit depths for wrought specimens of 1018 steel exposed for 1000 hours to deaerated simulated basalt groundwater at 250 C	3-125
Table 3.32. Corrosion rates calculated from weight loss and pit depths for cast specimens of clean 1018 steel exposed for 1000 hours to deaerated simulated basalt groundwater at 250 C	3-126

LIST OF TABLES
(Continued)

	<u>Page</u>
Table 3.33. Corrosion rates calculated from weight loss and pit depths for wrought specimens of 1018 steel exposed for 1000 hours to deaerated simulated 10X basalt groundwater at 250 C	3-126
Table 3.34. Results of EDX and XRD analyses of cast steel specimen exposed for 1000 hours in 250 C deaerated simulated basalt groundwater containing crushed basalt	3-127
Table 3.35. Corrosion rates calculated from weight loss and pit depths for duplicate specimens of clean cast 1018 steel exposed for 1000 hours to deaerated simulated 10X basalt groundwater at 250 C	3-129
Table 3.36. Corrosion rates calculated from weight loss and pit depths for duplicate specimens of clean wrought 1018 steel exposed for 1000 hours to deaerated simulated 10X basalt groundwater at 250 C	3-129
Table 3.37. Corrosion rates calculated from weight loss and pit depths for duplicate specimens of cast 1018 steel exposed for 1000 hours to deaerated simulated 10X basalt groundwater at 250 C	3-130
Table 3.38. Corrosion rates calculated from weight loss and pit depths for duplicate specimens of wrought 1018 steel exposed for 1000 hours to deaerated simulated 10X basalt groundwater at 250 C	3-130
Table 3.39. Summary of the effects of various ions on the corrosion of iron-base alloys	3-138
Table 3.40. Effect of electrochemical potential on the time to failure and the mechanical properties of cold-rolled 1018 carbon steel specimens in slow strain rate tests in basalt groundwater at 90 C and a strain rate of 6×10^{-7} sec ⁻¹	3-142
Table 3.41. Compositions of solutions from statistical design matrix that were used in the slow strain rate experiments	3-143
Table 3.42. Summary of potentiodynamic polarization parameters for 1020 carbon steel in the test solutions used in the SSR studies	3-144

LIST OF TABLES
(Continued)

	<u>Page</u>
Table 3.43. Summary of results of SSR experiments performed on solutions from potentiodynamic polarization matrix at 75 C and a strain rate of $2 \times 10^{-7} \text{ sec}^{-1}$	3-145
Table 3.44. Effect of various solutions and slurries containing Fe (III) and/or chloride on cracking at 316 C	3-150
Table 3.45. Summary of results of slow strain rate experiments performed on hot-rolled 1020 carbon steel in FeCl_3 solutions at 315 C and at various strain rates	3-151
Table 3.46. Summary of results of slow strain rate experiments performed on hot-rolled 1020 carbon steel in aqueous $5 \times 10^{-4} \text{ M FeCl}_3$ at a strain rate of $1 \times 10^{-7} \text{ sec}^{-1}$	3-154
Table 3.47. Summary of results of potentiodynamic-polarization experiments performed on 1020 carbon steel in deaerated nitrate solutions at 90 C and a scan rate of 18 V/hr	3-159
Table 3.48. Summary of results of slow strain experiments performed on hot-rolled 1020 carbon steel in nitrate solutions at 80 C and a strain rate of $2 \times 10^{-7} \text{ sec}^{-1}$	3-159
Table 3.49. Compositions and mechanical properties for Type 304L stainless steel stock used in the SCC tests	3-164
Table 3.50. Nominal composition of simulated tuff groundwater	3-165
Table 4.1. Composition of glass frits used at Savannah River Laboratory	4-2
Table 4.2. Wastage of Type 304 stainless steel in 72-68 waste glass over a 24-hour period	4-5
Table 4.3. Corrosion rates of Type 304 or 304L stainless steel exposed to various corrosive agents	4-7
Table 4.4. Certified analyses of Type 304L stainless steel	4-8
Table 4.5. Certified analysis of CF8 alloy	4-8
Table 4.6. Composition of PNL 76-68 glass	4-10

LIST OF FIGURES

	<u>Page</u>
Figure 2.1. Complex mechanical-thermal-hydrogen environment anticipated in service for a container material	2-7
Figure 2.2. Breakdown of technical approach showing various factors studied to assess effects of hydrogen on container integrity	2-9
Figure 2.3. Full longitudinal section through casting of clean steel	2-12
Figure 2.4. Full longitudinal section through casting of doped steel	2-13
Figure 2.5a. Microstructure of clean steel	2-14
Figure 2.5b. Microstructure of doped steel	2-15
Figure 2.6. Microstructure of clean steel after hot rolling and after annealing	2-16
Figure 2.7. Microstructure of doped steel after hot rolling and after annealing	2-17
Figure 2.8. Photomacrograph of cast steel plate NRC-9 provided by Colorado School of Mines	2-20
Figure 2.9. Photomacrograph of cast steel plate NCR-11 provided by Colorado School of Mines	2-21
Figure 2.10. Transverse section through iron ingot that were provided by ARMCO	2-22
Figure 2.11. Photomicrographs of iron ingot showing fine precipitates at grain boundaries and in the matrix	2-23
Figure 2.12. Compact-tension specimen design for fracture-mechanics experiments	2-24
Figure 2.13. Ductility of clean and doped steels tension tested in 1000 psig hydrogen or nitrogen	2-32
Figure 2.14. Fracture surfaces of clean cast steel	2-34
Figure 2.15. Fracture surface of doped as-cast steel	2-35

LIST OF FIGURES
(Continued)

	<u>Page</u>
Figure 2.16. Fractured tensile specimens prepared from welded cast-steel plates provided by Colorado School of Mines	2-37
Figure 2.17. J-resistance curves for the as-cast clean steel tested in nitrogen or in hydrogen	2-39
Figure 2.18. J-resistance curves for specimens for plate NRC-11, notched in the heat-affected zone	2-42
Figure 2.19. Photomicrographs comparing the microstructures in the heat-affected zone of Plate NRC-11 with the microstructures of the clean steel as cast and as annealed	2-44
Figure 2.20. J-resistance curves for iron specimens	2-45
Figure 2.21. Hydrogen content versus time of exposure to simulated basaltic groundwater for as-cast clean and doped steels	2-50
Figure 2.22. Typical raw-data generated during the fracture toughness experiments, showing load and electric potential plotted versus displacement	2-53
Figure 2.23. Load-displacement curves of some compact-tension specimens, pre-exposed to hydrogen at elevated temperatures, and subsequently loaded to failure in hydrogen at room temperature	2-54
Figure 2.24. Load-displacement curves of compact-tension specimens, pre-exposed to helium at elevated temperatures, and subsequently loaded to failure in helium at room temperature	2-55
Figure 2.25. Load-displacement curves of unexposed and pre-exposed specimens, tested at 260 C (500 F)	2-56
Figure 2.26. Typical J-resistance curve generated for pre-exposed specimen	2-58
Figure 2.27. Bar-chart showing J_{IC} , dJ/da , and composite parameter J_G for various pre-exposure conditions	2-62
Figure 2.28. Bar-chart showing comparison of J_{IC} , dJ/da , and J_G for specimens tested at room-temperature or at 260 C (500 F)	2-64

LIST OF FIGURES
(Continued)

	<u>Page</u>
Figure 2.29. Scanning electron micrograph of fracture surface of specimen, pre-exposed to helium at 1100 F for 50 hours, and subsequently fracture tested in helium at room temperature	2-65
Figure 2.30. Fracture surface of specimen, pre-exposed to hydrogen at 1100 F for 50 hours, and subsequently fracture tested in hydrogen at room temperature	2-66
Figure 2.31. Fracture surface of specimen, pre-exposed to hydrogen for 250 hours at various temperatures, and subsequently fracture tested at room temperature in hydrogen	2-67
Figure 2.32. Fracture surface of specimen, pre-exposed to hydrogen at 1100 F for 250 hours, and subsequently fracture tested in hydrogen at room temperature	2-68
Figure 2.33. Microstructure of a specimen pre-exposed in hydrogen at 260 C (500 F) for 250 hours	2-69
Figure 2.34. Microstructure of a specimen pre-exposed in hydrogen at 399 C (750 F) for 250 hours	2-69
Figure 2.35. Crack-like cavities observed in the microstructure of a specimen, exposed to hydrogen at 399 C (750 F) for 250 hours	2-70
Figure 2.36. Microstructure near the fracture surface of a specimen, pre-exposed to hydrogen at 1100 F for 250 hours, and subsequently fracture tested in hydrogen at room temperature	2-71
Figure 2.37. High-magnification photomicrograph of a specimen exposed to hydrogen at 593 C (1100 F) for 250 hours	2-72
Figure 2.38. Cavities nucleating along ferrite-pearlite boundary, for a specimen exposed to hydrogen at 750 F for 250 hours	2-73
Figure 2.39. Generalized representations of the applied J integral as a function of flaw depth and applied hoop stress for a cylinder with an axial surface flaw	2-75

LIST OF FIGURES
(Continued)

	<u>Page</u>
Figure 2.40. Time for attack of carbon steel in hydrogen service	2-78
Figure 2.41. Plot of J_G versus times of pre-exposure in hydrogen at various temperatures. All the specimens were fracture tested in hydrogen at room temperature	2-80
Figure 2.42. Rate of decrease in J_G versus temperature of pre-exposure in hydrogen	2-82
Figure 2.43. Sketch, illustrating possible reason for the observed peak in rate of damage (measured in terms of J_G/dt) of specimens	2-83
Figure 2.44. Rate of decrease of J_G plotted versus inverse of absolute temperature	2-84
Figure 3.1. Schematic of heat-transfer and thermogalvanic specimens	3-5
Figure 3.2. $1/PR$ as a function of exposure time for Titanium Grade 12 exposed to deaerated Brine A at 250 C	3-10
Figure 3.3. Low-power optical photographs of front (a) and back (b) faces of Titanium Grade 12 crevice specimens exposed to Brine A for 900 hours at 250 C	3-11
Figure 3.4. Low-power optical photograph of Titanium Grade 12 thermogalvanic specimens showing deposit on heated specimen	3-13
Figure 3.5. Galvanic current density as a function of exposure time for a heated Titanium Grade 12 specimen coupled to an unheated specimen ($\Delta T = 20$ C) having equal surface areas in deaerated Brine A at 250 C	3-18
Figure 3.6. $1/PR$ as a function of exposure time for heated and unheated ($\Delta T = 20$ C) Titanium Grade 12 specimens exposed in deaerated Brine A at 250 C	3-20
Figure 3.7. Low-power optical photograph of canister, specimen rack, and heat-transfer specimen following testing	3-22

LIST OF FIGURES
(Continued)

	<u>Page</u>
Figure 3.8. Low-power optical photograph of crevice specimens exposed to vapor and liquid phases in the third autoclave exposure	3-23
Figure 3.9. Low-power optical photograph of U-bend specimens exposed to vapor in the third autoclave exposure	3-24
Figure 3.10. Rate of deposit growth, averaged over 3-hour tests, as a function of solution temperature and ΔT on a Titanium Grade 12 specimen exposed to naturally aerated Brine A	3-25
Figure 3.11. Data shown in Figure 3.10 given as rate of weight gain as a function of $1/T$	3-26
Figure 3.12. Low-power optical photograph of Titanium Grade 12 heat transfer specimen exposed for 4 hours to naturally aerated Brine A at 65 C ($\Delta T = 7$ C)	3-27
Figure 3.13. Specimen temperature as a function of distance from solution-vapor interface and solution temperature for Titanium Grade 12 in Brine A with a fixed ΔT ($T_{\text{heated specimen}} - T_{\text{solution}}$)	3-29
Figure 3.14. Specimen temperature as a function of distance from solution-vapor interface and ΔT for Titanium Grade 12 in Brine A at 100 C	3-30
Figure 3.15. SEM photograph of fracture surface of Titanium Grade 12 specimen after slow strain rate testing in deaerated Brine A at 250 C at a strain rate of $1 \times 10^{-7} \text{ sec}^{-1}$	3-31
Figure 3.16. Photomicrograph of metallographic section of specimen from Figure 3.15	3-32
Figure 3.17. Higher magnification photomicrograph of right edge of fracture surface shown in Figure 3.16	3-33
Figure 3.18. Schematic of typical anodic potentiodynamic polarization curves	3-34
Figure 3.19. Schematic of slow scan and fast scan potentiodynamic polarization curves for a metal in an SCC environment	3-35

LIST OF FIGURES
(Continued)

	<u>Page</u>
Figure 3.20. Three-compartment polarization cell design	3-36
Figure 3.21. Potentiodynamic polarization curve for cast, doped BCL steel in basalt groundwater at 90 C polarized with a scan rate of 0.6 V/hr	3-41
Figure 3.22. Potentiodynamic polarization curves for Specimens 1 and 2 of Ferrovac E in basalt groundwater at 90 C polarized with a scan rate of 0.6 V/hr	3-42
Figure 3.23. Optical photographs of Ferrovac E Specimen 2 following potentiodynamic polarization testing in deaerated basalt groundwater at 90 C	3-44
Figure 3.24. Electrochemical potential parameters taken from potentiodynamic polarization curves for wrought doped and clean cast BCL steels in deaerated simulated basalt groundwater at 90 C	3-45
Figure 3.25. Current parameters taken from potentiodynamic polarization curves for wrought doped and clean cast BCL steels in deaerated simulated basalt groundwater at 90 C	3-46
Figure 3.26. Effect of scan rate on the polarization behavior of cast doped BCL steel in deaerated basalt groundwater at 90 C	3-49
Figure 3.27. Potentiodynamic polarization curve for the wrought doped BCL steel in basalt groundwater at 250 C with a scan rate of 0.6 V/hr	3-50
Figure 3.28. Schematic showing the relative magnitude and direction of significant main effects and two-factor interactions on E_{cor}	3-64
Figure 3.29. Schematic showing the relative magnitude and direction of significant main Effects and two-factor interactions on i_{cor}	3-65
Figure 3.30. Schematic showing the relative magnitude and direction of significant main effects and two-factor interactions on i_{max}	3-66

LIST OF FIGURES
(Continued)

	<u>Page</u>
Figure 3.31. Schematic showing the relative magnitude and direction of significant main effects and two-factor interactions on i_{pas}	3-67
Figure 3.32. Schematic showing the relative magnitude and direction of significant main effects and two-factor interactions on E_{pit}	3-68
Figure 3.33. Schematic showing the relative magnitude and direction of significant main effects and two-factor interactions on E_{prot}	3-69
Figure 3.34. Free-corrosion potential as a function of exposure time for 1020 carbon steel specimens in deaerated basalt groundwater at 90 C with continuous H_2O_2 additions of 6.5 ppm/min	3-75
Figure 3.35. Potentiodynamic polarization curve for 1020 carbon steel under same conditions as for Figure 3.34	3-76
Figure 3.36. Free-corrosion potential as a function of exposure time for 1020 carbon steel specimens in deaerated basalt groundwater at 90 C with continuous H_2O_2 additions of 65 ppm/min	3-76
Figure 3.37. Potentiodynamic polarization curves for 1020 carbon steel under same conditions as for Figure 3.36	3-77
Figure 3.38. Free-corrosion potential as a function of exposure time for 1020 carbon steel specimen in deaerated basalt groundwater at 90 C with continuous $HClO_4$ additions of 2.0 ppm/min	3-78
Figure 3.39. Potentiodynamic polarization curves for 1020 carbon steel under same conditions as for Figure 3.38	3-78
Figure 3.40. Pit geometries used in long-term exposure tests	3-82
Figure 3.41. Schematic of pit-propagation monitor	3-84

LIST OF FIGURES
(Continued)

	<u>Page</u>
Figure 3.42. Electrochemical potential as a function of exposure time for mechanically prepitted 1018 carbon steel specimens in basalt groundwater containing crushed basalt at 90 C	3-86
Figure 3.43. Low-power photograph of prepitted hot-rolled 1018 carbon steel specimens following exposure in oxygenated and deaerated simulated basalt groundwater containing crushed basalt at 90 C	3-88
Figure 3.44. Optical photomicrograph of 1:2 aspect ratio 0.53-mm-diameter pit	3-89
Figure 3.45. Optical photomicrograph of 1:5 aspect ratio 0.53-mm-diameter pit	3-89
Figure 3.46. Optical photomicrographs of prepitted specimen (0.53-mm diameter pits) of hot-rolled 1018 carbon steel following exposure in oxygenated simulated basalt groundwater containing crushed basalt for 238 days (5712 hours)	3-91
Figure 3.47. Results of 1000-hour weight-loss tests performed on simulated pits in deaerated basalt groundwater at 90 C	3-92
Figure 3.48. Results of 1000-hour weight-loss tests performed on simulated pits in aerated basalt groundwater at 90 C	3-93
Figure 3.49. Results of 1000-hour weight-loss tests performed on simulated pits in an aerated pitting solution (Number 47 from potentiodynamic polarization studies) at 90 C	3-94
Figure 3.50. Effect of aspect ratio (diameter to depth) and pit-wall reactivity in the corrosion rate of pit and BES specimens in 1000-hour weight-loss tests	3-96
Figure 3.51. Current density as a function of exposure time for pit propagation experiments performed at diameter-to-depth ratios of 1:1, 1:5, and 1:10 in oxygenated basalt groundwater at 75 C	3-99

LIST OF FIGURES
(Continued)

	<u>Page</u>
Figure 3.52. Coupled current density as a function of exposure time and pit-wall reactivity for pit-propagation Experiment 17 performed at a diameter-to-depth ratio of 1:5 in aerated basalt groundwater at 25 C	3-105
Figure 3.53. Coupled potential as a function of exposure time for pit-propagation Experiment 17 performed at a diameter-to-depth ratio of 1:5 in aerated basalt groundwater at 25 C	3-106
Figure 3.54. Uncoupled potential as a function of exposure time for pit-propagation Experiment 17 performed at a diameter-to-depth ratio of 1:5 in aerated basalt groundwater at 25 C	3-107
Figure 3.55. Potential for pit specimen as a function of microcapillary probe position down the pit when the pit specimen and BES were uncoupled; Experiment 17 in aerated basalt groundwater at 25 C	3-108
Figure 3.56. Potential for pit specimen as a function of microcapillary probe position down the pit where the pit specimen and BES specimen were coupled; Experiment 17 in aerated basalt groundwater at 25 C	3-109
Figure 3.57. Coupled current density as a function of exposure time and pit-wall reactivity for Experiment 26 performed at a diameter-to-depth ratio of 1:5 in aerated solution No. 30 at 25 C	3-114
Figure 3.58. Potential for pit specimens as a function of microcapillary probe position down pit when the pit and BES specimens were coupled; carbon steel in aerated solution No. 30 (Experiment 26) at 25 C	3-115
Figure 3.59. Coupled current density as a function of exposure time and pit wall reactivity for Experiment 31 performed at a diameter-to-depth ratio of 1:5 in aerated solution No. 47 (Experiment 31) at 25 C	3-116

LIST OF FIGURES
(Continued)

	<u>Page</u>
Figure 3.60. Potential for pit specimens as a function of microcapillary probe position down pit when the pit and BES specimens were coupled (open symbols); carbon steel in aerated solution No. 47 at 25 C (Experiment 31)	3-117
Figure 3.61. Coupled potential as a function of exposure time for experiment performed at a diameter-to-depth ratio of 1:5 in aerated Solution No. 47 (Experiment 31) at 25 C	3-119
Figure 3.62. Schematic showing the postulated current behavior for nonreactive- and reactive-wall pits	3-122
Figure 3.63. SEM photograph of pit found in the crevice region of a cast clean 1018 steel specimen exposed for 1000 hours in 250 C deaerated simulated basalt groundwater containing crushed basalt	3-128
Figure 3.64. 1/PR as a function of exposure time for cast clean 1018 steel and platinum exposed in deaerated simulated basalt groundwater at 250 C containing crushed basalt	3-131
Figure 3.65. Graphical representation of electrode kinetics for a corroding metal where the oxidation and reduction reactions are under activation control	3-132
Figure 3.66. Potential as a function of exposure time for cast clean 1018 steel and platinum exposed at 250 C in deaerated simulated basalt groundwater containing crushed basalt	3-134
Figure 3.67. Measured stress corrosion crack velocities and current densities passed at a relatively bare surface for ferritic steel in a variety of solutions	3-136
Figure 3.68. Potential-pH diagram for iron with cracking domains for some of the potent cracking agents	3-139
Figure 3.69. Cracking velocity as a function of maximum current ratio (between fast and slow scan polarization curves) for SSR experiments performed in solutions from the statistical design matrix	3-147

LIST OF FIGURES
(Continued)

	<u>Page</u>
Figure 3.70. Cracking velocity as a function of maximum current from fast scan polarization curves for SSR experiments performed in solutions from the statistical design matrix	3-148
Figure 3.71. Cracking velocity as a function of maximum current difference (between fast and slow scan polarization curves) for SSR experiments performed in solutions from the statistical design matrix	3-149
Figure 3.72. Optical photograph of metallographic section of hot-rolled 1020 carbon steel specimen tested in 0.001 M FeCl ₃ at 315 C and a strain rate of 1 x 10 ⁻⁸ /s	3-151
Figure 3.73. Optical photograph of metallographic section of hot-rolled 1020 carbon steel specimen tested in 0.0005 M FeCl ₃ at 315 C and a strain rate of 1 x 10 ⁻⁷ /sec	3-153
Figure 3.74. Crack velocity as a function of temperature for hot-rolled 1020 carbon steel tested in 5 x 10 ⁻⁴ M FeCl ₃ at a strain rate of 1 x 10 ⁻⁷ /sec	3-155
Figure 3.75. Optical photographs of hot-rolled 1020 carbon steel specimen following slow strain rate testing at 125 C in aqueous 5 x 10 ⁻⁴ M FeCl ₃ at a strain rate of 1 x 10 ⁻⁷ sec ⁻¹	3-156
Figure 3.76. Optical photographs of hot-rolled 1020 carbon steel specimen following slow strain testing in aqueous 5 x 10 ⁻⁴ M FeCl ₃ at a rate of 1 x 10 ⁻⁷ sec ⁻¹ with an initial pH of 4.6	3-157
Figure 3.77. Crack velocity as a function of concentration for aqueous solutions of NH ₄ NO ₃ and NaNO ₃	3-160
Figure 3.78. Optical photographs of metallographic section of SSR specimen following testing in 0.1 M NaNO ₃ at 80 C	3-161
Figure 4.1. Penetration of Type 304 stainless steel as a function of exposure time at 1050 C	4-3
Figure 4.2. Corrosion rate of Type 304 stainless steel in 72-68 waste glass as a function of temperature	4-4

LIST OF FIGURES
(Continued)

	<u>Page</u>
Figure 4.3. Effect of exposure time on pit development at 900 C	4-12
Figure 4.4. Effect of exposure time on pit development at 700 C	4-13
Figure 4.5. Effect of exposure time on pit development at 500 C	4-14
Figure 4.6. Effect of exposure time on pit development at 300 C	4-15
Figure 4.7. Pitting penetration rates as a function of time	4-16
Figure 4.8. Pitting penetration rates for longest exposure times as a function of temperature	4-17
Figure 4.9. Energy dispersive X-ray analysis of 900 C specimen	4-19
Figure 4.10. Energy dispersive X-ray analysis of 900 C specimen	4-20
Figure 4.11. Photomicrographs of Type 304L and CF8 stainless steels	4-23
Figure 5.1. Illustration of pit configuration used with binary-electrolyte model	5-6
Figure 5.2. Variation of potential with distance for inert-wall pit-growth model for selected values of c_h^+/c_o^+ , where $c_h^+ \equiv c_+(h)$ and $c_o^+ \equiv c_+(0)$	5-10
Figure 5.3. Schematic illustration of pit configuration used with binary-electrolyte model, showing the current densities associated with cation transport	5-12
Figure 5.4. Variation of cation concentration with distance along pit length for example of active-wall and inert-wall pits discussed in text	5-19
Figure 5.5. Variation of electrostatic potential with distance along pit length for example of active-wall and inert-wall pits discussed in text	5-20

LIST OF FIGURES
(Continued)

	<u>Page</u>
Figure 5.6. Variation of current density at and normal to pit wall with distance along pit length for example of active-wall pit discussed in text	5-21
Figure 5.7. Selected concentration profiles calculated using one-species model with maximum-rate kinetics and $g = 0$	5-30
Figure 5.8. Selected concentration profiles calculated using one-species model with maximum-rate kinetics and $g = 1$, $\epsilon = 1$	5-30
Figure 5.9. Selected concentration profiles calculated using one-species model with maximum-rate kinetics and $g = 10$, $\epsilon = 1$	5-31
Figure 5.10. Selected concentration profiles calculated using one-species model with maximum-rate kinetics and $g = 10$, $\epsilon = 1$	5-31
Figure 5.11. Corrosion rate calculated as a function of time for one-species model with maximum-rate kinetics	5-33
Figure 5.12. Corrosion depth calculated as a function of time for one species model with maximum-rate kinetics	5-33
Figure 5.13. Selected concentration profiles calculated for oxidizing species using a two-species model with maximum-rate kinetics, and $g = 10$, $\epsilon = 2$	5-35
Figure 5.14. Selected profiles calculated for reducing species using the same model as in Figure 5.13	5-35
Figure 5.15. Comparison of concentration profiles calculated for oxidizing species using one-species and two-species models	5-36
Figure 5.16. Corrosion rate calculated as a function of time for two-species model, with maximum-rate kinetics and $g = 10$, $\epsilon = 2$	5-37
Figure 5.17. Corrosion depth calculated as a function of time for two-species model with maximum-rate kinetics and $g = 10$, $\epsilon = 2$	5-37

LIST OF FIGURES
(Continued)

	<u>Page</u>
Figure 5.18. Selected concentration profiles calculates using one-species model with film-growth kinetics and $g = 0$	5-38
Figure 5.19. Selected concentration profiles calculated using one-species model with film-growth kine- tics and $g = 10$, $\epsilon = 2$	5-40
Figure 5.20. Corrosion rate calculated as a function of time for one-species model with film-growth kinetics	5-40
Figure 5.21. Corrosion depth calculated as a function of time for one-species model with film-growth kinetics	5-41

CONTRIBUTORS

J. A. Beavers	H. J. Cialone
N. G. Thompson	B. S. Majumdar
A. J. Markworth	J. K. McCoy

EDITOR

T. Righter

EXECUTIVE SUMMARY

The Department of Energy (DOE) is conducting a large program for the disposal of high-level radioactive wastes in deep-mined geologic repositories. The Nuclear Regulatory Commission (NRC) will review and determine the adequacy of DOE's application for the construction and operation of the repositories. To assist in evaluating DOE's application, the NRC's Office of Nuclear Regulatory Research is developing an understanding of the long-term performance of geologic repositories. As part of this effort, Battelle has investigated, over a 5-year period, the long-term performance of materials used for high-level waste packages. The program, which is now concluded, was conducted in three parallel efforts: waste-form studies, container-material studies, and system performance studies. This report gives the final results of experimental and modeling studies that comprise the container materials task.

Hydrogen embrittlement studies were conducted to identify material and environmental factors leading to hydrogen degradation of container materials. The extent of hydrogen degradation of the properties of any metal exposed to hydrogen depends on numerous factors. Conditions in which degradation appear to be most severe include long-term exposure to high-pressure, elevated-temperature hydrogen. Hydrogen embrittlement is also promoted in regions which have undergone some form of microstructural transformation, such as in the weld heat-affected zone. Findings from these studies demonstrate that hydrogen degradation is an important consideration in evaluating container integrity.

A broad scope of experimental work was performed to identify potential corrosion failure modes for overpack materials. The experiments also evaluated the influence of environmental and metallurgical variables on rates of corrosion attack for those modes. Some emphasis was placed on Titanium Grade 12 in a salt environment and on Type 304L stainless steel in a simulated tuff environment. Most of the work, however, focused on low-carbon steel in a simulated basalt environment. A variety of tests, including electrochemical techniques, long-term exposures, and mechanical tests, was used to identify potential failure modes. Results of these studies identified potential cracking agents and demonstrated the need to further define exposure environments.

Studies were conducted on the possible internal corrosion of the canister by the glass waste form. The canister is the innermost metallic enclosure and is in direct contact with the waste. Canister corrosion could occur during the relatively short period of time when the glass is molten and during the long period of time when it is still hot in storage. To determine the long-term corrosive effects on the canister materials, coupons of Type 304L stainless steel and its casting equivalent, CF8 alloy, were exposed to PNL 76-68 waste glass at elevated temperatures. The pits produced by corrosion were measured, and the mechanism of corrosive attack was studied. It was found that, although the number of small pits increases with time and temperature, pit depths increase very slowly with time.

Modeling studies were conducted as a parallel effort to the experimental studies. The objective of the modeling work was to develop comprehensive, physically realistic models for general and localized (pitting) corrosion of the metallic container by the groundwater. The general corrosion model describes a metal surface in contact with an aqueous environment subjected to gamma irradiation. The model is applied to simplified examples to demonstrate effects of radiolytic production and film-growth kinetics on the overall corrosion rate. Pitting modeling centered on pit-initiation kinetics, pit-growth kinetics, and the evolution of the pit-depth distribution. Based on these aspects of the model, the pit-depth distribution could be generalized.

1. INTRODUCTION

The Waste Policy Act of 1982 delegates to the Department of Energy (DOE) the authority for siting, construction, and operation of deep-mined geologic repositories for the disposal of high-level waste and spent fuel. The Nuclear Regulatory Commission (NRC) has the responsibility to regulate the activities of DOE to assure that the health and safety of the repository workers and of the public are adequately protected. Prior to construction, the DOE will submit a license application to the NRC describing in detail the proposed repository. The DOE has been directed to take a multiple-barrier approach to the isolation of radioactive wastes, with the waste package, the underground facility, and the natural geohydrologic features of the site being the major barriers. Since NRC's compliance assessment requires the technical capability to understand relevant phenomena and processes relating to the long-term performance of the multiple barriers, the NRC's Office of Nuclear Regulatory Research established this program at Battelle to provide input to the assessment of the waste package.

The waste package is the center of study of this research program. The program's objective was to provide an improved understanding of the long-term performance of the materials used for the high-level waste package. More specifically, processes were identified that tend to degrade the performance of the waste-package materials, and experiments were performed to produce data that were otherwise lacking on material performance. Processes also were analytically modeled, utilizing experimental data, to better understand long-term effects. The principal task areas for this program were waste form studies, system performance studies, and container materials studies.

1.1 Task Objectives

The container-materials studies, the subject of this final topical report, focused on those processes that can cause degradation of the waste package container. The container consists of one or more concentric metallic enclosures that act as a barrier against the ingress of groundwater (or brine) to the waste form and the egress of radionuclides from the waste form to the repository. An innermost metallic enclosure, called the canister, may be used to contain the waste form. The most probable canister material is Type 304L stainless steel. A small portion of the container-materials effort was devoted to studying the possible internal corrosion of the canister due to contact with molten or hot glass for different periods of time.

An outer enclosure is called the overpack. At the onset of the project, the reference overpack consisted of a thick-walled steel container covered with a thin-walled shell of a titanium alloy. Subsequently, the use of a titanium alloy shell has been less favored by DOE. Hence, the major recent emphasis has been on cast and wrought low-carbon steels.

The use of low-carbon steel in a wet environment for a long-life container requires that the steel be thick enough to sustain the loss of metal by corrosion without penetration over the period of interest. For general corrosion and localized corrosion processes such as pitting or crevice corrosion, rates of attack may be sufficiently low such that the overpack wall thickness can be adjusted to compensate for the corrosion loss. On the other

hand, cracking rates from such processes as stress-corrosion cracking or hydrogen embrittlement may be so high as to preclude the use of cracking-prone materials for the overpack.

The initial approach for the carbon steel studies was to investigate corrosion behavior in simulated repository environments using potentiodynamic polarization techniques. The effort was directed at roughly identifying ranges of expected behavior and evaluating the influence of metallurgical and environmental variables on corrosion. Subsequent experiments focused on studying two forms of localized corrosion--pitting and stress-corrosion cracking--in greater detail. Propagation models were evaluated in the pitting studies, while critical cracking species were identified and evaluated in the stress-corrosion studies.

Hydrogen-embrittlement experiments were started because of the high probability that hydrogen will be generated in a repository environment by radiolytic and corrosion reactions. This form of material degradation is also important since hydrogen-assisted cracking would be catastrophic. Cast-steel overpacks are likely to contain numerous crack-like casting defects as well as welding defects produced in the closure of the overpack. Thus, a fracture-mechanics study was conducted to evaluate the effects of hydrogen, under anticipated salt-repository conditions, on the integrity of the overpack. Comparative testing of specimens in high-pressure hydrogen and an inert environment at elevated temperatures was performed to provide information on the effects of hydrogen on crack growth under conditions in which hydrogen attack would be predicted.

Container corrosion processes were also studied by modeling, with the focus on general corrosion and pitting corrosion. These efforts were undertaken to construct more comprehensive and physically realistic corrosion models. Comparison of results between those conducting the modeling studies and the experimental studies was promoted to provide mutual direction to both studies and to identify specific data requirements.

1.2 Report Organization

This topical report complements the final reports for other program tasks (Long-Term Performance of Spent-Fuel Waste Forms, NUREG/CR-4954; Long-Term Performance of High-Level Glass Waste Forms, NUREG/CR-4795; and System Performance of High-Level Waste Package Components, NUREG/CR-4956).

Chapter 2 describes studies to assess the magnitude and nature of hydrogen-embrittlement effects on steel. Chapter 3 describes studies identifying potential corrosion failure modes for candidate overpack materials. Chapter 4 presents results of a study conducted earlier in the program on canister pitting. Chapter 5 presents detailed descriptions of pitting and general corrosion modeling developed in this program. Finally, the results of these studies are set out in Chapter 6.

Appendices A through D provide additional data supporting the overpack corrosion studies; Appendix E provides user documentation for a corrosion computer code; and Appendix F provides a listing of quality assurance procedures for experiments performed in this task.

2. HYDROGEN EMBRITTLEMENT

Hydrogen embrittlement of waste containers is an important concern in assessing waste-container integrity for two reasons: (1) there is a high probability of hydrogen generation in a repository environment, and (2) any failure resulting from hydrogen embrittlement will likely be catastrophic, as compared with a more predictable failure mode such as general corrosion. The studies in this program were undertaken to assess the magnitude and nature of hydrogen-embrittlement effects that may be encountered by waste containers. This research has been conducted on several levels, including analysis of data in the technical literature, acquisition of data through personal contacts with experts in the field, and performance of selected laboratory experiments.

2.1 Background

In general, the direction of experimental research on hydrogen embrittlement has been dictated by the approaches employed in, and the findings from, the research programs being conducted independently by the various Department of Energy (DOE) contractors working to develop a waste-containment design. Changes in direction of the research were made with the guidance and concurrence of the cognizant NRC personnel. Attempts to anticipate the direction of the DOE research met with limited success. For some candidate container materials, such as Titanium Grade 12, the laboratory work being performed by DOE was extensive enough so that the Battelle team could monitor its progress without performing additional experiments. When DOE began to consider low-carbon cast steel, Battelle began studies of hydrogen embrittlement in that material because of the lack of such research and the need for more information than was available in the literature. The anticipated use of direct-reduced (commercial-purity) iron, for improved resistance to corrosion and environmentally enhanced cracking, led to limited studies with that material; however, these investigations were discontinued when it became clear that iron was no longer under consideration by DOE.

2.1.1 Sources of Hydrogen

Two principal sources of hydrogen in a repository are anticipated. Both radiolytic reactions and corrosion reactions can produce high fugacities of hydrogen. Corrosion reactions between the groundwater and the container metal are expected to provide a hydrogen-charging effect, in which the metal absorbs relatively high concentrations of atomic hydrogen. Radiolytic reactions also could provide some measure of hydrogen charging into the metal and thereby produce gaseous hydrogen within the repository. For salt repositories, which will be sealed, hydrogen pressures¹ up to 6.9 MPa (1000 psi) have been predicted.

¹Note that these pressures are limited to the surface region and are related to the chemical potential which drives hydrogen into the material. The pressures are not bulk pressures.

Hydrogen also may be present in waste containers in the as-fabricated condition. Historically, problems have been encountered with heavy steel castings that have absorbed hydrogen during casting, resulting in numerous casting defects or reductions in mechanical properties (Refs. 2.1, 2.2). However, for this program it is assumed that appropriate casting/processing and inspection procedures will be employed to avoid the presence of hydrogen in castings. Similarly, hydrogen may be picked up by the container during welding; again, it is assumed that suitable procedures will be followed to avoid such problems.

2.1.2 Candidate Container Materials

Several design/material concepts have been considered by DOE during the course of this program. During the first two years of the project, a multi-wall container design, comprising a 304L stainless steel canister, a low-carbon cast-steel structural overpack, and a Titanium Grade 12 corrosion-resistant overpack, was being evaluated.

In about the second year of the program, the titanium alloy was eliminated from the design concept by DOE. It was envisioned at that time that the container would consist of only the stainless steel canister and the cast-steel structural overpack, which may or may not be thick enough to provide self-shielding. The composition under consideration was a low-carbon steel with low concentrations of residual impurities for weldability in the field. This candidate specification was based on ASTM Standard A216, Grade WCA, with the composition shown in Table 2.1.

Table 2.1. Specified composition for ASTM A216, Grade WCA, cast carbon steel.

Maximum Content, weight percent									
C	Mn	P	S	Si	Cu*	Ni*	Cr*	Mo*	V*
0.25	0.70	0.04	0.045	0.60	0.50	0.50	0.40	0.25	0.03

*Total content of these residual elements not to exceed 1.00 percent.

Because of the large mass of steel involved in a waste package, the overpacks would likely be cast in a sand mold. Some consideration was given to whether the cast steel structural overpack could be produced by centrifugal casting (also in a sand mold). Centrifugal casting provides better feeding of the molten metal and therefore reduces shrinkage defects. However, limitations on wall thickness for a given casting diameter may rule out the use of centrifugal casting for some self-shielded container designs.

During the third year of the program, there were indications that DOE might consider using pure iron as an overpack material. The advantage of this material is improved corrosion resistance; however, costs could become quite high, depending on the purity required. Direct reduced iron, which is used as feedstock in the production of stainless steel, is relatively pure and is produced commercially in large quantities; thus, it could be a candidate material. However, DOE interest in pure iron did not develop as expected.

2.1.3 Effects Considered

The hydrogen-embrittlement effects which were considered were selected on the basis of the behavior of the candidate materials and other similar materials under predicted repository conditions, as reported in the technical literature. The extent of hydrogen degradation of the properties of any metal exposed to hydrogen depends on numerous material and environmental factors. Material factors that influence hydrogen embrittlement include alloy composition, microstructure, impurity segregation, yield strength, and whether the material is a hydride former. Other factors, such as hydrogen fugacity, temperature and temperature transients, the presence of stress concentrators or cracks, and the plastic deformation rate also play a major role in hydrogen embrittlement.

Depending on which material and environmental factors exist in a repository, different hydrogen-embrittlement effects may be operative. In discussing the effects which were considered in this program, it is useful to review the various hydrogen effects which have been observed in metals. The following paragraphs provide a brief summary of the effects and address the various factors which influence the magnitudes of the effects. Following this summary, the specific phenomena that were studied are discussed in detail.

The effects of hydrogen on metals can be divided into seven categories as follows:

- (1) Opening of the lattice
- (2) Shatter cracks, flakes, and fisheyes
- (3) Hydrogen attack
- (4) Blistering
- (5) Loss of ductility
- (6) Delayed brittle failure (hydrogen-stress cracking)
- (7) Hydrogen-environment embrittlement.

These categories were developed for convenience in describing and understanding the causes of the various hydrogen-embrittlement phenomena observed in the laboratory and in practice. In many cases, the categories partially overlap. In addition, more than one embrittlement mechanism may be operative, giving rise to interactions among the effects. The first six categories deal with hydrogen contained internally in the metal, having been absorbed from various sources such as moisture during processing or corrosion reactions in service. The seventh category is concerned with various forms of embrittlement caused by hydrogen on the surface of the metal, often referred to as external hydrogen. Embrittlement caused by external hydrogen

is similar in nature to internal-hydrogen embrittlement, although the magnitude of the effect differs, as is discussed below. Both internal and external hydrogen sources are anticipated in a repository.

Two categories of hydrogen effects do not apply to a waste repository. The condition known as "opening of the lattice" is a reaction that occurs in some alloys when they are subjected to extremely high hydrogen pressures at near-ambient temperature. This condition results in the metal becoming laced with small fissures. The lowest known hydrogen pressure at which this phenomenon has occurred in steel is approximately 207 MPa (30,000 psi). Such pressures are much higher than any which are likely to be encountered in a repository. The second category, including shatter cracks, flakes, and fisheyes, describes defects due to hydrogen absorbed in steels during production. These defects have been observed primarily in heavy forgings; they develop by segregation of atomic hydrogen to voids or discontinuities, such as microshrinkage cavities or gas holes, and subsequent precipitation of hydrogen at those sites as a high-pressure gas. Appropriate control of steelmaking practice and inspection of the containers are measures to reduce the incidence of such defects.

Hydrogen attack may be an important effect in waste repositories. When steels are exposed to high-pressure, high-temperature hydrogen for long times the hydrogen reacts with the carbon contained in the carbides in the steel. For plain-carbon steels, the minimum temperature for hydrogen attack is about 200 C (400 F). Repository temperatures are estimated to be 250 C (482 F) at the start of storage, gradually decreasing to 150 C (302 F) (Ref. 2.3). The reaction between carbon and hydrogen results in decarburization of the steel and formation of cavities at grain boundaries and ferrite-pearlite interfaces. This may be followed eventually by internal fissuring and blistering, as high internal pressures of methane build up inside cavities with the continuing reaction. This kind of damage leads to losses in strength, ductility, and toughness. The severity of hydrogen attack depends on the temperature and hydrogen pressure, as well as on the composition and processing of the steel. This dependence is described by the Nelson curves, which indicate hydrogen temperature-pressure conditions that have led to past failures in service, contrasted with conditions where no failures have been reported. The Nelson curves are presented, and periodically updated, in Publication 941 of the American Petroleum Institute (API). The curves are based on service experience in petrochemical plants; revisions may be published when new failures are reported, or by consensus of the members of the API Refining Department. Because the Nelson curves are based on service experience, which spans a period of approximately 40 years, they may be nonconservative for predicting hydrogen attack in a waste repository over a period of 1000 years. Also, long-term exposure to hydrogen at the elevated temperature may reduce the subsequent resistance to fracture at lower temperatures as the container cools.

Hydrogen blistering also may be encountered in a repository. It occurs when atomic hydrogen enters the metal, usually from a corrosive environment, and deposits as molecular hydrogen at an internal defect such as a lamination or nonmetallic inclusion. Such cases require that corrosion of the metal liberate high-fugacity atomic hydrogen, which is subsequently absorbed by the

metal. This hydrogen effect can be similar in nature to shatter cracks, flakes, and fisheyes, but it develops as a result of hydrogen generated from the service environment.

Loss of ductility (tensile elongation and reduction in area) is exhibited by a wide range of metals when they contain a sufficient concentration of hydrogen. In some metals, hydrogen reduces the ductility by enhancing the normal fracture mode which would proceed in the absence of hydrogen. Typically, those metals do not undergo significant changes in ultimate tensile strength, as the effects of hydrogen are most prevalent in the latter stages of fracture, and therefore such metals are not severely degraded by hydrogen. Metals which are more sensitive to hydrogen embrittlement, such as high-strength steels, often undergo a change in fracture mode from a normally ductile mode (such as microvoid coalescence) to a brittle mode (such as cleavage), and also experience significant reductions in ultimate tensile strength. A general rule is that the degree of loss in ductility increases with increasing strength level of the metal, provided that all other factors are held constant.

Hydrogen-induced, delayed brittle failure is an embrittlement mechanism in which a brittle-type failure occurs in a nominally ductile material at applied stresses below the yield strength. This failure occurs while the metal is under sustained load. In steels, delayed brittle failure, or hydrogen-stress cracking, is promoted by high yield strengths and severe hydrogen environments; steels with yield strengths below 480 MPa (70,000 psi) appear to be immune to hydrogen-stress cracking, even under the most severe conditions. Thus, for the types of steels under consideration for waste packaging, hydrogen-stress cracking probably will not be encountered. However, titanium alloys, which are hydride formers, also can undergo delayed brittle failure. In titanium alloys, appreciable hydrogen may be contained in the metal from processing, although usually it is absorbed from the environment. Failure occurs when diffusion of the hydrogen to regions of high local stress causes the formation of brittle metal hydrides that are oriented normal to the applied tensile stresses. Considerable difficulty with hydrogen embrittlement of Titanium Grade 12 by this mechanism has been encountered in DOE and NRC studies (Refs. 2.4, 2.5).

Hydrogen-environment embrittlement occurs when metals are stressed in a hydrogen environment, usually gaseous. Of the waste-package materials under consideration, the ferrous materials are most likely to experience this degradation mode. The severity of embrittlement depends on the hydrogen pressure and temperature. Embrittlement generally increases with the square root of the hydrogen partial pressure. The temperature dependence of embrittlement displays a maximum at an intermediate temperature, with the maximum embrittlement occurring at temperatures from about -40 to +40 C (-41 to +104 F) for most engineering alloys. In addition, when localized plastic deformation occurs, such as at a notch or stress raiser, the severity of embrittlement is increased. Hydrogen environment embrittlement manifests itself in many ways, including losses in tensile ductility, notched-bar strength, and notched-bar elongation, reductions in fracture toughness (resistance to crack initiation and growth), and enhancement of fatigue-crack initiation and growth. Ductility losses with external hydrogen

proceed in a manner similar to ductility losses with internal hydrogen, although in many cases external hydrogen produces a more marked loss than internal hydrogen at equivalent fugacity. Reductions in fracture toughness can lead to subcritical-crack (that is, a crack which would not grow under the service stresses in an inert environment) growth under sustained load, a situation analogous to hydrogen-stress cracking under the influence of internal hydrogen. This situation may be the most important with regard to long-term integrity of waste packages.

The hydrogen-embrittlement effects that were considered in this program are losses in ductility (with external hydrogen, which is expected to be the more severe case), reductions in fracture toughness, subcritical-crack growth, hydrogen attack, and interactions between hydrogen attack and fracture-toughness reductions. Mechanical degradation effects, and the influence of hydrogen-induced fracture-toughness reductions on those effects, are examined in a subsequent section. Experiments were performed to determine the amount of hydrogen that would be absorbed by a cast-steel overpack in a basalt repository and to assess the extent of blistering that might occur. Effects such as opening of the lattice, shatter cracks, flakes, and fisheyes were not considered because they are not relevant to the application. In addition, delayed brittle failure, while relevant for titanium alloys, was not considered because Titanium Grade 12 was deemphasized early in the program. Also, hydrogen-enhanced fatigue was not considered because no source of cyclic loading or straining is expected in a repository.

2.2 Objectives and Approach

2.2.1 Objectives

The objectives of the hydrogen-embrittlement studies were to (1) improve the understanding of the potential degradation mechanisms associated with hydrogen that could induce premature failure of a waste container, and (2) indicate which areas require further evaluation by NRC or demonstration by DOE. Only those hydrogen effects which conceivably could be encountered in a repository were considered. Particular attention was given to the effects on embrittlement behavior of metallurgical variables, such as impurity content and heat treatment, which are more readily controlled than environmental variables. However, the hydrogen studies were not intended to provide information for predicting container life; instead, the results of these studies suggest potential failure mechanisms.

2.2.2 Approach

Figure 2.1 illustrates the complex thermal-mechanical-environmental conditions to which the container material will be subjected in service. The only factor over which there is some degree of control is the alloy composition and microstructure. The service conditions, outlined by circles, are the driving forces that will determine container integrity for a given material condition. The overall goal of material characterization is to assess whether the container will be able to withstand service exposures over a very long time period (for example, 1000 years) without failure.

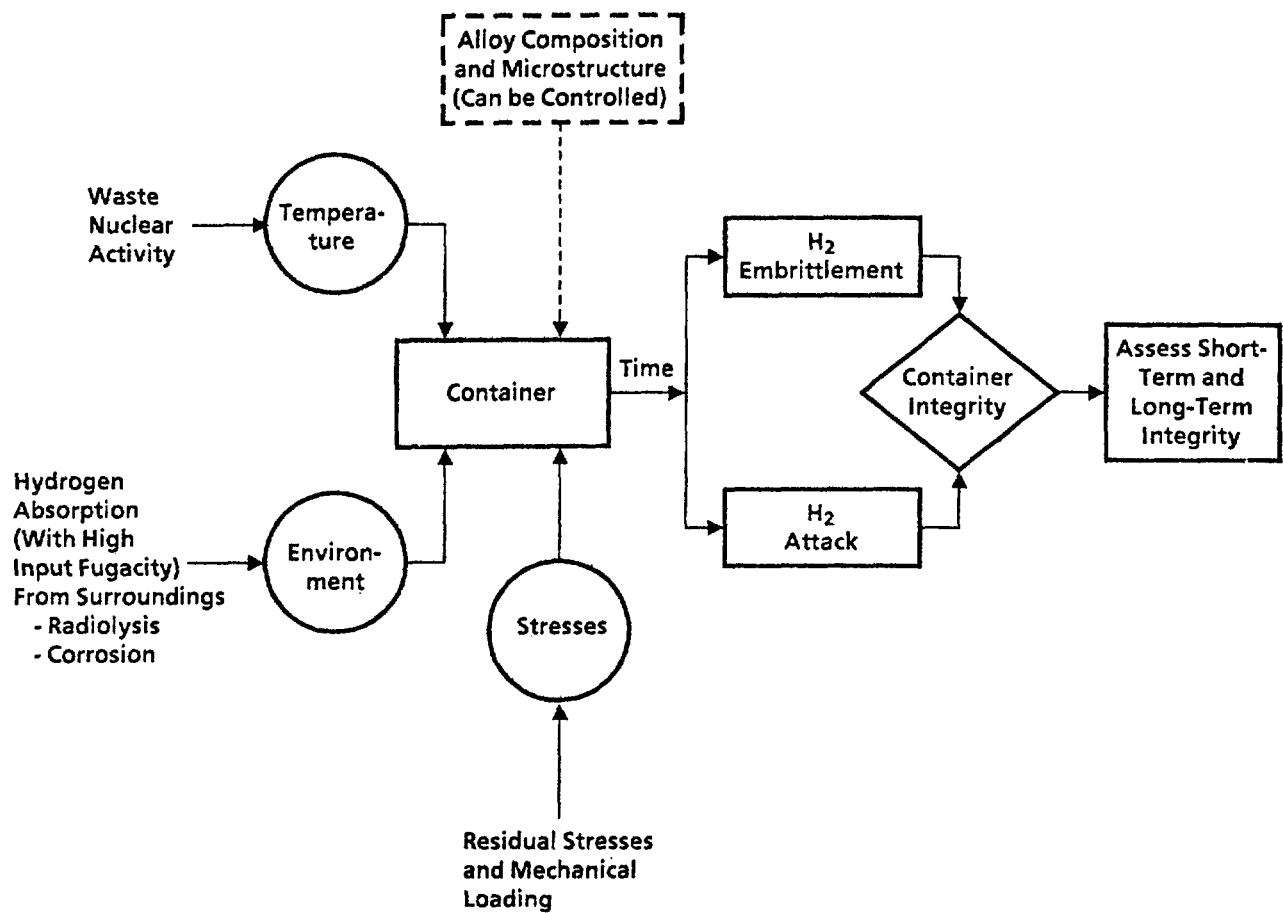


Figure 2.1. Complex mechanical-thermal-hydrogen environment anticipated in service for a container material.

major mechanisms of failure that are anticipated in service are embrittlement and hydrogen attack. Thus, it is necessary to assess the magnitude of these effects on short-term and long-term container integrity. The nomenclature "short-term" refers to the time period very early in the life of the repository when temperature is still in the neighborhood of 260 C (500 F). Hydrogen-environment embrittlement (discussed in Section 2.1.3) would be the primary failure mechanism under such conditions. "Long-term" refers to the extended exposure of the container material to a hydrogen environment and subsequent failure at temperatures ranging from 260 C (500 F) to room temperature. Both hydrogen embrittlement and hydrogen attack could play important roles in determining failure under long-term conditions.

Figure 2.1 shows that a multitude of factors, including those that are associated with material composition, make assessment of container integrity extremely complex. The problem is compounded by the lack of accurate estimates on hydrogen fugacity anticipated in service. In the present study, experiments were conducted with hydrogen pressures in the range 4.8 MPa to 6.9 MPa (700 psi to 1000 psi), a convenient level which appears to represent an upper bound.

The approach used in these studies was to subdivide the complex system into a number of smaller subsystems (Figure 2.2). The first phase of the work involved determining how short-term hydrogen embrittlement was affected by composition, processing, and microstructure of the material (Figure 2.2a). Steels were obtained from various sources, and some were specially cast to contain controlled residual impurity levels. Embrittlement effect was measured in terms of reduction in conventional mechanical properties, namely tensile strength, elongation to failure, and reduction in area. Experiments involved tensile tests of unexposed specimens in nitrogen and hydrogen environments at room temperature. The details are discussed in Sections 2.3.1, 2.3.2, and 2.4.1.

In the second phase of the work, hydrogen embrittlement of the same series of material was evaluated by fracture toughness tests (Figure 2.2b). Comparative J-integral tests were run in nitrogen and hydrogen to determine how hydrogen affected crack initiation toughness (J_{IC}) and tearing resistance to further crack growth (dJ/da) of the material. Special attention was focused on determining the microstructural influence, such as effects of residual impurities and heat-treatments, on hydrogen embrittlement at room temperature. It was found that the fracture toughness results were much more sensitive to hydrogen than tensile test results. Details of this second phase are discussed in Sections 2.3.1, 2.3.2, and 2.4.2.

In the third phase of the work, both short-term and long-term integrity of a container material was evaluated in high-pressure, elevated temperature hydrogen (Figure 2.2c). Hydrogen-induced damage was measured for a clean cast steel in terms of effects on fracture toughness properties. Thus, microstructure and residual impurity concentration was not a variable in this series of experiments. Fracture toughness specimens, which were either unexposed or were pre-exposed to hydrogen and helium at various temperatures for different time periods, were fracture tested at 260 C (500 F) and at

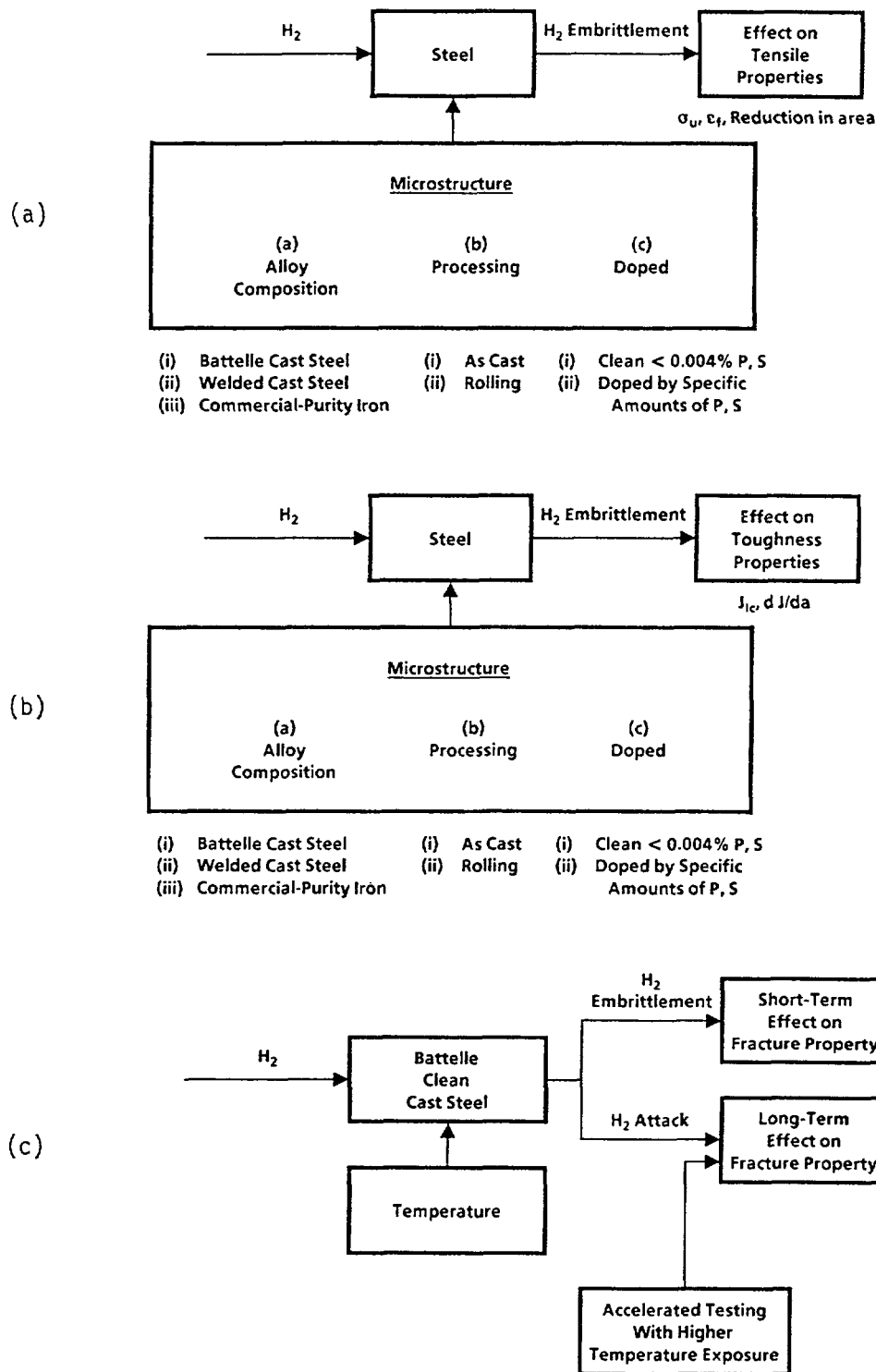


Figure 2.2. Breakdown of technical approach showing various factors studied to assess effects of hydrogen on container integrity.

room temperature. Accelerated tests were conducted by exposing specimens at temperatures above 260 C (500 F) for short times to simulate long-time service exposure at lower temperatures. Details of this phase of experiments are discussed in Sections 2.3.4, 2.4.4, and 2.5.2.

2.2.3 Materials Studied

Most of the research focused on low-carbon cast steels because the cast-steel overpack is expected to provide structural integrity to the container. Three steels with compositions satisfying the ASTM Standard A216, Grade WCA, were studied. In addition, one steel with a higher manganese content than that specified in the standard was included in the investigation. The steels were studied in the as-cast, annealed, hot-rolled, and as-welded conditions. Some experiments also were conducted with samples of direct-reduced iron in the as-cast condition.

No hydrogen-embrittlement experiments were conducted with Titanium Grade 12. While Titanium Grade 12 is resistant to general corrosion and provides improved resistance to crevice corrosion compared with other titanium alloys, DOE and NRC researchers found it to be extremely sensitive to hydrogen embrittlement (Refs. 2.4, 2.5). This sensitivity was one reason DOE eliminated that alloy from consideration. In addition, hydrogen-embrittlement experiments were not conducted with the stainless-steel canister alloy, in part because of the high resistance of most austenitic stainless steels to hydrogen embrittlement, and in part because DOE was taking no credit for the integrity of the canister for a basalt repository.

2.3 Experimental Procedures

2.3.1 Material/Specimen Preparation

Materials from three different sources were used for the investigation:

- Battelle steel castings
- welded steel castings
- iron castings.

The preparation and microstructure of these materials are discussed as follows in Sections 2.3.1.1 through 2.3.1.3, respectively.

2.3.1.1 Battelle Steel Castings

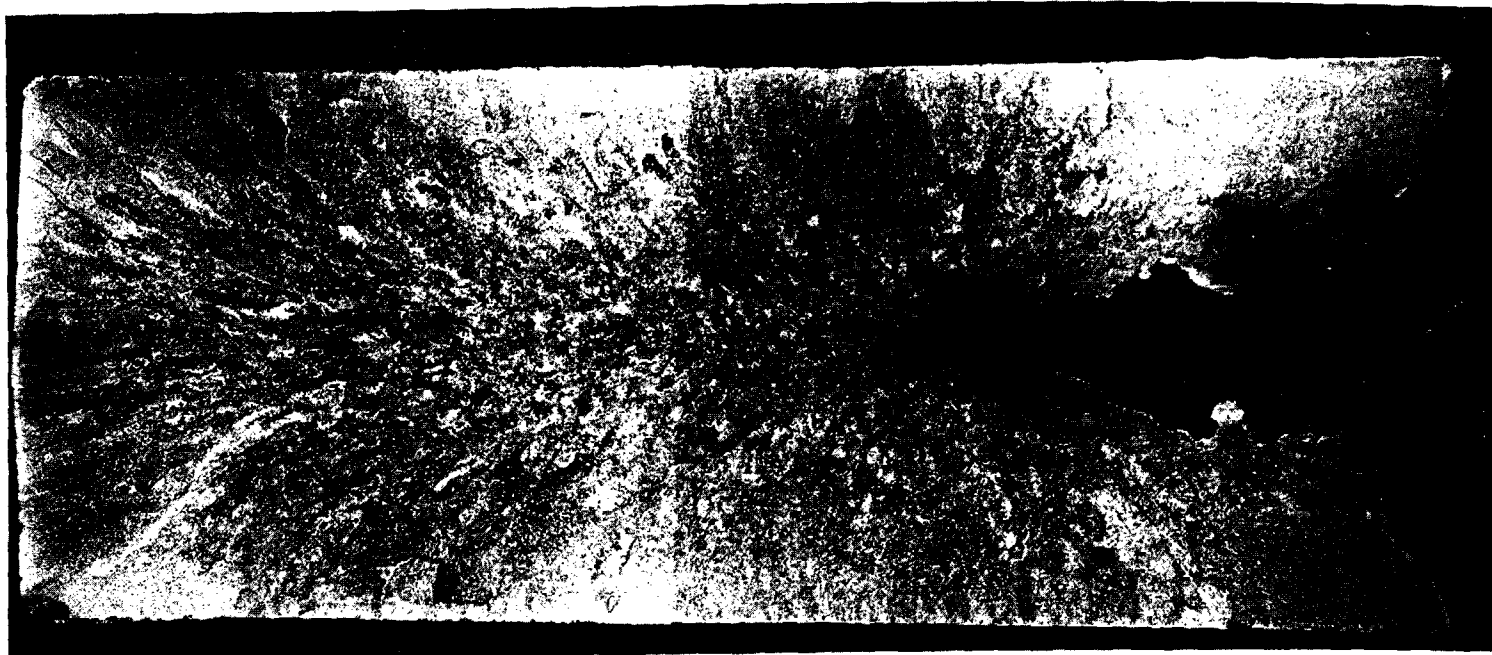
Two ingot-shaped steel castings were prepared for hydrogen embrittlement studies in this program. At the time the castings were prepared, a nominal composition was selected by Battelle that was representative of commercially available cast steel with reasonable weldability. Subsequently, DOE indicated that its cast steel composition for a salt repository would be similar to ASTM A216, Grade WCA (Ref. 2.6); the Battelle composition targets were within the composition specification for that steel. One of the castings was made with very low impurity content; the other, with the same nominal composition, was prepared with the intentional addition of metalloid impurities (sulfur and phosphorus) to a level that was typical of steel castings

that are readily available commercially. Thus, comparisons between the "clean" and "doped" castings would provide an indication of the effects of metalloid impurities on the hydrogen embrittlement sensitivity of the cast steel, and whether more restrictive composition specifications may be needed. Co-segregation of hydrogen and metalloid impurities has been shown to increase the extent of embrittlement.

The castings were prepared from a split heat; after the clean casting was poured, the remaining molten metal was doped with ferrophosphorus and ferro-sulfur before pouring the second casting. The castings were cast into sand molds, with nominal dimensions of 8 x 8 x 20 in, so as to approximate the slow cooling rates from casting that would be experienced in casting a large structural overpack. Figures 2.3 and 2.4 present full longitudinal sections prepared from each casting and show the solidification structures of the castings. Large columnar grains, emanating from the mold surface toward the interior of each of the castings, can be seen in the figures. The figures illustrate that no macroporosity was present in the castings, an observation which was confirmed by radiography. Both castings underwent considerable "pipe" during solidification. All specimens for testing and analysis were prepared from portions of the castings located at least 1 inch below the deepest penetration of the pipe.

Spectrographic chemical analyses were performed on samples removed from several locations in each casting. The average compositions are presented in Table 2.2, which includes the specified composition limits and ranges for ASTM A216, Grade WCA, for comparison. The average compositions of both castings satisfy the requirements of ASTM A216, Grade WCA, steel castings. There was little variation in composition at different locations in each casting.

Comparison between the etched surfaces of the castings, shown in Figures 2.3 and 2.4, indicates that the addition of metalloid impurities may have influenced the solidification structure. The macrostructure of the doped steel appears much finer than that of the clean steel. The microstructures of the clean and doped steels, viewed from three orientations, are shown in Figure 2.5a and b. Both steels contained mixtures of ferrite (light constituent) and pearlite (dark constituent), although there was considerable difference in the morphology of those constituents. The figure shows that the clean steel had an acicular, "feathery" structure, whereas the doped steel had a more equiaxed-grain microstructure. In addition, virtually no inclusions were present in the clean steel. The doped steel contained numerous Type II (Ref. 2.7) manganese sulfide inclusions that were aligned along prior-austenite grain boundaries, forming a nearly continuous film on those boundaries. When manganese sulfide inclusions form with this morphology, they can influence the fracture behavior markedly, as was observed in this program. The difference in grain structure for the two castings would suggest a higher cooling rate after casting for the clean steel, but the heat records indicate that the cooling rates were similar for both castings. Therefore, the solidification structure apparently was influenced by the presence of impurities, probably by way of the nonmetallic inclusions acting as grain nucleation sites.



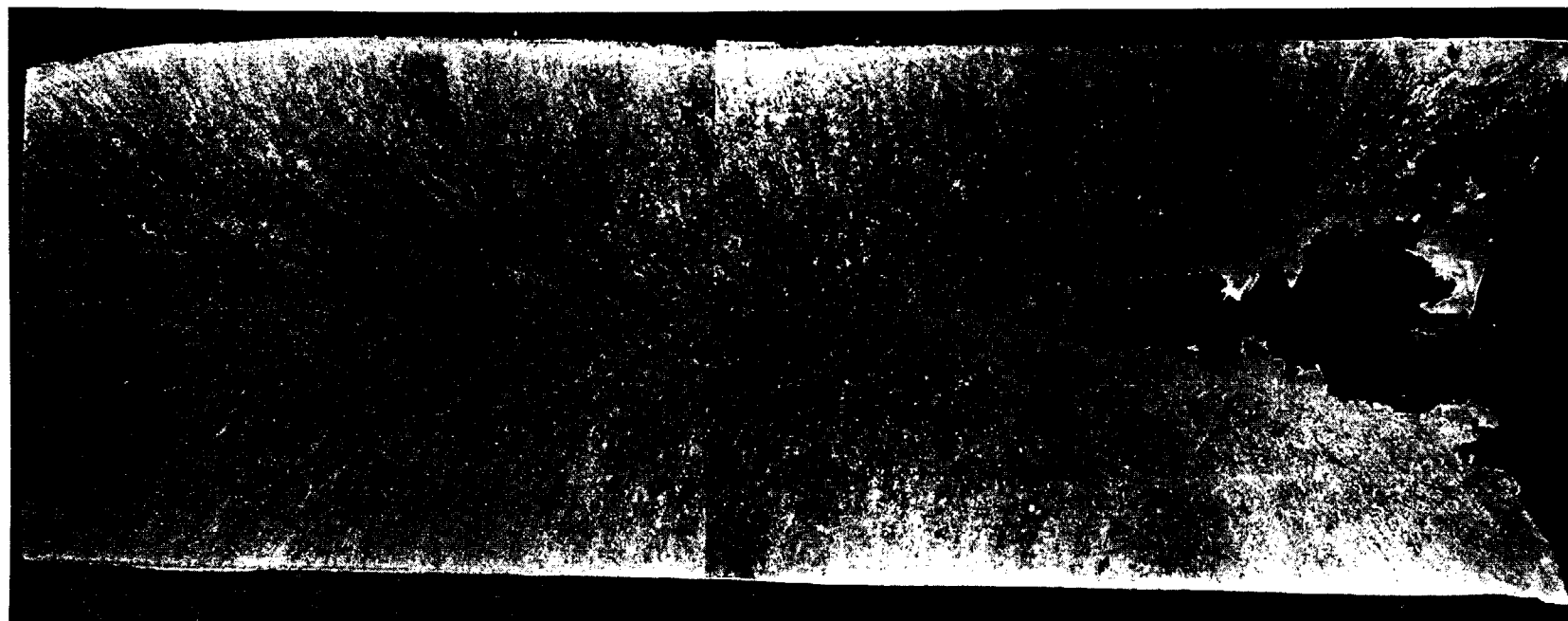
3/8X

10-Percent Nital Etch

OL531

Figure 2.3. Full longitudinal section through casting of clean steel.

2-13



3/8X

10-Percent Nital Etch

OL533

Figure 2.4. Full longitudinal section through casting of doped steel.

Table 2.2. Chemical compositions of steels cast by Battelle.

Steel	Content, weight percent										
	C	Mn	P	S	Si	Al	Cu	Ni	Cr	Mo	V
Clean	0.18	0.49	0.004	0.002	0.30	0.10	0.006	0.002	0.007	0.000	0.000
Doped	0.17	0.55	0.029	0.036	0.35	0.14	0.007	0.004	0.011	0.000	0.006
WCA(a)	0.25	0.70	0.04	0.045	0.60	--	0.50(b)	0.50(b)	0.40(b)	0.25(b)	0.03(b)

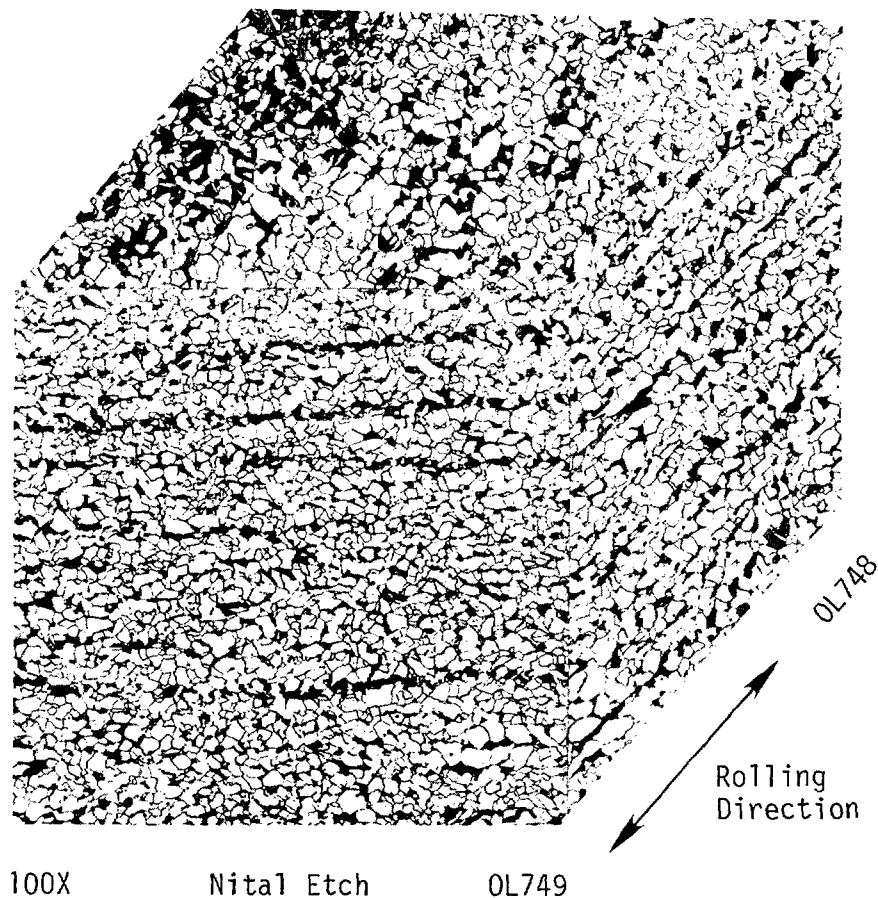
(a) Maximum specified content for ASTM A216, Grade WCA cast steel.

(b) The sum of the copper, nickel, chromium, molybdenum, and vanadium contents not to exceed 1.00 percent by weight, and the carbon equivalent shall not exceed 0.50 [carbon equivalent = $C + Mn/6 + (Cr + Mo + V)/5 + (Ni + Cu)/15$].



Figure 2.5a. Microstructure of clean steel.

OL750



100X

Nital Etch

OL749

Hot Rolled

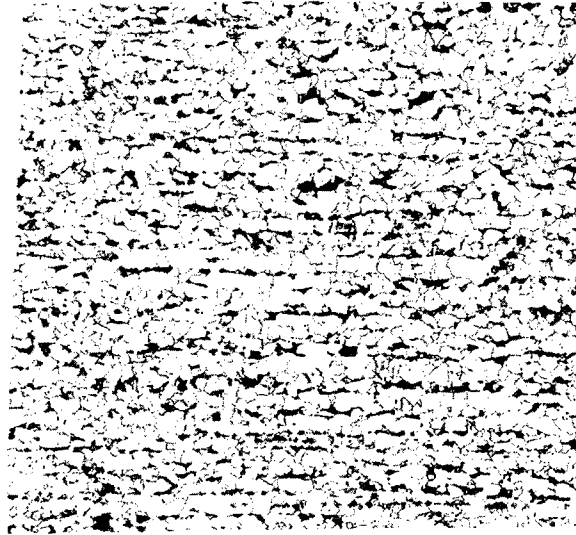
Figure 2.5b. Microstructure of doped steel.

After being sectioned longitudinally, one half of each casting was hot rolled, parallel to the rolling direction, to plate form, with a thickness reduction of 8:1. During rolling, the metal temperature was between about 900 and 1000 C (between 1652 and 1832 F). In addition, portions of the as-cast halves of the castings were annealed by heating in argon to 900 C (1652 F), holding at temperature for 2 hours, and furnace cooling to room temperature at a rate of approximately 50 C/hr (90 F/hr). The resulting microstructures are shown in Figures 2.6 and 2.7.

The microstructures of the clean and doped steels in the hot-rolled condition were very similar, as shown in Figures 2.6a and 2.7a. Both steels exhibited microstructures in which the ferrite and pearlite grains were banded in the direction of rolling. The only difference was that the doped

Hot
rolled

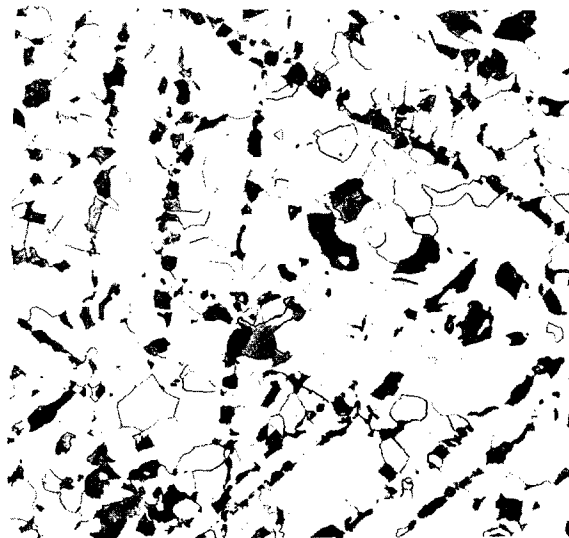
100 μ m



100X Picral + Nital Etch

0L753

Annealed



100X Picral + Nital Etch

3L128

Figure 2.6. Microstructure of clean steel after hot rolling and after annealing.

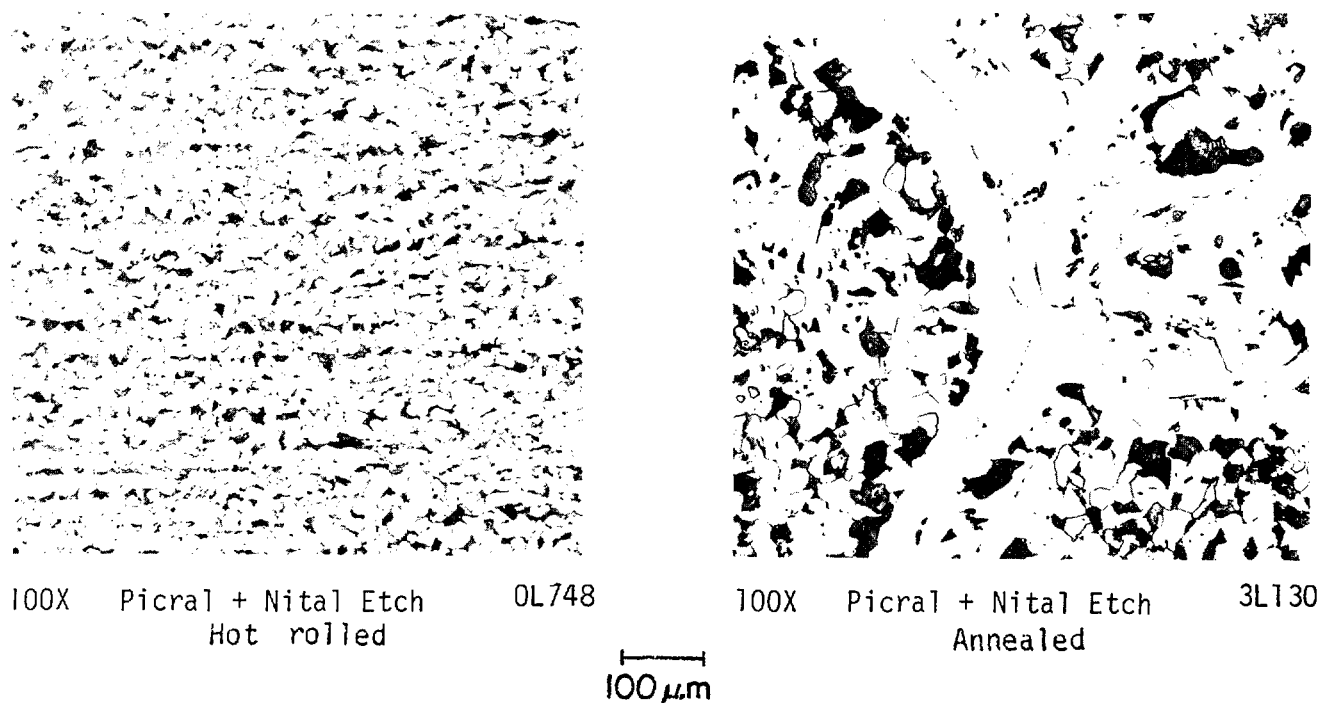


Figure 2.7. Microstructure of doped steel after hot rolling and after annealing.

steel contained numerous manganese sulfide inclusions that were elongated in the rolling direction, which are not visible in the photomicrographs in the figures. The annealed portions of the castings exhibited microstructures that reflected the original microstructures as cast. In both steels, the ferrite and pearlite grains were much finer in the after-annealed condition than in the as-cast condition, as shown in Figures 2.6b and 2.7b. In the clean steel, the refined pearlite grains were aligned in bands that appeared to be oriented randomly, unlike the banding observed in the hot-rolled portions of the castings. The bands of pearlite in the annealed clean steel probably were associated with the acicular structure in the as-cast condition. The pearlite in the annealed doped steel was more evenly distributed, having formed from the more equiaxed as-cast structure. The manganese sulfide inclusions were not affected by the annealing heat treatment, and remained situated on the as-cast grain boundaries.

Portions of the ingots were hot-rolled to develop correlations between the hydrogen-embrittlement characteristics of cast and hot-rolled steels with identical chemical compositions. Such a correlation would make it possible to refer to the large body of information available in the technical literature on hydrogen embrittlement of wrought steels, to gain insight into the effects of hydrogen on cast steels. Apart from early work by Sims and his co-workers, who identified steel-industry problems with heavy castings as a

hydrogen-embrittlement phenomenon (Refs. 2.1, 2.2), there has been very little published research on hydrogen embrittlement of cast steels or the effects of metallurgical and environmental variables on embrittlement. Unfortunately, as described subsequently in this report, there was very little correlation between hydrogen-embrittlement effects on rolled and cast steel. The purpose of annealing portions of the castings was to assess the effects of heat treatment on sensitivity to hydrogen embrittlement. In practice, steel castings that do not meet minimum strength requirements often are heat treated in a similar manner, in an effort to increase the strength to an acceptable level.

2.3.1.2 Welded Steel Castings

Two plate samples cast and welded by the Colorado School of Mines, under contract with the NRC through Manufacturing Sciences Corporation to study waste-package manufacturing variables, were also prepared for evaluation in the hydrogen-embrittlement studies. One of the sample plates met the composition requirements for ASTM A216, Grade WCA, steel; the other had a higher manganese content. The chemical compositions of the plates, reported to Battelle by Colorado School of Mines, are presented in Table 2.3. The table also includes the specified composition for ASTM A216, Grade WCA steel, for comparison.

Table 2.3. Chemical compositions of cast-steel sample plates provided by Colorado School of Mines(a).

Steel	Content, weight percent										
	C	Mn	P	S	Si	Al	Cu	Ni	Cr	Mo	V
NRC-9	0.20	0.50	0.008	0.01	0.33	0.054	(b)	(b)	(b)	(b)	(b)
NRC-11	0.15	0.97	0.015	0.01	0.19	0.034	(b)	(b)	(b)	(b)	(b)
WCA(c)	0.25	0.70	0.04	0.045	0.60	--	0.50(d)	0.50(d)	0.40(d)	0.25(d)	0.03(d)

(a) Reported by Colorado School of Mines.

(b) Not reported.

(c) Maximum specified content for ASMT A216, Grade WCA cast steel.

(d) The sum of the copper, nickel, chromium, molybdenum, and vanadium contents not to exceed 1.00 percent by weight, and the carbon equivalent shall not exceed 0.50 [carbon equivalent = $C + Mn/6 + (Cr + Mo + V)/5 + (Ni + Cu)/15$].

The sample plates were cast approximately 3.8 cm (1.5 in) thick by 15.2 cm (6 in) long, with a trapezoidal cross section that was approximately 4 in wide at mid-height. The castings were sectioned in half longitudinally, and then one as-cast edge and one sawcut edge were welded together. The two edges were butted against each other, forming a half-K groove, and then

joined by multiple-pass submerged-arc welding with a Tibor 22 low carbon welding wire in combination with an Orkelon OP121-TT flux. The composition of the welding wire in weight-percent, reported by Colorado School of Mines, was 0.059 C, 1.48 Mn, 0.009 P, 0.008 S, 0.04 Si, and 0.03 Al. A backing plate of AISI 1018 steel was used to minimize distortion during welding.

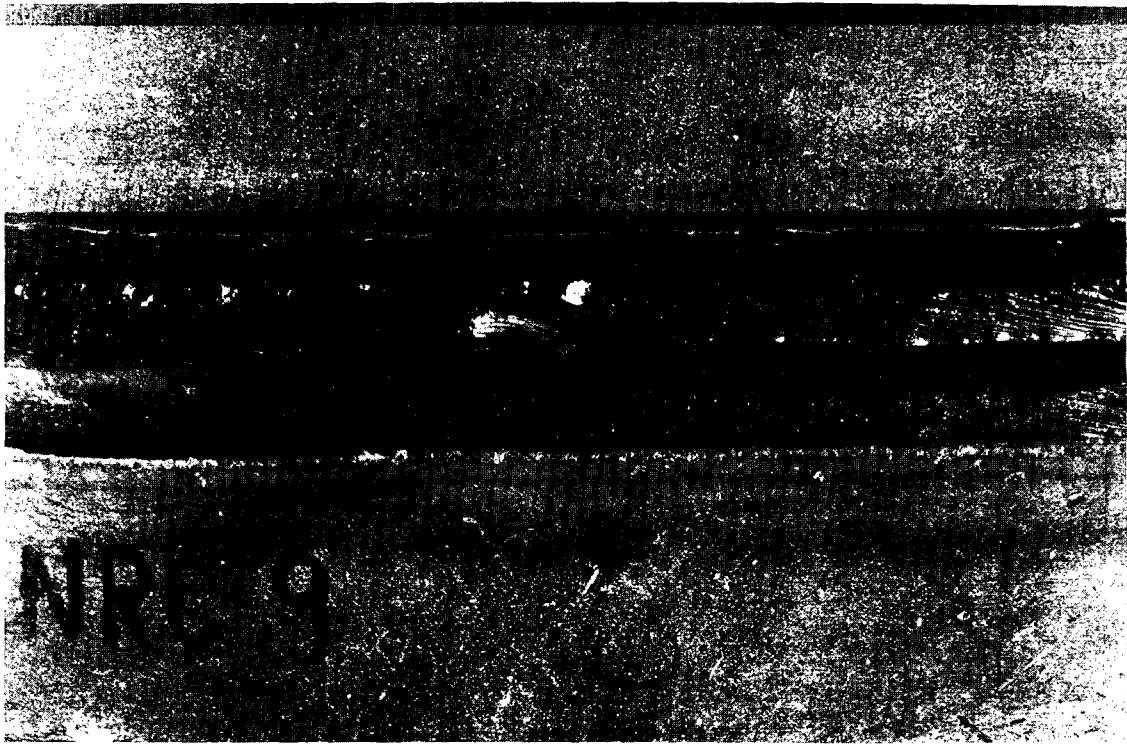
Figures 2.8 and 2.9 present photomacrographs of the welded plates, which are identified by the code numbers assigned by the Colorado School of Mines. Part (b) of each photomacrograph presents a cross sectional view through the weld, showing the multiple welding passes that were used--ten for Sample NRC-9 and nine for Sample NRC-11. The figures also show that the weld heat-affected zones to one side of the weld were oriented approximately straight through the thickness, which was the reason for using a half-K groove. This alignment of heat-affected zones made it possible to prepare fracture-mechanics specimens to measure the effects of hydrogen on the resistance to crack growth in the heat-affected zone.

2.3.1.3 Iron Castings

Twelve small laboratory ingots of direct-reduced iron, 2.5 x 7.6 x 17.8 cm (approximately 1 in thick, 3 in wide, and 7 in long), were provided by Armco, Inc., for examination in this program. When produced in commercial rather than laboratory quantities, this material normally is used as feed-stock in the production of stainless steel alloys. Thus, it is a material which could be made in large quantities at relatively low cost, using existing facilities, and may be a viable overpack material. Research with this iron was initiated because of a perceived shift in interest by DOE toward pure iron overpacks, presumably for improved corrosion resistance. Since that interest never developed beyond the initial stage, research with the direct-reduced iron in this program was limited.

Table 2.4 presents the average chemical composition for the ingots that were used in this program. The compositions were determined by spectrographic analysis. The table shows that there was little variability in composition among the twelve ingots. The carbon, manganese, phosphorus, and sulfur contents all were relatively low. The higher silicon content resulted from deoxidation. The relatively high contents of copper, chromium, nickel, and molybdenum reflect the intended use of the iron in production as a precursor for stainless steel.

Figure 2.10 presents a photomacrograph of a transverse section through one of the ingots. The figure illustrates the solidification pattern and the very coarse grain size that was apparent in all of the castings. The coarse grain size is further illustrated in Figure 2.11, which presents photomicrographs showing the ferritic microstructure of the ingot shown in Figure 2.10. The photomicrograph in Figure 2.11a shows very fine particles present in the grains, and somewhat coarser particles present on the grain boundaries. These particles exhibited a lamellar structure, as shown in Figure 2.11b, and may have been fine pearlite precipitates. No inclusions were observed.

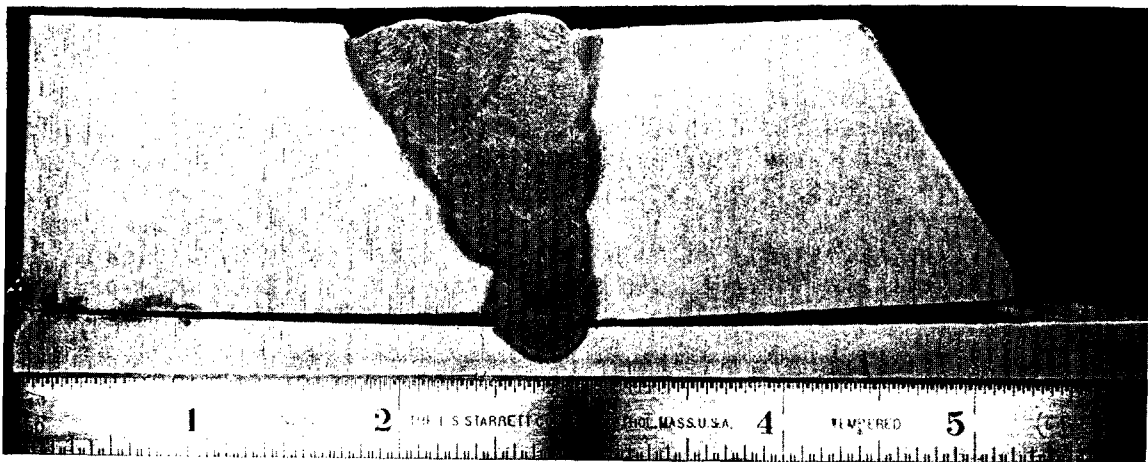


1X

As Received

1M951

a. Top View



1X

10-Percent Nital Etch

1M953

b. Side View

Figure 2.8. Photomicrograph of cast steel plate NRC-9 provided by Colorado School of Mines.



1X

As Received

1M952

a. Top View



1X

10-Percent Nital Etch

1M954

b. Side View

Figure 2.9. Photomicrograph of cast steel plate NCR-11 provided by Colorado School of Mines.

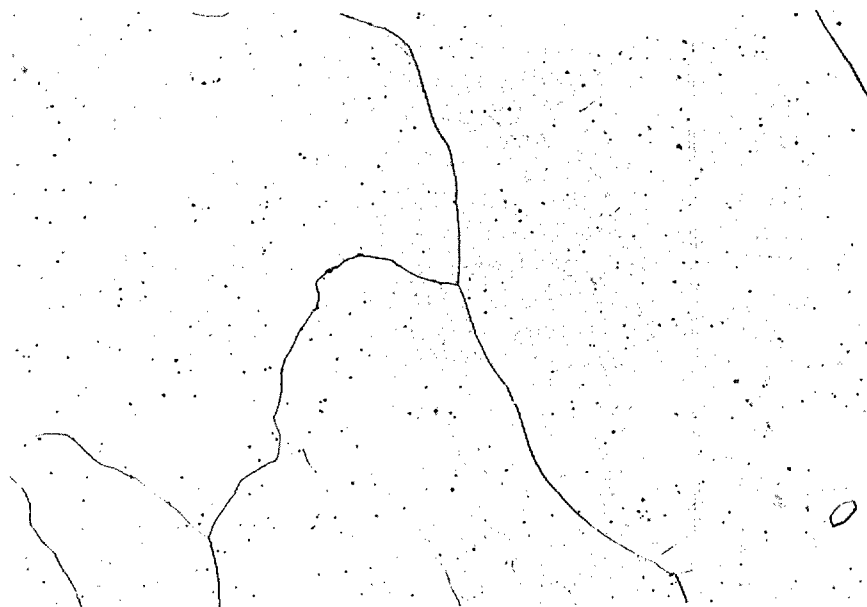
Table 2.4. Average chemical composition of iron ingots.

Element	Content, weight percent	
	Average	Range
Carbon	0.001	0.000 - 0.002
Manganese	0.004	0.003 - 0.004
Phosphorus	0.002	0.002 - 0.003
Sulfur	0.004	0.003 - 0.004
Silicon	0.17	0.16 - 0.18
Aluminum	0.001	0.000 - 0.001
Copper	0.069	0.066 - 0.072
Nickel	0.021	0.017 - 0.022
Chromium	0.046	0.041 - 0.049
Molybdenum	0.044	0.034 - 0.048
Vanadium	0.001	0.000 - 0.001



7L387

Figure 2.10. Transverse section through iron ingot that were provided by ARMCO.

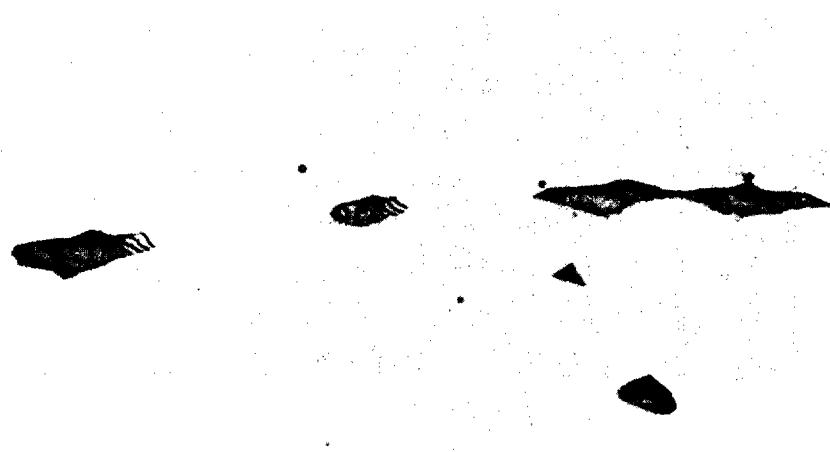


100X

Nital Etch

7L368

a. Overall View



1000X

Nital Etch

7L373

b. Grain-Boundary Precipitates

Figure 2.11. Photomicrographs of iron ingot showing fine precipitates at grain boundaries and in the matrix.

2.3.1.4 Test Specimens

Three types of test specimens were prepared from the sample castings: standard round tension specimens, standard fracture-mechanics (compact-tension) specimens, and exposure-coupon specimens. The specimen dimensions were varied in accordance with the casting size and the specimen orientation in the casting. The tension specimens were prepared according to ASTM Standard E8, "Tension Testing of Metallic Materials", using Specimen Design 1 in Figure 9 of the Standard. The compact-tension (CT) specimens were prepared according to ASTM Standard E813, "Standard Test Method for J_{IC} , A Measure of Fracture Toughness"; Figure 2.12 shows the specimen design. Both 1T (thickness $B = 2.54$ cm) and 1/2T (thickness $B = 1.27$ cm) CT specimens were prepared. Exposure coupons were prepared only from the Battelle castings. All of the exposure coupons were 0.635-cm (0.25-in) diameter by 2.54-cm (1-in) long solid cylinders.

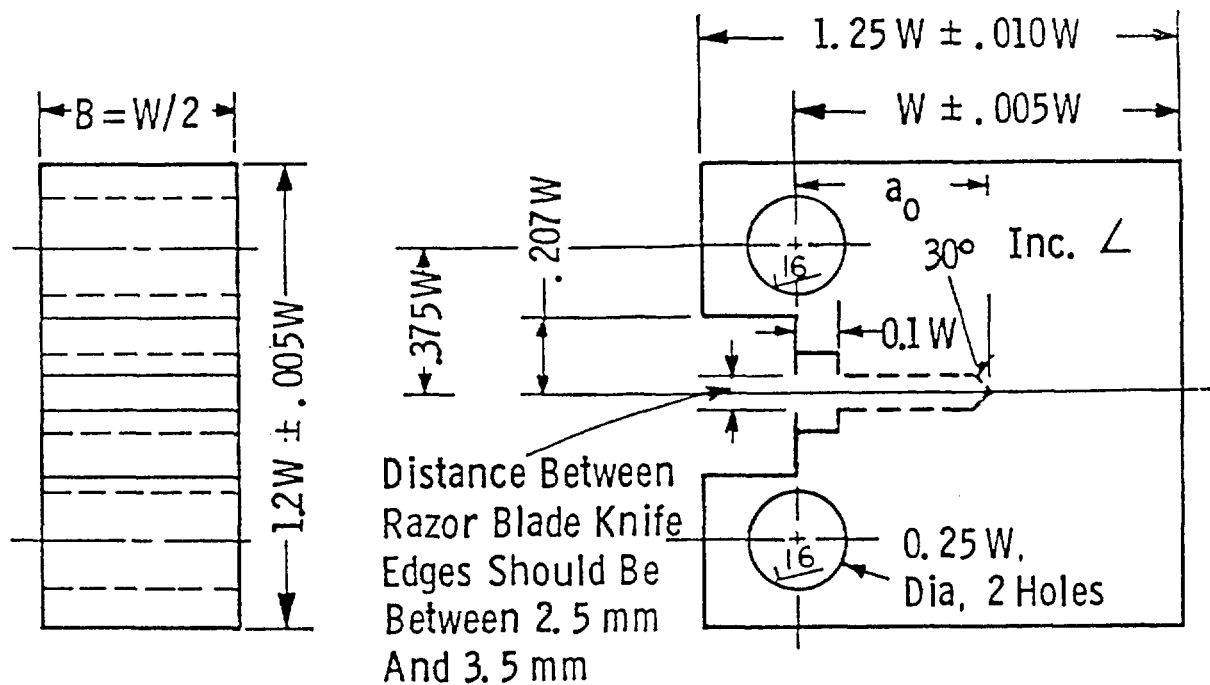


Figure 2.12. Compact-tension specimen design for fracture-mechanics experiments.

Note: $B = 2.54$ cm for 1T specimen, 1.27 cm for 1/2T specimens.

For the clean and doped steel castings prepared by Ba specimens were prepared with their axes parallel and length of the casting, or the direction of pouring. responded to the longitudinal and transverse orienta the plates that were rolled from one-half of each ca both orientations had a 0.635-cm (0.25-in) diameter 2.54 cm (1 in) long. The CT specimens from those c crack growth parallel to the columnar grains, which tural overpack, would correspond with crack growth the waste package toward the interior of the waste packi- ture toughness experiments were conducted with 1T CT specimens; later ex- iments were conducted with 1/2T CT specimens. Exposure coupons were pre- pared with their axes in the longitudinal orientation.

oriented for
to the le
tially
from +

2

Tensile specimens from the welded steel castings were oriented transverse to the weld. The specimens had gage sections that were nominally 1.27 cm (0.5 in) in diameter x 5.08 cm (2 in) in length, but the specimens that were located farthest from the root pass of the weld had to be further machined to a 0.635-cm (0.25-in) diameter gage section to remove surface defects that were associated with inclusions and/or porosity. For all of the tension specimens, the reduced section contained weld metal, heat-affected zone (HAZ), and base metal. It was anticipated that this specimen design would make it possible to identify the portion of the weld region that was most sensitive to hydrogen embrittlement, by determining which portion of the microstructure initiated fracture in a hydrogen environment. Then, the 1/2T CT specimens, which were oriented for crack growth parallel to the weld (with the crack plane normal to the plate width), would be notched in the most sensitive region to provide a worst-case assessment of the effect of hydrogen on the fracture toughness in the weld region. However, as discussed in detail in a subsequent section, the tension specimens did not provide sufficient information regarding the sensitivity to hydrogen embrittlement of the weld region. Therefore, CT specimens were used, based on observations in this program that fracture properties of cast steel were more sensitive to hydrogen embrittlement than tensile properties. In the CT specimens, notches were cut approximately in the center of the HAZ because of common service experience that hydrogen embrittlement occurs predominantly in the HAZ of welded structural steels. The CT specimens were prepared only from Plate NRC-11. All specimens, including tension and CT specimens, were located at two different locations (based on the tensile axis or the center of the crack plane) with respect to the root pass of the weld. Those locations were approximately 1/4 of the plate thickness from the root pass, and 3/4 of the plate thickness from the root pass. Specimens that were farther from the root pass had a broader HAZ, because the adjacent volume of weld metal was greater, as seen in Figures 2.8b and 2.9b.

Both transverse and longitudinal tension specimens were prepared from the iron castings. The longitudinal specimens (tensile axis parallel to the pouring direction, or the length of the ingot) had a 1.27-cm (0.5-in) diameter gauge section that was 5.08 cm (2 in) long, whereas the transverse specimens (tensile axis perpendicular to the pouring direction and parallel to the width of the ingot) had a 0.635-cm (0.25-in) diameter gauge section that was 2.54 cm (1 in) long. In addition, 1T CT specimens were prepared,

for crack growth across the width of the ingot (that is, transverse length of the ingot). This orientation provided crack growth essentially parallel to the columnar grains, for comparison with the CT specimens of the Battelle castings.

2.3.2 Hydrogen-Embrittlement Experiments to Assess Role of Composition, Processing, and Dopants

Experiments to assess the potential for hydrogen embrittlement of the test materials (refer to Figures 2.2a and 2.2b) consisted of tension tests and elastic-plastic fracture-toughness (J-integral) experiments. Parallel experiments were conducted in hydrogen and inert (nitrogen or helium) environments. The degree of degradation was based on the differences in mechanical and fracture properties in the two environments. The hydrogen environment consisted of gaseous hydrogen at a pressure of 6.9 MPa (1000 psi). All experiments were conducted at room temperature.

The tension tests were conducted at an engineering-strain rate of 10^{-4} sec^{-1} . Strength and ductility properties were measured, and the fracture surfaces were examined in a scanning electron microscope (SEM) to determine whether hydrogen affected the fracture mode. For the tensile properties, the principal indicator of embrittlement was a loss in reduction of area. Typically, elongation also is reduced by hydrogen, but to a lesser degree than the reduction of area. Unless severe embrittlement occurs, there usually is no effect of hydrogen on the strength properties.

The J-integral experiments were conducted in accordance with ASTM Standard E813, "Standard Test Method for J_{IC} , a Measure of Fracture Toughness". The test consisted of imposing a steady load-line displacement rate, while monitoring the applied load required to maintain the displacement, and the crack length. Crack growth was monitored continuously by a direct-current electric-potential-drop method, so that J-integral data could be obtained from a single specimen; thus, replicate tests provided information regarding the reproducibility of the observed hydrogen effects on fracture resistance. The J-integral elastic-plastic fracture-toughness test is useful for characterizing the crack-growth resistance of a ductile metal. Two fracture-toughness properties are obtained from this test: (1) the fracture toughness, J_{IC} , which is a measure of the work required to initiate a crack*, and (2) the tearing resistance, dJ/da , which is a measure of the resistance of the metal to subsequent unstable plastic crack growth. Reductions in these properties in a hydrogen environment, relative to an inert environment, indicate the degree of hydrogen degradation.

2.3.3 Hydrogen Absorption Experiments

Hydrogen-absorption experiments were conducted by immersing the exposure coupons into a simulated basaltic groundwater environment at a temperature

*The magnitude of stresses and strains ahead of the crack tip at the instant of crack initiation, are also directly controlled by the value of J_{IC} .

of 250 C (482 F). The specific environment that was used is described in Section 2.4.3. The purpose of the hydrogen absorption experiments was to determine whether significant concentrations of hydrogen could develop in an overpack as a result of corrosion reactions with the groundwater.

2.3.4 Experiments Involving High-Pressure Hydrogen at Moderately Elevated Temperatures

The objectives of this phase of the work were twofold:

- (1) To evaluate short-term effects of high-pressure hydrogen on fracture resistance of cast steel at 260 C (500 F), which is the temperature expected early in the life of the repositories.
- (2) To estimate long-term effects of hydrogen exposure at elevated temperatures on fracture resistance of cast steel.

The short-term effects of hydrogen at 260 C (500 F) were assessed by conducting J_{IC} tests in an atmosphere of 4.5 MPa (700 psi) hydrogen at 260 C (500 F). Compact-tension type specimens, which were not previously exposed to hydrogen, were used for the fracture experiments. Conversely, long-term effects of hydrogen were evaluated by pre-exposing compact-tension type specimens in 6.9 MPa (1000 psi) hydrogen at elevated temperatures for various lengths of times, and subsequently determining J_{IC} and dJ/da in 4.5 MPa (700 psi) hydrogen at 260 C (500 F) or at room temperature*. Exposure temperatures above 260 C (500 F) were used to accelerate the damage kinetics, so that relatively short-duration exposures at higher temperatures could simulate very long exposure times (1000 years) at 260 C (500 F) and below. However, care was taken in the analysis to avoid effects of gross hydrogen attack, since the anticipated repository conditions lie below the Nelson curve for carbon steels.

The experiments were limited to fracture toughness tests, since previous room temperature experiments had indicated that toughness and tearing resistance were more sensitive to hydrogen degradation than other mechanical properties, such as tensile strength, elongation, or reduction in area. Companion tests were conducted in helium with and without pre-exposures in helium. The purpose of these tests was to evaluate the effect of temperature alone on fracture properties, so that the results would provide baseline data with which to compare the results of experiments utilizing hydrogen. Table 2.5 shows the test matrix for the fracture experiments with high-pressure elevated-temperature hydrogen and helium.

*Fracture tests were conducted at 260 C (500 F) to simulate possible fracture events in repositories when temperature is relatively warm. The room temperature fracture tests would correspond to conditions after a long time in the repositories, when temperature had decreased.

Table 2.5. Test matrix involving high-pressure hydrogen and helium at elevated temperatures, for assessing short-term and long-term effects of pre-exposure.

Pre-Exposure Conditions			Test Conditions		Specimen No.
Environment	Temperature (F)	Period (hours)	Environment	Temperature (F)	
H ₂	500	5	H ₂	RT*	12
		50	H ₂	RT	23
		250	H ₂	RT	18
He	500	50	He	RT	21
		250	He	RT	14
H ₂	625	5	H ₂	RT	30
		250	H ₂	RT	34
H ₂	750	5	H ₂	RT	27
		50	H ₂	RT	28
		250	H ₂	RT	24, 35
He	750	50	He	RT	26
		250	He	RT	11
H ₂	850	5	H ₂	RT	33
		50	H ₂	RT	31
He	850	50	He	RT	29
H ₂	1100	5	H ₂	RT	19
		50	H ₂	RT	17
		250	H ₂	RT	4
He	1100	5	He	RT	22
		50	He	RT	15
		250	He	RT	6
None	None	None	H ₂	500	13
		None	He	500	10
H ₂	1100	250	H ₂	500	5
He	1100	250	He	500	7

*RT = room temperature.

Compact-tension type specimens were machined from the Battelle clean cast steel, and precracked to a/W of approximately 0.6. In the case of long-term tests, the specimens were preexposed in hydrogen or helium gas at temperatures ranging from 260 to 593 C (500 to 1100 F). Stainless steel autoclaves were used for exposing specimens in 6.9 MPa (1000 psi) hydrogen. Helium

exposures were performed on companion specimens in sealed glass tubes, which were initially evacuated and then backfilled with approximately one-eighth atmosphere helium. Since the primary purpose of the helium exposures was to determine the effect of the elevated temperature alone on fracture properties, the lower pressure for the reference specimens was deemed adequate.

After pre-exposure the specimens were stored in liquid nitrogen to minimize loss of hydrogen from the specimens prior to the tests. Fracture tests were usually conducted within a few hours after removal from the autoclave.

Fracture toughness, J_{IC} , and tearing resistance, dJ/da , were determined for unexposed and pre-exposed specimens, using procedures generally in accord with guidelines specified in ASTM E813. Specimens were tested in 4.8 MPa (700 psi) hydrogen or helium gas, at room temperature or at 260 C (500 F). For conducting tests at 260 C (500 F), heating was performed by attaching tubular heaters to the clevis grips; the heaters were encased in metal sheaths to prevent contamination of the environment.

Single specimen J-integral testing procedures, similar to those described earlier in Section 2.3.2, were followed for determining fracture parameters. The current through electric potential input leads was maintained at a level sufficient to ensure approximately 320 μ V electric potential (EP) output at the start of the test. Loading was continued until the electric potential drop increased by approximately 50 μ V. This increase corresponded to crack growth in the range of 1 to 3 mm.

J-integral testing, according to ASTM E813, requires accurate determination of load-line displacement at the crack mouth (crack opening displacement). This procedure was followed in the experiments with unexposed specimens tested at room temperature (Section 2.3.2 of this report), but it could not be followed with pre-exposed specimens or with specimens tested at 260 C (500 F) because of space and temperature limitations. Instead, displacements were monitored by the stroke displacement of the servohydraulic system. The fixture compliance was obtained by measuring the difference between crack opening displacement and stroke displacement of a dummy specimen for a range of applied loads comparable to the range used in the fracture tests. Also, during subsequent J-integral testing, the specimen compliance based on linear-elastic region of load-elongation curve was compared with theoretical elastic compliance tabulated in ASTM E813. This comparison provided a separate estimate of fixture compliance. The fixture compliance obtained by various procedures ranged between 1.14×10^{-7} and 1.6×10^{-7} m/N (2.0×10^{-5} and 2.8×10^{-5} in/lb). The small variation in fixture compliance gave confidence to the validity of using a load-dependent scaling factor to calculate crack opening displacement from measured stroke displacement. Data on load, displacement and electric potential were stored on a computerized data-acquisition system for subsequent analysis.

After fracture testing, fractographic examinations in an SEM were conducted on selected specimens. In addition, some specimen halves were sectioned perpendicular to the crack plane and parallel to the side surface. These sections were polished metallographically and etched lightly to reveal cavities formed during hydrogen exposure. Such metallographic sections also

allowed investigation of changes in microstructure which occurred with elevated-temperature exposure in hydrogen or helium.

2.4 Results

2.4.1 Effects of Hydrogen on Tensile Properties

2.4.1.1 Battelle Cast Steel--Effects of Hydrogen on Tensile Properties

Table 2.6 presents the results of the tensile tests performed with specimens from the steel castings prepared by Battelle for this study. The results presented are averages for replicate tests. Between two and four tests were conducted for each condition, depending on the amount of material available and the degree of reproducibility initially observed between duplicate specimens. The table also presents, for comparison, the specified minimum tensile properties for ASTM A216, Grade WCA cast steel, as well as the tensile properties for the portions of the Battelle castings that were wrought (hot rolled).

The data in Table 2.6 show that the principal effect of hydrogen was to limit the reduction of area at fracture. There was also some reduction in elongation at fracture due to hydrogen, but no significant effect on the yield or the ultimate tensile strength. These observations are typical for low and medium strength steels that are deformed in a hydrogen environment. In addition, the strength properties of the Battelle steels were not affected significantly by impurity content (clean versus doped steel) or by orientation. However, strength and ductility were affected by annealing and hot-working, as may be observed from the data in Table 2.6.

The ductilities of the Battelle steels were influenced by many factors, especially impurity content and environment. Figure 2.13 compares the reduction in area for each material condition. For material in the as-cast condition, considerable scatter in the ductility data was observed for replicate specimens, presumably as a result of the inhomogeneity of the castings and the small specimen size relative to the grain size. To reduce the scatter in the data, the results in Figure 2.13 were obtained by averaging the data for both orientations. Averaging may mask, to some extent, the effect of structure (orientation) on ductility; however, the variation with orientation was small compared with the effects of processing and of impurity content. For the clean steel, annealing increased the ductility when tested in nitrogen over that for the as-cast condition, and decreased slightly the ductility loss when tested in hydrogen. Hot rolling further increased the ductility when tested in nitrogen, and decreased the ductility loss when tested in hydrogen. The doped steel exhibited considerably less ductility than did the clean steel in either test environment, particularly in the as-cast and the annealed conditions. The inherent ductility was so low for the doped steel in those conditions that the effect of hydrogen on ductility was minimal, as is illustrated in Figure 2.13. This low ductility was related to the manganese sulfide inclusions that were on the as-cast grain boundaries, as is discussed in the following section. No beneficial

Table 2.6. Tensile properties of Battelle steels.

Steel and Condition	Test Environment	Ultimate Tensile Strength, MPa (ksi)		Yield Strength, MPa (ksi)		Percent Elongation in 1 Inch	Reduction in Area, percent
<u>Longitudinal Orientation</u>							
Clean, as cast	6.9 MPa N2	331	(48)	131	(19)	23	31
	6.9 MPa H2	338	(49)	124	(18)	15	20
Clean, annealed	6.9 MPa N2	400	(58)	207	(30)	37	56
	6.9 MPa H2	407	(59)	214	(31)	36	59
Clean, wrought	6.9 MPa N2	434	(63)	290	(42)	39	66
	6.9 MPa H2	427	(62)	290	(42)	40	63
Doped, as cast	6.9 MPa N2	352	(51)	165	(24)	26	36
	6.9 MPa H2	345	(50)	152	(22)	15	18
Doped, annealed	6.9 MPa N2	379	(55)	221	(32)	14	28
	6.9 MPa H2	386	(56)	221	(32)	13	23
Doped wrought	6.9 MPa N2	462	(67)	290	(42)	34	53
	6.9 MPa H2	462	(67)	296	(43)	34	40
<u>Transverse Orientation</u>							
Clean, as cast	6.9 MPa N2	345	(50)	145	(21)	29	50
	6.9 MPa H2	352	(51)	152	(22)	28	41
Clean, annealed	6.9 MPa N2	400	(58)	207	(30)	39	67
	6.9 MPa H2	407	(59)	207	(30)	32	37
Clean, wrought	6.9 MPa N2	441	(64)	283	(41)	41	63
	6.9 MPa H2	427	(62)	269	(39)	35	48
Doped, as cast	6.9 MPa N2	352	(51)	172	(25)	13	16
	6.9 MPa H2	345	(50)	152	(22)	15	20
Doped, annealed	6.9 MPa N2	400	(58)	221	(32)	17	20
	6.9 MPa H2	407	(59)	221	(32)	15	23
Doped, wrought	6.9 MPa N2	448	(65)	269	(39)	39	63
	6.9 MPa H2	448	(65)	283	(41)	34	37
<u>ASTM A216 Grade WCA--Unspecified Orientation</u>							
As Cast or Heat Treated	Lab Air	(60-85)		(30 min)	24 min	35 min	

not qualified

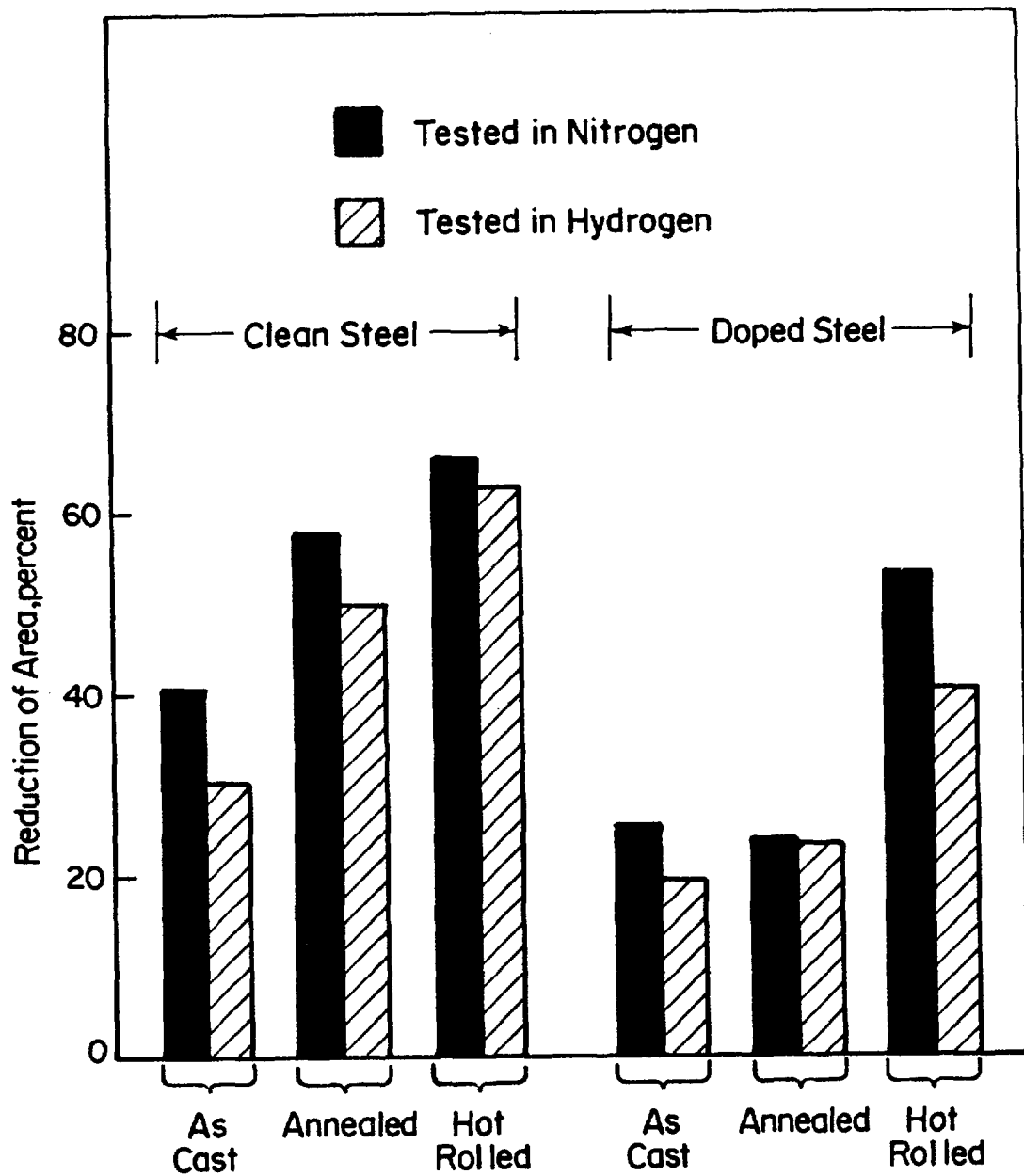


Figure 2.13. Ductility of clean and doped steels tension tested in 1000 psig hydrogen or nitrogen.

effect on ductility by annealing was observed for the doped steel. However, hot rolling provided some improvement in ductility.

Fracture surfaces of the Battelle steels were examined in the scanning electron microscope to determine the dominant fracture mode for each material condition and environment. For the clean steel, fracture was strongly

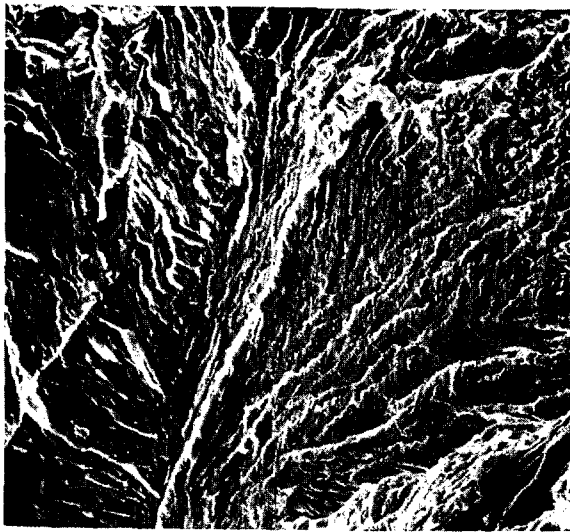
influenced by the hydrogen environment. In nitrogen, the as-cast clean steel fractured by a combination of tearing (failure with limited ductility) and some ductile dimpled rupture. In hydrogen, the clean steel failed by tearing in some regions and cleavage (brittle fracture) in others. Hydrogen also reduced local plastic deformation in the annealed clean steel. Annealing caused the fracture behavior in nitrogen to change to completely dimpled rupture, whereas the fracture mode in hydrogen changed to dimpled rupture plus tearing. Figure 2.14 presents examples of dimpled rupture, tearing, and cleavage in the clean steel. The figure shows the extent to which localized plastic deformation was reduced by hydrogen. This reduction was more pronounced in the as-cast condition than in the annealed condition. The refinement of the grains and redistribution of segregated impurities during annealing probably account for the increased resistance of the annealed steel to degradation by hydrogen. The fractographic evidence shown in Figure 2.14 suggests that the inherent resistance to fracture of the clean steel may be affected strongly by hydrogen as a result of reduced crack-tip deformation; this was studied further with fracture-toughness tests with precracked specimens, as is discussed in a subsequent section.

The doped steel in both the as-cast and annealed conditions fractured primarily along as-cast grain boundaries by delamination at manganese sulfide inclusions (that is, separation at the matrix-inclusion interfaces), as is shown in Figure 2.15. In addition, some tearing was observed. The fractographic appearances of as-cast and annealed doped-steel specimens tested in hydrogen and nitrogen were virtually identical. Hydrogen apparently had little effect on the process of delamination at manganese sulfide inclusions. It is not clear at this time to what extent the effects observed with respect to the manganese sulfide inclusions are representative of other cast steels with similar compositions but with inclusions that are more uniformly distributed.

In the hot-rolled condition, the clean and doped steels fractured by dimpled rupture, or microvoid coalescence, both in hydrogen and in nitrogen. This behavior is consistent with that of other wrought steels reported widely in the literature (for example, in Refs. 2.8 and 2.9). In the hot-rolled condition, the doped steel was slightly more susceptible to hydrogen-induced ductility losses than the clean steel. The dimples on the fracture surfaces of the doped steel consisted of a mixture of fine (initiated at carbide-ferrite interfaces) and coarse (initiated at MnS-matrix interfaces) dimples, whereas the dimples in the clean steel were almost uniformly fine.

2.4.1.2 Welded Steel Castings

Table 2.7 presents the average tensile properties that were determined for the welded cast steel specimens that were provided by the Colorado School of Mines. The table shows that there was no significant difference between the tensile properties of the welded-plate samples in nitrogen and in hydrogen, except for a slight loss in reduction in area in hydrogen. In all of those tensile tests, fracture occurred in the base metal. In addition, many of the specimens developed two necks (regions of localized plastic deformation) in the portions of the reduced section that contained base metal on either



40436

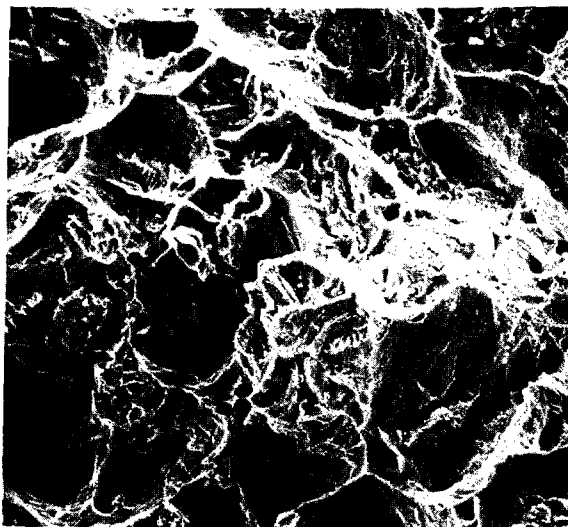
a. As cast; tested in nitrogen.



40411

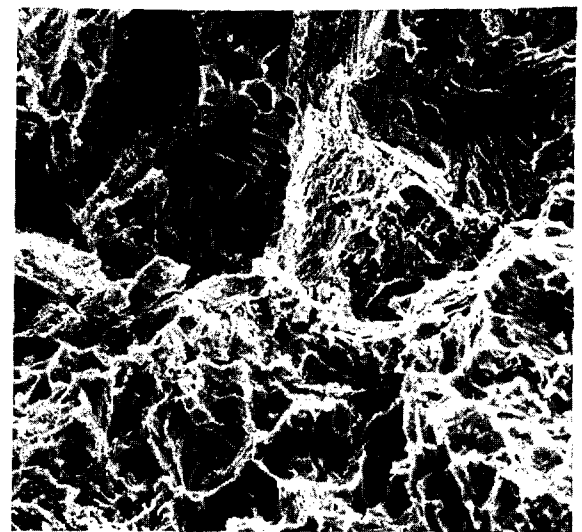
b. As cast; tested in hydrogen.

20 μ m



42935

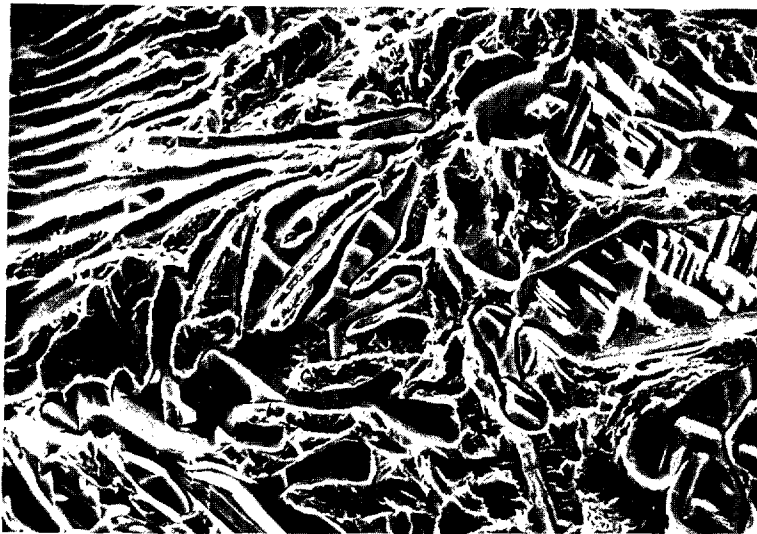
c. Annealed; tested in nitrogen.




42930

d. Annealed; tested in hydrogen.

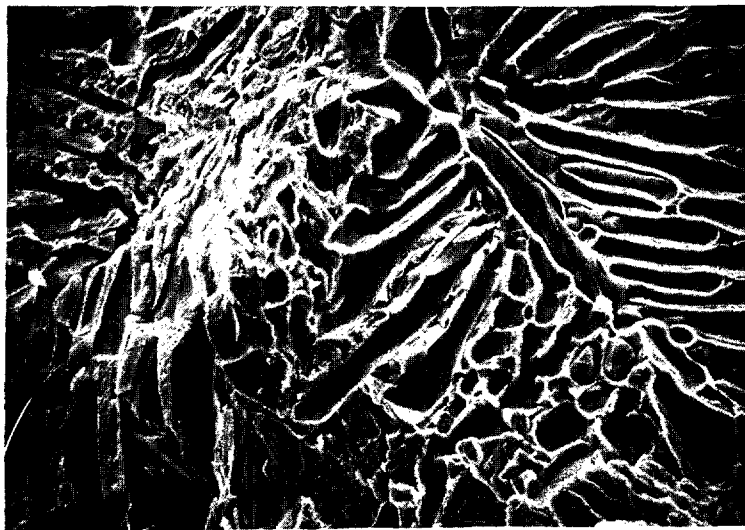
Figure 2.14. Fracture surfaces of clean cast steel.





 20 μm

40422

a. Tested in nitrogen.




 20 μm

40430

b. Tested in Hydrogen.

Figure 2.15. Fracture surface of doped as-cast steel.

Table 2.7. Tensile properties of welded cast-steel plates.

Test Environment	Yield Strength, MPa (ksi)	Ultimate Tensile Strength, MPa (ksi)	Percentage Elongation* in 2 Inches	Reduction in Area, percent
<u>Plate NRC-9</u>				
6.9 MPa N ₂	308 (45)	372 (54)	12.3	49.6
6.9 MPa H ₂	306 (44)	341 (50)	12.5	43.6
<u>Plate NRC-11</u>				
6.9 MPa N ₂	290 (42)	429 (62)	12.3	42.0
6.9 MPa H ₂	298 (43)	435 (63)	13.1	41.6

*The percentage elongation data are not reliable measures of ductility for these tension specimens because many of the specimens formed two necks during the tension tests.

side of the weld. Figure 2.16 presents examples of the double necking for specimens tested in each environment. The formation of two necks in many, but not all, of the specimens makes comparisons among the total-elongation values of specimens to infer the effect of hydrogen unreliable. However, comparing the reduction-of-area values for specimens tested in hydrogen with those for comparable specimens tested in nitrogen shows that there was only a slight reduction in ductility in the base metal: 12 percent for Plate NRC-9 and 1.0 percent for Plate NRC-11. Hydrogen promoted the formation of surface cracks, as is shown in Figure 2.16b.

The formation of double necks in the base metal of the welded plates in both environments indicates that the base metal had significantly lower strength than the weld metal or the HAZ. The relatively small reductions in ductility by hydrogen suggest that the location of the failure in the base metal was not a result of the base metal being particularly sensitive to hydrogen degradation, particularly because all failures (in both environments) were consistently located in the base metal. For Plate NRC-9, the weld-metal hardness was 94 Rockwell B, compared with a base-metal hardness of 71 Rockwell B. Similarly, for Plate NRC-11, the weld-metal hardness was 90 Rockwell B and the base-metal hardness was 69 Rockwell B. Thus, the weld metal was strong enough to resist plastic deformation at stresses below which ductile fracture occurred in the base metal. In addition, the weld probably constrained flow in the adjacent HAZ. However, the weld strength was not so high that hydrogen degradation occurred in the absence of plastic deformation.

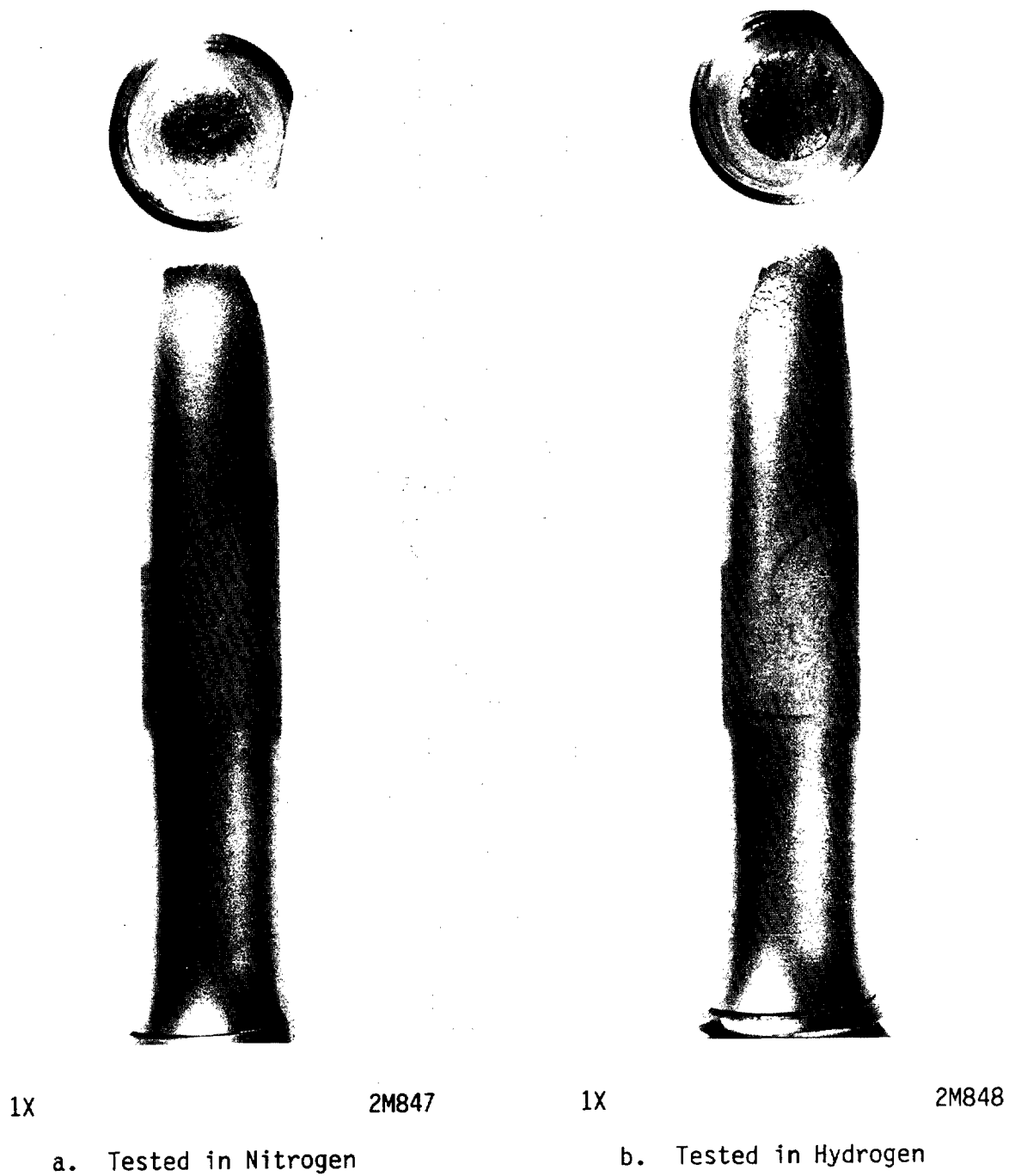


Figure 2.16. Fractured tensile specimens prepared from welded cast-steel plates provided by Colorado School of Mines.

Mild steels usually must undergo plastic deformation for hydrogen degradation to occur, even though hydrogen embrittlement may occur in very high-strength steels at stresses below the yield strength. Thus, no degradation of the HAZ (or the weld) was observed, contrary to expectations based on the previous work with annealed cast steel. However, if a defect is present in or near the HAZ, such as could occur in a field-welded container, stresses and strains could be concentrated in that potentially sensitive area, and hydrogen degradation then could occur. Therefore, fracture-toughness experiments were conducted with specimens that were notched and fatigue pre-cracked in the HAZ. The results of those experiments are discussed in Section 2.4.2.1.

2.4.1.3 Commercial-Purity Iron

The results of the tensile tests with the commercial-purity iron in nitrogen or in hydrogen are presented in Table 2.8. The results indicate that, as expected based on the results with the steels and information in the literature, hydrogen had no effect on the strength properties. Hydrogen did reduce the ductility in both orientations, but to a greater extent in the transverse orientation. The reduction in area was decreased approximately 36 percent in the transverse specimens and approximately 17 percent in the longitudinal specimens. However, it should be noted that the absolute value of the reduction in area was greater for the transverse specimens in both environments. In neither case was the loss of reduction in area so great as to indicate severe hydrogen embrittlement.

Table 2.8. Tensile properties of iron ingots.

Test Environment	Yield Strength, MPa (ksi)	Ultimate Tensile Strength, MPa (ksi)	Percentage Elongation ^(a) in 2 Inches	Reduction in Area, percent
<u>Longitudinal Orientation^(b)</u>				
6.9 MPa N ₂	74 (11)	213 (31)	25.1	21.1
6.9 MPa H ₂	72 (11)	219 (32)	24.9	17.6
<u>Transverse Orientation^(b)</u>				
6.9 MPa N ₂	65 (9)	188 (27)	31.3	55.2
6.9 MPa H ₂	69 (10)	190 (28)	23.6	35.2

(a) Percentage elongation was measured in a gage length that was equal to four times the diameter.

(b) Longitudinal orientation indicates that the specimen axis was oriented parallel to the pouring direction, or the length of the ingot. Transverse orientation indicates that the specimen axis was oriented transverse to the pouring direction, or parallel to the width of the ingot.

2.4.2 Effects of Hydrogen on Fracture Toughness

2.4.2.1 Battelle Cast Steel and Welded Steel Plates

The results of the fracture-toughness tests with the clean Battelle steel in the as-cast condition are presented in Figure 2.17, which presents a plot of the J-integral versus crack growth for each test environment. The plot of J-integral versus crack growth is referred to as the J-resistance curve, which provides information regarding the material's resistance to crack initiation and growth. Each J-resistance curve in Figure 2.17 is a composite curve for two tests.

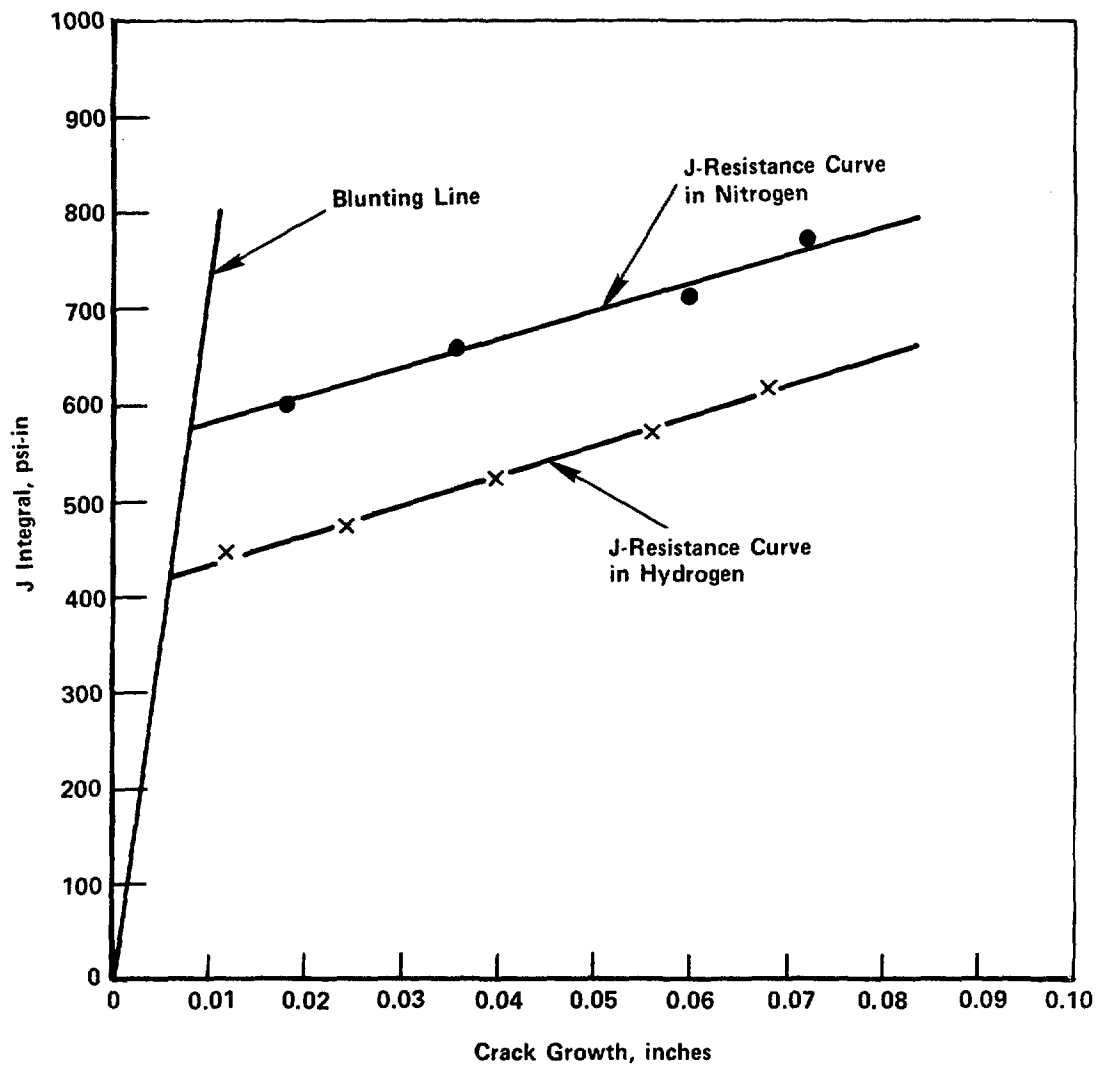


Figure 2.17. J-resistance curves for the as-cast clean steel tested in nitrogen or in hydrogen.

The fracture toughness, J_{IC} , is determined by the intersection of the J-resistance curve with the blunting line, which is an approximation of the extent of apparent crack growth that results from crack-tip blunting processes. The blunting line is defined by the expression $(\Delta)a_b = J/2(\sigma)_0$, where $(\Delta)a_b$ is the apparent crack growth from crack-tip blunting and $(\sigma)_0$ is the flow stress (estimated as the average of the yield strength and the ultimate tensile strength). The tearing resistance, dJ/da , is given by the slope of the J-resistance curve and provides an indication of the resistance of the material to subsequent crack growth. Reductions in J_{IC} and dJ/da in a hydrogen versus nitrogen indicate the degree of hydrogen degradation of the resistance to fracture.

The data in Figure 2.17 indicate a moderate reduction in the fracture toughness of the as-cast clean steel by hydrogen. J_{IC} was reduced from approximately 100 kJ/m^2 (575 psi-in) in nitrogen to approximately 70 kJ/m^2 (420 psi-in) in hydrogen, a loss in fracture toughness of about 27 percent. There was no significant effect of hydrogen on the tearing resistance of the as-cast steel, which in fact was nearly 8 percent higher in the hydrogen environment; this appears to be within the scatter of the tearing-resistance measurement.

Table 2.9 summarizes the fracture-toughness data for the clean steel in the as-cast, annealed, and hot-rolled conditions, as well as the doped Battelle steel and one of the welded cast-steel plates, Plate NRC-11, in the weld HAZ near the root pass and the final pass. The table shows that hydrogen reduced the fracture toughness in all cases, except for the HAZ of Plate NRC-11 near the final weld pass. The percentage reductions in J_{IC} in hydrogen were as follows:

<u>Steel and Condition</u>	<u>J_{IC} Reduction in Hydrogen, percent</u>
Clean; as cast	27
Clean; annealed	88
Clean; wrought	95
Doped; as cast	66
Doped; annealed	88
Doped; wrought	69
HAZ; first pass	65
HAZ; final pass	-9

In most cases, hydrogen induced a very large reduction in fracture toughness. The reduction in J_{IC} for the clean steel in the as-cast condition was relatively low compared with the annealed and wrought conditions, and with the doped steel in all conditions. The HAZ of the welded plate exhibited no toughness loss due to hydrogen; in fact, the fracture toughness was slightly higher in hydrogen than in nitrogen.

Table 2.9. Room-temperature fracture-toughness data for cast steels.

Steel Condition	Test Environment	Fracture Toughness (J_{IC}) kJ/m ² (psi-in)	Tearing Resistance (dJ/da), MPa (psi)
<u>Clean Steel</u>			
As Cast	6.9 MPa N ₂	100 (575)	18.8 (2,730)
	6.9 MPa H ₂	70 (420)	20.3 (2,940)
Annealed	6.9 MPa N ₂	90 (542)	45.3 (6,570)
	6.9 MPa H ₂	10 (65)	10.8 (1,560)
Wrought	6.9 MPa N ₂	220 (1,265)	48.9 (7,090)
	6.9 MPa H ₂	10 (65)	35.5 (5,150)
<u>Doped Steel</u>			
As Cast	6.9 MPa N ₂	120 (658)	21.7 (3,150)
	6.9 MPa H ₂	40 (225)	20.3 (2,940)
Annealed	6.9 MPa N ₂	40 (245)	54.3 (7,880)
	6.9 MPa H ₂	10 (30)	10.8 (1,560)
Wrought	6.9 MPa N ₂	110 (605)	27.1 (3,930)
	6.9 MPa H ₂	30 (185)	30.5 (4,420)
<u>Welded Plate NRC-11</u>			
Root Pass*	6.9 MPa N ₂	340 (1,910)	201.8 (29,270)
	6.9 MPa H ₂	120 (680)	50.1 (7,270)
Final Pass*	6.9 MPa N ₂	210 (1,200)	95.1 (13,790)
	6.9 MPa H ₂	230 (1,310)	51.1 (7,410)

*Approximate location of machined notch in CT specimen with respect to the weld.

The tearing resistance was reduced substantially only in some conditions. For the Battelle steels, large reductions in the tearing resistance were observed in the annealed condition only; the reductions were approximately 76 percent for the clean steel and 80 percent for the doped steel. A moderate reduction (approximately 27 percent) in tearing resistance was observed for the clean steel in the hot-rolled condition, but the tearing resistance was essentially unaffected for the hot-rolled doped steel and for both steels in the as-cast condition. The tearing resistance was reduced significantly in the HAZ of welded Plate NRC-11, with a greater reduction in the portion of the HAZ that was near the root pass (75 percent reduction near the root pass versus 46 percent reduction near the final pass).

This difference between HAZ material near the first and last weld passes in Plate NRC-11 is illustrated in Figure 2.18 which presents the J-resistance

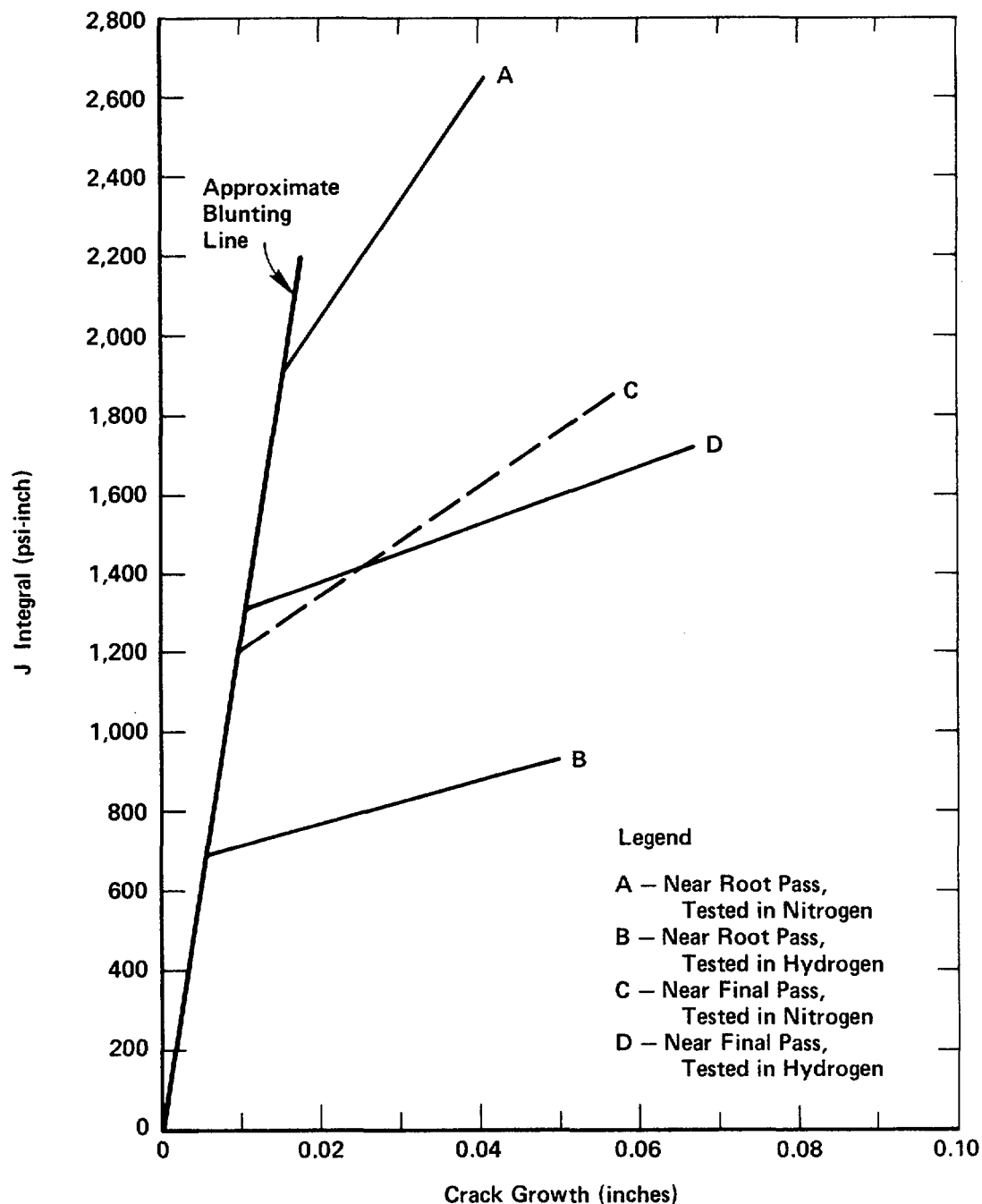


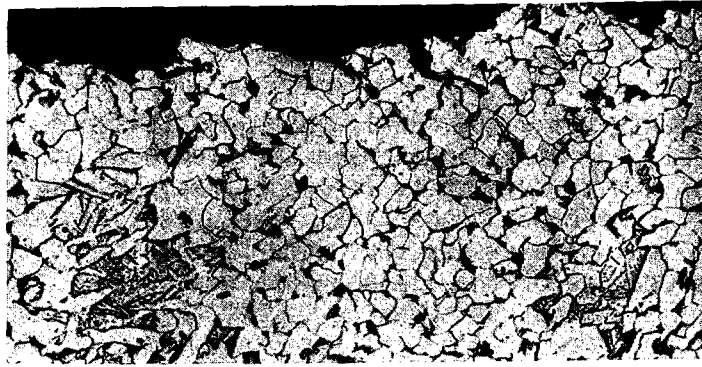
Figure 2.18. J-resistance curves for specimens for plate NRC-11, notched in the heat-affected zone.

The J-resistance curve for the material near the final weld passes that was tested in nitrogen (Curve C) is presented as a broken line because the data were not sufficient to fully define the J-resistance curve.

curves for specimens from Plate NRC-11 that were tested in hydrogen and in nitrogen. Separate curves are presented for specimens that were located at different locations with respect to the root pass, because of the significant differences in fracture properties. The J-resistance curve for specimens nearer the final weld passes that were tested in nitrogen (Curve C) is only approximate because of the limited data available. Tests with material from the location could not be repeated to better define the J-resistance curve because all of the material in that plate had been consumed. J-resistance Curves B and D, for specimens that were tested in hydrogen, displayed different values of J_{IC} , or the J-integral value at which the curves intersect the blunting line. However, the tearing-resistance values, or the slopes of the curves (dJ/da), do not differ substantially. Curves A and C, for specimens that were tested in nitrogen, appear to have differing values of both J_{IC} and dJ/da , although the magnitudes of those differences are uncertain because of the uncertainties in establishing Curve C with limited data. Thus, there were differences in the baseline fracture properties of the HAZ at those two locations, independent of any environmental effects.

The smaller reduction in fracture properties in material nearer the final weld passes indicates less sensitivity to hydrogen degradation near the final pass than near the root pass for Plate NRC-11. However, it should be noted that the reference fracture properties for the material nearer the final passes tested in nitrogen were approximate, and that larger reductions in J_{IC} and the tearing resistance may have occurred than are apparent. Alternatively, the apparent difference in sensitivity to hydrogen degradation may be real, and could be related to the different thermal cycles at those locations. Material nearer the root pass probably underwent a more rapid heating and cooling cycle compared with material nearer the final passes because there were fewer prior passes to provide preheat and there was less adjacent weld metal to act as a heat source. It was observed that the HAZ was approximately 30 percent wider and appeared more diffuse in specimens located near the final passes than in specimens located near the root pass.

The data in Table 2.9 also indicate that the fracture properties for the HAZ of the welded plate were considerably higher than those of the Battelle cast steels. The reason for the high fracture toughness of the HAZ probably is related to the very refined microstructure that was present in the heat-affected zones of the welded plates. Figure 2.19 compares the microstructure of the clean steel as cast and as annealed with that in the region of the HAZ where crack growth occurred. The microstructure in the HAZ was considerably finer than that in the Battelle cast steel in either the as-cast or the as-annealed condition. In fact, the microstructure in the HAZ was so fine that the photomicrograph in Figure 2.17a was taken at a magnification of 500X to reveal the microstructural features, rather than at 100X as in Figures 2.17b and 2.17c. The finer structure in the HAZ of the welded plate probably was due to the fine initial grain size of the plate as-cast, which was a result of the small section size. Thus, the plates may have undergone a higher cooling rate during solidification, despite efforts to insulate the plates when they were cast to simulate cooling rates in larger castings. The clean and doped castings that were prepared at Battelle were originally



500X

Picral Etch

5M221

a. Plate NRC-11 Heat-Affected Zone in Region of Crack Growth

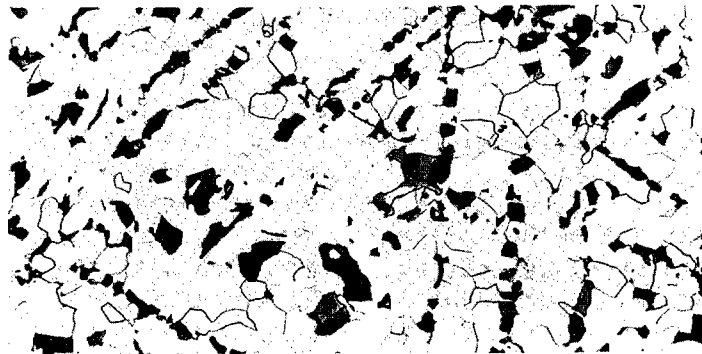


100X

Picral Etch

0L746

b. Clean Steel As Cast



100X

Picral Etch

3L128

c. Clean Steel as Annealed

Figure 2.19. Photomicrographs comparing the microstructures in the heat-affected zone of Plate NRC-11 with the microstructures of the clean steel as cast and as annealed.

cast with 8-in-square cross section to more closely simulate the slow cooling that would occur during solidification of a waste canister.

2.4.2.2 Commercial-Purity Iron

Figure 2.20 presents approximate J-resistance curves for the commercial-purity iron that was generated from the fracture-toughness-experiment data. There was some uncertainty in determining the actual crack lengths for reasons discussed later in this section. The J-resistance curves indicate that the fracture toughness values in the nitrogen (Ref. 2) and hydrogen environments were approximately 80 kJ/m^2 (440 psi-in) and 4 kJ/m^2 (20 psi-in), respectively. As with the cast steels, hydrogen dramatically reduced the resistance to initiation of ductile cracking (J_{IC}). The tearing-resistance values also were extremely low, and a greater amount of rapid crack growth was observed in both environments than had been anticipated based on the experiments with the cast steels.

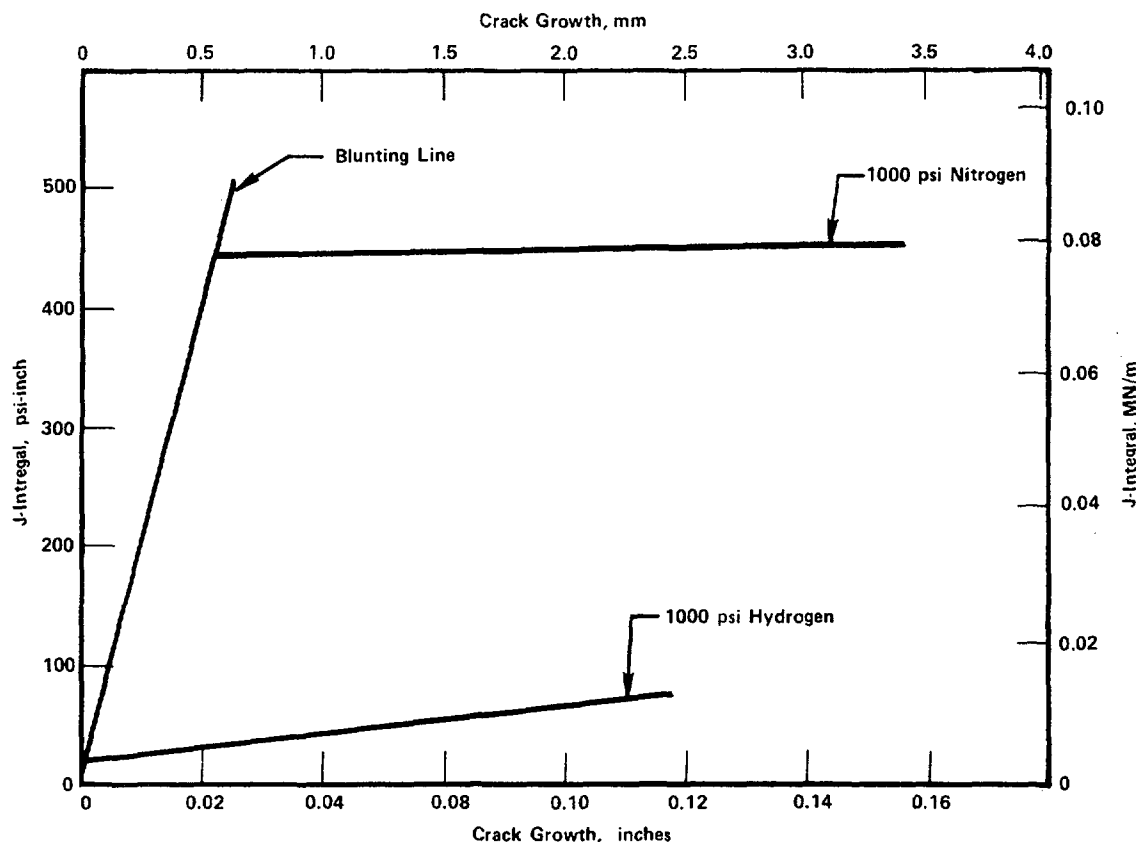


Figure 2.20. J-resistance curves for iron specimens.

These results suggest that fracturing proceeded in an elastic or brittle manner, with little or no plastic deformation preceding crack initiation. In essence, this is what occurred in the experiments, except that there was some ductile behavior prior to crack initiation--sufficient to rule out standard linear-elastic quantification of the fracture behavior. Continuous monitoring of crack length during the fracture-toughness experiments, using a direct-current electric-potential-drop method, provided an indication of the manner in which cracking occurred in this environment. In the nitrogen environment, the specimen was loaded elastically at first, and then plastic deformation at the crack tip occurred as the specimen was loaded further. Following what appeared to be a significant amount of plastic deformation, such that standard linear-elastic measures of fracture toughness could not be determined with validity, a sudden drop in load was detected. This load drop was accompanied by a rapid rise in the signal from the electric-potential-drop probes, indicating a rapid increase in crack length. This "pop-in" form of crack initiation sometimes is observed in brittle, high-strength materials, but typically it is not preceded by any appreciable deformation. Thus, standard test methods could not be applied to interpret the results of these experiments.

However, some comparisons may be made between the cracking behavior in the nitrogen and hydrogen environments. Crack growth in the hydrogen environment proceeded in a manner similar to that described above for crack growth in nitrogen, except that pop-in crack initiation was preceded by a small amount of steady, possibly ductile, crack growth. This is reflected in the J-resistance curves, which indicate that hydrogen promoted a large reduction in resistance to crack initiation. However, because of the rapid nature of the subsequent pop-in cracking, the precise crack length indicated by the electric-potential-drop probes at a given point in an experiment was uncertain with the calibration procedure used. Thus, the J-resistance curves in Figure 2.20 are only approximate, and the extent of cracking in the hydrogen environment prior to pop-in is not known precisely.

The fracture-toughness-test results indicate that the iron samples that were studied underwent large reductions in J_{IC} when exposed to hydrogen and had extremely low resistance to crack growth in both environments. In addition, observations during the tests suggest that the iron may be subject to rapid cracking, independent of environment. The presence of a hydrogen environment also promoted steady cracking prior to pop-in cracking. This behavior may indicate a sensitivity of this material to sustained-load subcritical crack growth. Therefore, subcritical-crack-growth experiments were performed to determine whether the iron was susceptible to this form of degradation. These experiments were nonstandardized tests that have been developed at Battelle to evaluate the sensitivity of a relatively ductile material to subcritical-crack growth in an aggressive environment.

The subcritical-crack-growth experiments were conducted with CT fracture-toughness specimens in the following manner. Each specimen was fatigue pre-cracked in the test environment, 6.9 MPa nitrogen or 6.9 MPa hydrogen. Then, a fixed load-line displacement was imposed on the specimen, and the load and crack length were monitored. If no subcritical crack growth was observed in a period of at least 1 hour, the displacement was increased and

another 1-hour hold period at fixed displacement was imposed. This sequence was repeated three times or until crack growth was detected.

The subcritical-crack-growth experiments provided no indication of crack growth at fixed displacement. In every load period, there was a small decrease in load and an apparent increase in crack length that was related to crack-tip relaxation processes. After completion of the test in nitrogen, the nitrogen was evaluated and replaced with hydrogen while the displacement was maintained. However, no crack growth was observed under those conditions, even when additional displacement increments were imposed. Thus, it appears that although the iron had low toughness in an inert environment and underwent significant loss in J_{IC} in hydrogen, it was not susceptible to subcritical-crack growth. It should be noted that the experiments with the commercial-purity iron were exploratory in nature, and no efforts were made to optimize the properties of the material. The fracture resistance most likely could be improved by optimizing the composition and/or subsequent heat treatments.

2.4.3 Hydrogen Absorption in Basalt-Repository Environment

Hydrogen-absorption determinations were made on as-cast and wrought specimens exposed to simulated basaltic groundwater at 250 C (500 F) to determine whether significant concentrations of hydrogen could be developed in cast-steel overpacks. In addition, some specimens were exposed to more concentrated basaltic groundwater containing ten times the nominal concentrations of the various components, as described in Chapter 3. Coupons 0.635 cm (1/4-in) in diameter by 2.54 cm (1 in) long were machined from both the clean and the doped steels. The coupons were exposed to the simulated basaltic groundwater environment under stagnant conditions for 500 to 2000 hours. Some of the as-cast coupons were thermally outgassed under vacuum for 24 hours at 250 C (500 F) prior to insertion in the autoclave to remove any diffusible hydrogen that might be present. After removal from the autoclave, the coupons were stored in liquid nitrogen to retain the hydrogen until they could be analyzed. Prior to analysis, the surfaces of the coupons were abraded with a file to remove oxide or other corrosion products that might influence the results of the analysis. The hydrogen contents of the coupons were determined using an Ithac-01 Hydrogen Determinator. The hydrogen was extracted from each coupon by an inert-gas-fusion method, and the amount present was determined by the change in thermal conductivity of the carrier gas; the sensitivity of the unit is 0.01 ppm hydrogen.

Table 2.10 presents the results of the hydrogen analyses. Three coupons were evaluated for each material condition. In addition, at least three coupons that were not exposed to the basaltic environment were analyzed to determine the initial hydrogen contents. The approximate hydrogen concentration due to exposure was determined from the difference between those two values.

The data in Table 2.10 exhibit wide scatter for replicate conditions. This scatter is particularly evident for the unexposed clean steel in the as-cast condition, which contained considerable dissolved hydrogen, the content of

Table 2.10. Hydrogen absorbed during exposure to simulated basalt groundwater.

Material	Thermally Outgassed Before Exposure(a)	Hydrogen Content of Exposed Specimens (ppm by weight)		Hydrogen Content of Unexposed Specimens (ppm by weight)		Average Hydrogen Concentration Absorbed During Exposure (ppm by weight)
		Range	Average	Range	Average	
<u>2000-Hour Exposure (Nominal Groundwater Composition)</u>						
<u>Clean Steel</u>						
As cast	Yes	3.29-5.74	4.65	2.78-5.73	4.43	0.22
As cast	No	3.92-4.99	4.43	0.32-3.39	1.98	2.45
Wrought	No	0.34-0.50	0.42	0.00-0.00	0.00	0.42
<u>Doped Steel</u>						
As cast	Yes	0.56-2.89	1.86	0.00-0.05	0.02	1.84
Wrought	No	0.00-0.17	0.09	0.00-0.09	0.02	0.07
<u>1100-Hour Exposure (Nominal Groundwater Composition)</u>						
<u>Clean Steel</u>						
As cast	No	0.88-1.20	0.99	0.32-3.39	1.98	-0.99(b)
Wrought	No	0.21-0.42	0.31	0.00-0.00	0.00	0.31
<u>Doped Steel</u>						
As cast	No	0.34-0.60	0.49	0.00-0.33	0.07	0.42
Wrought	No	0.28-0.39	0.34	0.00-0.09	0.02	0.32
<u>550-Hour Exposure (Nominal Groundwater Composition)</u>						
<u>Clean Steel</u>						
As cast	No	6.49-7.10	6.69	0.32-3.39	1.98	4.71
As cast	Yes	4.48-6.80	5.67	2.78-5.73	4.43	1.24
<u>Doped Steel</u>						
As cast	Yes	1.04-3.56	2.61	0.00-0.05	0.02	2.59
<u>1000-Hour Exposure (10X Nominal Groundwater Composition)</u>						
<u>Clean Steel</u>						
As cast	No	0.81-2.29	1.42	0.32-3.39	1.98	-0.56(b)
<u>Doped Steel</u>						
As cast	No	0.00-0.44	0.20	0.00-0.33	0.07	0.20

(a) Thermal outgassing was performed by heating to 250 C in a vacuum for 24 hours to drive off diffusible hydrogen.

(b) Probably an anomaly resulting from the wide specimen-to-specimen variation in initial hydrogen content.

which varied widely from one location in the casting to another (from 0.32 to 3.39 ppm), although no systematic pattern of variation was observed. Thermal outgassing did not reduce the hydrogen content of the as-cast clean steel; in fact, the average hydrogen content of outgassed specimens was more than twice that of specimens that were not outgassed. This indicates the approximate magnitude of variation in hydrogen content which can be attributed to specimen-to-specimen scatter, and suggests that most of the pre-existing hydrogen probably was nondiffusible; that is, it was in the form of gaseous hydrogen in pores or at internal interfaces. Specimen-to-specimen variations in the initial hydrogen content of the clean steel may then be related to variations in porosity or interface content, although such a correlation was not attempted.

Hot rolling eliminated virtually all of the pre-existing hydrogen in the clean steel. The doped steel contained very little hydrogen in the as-cast condition (less than 0.1 ppm average) and exhibited little scatter in initial hydrogen content. However, after exposure to the simulated basaltic groundwater, both the clean and doped steels in the as-cast condition exhibited considerable scatter in hydrogen content. The magnitude of the scatter was comparable for both steels, as illustrated in Figure 2.21. Since thermal outgassing apparently had no effect on initial hydrogen content, data for outgassed specimens were not differentiated from data for specimens that were not outgassed. For either steel in Figure 2.21, the hydrogen content did not increase with greater exposure time over the level achieved with 550 hours' exposure, suggesting that an "equilibrium" level of hydrogen was reached within 550 hours.

The scatter in the data for the doped steel after exposure to the basaltic groundwater, compared with the reproducibility of the data for unexposed doped-steel specimens, indicates that the scatter in hydrogen contents results primarily from specimen-to-specimen variability in reactions with the groundwater or in absorption of hydrogen produced by those reactions. However, since concentrating the groundwater composition to ten times the nominal composition had little, if any, effect on hydrogen absorption, the variability of reaction was probably related to the specimens rather than the environment. The corrosion data, discussed in Chapter 3, did not exhibit much specimen-to-specimen variability. Therefore, the scatter observed in the hydrogen-absorption determinations probably arose from variations in the absorption of hydrogen generated by the corrosion reactions and therefore, may be related to differences in the surface conditions of the specimens.

The scatter in the hydrogen-absorption data causes difficulty in evaluating the effect of corrosion reactions with groundwater on hydrogen absorption by cast-steel overpacks. It appears, however, that the steels absorbed approximately 3 ppm or less hydrogen in the as-cast condition and approximately 0.5 ppm or less hydrogen in the wrought condition. Therefore, cast-steel overpacks might be expected to absorb several times more hydrogen from groundwater corrosion reactions than would their wrought-steel counterparts. However, in either case, the concentration of hydrogen absorbed was not particularly high in comparison with that which could be obtained with cathodic charging methods (by which hydrogen contents of 5 to 10 ppm usually can be

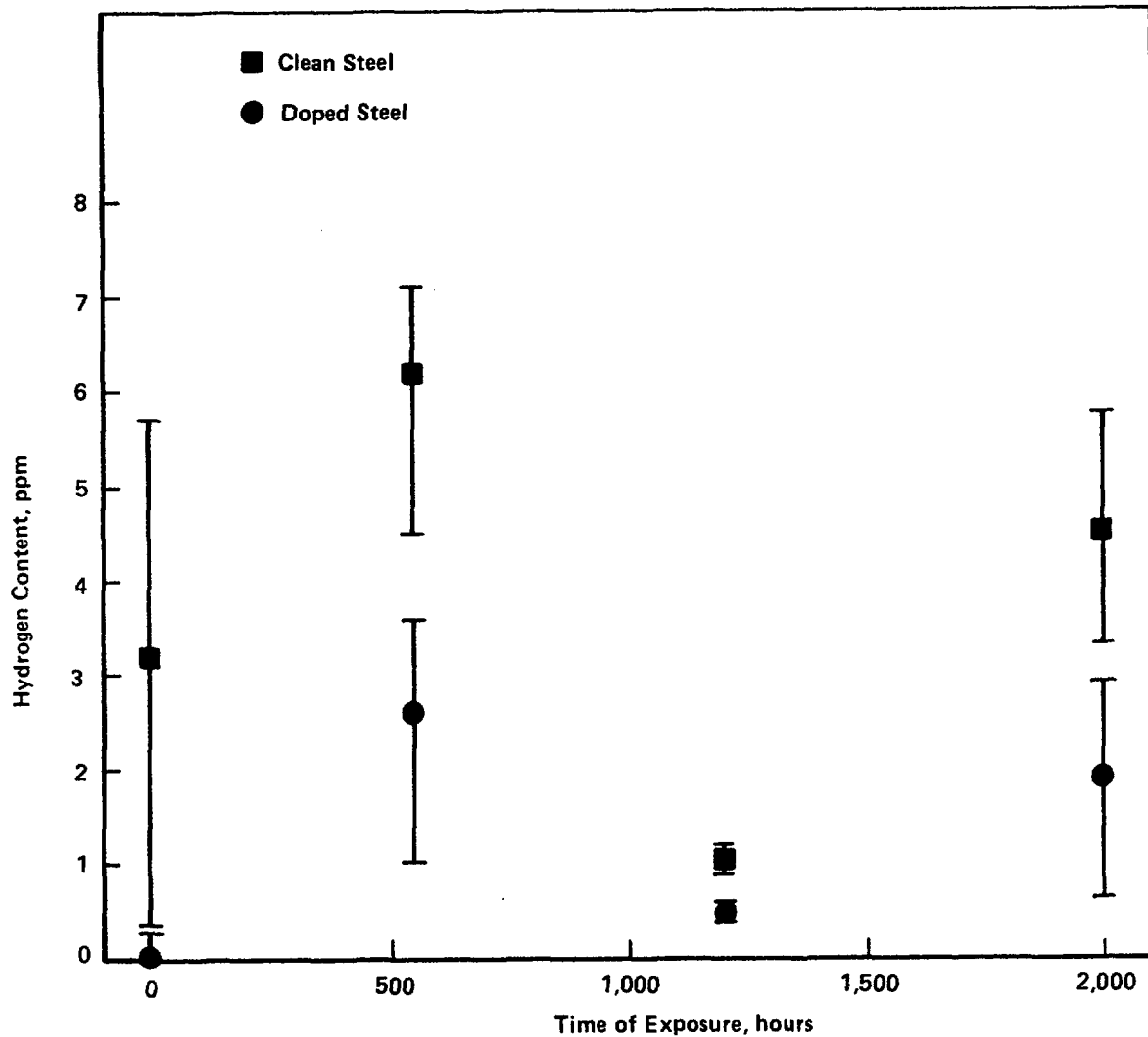


Figure 2.21. Hydrogen content versus time of exposure to simulated basaltic groundwater for as-cast clean and doped steels.

generated), so that testing of cathodically charged specimens would not be representative of anticipated repository conditions. Thus, experiments in gaseous hydrogen should provide a realistic assessment of embrittlement characteristics in a repository for two reasons: (1) hydrogen pressures of approximately 1000 to 2000 psi as a result of radiolytic reactions have been estimated for a sealed repository, and (2) the absorption of up to 3 ppm of hydrogen from corrosion reactions should not substantially alter the magnitude or character of the embrittlement observed in gaseous hydrogen because the solubility of hydrogen at 1000 psi at room temperature is 0.5 to 1.0 ppm (Ref. 2.10) in α -iron (ferrite).

2.4.4 Short-Term and Long-Term Effects of Hydrogen at Moderately Elevated Temperatures

2.4.4.1 Test Data

Table 2.11 summarizes general features of the fracture toughness test results for 1/2T CT specimens that were either unexposed or pre-exposed for various lengths of time at various temperatures in hydrogen or helium environments, and subsequently fracture tested at room temperature or at 260 C (500 F). The data include the extent of crack growth, maximum load, total displacement, and tentative J_{IC} , and they provide an initial estimate of how pre-exposure affected subsequent fracture and load bearing capacity.

In Figure 2.22 the load and electric potential (EP) are plotted versus displacement, for a specimen exposed to hydrogen at 454 C (850 F) for 5 hours. In the figure, the electric potential at the start of the test (EP_0) has been subtracted from total electric potential output, and the result has been magnified 30 times. This type of plot was typical of most experiments and the data were used for estimating the J-resistance curve and determining J_{IC} and dJ/da .

Figures 2.23 and 2.24 contain load-versus-displacement curves for some of the specimens exposed in hydrogen and helium, respectively. All of the specimens represented were tested at room temperature. The plots illustrate the effects of exposure on the load-displacement curves. Since all specimens had approximately the same precrack length, the relative magnitudes of damage can be qualitatively assessed from the curves. Longer exposures at a certain temperature in hydrogen led to monotonically increasing loss of load bearing capacity. The trend existed at 260 C (500 F) (compare curves 12, 23, and 18 in Figure 2.23).

Figure 2.25 contains load-displacement curves obtained from testing at room temperature and at 260 C (500 F). The figure shows the strong effect of pre-exposure environment on subsequent load-displacement curves (compare curves 7 and 5). For the unexposed specimens (curves 10 and 13), the difference in load-elongation curves was much less. However, the extents of crack growth were different, and the combined effects are best illustrated by the J-integral data in the next section.

While Figures 2.23 to 2.25 provide qualitative evaluations of hydrogen degradation at elevated temperatures, they are insufficient for quantitative comparisons. The data missing from these curves are crack-initiation points and extents of crack growth for each specimen. These were obtained by analysis of EP data as well as from fracture surface observations.

Table 2.11. Results of fracture toughness experiments with high-pressure, elevated-temperature hydrogen or helium.

Sample No.	Exposure Conditions			Test Conditions		Pre-Crack Length (mm)	Final Crack Length (mm)	Max. Load (lb)	Total Displ. (in)	J_{Ic} (kJ/m ²)
	Env.	Temp. (F)	Time (hrs)	Env.	Temp. (F)					
12	H ₂	500	5	H ₂	RT*	15	17.1	1154	0.117	152
23			50		RT	15.4	17.3	981	0.096	100
18			250		RT	16.4	19.3	950	0.080	103
21	He	500	50	He	RT	15.5	18.2	1375	0.219	345
14			250		RT	15.5	16.8	1510	0.225	447
30	H ₂	625	5	H ₂	RT	15.9	17.5	1425	0.151	325
34			250		RT	15.3	18.9	1172	0.113	139.5
27	H ₂	750	5	H ₂	RT	15.6	18.6	1020	0.073	68.6
28			50		RT	15.6	17.9	981	0.089	75.6
24			250		RT	15.6	17.8	832	0.050	17.1
26	He	750	50	He	RT	15.8	18.4	1490	0.234	414
11			250		RT	15.5	18.9	1515	0.221	282
25			50	H ₂	RT	15.3	17.6	983	0.097	64.9
35	H ₂	750	250	H ₂	RT	15.6	24.2	559	0.028	6.31
33	H ₂	850	5	H ₂	RT	15.3	18.6	1200	0.151	167
31			50		RT	15.5	23.8	561	0.031	11.4
29	He	850	50	He	RT	15.5	18.7	1556	0.235	431
19	H ₂	1100	5	H ₂	RT	15.7	17.5	895	0.084	66.6
17			50		RT	15.6	17.3	743	0.068	33.6
4			250		RT	15.2	20.3	650	0.119	67.9
22	He	1100	5	He	RT	15.5	17.1	1272	0.202	341
15			50		RT	15.6	17.1	1230	0.140	151
6			250		RT	15.8	18	1200	0.131	149
13	-	-	-	H ₂	500	15.4	16.3	1389	0.128	239
10	-	-	-	He	500	15.6	16.3	1476	0.138	182
5	H ₂	1100	250	H ₂	500	15.7	18.8	690	0.098	63.5
7	He	1100	250	He	500	15.5	17.2	1190	0.139	115

*RT = room temperature.

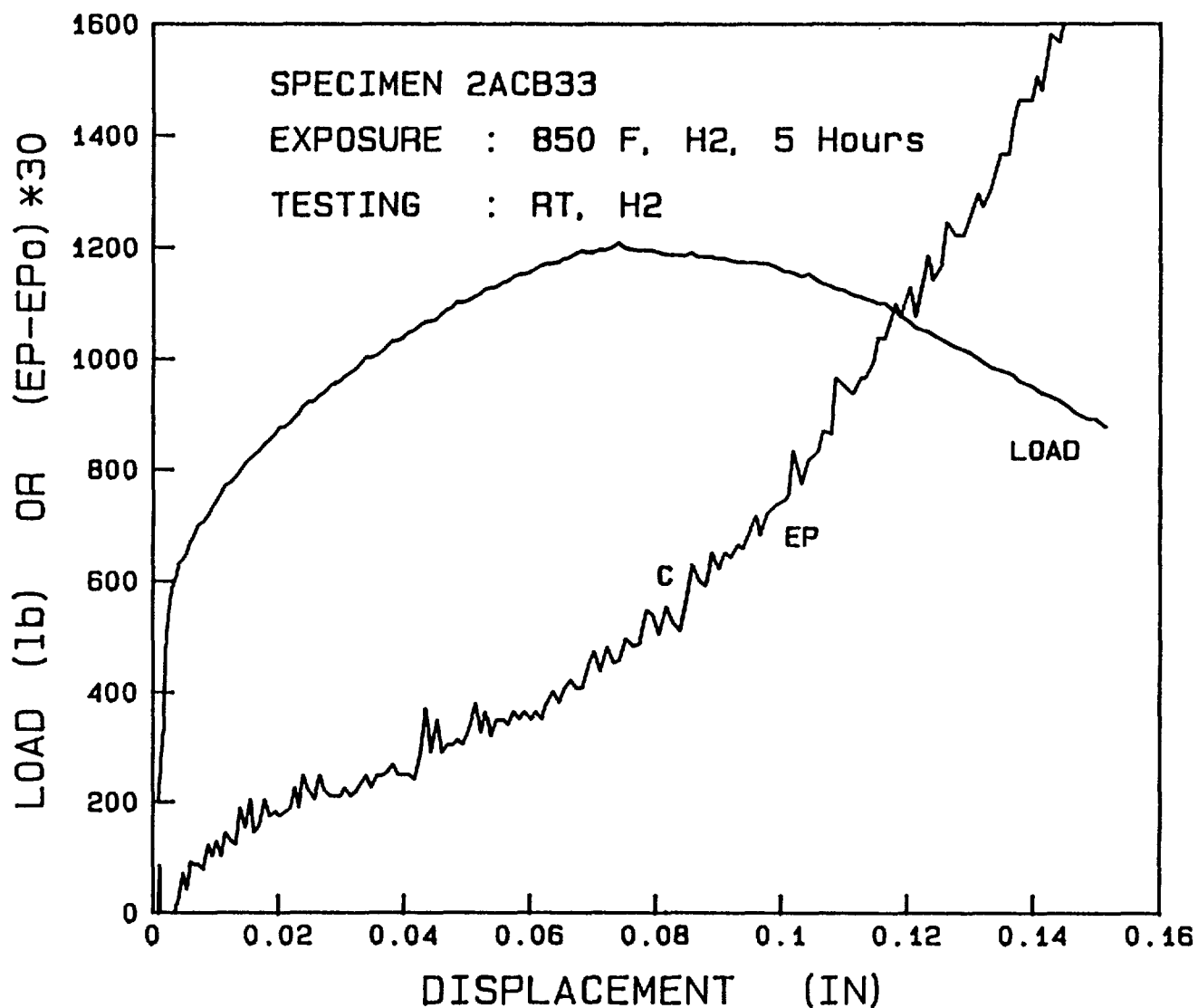


Figure 2.22. Typical raw data generated during the fracture toughness experiments, showing load and electric potential plotted versus displacement. The electric potential (microvolts) increment from the start of the test has been magnified thirty times. Point C corresponds to the location where crack initiation is assumed to have occurred, and is obtained by noting when rate of increase of EP changes rapidly.

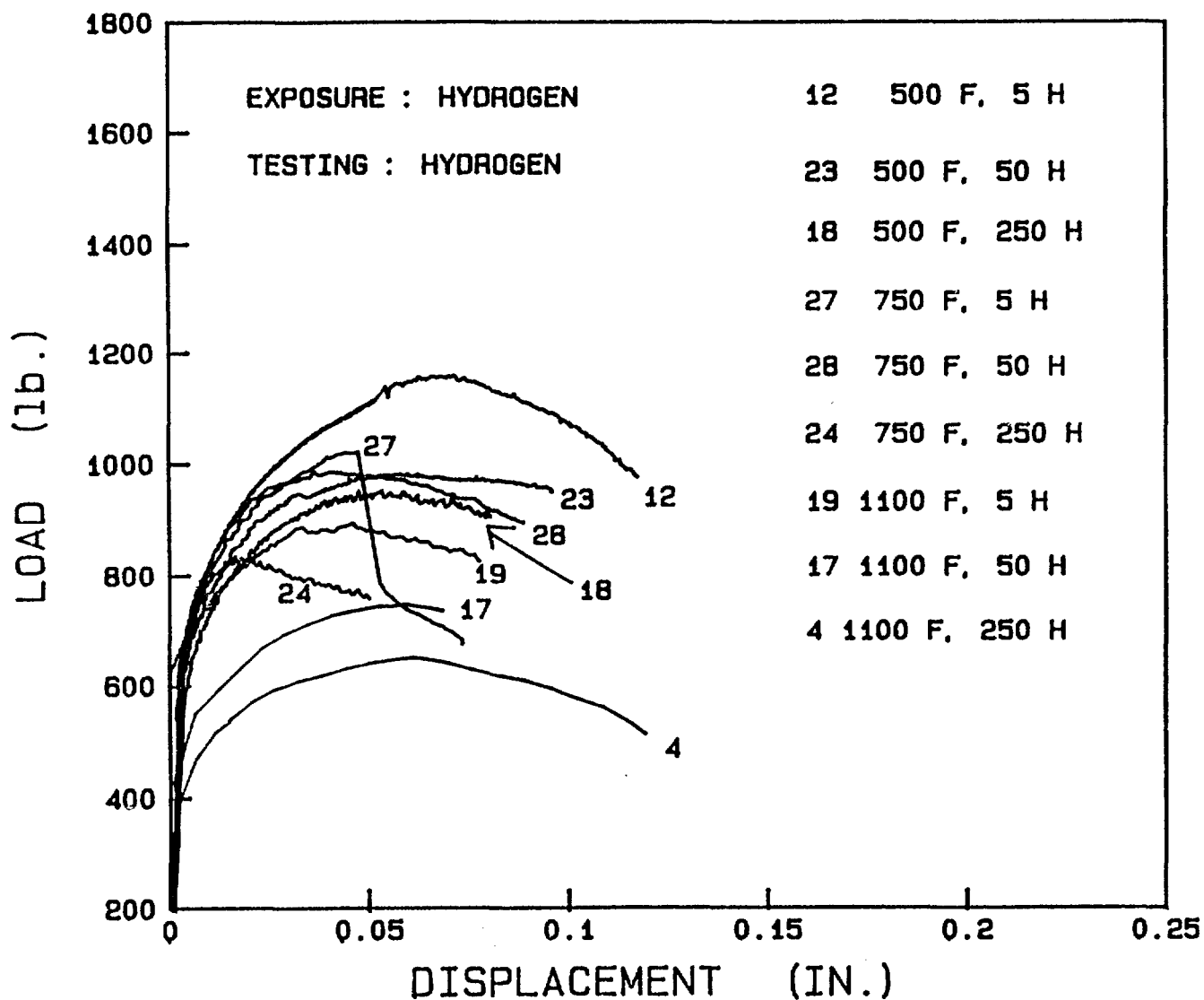


Figure 2.23. Load-displacement curves of some compact-tension specimens, pre-exposed to hydrogen at elevated temperatures, and subsequently loaded to failure in hydrogen at room temperature. The curves are identified by specimen number.

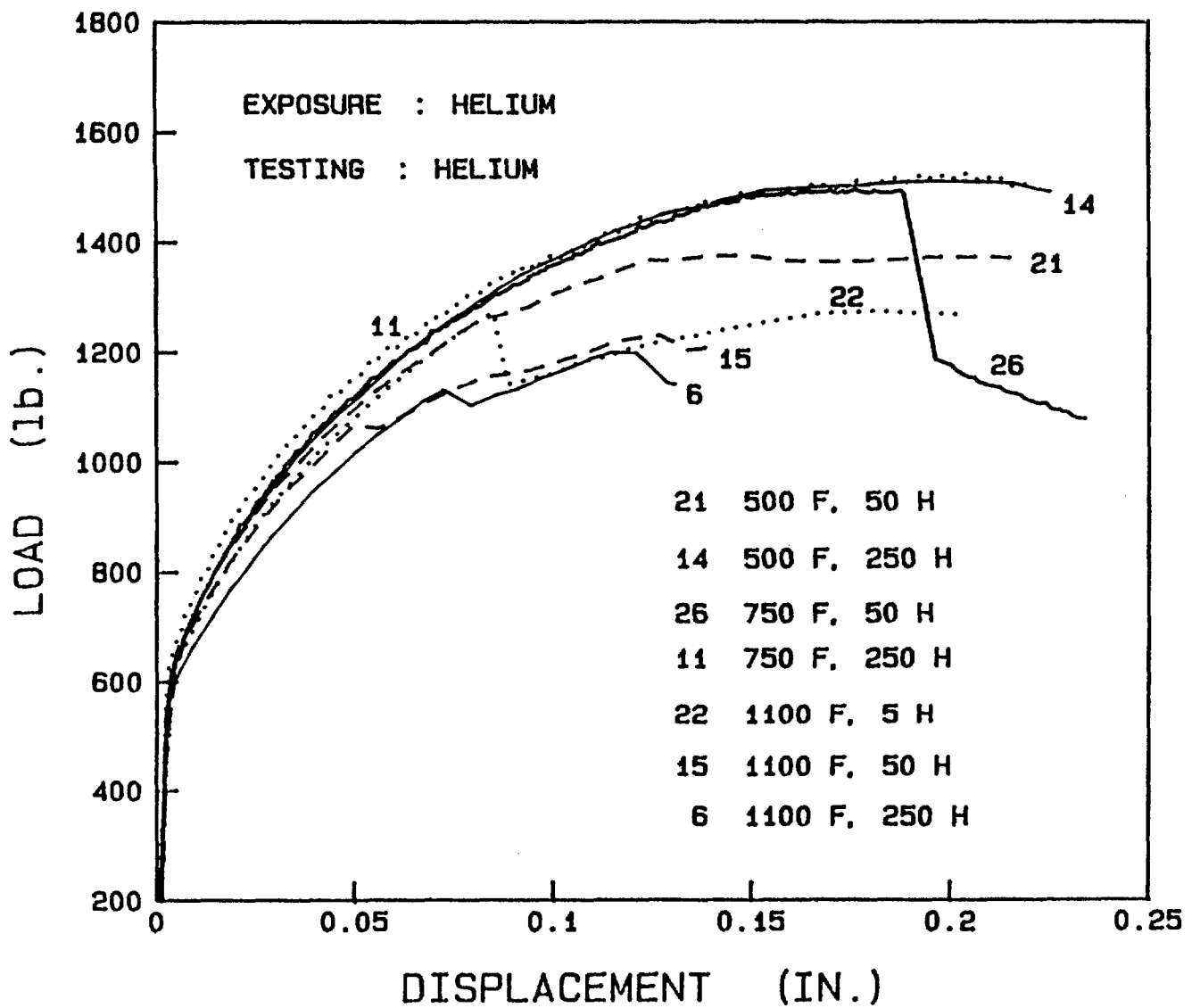


Figure 2.24. Load-displacement curves of compact-tension specimens, pre-exposed to helium at elevated temperatures, and subsequently loaded to failure in helium at room temperature. The curves are identified by specimen numbers.

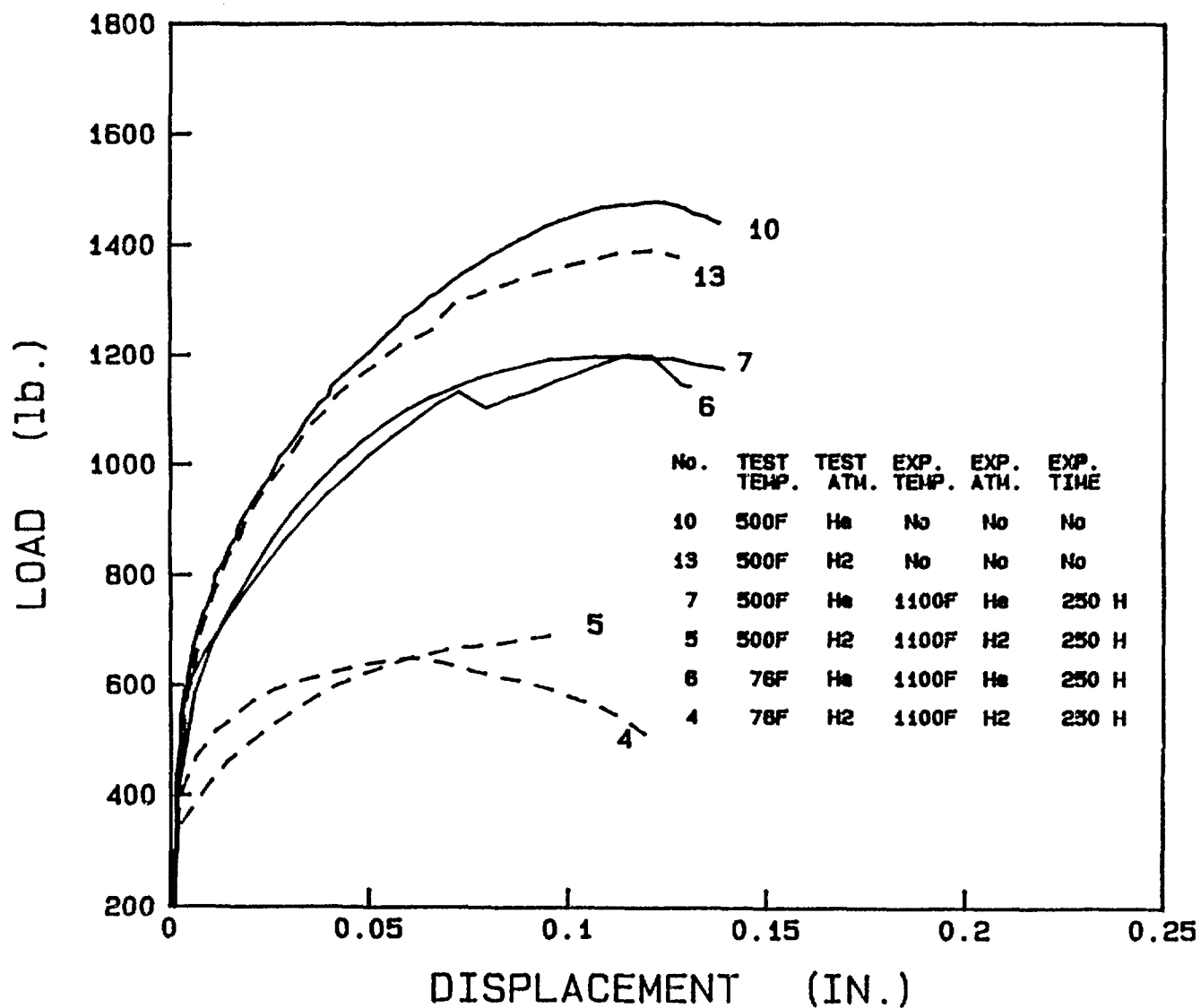


Figure 2.25. Load-displacement curves of unexposed and pre-exposed specimens, tested at 260 C (500 F). The pre-exposure and testing conditions are indicated in the figure. Data on 593 C (1100 F) pre-exposed specimens, tested at room temperature, are included for comparison.

2.4.4.2 J-Integral Results

The load-displacement and EP data were used to generate J-integral curves as described in Section 2.4.2.1. Figure 2.26 shows the J-resistance curve for the specimen of Figure 2.22. As with the unexposed specimens, discussed in Section 2.4.2.1, degradation of fracture properties was evaluated by determining the effect of exposure on fracture toughness*, J_{IC} , and on tearing resistance, dJ/da .

The EP data indicate that cracking generally initiated slightly before maximum load was attained. In certain cases, and this was especially true for the helium-exposed specimens, cracking initiated with a large load drop, indicating "pop-in" behavior, which is typical of brittle fracture. As with commercial-purity iron, the fracture mode was cleavage under such circumstances, and therefore dJ/da may not be appropriate for characterizing crack growth. Generally, dJ/da is associated with ductile tearing, and usually it has a positive value. Under purely cleavage conditions dJ/da may be zero or even negative, and it is not clear at present what such values signify, other than indicate brittle fracture mode. However, J_{IC} remains significant, since it determines the conditions which lead to crack initiation from a microstructural site ahead of the crack tip.

2.4.4.3 Short-Term Effects of Elevated Temperature Hydrogen

Table 2.12 lists J_{IC} and dJ/da values for unexposed specimens, which were tested in helium or hydrogen at 260 C (500 F). For comparison, data are included on unexposed clean-cast-steel specimens, which were fracture tested at room temperature (refer to Section 2.3.2 of this report). Table 2.12 also contains data on an additional fracture parameter, J_G , which corresponds to the J-integral that must be exceeded to grow the crack beyond a crack length increment of 1.5 mm; its significance is discussed in detail in the next section. Together, these results provide a measure of the short-term effects of hydrogen at 260 C (500 F) and at room temperature.

Tests conducted in helium (or nitrogen) with no prior exposure show that J_{IC} increased from 100 kJ/m² at room temperature to 311 kJ/m² at 260 C (500 F), an increase of 211 percent. The corresponding increase in dJ/da was 260 percent. These results reflect the greater inherent ductility of the material at 260 C (500 F) compared to room temperature.

Comparison of J_{IC} and dJ/da values of unexposed specimens, tested at room temperature, show that J_{IC} was 30 percent less in hydrogen than in nitrogen, while dJ/da was relatively unaffected by the environment (Table 2.9). On the other hand, while at 500 F J_{IC} was only 17.7 percent less in hydrogen

*Actually, the terminology J_Q should be used rather than J_{IC} , since the size requirements according to ASTM E813 were not strictly met in all specimens (only half of all specimens tested satisfied size requirements). To prevent confusion of terms, and to retain the more familiar expression, namely J_{IC} , we tentatively refer to all J_Q as J_{IC} .

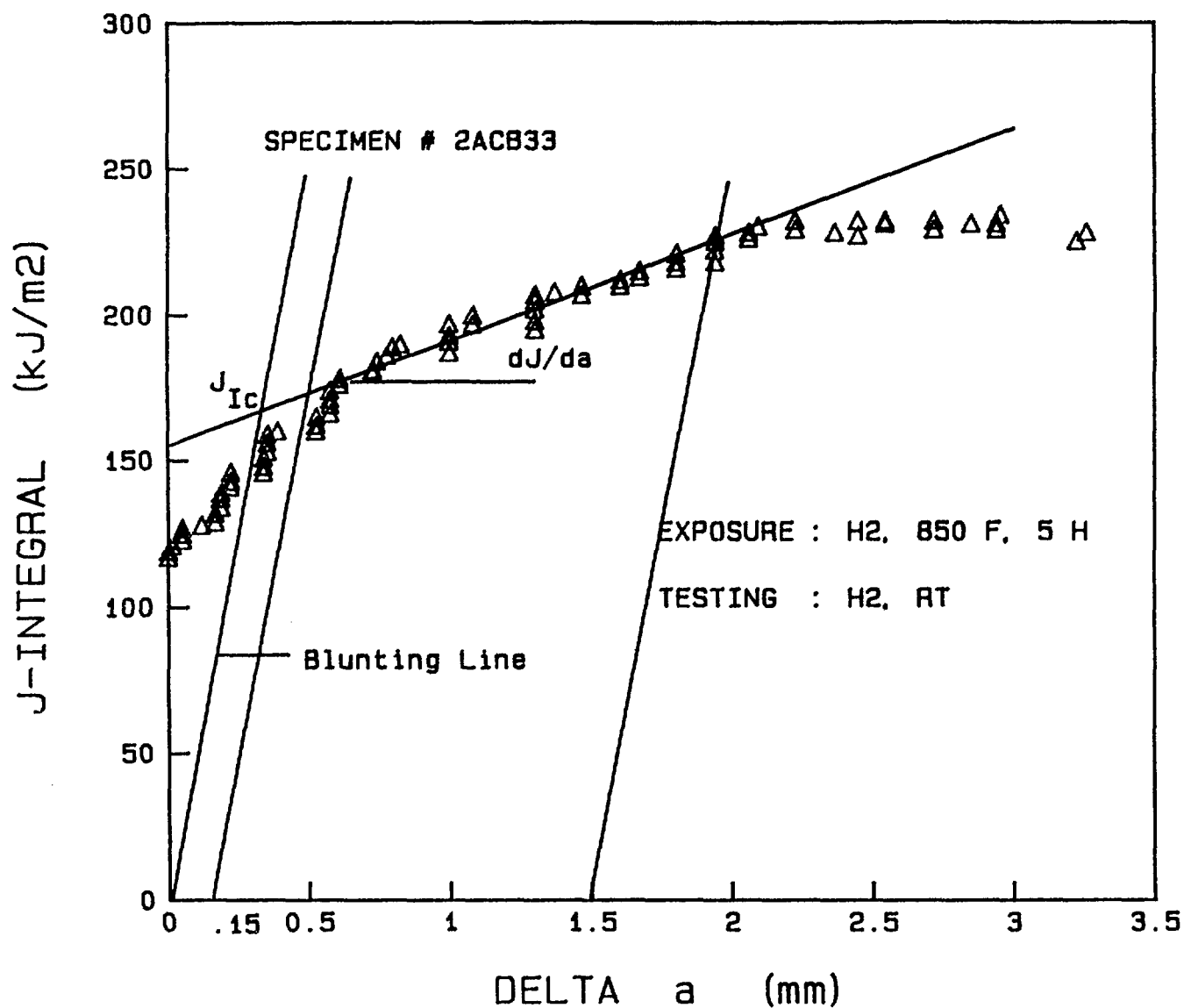


Figure 2.26. Typical J-resistance curve generated for pre-exposed specimen. The blunting line, 0.15 mm offset line, and 1.5 mm offset line are indicated. Tearing resistance dJ/da is obtained by linear least-square-fit through data between the two offset lines.

Table 2.12. Short-term effects of elevated-temperature hydrogen.

Specimen Number	Test Conditions		J_{IC} (kJ/m ²)	dJ/da (MPa)	J_G (kJ/m ²)
	Temperature (F)	Environment			
13	500	Hydrogen	256	28.7	299.1
10	500	Helium	311	73.3	420.9
CS1	Room Temperature	Hydrogen	70	20.3	100.5
CS2	Room Temperature	Nitrogen	100	18.8	128.2

than in helium, the loss of dJ/da due to hydrogen was much larger; approximately 60 percent. These differences in trends for J_{IC} and dJ/da can be rationalized on the basis that the crack initiation toughness, J_{IC} , is largely stress controlled, while tearing resistance dJ/da provides a measure of ductility, and is primarily controlled by the total strain-to-failure. The increased ductility of the material at 260 C (500 F) compared to that at room temperature may thus explain why, at room temperature, hydrogen had larger effect on J_{IC} than on dJ/da, while at 260 C (500 F) dJ/da was degraded more in comparison to J_{IC} .

As will be discussed in the next section, J_G is a composite parameter that reflects the material's resistance both to initiation and propagation of the crack. The data in Table 2.12 show that J_G decreased by approximately 22 percent in going from nitrogen to hydrogen environment at room temperature. At 260 C (500 F) the decrease in J_G was approximately 29 percent. Thus, the material seems to be slightly more sensitive to hydrogen degradation at 260 C (500 F) than at room temperature. This finding is in contrast to many statements in the technical literature that suggest hydrogen embrittlement is not observed at temperatures above 100 C (212 F). Such generalizations are based on smooth-bar tensile data and do not consider crack-tip interactions with hydrogen, as was done in the present investigation.

2.4.4.4 Long-Term Effects of Elevated-Temperature Hydrogen

Table 2.13 summarizes the J_{IC} and dJ/da values for specimens which were fracture tested at room temperature or 260 C (500 F), following pre-exposure to hydrogen or helium. Data on unexposed specimens are also included (from Table 2.13) for comparison. The table contains two sets of results. In one set, J-integral results are tabulated for unexposed and pre-exposed specimens, which were fracture tested at 260 C (500 F). Comparison of results in this set allows an evaluation of long-term effect of hydrogen on subsequent fracture resistance at initial repository temperatures. In the other set of results, J-integral values are tabulated for specimens which were pre-exposed in hydrogen or helium for various temperature/time combinations, and then fracture tested at room temperature. These results allow an assessment

Table 2.13. Long-term effects of elevated-temperature hydrogen.

Specimen Number	Pre-Exposure Conditions			Test Conditions		J_{Ic} (kJ/m ²)	dJ/da (MPa)	J_G (kJ/m ²)
	Environment	Temperature (F)	Time (hours)	Environment	Temperature (F)			
12	H ₂	500	5	H ₂	RT	155.1	18.9	183.4
23			50			87.9	32.6	136.8
18			250			103.8	7.5	115.0
21	He	500	50	He	RT	369	21.1	400.6
14			250			495.6	36.3	550.0
30	H ₂	625	5	H ₂	RT	325	0	325.0
34			250			139.5	6.2	147.0
27	H ₂	750	5	H ₂	RT	69.7	25.1	107.3
28			50			76.3	29	119.8
24			250			11.4	27.8	53.1
35			250			6.3	3.1	11.0
26	He	750	50	He	RT	461.2	0	461.2
11			250			323.7	32.1	371.9
33	H ₂	850	5	H ₂	RT	166.7	35	219.2
31			50			11.4	0.8	12.6
29	He	850	50	He	RT	431	0	431
19	H ₂	1100	5	H ₂	RT	74.4	25.3	112.3
17			50			36.2	27.9	78.0
4			250			68.3	6.1	77.5
22	He	1100	5	He	RT	369	18.7	397.1
15			50			181.5	80.8	302.7
6			250			156.6	39.7	216.2
5	H ₂	1100	250	H ₂	500	69	5.8	77.7
7	He	1100	250	He	500	145.3	82	268.3
13	None	None	None	H ₂	500	256	28.7	299.1
10	None	None	None	He	500	311	73.3	420.9
CS1	None	None	None	H ₂	RT	70	20.3	100.5
CS2	None	None	None	N ₂	RT	100	18.8	128.2

of the effect of long-term elevated-temperature exposure in hydrogen on fracture resistance of the material, when temperatures in the repositories decrease. As already mentioned, exposure temperatures above 260 C (500 F) were used so that relatively short duration exposures at those temperatures could simulate long duration service exposures at 260 C (500 F). Together, these results provide a measure of long-term effects of elevated temperature hydrogen on container integrity.

Figure 2.27 is a bar chart which allows comparison of J_{IC} and dJ/da values obtained from experiments involving pre-exposure to hydrogen or helium. In this figure the left-most bar for each specimen number corresponds to J_{IC} (kJ/m^2), while the middle bar corresponds to dJ/da (MPa or MN/m^2). The right-most bar for each specimen is an additional fracture parameter, J_G , which is discussed in detail in the next paragraph. By comparing results for hydrogen and helium-exposed specimens, it is quite clear that hydrogen reduced fracture properties significantly. It should however be noted that in some cases the helium-exposed specimens had lower dJ/da values than corresponding hydrogen-exposed specimens. The difference was a result of "pop-in" fracture that was observed in these specimens. Table 2.13 shows that J_{IC} was quite large despite the low dJ/da values. Presumably the stress and strain distributions ahead of the crack tip (Refs. 2.13, 2.14), which are controlled by magnitude of J-integral, were sufficient to trigger particle-induced cleavage, in accordance with well-established theory of cleavage fracture (Ref. 2.15). Therefore, while comparing results of companion hydrogen and helium tests, it is necessary to consider both J_{IC} and dJ/da . Hence, another parameter, J_G , which is a composite of J_{IC} and dJ/da , was developed to allow convenient comparisons to be made between the results of various fracture tests. In Figure 2.27, J_G is represented by the right-most bar for each specimen.

The parameter J_G corresponds to the J-integral at a crack increment (Δa) of 1.5 mm. It is the J-integral value necessary to initiate and grow the crack by 1.5 mm; this level of J-integral must be exceeded to further propagate the crack. Mathematically, J_G is defined as $J_G = J_{IC} + (dJ/da) \cdot (1.5 \text{ mm})$. A crack increment of 1.5 mm was chosen since that distance spans approximately 10 pearlite colonies. The rationale behind the choice of pearlite colonies as a critical microstructural feature is that hydrogen attack occurs predominantly at ferrite/pearlite boundaries. These sites, and ferrite-carbide interfaces, located within the colonies, act as traps for hydrogen so that hydrogen embrittlement would additionally be affected by the location of a colony with respect to the crack tip. Thus, the J-integral required for crack extension over a reasonable multiple of such microstructural features should provide an indication of the resistance to steady-state crack growth.

Measuring the resistance to crack extension over 10 pearlite colonies reduces the degree of data scatter associated with any favored location or orientation of a single pearlite colony with respect to the crack tip. Note that J_G incorporates both crack initiation (J_{IC}) and crack propagation (dJ/da) conditions, and hence, provides a combined measure by which to compare short-term and long-term effects of high-pressure hydrogen. Figure 2.27 shows that J_G monotonically decreased with the time of pre-exposure in hydrogen at 260 C (500 F), indicating a steady time-dependent decline in

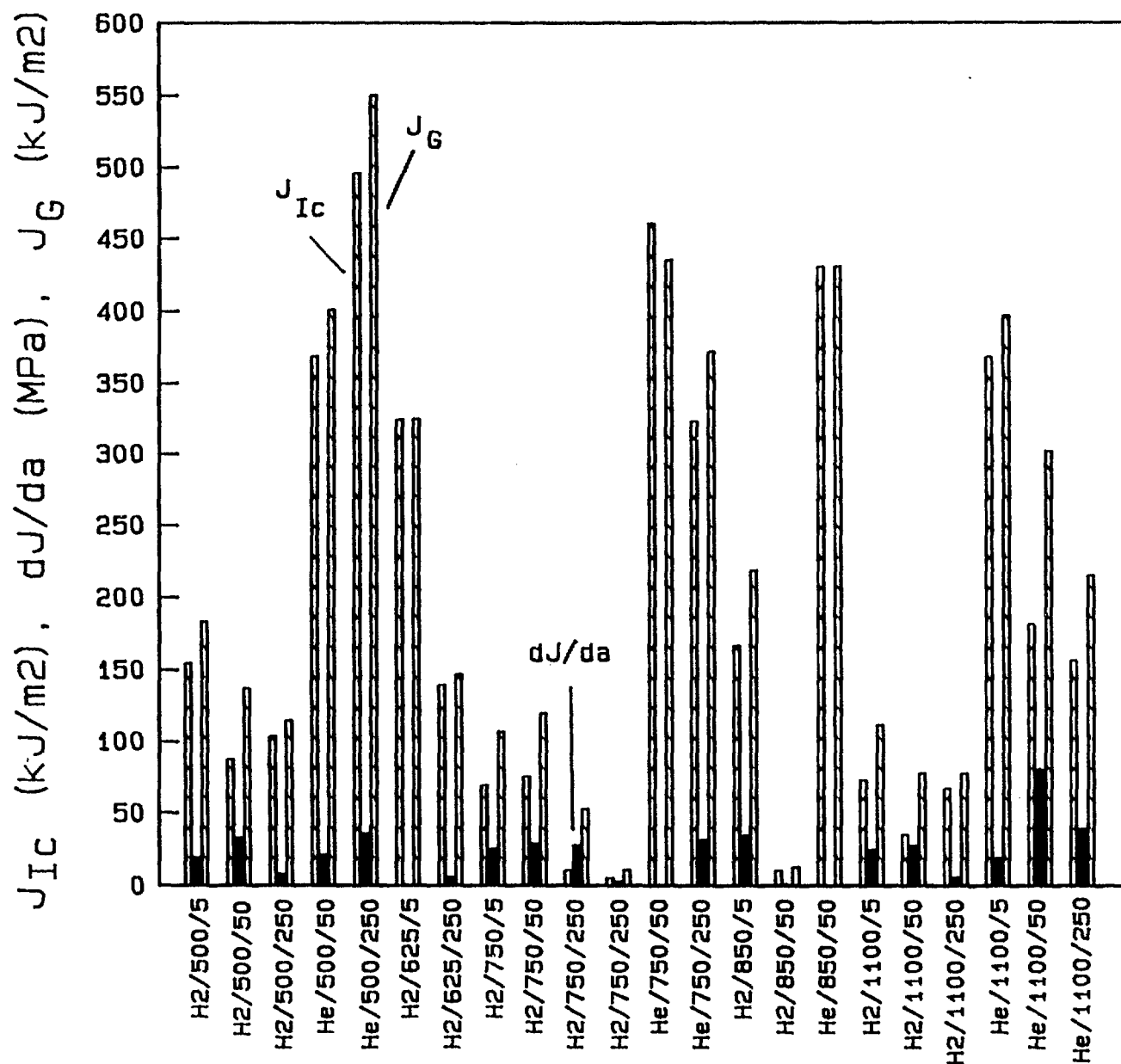


Figure 2.27. Bar-chart showing J_{IC} , dJ/da , and composite parameter J_G for various pre-exposure conditions. For each specimen, the left bar corresponds to J_{IC} , the middle bar to dJ/da , and the right bar to J_G . The legends along the abscissa correspond to environment, temperature ($^{\circ}F$), and time (hours) of pre-exposure. Fracture tests were conducted at room temperature, and the test environment corresponded to the gas in which specimens were pre-exposed.

fracture resistance. This behavior may be contrasted with that of dJ/da , which shows a peak in dJ/da at 260 C (500 F) in hydrogen.

Comparison of results on helium and hydrogen pre-exposed specimens (Figure 2.27) shows that hydrogen pre-exposure at all temperatures led to significant loss in fracture resistance at room temperature. Also, at a given pre-exposure temperature, greater time of exposure to hydrogen led to larger loss in J_G . Figure 2.27 shows that the maximum loss in J_G occurred in the range of 399 to 454 C (750 to 850 F). The microstructure of pre-exposed specimens indicated that hydrogen attack occurred at all temperatures above 399 C (750 F). However, this damage mechanism is insufficient to account for all the observations. For example, activation energy analysis, discussed in Section 2.5.2, showed that the activation energy associated with loss in J_G was well below that for any of the well-known mechanisms of hydrogen attack. Also, it is difficult to explain why J_G was lower for pre-exposures in the range of 399 to 454 C (750 to 850 F) than for pre-exposures at 593 C (1100 F). A number of competing hydrogen degradation mechanisms may have operated at elevated temperatures. The combined effect of these mechanisms on subsequent flow and fracture behavior of the material ahead of the crack tip, loaded at room temperature, may be responsible for the peak in loss of J_G .

Figure 2.28 is a bar chart similar to Figure 2.28 and contains data selected to allow comparison of results from fracture tests conducted at room temperature and at 260 C (500 F). Specimens that were pre-exposed to hydrogen at 593 C (1100 F) for 250 hours and tested at room temperature exhibited a reduction in J_G of approximately 23 percent compared with specimens that were not pre-exposed but tested in hydrogen. The value of J_G was 100.5 kJ/m² at no prior exposure and 77.5 kJ/m² for the 593 C (1100 F) exposure. Tests in hydrogen at 260 C (500 F) show that J_G was reduced from 299.1 kJ/m² at no prior exposure to 77.7 kJ/m² with 1100 F/250 hour pre-exposure in hydrogen. The larger difference in J_G at 260 C (500 F), approximately 74 percent (compared to only 23 percent at room temperature), suggests that the steel is more sensitive to hydrogen-induced damage at 260 C (500 F) than at room temperature. This result may be important in designing future experiments for assessing overpack integrity following service exposure.

2.4.4.5 Fractography

Figure 2.29 is a scanning-electron micrograph of the fracture surface at the crack initiation region for a specimen tested at room temperature in helium, following 50 hours pre-exposure in helium at 593 C (1100 F). The fracture is predominantly cleavage, with small interspersed regions of ductile fracture. Figure 2.30 is a fractograph of the companion specimen which was tested in hydrogen after 50 hours pre-exposure at 593 C (1100 F) in hydrogen. There are large regions of quasi-cleavage, which are different in appearance from the clean cleavage regions observed in Figure 2.29. A significant number of fine voids may be observed on the fracture surface in Figure 2.30. These voids were probably formed by hydrogen attack at elevated temperatures.

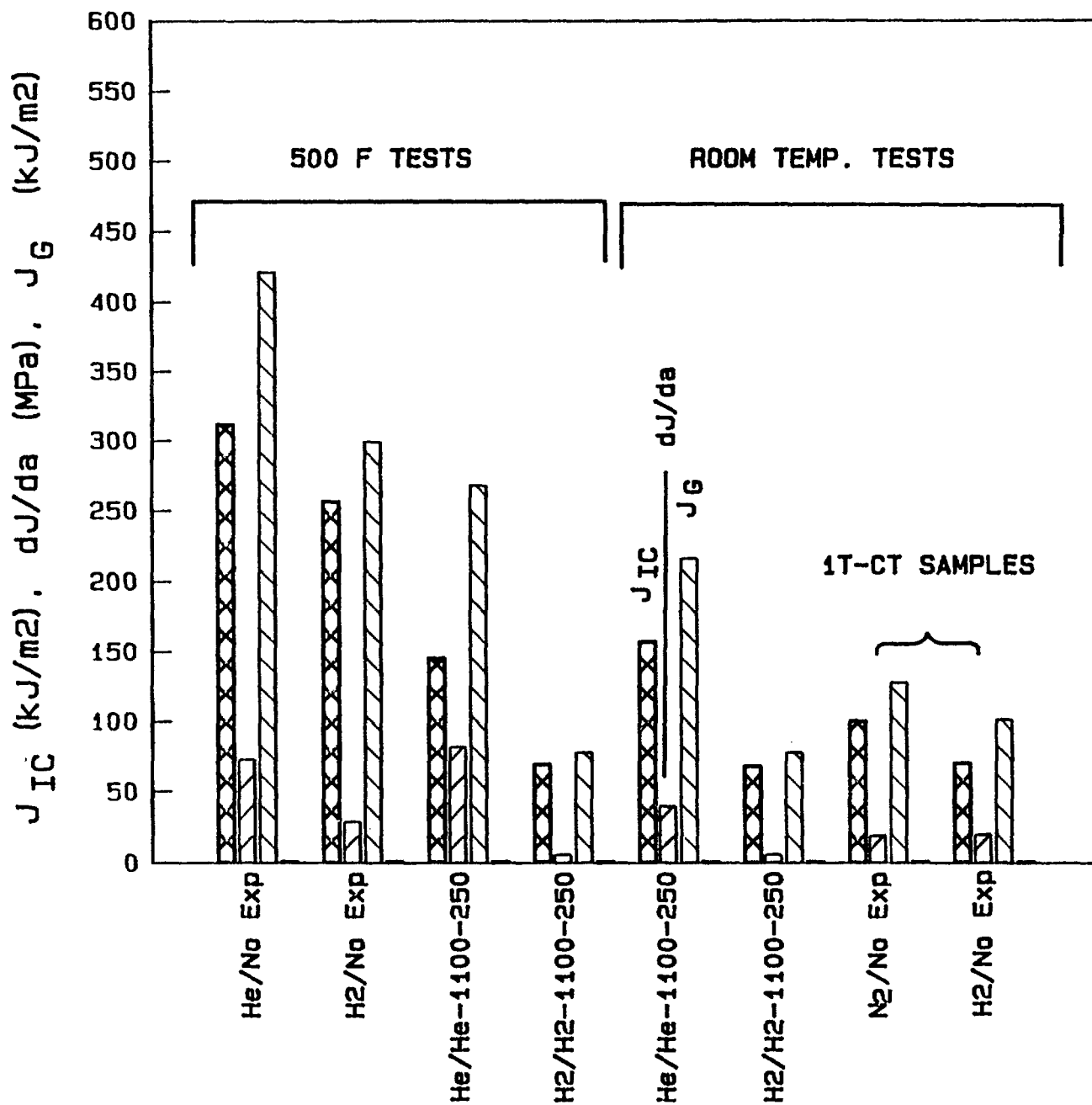


Figure 2.28. Bar-chart showing comparison of J_{IC} , dJ/da , and J_G for specimens tested at room-temperature or at 260 C (500 F).

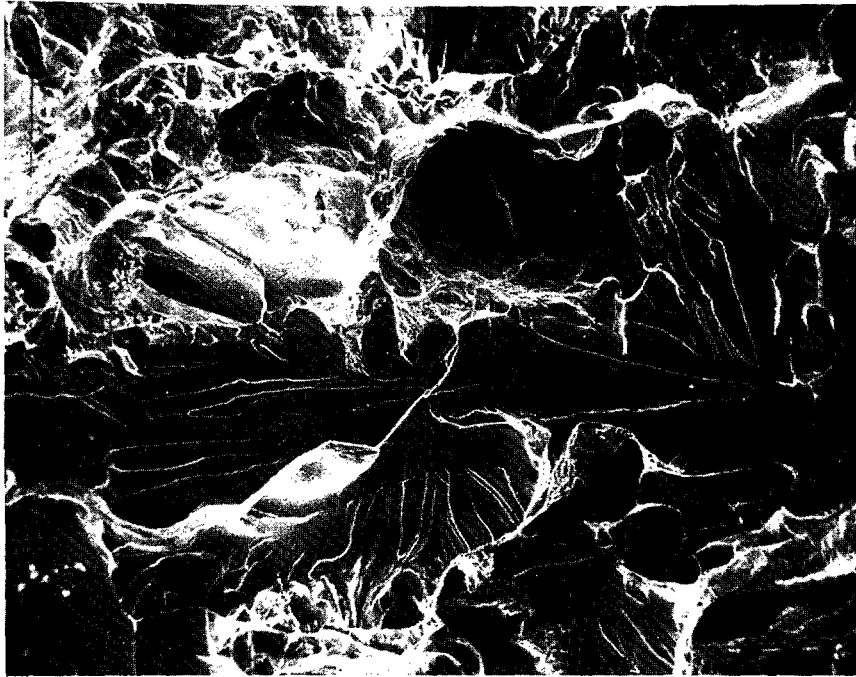


Figure 2.29. Scanning electron micrograph of fracture surface of specimen, pre-exposed to helium at 1100 F for 50 hours, and subsequently fracture tested in helium at room temperature. Magnification 250X.

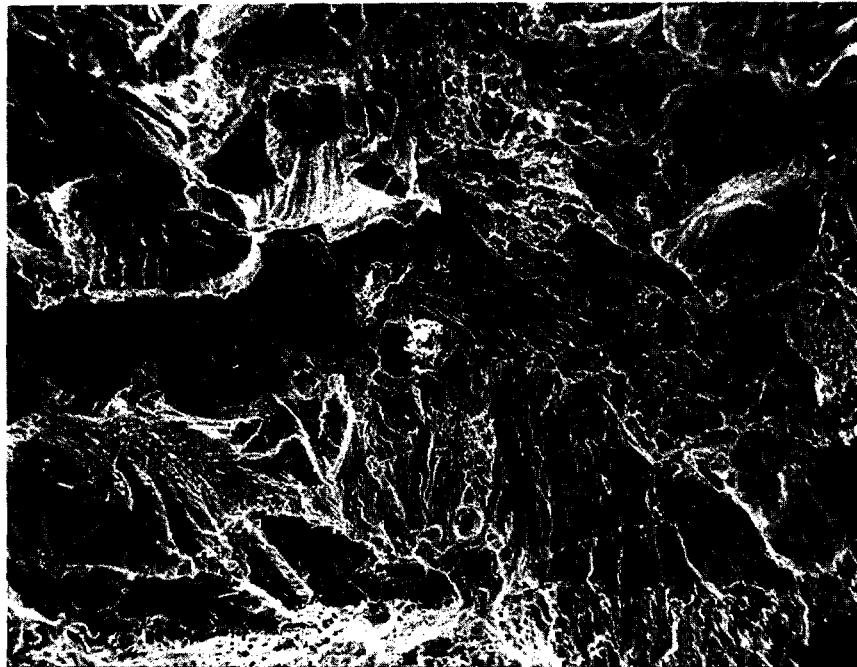
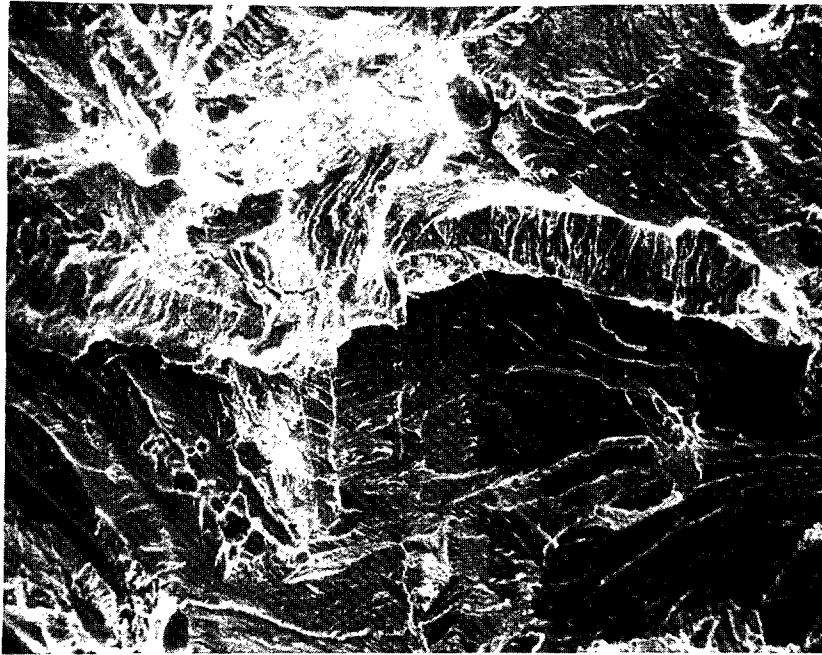


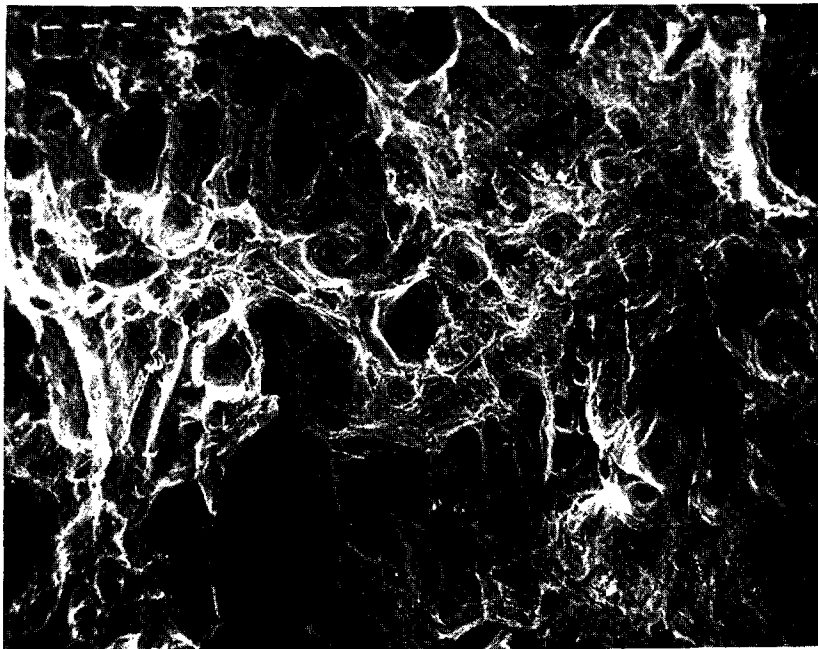
Figure 2.30. Fracture surface of specimen, pre-exposed to hydrogen at 1100 F for 50 hours, and subsequently fracture tested in hydrogen at room temperature. Magnification 250X.

Figure 2.31 presents fractographs from the tearing (crack-growth) regions of specimens that were tested in hydrogen following 250 hours pre-exposure in hydrogen at temperatures of 260 and 399 C (500 and 750 F). With pre-exposure at 260 C (500 F), fracture is quasi-cleavage with fine tongues on the cleavage facets (Figure 2.31a). The fracture surface also contains a number of voids; it is not clear whether those voids were solely a result of hydrogen exposure at 260 C (500 F). Microstructures away from the fracture surface of exposed specimens (to be discussed later) indicated no optically resolvable void formation at 260 C (500 F), but incipient voids may have been present which became visible with the plastic deformation associated with fracture testing.

Some quasi-cleavage is also observed following 250 hours of exposure in hydrogen at 399 C (750 F). However, the fracture is primarily microvoid coalescence, with some isolated facets which may be a result of fracture along pearlite-colony boundaries. Such regions are shown in Figure 2.31b. The same trend continues with pre-exposure at 593 C (1100 F) in hydrogen. Figure 2.32 shows that the extent of quasi-cleavage was reduced, and fracture was predominantly microvoid coalescence. The voids on the fracture surface appear to be associated with prior-austenite grain boundaries, although the fracture was ductile rather than brittle intergranular. The specimen in Figure 2.32 was largely de-carburized during pre-exposure in hydrogen, and



(a) 500 F pre-exposure



(b) 750 F pre-exposure

Figure 2.31. Fracture surface of specimen, pre-exposed to hydrogen for 250 hours at various temperatures, and subsequently fracture tested at room temperature in hydrogen. Magnification 170X.

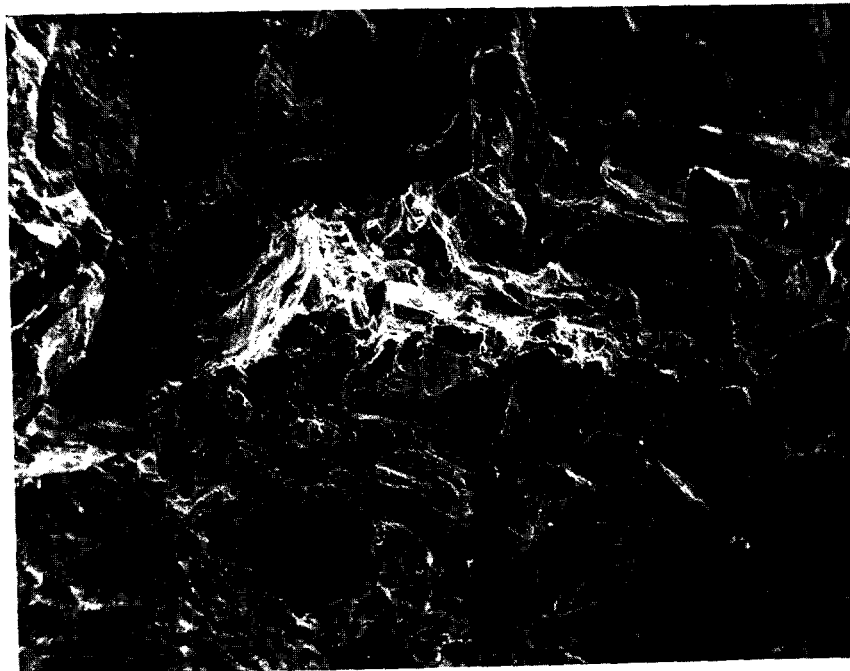


Figure 2.32. Fracture surface of specimen, pre-exposed to hydrogen at 1100 F for 250 hours, and subsequently fracture tested in hydrogen at room temperature. Magnification 150X.

hence the enhanced growth of voids may be expected as a result of the reduced flow stress of the material accompanying decarburization.

2.4.4.6 Microstructure

Figure 2.33 shows the microstructure near the fracture surface of a specimen that had been exposed to hydrogen at 260 C (500 F) for 250 hours, and tested at room temperature. There is no discernible difference between this microstructure and that of the unexposed material (Figure 2.5a). The top white region of the micrograph corresponds to a nickel coating which was applied to the fractured surface prior to sectioning to retain the edge during metallographic polishing. Optical observations did not indicate any signs of bubble formation following 250 hours of exposure at 260 C (500 F). Deformation-induced voids are seen adjacent to the fracture surface, and their concentration is greater compared to a specimen which was exposed to helium at 593 C (1100 F) for 50 hours. These observations seem to imply that pre-exposure at 260 C (500 F) aids in void formation during crack growth at room temperature. This may explain the monotonic decrease in J_G following exposure in hydrogen at 260 C (500 F).

Figure 2.34 is a photomicrograph near the fracture surface of a specimen which was pre-exposed for 250 hours in hydrogen at a temperature of 399 C (750 F). A large number of crack-like cavities may be seen throughout the specimen. Most interestingly, the cavities do not seem to be associated

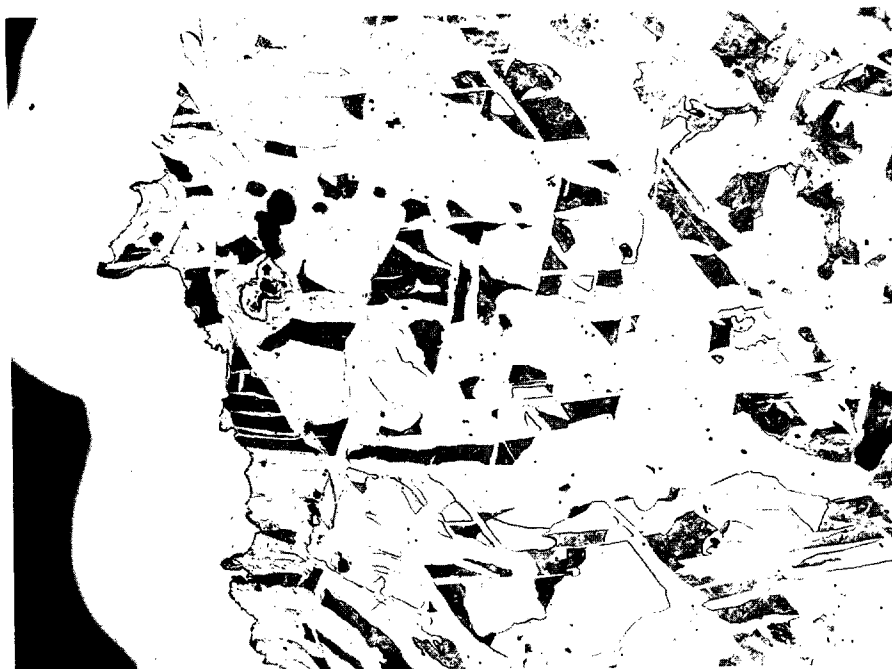


Figure 2.33. Microstructure of a specimen pre-exposed in hydrogen at 260 C (500 F) for 250 hours. The white band towards the top of the micrograph corresponds to a nickel coating which was applied to the fracture surface before sectioning. Magnification 50X.

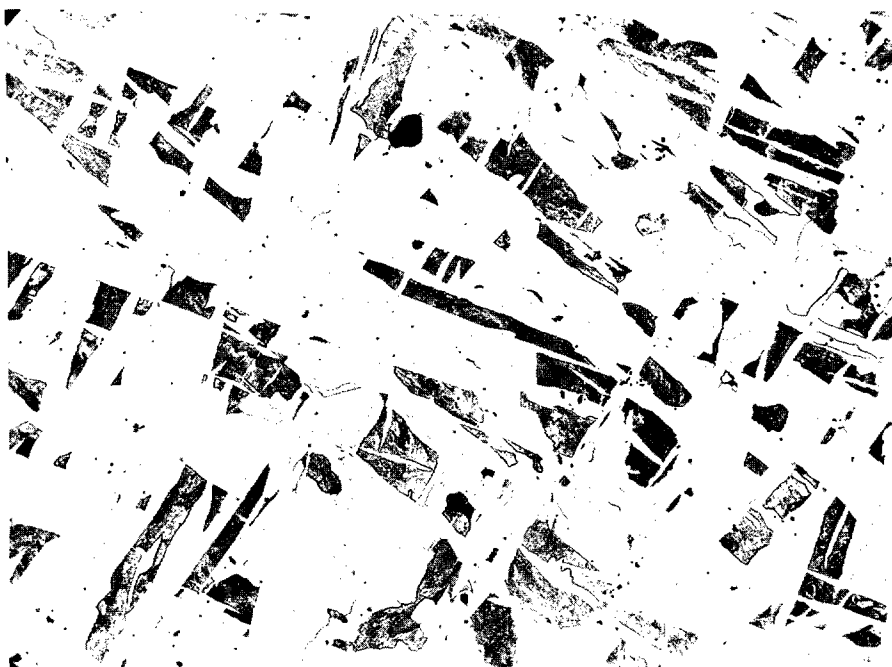


Figure 2.34. Microstructure of a specimen pre-exposed in hydrogen at 399 C (750 F) for 250 hours. Magnification 50X.

with large pearlite colonies. This observation is at first surprising, considering that almost all theories of elevated temperature hydrogen attack (Ref. 2.16) involve some form of carbide dissolution. Figure 2.35 is a high-magnification photomicrograph that better illustrates the phenomenon. Careful examination of the virgin microstructure showed that the clean cast steel contained a large number of stringer-like carbides along grain boundaries. Figure 2.34 shows some of those carbide stringers which have not been attacked by hydrogen (arrows). Since these stringers lie along boundaries, they dissolve readily and give rise to methane bubbles. Also, because of the stringer shape, the resulting cavities are crack-like. This explains why the specimen showed a preference for crack-like cavities, which were not associated with large pearlite colonies. However, once these cavities were formed, cavities nucleated adjacent to larger pearlite colonies, as is described in the next paragraph. Thus, it may be worthwhile to take steps to reduce the concentration of stringer-like carbides at grain boundaries in the material--although their removal may only delay degradation because pearlite-colony boundaries would still be available to nucleate cavities.



Figure 2.35. Crack-like cavities observed in the microstructure of a specimen, exposed to hydrogen at 399 C (750 F) for 250 hours. Many of these cavities are apparently unassociated with larger pearlite colonies. Magnification 400X.

Figure 2.36 is a photomicrograph near the fracture surface of a specimen pre-exposed in hydrogen for 250 hours at 593 C (1100 F). The crack-initiating region is in the middle of the micrograph. The figure shows extensive deformation and void formation associated with fracture. Pearlite colonies cannot easily be distinguished in this figure since the steel has

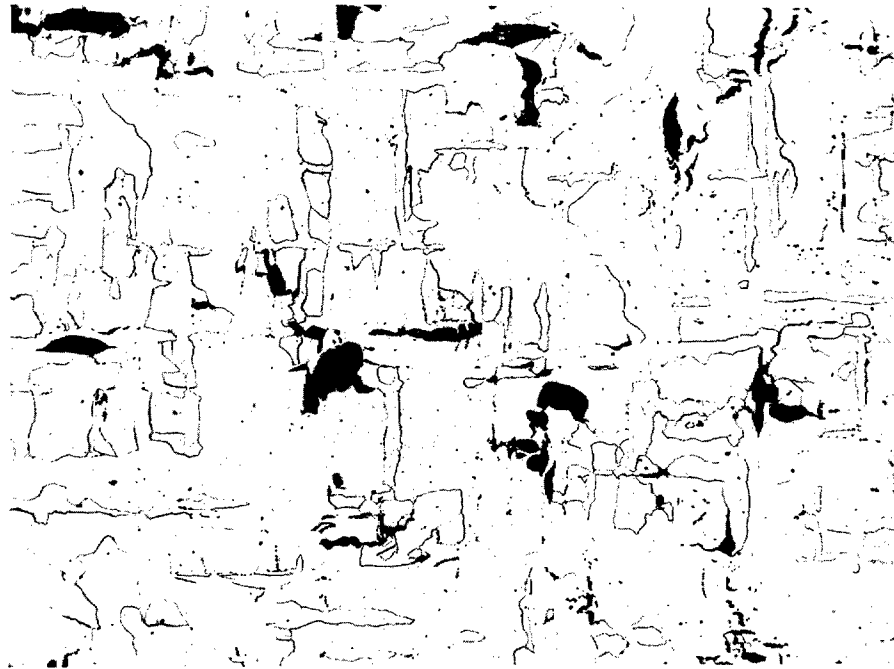


Figure 2.36. Microstructure near the fracture surface of a specimen, pre-exposed to hydrogen at 1100 F for 250 hours, and subsequently fracture tested in hydrogen at room temperature.

been almost completely decarburized. Large voids have opened up at boundaries of prior pearlite colonies and ferrite grains. Hardness measurements indicated that this steel had a hardness of only Rockwell B25, compared with a hardness of Rockwell B59 for the as-cast material.

Figure 2.37 shows a high-magnification photomicrograph of cavities nucleating at prior-austenite and ferrite-pearlite boundaries. Cavities are largely absent from within the grains, confirming that cavity formation involves carbide (that is, the cementite in pearlite) dissolution, the transport of free carbon to grain boundaries, and their subsequent reaction with hydrogen to form nonsoluble methane bubbles at grain boundaries. Direct support of this mechanism is obtained from photomicrograph Figure 2.38, which shows a carbide-free zone adjacent to a ferrite-pearlite boundary. Such direct evidence of the cavity-formation mechanism was not found in the technical literature. The clear demarcation and smooth boundary of the carbide-free zone is also noteworthy. The smooth boundary seems to imply that, among the various reactions that lead to bubble formation, carbon transport is probably rate limiting. Thus, if any cementite ribbon were to dissolve preferentially, a larger distance from grain boundary would reduce diffusion-controlled carbon flux within the carbide-free zone; this would consequently slow down the cementite dissolution. On the other hand, if carbide dissolution were rate limiting, then carbon from any excess dissolution of carbide would be immediately transported to the grain boundary, and hence the carbide-free zone could have a rough boundary. For a similar



Figure 2.37. High-magnification photomicrograph of a specimen exposed to hydrogen at 593 C (1100 F) for 250 hours. Cavities may be observed nucleating at prior-austenite and ferrite-pearlite boundaries. Magnification 400X.

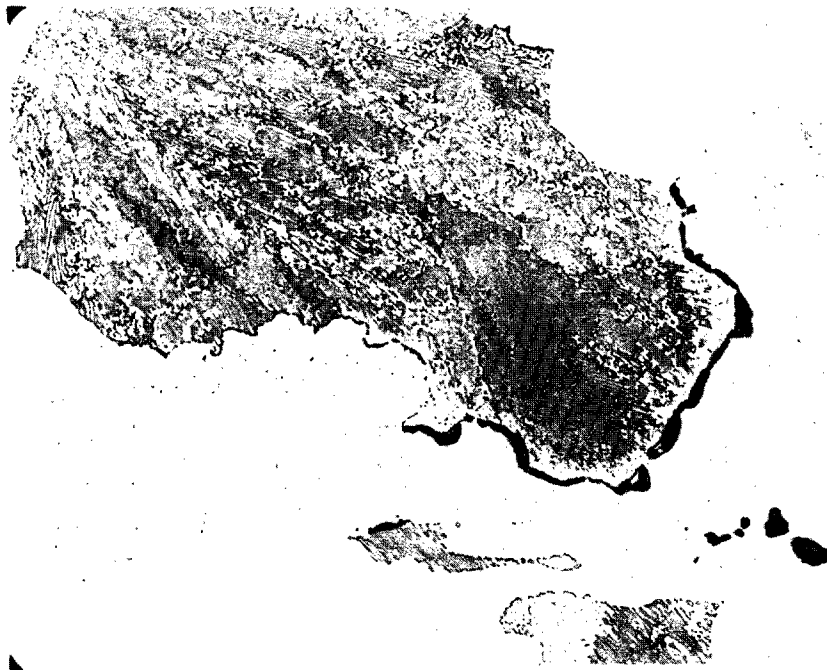


Figure 2.38. Cavities nucleating along ferrite-pearlite boundary, for a specimen exposed to hydrogen at 750 F for 250 hours. The uniform width of pearlite-free zone adjacent to the cavi-tated boundary is noteworthy. Magnification 750X.

reason, methane reaction-limited bubble formation also seems unlikely. Further research into aspects of bubble formation is outside the scope of this investigation.

2.5 Discussion

2.5.1 Mechanical Degradation Analysis

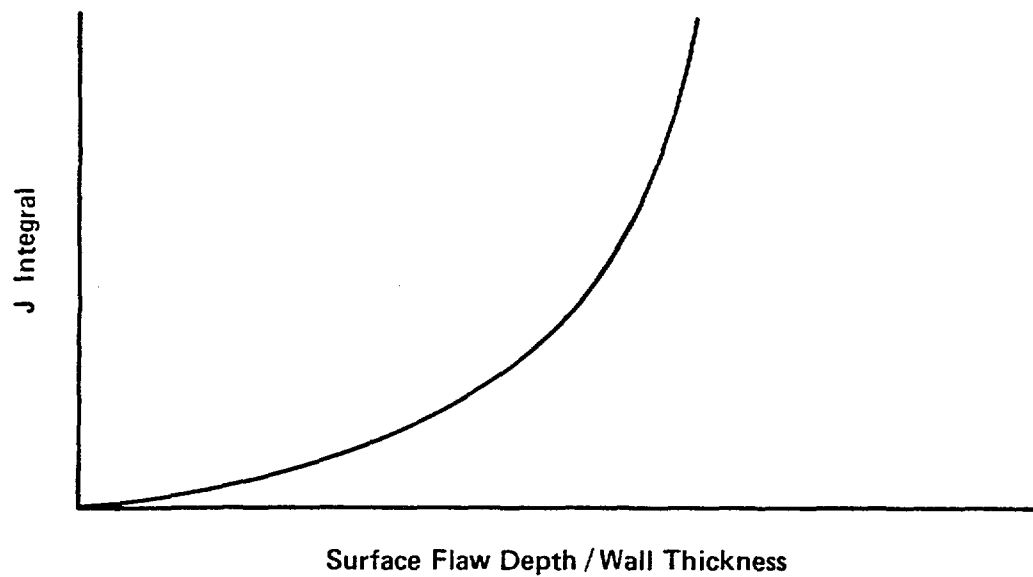
The most commonly used method for assessing degradation of mechanical properties is the threshold stress intensity, which is designated K_{ISCC} when the degradation occurs by stress-corrosion cracking and K_{IH} when the degradation occurs by hydrogen embrittlement. The value of K_{ISCC} or K_{IH} is influenced by the environmental conditions and by the compatibility of the container material with the environment. When the applied stress intensity, K_I (which depends on the dimensions of the waste container, the applied stresses, and the depth, length, shape, and location of the largest pre-existing flaw such as at a weld), exceeds K_{ISCC} or K_{IH} for the repository conditions, subcritical crack growth occurs. Assuming the applied stresses are constant, the flaw or crack will grow and the value of K_I will increase until it reaches the value K_{IC} , which is the critical stress intensity or fracture toughness. The value of K_{IC} is a material property which is independent of environment. When K_I exceeds K_{IC} , unstable crack growth occurs. Thus, stress-corrosion cracking and hydrogen embrittlement can induce premature growth of flaws at

stress intensities below the K_{IC} , and this subcritical crack growth can lead to the development of a critical flaw which grows in an unstable manner when K_I reaches K_{IC} .

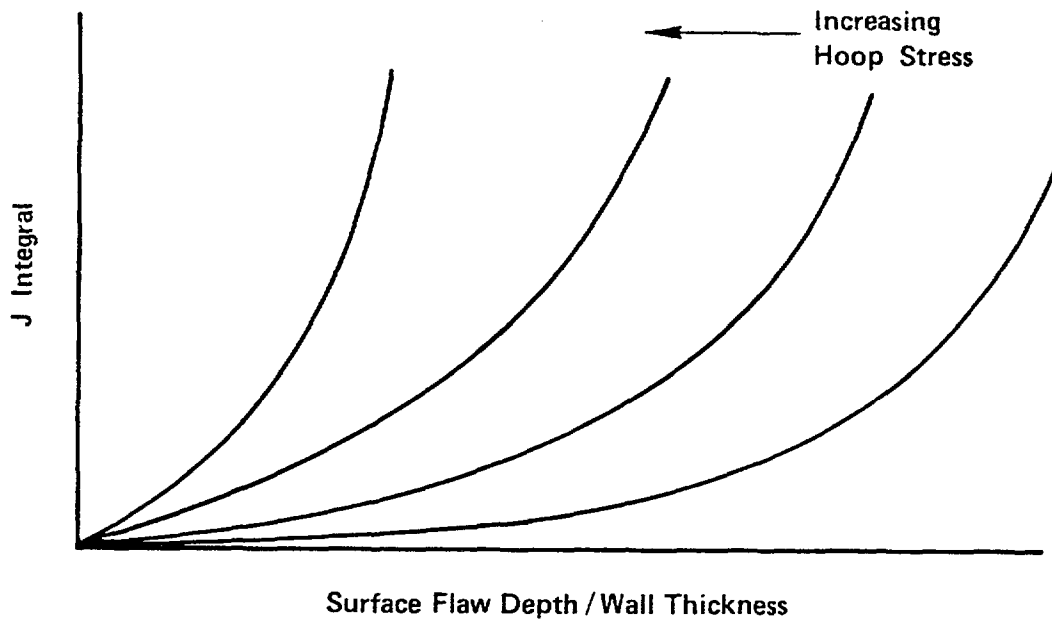
To apply the threshold stress intensity concept to an assessment of container degradation requires an understanding of the influence of environmental variables on K_{ISCC} and K_{IH} , knowledge of the environmental conditions in a repository, and calculation of the applied K_I values at pre-existing flaws in the container. The first two issues have been addressed in this program and in other investigations. Calculation of the applied K_I values for cylindrical components with surface flaws has been progressing for over ten years and is relatively straightforward. The principal limitation of such an approach is that the calculations assume that the materials are linear-elastic, and that virtually no plastic deformation takes place. However, for most engineering materials, this is not the case. Therefore, more recent studies in fracture have dealt with elastic-plastic materials through the use of the J-integral. With a J-integral approach, appreciable crack-tip plastic deformation, which acts to retard flaw growth, can be accounted for. This is the approach that has been taken in the hydrogen-embrittlement studies.

In a laboratory J-integral experiment, two properties are determined. One is J_{IC} , which is related to K_{IC} for elastic materials and represents the work required to initiate a crack from a pre-existing flaw. The second property represents the additional work required to cause that crack to grow in a ductile material. Frequently, this property is referred to as the tearing resistance, dJ/da , where a is the crack length. Alternatively, the tearing modulus, which is proportional to the tearing resistance but is normalized to the material's tensile properties, is used. In a ductile material, a crack is initiated when the applied J-integral exceeds J_{IC} . However, the crack will remain stable unless the applied J-integral is increased further. The crack grows in a steady manner with increasing applied J-integral until the increase in applied J-integral with flaw growth is greater than the tearing resistance for the material; thereafter, crack growth is unstable. Thus, container integrity can be degraded if the value of J_{IC} and/or dJ/da are reduced by hydrogen embrittlement.

For a cylindrical structure with an axially oriented surface flaw, an approximation of the relationship between the applied J integral to the flaw size is shown schematically in Figure 2.39a. As the flaw grows, the J-integral increases, and the J-versus-flaw-depth curve becomes steeper. Figure 2.39b shows how the applied circumferential, or hoop, stress influences that relationship. In general, for a given flaw depth, a high hoop stress gives a high J-integral and a steeper curve. A crack will initiate from a pre-existing flaw when the flaw depth and applied hoop stress combine to produce an applied J-integral that exceeds J_{IC} for the container material and its environmental conditions. Instability will occur if the slope of the J-versus-flaw-depth curve in Figure 2.39 exceeds the tearing resistance. In that regard, reductions of the tearing resistance by hydrogen embrittlement probably are more significant to container integrity than are reductions in J_{IC} .



a. Effect of Flaw Depth on J Integral



b. Effect of Hoop Stress on J Integral

Figure 2.39. Generalized representations of the applied J integral as a function of flaw depth and applied hoop stress for a cylinder with an axial surface flaw.

Application of a J-integral approach to assessing container degradation requires an understanding of the influences of environmental variables on J_{IC} and dJ/da , knowledge of the repository conditions, and calculation of the applied J-integral as a function of flaw dimension, location, and orientation, and applied stress. The J-integral aptly describes ductile engineering materials. However, at present, determination of the applied J-integral for various structures is not straightforward. Some progress in analytical methods has been made in recent years, but extensive simplifying assumptions are usually required. Therefore, the approach in this program has been to assess the potential for degradation of container integrity by hydrogen embrittlement primarily by comparing fracture-toughness properties (J_{IC} and dJ/da) in a hydrogen environment with those in an inert environment (nitrogen or helium).

2.5.2 Summary of Hydrogen Effects

The results of the room temperature tensile and fracture tests have shown that fracture toughness properties are much more sensitive to hydrogen effects than tensile properties. This may be observed by comparing the results of Tables 2.6 and 2.9. These results imply that future investigations should consider fracture toughness measurements for assessing integrity of containers under the thermal-mechanical-environmental conditions anticipated in service. Conventional testing, involving tensile testing in hydrogen environments, may not be sensitive enough to determine the effects of hydrogen. Also, because the primary concern is container integrity, design and life assessment should be based on fracture mechanics considerations rather than on simply tensile strengths and reductions in area.

Table 2.9 shows that the maximum decreases in J_{IC} due to hydrogen occur for the cast-wrought, cast-annealed, doped-wrought and doped-annealed steels. Table 2.6 shows that these are also the steels which have the largest tensile strengths. Such a correlation between J_{IC} and tensile strength can be rationalized on the basis of the well-known observation that hydrogen embrittlement is greater for materials with larger tensile strengths. It may be noted from Table 2.6 that hydrogen has little effect on tensile properties of these steels. On the other hand Table 2.9 clearly points out that the higher strength steels are much more prone to hydrogen embrittlement.

Table 2.9 also shows that the annealed steels are much more sensitive to hydrogen embrittlement than the as-cast steels. The reason for this is not very clear at present, although redistribution of residual impurity could play a role in the case of the doped steel. In the case of the clean cast steel the reason is much less clear. In any case, the results point out that thermal history and heat treatment of cast steels and heat-affected zones are important parameters that govern sensitivity to hydrogen embrittlement. These parameters need to be carefully studied while assessing container integrity.

Tables 2.6 and 2.9 show that residual impurity levels seem to have less effect in hydrogen embrittlement of as-cast steels, compared to wrought steels. This would imply that commercial purity levels of cast steel may be sufficient for fabricating repository containers. However, the tests on

doped steels were limited to short-time, room-temperature tests. Tests involving long-time, elevated-temperature exposure to hydrogen are necessary to ascertain that commercial purity levels are not worse than high purity levels for the long-term integrity of the containers.

2.5.2.1 Discussion on Short-Term and Long-Term Effects of High-Pressure Hydrogen at Moderately Elevated Temperatures

The experiments with elevated-temperature, high-pressure hydrogen have shown a significant effect of long-term exposure to hydrogen at moderately elevated temperatures. The specific scenario under consideration was one in which exposure at conditions below the Nelson curve (that is, where hydrogen attack has not been observed in carbon steels) results in incipient damage, and subsequent stressing at lower temperatures (for example, after many years in the repository) results in enhanced flaw growth. This scenario could lead to reduced container integrity.

The results of the fracture toughness tests show that pre-exposure to 6.9 MPa (1000 psi) hydrogen has significant effects on J_{IC} , dJ/da , and the composite fracture parameter J_G . It may be remembered that J_{IC}^* is a measure of the work needed for crack initiation, dJ/da represents the material's resistance to further crack propagation once a crack is initiated, and J_G is a composite parameter representing the J-integral that must be exceeded to initiate and extend the crack beyond 1.5 mm, or approximately 10 pearlite colonies. Since J_G incorporates both crack initiation and crack-propagation events, it should be a useful quantitative measure for assessing material degradation due to exposure in hydrogen.

It was observed that J_G decreased continuously with the time of exposure at 260 C (500 F). This behavior would suggest some form of hydrogen embrittlement or incipient attack even at 260 C (500 F). This conclusion indicates that damage was not classical hydrogen attack as described by the Nelson curves for carbon steel (Refs. 2.11, 2.12). Figure 2.40, which is reproduced from Figure 4 of API Publication No. 941 (Ref. 2.12), shows that no hydrogen attack has been reported for exposures up to 10,000 hours for carbon steels exposed to 6.9 MPa (1000 psi) hydrogen at 260 C (500 F). On the other hand, significant degradation in fracture properties was observed in the present study for exposure times as low as 250 hours. Throughout this study it has been shown that crack-growth experiments are more sensitive to hydrogen degradation effects than conventional tensile tests. More importantly, there was a very high rate of reduction in J_G with exposure time at 260 C (500 F). These results indicate that there is the possibility of significant degradation of the overpack integrity if hydrogen is generated in the repository, although further studies are needed to define limiting temperature/hydrogen partial pressure conditions for degradation.

*Alternately, J_{IC} controls the level of stress and strain distribution ahead of the crack tip, for initiation of crack growth.

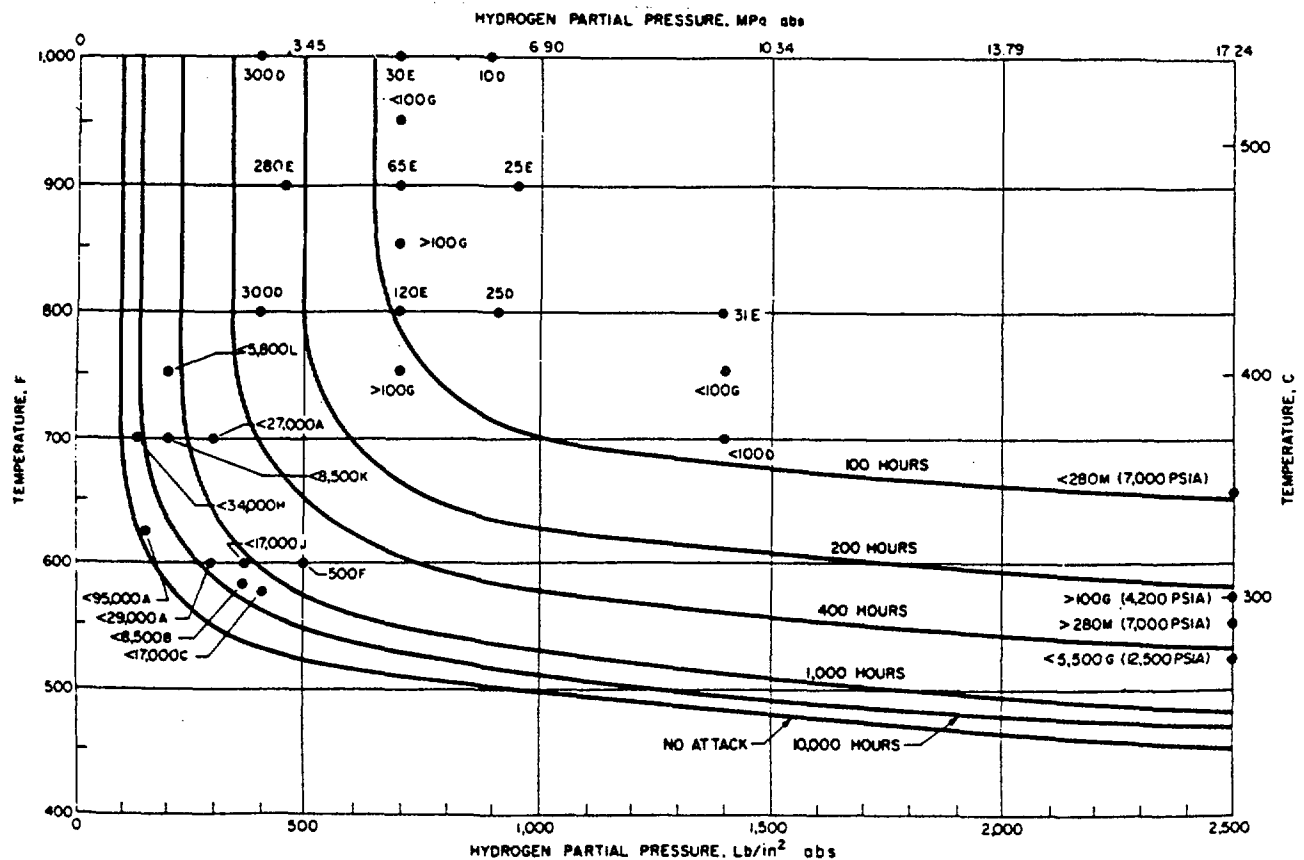


Figure 2.40. Time for attack of carbon steel in hydrogen service (Figure 4 of Ref. 2.12, API Publ. 941).

Thus, the results of the present experiments suggest that, for the case of a waste container, selection of materials based on Nelson curves may not provide conservative estimates of hydrogen temperature-pressure conditions which assure no failure due to long-term hydrogen exposure. The presence of stress-concentrating flaws--coupled with mechanical and residual stresses, steadily decreasing repository temperatures, and increasing hydrogen pressures--may aggravate hydrogen degradation and must be taken into account. Consequently, in selecting and evaluating container materials it is necessary to determine appropriate fracture mechanics parameters, following various periods of hydrogen exposure, to assure that fracture resistance is not degraded by long periods of exposure at 260 C (500 F). This is an important recommendation based on present results.

Comparison of the results of fracture toughness tests conducted on unexposed specimens at room temperature and at 260 C (500 F) (Figure 2.28) indicate that the material is more sensitive to hydrogen degradation at 260 C (500 F). The reduction in short-term fracture resistance at 260 C (500 F) seems to be a combination of elevated temperature hydrogen embrittlement and incipient hydrogen attack, aided by higher hydrogen diffusivity at 260 C (500 F) compared to room temperature. Experiments with pre-exposed specimens also indicate that the reduction in fracture resistance is greater when J_{IC} tests are conducted in hydrogen at 260 C (500 F) than when they are conducted at room temperature. Accordingly, it may be better to assess long-term damage by conducting fracture toughness tests on pre-exposed specimens at 260 C (500 F). This conclusion is, of course, based on only two extreme exposure conditions--namely, no exposure, and exposure at 593 C (1100 F) for 250 hours. Further experiments involving lower temperatures of pre-exposures are necessary to verify the general validity of this conclusion.

Figure 2.41 is a series of constant-temperature plots of J_G versus time of exposure in hydrogen for the pre-exposure temperatures used in this study. The overall trend is that damage, measured in terms of the decrease in J_G , increases with time of exposure. However, the rates are different at different temperatures, suggesting different damage kinetics at different temperatures. Also, at 1100 F there appears to be a saturation in the extent of damage with time, which appears to be related to gross hydrogen attack, although further study is necessary to verify this apparent behavior. It should be noted that 250 hours of exposure at 593 C (1100 F) led to extensive decarburization. Therefore, reductions in toughness by hydrogen attack probably were balanced by improvements in ductility due to decarburization.

For the purpose of comparing kinetics, it was assumed that damage increases linearly with time. Accordingly, a linear least-squares fit was used at each temperature to determine rates of decrease of J_G with time of exposure. The only exception was at 593 C (1100 F), where the data point at 250 hours was neglected due to extreme decarburization of the sample; as indicated previously, gross hydrogen attack was not an issue in this study. The rate of decrease of J_G for each exposure temperature is tabulated in Table 2.14, and also is plotted versus temperature of exposure in Figure 2.42. It is difficult to explain the peak in the rate of damage that is observed at 454 C (850 F). The data at that temperature were limited and may have been insufficient to accurately estimate the rate of damage. However, Figure 2.27 clearly shows that hydrogen pre-exposures were most damaging at 399 and 454 C (750 and 850 F), so that some form of peak in damage rate in the temperature regime may indeed exist.

A possible explanation for a peak in damage rate is the competition of hydrogen embrittlement with hydrogen attack. Pre-exposure at elevated temperatures could soften the material due to some form of decarburization, and the lower flow stress would make the material less sensitive to hydrogen embrittlement at room temperature. This behavior is indicated by curve I in Figure 2.43. On the other hand, as the temperature of exposure is increased, a greater number of cavities would form at ferrite-pearlite boundaries. Such cavitation damage would reduce ductility and fracture resistance at room temperature, with the damage increasing with greater pre-

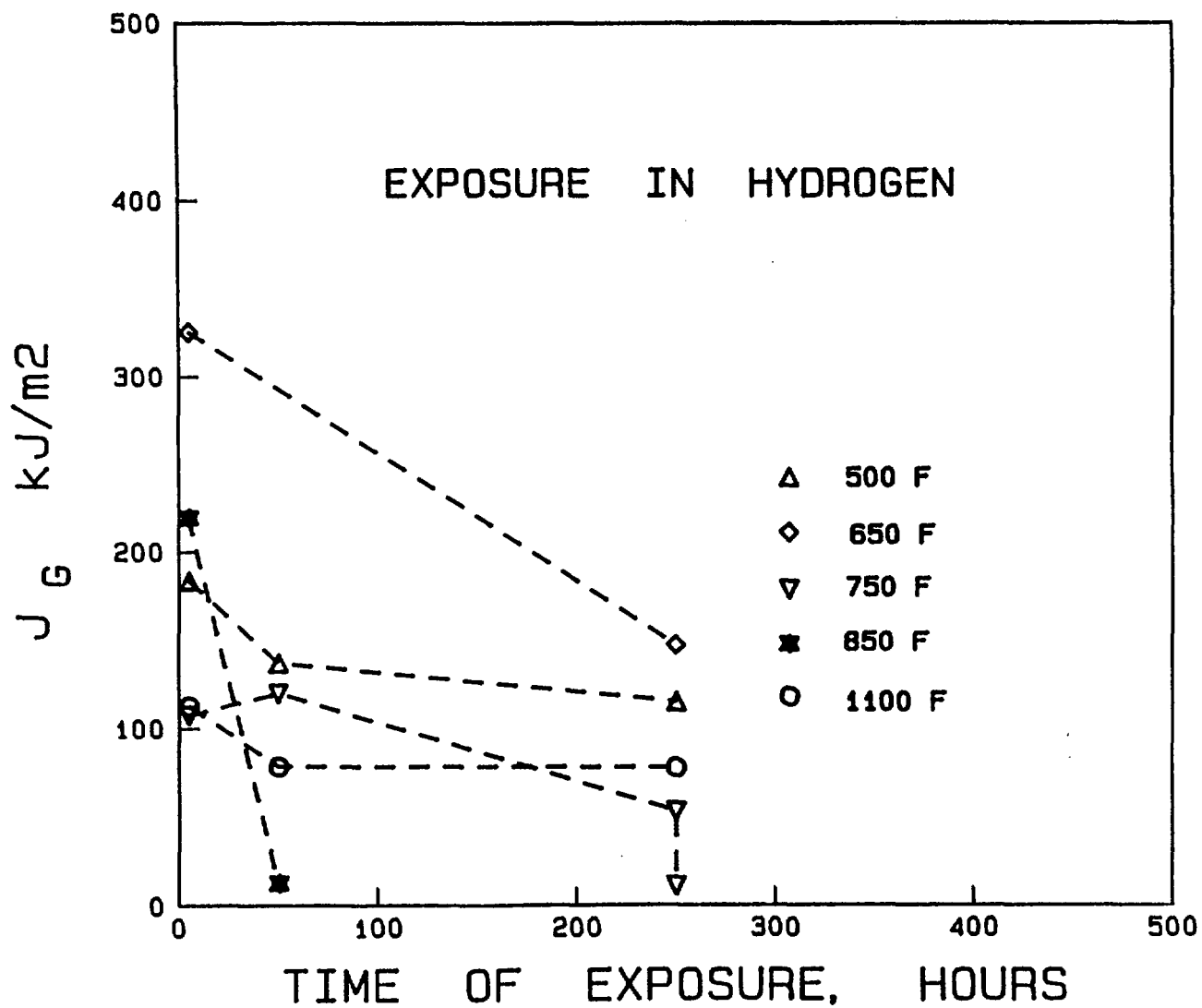


Figure 2.41. Plot of J_G versus times of pre-exposure in hydrogen at various temperatures. All the specimens were fracture tested in hydrogen at room temperature.

Table 2.14. Rate of decrease of J_G at various temperatures, for specimens pre-exposed to hydrogen and subsequently fracture tested at room temperature.

Temperature of Pre-exposure (F)	dJ_G/dt (kJ/m ² hr)
500	0.23
625	0.75
750	0.26
850	4.59
1100	0.76

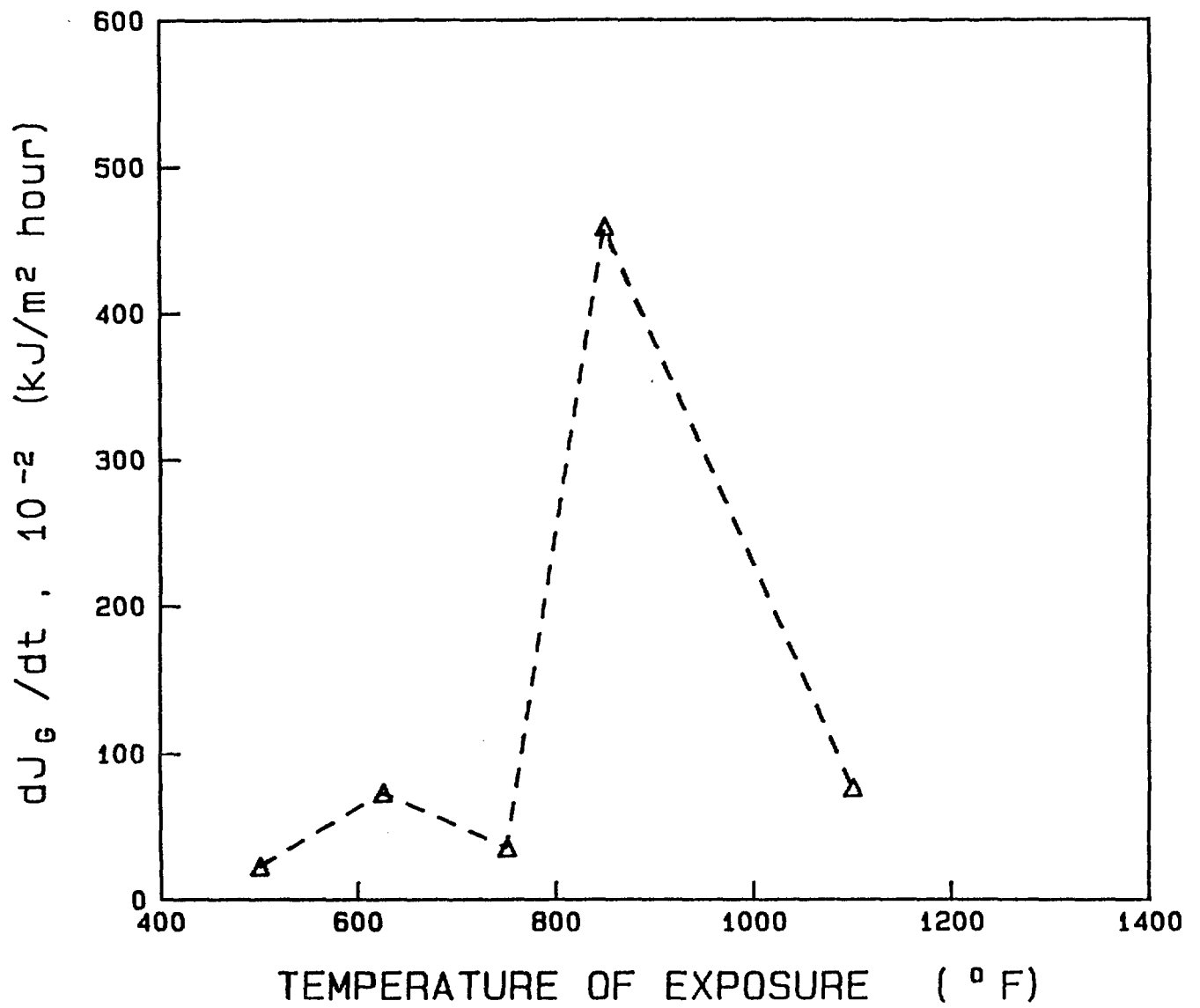


Figure 2.42. Rate of decrease in JG versus temperature of pre-exposure in hydrogen.

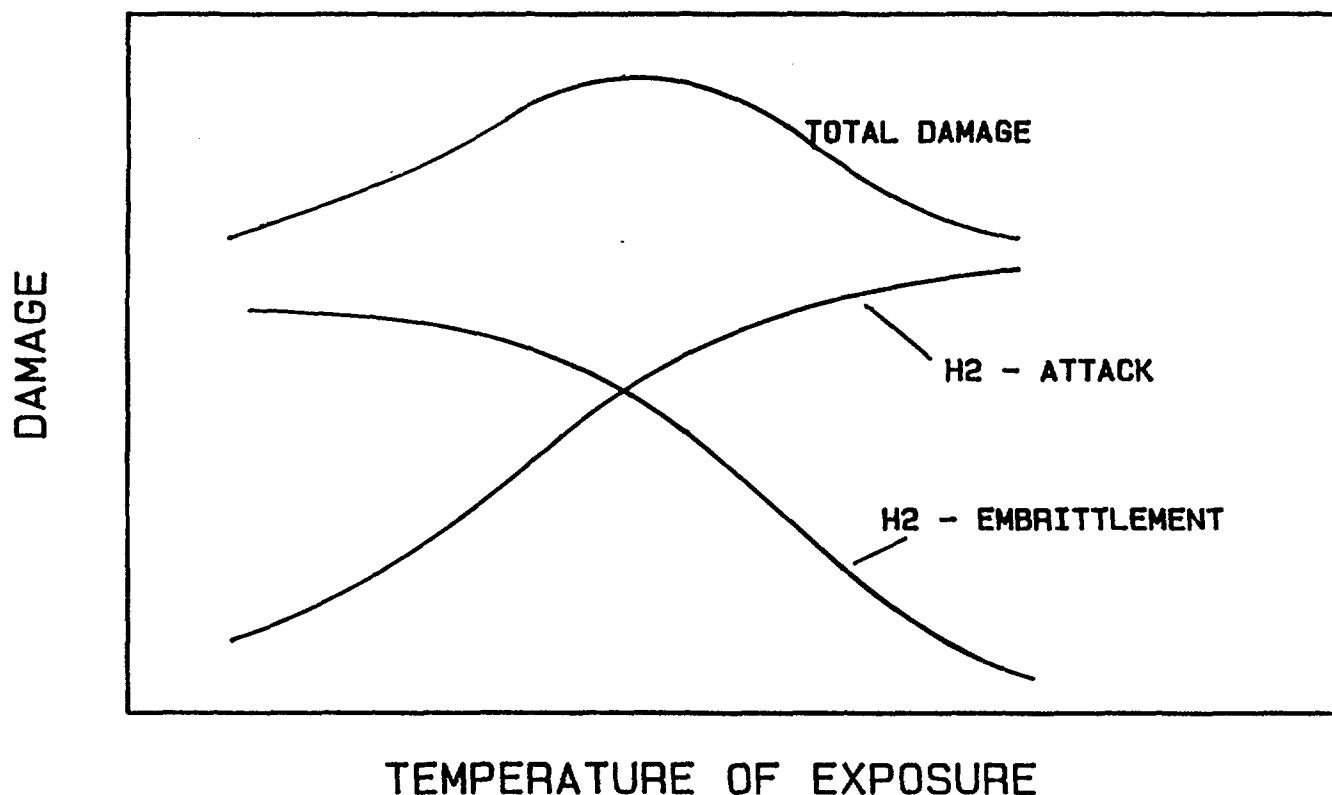


Figure 2.43. Sketch, illustrating possible reason for the observed peak in rate of damage (measured in terms of J_G/dt) of specimens pre-exposed to hydrogen at various temperatures, and subsequently fracture tested in hydrogen at room temperature.

exposure temperatures. This behavior is illustrated by curve II in Figure 2.43. The sum total of these effects would give rise to a peak in degradation, as is illustrated by curve III in Figure 2.43. Further investigation into the mechanism was outside the scope of this research. Nevertheless it should be useful to know the occurrence and temperature of a similar peak when selecting and evaluating container material.

In Figure 2.44 the logarithm of the rate of damage, which is represented by dJ_G/dt , is plotted versus the inverse of temperature. The purpose of such a plot is to determine the activation energy associated with a rate-limiting reaction process. In the present case, the activation energy may help in identifying the metallurgical process which is responsible for degradation in fracture properties. Figure 2.44 shows quite a large scatter, suggesting that more than one mechanism, with different temperature dependencies, may be operating simultaneously.

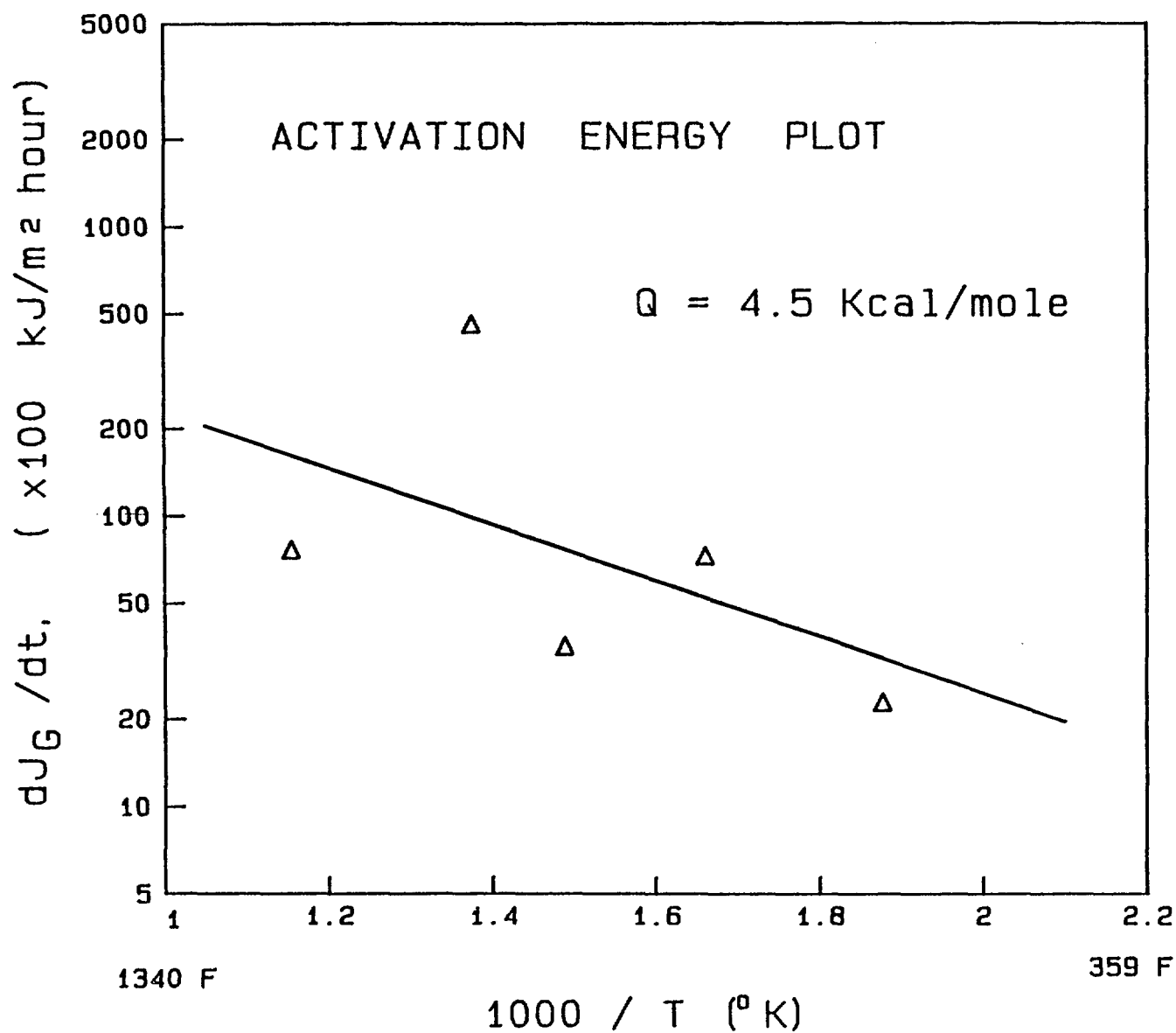


Figure 2.44. Rate of decrease of JG plotted versus inverse of absolute temperature. The solid line is a least squares fit, and it yields an activation energy of approximately 4.5 kcal/mole.

The least-squares fit to the data points in Figure 2.44 is indicated by the solid line. The line is defined by the equation

$$dJ_G/dt = 21.51 \exp [-2241/T] \quad (2-1)$$

where J_G is in kJ/m^2 , t is time in hours, and T is temperature in degrees Kelvin. Rewriting the equation in the familiar form

$$dJ_G/dt = 21.51 \exp [-Q/RT] \quad (2-2)$$

an activation energy Q of 4.5 kcal/mole is obtained. Here R is the universal gas constant.

Table 2.15 lists activation energies for various processes associated with hydrogen interactions with steel. The above activation energy for damage in the clean cast steel is closest to the activation energy for hydrogen permeability in steel, and is much lower than the activation energy associated with the incubation time for hydrogen attack (Refs. 2.16, 2.17). The latter activation energy of 14.6 kcal/mole was obtained from experiments involving tensile testing at room temperature following elevated temperature (800 to 1000 F) hydrogen exposure. Incubation times were based on times of exposure which produced a rapid decrease in reduction of area. The fact that the activation energy for damage determined in the present study using fracture mechanics techniques is much lower than Weiner's value (Ref. 2.17) supports the conclusion that fracture mechanics techniques are more sensitive to damage accumulation than conventional methods of evaluating hydrogen damage, and this helps to explain the disagreement between the present results and the Nelson curves. Hence, damage seems to be rate limited by the permeability of hydrogen into the material, with the magnitude of damage controlled by the accumulation of hydrogen in the matrix as well as at potential crack nucleating sites (such as carbide-ferrite interfaces).

J-integral tests have also been conducted (Ref. 2.18) on hydrogen-exposed 2.25 Cr-1 Mo steel. Specimens were exposed to 24.1 MPa (3500 psi) hydrogen at 454 C (850 F) for 6 months, and were subsequently tested in air at room temperature as well as at 454 C (850 F). Room temperature tests indicated more than 15-fold decrease in J_{IC} and almost a three-fold decrease in dJ/da . These results are in agreement with the Nelson curve, which predicts failure under the stated hydrogen pressure-temperature conditions. Since exposures were limited to one temperature, an activation energy could not be obtained from those results. In any case, the substantial reductions in J and dJ/da are similar to the present results on cast steel, where significant material degradation was observed after only 50 hours of pre-exposure at 454 C (850 F).

In the present study, fractographs indicated that helium-exposed specimens failed predominantly by cleavage. Cracking in these specimens generally

Table 2.15. Activation energies of various processes related to hydrogen in iron and steels.

Mechanism	Activation Energy (KCal/mole)	Reference
Hydrogen diffusion in Fe - lattice	1.6	R1, R2, R7
Hydrogen solubility in Fe	6.8	R1, R7
Permeability of hydrogen in steels	6.5	R3, R7
Carbon diffusion	20.1	R4
Incubation time for hydrogen attack	14.6	R5
Hydrogen attack of 2.25 (γ - 1Mo steels)	45 - 60	R6
Present results	4.5	

References:

- R1 N. R. Quick and H. H. Johnson, Acta Metallurgica, Vol. 26, pp. 903-907, (1978).
- R2 H. G. Nelson and J. E. Stein, NASA Report TND-7265, NASA, Ames Research Center, Moffett Field, CA (1973).
- R3 R. A. Oriani, Acta Metallurgica, Vol. 18, pp. 147-158 (1970).
- R4 C. A. Wert, Physical Review, Vol. 79, pp. 601 (1950).
- R5 L. C. Wiener, Corrosion, Vol. 17, pp. 137-143 (1961).
- R6 T. A. Parthasarathy, H. F. Lopez, and P. G. Shewmon, Metall. Trans., Vol. 16A, pp. 1143-1149 (1985).
- R7 J. P. Hirth, "Effect of Hydrogen on Properties of Iron and Steel," Metallurgical Transactions, Vol. 11, pp. 861-890 (1980).

initiated at large J_{IC} , so that stresses were large enough to trigger cleavage. Cleavage also occurred with hydrogen-exposed specimens. At 500 F there was rough cleavage, while at 399 and 593 C (750 and 1100 F) ductile failure was primarily observed. However, of more significance to the present work is the fact that in room-temperature tests following 260 C (500 F) pre-exposure, cleavage occurred at lower J_{IC} for specimens with hydrogen pre-exposure than for specimens with helium pre-exposure. Some of the short-time pre-exposures in hydrogen at higher temperatures also produced cleavage fracture, and in these cases J_{IC} was also lower for hydrogen pre-exposed specimens than for helium pre-exposed specimens. These observations would imply some form of hydrogen embrittlement, with cleavage aided by the excess concentration of hydrogen accumulated in the hydrostatically stressed region ahead of the crack tip by diffusion at room temperature.

The fractographic and activation-energy evidence suggests that the predominant form of damage at 260 C (500 F) is hydrogen accumulation, which gives

rise to hydrogen embrittlement and incipient attack. Since J_g monotonically decreased with pre-exposure time, the 250-hour exposure apparently was not sufficient to saturate the matrix as well as all traps, particularly those which are potential sites for crack nucleation. Thus, continued damage with further exposure at 260 C (500 F) should be anticipated.

Microstructures of exposed specimens showed no evidence of cavity formation by hydrogen attack at 260 C (500 F), at least within the resolution of the optical microscope. However, this does not guarantee that attack would not occur after a longer period at 260 C (500 F). Consider, for example, that the rate-limiting step for cavity formation is carbon diffusion, with an activation energy of 20.1 kcal/mole. If the rate of damage is considered proportional to the rate of carbon diffusion away from pearlite to grain boundary interfaces, then equivalent times of damage at 260 and 399 C (500 and 750 F) are given by

$$\frac{t_{500F}}{t_{750F}} = \exp \left(\frac{[20.1 \times 4.2 \times 1000]}{8.3} \right) \times \left(\frac{1}{533} - \frac{1}{672} \right) = 51.7 \quad (2-3)$$

Thus, 250 hours of exposure at 399 C (750 F) is equivalent to approximately 1-1/2 years of exposure at 260 C (500 F). Considering that crack-like cavities were seen in the microstructure only after 250 hours of exposure at 399 C (750 F), the pre-exposure times that were used in the investigation at 260 C (500 F) would be far too short to produce any cavity in the microstructure. The above simple calculation (Eq. 2-3) also serves to illustrate the concern with regard to container integrity. A period of 1-1/2 years is certainly short with respect to the total life of the repository. This was the reason for conducting accelerated tests. Unfortunately, the present data are insufficient to provide a model for long-term damage at temperatures of 260 C (500 F) and lower because of the complication in interpretation arising from competing and complementary mechanisms.

In summary, the results of the long-term pre-exposure experiments have tentatively identified hydrogen embrittlement as the principal degradation mechanism for pre-exposures at 260 C (500 F). This finding is consistent with the substantial short-term degradation in fracture resistance for unexposed specimens tested at 260 C (500 F). However, since exposures were limited to only 250 hours of duration, it is premature to conclude that hydrogen attack would not occur after much longer exposure periods at 260 C (500 F). Accelerated tests conducted at higher temperatures suggest a combination of damage mechanisms, and there is too much variation in damage rates to make a firm conclusion regarding the rate-controlling step at different temperatures. It is also difficult to assess at present whether the rate of decrease of J_g would remain constant with time, or whether it would stabilize to a plateau. Longer-duration exposures need to be conducted at temperatures in the vicinity of 260 C (500 F) to develop a realistic model for degradation of fracture resistance.

2.5.3 Areas of Most Severe Degradation and Implications for Long-Term Integrity of Waste Containers

This study has shown that enhanced crack growth can occur at elevated temperatures, as well as at room temperature. Two areas have been identified in which degradation appears to be most severe: (1) hydrogen-enhanced crack growth after long-term exposure to high-pressure, elevated-temperature hydrogen, and (2) hydrogen embrittlement of regions which undergo some form of microstructural transformation. Thus, long-term integrity of waste containers clearly can be influenced by hydrogen degradation. Hydrogen embrittlement, taking the form of enhanced crack growth from a pre-existing flaw, can occur at any point in the life of the container, provided that the necessary hydrogen fugacity, applied stress state, and flaw dimensions are present. Short-term effects appear worst in steel which has undergone thermally-induced microstructural evolution, such as in a weld heat-affected zone or in an annealed overpack. A longer term degradation phenomenon, termed "incipient attack" in this work, also can occur with extended exposure to hydrogen at moderately elevated temperatures. This phenomenon becomes apparent in the presence of a stress concentrator, such as a flaw or a crack, and could result in failure of the container as its temperature decreases.

2.6 Conclusions and Recommendations

The findings of this program have demonstrated that hydrogen degradation is an important consideration in evaluating container integrity, and that further research is needed in this area. It appears particularly important to investigate further the effect of long-term exposure to hydrogen at temperatures below the level at which hydrogen attack would be expected, to understand the extent of "incipient attack" which may develop. In addition, effects of hydrogen on regions which undergo thermally induced microstructural transformations, such as in the weld heat-affected zone, should be studied.

2.7 References for Chapter 2

- (2.1) C. E. Sims, G. A. Moore, and D. W. Williams, Trans. AIME 176, 283 (1948).
- (2.2) C. E. Sims, Trans. AIME 188, 1321 (1950).
- (2.3) L. A. James and L. D. Blackburn, "BWIP Crack Growth Studies," Rockwell Hanford Report No. SD-BWI-TI-120, January 1983.
- (2.4) T. M. Ahn and P. Soo, "Container Assessment--Corrosion Study of HLW Container Materials," Brookhaven National Laboratory Report, June 1983.
- (2.5) T. F. Archbold and D. H. Pelonis, "Assessment of Delayed Failure Models in Titanium and Titanium Alloys," PNL-4127/UC-70 (December 1981).

- (2.6) S. J. Basham, Jr., "Waste Package for a Repository Located in Salt," Proceedings of the 1983 Civilian Radioactive Waste Management Information Meeting, December 12-15, 1983, Washington, DC, CONF-831217, February 1984.
- (2.7) C. E. Sims and F. B. Dahle, Trans. AFS 57, 233 (1938).
- (2.8) R. Gerber, I. M. Bernstein and A. W. Thompson, Scr. Metall. 10, 341 (1976).
- (2.9) H. Cialone and R. J. Agavo, Metall. Trans. A, 12A 1373 (1981).
- (2.10) M. L. Hill and E. W. Johnson, "The Solubility of Hydrogen in Alpha Iron," Transactions, TMS-AIME 221, 662-629 (1961).
- (2.11) G. A. Nelson, "Hydrogenation Plant Steels," Proc. API 29M, 163-72 (1949).
- (2.12) American Petroleum Institute, Steels for Hydrogen Service at Elevated Temperatures and Pressures in Petroleum Refineries and Petrochemical Plants, API Publication No. 941, Second Ed., June (1977).
- (2.13) J. W. Hutchinson, "Singular Behavior at the End of a Tensile Crack in a Hardening Material," Journal of the Mechanics and Physics of Solids 16, 13-31 (1968).
- (2.14) J. R. Rice and G. F. Rosengren, "Plain Strain Deformation Near a Crack Tip in a Power-Law Hardening Material," Journal of the Mechanics and Physics of Solids 16, 1-12 (1968).
- (2.15) R. O. Ritchie, J. F. Knott, and J. R. Rice, "On the Relationship Between Critical Tensile Stress and Fracture Toughness in Mild Steel," Journal of the Mechanics and Physics of Solids 21, 395-410 (1973).
- (2.16) P. G. Shewmon, "Hydrogen Attack of Carbon Steel," Metallurgical Transactions, 7A, 279-286 (1976).
- (2.17) L. C. Wiener, Corrosion 17, 137-143 (1961).
- (2.18) J. D. Landes and D. E. McCabe, "The Effect of Hydrogen Exposure on Fracture," Hydrogen Effects in Metals, I. M. Bernstein and A. W. Thomson (eds.), Publication of Metallurgical Society of AIME, 933-941 (1981).

3. OVERPACK CORROSION

Two design concepts have been considered for the overpack: a corrosion-resistant and a corrosion-allowance design. In the former, a thin-walled overpack of a highly corrosion-resistant material such as Titanium Grade 12 or Hastelloy Alloy C276 is used. The material is selected to have very low general corrosion rates in the expected repository environments and to resist localized forms of corrosion such as pitting and stress-corrosion cracking (SCC). In the corrosion-allowance design, an overpack of a corrosion-allowance material is selected and the wall is made sufficiently thick to allow for measurable corrosion during the overpack life.

Both designs have advantages and disadvantages. The corrosion-resistant design allows for a much lighter waste package that is easier to close. On the other hand, the corrosion-resistant materials generally rely on a passive oxide film for their corrosion resistance and, under some conditions, these films may break down locally, resulting in pitting or SCC. The corrosion-allowance materials are less susceptible to localized corrosion, and it may be possible to adjust the thickness of the overpack to account for pitting or crevice corrosion. However, SCC velocities are probably too high for this approach to be effective, and corrosion-allowance materials such as carbon steel are susceptible to SCC under some environmental conditions. Therefore, SCC must not occur for successful containment using a corrosion-allowance or a corrosion-resistance material.

The overall objective of the overpack corrosion studies was to identify potential corrosion failure modes for candidate overpack materials and to evaluate the influence of environmental and metallurgical variables on rates of corrosion attack for those modes. Initial emphasis was placed on a corrosion-resistant material, Titanium Grade 12, in simulated salt repository environments. However, this material became less favored by DOE and, after the first year, the effort was shifted to low-carbon steel. The latter studies were performed in a simulated basalt repository environment. Limited studies also were performed on Type 316L stainless steel in a simulated tuff repository environment.

For these systems, a combination of electrochemical techniques, long-term exposures, and mechanical test techniques were used to evaluate potential failure modes.

3.1 Titanium Grade 12-Salt System

3.1.1 Task Objective

The objectives of the Titanium Grade 12 - salt system experiments were to confirm experimental results found in the literature and to investigate relevant environmental effects and potential failure modes that have not been previously studied. These effects include thermogalvanic corrosion, heat transfer, and the influence of surface iron particles.

3.1.2 Experimental Approach

Three autoclave exposures were performed on the Titanium Grade 12 salt system. General, pitting, crevice, thermogalvanic, and stress corrosion were evaluated in these experiments by means of electrochemical techniques and coupon exposures. In addition, one slow strain rate test and several deposit-growth experiments were performed. Details of the experimental procedures and results are given below.

3.1.2.1 Materials

Titanium Grade 12, in the form of both sheet and rod stock, was obtained for the experimental studies. Chemical analyses for these materials are given in Table 3.1.

3.1.2.2 Specimen Preparation and Examination

For the first autoclave exposure, a total of ten gravimetric specimens, two crevice-corrosion specimens, two U-bend specimens, and two polarization-resistant specimens were exposed in deaerated Brine A at 250 C. The gravimetric and crevice-corrosion specimens had dimensions of 2.5 cm x 2.5 cm x 0.3 cm. The U-bend specimens had dimensions of 2.5 cm x 10 cm x 0.3 cm with a longitudinal (L) orientation, where the long direction of the specimen was parallel to the rolling direction of the sheet stock. The polarization-resistance specimens had dimensions of 25.4 cm x 0.48 cm diameter.

The specimens were machined to the appropriate dimensions and the corners rounded to approximately a 0.3-cm radius on a belt sander, using a clean 180-grit belt. All surfaces were wet abraded with clean 180, 320, and 400 silicon carbide paper in sequence. The specimens were marked with identification numbers and were cleaned in an ultrasonic bath containing acetone for 10 minutes at room temperature, rinsed in distilled water, rinsed with acetone, and air dried. To embed iron in the surface, five of the gravimetric specimens were then wet abraded on a clean 120-grit belt on which a specimen of 1020 carbon steel had been previously ground. These iron-embedded specimens were then ultrasonically cleaned as described above and stored in a desiccator.

The remaining specimens were pickled for 6 minutes at 55 C in a bath containing 35 volume percent of reagent-grade nitric acid (70 percent), 5 volume percent of reagent-grade hydrofluoric acid (60 percent), and the balance deionized water. Following pickling, the specimens were rinsed in tap water, cleaned ultrasonically, and rinsed as described above. The surface areas of all specimens were accurately measured to the nearest 0.01 cm². The specimens were then oven dried at 100 C for 15 minutes and weighed to the nearest 0.1 mg.

The U-bend specimens were prepared by first drilling 0.8-cm holes 1.2 cm from each end, and bending the specimens in a jig, as described in ASTM G30, such that the legs of the U-bends were 25 degrees off parallel. A Titanium Grade 12 bolt 0.635 cm in diameter was then inserted through the drilled holes and tightened until the legs of the specimens were parallel.

Table 3.1. Certified chemical analyses for Titanium Grade 12 material.

Form	Vendor	Heat	Chemical Composition, Weight Percent							
			N	C	H	Fe	O	Mo	Ni	Ti
0.035 in Sheet	Titanium Industries	P0822	0.016	0.013	0.01	0.09	0.15	0.29	0.82	Balance
0.5 in Dia. Rod	Titanium Industries	DJ07	0.011	0.011	0.0031	0.06	0.15	0.28	0.73	Balance
0.187 in Dia. Rod	Titanium Wire Corp.	P0822	0.016	0.013	0.01	0.09	0.15	0.29	0.82	Balance
	ASTM Specification		0.03	0.10	0.015	0.30	0.250	0.2-0.4	0.6-0.9	Balance

The crevice-corrosion specimens were prepared by drilling a hole in the center of each specimen and attaching serrated PTFE washers to each side of the specimen with a Titanium Grade 12 bolt.

For the second autoclave exposure, a total of six U-bend specimens, two polarization-resistance specimens, two heat-transfer specimens, and two thermogalvanic-corrosion specimens were exposed to deaerated Brine A at 250 C. The thermogalvanic and heat-transfer specimens had the geometry and dimensions shown in Figure 3.1. All other specimen dimensions were the same as those used in the first autoclave exposure.

Two of the U-bend specimens were unwelded and were oriented in the transverse orientation (T), with the long direction of the specimen perpendicular to the rolling direction of the sheet stock. The remaining four U-bend specimens contained welds that were oriented parallel to the long direction of the specimen; two specimens had the L orientation and two had the T orientation. The surfaces of all unwelded specimens were prepared as described for the first autoclave exposure. Surfaces of welded specimens were cleaned prior to welding according to standard welding procedures and were ultrasonically cleaned prior to exposure. Neither abrasion nor pickling were performed on these specimens.

For the third autoclave exposure, a total of eight weight-loss specimens, four crevice specimens, four U-bend specimens, and two heat-transfer specimens were exposed to deaerated Brine A at 250 C. For the weight-loss, crevice, and U-bend specimens, half were exposed to vapor and half to liquid. The U-bend specimens had the L orientation. All specimens were prepared as described above.

Following the autoclave exposures, all specimens were optically examined, scrubbed with hard rubber to remove loosely adherent deposits, ultrasonically cleaned in acetone, rinsed in deionized water, and oven dried for 15 minutes at 100 C. Specimens were then reweighed. Selected specimens also were metallographically sectioned and examined for evidence of localized attack.

For the deposit-growth experiments, a single heat-transfer specimen of Titanium Grade 12 was used. This specimen was prepared as described above. In several of the experiments, thermocouples were attached to the OD surface of the specimen by inserting the thermocouples in small machined holes.

The slow strain rate specimen had dimensions of 12 cm x 0.476 cm in diameter with a centered gauge section 1.27 cm x 0.25 cm in diameter. The gauge section of the specimen was abraded with Nos. 180, 320, and 400 silicon carbide paper and cleaned and pickled as previously described.

3.1.2.3 Solution Preparation

All experiments were performed in a high-magnesium brine referenced in the literature as Brine A. The concentration of the major constituents of Brine A are 42,000 ppm Na^+ , 30,000 ppm K^+ , 35,000 ppm Mg^{++} , 600 ppm Ca^{++} , 5 ppm Sr^{++} , 190,000 ppm Cl^- , 3,500 ppm SO_4^{--} , 10 ppm I^- , 700 ppm HCO_3^- ,

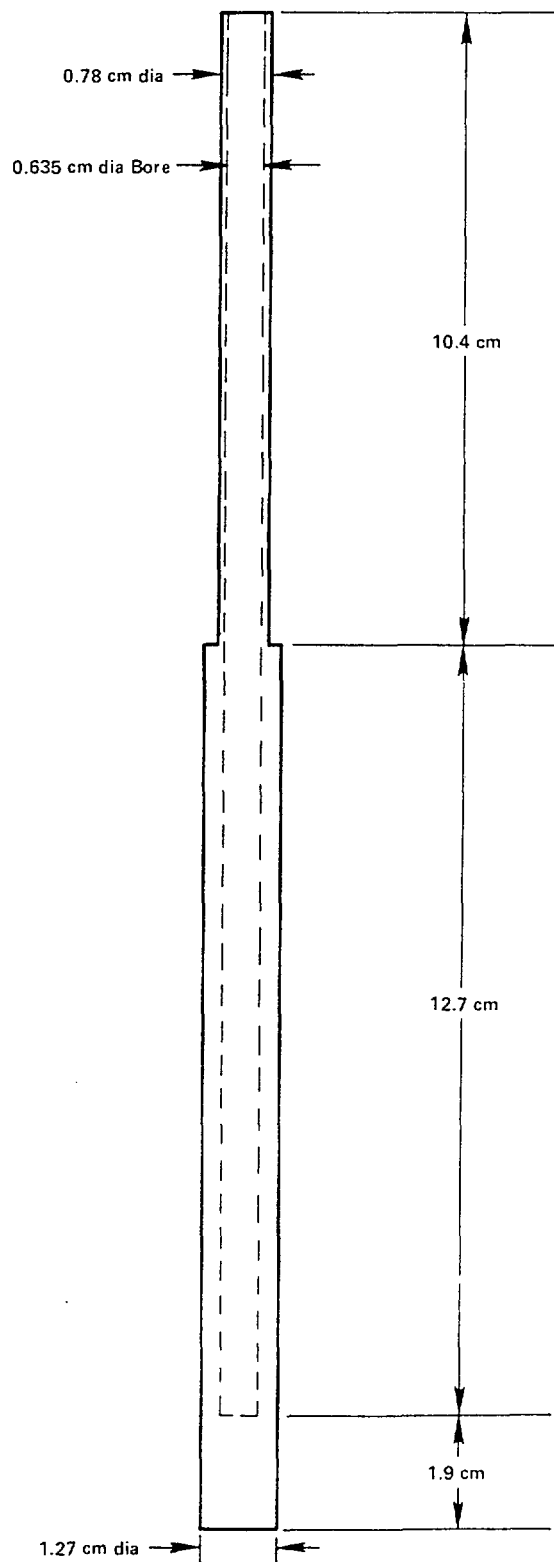


Figure 3.1. Schematic of heat-transfer and thermogalvanic specimens.

1,200 ppm BO_3^{3-} , and 400 ppm Br^- by weight. The solution was prepared from a formulation obtained from Sandia National Laboratories as follows. Master Solution 1 was prepared by dissolving in 500 mL of deionized water the following:

CsCl	0.52 g
LiCl	50.00 g
RbCl	10.87 g
$\text{SrCl}_2 \cdot 6\text{H}_2\text{O}$	6.00 g
KI	5.20 g

and by diluting to 1 liter with deionized water. Master Solution 2 was prepared by dissolving in 500 mL of deionized water the following:

$\text{FeCl}_3 \cdot 6\text{H}_2\text{O}$	5.00 g
HCl (concentrated)	5.00 mL

and by diluting to 1 liter with deionized water. A third solution was then prepared by dissolving in 1 liter of deionized water the following:

NaCl	200.20 g
Na_2SO_4	12.40 g
$\text{Na}_2\text{B}_4\text{O}_7 \cdot 10\text{H}_2\text{O}$	3.90 g
NaHCO_3	1.92 g
NaBr	1.04 g
KCl	114.40 g
$\text{MgCl}_2 \cdot 6\text{H}_2\text{O}$	584.20 g
CaCl_2 (anhydrous)	3.32 g

Five mL of master Solution 1 and 5 mL of master Solution 2 were then added to the above solution and the solution was diluted to 2 liters with deionized water. The pH was then adjusted to 6.5 ± 0.1 with HCl or NaOH and the solution was stored in a cleaned, capped polyethylene bottle until used.

3.1.2.4 Autoclave Exposures

The Hastelloy Alloy C276 autoclave and the Titanium Grade 12 liner for the autoclave were first rinsed with deionized water and then dried. Ten mL of deionized water were then poured into the autoclave and the liner was installed. The isothermal polarization-resistance specimens were attached to threaded Type 316 stainless steel rods, which were then inserted in adjacent, electrically insulated Conax® fittings located in the autoclave head. The specimens were flush with the fitting such that the stainless steel rod was isolated from the test environment. For the first autoclave exposure, all other specimens were suspended from a Titanium Grade 12 rack that was placed in the autoclave such that the specimens were totally immersed during exposure. For the second autoclave exposure, the heat-transfer and thermogalvanic-corrosion specimens were inserted in electrically insulated Conax fittings located in the autoclave head. Other specimens were suspended as described above.

For the third autoclave exposure, a sealed internal canister of Titanium Grade 12 was fitted inside the Hastelloy Alloy C276 autoclave, isolating the test environment from the autoclave head and body. This precaution was taken to prevent contamination of the test solution by corrosion products from the autoclave head. Other test conditions were the same as those used in the second autoclave test.

The test solution was deaerated by sparging with nitrogen for 30 minutes and then added to the autoclave.* The autoclave head was installed and the solution was further deaerated by sparging with nitrogen through a 6-mm-diameter Tygon® tube for 2 hours. The autoclave was then evacuated with a mechanical pump for 30 minutes and backfilled with nitrogen. For the second and third autoclave exposures, resistance heaters with calibrated thermocouples were inserted in the heat-transfer specimens and in one of the thermogalvanic-corrosion specimens. The autoclave was then heated to 250 C, and the thermogalvanic and heat-transfer specimens were heated to approximately 270 C, giving a ΔT of approximately 20 C. During the course of the experiments, the temperature and pressure of the system were monitored.

The polarization resistances of the isothermal and heat-transfer specimens were measured periodically by applying a potential of 10 mV between identical specimens and measuring the ensuing current flow across a precision resistor. When polarization-resistance measurements were not being taken, the specimens were electrically shorted to maintain their identical nature.

The galvanic current flow between the heated and unheated thermogalvanic specimens having identical surface areas was measured periodically in the second and third autoclave exposures by means of a zero-resistance ammeter (ZRA). When measurements were not being taken, these specimens were electrically shorted.

At the completion of the exposure period, the heaters were turned off and the autoclave was allowed to cool to room temperature. The autoclave head was then opened and the solution was removed and stored in a capped polyethylene bottle. The specimens were then optically examined, cleaned, and weighed as previously described. Selected specimens were also metallographically examined.

3.1.2.5 Deposit-Growth Studies

In support of the autoclave exposures of the Titanium Grade 12 - salt system, the effect of temperature difference between a heated specimen and the bulk solution (ΔT) on the rate of deposit buildup on the surface exposed to the vapor was studied. The tests were performed for 3 hours at ambient pressure over a solution temperature range of 40 to 100 C and a ΔT range of 5 to 15 C using a heat-transfer specimen.

*In the third autoclave test, the solution was added to the canister.

3.1.2.6 Slow Strain Rate Tests

A single slow strain rate test was performed on a Titanium Grade 12 specimen in deaerated Brine A at 250 C. The specimen was prepared as previously described and then mounted to a Titanium Grade 12 pull rod and to a specimen end support. The specimen and pull rod were electrically isolated from the end support with PTFE washers and heat-shrinkable tetrafluoroethylene (TFE) tubing. The solution was deaerated as described previously prior to closure of the autoclave. The autoclave was then heated to 250 C, and the specimen was preloaded to approximately 45 MPa and strained to failure at a rate of 1×10^{-7} /sec. The heater was then turned off and the autoclave was allowed to cool to room temperature. The specimen was then removed and examined optically and in the scanning electron microscope. The fracture surface of the specimen was also examined metallographically.

3.1.3 Results and Discussion

3.1.3.1 First Autoclave Exposure

The objectives of the first autoclave exposure were threefold: to test out the system, to reproduce results reported in the literature, and to examine the influence of embedded iron on corrosion performance. The latter is of concern since iron is known to degrade the performance of titanium and the container may be in contact with ferrous equipment during manufacture and handling.

This exposure was run on Titanium Grade 12 at 250 C in deaerated Brine A. Included in the autoclave were ten gravimetric specimens, five having a pickled surface treatment and five in which iron particles were embedded. Also included were duplicate crevice-corrosion specimens of each of the two surface treatments; duplicate U-bend SCC specimens; and two polarization-resistance specimens. Experimental results and discussion are given below.

General Corrosion. Results of weight-change measurements performed on unscaled specimens are given in Table 3.2. The data show that the pickled specimens gained weight as a result of the exposure. The weight gains were converted to corrosion rates, assuming all metallic titanium was converted to TiO_2 and no titanium was dissolved in the solution. The resulting corrosion rate, $1.7 \times 10^{-1} \mu\text{m/y}$, is somewhat less than that reported in the literature (Ref. 3.2).

The minor discrepancy between the results is probably due to the different surface treatments used; Braithwaite (Ref. 3.1) abraded the surfaces prior to exposure, whereas a pickled surface was used in the present studies. It should be noted that a pickled surface treatment more closely represents a commercial surface treatment.

Results for the specimens having an iron-embedded surface treatment are also given in Table 3.2. The data show that weight changes for these specimens were erratic: two specimens gained weight, two specimens lost weight, and one showed no weight change. Although the data could not easily be converted to corrosion rates, it is probable that these specimens exhibited

Table 3.2. Results of gravimetric measurements performed on Titanium Grade 12 specimens exposed 900 hours to deaerated Brine A at 250 C (first autoclave exposure).

Specimen Type	Surface Treatment	Weight Change, g/cm ² (a)	Corrosion Rate, $\mu\text{m/y}$ (b)
Gravimetric	Pickled	$+1.31 \times 10^{-5}$	1.70×10^{-1}
Gravimetric	Iron Embedded	$+2.10 \times 10^{-5}(c)$	-
Gravimetric	Iron Embedded	$-6.00 \times 10^{-6}(c)$	-
Crevice	Pickled	$+4.95 \times 10^{-5}$	6.4×10^{-1}
Crevice	Iron Embedded	$+3.69 \times 10^{-5}$	-

(a) Averaged for five specimens.

(b) Calculated assuming that weight gain was the result of TiO_2 formation.

(c) Three groupings: one group of two specimens gained weight, one group of two specimens lost weight, and one specimen had no weight change.

higher corrosion rates since their surfaces were a dark straw color, whereas the surfaces of the pickled specimens were metallic gray. There was no evidence of pitting or other forms of localized attack on specimens having either surface treatment.

Results of the polarization-resistance (PR) measurements performed on duplicate specimens of Titanium Grade 12 in deaerated Brine A at 250 C are given in Figure 3.2. The data are plotted as $1/\text{PR}$ (mhos/cm^2) as a function of exposure time; $1/\text{PR}$ was constant at $\sim 2 \times 10^{-5}$ mhos/cm^2 for approximately the first 150 hours, then increased over the next 400 hours to approximately 1×10^{-4} mhos/cm^2 and finally appeared to fluctuate around this value for the remainder of the exposure. A value of 1×10^{-4} mhos/cm^2 for $1/\text{PR}$ corresponds to a corrosion rate of approximately 20 $\mu\text{m/y}$, assuming Tafel slopes of 100 mV/decade for the anodic and cathodic reactions and an ionic value of +4 for titanium. This corrosion rate is approximately two orders of magnitude greater than the value predicted from gravimetric measurements. Two possible explanations for this discrepancy are that either the titanium acts as a hydrogen electrode and the exchange current for this reaction is much higher than the corrosion current, or that oxidation of some other species in solution contributes a net current.

Crevice Corrosion. Duplicate crevice-corrosion specimens of Titanium Grade 12 with pickled and iron-embedded surfaces were exposed in the first autoclave test. Following exposure, the specimens were optically examined and gravimetric measurements were performed. Results of the gravimetric

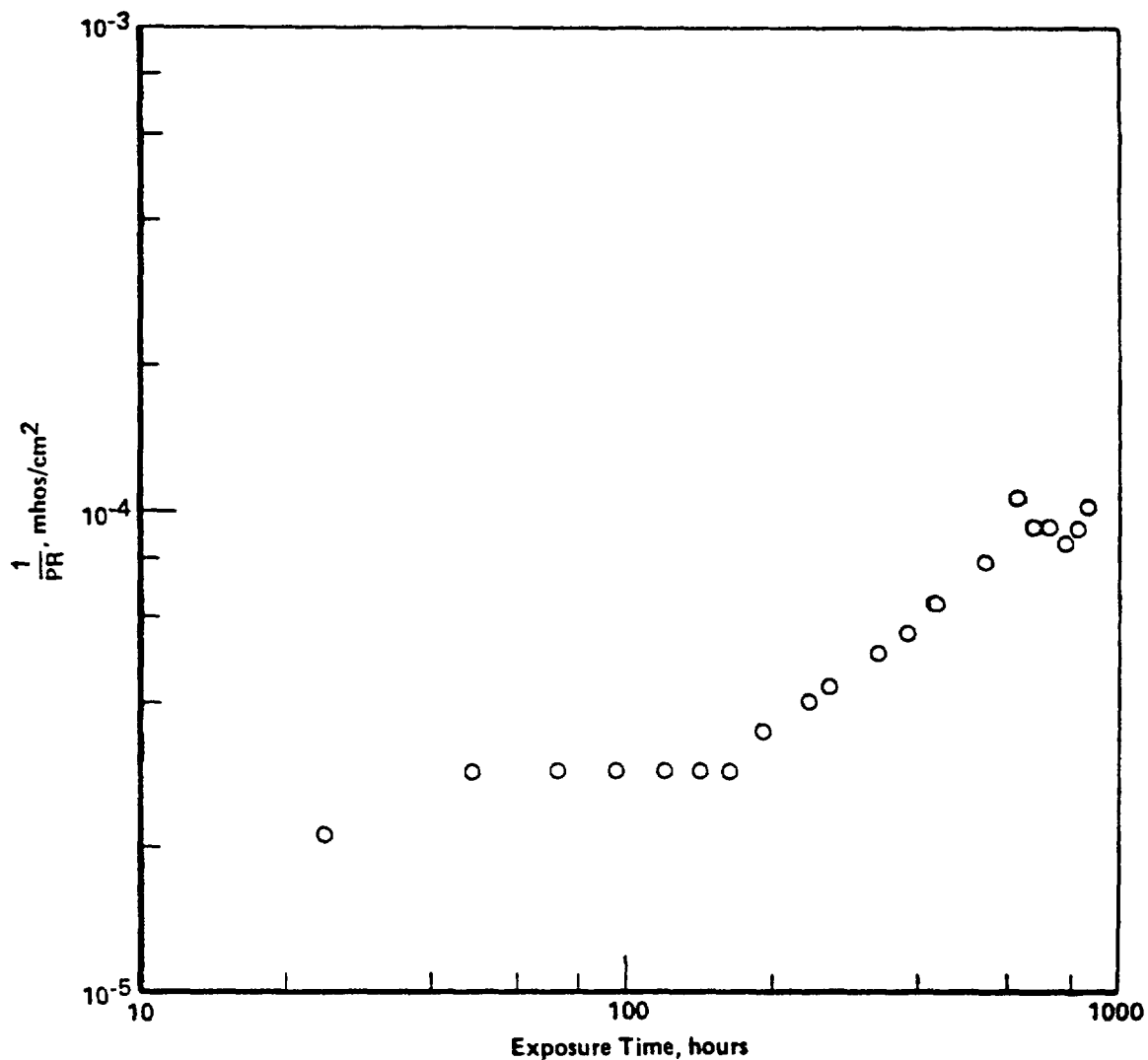


Figure 3.2. $1/PR$ as a function of exposure time for Titanium Grade 12 exposed to deaerated Brine A at 250 C.

measurements, given in Table 3.2, show that the crevice specimens gained more weight than the uncreviced specimens, suggesting that the presence of crevices led to higher rates of attack. This conclusion is consistent with results of optical examination of the specimens. Interference colors were evident in the creviced region of the specimens, suggesting that thicker films are present in these regions (see Figure 3.3). These observations are similar to those reported by Ahn and Soo (Ref. 3.2) and may be an indication of incipient crevice corrosion. The presence of iron did not appear to significantly influence crevice-corrosion behavior.

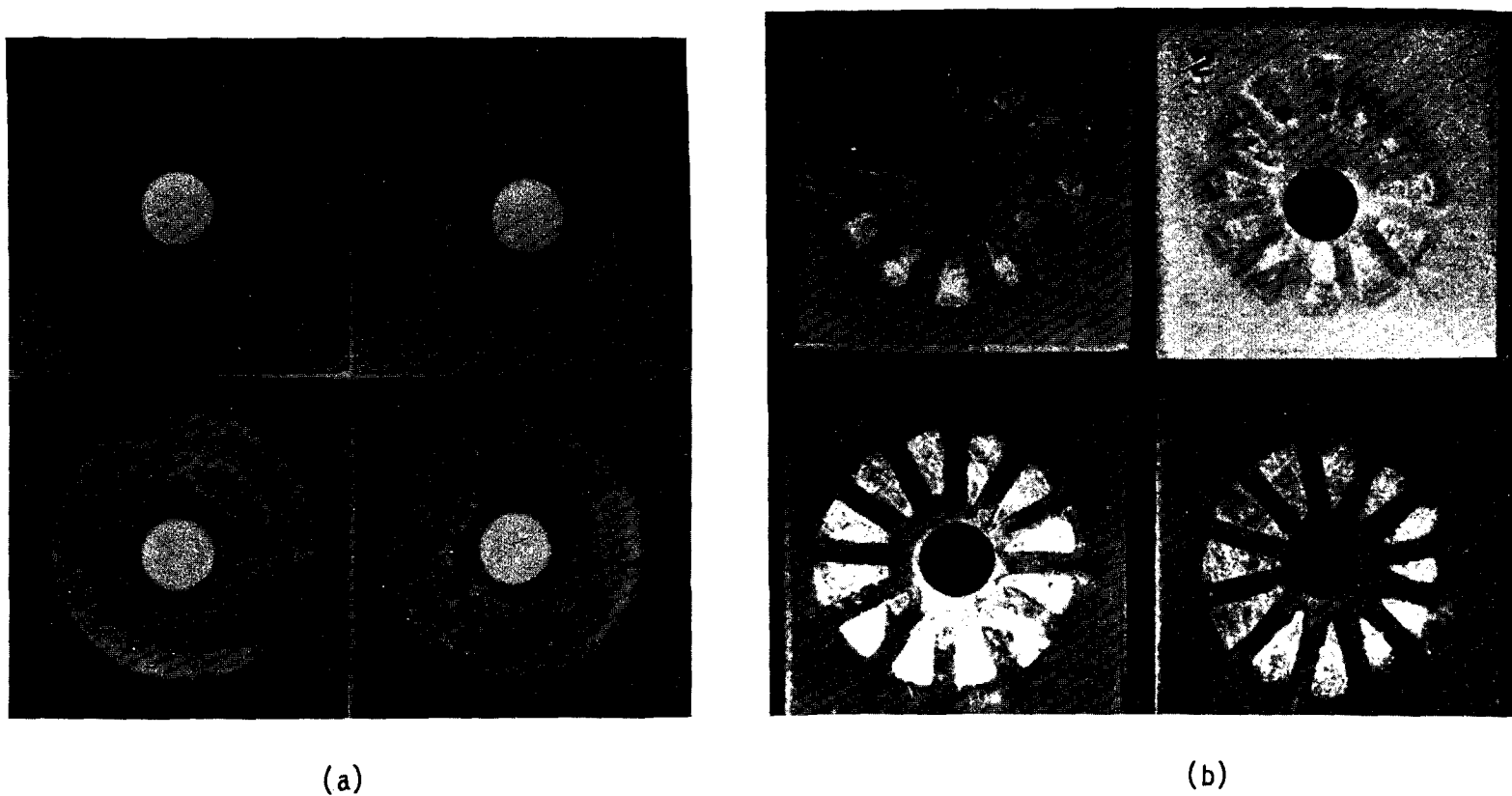


Figure 3.3. Low-power optical photographs of front (a) and back (b) faces of Titanium Grade 12 crevice specimens exposed to Brine A for 900 hours at 250 C.

Specimens 1 and 2 had a pickled surface treatment while Specimens 3 and 4 had an iron-embedded surface treatment.

Stress-Corrosion Cracking. The two U-bend specimens of Titanium Grade 12 included in the first autoclave exposure were oriented such that the maximum stress was parallel to the rolling direction in the plate stock. No cracking was observed. However, this orientation generally is considered to be the least susceptible orientation for SCC of titanium.

3.1.3.2 Second Autoclave Exposure

The objectives of the second autoclave exposure were to study the effect of heat transfer and thermal gradients (thermogalvanic corrosion) on pitting and general corrosion and to evaluate the influence of welding and metallurgical orientation on SCC. Isothermal polarization-resistance specimens were included in the exposure to study the anomalous electrochemical behavior observed in the first autoclave exposure.

Rather peculiar behavior was observed throughout this second autoclave exposure. Immediately following autoclave heatup, pressure in the system stabilized at the autogeneous value, approximately 3.45 MPa (500 psi), as in the first autoclave exposure. However, whereas the pressure in the autoclave in the first exposure maintained a steady value throughout the test, a steady increase in pressure was observed in the second autoclave exposure, up to a value of 6.6 MPa (950 psi) within approximately 350 hours. The pressure then decreased to approximately 6.2 MPa (900 psi) within 4 days; at this point a leak in an autoclave head fitting was noticed. The heaters were then shut off and the autoclave was allowed to cool to room temperature and ambient pressure. The leak was repaired and the system was vacuum tested, blanketed with nitrogen, and reheated to 250 C. The pressure in the system achieved a value somewhat higher than that observed upon initial heatup: 3.9 MPa (560 psi) versus 3.45 MPa (500 psi). As in the initial heatup, the pressure gradually increased with exposure time thereafter, reaching a value of 5.8 MPa (840 psi) prior to shutdown.

Following a total of 1,000 hours at 250 C, the heaters were turned off and the autoclave was allowed to cool to room temperature, whereupon the pressure returned to approximately 1 atm. The autoclave was then opened and the specimens were examined. A significant deposit buildup had occurred on the heated specimens in the region exposed in the vapor space in the autoclave, whereas there was no evidence of deposit buildup on the unheated specimens. Low-power optical photographs of the thermogalvanic specimens are shown in Figure 3.4. The deposits were primarily light gray to dark gray in color. A dark green color was evident in the region of the deposit nearest to the liquid-vapor interface, while yellow-white deposits were scattered over the gray deposits and were concentrated adjacent to, and above, the dark green deposits.

Energy-dispersive spectrographic (EDS) and X-ray diffraction (XRD) analyses were performed on the deposits. Results of these analyses are given in Tables 3.3 and 3.4. These data show that the deposits were composed of sodium and magnesium salts, magnesium hydroxide, and chromium and nickel. The presence of significant quantities of chromium and nickel indicates that severe attack of the autoclave or the fittings had occurred. Examination of these components confirmed that both the fittings and the autoclave head had



a
Heated

b
Isothermal

Figure 3.4. Low-power optical photograph of Titanium Grade 12 thermo-galvanic specimens showing deposit on heated specimen.

Table 3.3. Results of EDS analyses of deposits found on one of the heated polarization-resistance specimens.

Deposit Color	Concentration, weight percent							
	Na	Mg	S	Cl	V	K	Cr	Ni
Green	8.6	10.6	1.5	33.8	0.6	1.2	26.7	16.9
White	34.6	-	-	63.3	-	-	-	2.1
Gray	5.8	13.1	1.6	26.0	-	0.6	0.9	52.1

Table 3.4. Results of XRD analyses of deposits found on one of the heated polarization-resistance specimens.

Deposit Color	Compounds Identified	Powder Diffraction Number
Green	NaCl	5-628
	MgCl ₂	3-854
	Mg(OH) ₃ Cl	12-410
	Mg ₂ Cl(OH) ₂	12-120
	MgClOH	24-276
White	NaCl	5-628
Gray	NaCl	5-628
	Mg(OH) ₂	7-239
	Ni metal	4-850

undergone severe attack. Some of the Type 316 stainless steel fittings failed in the threads during removal due to severe general corrosion, while evidence of pitting and surface etching of the Hastelloy Alloy C276 autoclave head was found. Since the autoclave is composed of a highly corrosion-resistant material, the observation of severe attack suggests that a very aggressive species was present in the autoclave's vapor space.

The pH of solution samples taken from the autoclave following exposure was measured with a glass electrode and found to be approximately 0.68. By comparison, the solution's initial pH was approximately 6.5. An inductively coupled argon plasma (ICAP) analysis of the solution indicated the presence of significant quantities of nickel, chromium, and iron, as shown in

Table 3.5. The probable source of these elements was the autoclave head that underwent severe vapor-phase attack.

Table 3.5. Results of ICAP analyses of test solution from the autoclave exposure of Titanium Grade 12 in Brine A where effect of heat transfer was studied.

Element*	µg/ml (ppm)
Arsenic	4.7
Boron	210
Calcium	560
Cobalt	590
Chromium	2,600
Copper	310
Iron	3,600
Magnesium	22,000
Manganese	210
Molybdenum	8.0
Sodium	37,000
Nickel	9,100
Phosphorus	8.3
Palladium	3.9
Selenium	2.5
Strontium	13.0
Zinc	7.6

*Only elements having a concentration greater than 1 ppm are reported.

The observation of a low-pH solution following exposure, coupled with the occurrence of severe vapor-phase attack of the Hastelloy Alloy C276 autoclave head, the presence of hydroxides of magnesium in the deposits, and the pressure buildup in the autoclave with exposure time, all point to a simple explanation for the peculiar phenomena observed: namely, the generation of hydrochloric acid in the vapor phase of the autoclave. It appears that hydrolysis of magnesium salts and their deposition as a basic salt in the vapor phase led to generation of hydrochloric acid. At the autoclave temperature, 250 C, this HCl would be present primarily as a vapor and thus would lead to a gradual increase in pressure with continued generation. Upon autoclave cooldown, the HCl would go into the liquid, lowering the pH and allowing the autoclave pressure to return to approximately ambient pressure at ambient temperature. The generation of hydrogen or of any other noncondensable gas would have produced a net pressure in the system at ambient temperature. A simple calculation of the expected pressure increase in

the autoclave, as a result of the acid generation and pH drop from 6.5 to approximately 0.7, was made based on an initial solution volume of 2.25 liters and a vapor volume (at temperature) of 0.5 liters. Assuming the pH is equal to the negative log of the hydrogen ion concentration, that is, not considering activity coefficients and also assuming ideal gas behavior, a pressure increase of approximately 3.7 MPa (540 psi) would be expected. This is in reasonably close agreement with the observed pressure increase of approximately 2.7 MPa (400 psi).

The formation of magnesium hydroxide on heated surfaces has been routinely observed in seawater desalination (Ref. 3.3). The commonly accepted mechanism for this process involves generating hydroxide by decomposition of the bicarbonate ion in the seawater. Since the bicarbonate composition of Brine A is reasonably low, 700 ppm, this mechanism probably is not applicable to this system. Moreover, such a mechanism does not involve generation of hydrochloric acid. The key to understanding the mechanism probably is related to the deposition that occurs in the vapor space. Under isothermal conditions where these deposits were not observed, the increased solubility of magnesium hydroxide with decreasing pH limits the progress of the reaction. On the other hand, deposition of magnesium hydroxide in the vapor space, which occurs under heat-transfer conditions, apparently allows the reaction to be self-sustaining.

Weight Loss. Results of the gravimetric measurements performed on the specimens in the second autoclave exposure are given in Table 3.6. These data show that Titanium Grade 12 performed surprisingly well, considering the aggressive nature of the environment that was generated in the autoclave. It should also be noted that no evidence of localized attack of the specimens was found. As shown in Table 3.6, rates of attack for the welded U-bend specimens exposed in the liquid phase were low and were similar to those measured for pickled gravimetric specimens in the first autoclave exposure. Rates of attack were higher for specimens that were partially exposed in the vapor. The portions of the specimens exposed in the vapor also were darker in color than the regions exposed in the liquid. However, the weight-loss data for the polarization-resistance specimens are of questionable validity because of the presence of corrosion products from the support rods, whereas the weight gain for the unheated member of the thermogalvanic couple may have represented thermogalvanic as well as vapor-phase effects.

Electrochemistry. Two types of electrochemical measurements were performed in the second autoclave exposure: galvanic current and polarization resistance. The objective of the galvanic-current experiment was to evaluate the potential influence of variation in the overpack skin temperature, as a function of location, on corrosion rates; this phenomenon is sometimes referred to as thermogalvanic corrosion. The galvanic current between a heated and an unheated specimen with equal surface areas was measured periodically by means of a ZRA. The heated specimen was maintained at 270 C by an internal resistance heater; the unheated specimen was equilibrated at the autoclave temperature (250 C). Before each measurement, the potential difference between the electrodes also was measured.

Table 3.6. Results of gravimetric measurements performed on Titanium Grade 12 specimens exposed 1,000 hours to deaerated Brine A at 250 C (second autoclave exposure).

Specimen Type	Number of Specimens	Weight Change g/cm ²	Corrosion Rate μm/y ^(b)
Unwelded U-bends	2	+4.04 x 10 ⁻⁶ -6.7 x 10 ⁻⁷	- -
Welded U-Bends	4	+1.29 x 10 ⁻⁵	1.67 x 10 ⁻¹
Heat Transfer	2	N/A(a)	-
Thermogalvanic Heated	1	N/A(a)	-
Unheated	1	+1.33 x 10 ⁻⁴	1.72
Isothermal Polarization Resistance ^(c)	2	-8.5 x 10 ⁻³	1.1 x 10 ²

(a) Not available--unable to remove deposits.

(b) Calculated assuming the weight gain was the result of TiO₂.

(c) Questionable data because of inability to remove all of the corrosion products from the Type 316 stainless steel support rod.

It was found that the heated specimen was noble to the unheated one by about 90 mV throughout the exposure, and that the galvanic-current flow was in the direction of the unheated specimen; that is, the unheated specimen was undergoing galvanic corrosion when contacted by the heated specimen, assuming that the current measured was a corrosion current. Actual current measurements are given in Figure 3.5. These data show that the current fluctuated over the initial 400 hours of exposure around a value of 8×10^{-5} A/cm². Converting this current to a corrosion rate by means of Faraday's Law, and assuming an ionic valence state of +4 for titanium, gives a value of 6.5×10^2 μm/year. This value is more than two orders of magnitude greater than the corrosion rate of the unheated specimen as measured gravimetrically (1.72 μm/year). As discussed above, a similar discrepancy was observed between corrosion rates of Titanium Grade 12 in Brine A predicted by polarization resistance and those predicted gravimetrically. This discrepancy is attributed to parasitic redox reactions in the solution that contributed a net current.

The corrosion rate of the unheated thermogalvanic specimen measured gravimetrically was greater, by an order of magnitude, than the corrosion rate of the gravimetric specimen from the previous autoclave exposure, or from immersed U-bend specimens in this autoclave exposure. Thus it appears that

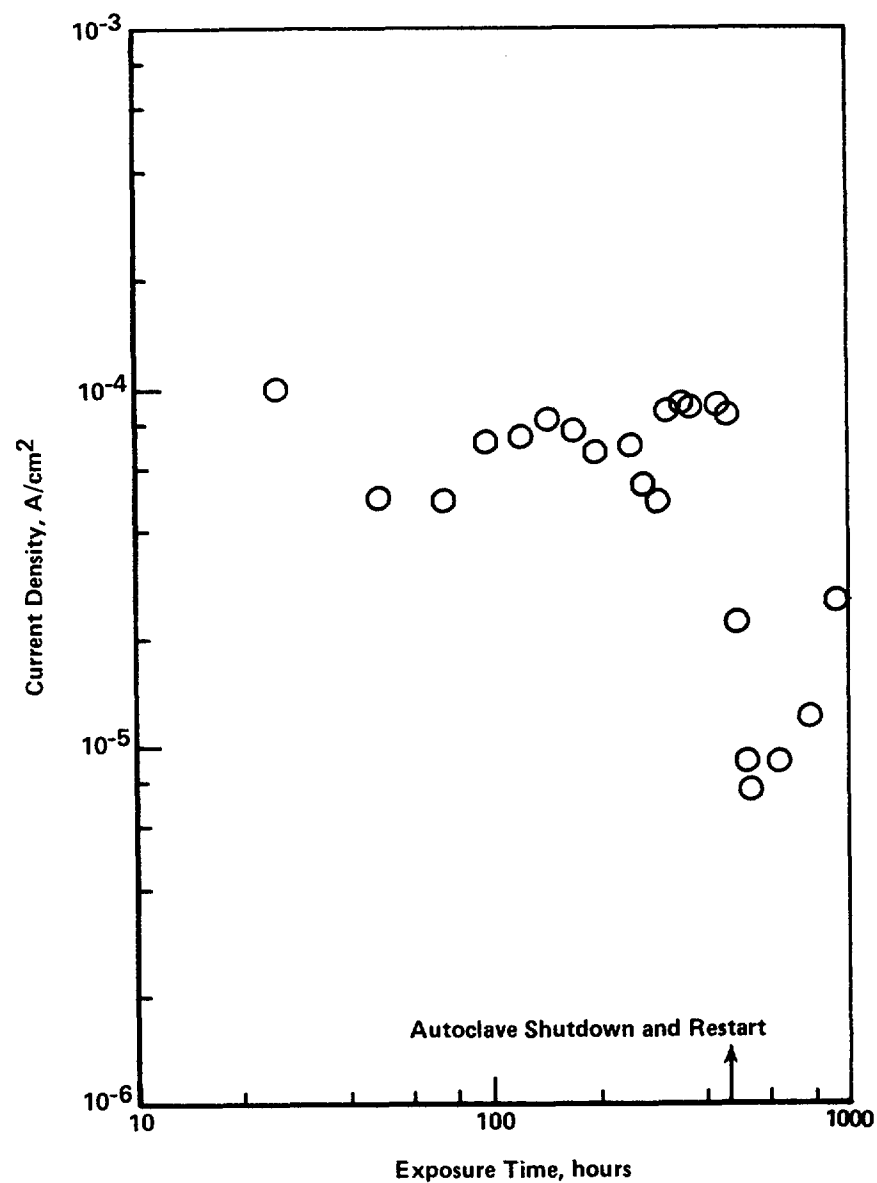


Figure 3.5. Galvanic current density as a function of exposure time for a heated Titanium Grade 12 specimen coupled to an unheated specimen ($\Delta T = 20$ C) having equal surface areas in deaerated Brine A at 250 C.

Heated specimen was noble with respect to unheated specimen throughout exposure.

the galvanic-current measurement successfully predicted the direction, but not the magnitude, of the galvanic effect. However, in this autoclave exposure, deposits built up on the heated specimens in the vapor phase, which apparently led to hydrolysis of salts in the deposits and to generation of HCl. The HCl in the vapor may have accelerated the corrosion rate of the electrodes, which passed through the vapor phase, more than that observed with the immersed U-bend specimens.

During this second autoclave exposure, pressure buildup in the autoclave promoted a leak after approximately 450 hours of exposure. As shown in Figure 3.5, galvanic currents measured after restarting the autoclave were considerably lower than those measured before shutdown. The data taken after autoclave startup, however, are not considered to be reliable since deposit buildup may have impinged on the autoclave head by this time and affected measurements.

Results of the polarization-resistance (PR) measurements performed in this autoclave exposure are summarized in Figure 3.6. These data show that the polarization-resistance values for the heated specimens were higher (that is, $1/PR$ values were lower) than those for the unheated specimens. This suggests that corrosion rates for the heated specimens were lower than those of the unheated specimens, a suggestion qualitatively consistent with the results of the galvanic-current measurements. Problems exist with the data, however. First of all, corrosion rates predicted from the polarization-resistance measurements are several orders of magnitude higher than those predicted gravimetrically, as was observed in the previous autoclave exposure. In addition, the polarization-resistance values for the unheated specimens measured in this autoclave exposure do not agree with those reported in the first autoclave exposure. This effect may have resulted from increased concentration of metal ions in the solution, as shown in Table 3.5. Finally, the measured polarization-resistance values for the heated specimens decreased with exposure time after about 300 hours; this may have been a real effect but more probably was a result of impingement of vapor-phase deposits onto the autoclave head.

Stress-Corrosion Cracking. Duplicate unwelded U-bends having a transverse orientation and duplicate welded U-bends having transverse and longitudinal orientations were exposed in the liquid phase in the second autoclave test. Following exposure, the specimens were optically examined, and no evidence of SCC or localized attack was observed.

3.1.3.3 Third Autoclave Exposure

The objective of the third autoclave exposure was to investigate the effect of heat transfer on Titanium Grade 12 corrosion, and to do so in the absence of contamination of the test environment with corrosion products from the autoclave. The latter was accomplished by fitting a sealed internal canister of Titanium Grade 12 inside the autoclave so that the test environment was isolated from the autoclave head and body.

The annular region between the autoclave and the connector was filled with an aqueous solution of 1,000 g/L sodium chloride. This solution was

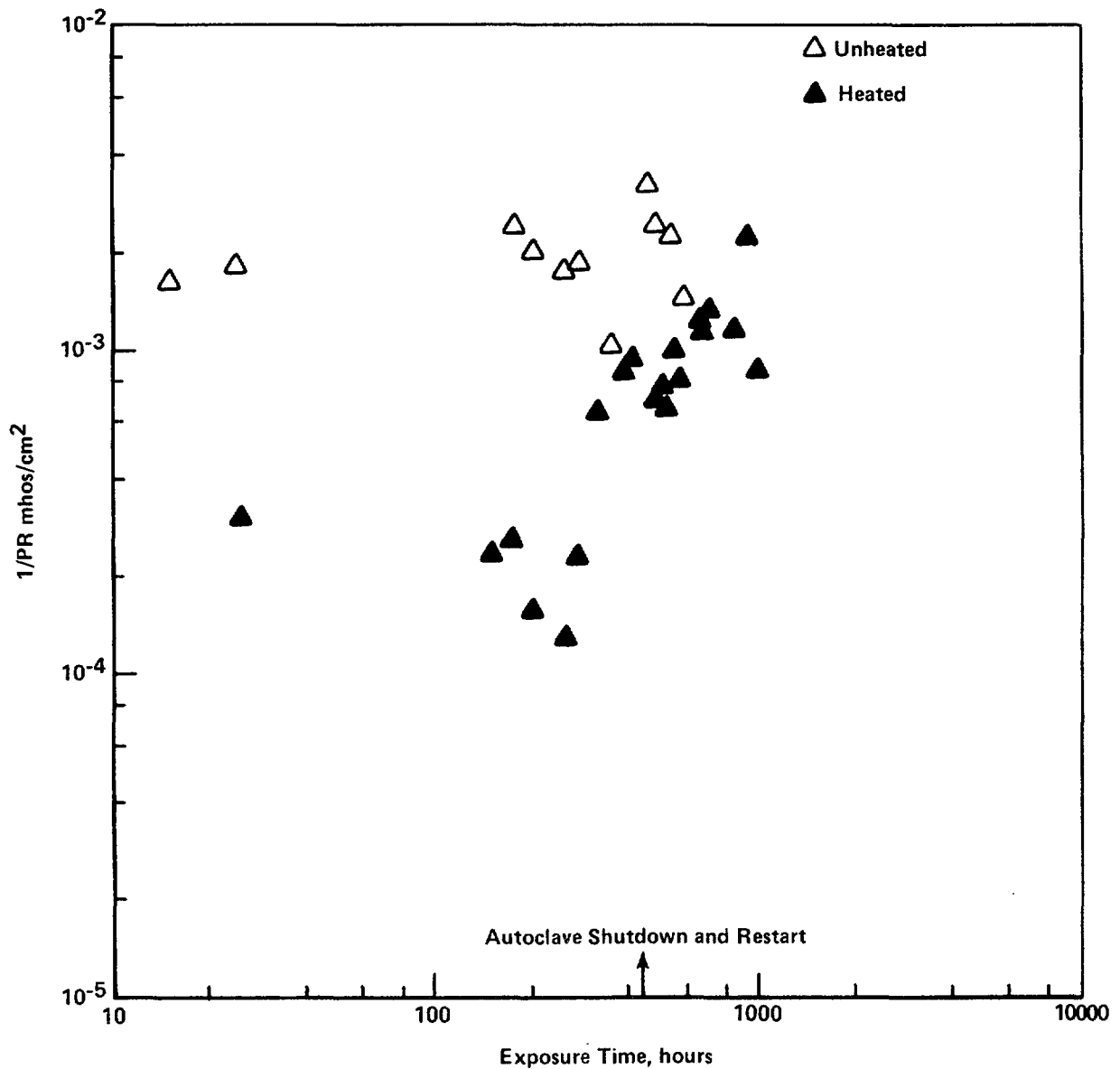


Figure 3.6. $1/PR$ as a function of exposure time for heated and unheated ($\Delta T = 20^\circ\text{C}$) Titanium Grade 12 specimens exposed in deaerated Brine A at 250°C .

selected to match the vapor pressure of Brine A, but to prevent HCl generation by hydrolysis of magnesium salts. The contents of the canister included four weight-loss specimens, two crevice specimens, and two U-bend specimens in each phase (liquid and vapor).

Unlike the results of the previous autoclave exposure, the pressure within the canister in this exposure did not increase with exposure time. When the

autoclave was opened at the end of the exposure, a deposit was found to have built up on the outside of the internal canister. The internal canister, which contained the actual specimens and Brine A, was cut open and only a small amount of deposit was found on the heated specimen (see Figure 3.7). The solution pH was measured using a glass electrode and was found to be 5.7. These observations suggest that the internal canister had become isothermal during the test and that the majority of the temperature drop had occurred between the canister's outside surface and the autoclave wall.

All of the specimens gained weight as a result of the exposure, and the weight changes were comparable with those previously reported, although the values for the gravimetric specimens immersed in the liquid were somewhat higher than those previously reported (see Table 3.7).

The specimens were optically examined and, as in the previous exposures, evidence of incipient attack was found within the crevices (see Figure 3.8). This attack appeared to have been somewhat more severe on the specimens exposed in the liquid, although the gravimetric results did not reflect this. Colored interference spots were evident on the specimens exposed to the vapor, suggesting that an aggressive condensate had formed on them (see Figure 3.9). No evidence of cracking was found in the U-bend specimens.

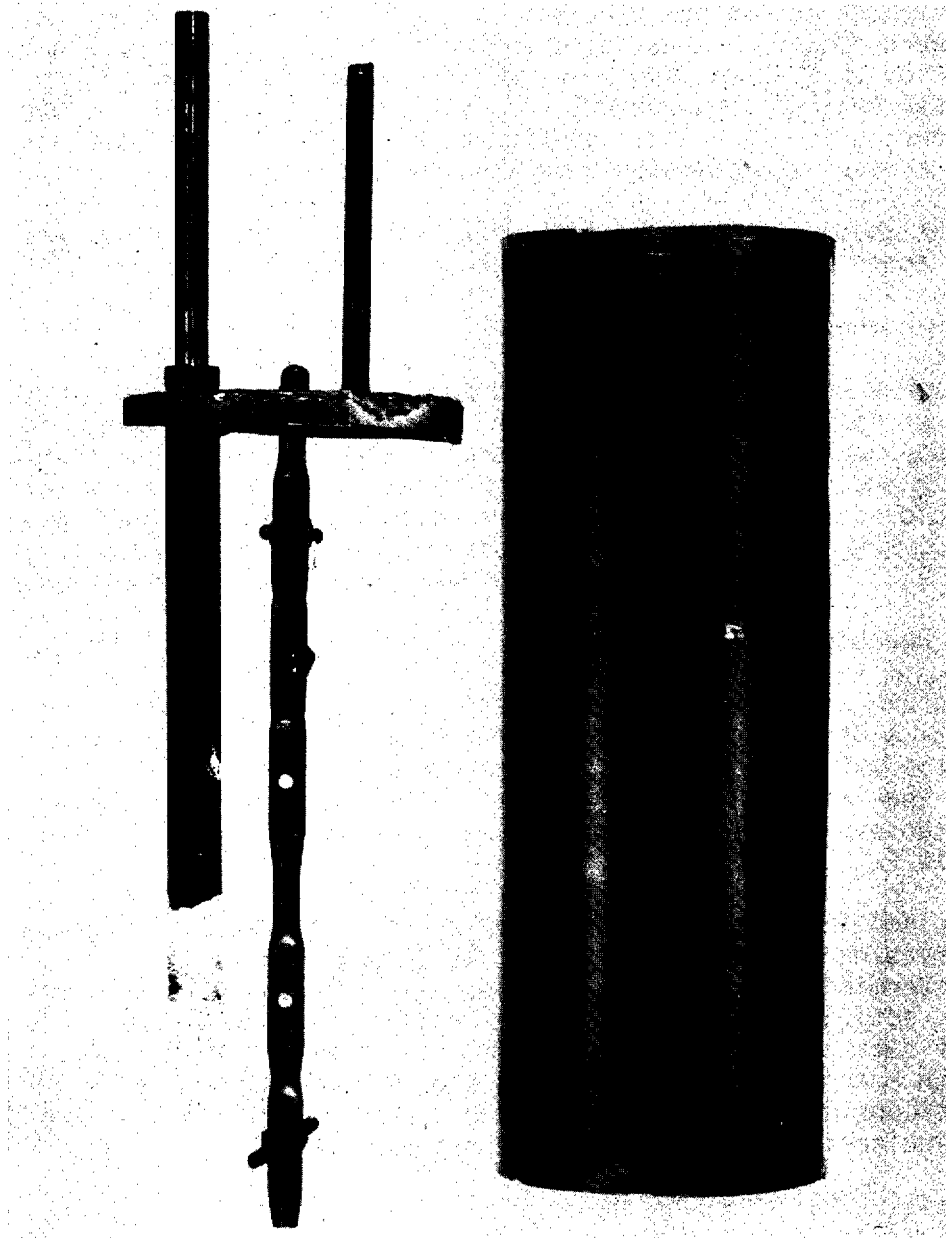
3.1.3.4 Deposit-Growth Studies

The objective of the deposit-growth studies was to investigate the mechanism and kinetics of the deposit growth that occurred on the heat-transfer specimen in the autoclave studies. The effect of temperature difference between a heated specimen (ΔT) and the bulk solution on the rate of deposit growth was studied over a solution temperature range of 40 to 100 C and a ΔT range of 5 to 15 C.

Results given in Figure 3.10 show that the rate of deposit growth increased with increasing temperature and ΔT . The data were plotted as a function of $1/T$ to determine whether the rate of deposit buildup could be described by a thermally activated process having a single activation energy. Figure 3.11 shows the data for $\Delta T = 5$ C falling on a reasonably straight line, with an activation energy of approximately 13 kcal/mole. Data for $\Delta T = 10$ C and 15 C have considerably more scatter and appear to fit lines having smaller slopes, indicating lower activation energies.

The deposits that formed on the specimens were optically examined, and selected samples were analyzed. In contrast to the multicolored deposits that formed in the autoclave tests, where significant contamination of the system had occurred from reactions with the autoclave head, deposits formed at ambient pressure were a uniform white color (see Figure 3.12). The deposits were found to contain approximately 68 percent chlorine, 15 percent potassium, 13 percent magnesium, 4 percent sodium, and a trace of sulfur, as determined by EDS analysis. X-ray diffraction analyses of the deposits indicated the presence of KOH, NaCl, and two hydrated magnesium chlorides.

Optical examination of the specimens during deposit formation suggested that the mechanism of formation is related to a wicking action whereby a thin



0.5X

2L354

Figure 3.7. Low-power optical photograph of canister, specimen rack, and heat-transfer specimen following testing.

Note the small amount of deposit present on the heat-transfer specimen (lower left).

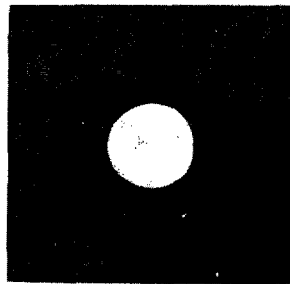
Table 3.7. Results of gravimetric measurements performed on Titanium Grade 12 specimens exposed for 1,000 hours to deaerated Brine A at 250 C (third autoclave exposure).

Specimen Type	Phase	Weight Change g/cm ²	Corrosion Rate μm/y ^(a)
Gravimetric	Vapor	+1.09 x 10 ⁻⁴ ^(b)	1.27
Crevice	Vapor	+3.68 x 10 ⁻⁵ ^(c)	4.29
Gravimetric	Liquid	+4.09 x 10 ⁻⁵ ^(b)	4.77
Crevice	Liquid	+3.95 x 10 ⁻⁵ ^(c)	4.61

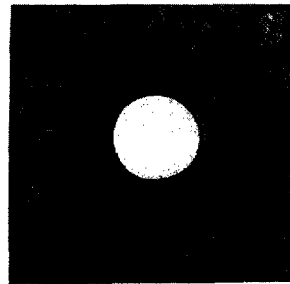
(a) Calculated assuming the weight gain was the result of TiO₂ formation.

(b) Averaged for four specimens.

(c) Averaged for two specimens.



vapor

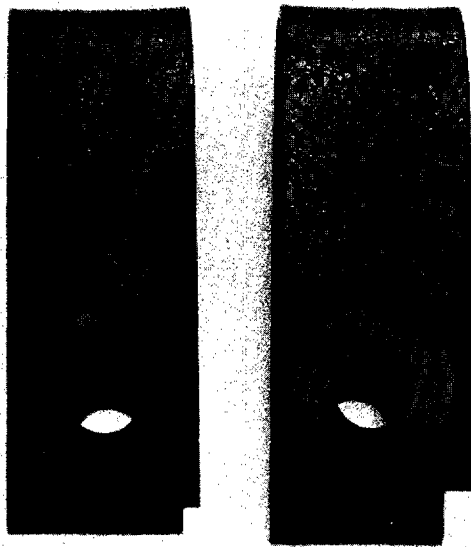


liquid

3X

2L464

Figure 3.8. Low-power optical photograph of crevice specimens exposed to vapor and liquid phases in the third autoclave exposure.



2X

2L465

Figure 3.9. Low-power optical photograph of U-bend specimens exposed to vapor in the third autoclave exposure.

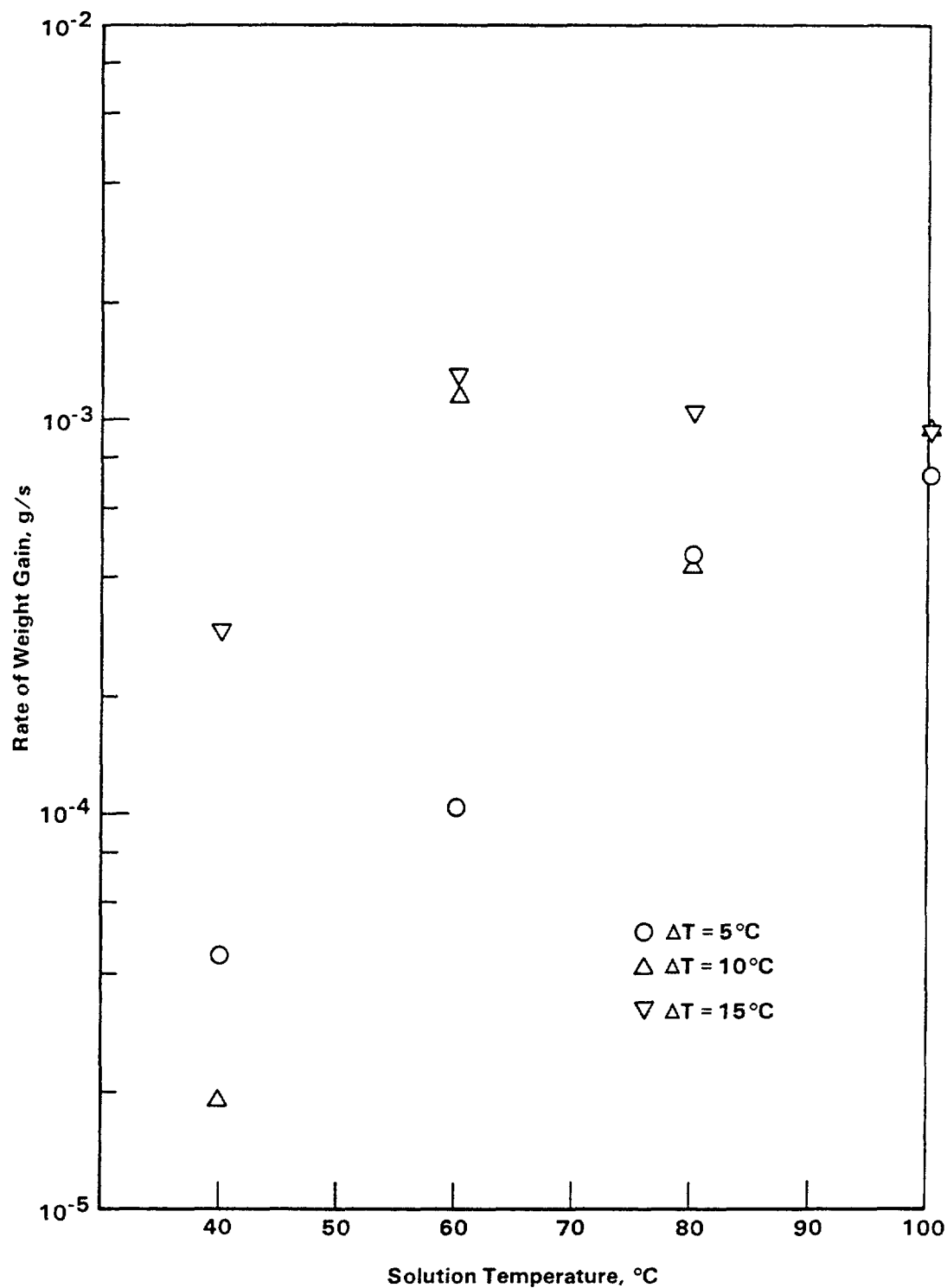


Figure 3.10. Rate of deposit growth, averaged over 3-hour tests, as a function of solution temperature and ΔT on a Titanium Grade 12 specimen exposed to naturally aerated Brine A.

$$\Delta T = T_{\text{heated specimen}} - T_{\text{solution}}$$

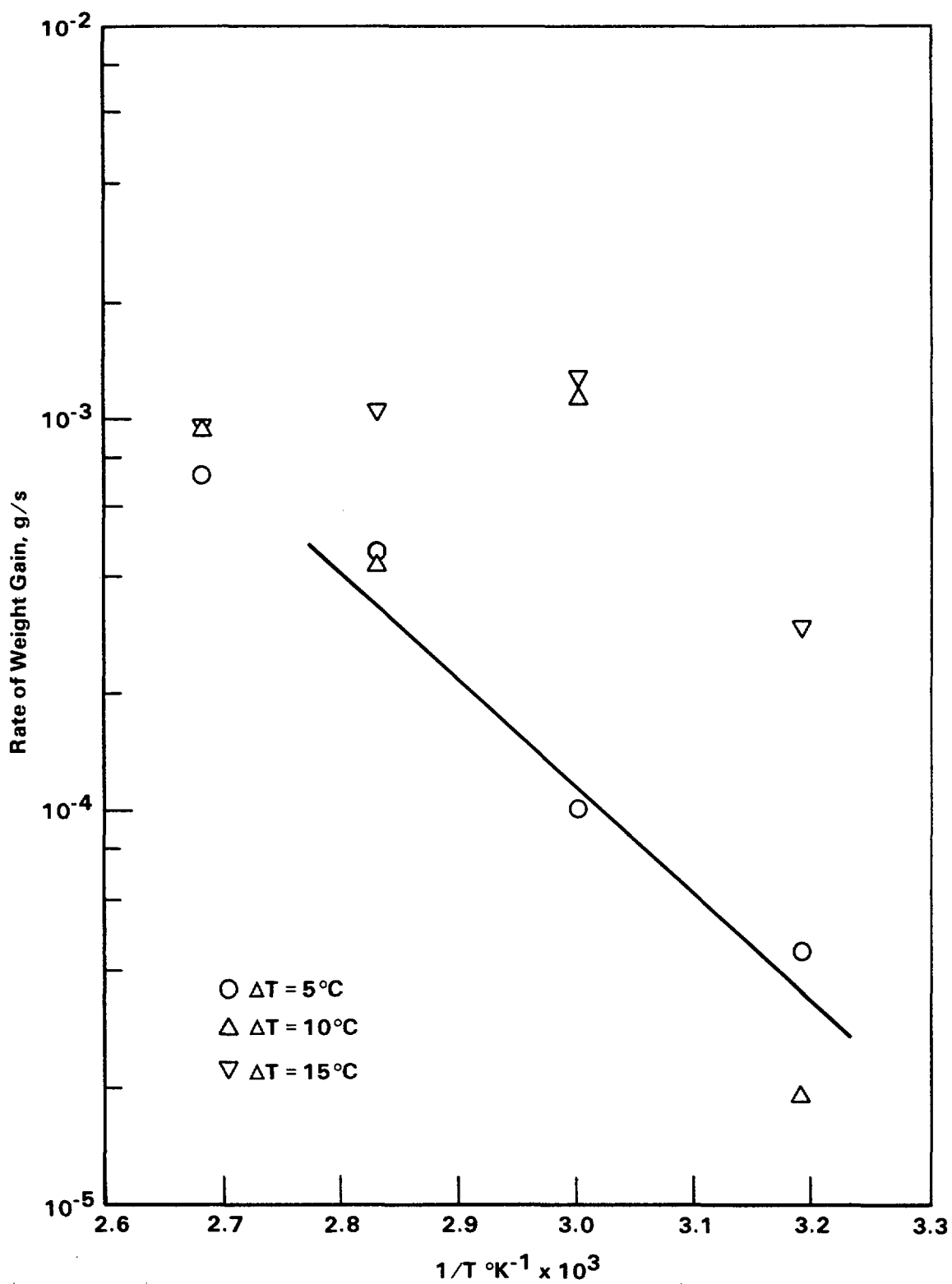
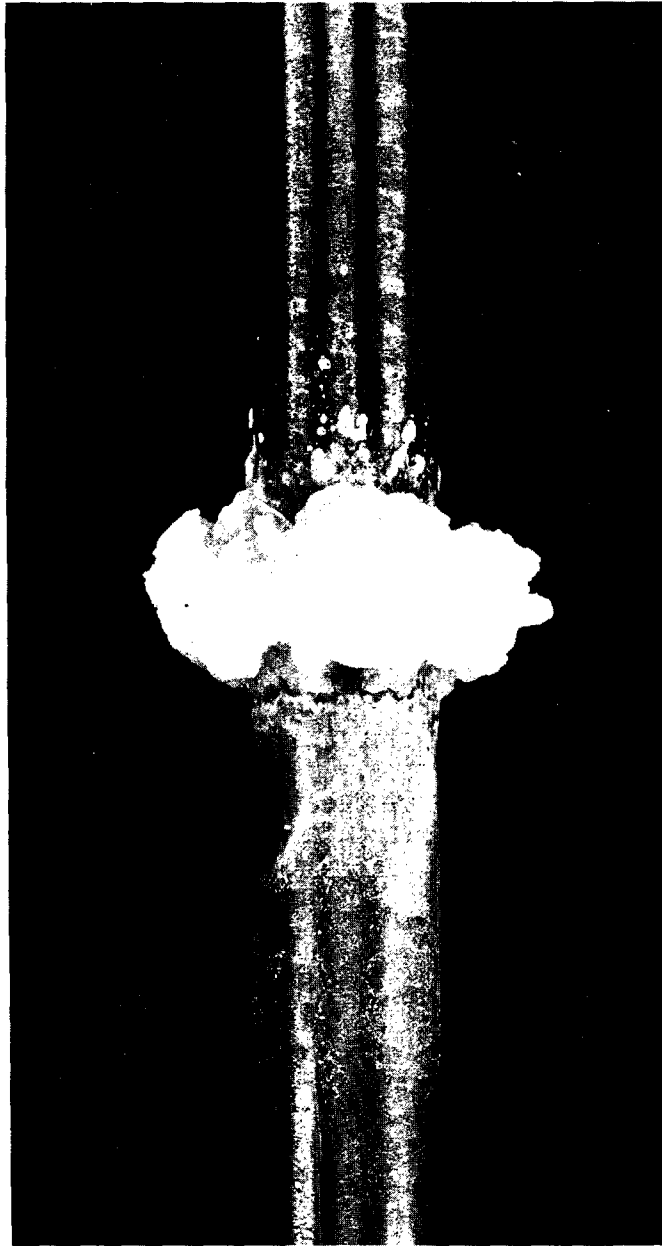


Figure 3.11. Data shown in Figure 3.10 given as rate of weight gain as a function of $1/T$.



2X

1L596

Figure 3.12. Low-power optical photograph of Titanium Grade 12 heat transfer specimen exposed for 4 hours to naturally aerated Brine A at 65 C ($\Delta T = 7$ C).

$\Delta T = T_{\text{heated specimen}} - T_{\text{solution}}$.

deposit initially forms on the specimens at the vapor-liquid interface, and solution then migrates up the specimen in the thin layer between specimen and deposit, ultimately depositing on the specimen. Such a mechanism may be driven by a large thermal gradient on the specimen surface. Accordingly, thermocouples were attached to the specimen in the vapor space, and the temperature was measured as a function of distance from the solution-vapor interface. Typical results of these measurements, given in Figures 3.13 and 3.14, show that the temperature of the specimen in the vapor was indeed much greater than that in the liquid and reached a maximum at about 2.5 cm from the solution-vapor interface.

3.1.3.5 Slow Strain Rate Studies

The objective of the slow strain rate test was to reproduce data found in the literature. A slow strain rate test was carried out on a Titanium Grade 12 tensile specimen at a strain rate of $1 \times 10^{-7} \text{ sec}^{-1}$ in Brine A at 250 C under deaerated conditions. The specimen failed after 350 hours, giving an elongation to failure of 13 percent and a reduction in area of 59 percent. After the test, the specimen was examined optically and in a scanning electron microscope (SEM). Figure 3.15 is an SEM fractograph for the specimen. With the exception of a narrow region at the edge, the fracture surface is typical of ductile failure. A closer examination of the narrow region suggested that the area had been mechanically damaged when the specimen was removed from the autoclave. The mechanical nature of the damage was confirmed on metallographic examination of the specimen (see Figures 3.16 and 3.17), which showed complete absence of cracking and high local deformation in the damaged area. The voids seen near the fracture surface in Figures 3.16 and 3.17 are due to strain-induced porosity, which is well-known to occur in titanium and its alloys at high strains (Ref. 3.4).

3.1.4 Conclusions

In these studies, Titanium Grade 12 exhibited good corrosion performance in deaerated Brine A under isothermal and heat-transfer conditions. General corrosion rates were very low and there was no evidence of stress corrosion under slow strain rate conditions or cracking in welded or unwelded specimens, either in the longitudinal or transverse orientation.

However, several potential problem areas were identified. Discoloration of surface films was observed within crevices on the specimens, which may be an indication of a decrease in the protective nature or possible breakdown of the passive films. This behavior has been reported elsewhere (Ref. 3.2). Similar discoloration was observed on uncreviced specimens in which iron particles were embedded prior to exposure.

Heat transfer, occurring on Titanium Grade 12 specimens in deaerated Brine A at 250 C, led to hydrolysis of magnesium chloride and to generation of significant quantities of HCl in the autoclave. Although the Titanium Grade 12 performed well in the aggressive HCl vapors generated, it is unlikely that this alloy has adequate corrosion resistance to guarantee, with some degree of certainty, an extended lifetime.

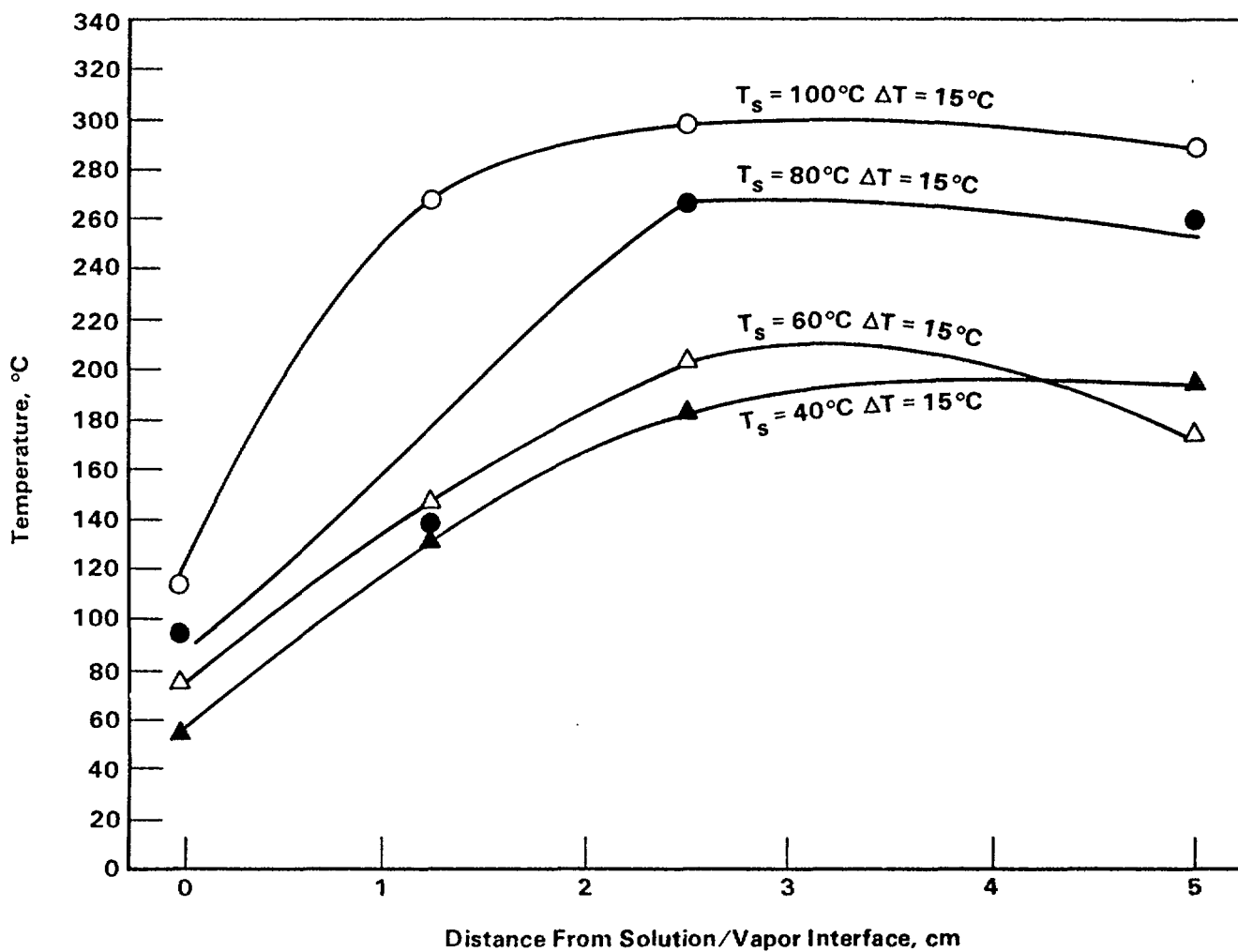


Figure 3.13. Specimen temperature as a function of distance from solution-vapor interface and solution temperature for Titanium Grade 12 in Brine A with a fixed ΔT ($T_{\text{heated specimen}} - T_{\text{solution}}$). Measurements were taken after an exposure time of 10 minutes.

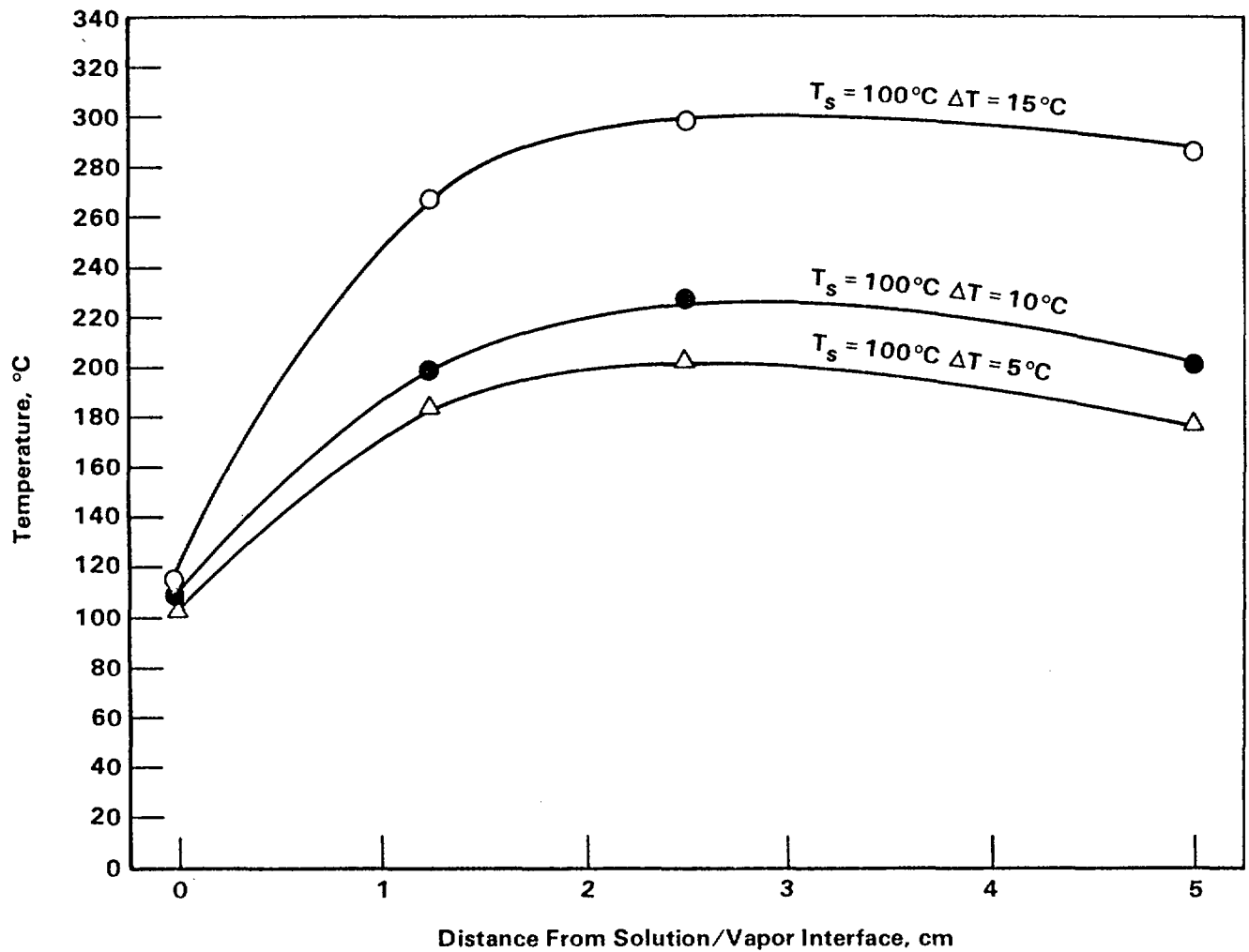


Figure 3.14. Specimen temperature as a function of distance from solution-vapor interface and ΔT for Titanium Grade 12 in Brine A at 100 C.

$$\Delta T = T_{\text{heated specimen}} - T_{\text{solution}}$$

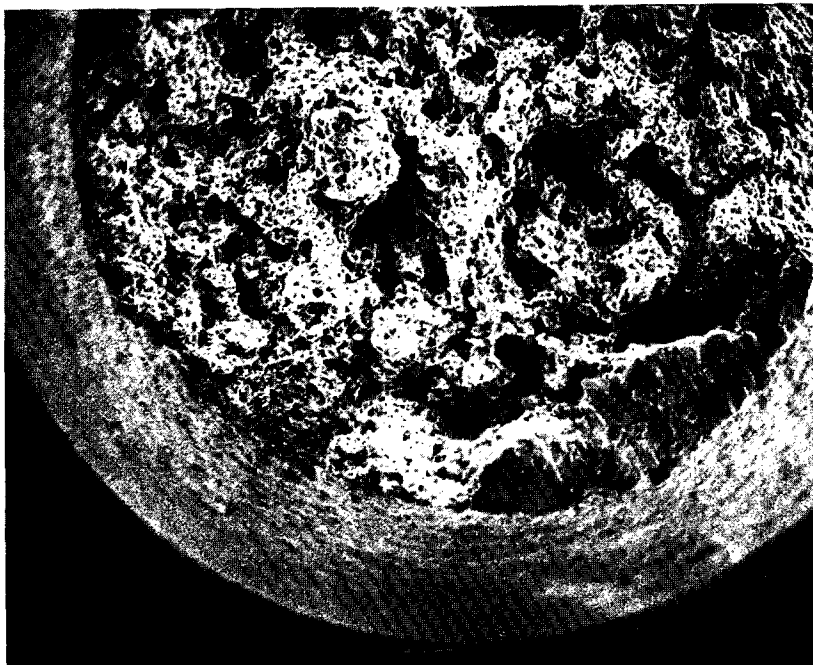


Figure 3.15. SEM photograph of fracture surface of Titanium Grade 12 specimen after slow strain rate testing in deaerated Brine A at 250 C at a strain rate of $1 \times 10^{-7} \text{ sec}^{-1}$.

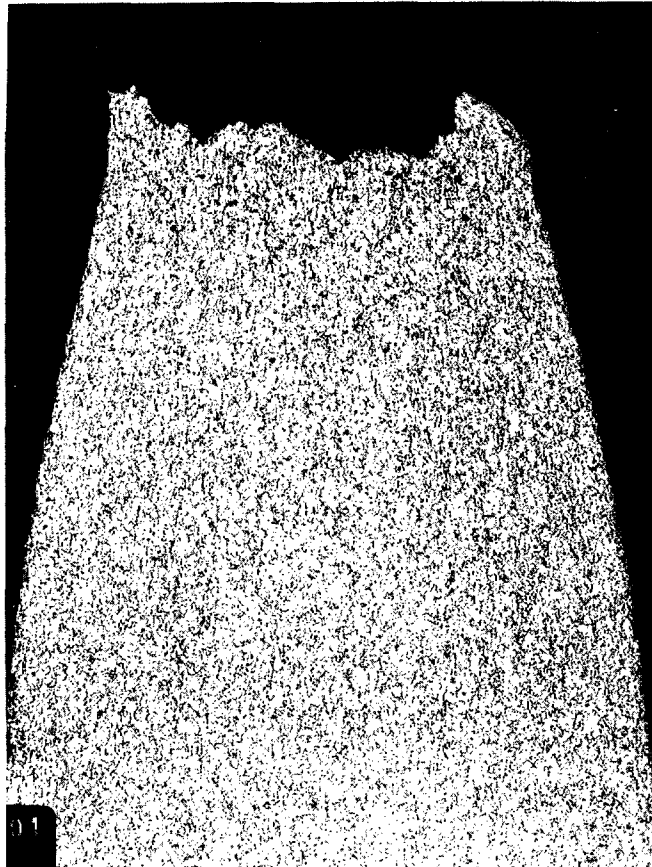


Figure 3.16. Photomicrograph of metallographic section of specimen from Figure 3.15.

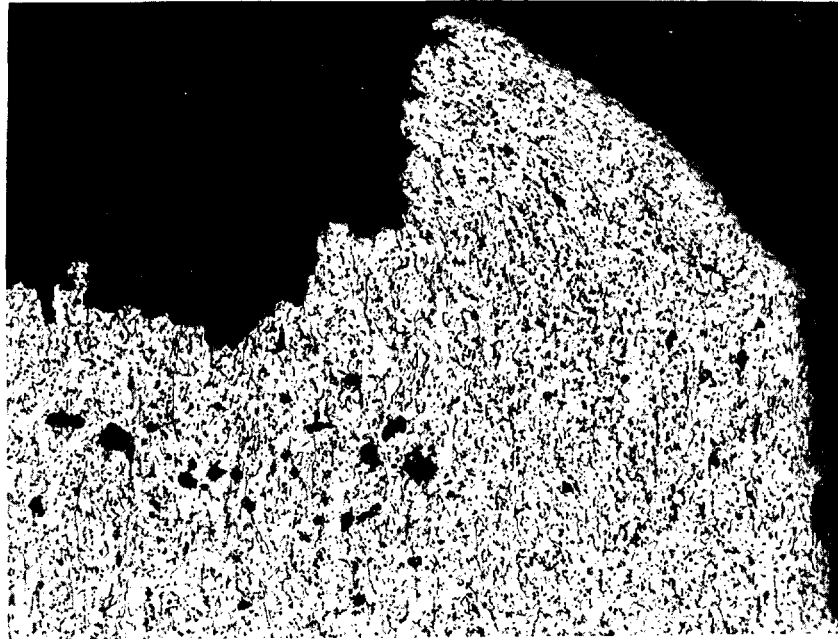


Figure 3.17. Higher magnification photomicrograph of right edge of fracture surface shown in Figure 3.16.

Note considerable plastic deformation in the damaged area in upper right-hand corner and strain-induced porosity (voids).

Finally, results of gravimetric and polarization-resistance measurements performed on isothermal specimens of Titanium Grade 12 in deaerated Brine A at 250 C indicate that parasitic redox reactions occurring in the solutions may preclude the use of electrochemistry for measuring corrosion rates in this system.

3.2 Carbon Steel-System

3.2.1 Potentiodynamic Polarization Studies

3.2.1.1 Objective

The objective of this task was to evaluate the influence of metallurgical and environmental variables on the general corrosion, pitting, and stress corrosion behavior of carbon steels in simulated basalt repository environments.

3.2.1.2 Experimental Approach

Potentiodynamic polarization techniques were used to evaluate the influence of metallurgical and environmental variables on the electrochemical behavior of carbon steels. The results of these analyses were then used to assess the tendency for general corrosion, stress-corrosion cracking (SCC), and pitting.

In the potentiodynamic polarization procedure, the polarity and magnitude of the current density between a metal specimen and an inert counter electrode are measured as functions of electrochemical potential. A polarization curve is then plotted as potential versus logarithm of current density. For the anodic portions of the curve, the current measured is equal to the corrosion rate of the specimen if two conditions are met: (1) the over-potential (difference between the free-corrosion and polarized potential) is large enough such that the rate of the cathodic reaction is negligible, and (2) the rates of parasitic oxidation reactions are negligible.

A schematic of anodic polarization curves showing several types of behavior is given in Figure 3.18. For the active-corrosion case, the anodic curve is linear on a potential versus logarithm of current (E -log i) plot, and the forward and reverse scans are coincident. The presence of a peak in the anodic portion of the curve, followed by decreasing current, generally indicates the onset of passivation. The occurrence of hysteresis between the forward and reverse scans indicates pitting. Where the hysteresis loop is very large, the protection potential, E_{prot} , may be very close to the free-corrosion potential, E_{cor} , indicating a high probability of pitting in service.

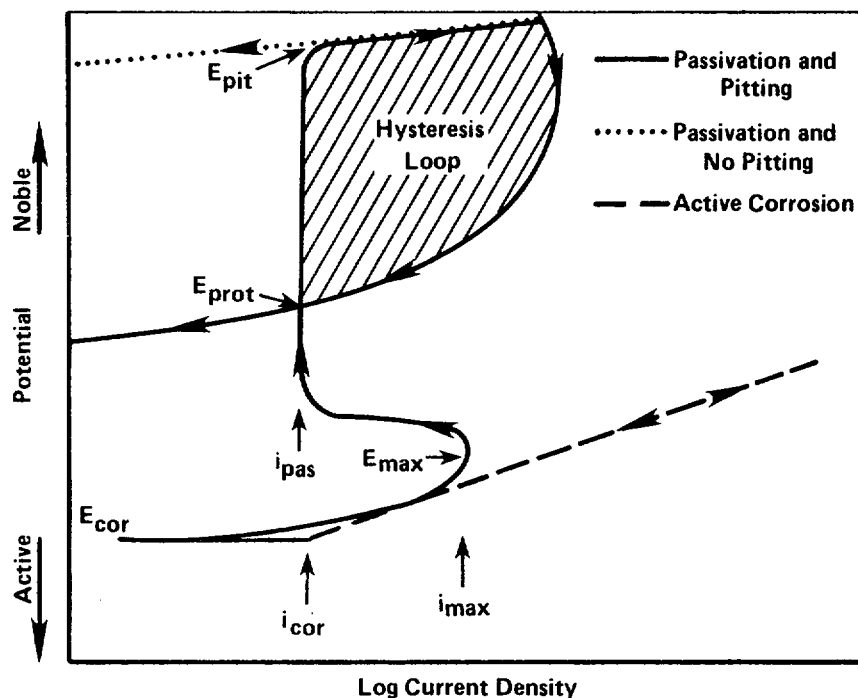


Figure 3.18. Schematic of typical anodic potentiodynamic polarization curves.

E_{cor} = corrosion potential; i_{cor} = current density at the free-corrosion potential; E_{max} = potential at the active peak; i_{max} = current density at active peak; i_{pas} = current density in passive range; E_{pit} = potential at which pits initiate on forward scan; and E_{prot} = potential at which pits repassivate on reverse scan.

The potentiodynamic polarization technique also has been found to be useful in identifying possible SCC environments for carbon steels. It has been shown (Ref. 3.5) that SCC is associated with environments that promote active-passive behavior and that the range of electrochemical potentials that promotes SCC is near to and more noble (positive) than E_{\max} . Moreover, it has been observed (Ref. 3.5) that severe cracking occurs in environments where i_{\max} on a fast scan (scan rate > 10 V/hr) is greater than about 1×10^{-3} A/cm², and where the fast scan exhibits currents at least an order of magnitude higher than those of the slow scan (scan rate < 1 V/hr) (see Figure 3.19).

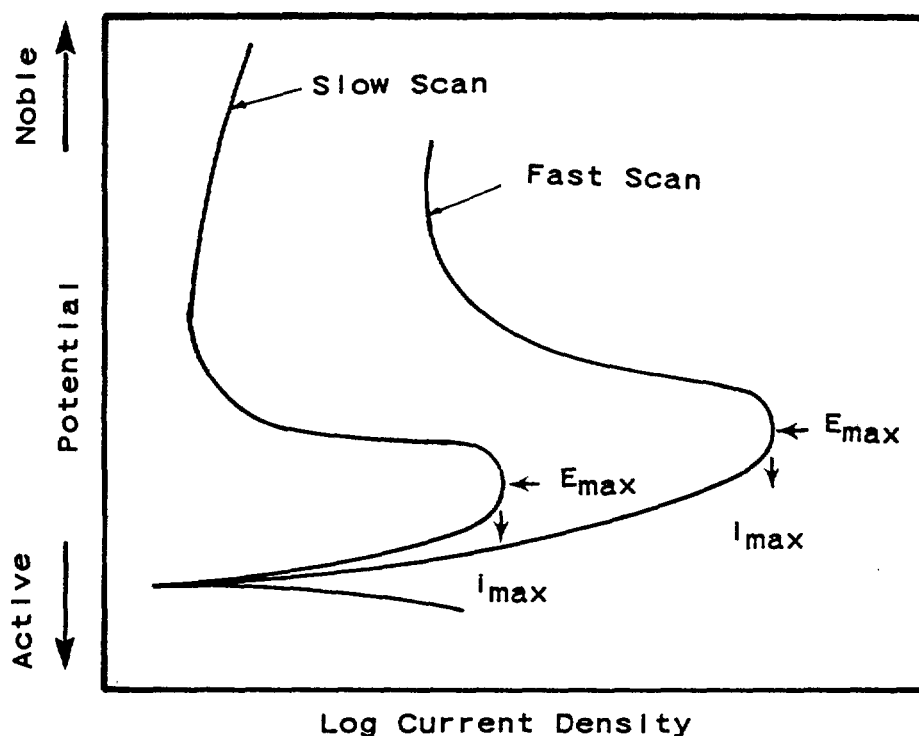


Figure 3.19. Schematic of slow scan and fast scan potentiodynamic polarization curves for a metal in an SCC environment.

The polarization behavior of candidate alloys was determined using conventional polarization techniques. The equipment used for these experiments included a PAR Model 173 potentiostat with an ECO Model 567 function generator, coupled to a computer data-acquisition system. A three-compartment electrochemical cell containing a saturated calomel reference electrode (SCE) and a platinum counter electrode was used. The three-compartment electrochemical cell, which is shown in Figure 3.20, separates the working electrode from the counter electrode, thus preventing solutions in the different compartments from mixing. The working-electrode specimens were cylindrical rods drilled and tapped at both ends and then sealed using PTFE

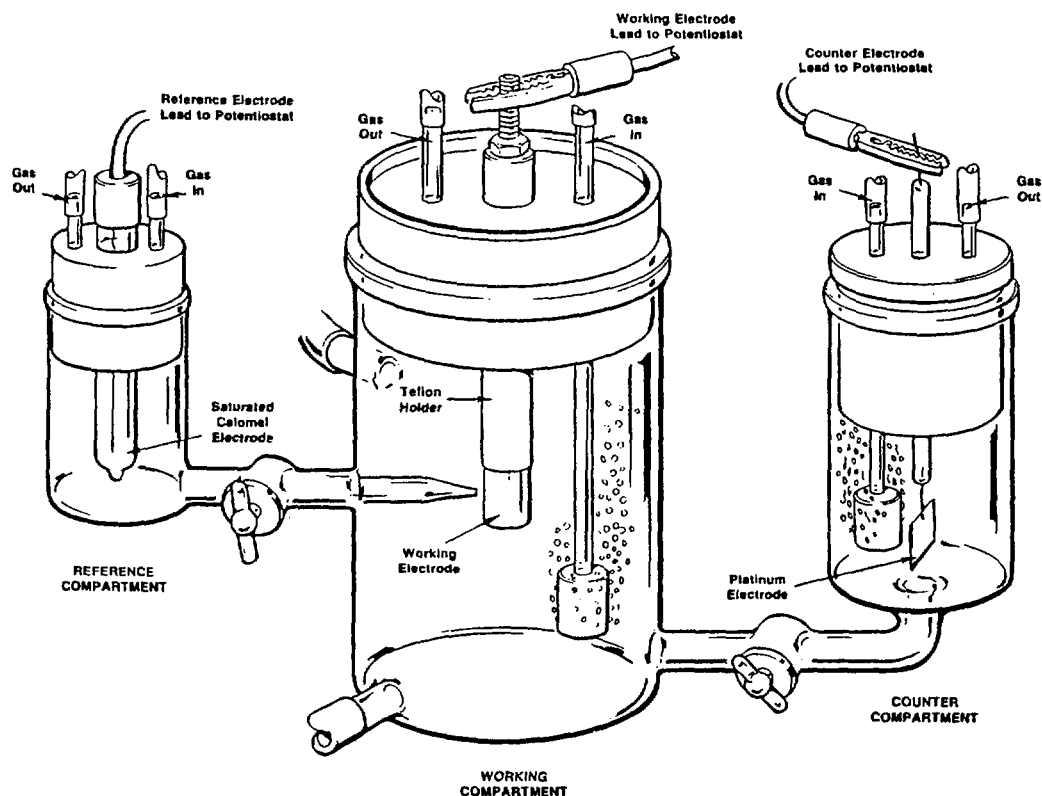


Figure 3.20. Three-compartment polarization cell design.

gaskets. The specimens were 0.6 cm in diameter and 1.9 cm in length; the actual area of each specimen was measured prior to immersion in the electrochemical cell. The electrodes were polished with successively finer grades of silicon carbide paper, finishing with a 600-grit paper.

Prior to testing, the working electrode remained in the test solution overnight while the solution was sparged with the desired gas mixture. The polarization scans were then performed approximately 16 hours after the working electrode was immersed in the cell. Partial cathodic and full anodic polarization curves were obtained by scanning at a rate of 0.6 V/hr, beginning the scan approximately 100 mV more negative than the free-corrosion potential. The current for the anodic curve was then scanned until it attained a density of approximately $3 \times 10^{-3} \text{ A/cm}^2$; the anodic scan was then reversed until repassivation occurred and the current changed polarity, becoming cathodic. When the polarization plot was completed, a new steel specimen was inserted into the polarization cell and immediately polarized to a potential of approximately -0.90 V (SCE). Within five minutes of immersion, a fast-anodic scan was performed using a scan rate of 18 V/hr. After the polarization scans were completed, the following polarization parameters were obtained from the polarization curves of potential

(E) versus the logarithm of current density ($\log i$): E_{cor} , i_{cor} , E_{max} , i_{max} (obtained from the fast-scan curves), i_{pas} , E_{pit} , and E_{prot} .

The potentiodynamic polarization technique was used in three separate studies: metallurgical studies of the effect of steel cleanliness and structure on electrochemical behavior in simulated basalt groundwater; preliminary environmental studies of the effect of the presence of basalt rock and concentration of the basalt groundwater on corrosion behavior; and a statistical matrix of experiments designed to evaluate the influence of 15 environmental species on corrosion behavior. The chemical composition and other data on the steels used in these studies are given in Table 3.8. Note that, with the exception of the metallurgical studies, hot-rolled 1020 carbon steel specimens were used for all potentiodynamic polarization experiments. Significant findings from these studies are given below.

3.2.1.3 Results of Metallurgical Studies

The majority of the metallurgical studies were performed in a single groundwater composition, which is referred to as basalt groundwater. This solution was prepared according to a published procedure (Ref. 3.6); the nominal composition is given in Table 3.9.

The metallurgical studies focused on the effects of steel cleanliness and structure on electrochemical behavior. Two steel compositions were examined, one ("doped" with phosphorus and sulfur) comparable to a 1018 composition, and one ("clean") having low phosphorus and sulfur (see Table 3.8). These two steels were tested in the as-cast condition and in the hot-rolled condition, giving four combinations. Information on the preparation procedures and characterization of these materials is provided in the 1983-1984 Annual Report for this program (Ref. 3.7).

Results of polarization tests performed on the materials at a scan rate of 0.6 V/hr in deaerated basalt groundwater at 90 C are summarized in Table 3.10 and a polarization curve is given in Figure 3.21. These data show that neither the cleanliness nor the structure of the steel had a pronounced effect on its electrochemical behavior in basalt groundwater.

As an extension of this work, polarization tests were run, in duplicate, on Ferrovac E in basalt groundwater at 90 C. Ferrovac E is a high-purity iron containing only trace quantities of impurities (Table 3.8) and represents an upper bound in cleanliness for a ferrous canister material. The results are summarized in Table 3.10 and Figure 3.22. Several features of the data are noteworthy. First of all, two types of behavior are readily apparent. In Specimen 1, the appearance of the polarization curve is similar to that reported for the other steels, exhibiting an active-to-passive transition, a passive region, and definite pitting and protection potentials. Values of the parameters for Ferrovac E are comparable to those previously reported for the other steels (see Table 3.10). On the other hand, the curve for Specimen 2 does not exhibit an active-to-passive transition, and the free-corrosion potential was in the passive potential range. The presence of a pitting potential and hysteresis on the reverse scan indicates that pitting had occurred on the specimen. The protection and pitting potentials for

Table 3.8. Chemical compositions and other data on steels used in the corrosion studies.

SAE Number or Designation	Thermomechanical Treatment	Tests Used In	Dimensions	Composition, weight percent										
				C	Mn	P	S	Si	Cu	Sn	Ni	Cr	Mo	Al
1018	Cold-Rolled	Slow Strain Rate	0.635 cm dia. rod	0.18	0.72	0.007	0.010	--	--	--	--	--	--	--
1018	Hot-Rolled	Pitting Exposures	7.6 cm x 15.2 cm strip	0.18	0.77	0.017	0.019	0.22	--	--	--	--	--	--
1020(a)	Hot-Rolled	Electrochemical Pitting Monitor, Potentiodynamic Polarization	1.27 cm rod	0.20	0.46	0.011	0.032	0.17	0.38	0.027	0.014	0.018	0.024	--
1020(a)	Hot-Rolled	Slow Strain Rate	0.635 cm diam. rod	0.22	0.55	0.01	0.037	--	--	--	--	--	--	--
Clean BCL Steel	Cast or Hot- Rolled	Potentiodynamic Polarization	Ingot	0.18	0.49	0.004	0.002	0.30	0.006	--	0.002	0.007	0.00	0.10
Doped BCL Steel	Cast or Hot- Rolled	Potentiodynamic Polarization	Ingot	0.17	0.55	0.029	0.036	0.35	0.007	--	0.004	0.011	0.00	0.14
Ferrovac E	Cast	Potentiodynamic Polarization	Ingot	0.003	Tr(b)	--	--	Tr	--	--	Nil(c)	Nil	Tr	Nil

(a) Hot-rolled 1018 carbon steel not available in rod form.

(b) Tr = Trace.

(c) Nil = None detected.

Table 3.9. Nominal compositions of test solutions.

	Concentration, mg/l															pH
	Na	K	Mg	Ca	Sr	Fe	Cl	F	Br	Si	SO ₄	CO ₃	HCO ₃	BO ₃	NO ₃	
Basalt Groundwater	360	3.4	0.03	2.8	--	--	310	33.4	--	35.5	175	(b)	(b)	--	--	9.8
Brine A(a)	42,000	30,000	35,000	600	5	--	190,000	--	400	--	3,500	--	700	1,200	--	6.5
Brine B	115,000	15	10	900	15	--	175,000	--	400	--	3,500	10	10	10	--	6.5

(a) ppm.

(b) 18.1 ppm total inorganic carbon.

Table 3.10. Summary of results of potentiodynamic polarization tests performed on cast and wrought steels in deaerated basalt groundwater at 90 C and a scan rate of 0.6 V/hr.

Material		$E_{cor},$ V (SCE)	$E_{max},$ V (SCE)	$E_{pit},$ V (SCE)	$E_{prot},$ V (SCE)	$i_{cor},$ V (SCE)	$i_{max},$ A/cm ²	$i_{pas},$ A/cm ²
Doped BCL Steel	Cast	-0.840	-0.745	-0.508	-0.698	3.7×10^{-6}	5.5×10^{-6}	4.6×10^{-6}
Doped BCL Steel	Wrought	-0.859	-0.793	-0.481	-0.659	6.8×10^{-6}	1.2×10^{-5}	5.7×10^{-6}
Clean BCL Steel	Cast	-0.859	-0.793	-0.471	-0.679	6.2×10^{-6}	1.0×10^{-6}	6.2×10^{-6}
Clean BCL Steel	Wrought	-0.859	-0.801	-0.508	-0.669	3.4×10^{-6}	5.2×10^{-6}	4.4×10^{-6}
Ferrovac E (1)		-0.869	-0.764	-0.432	-0.679	6.2×10^{-6}	1.2×10^{-5}	6.2×10^{-6}
Ferrovac E (2)		-0.754	*	-0.461	-0.764	1.9×10^{-7}	*	4.4×10^{-7}

*The free-corrosion potential of the specimen was more noble than the potential at maximum current (E_{max}).

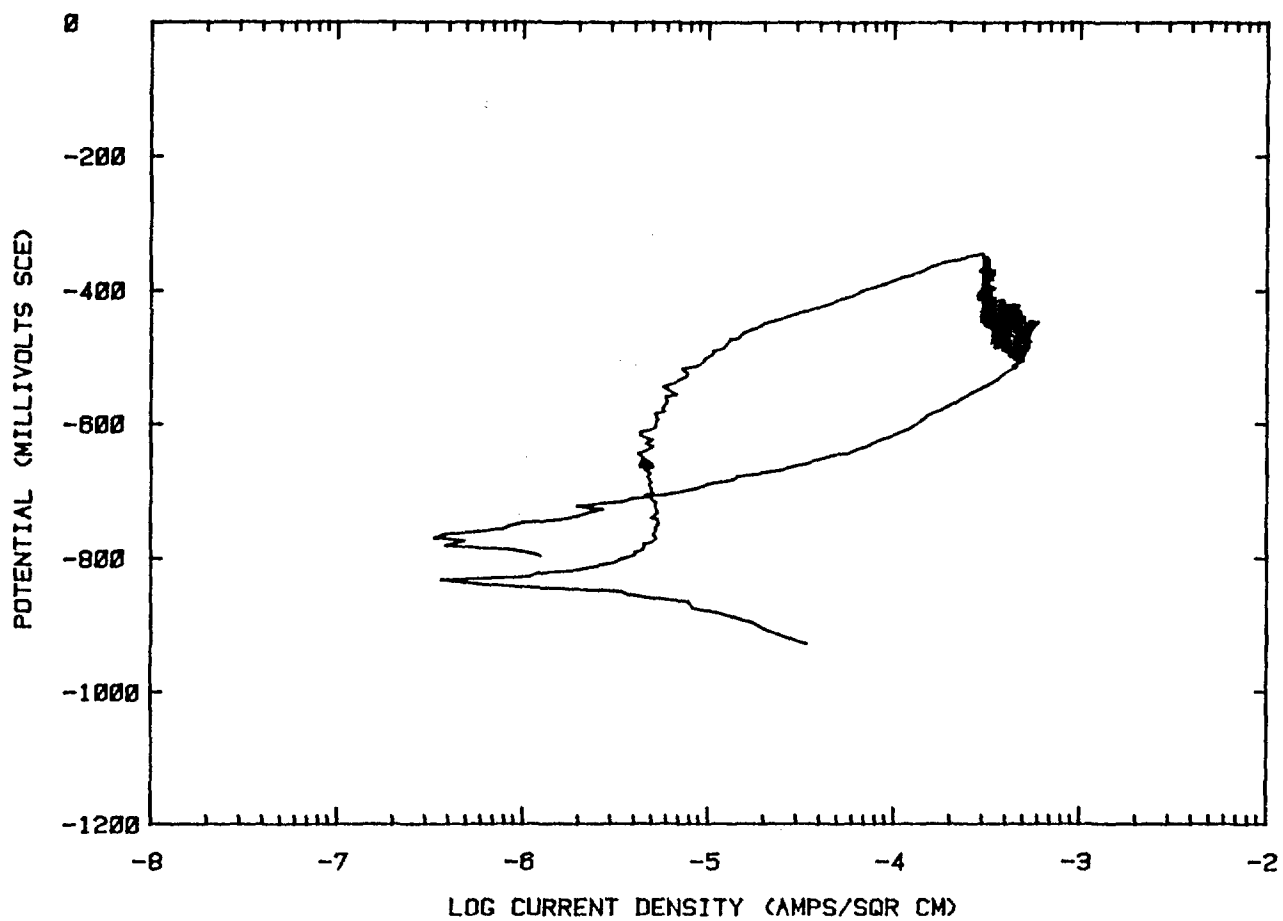
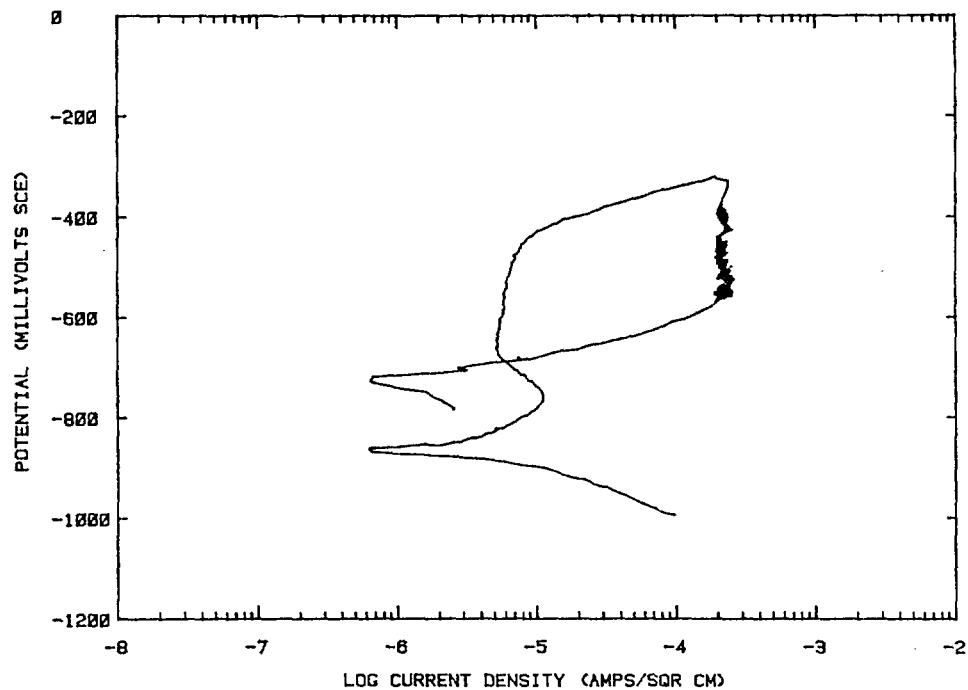
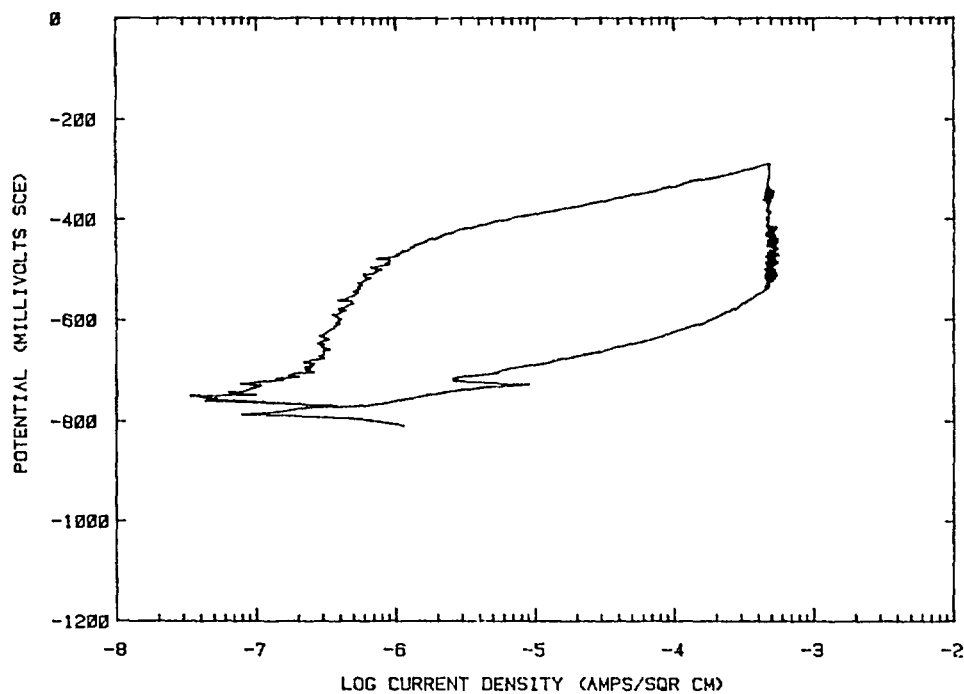


Figure 3.21. Potentiodynamic polarization curve for cast, doped BCL steel in basalt groundwater at 90 C polarized with a scan rate of 0.6 V/hr.



(a) Specimen 1



(b) Specimen 2

Figure 3.22. Potentiodynamic polarization curves for Specimens 1 and 2 of Ferrovac E in basalt groundwater at 90 C polarized with a scan rate of 0.6 V/hr.

Specimen 1 and 2 were similar, whereas the value for E_{cor} for Specimen 2 was more noble than that for Specimen 1. The most reasonable explanation for this behavior is that the solution in the cell containing the latter sample was contaminated with trace quantities of O_2 that spontaneously passivated the specimen.

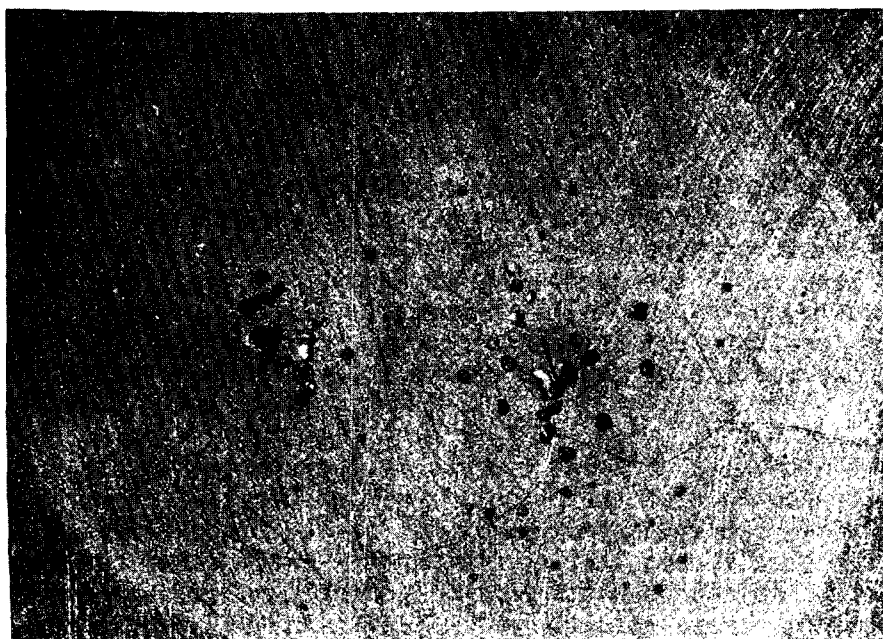
The standard procedure used for these electrochemical experiments was to allow the specimens to equilibrate in the solution overnight before beginning the polarization experiment. Periodically, during this equilibration period, the Ferrovac E specimens were visually examined, and evidence of pit initiation was found on the polished surfaces of both specimens. Following the polarization test, the attack on the specimen surfaces was somewhat greater, as one would expect based on the polarization behavior (see Figure 3.23).

In summary, the results of these experimental studies indicate that variation in the composition of the steels from high-purity Ferrovac E to 1018 carbon steel does not have a marked effect on the electrochemical behavior in a simulated basalt repository environment. Since close correlation between electrochemical behavior and pit initiation has been established for many environments, these results indicate that minor variation in the composition of carbon steel or the use of a high-purity steel will not have a marked influence on pit initiation.

The influence of steel composition on SCC cannot be fully assessed on the basis of these electrochemical data. Although the electrochemical behavior of Ferrovac E was not markedly different from 1018 carbon steel, it is well known that carbon content of steel can greatly influence SCC susceptibility, and the carbon content of these steels is considerably different. Thus, it is clear that properties other than the bulk electrochemical response must be considered in assessing the influence of metallurgical variables on SCC susceptibility. Since SCC in this system is intergranular in nature, the chemistry and electrochemistry of the grain boundaries, as influenced by bulk composition, also must be considered. In addition, the influence of steel composition on mechanical response of the material to the applied load must also be taken into account in assessing the influence of composition on SCC susceptibility.

3.2.1.4 Results of Preliminary Environmental Studies

Effect of Basalt Rock and Concentration of Basalt Groundwater. Potentiodynamic polarization curves were obtained on two of the steels characterized in Table 3.8: a wrought, doped BCL steel and a clean, cast BCL steel. These were tested in the standard basalt groundwater (1X) and a 10-fold concentration of this groundwater (10X) both in the presence of crushed basalt and in its absence. In the former tests, the solutions were equilibrated with crushed basalt by boiling overnight. Results of these studies, summarized in Figures 3.24 and 3.25, show small but systematic effects of groundwater chemistry on the electrochemical parameters. The corrosion potential (E_{cor}) and the potential at the current peak (E_{max}) shifted to slightly more negative values, and the passive current density (i_{pas}) decreased slightly upon increasing the solution concentration. A similar analysis of the



20X

6L617



4X

6L616

Figure 3.23. Optical photographs of Ferrovac E Specimen 2 following potentiodynamic polarization testing in deaerated basalt groundwater at 90 C.

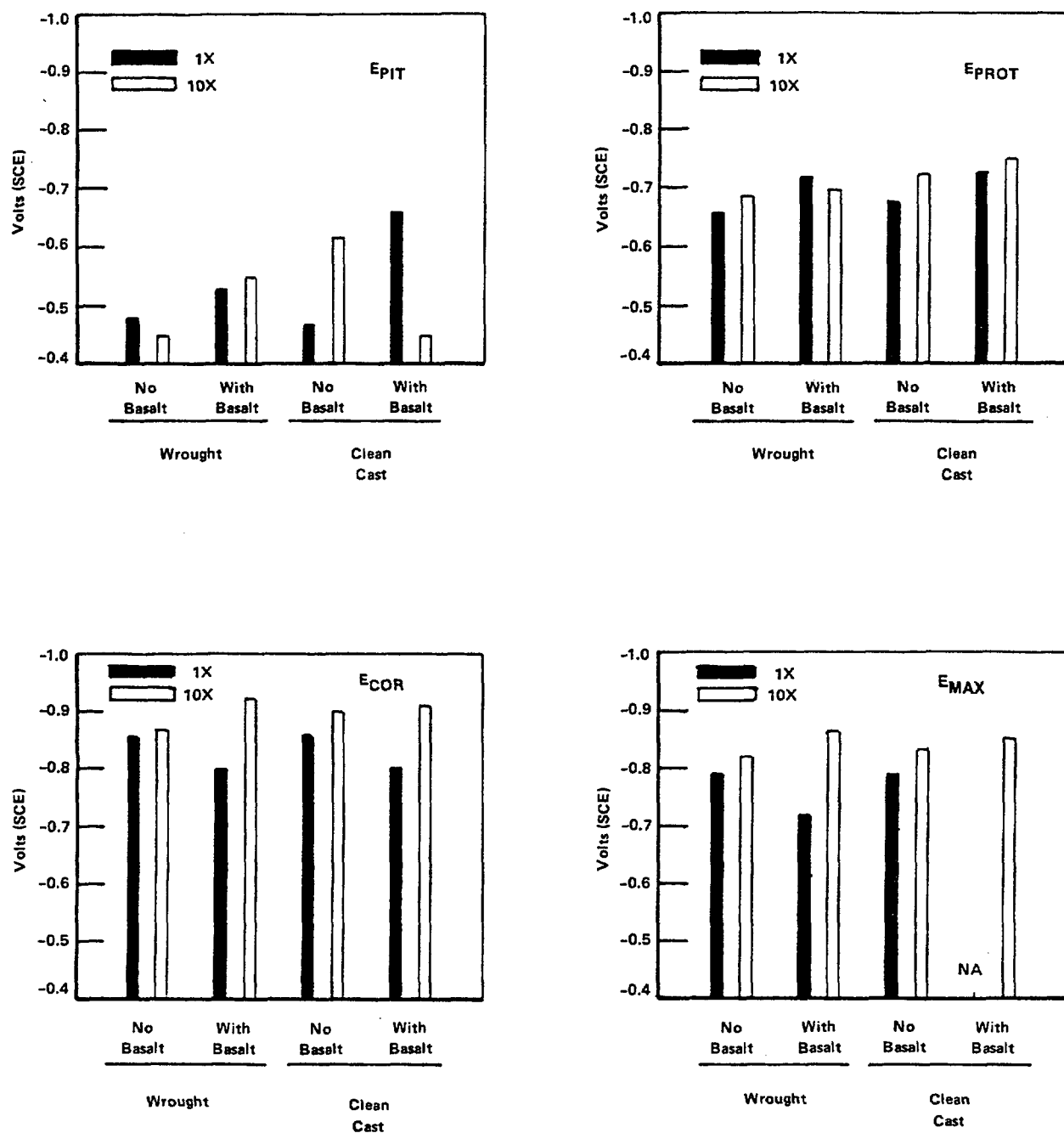


Figure 3.24. Electrochemical potential parameters taken from potentiodynamic polarization curves for wrought doped and clean cast BCL steels in deaerated simulated basalt groundwater at 90 C.

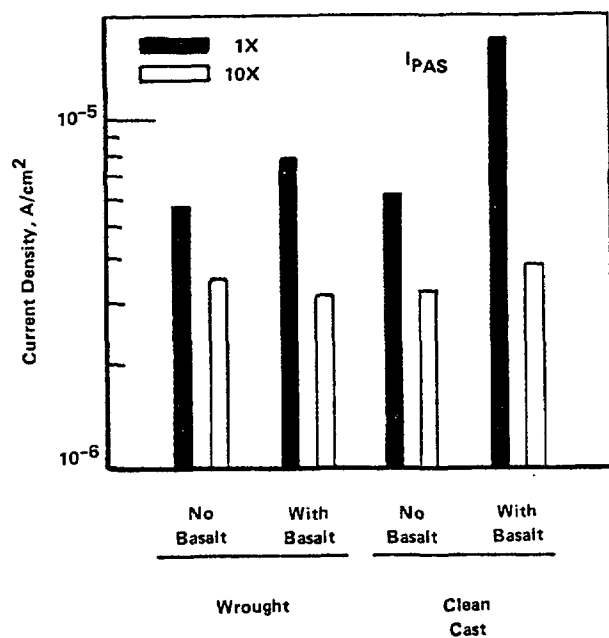
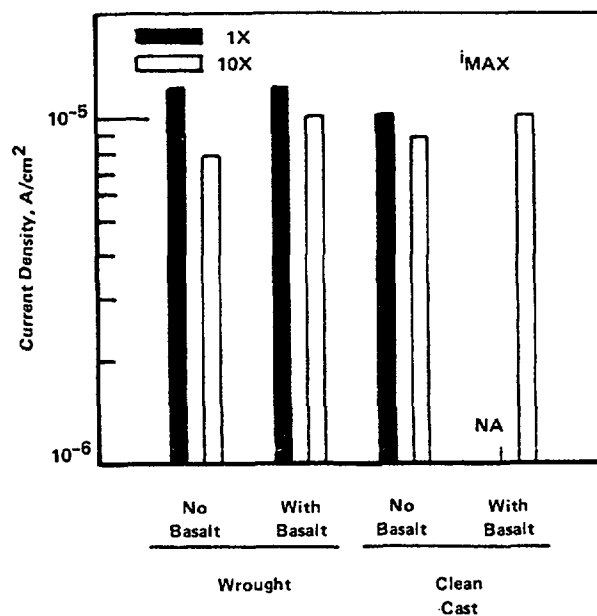
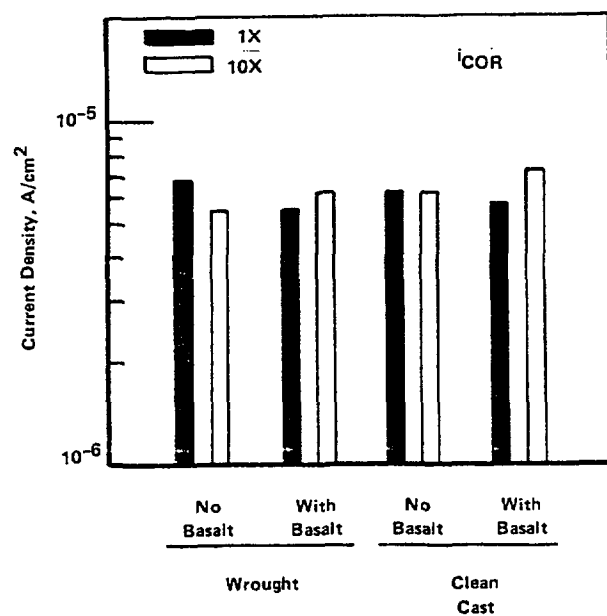


Figure 3.25. Current parameters taken from potentiodynamic polarization curves for wrought doped and clean cast BCL steels in deaerated simulated basalt groundwater at 90 C.

effect of leaching of the basalt rock on these parameters indicated no systematic effect on the electrochemical parameters measured. Since the systematic shifts in these parameters were small, their relevance is difficult to ascertain with respect to waste-package performance.

Effect of Electrochemical-Potential Scan Rate. The effect of scan rate on the polarization behavior of two steels was studied in a 1X basalt groundwater at 90 C. These experiments provided information on the most likely potential ranges for stress-corrosion cracking susceptibility of the steels in repository environments. In the fast-scan tests (18 V/hr), the curves were generated as soon as the specimen contacted the solution, whereas in the slow-scan tests (0.6 V/hr), the specimens were allowed to equilibrate with the solution overnight. The aim of the fast-scan polarization tests was to obtain the maximum current density on relatively bare metal surfaces.

Results of these experiments, summarized in Table 3.11, show that passive currents are considerably higher at the faster scan rates than at the lower scan rates, as expected. An example is given in Figure 3.26. Empirically, it has been shown that stress-corrosion susceptibility of carbon steel reaches a maximum where the differences in current density between the fast and slow polarization scans are large. On this basis, one would expect that the most likely range for SCC of carbon steel in basalt groundwater is between -0.78 V and -0.65 V (SCE). However, the differences in current between the fast and slow scans are small in comparison to potent cracking systems, and thus one would not expect a high degree of susceptibility to SCC at 90 C in the 1X basalt groundwater.

Effect of Temperature. A potentiodynamic polarization curve was obtained for the wrought, doped carbon steel in deaerated basalt groundwater at 250 C and at a scan rate of 0.6 V/hr. In this test, a pressure-balanced external Ag/AgCl reference electrode and an internal platinum counter electrode were used. With the exception of the modifications necessitated by the cell design, the experimental procedure used for the high-pressure test was similar to that used at ambient pressure. The results, given in Figure 3.27, show that the behavior of the steel at 250 C was qualitatively similar to that observed at 90 C, exhibiting an active-passive transition and pitting and protection potentials. Values for i_{cor} , i_{max} , and i_{pas} were somewhat higher at 250 C than at 90 C. The higher peak current may indicate that SCC is more likely at 250 C than at 90 C. On the other hand, the hysteresis loop area at 250 C appears to be somewhat smaller than at 90 C. Because the polarization behavior is qualitatively similar at 250 C to that observed at 90 C, the majority of the subsequent polarization studies were performed at 90 C.

3.2.1.5 Statistical Environmental Studies

As discussed previously, results of the potentiodynamic polarization studies indicate that a uniform tenfold increase in chemical concentration of the groundwater did not have a pronounced effect on the electrochemical behavior. On the other hand, the literature survey (Ref. 3.5) identified many species that are present in the groundwater or that may intrude into the repository or be generated by radiolysis that may significantly affect the

Table 3.11. Summary of results of potentiodynamic polarization tests performed on doped cast BCL steel and clean wrought BCL steel in deaerated basalt groundwater at 90 C comparing fast scan rate and slow scan rate data.

Material	Scan Rate, V/hr	E_{cor} , V (SCE)	E_{max} , V (SCE)	E_{pit} , V (SCE)	E_{prot} , V (SCE)	i_{cor} , A/cm ²	i_{max} , A/cm ²	i_{pas} , A/cm ²
Doped Cast*	0.6	-0.858	-0.745	-0.508	-0.698	3.7×10^{-6}	5.5×10^{-6}	4.6×10^{-6}
Doped Cast	18	-0.886	*	-0.518	-0.669	1.9×10^{-5}	*	8.2×10^{-5}
Clean Wrought	0.6	-0.859	-0.801	-0.508	-0.669	3.4×10^{-6}	5.2×10^{-6}	4.4×10^{-6}
Clean Wrought	18	-0.896	*	-0.491	-0.649	1.5×10^{-5}	*	9.0×10^{-5}

*Polarization behavior did not exhibit a maximum current peak.

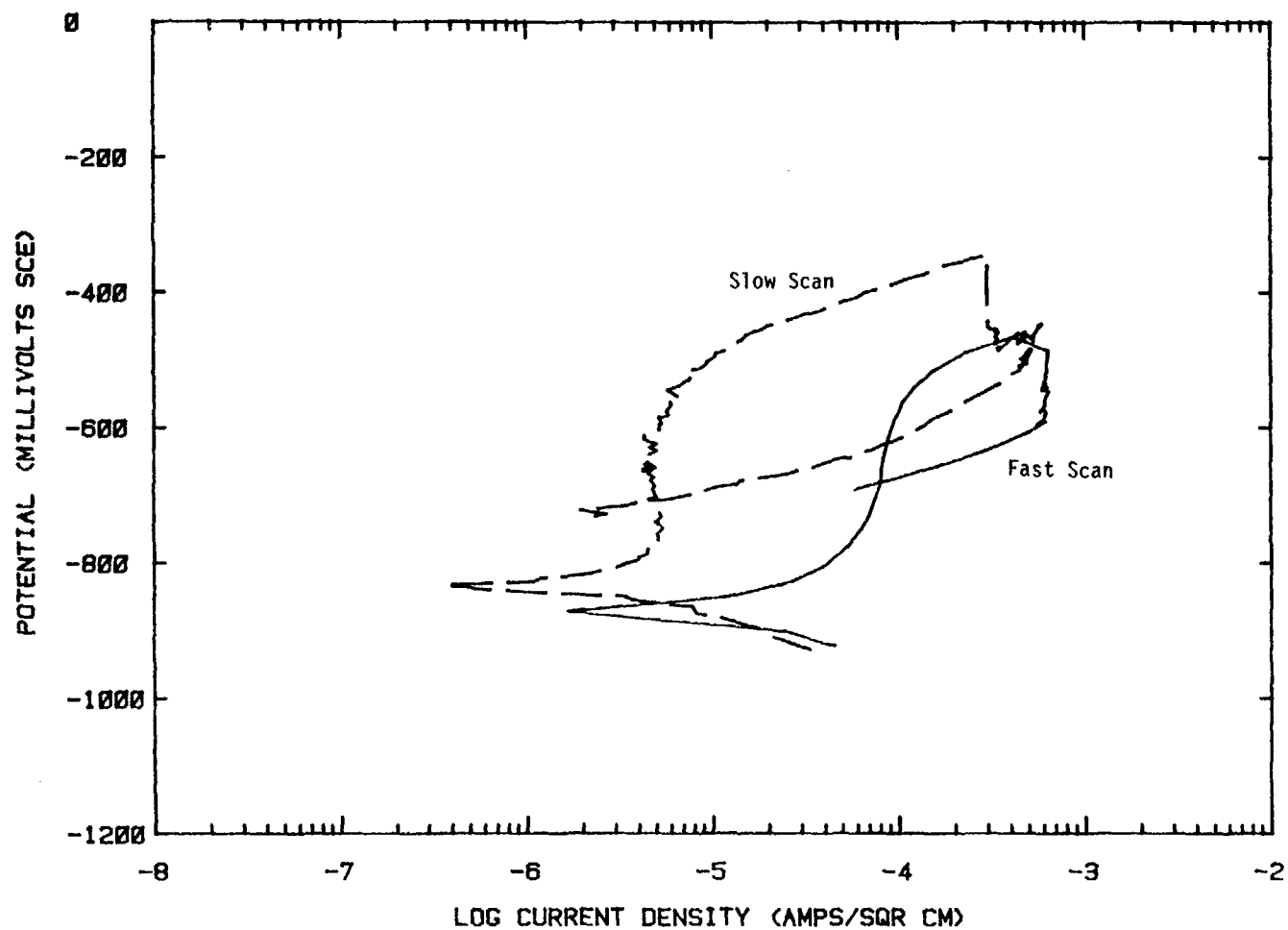


Figure 3.26. Effect of scan rate on the polarization behavior of cast doped BCL steel in deaerated basalt groundwater at 90 C.

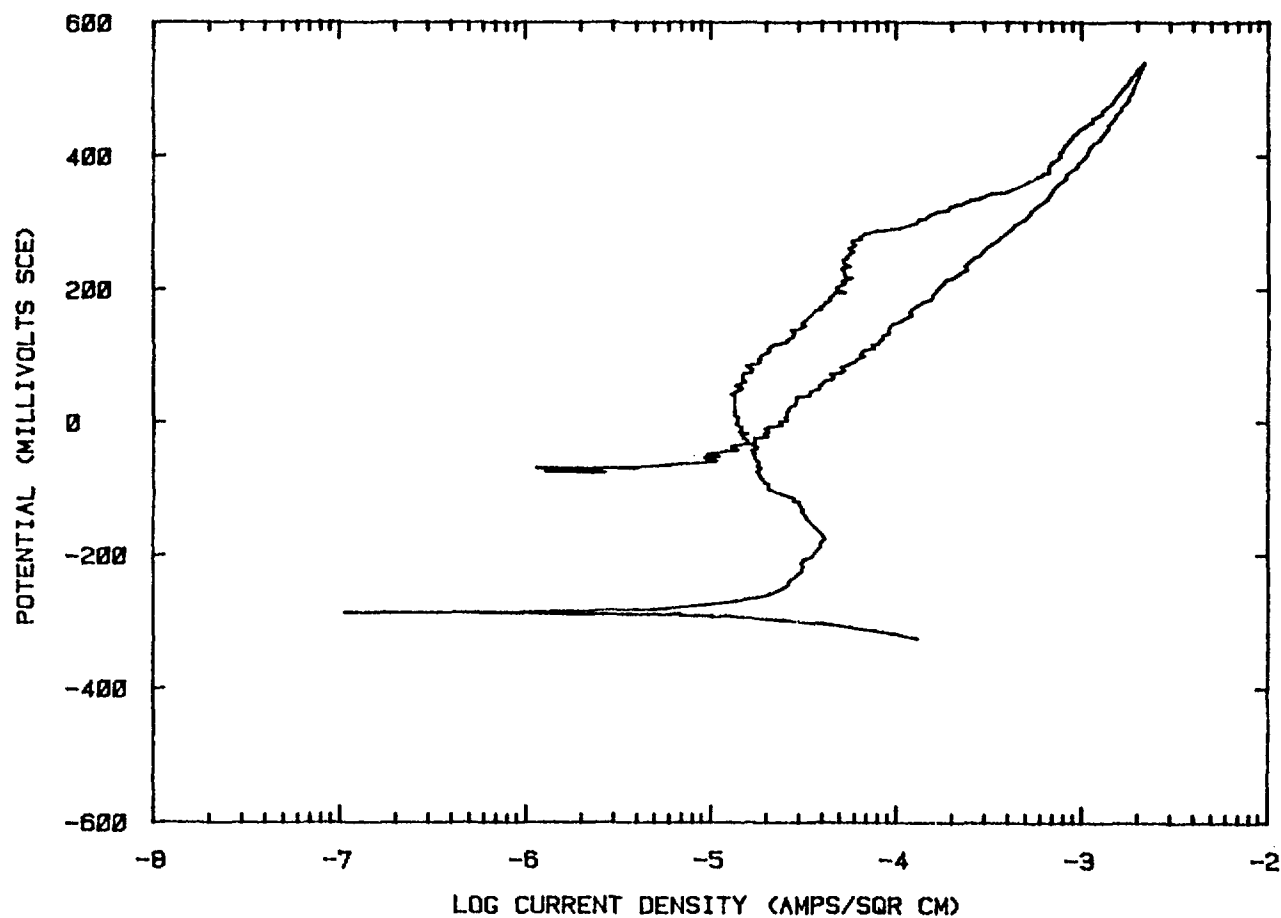


Figure 3.27. Potentiodynamic polarization curve for the wrought doped BCL steel in basalt groundwater at 250 C with a scan rate of 0.6 V/hr.

localized corrosion behavior of carbon steel. Accordingly, electrochemical studies were undertaken to evaluate the influence of these species on electrochemical behavior. Because of the large number of species considered, a statistical approach was used.

A literature survey of the chemical species selected for the investigation was the basis for determining the high and low concentrations to be used in the experiments. The low concentration was based on that present in typical basalt groundwater. The high concentration was typically 2 to 4 orders of magnitude higher than the low concentration.

Table 3.12 gives the 15 species and their concentrations selected for examination during the preliminary two-level design matrix. These included species present in the groundwater, those that may leach from the backfill, radiolysis products, and species that may intrude into the repository.

Table 3.13 shows typical concentrations reported in the literature for the 15 species examined, as well as concentrations of other species. Species such as sodium (Na^+), potassium (K^+), calcium (Ca^{+2}), and sulfate (SO_4^{-2}) were also included in the experimental matrix, but not as controlled variables. The concentrations of potassium and calcium were maintained constant, while sodium and sulfate ions were used to balance the cation and anion concentrations required for the 15 species added as variables. Justifications for the species examined in this task were presented elsewhere (Ref. 3.14).

All experiments were performed on a commercially available, hot-rolled 1020 carbon steel at 90 C in argon-purified simulated groundwater solutions. The composition of the steel is given in Table 3.8. The parameters analyzed were E_{cor} , E_{prot} , E_{pit} , i_{cor} , i_{max} , and i_{pas} , as defined in Figure 3.18. The studies, described in the following sections, were divided into three subtasks: the screening matrix, the main matrix, and effects of single species.

Screening Matrix of Experiments. The purpose of the screening matrix of experiments was to determine which of the 15 species discussed above have a significant effect on general corrosion, SCC, and pitting corrosion. The screening matrix was used to select the species that significantly affect corrosion, for examination in the main matrix.

To estimate the individual main effects of each of the 15 species, a statistical design was used to define the optimal compositions of the test solutions. The statistical design was a partial factorial design of resolution IV. This design permits the main-effect terms of the 15 variables to be estimated free and clear of other main-effect terms and of any two-factor interactions. Three-factor and greater interactions still confound the main-effect terms; however, these usually contribute only a small response compared to the main-effect term response. Consequently, a good estimate of the main-effect terms was calculated at the end of the screening matrix of experiments. Four experiments were also performed using the midpoint of each species concentration to provide an estimate of error for the polarization experiments.

Table 3.12. High and low concentrations of species selected for evaluation in the electrochemical experiments.

Species	High Concentration	Low Concentration
1. pH	9.3	6.0
2. Cl^{-1}	100,000 ppm	100 ppm
3. F^{-1}	10,000 ppm	10 ppm
4. $\text{Fe}^{+2}/\text{Fe}^{+3}$	100 ppm	0.05 ppm
5. Al^{+3}	1,000 ppm	0.1 ppm
6. $\text{CO}_3^{-2}/\text{HCO}_3^{-1}$	1 M	0.001 M
7. $\text{NO}_3^{-1}/\text{NO}_2^{-1}$	1,000 ppm [N]	0.1 ppm [N]
8. PO_4^{-3}	1,000 ppm [P]	0.1 ppm [P]
9. $\text{BO}_3^{-3}/\text{B}_4\text{O}_7^{-2}$	1,000 ppm [B]	1 ppm [B]
10. SiO_3^{-2}	1,000 ppm [Si]	10 ppm [Si]
11. H_2O_2	100 ppm	0
12. ClO_4^{-1}	100 ppm	0
13. O_2	2% (Vapor)	0
14. CO	1% (Vapor)	0
15. H_2	80% (Vapor)	1%

Table 3.13. Concentrations of species in basalt groundwater or in actual or simulated basalt repository environments.

	Ref. 3.8	Ref. 3.9	Ref. 3.10	Ref. 3.11	Ref. 3.12	Ref. 3.13
1. pH	9.7 (5.7)					
2. Cl ⁻¹	98-297(500) ppm					
3. F ⁻¹	11-42(50) ppm					4%[Fe ₂ O ₃](c)
4. Fe ⁺² /Fe ⁺³	0-0.6(0.5)[Fe ⁺²] ppm	0.009 ppm				18%[Al ₂ O ₃](c)
5. Al ⁺³	0.02(20) ppm	0.007 ppm				
6. CO ₃ ⁻² /HCO ₃ ⁻¹	4-55/45-118(70/200) ppm					
7. NO ₃ ⁻¹ /NO ₂ ⁻¹						
8. PO ₄ ⁻³		0.2[P] ppm				0.08%[P ₂ O ₅](c)
9. BO ₃ ⁻³ /B ₄ O ₇ ⁻²	0-1.5(5)[B ⁺³] ppm	1.3 [B] ppm				
10. SiO ₃ ⁻²	30-170(2000)[Si] ppm				30[SiO ₂] ppm	59%[SiO ₂](c)
11. H ₂ O ₂				0.34 ppm		
12. ClO ₄ ⁻²						
13. O ₂				3.2 ppm	0.5%(b)	
14. CO						
15. H ₂				0.02 ppm	76.6%(b)	
Na ⁺¹	161-350(500)					2.2%(c)
K ⁺¹	3-25(100)					0.7%[K ₂ O](c)
Ca ⁺²	0.8-10(100)					1.7%[CaO](c)
Mg ⁺²	0-0.2(50)					2.1%[MgO](c)
SO ₄ ⁻²	4-197(200)				300 ppm	
S ⁻²	0(100)					
N ₂			25 ppm(a)		29.3%(b)	
CH ₄			700 ppm(a)		0.3%(b)	
CO ₂					2.3%(b)	
E _H	-0.5 to -0.53(+0.2 to -0.4)VSHE					

(a)Measurements at 25 C.

(b)Composition of gas phase for simulated irradiated Grande Ronde basalt groundwater.

(c)Composition of bentonite.

At the completion of the screening matrix of experiments, a regression analysis was performed on the different corrosion parameters with the aid of a multiple regression routine on the MINITAB* statistical computer program. The regression analysis calculated the "F" ratio and the regression coefficient for each of the 15 species. The "F" statistic is a ratio of two variances, that is, the sum of squares explained by each factor when entered in the equation, divided by the residual mean square (error). In general, when the calculated "F" ratio for a factor is large, it means that a large amount of experimental variation is explained by this term compared to the error variation. If a calculated "F" ratio exceeds the appropriate tabulated "F" value, then it can be assumed that the solution variable has a statistically significant effect on a particular polarization parameter. A 90-percent probability that a species is significant is usually acceptable for most experimental work and implies that one accepts a 10-percent chance of being wrong in assuming the factor has a significant effect.

The regression coefficients are multiplicative terms for the factors in a regression equation and were determined by a linear least square fit of the data. The regression coefficients determined in this study were calculated based on the high and low concentrations (+1 and -1) of the various chemical species. For the screening matrix, these factors were based on the design concentration range of the species indicated in Table 3.12. Because precipitation occurred in several solutions, the actual concentrations achieved in the test solutions were not the designed values. Therefore, the regression coefficients provide relative magnitudes of the measured effects only and were not meant to give a quantitative measure of the effects.

Polarization experiments were performed and polarization curves obtained for each of 33 solutions. A wide range of behavior was observed by varying the concentration of the 15 species used in the screening matrix of experiments. Not all of the polarization parameters could be selected from the curves in all cases. Table 3.14 shows the polarization parameter values for 1020 carbon steel in quadruplicate tests in solution 33. The variations in the polarization parameters for these tests indicate the reproducibility of the data obtained.

Results of the statistical analysis performed on the polarization data are given in Table 3.15. These data indicate the main effect for each of the 15 species on the six polarization parameters examined: E_{cor} , $\log i_{cor}$, $\log i_{pas}$, E_{pit} , and E_{prot} from the slow scan rate curves, and $\log i_{max}$ from the fast scan rate curves. The "F" value indicates the significance of the species, and the coefficient indicates the relative magnitude of the effect. Coefficients are given only for those species that have a significant effect, based on a 75-percent or greater probability. For the majority of the discussions, a 90-percent or greater probability is typically required before an effect is considered significant. A positive coefficient indicates that an increase in concentration increases the value of the

*Minitab Project, Statistics Dept., 215 Pond Laboratory, The Pennsylvania State University, University Park, PA, 16802, 1981.

Table 3.14. Experimentally measured polarization parameters for solution 33 which represented the mid-point concentration of species defined in Table 3.12 (4 replicates, A to D).

Solution	i_{cor} , A/cm ²	E_{cor} , V (SCE)	i_{pas} , A/cm ²	E_{pit} , V (SCE)	E_{prot} , V (SCE)	$i_{max(fast)}$, A/cm ²
33A	2.50×10^{-6}	-0.544	6.25×10^{-6}	-0.293	-0.576	1.12×10^{-4}
33B	1.10×10^{-6}	-0.0466	3.73×10^{-6}	-0.310	-0.576	1.17×10^{-4}
33C	1.37×10^{-6}	-0.530	4.27×10^{-6}	-0.232	-0.576	8.97×10^{-5}
33D	1.48×10^{-6}	-0.530	4.61×10^{-6}	-0.310	-0.576	1.11×10^{-4}

Table 3.15. Results of statistical analysis indicating the effect of each chemical species on the polarization parameters measured by potentiodynamic polarization.

	E_{cor}		$\log i_{cor}$		$\log i_{max}$		$\log i_{pas}$		E_{pit}		E_{prot}	
	F	Coef	F	Coef	F	Coef	F	Coef	F	Coef	F	Coef
pH	0.5		6.4	-0.34*	0.0		174	-0.18*	27	+0.31*	13	+0.22*
Cl	7.6	-0.06*	0.2		7.1	-0.23*	34	+0.06*	26	-0.25*	30	-0.32*
F	0.5		1.0		1.8	+0.11**	39	-0.08*	0.0		0.3	
Fe	0.9		0.9		0.2		86	+0.41*	0.0		0.3	
Al	1.1		0.8		0.0		36	+0.03*	1.7		0.1	
CO ₃ /HCO ₃	8.4	-0.07*	0.3		25.1	+0.43*	3.6	-0.16**	2.9	+0.06**	0.9	
NO ₃ /NO ₂	15.0	+0.09*	1.1		0.9		19	+0.64*	4.0	+0.13**	0.1	
PO ₄	1.1		0.4		0.3		28	+0.10*	0.3		2.6	-0.10**
BO ₃ /B ₄ O ₇	1.9	+0.03**	0.1		1.3		29	+0.78*	6.0	+0.14*	5.1	+0.13*
SiO ₃	1.1		7.2	-0.36*	0.2		138	-0.85*	0.0		0.1	
H ₂ O ₂	0.3		4.2	+0.27*	0.4		16	+0.25*	0.0		0.2	
ClO ₄	0.2		0.1		0.0		1.2		0.2		1.3	
O ₂	3.9	+0.05*	0.5		0.0		1.3		9.3	+0.13*	8.2	+0.15*
CO	0.1		0.1		0.0		22	-0.64*	1.1		0.0	
H ₂	0.0		1.7	+0.17**	0.2		0.3		1.2		0.1	

*Greater than 90 percent probability that effect is significant.

**Greater than 75 percent but less than 90 percent probability that effect is significant.

parameter, and a negative coefficient indicates that an increase in concentration of the species decreases the value of the parameter. Table 3.15 indicates that most species have an effect on at least one polarization parameter, with the exceptions of perchlorate (ClO_4^-) and hydrogen (H_2), based on a 90-percent or greater probability of significance.

Table 3.16 summarizes the statistical analysis results for the main effects of the chemical species examined in the screening tests. Arrows are used to indicate the direction of the effect for each species that had a significant effect, based on a 90-percent or greater probability. Many of the effects were expected, such as O_2 and NO_3^- increasing E_{cor} and Cl^- decreasing E_{pit} . Other effects, such as Cl^- decreasing E_{cor} , were not particularly expected, but can be explained since Cl^- would tend to make the steel more active. It is also noteworthy that several species had a significant effect on i_{pas} . Referring back to Table 3.15, $\text{NO}_3^-/\text{NO}_2^-$ and $\text{BO}_3^{3-}/\text{B}_4\text{O}_7^{2-}$ had very large coefficients, indicating that these species greatly increased the passive current density with an increase in concentration, while SiO_3^{2-} and CO had large negative coefficients, indicating that these species greatly decreased i_{pas} with an increase in concentration.

The polarization parameter i_{max} , which is the maximum current density during the active peak, as measured with the fast-scan technique, has been used to indicate the tendency for SCC. Generally, a higher SCC tendency is indicated by a larger i_{max} . As expected, $\text{CO}_3^{2-}/\text{HCO}_3^-$ produced a significant increase in i_{max} with increasing concentrations. Chloride, on the other hand, decreased i_{max} with increasing concentration.

Pitting behavior also was affected significantly by some of the species. Chloride, as expected, tended to decrease E_{pit} and E_{prot} , indicating more severe pitting conditions. Oxygen, $\text{BO}_3/\text{B}_4\text{O}_7$, and pH all tended to increase E_{pit} and E_{prot} with increasing concentration.

Based on the results of the statistical analysis, 11 species were selected for examination in the main matrix of experiments. As shown in Table 3.16, H_2 and ClO_4^- had no effect on the polarization parameters measured, based on a 90-percent or greater probability of significance; therefore, these two species were removed from further consideration. It should be noted that ClO_4^- may have an effect that lasts for only a short period, and that it might have been overlooked in the present experiments. Therefore, additional work was performed to consider the effects of ClO_4^- . The other two species not considered in the main matrix of experiments were Al^{+3} and PO_4^{3-} ; these species were removed since they only affected i_{pas} , and the coefficients of the effects (see Table 3.15) were less than those of the other species. Fluoride also had only a small effect on i_{pas} but showed an effect on i_{max} with a probability of significance greater than 75 percent, but less than 90 percent. The decision, therefore, was made to retain fluoride in the main matrix.

Several of the two-factor interactions of the 15 species examined were significant. Of particular interest to this program are interactions that are important when considering i_{max} , which indicates the tendency for SCC, and when considering E_{pit} and E_{prot} , which indicate the tendency for pitting.

Table 3.16. Summary of results of statistical analysis for the main effects of the chemical species based on a 90-percent or greater probability of significance.

	E_{cor}	$\log i_{cor}$	$\log i_{max}$	$\log i_{pas}$	E_{pit}	E_{prot}
pH	-	↓	-	↓	↑	↑
Cl	↓	-	↓	↑	↓	↓
F	-	-	-	↓	-	-
Fe	-	-	-	↑	-	-
Al	-	-	-	↑	-	-
CO ₃ /HCO ₃	↓	-	↑	-	-	-
NO ₃ /NO ₂	↑	-	-	↑	-	-
PO ₄	-	-	-	↑	-	-
BO ₃ /B ₄ O ₇	-	-	-	↑	↑	↑
SiO ₃	-	↓	-	↓	-	-
H ₂ O ₂	-	↑	-	↑	-	-
ClO ₄	-	-	-	-	-	-
O ₂	↑	-	-	-	↑	↑
CO	-	-	-	↓	-	-
H ₂	-	-	-	-	-	-

↑ means that an increase in the control parameter (e.g., pH) resulted in an increase in the response parameter. ↓ means that an increase in the control parameter resulted in a decrease in the response parameter.

However, the two-factor interactions were always confounded with several others, and individual two-factor interaction effects could not be determined from the preliminary matrix analysis.

Main Matrix of Experiments. The primary purpose of the main matrix of experiments was to examine the two-factor interactions significantly affecting the corrosion behavior of carbon steel. Also, an improved estimate of the main effect of each of the 11 species in the main matrix of experiments was determined with the aid of the larger database available. Table 3.17 shows the 11 species included in the main test matrix and the 21 two-factor interactions, that were also examined. The interactions included in Table 3.17 were based on (1) the results of the preliminary matrix analysis

Table 3.17. Main effects and interactions selected from screening tests which were examined in main test matrix.

Main Effects	Two-Factor Interactions	
pH	pH x Cl	Cl x H ₂ O ₂
Cl	pH x CO ₃	CO ₃ x H ₂ O ₂
F	pH x NO ₃	CO ₃ x O ₂
Fe	pH x BO ₃	NO ₃ x BO ₃
CO ₃ /HCO ₃	pH x SiO ₃	NO ₃ x O ₂
NO ₃ /NO ₂	pH x H ₂ O ₂	NO ₃ x SiO ₃
BO ₃ /B ₄ O ₇	pH x O ₂	BO ₃ x SiO ₃
SiO ₃	pH x CO	BO ₃ x H ₂ O ₂
H ₂ O ₂	Cl x CO ₃	SiO ₂ x O ₂
O ₂	Cl x NO ₃	H ₂ O ₂ x O ₂
CO	Cl x BO ₃	

of group-interaction effects on the polarization parameters, and (2) past experience.

The design of the main matrix of experiments was accomplished with a computer-aided design program called COED (Computer Optimized Experimental Design). The COED program is an interactive computer program that allows scientists involved in experimental investigations to plan their experiments to obtain maximum information at minimum cost. COED picks an optimal subset of experiments to be run from the total number of possible experiments. The selection process is based on determinant optimality theory; that is, it determines the experiments that minimize the error of prediction at each possible experimental design point. COED can be used to generate an entire experimental design or to build upon an existing experimental effort.

In this case, the COED program was used to select 30 additional experiments, which, when combined with the preliminary matrix experiments, allowed for the estimation of the 21 two-factor interactions listed in Table 3.17. The ability to estimate the main effects listed in the table carries over from the preliminary matrix. Table 3.18 gives the design matrix for the 30 additional test solutions selected by COED for the main matrix of experiments. The pluses and minuses refer to the high and low concentration values given in Table 3.12, except in the case of pH. In the main matrix of experiments, the nominal high and low values for pH were 11.5 and 6.0, respectively, compared to 9.3 and 6.0 in the screening matrix.

In an initial analysis of the main matrix data, the design concentrations given in Table 3.12 were used. Therefore, as in the screening matrix, the accuracy of the analysis was reduced because the design concentrations were not achieved. To improve the analysis, the solutions were analyzed and the actual elemental concentrations were then used in a subsequent analysis.

Table 3.18. Experimental design developed utilizing COED for main matrix of experiments.*

Experiment	pH	Cl	F	Fe	CO ₃ /HCO ₃	NO ₃ /NO ₂	BO ₃ /B ₄ O ₇	SiO ₃	H ₂ O ₂	O ₂	CO
37	+	+	-	+	+	+	-	-	-	-	+
38	+	-	+	-	+	+	-	+	+	-	-
39	+	+	-	+	+	-	-	+	+	+	-
40	+	+	-	+	+	-	-	+	+	+	-
41	+	-	-	+	-	+	+	+	+	+	+
42	-	-	-	-	+	+	-	+	-	-	+
43	-	+	-	-	+	+	+	-	+	-	+
44	+	-	+	-	-	+	+	+	-	-	+
45	-	+	-	+	-	-	+	+	+	+	+
46	+	-	-	-	+	+	+	-	+	-	-
47	+	-	-	+	-	+	-	-	-	+	-
48	+	+	+	-	-	+	-	-	+	-	+
49	+	-	+	-	+	-	+	+	-	+	-
50	+	-	+	-	-	-	-	-	+	+	+
51	+	-	-	+	+	+	+	-	-	+	+
52	+	-	-	+	-	-	-	+	+	-	-
53	+	+	-	+	-	-	+	+	-	+	+
54	+	+	-	-	-	-	-	-	-	-	-
55	+	+	+	-	+	-	+	-	+	+	-
56	=	-	-	+	-	-	+	-	+	-	-
57	-	-	+	+	-	+	+	+	+	-	-
58	+	-	-	+	+	-	-	+	-	-	+
59	-	-	+	+	+	+	-	-	+	+	+
60	+	+	-	-	+	+	+	+	-	-	-
61	-	-	-	+	-	-	+	-	-	+	+
62	+	+	+	+	+	-	+	-	-	-	-
63	+	+	+	-	+	-	+	+	+	-	+
64	+	+	+	+	-	+	+	-	+	+	-
65	+	+	-	+	+	+	-	+	-	+	+
66	+	-	-	+	+	-	-	-	+	+	+

*(+) and (-) refer to the high and low concentrations, respectively, as indicated in Table 3.12 (except for pH). Solutions 1 through 33 comprise the preliminary matrix.

During the polarization experiments, solution samples were collected. As part of the collection procedure, a filtering process removed any precipitate present in the test solution. Therefore, the samples consisted of only the dissolved species present when the tests were performed. Prior to analysis, any precipitates that formed during storage of the samples were redissolved so that the analysis provided elemental concentrations representative of those present in solution at the time of testing.

Analyses for fluoride, iron, and silicon were performed on all solutions. Spot analyses were performed for chloride, nitrogen, and boron depending on whether precipitates were observed during testing and whether the high or low concentration was used for a particular solution. Because peroxide is a nonstable species, the design concentration was used, although it was realized that that concentration probably was not achieved during testing. The pH of the test solution, as measured immediately after testing, was used in this analysis. The carbonate/bicarbonate concentration was determined through equilibrium calculations based on the hardness of the solution and pH. Design concentrations were used for oxygen and carbon monoxide. The concentrations used in the statistical analysis for the chemical variables in each of the 66 experiments are given in Table A.1, Appendix A. Table 3.19 gives the range and median values of the solution variables measured.

Table 3.19. Measured range and median values of solution variables in main matrix of experiments.

	Range	Median
pH	5.3 - 13	9.15
Cl	100 - 114,000 g/m ³	57,100 g/m ³
F	10 - 8,200 g/m ³	4,105 g/m ³
Fe	0.1 - 23 g/m ³	11.55 g/m ³
CO ₃ /HCO ₃	60 - 239,000 g/m ³	119,530 g/m ³
N	0.2 - 2,000 g/m ³	1,000 g/m ³
B	1 - 2,080 g/m ³	1,040 g/m ³
Si	14 - 1,360 g/m ³	687 g/m ³
H ₂ O ₂	0 - 100 g/m ³	50 g/m ³
O ₂	0 - 2% (Vapor)	1%
CO	0 - 1% (Vapor)	0.5%

A close examination of the measured values of the solution variables (Table 3.19) as compared to the designed values (Table 3.12) indicates a significant discrepancy. As was expected, the carbonate-to-bicarbonate ratio was highly dependent upon pH. Furthermore, the total carbonate/bicarbonate concentration varied significantly from the high and low values of the design matrix, with the low values being quite often higher than designed. Both silicon and iron also varied significantly from their designed concentrations for both high and low concentrations. For silicon this may be partly due to (1) leaching from the walls of the glass cell, especially when fluoride was present, and (2) limited solubility. Iron deviated from designed values due to limited solubility and corrosion-product formation. The high concentration for fluoride was typically less than half the designed 10,000 g/m³ value due to limited solubility. Due primarily to the fact that the designed concentrations were not always achieved, a high degree of unwanted correlation existed between certain main-effect and interaction terms. It is desired that all main-effect terms and interaction terms be independent of one another. Table 3.20 gives the terms that had a high degree of correlation.

Table 3.20. Terms that had a high degree of correlation.

Main-Effect Terms	Interaction Terms
pH and	CO ₃
F and	SiO ₃
CO ₃ and	pH x CO ₃
SiO ₃ and	SiO ₃ x O ₂
SiO ₃ and	pH x SiO ₃
SiO ₃ and	BO ₃ x SiO ₃
pH and	pH x SiO ₃
BO ₃ and	BO ₃ x SiO ₃
O ₂ and	NO ₃ x O ₂
O ₂ and	H ₂ O ₂ x O ₂
pH x CO ₃ and	pH x SiO ₃
pH x Cl and	Cl x CO ₃
pH x H ₂ O ₂ and	CO ₃ x H ₂ O ₂
pH x O ₂ and	CO ₃ x O ₂
NO ₃ x SiO ₃ and	BO ₃ x SiO ₃

The final regression model was based on a step-wise regression analysis. This technique begins with no variables in the model and adds variables one at a time. For each variable, an F statistic is calculated that reflects the variable's contribution to the model if it were to be included next. The variable contributing most to the model is added provided that the F statistic is significant at the 15 percent level. After a variable is added, however, a backward elimination is performed to delete any variable that does not contribute significantly to the model. This process continues until no variables can be added or deleted. Tables A.2 and A.3 (Appendix A) present the coefficients and significance levels for the main-effect terms and two-factor interaction terms in the final model, respectively. The final model included all terms with a 15 percent or less chance of not being significant. Coefficients are presented for each term present in the model, with a positive value indicating that the parameter increases with increasing concentration and a negative value indicating that a parameter decreases with increasing concentration.

Figures 3.28 to 3.33 represent the main-effect terms and interaction terms for each corrosion parameter. Because the analysis represents normalized concentrations from +1 to -1 for each variable, comparisons of the relative magnitude of the effect can be made for the concentration ranges examined. Figures 3.28 to 3.33 present the data in such a way that determining the significance of a main-effect term and its interactions is relatively easy. For example, from Figure 3.28 it is seen that iron has the largest main effect on E_{cor} ; E_{cor} decreases with increasing iron concentration. Furthermore, no iron interactions were shown to be significant (follow the iron lines through the interaction triangle). Nitrate, on the other hand, tends to increase E_{cor} with increasing concentration, and the nitrate x pH two-factor interaction is significant. Chloride also is shown to decrease E_{cor} with increasing chloride concentration. The effects of chloride and nitrate are easily explained, but the relatively large decrease of E_{cor} due to iron is more difficult to explain. Iron was added as equal amounts of ferric and ferrous ions, and, because E_{cor} decreases with increasing iron, it appears that the effect of the ferrous ions is dominating.

Several main effects were shown to be significant for the parameter of maximum active current density, i_{max} . This parameter is important because a high value of i_{max} suggests the possibility for SCC. Figure 3.30 shows that pH and chloride produce a decrease in i_{max} with an increase in the value of the variable. Fluoride, iron, and carbonate tend to increase i_{max} with increasing concentration. The pH x carbonate interaction is the most significant interaction term for i_{max} present in the model. Table 3.20 indicates that some of the factors in the i_{max} model are highly correlated: (1) pH and carbonate, (2) carbonate and pH x carbonate, and (3) pH x chloride and chloride x carbonate. A consequence of these correlations is a decreased ability of the model to predict electrochemical behavior, especially beyond the ranges for concentrations of the variables contained in the model.

The pitting tendency for a solution can be described by E_{pit} and E_{prot} . A variable that tends to decrease either of these parameters would typically be considered to promote pitting. To determine whether pitting would occur in any given environment, E_{cor} would also have to be considered. From

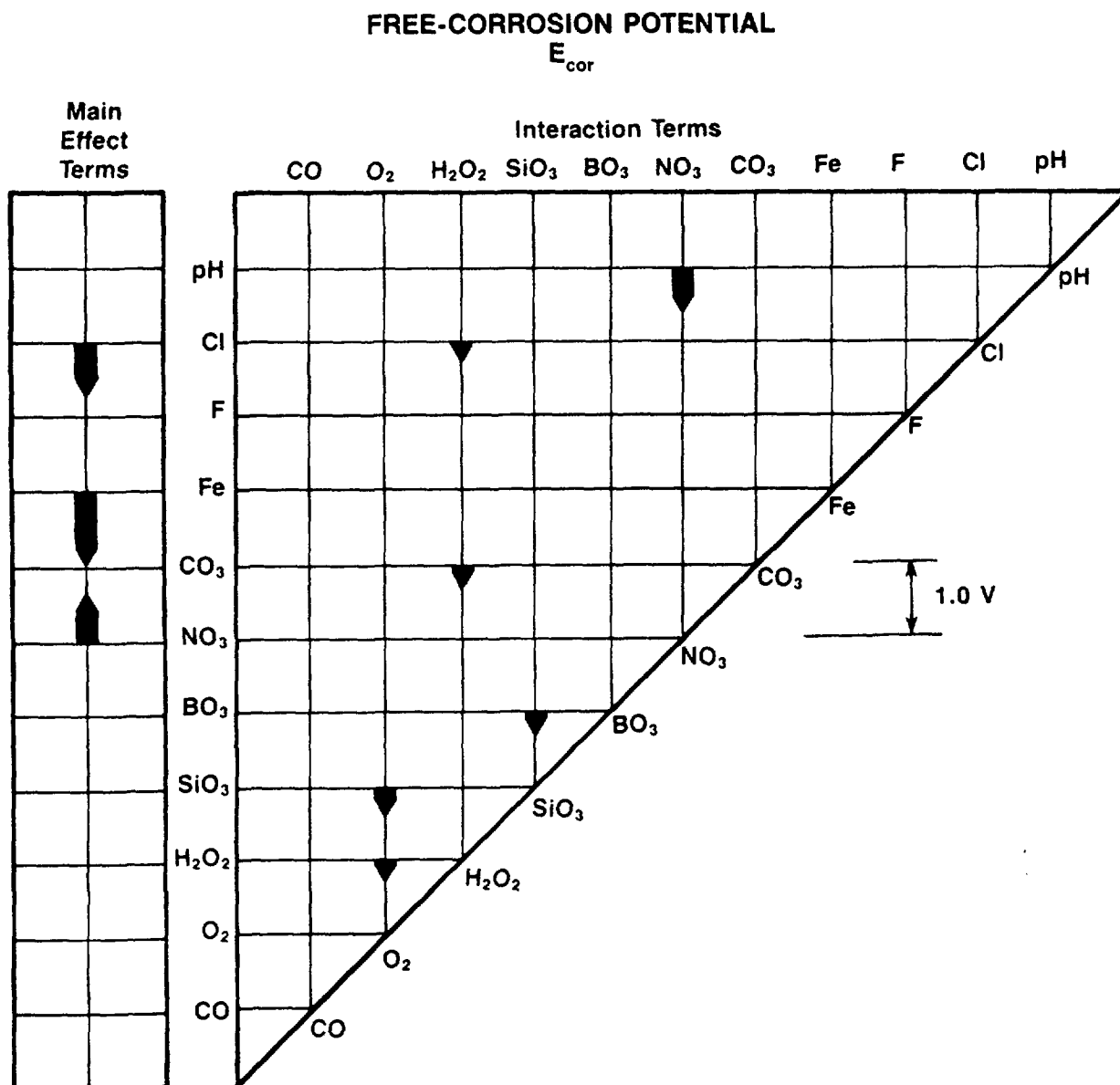


Figure 3.28. Schematic showing the relative magnitude and direction of significant main effects and two-factor interactions on E_{cor} .

The direction of the arrow indicates the direction of effect of that single species (left) or that two-factor interaction (right) on E_{cor} . The length of the arrow indicates the magnitude. For example, NO₃ increased E_{cor} by about 0.67 V while the BO₃ x SiO₃ interaction decreased E_{cor} by about 0.25 V.

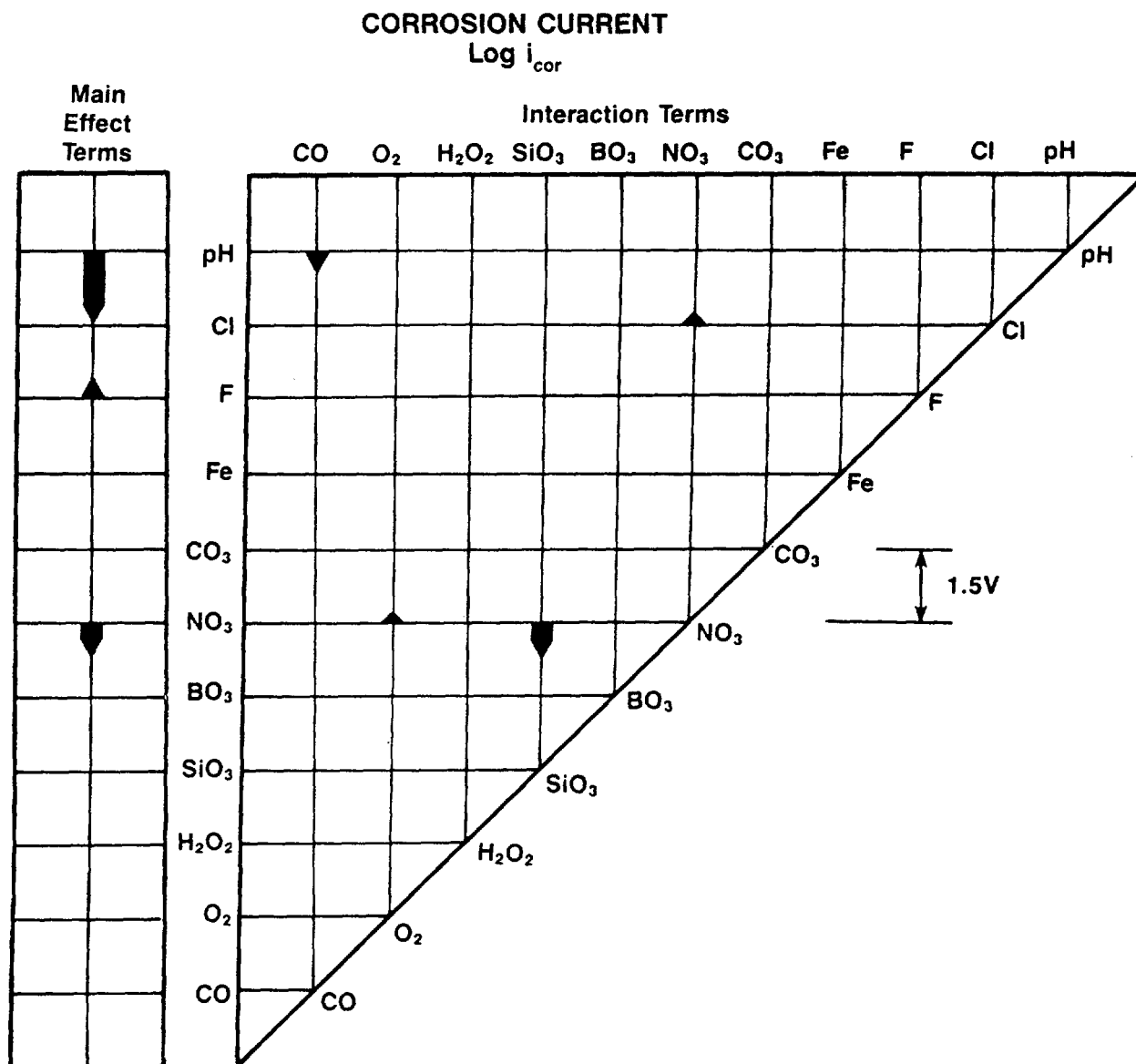


Figure 3.29. Schematic showing the relative magnitude and direction of significant main effects and two-factor interactions on i_{cor} .

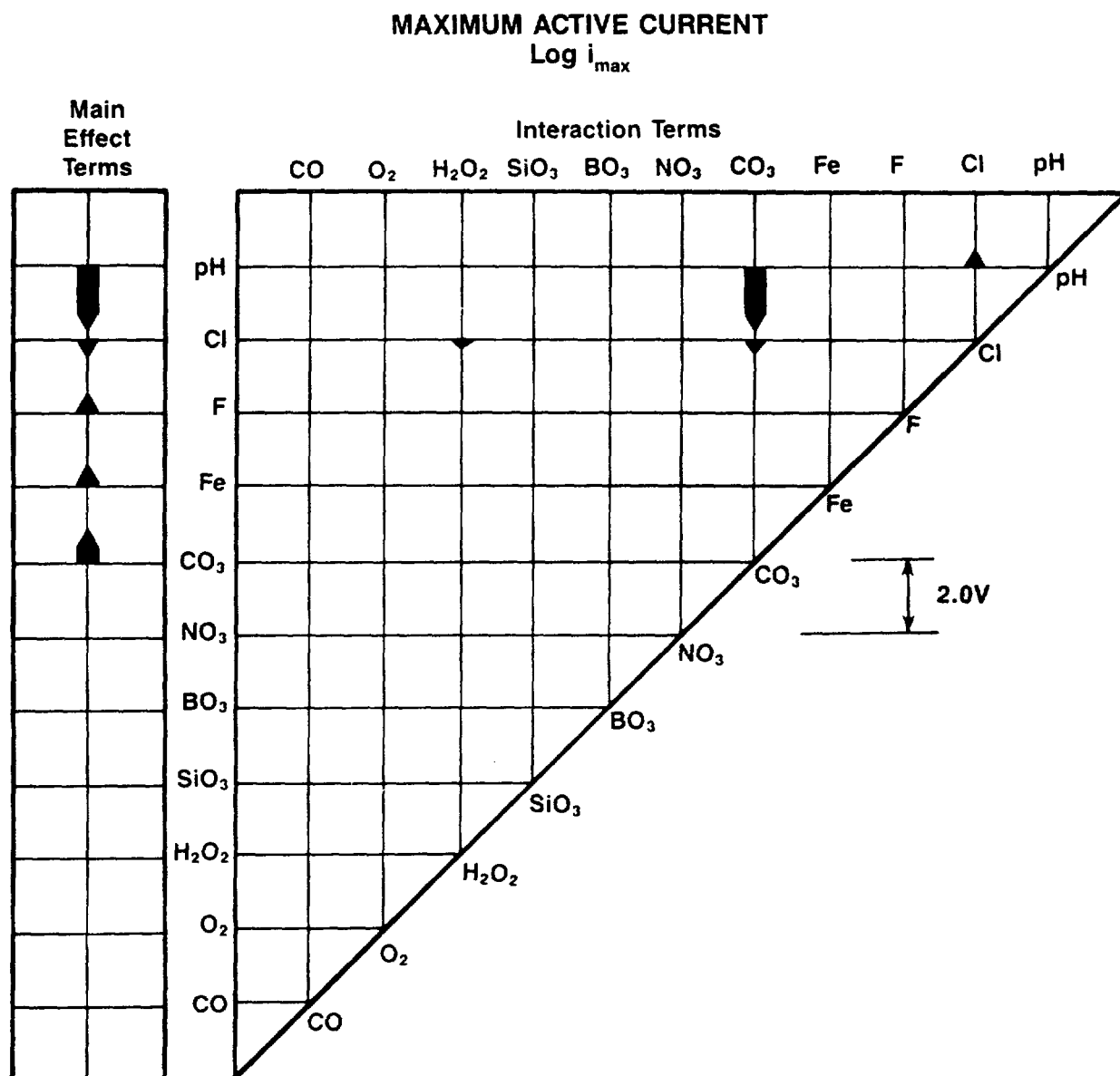


Figure 3.30. Schematic showing the relative magnitude and direction of significant main effects and two-factor interactions on i_{max} .

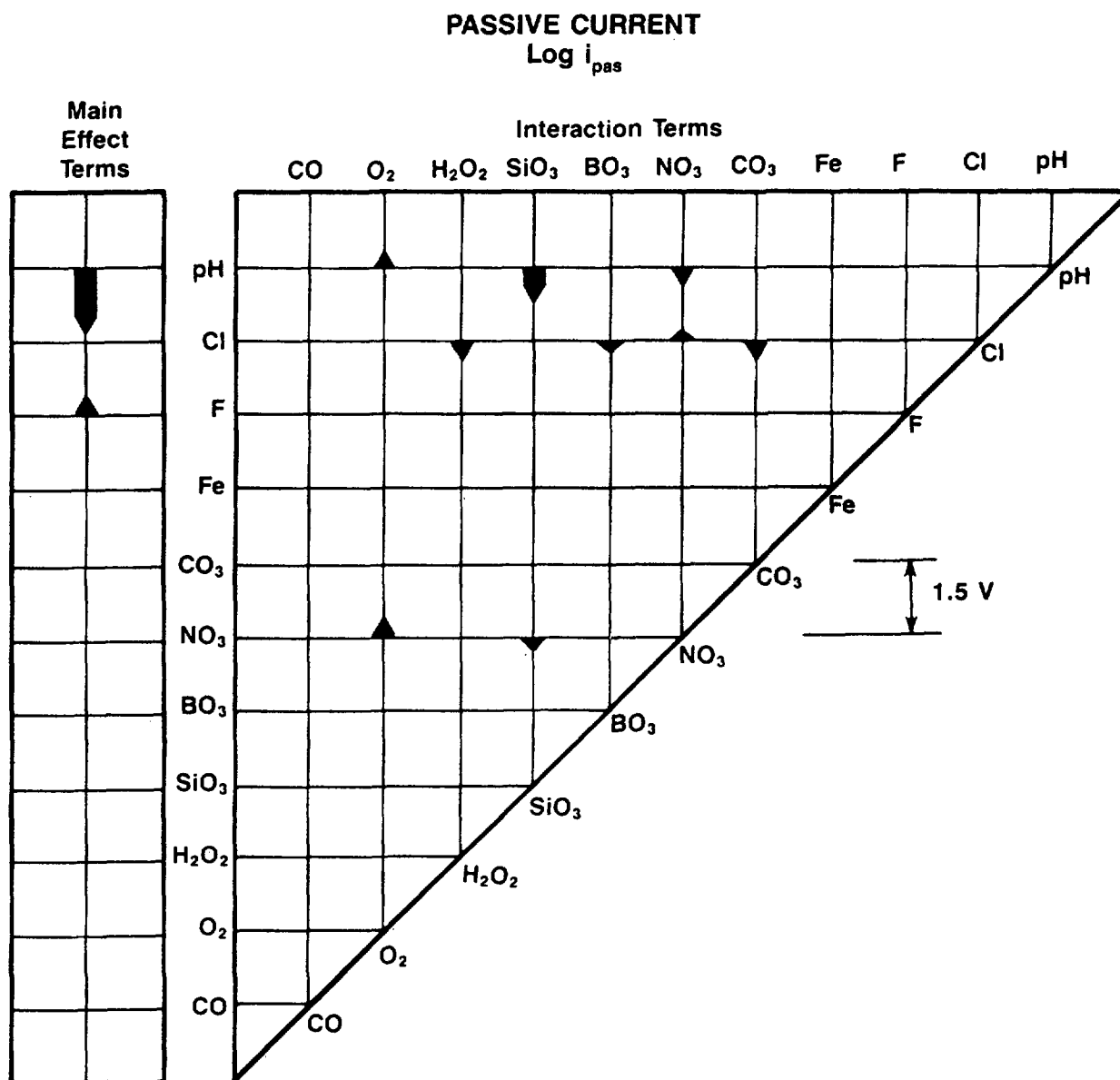


Figure 3.31. Schematic showing the relative magnitude and direction of significant main effects and two-factor interactions on i_{pas} .

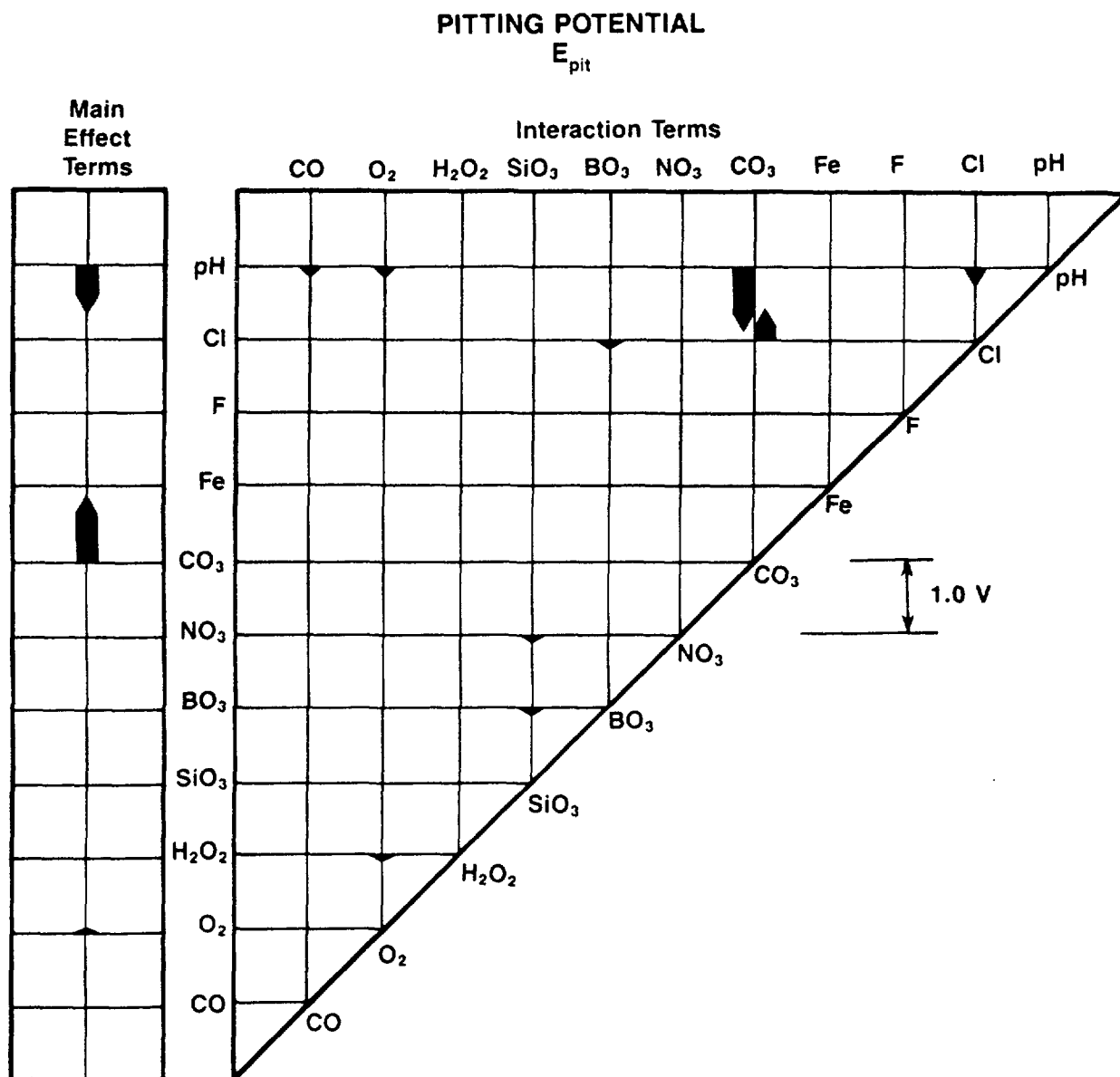


Figure 3.32. Schematic showing the relative magnitude and direction of significant main effects and two-factor interactions on E_{pit} .

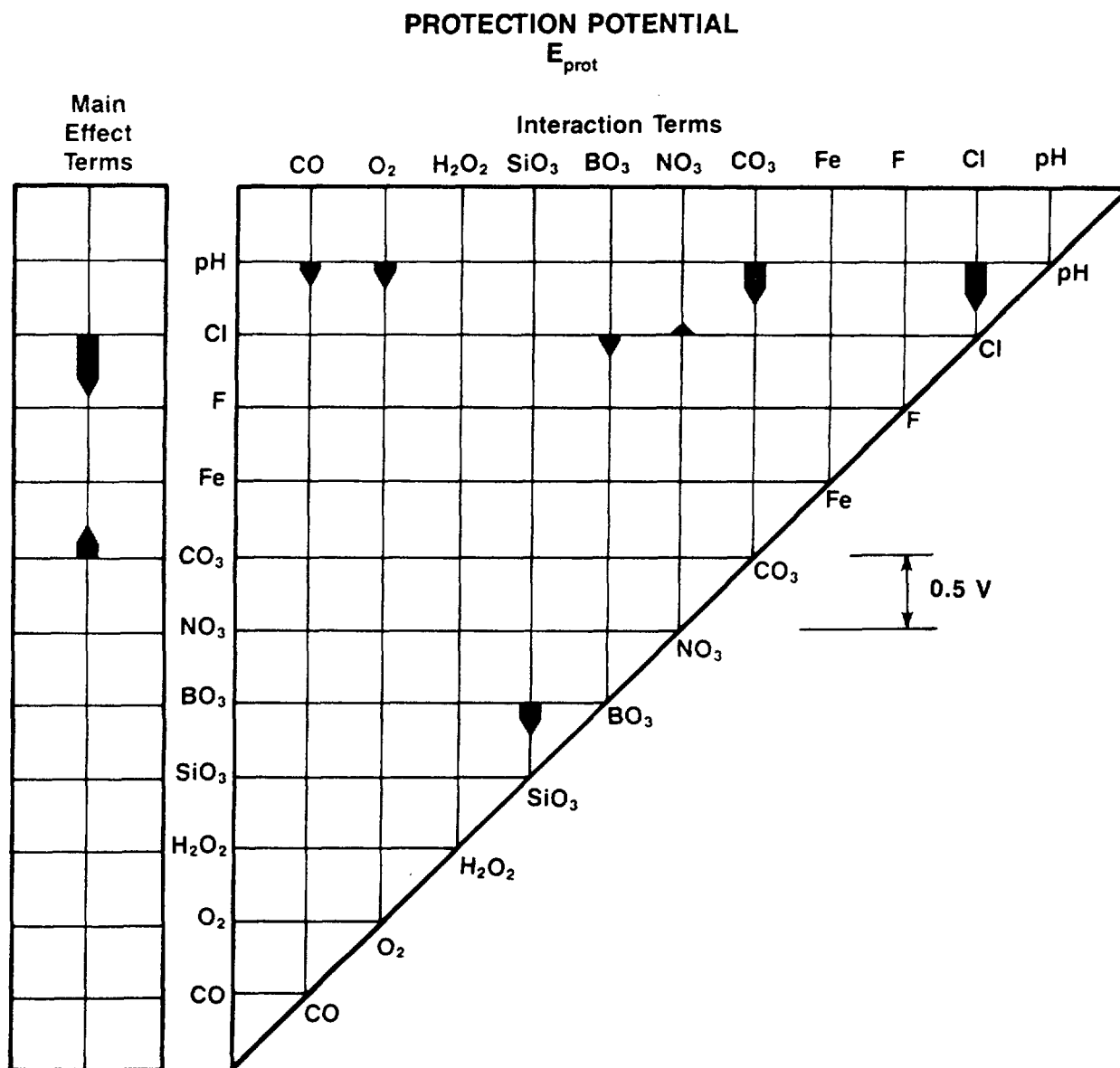


Figure 3.33. Schematic showing the relative magnitude and direction of significant main effects and two-factor interactions on E_{prot} .

Figures 3.32 and 3.33, pH, chloride, and carbonate were the only main effects shown to have a significant effect on either E_{prot} or E_{pit} . A decrease in pH tended to increase E_{pit} ; a decrease in chloride tended to increase E_{prot} ; and an increase in carbonate tended to increase both E_{pit} and E_{prot} . Furthermore, various interactions with pH or with chloride tended to explain the majority of the significant interaction terms. It

should be noted, however, that E_{pit} had several variables included in the model which, in Table 3.20, show a high degree of correlation: (1) pH and carbonate, (2) carbonate and pH x carbonate, (3) oxygen and peroxide x oxygen, (4) pH x chloride and chloride x carbonate, and (5) borate x silicate and nitrate x silicate. As discussed for i_{max} , high correlation of these factors makes predictions and extrapolation of the data outside of the ranges present in the model much less accurate.

To perform a statistical analysis of the main-effect and interaction terms, the data (given in Tables A.2 and A.3 in Appendix A) were normalized to a range of +1 to -1 for each variable using the following transformation:

$$X_i^* = 2 \left(\frac{X_i - L_i}{M_i - L_i} \right) - 1 \quad (3-1)$$

where X^* is the transformed concentration of variable i , X_i is the actual concentration, L_i is the minimum concentration, and M_i is the maximum concentration. The equation for any particular parameter, Y , can be expressed as follows:

$$Y = a_0 + b_i X_i^* + c_{ij} X_i^* X_j^* \quad (3-2)$$

where a_0 is the intercept, b_i is the coefficient for the main-effect terms, and c_{ij} is the coefficient for the two-factor interaction terms.

The transformation (Eq. 3-1) is such that at the maximum concentration, $X_i^* = +1$; when X_i equals the minimum concentration, $X_i^* = -1$; and when X_i equals the median concentration, $X_i^* = 0$. For this discussion, the median concentration will be referred to as an average concentration. Therefore, for an average solution (a solution with all variables set to their median concentrations), the parameter Y is equal to a_0 , since X_i^* is equal to 0 for all variables. For solutions other than an average solution, the effect of the solution concentration on the corrosion parameter Y can be calculated using Eqs. 3-1 and 3-2.

Table 3.21 shows the effect of the concentration range for each variable with all other variables held at their median values. With all other variables held at their median values, all of the terms in the model go to 0 except for the variable of interest. For example, with all variables held at their median values except for chloride, E_{cor} is given as follows:

$$E_{cor} = -0.664 - 0.072 X_{Cl}^* \quad (3-3)$$

Table 3.21. Effect of concentration range for each variable (with all other variables held at their median values) on the corrosion parameters.

Variable	Range	Effects on Corrosion Parameters					
		E_{cor} V (SCE)	i_{cor} A/cm ²	i_{max} A/cm ²	i_{pas} A/cm ²	E_{pit} V (SCE)	E_{prot} V (SCE)
pH	5.3 to 13	-	1.3×10^{-4} to 1.6×10^{-7}	3.5×10^{-1} to 1.7×10^{-5}	3.9×10^{-4} to 5.2×10^{-7}	+1.39 to +0.08	-
Cl	100 to 114,000 g/m ³	-0.59 to 0.74	-	5.0×10^{-3} to 1.2×10^{-3}	-	-	+0.32 to -0.51
F	10 to 8,200 g/m ²	-	1.8×10^{-6} to 1.2×10^{-5}	1.2×10^{-3} to 4.9×10^{-3}	7.7×10^{-6} to 2.7×10^{-5}	-	-
Fe	0.1 to 23 g/m ³	-0.55 to -0.78	-	6.2×10^{-4} to 1.0×10^{-2}	-	-	-
CO ₃	60 to 239,000 g/m ³	-	-	2.2×10^{-4} to 2.7×10^{-2}	-	-	-
NO ₃	0.2 to 2,000 g/m ³	-0.72 to -0.60	2.0×10^{-5} to 1.1×10^{-6}	-	-	-0.19 to +1.66	-0.33 to +0.14
BO ₃	1 to 2,080 g/m ³	-	-	-	-	-	-
SiO ₃	14 to 1,360 g/m ³	-	-	-	-	-	-
H ₂ O ₂	0 to 100 g/m ³	-	-	-	-	-	-
O ₂	0 to 2% (Vapor)	-	-	-	-	+0.67 to -0.80	-
CO	0 to 1% (Vapor)	-	-	-	-	-	-

where X_{Cl}^* is given as follows:

$$X_{Cl}^* = 2 \left(\frac{X_{Cl} - 100}{114,000 - 100} \right) - 1 \quad . \quad (3-4)$$

Therefore, Table 3.21 shows the magnitude of the effect of varying any particular variable in an otherwise "average" solution.

The effect of iron in Table 3.21 on i_{max} is of interest because i_{max} has been shown to be related to SCC. Within a concentration range of 0.1 to 23 g/m³, the model predicted that i_{max} would increase from 6×10^{-4} to 1×10^{-2} A/cm². Also, the effect of pH on i_{max} and E_{pit} is worth noting, but it should also be recalled that pH and carbonate are highly correlated (see Table 3.20). The large increase in i_{max} at low pH values probably indicates an increase in active corrosion behavior as opposed to an increase in i_{max} , followed by passivation behavior. Therefore, care should be exercised in making predictions with the model.

Selected Two-Factor Interactions. This section presents the results of potentiodynamic polarization studies of five two-factor interactions selected for further examination. Potentiodynamic polarization curves were performed for the low-low, high-low, high-high, and low-high conditions for the following interactions: chloride x carbonate, chloride x borate, pH x chloride, pH x borate, and nitrate x oxygen. These interactions were selected based on the preliminary results and thus the importance changed once the final regression model was completed. For example, the interaction of pH x borate was not shown as being significant in the final model. Also, these polarization curves permit a comparison to be made between experimental results and the predictions based on the regression model.

The potentiodynamic polarization curves for the chloride x carbonate and nitrate x oxygen interactions are presented in the second quarterly report for Year Four (Ref. 3.15). Solutions used in these experiments were formulated by adding the high or low concentrations of the interaction variables to the simulated basalt groundwater. The composition of the simulated basalt groundwater is given in Table 3.9. For purposes of verifying the regression model, all of the variables were assumed to be at their low values except for the interaction variables being examined and except for pH. When pH was included in the interaction, the low value of pH was 6 and the high value of pH was 11.5. When pH was not in the interaction term being examined, the pH was assumed to be 9, which was the approximate value of the simulated basalt groundwater used in the potentiodynamic polarization experiments. With these considerations, the solutions used in the potentiodynamic polarization experiments simulated the solution described in the model.

Table 3.22 presents the predictions for the corrosion parameters compared to the experimentally measured values. The quantitative agreements between the

Table 3.22. Model predictions for corrosion parameters compared to measured values for several solutions used in examining two-factor interactions.

Condition	E_{cor} , V (SCE)		i_{cor} , A/cm ²		i_{max} , A/cm ²		i_{pas} , A/cm ²		E_{pit} , V (SCE)		E_{prot} , V (SCE)	
	Exp. (a)	Model (b)	Exp.	Model	Exp.	Model	Exp.	Model	Exp.	Model	Exp.	Model
Low Cl + Low CO ₃ (c)	-0.65	-0.71	1.4x10 ⁻⁷	5.3x10 ⁻⁶	2.8x10 ⁻⁵	2.9x10 ⁻⁵	-	4.2x10 ⁻⁶	-0.51	-0.26	-0.83	-0.17
High Cl + Low CO ₃ (c)	-0.66	-0.80	5.7x10 ⁻⁷	1.9x10 ⁻⁶	4.5x10 ⁻⁵	3.0x10 ⁻⁵	-	2.2x10 ⁻⁵	-0.55	-0.84	-0.66	-0.89
High Cl + High CO ₃ (c)	-0.96	-0.74	1.0x10 ⁻⁵	1.9x10 ⁻⁶	8.9x10 ⁻³	4.8x10 ⁻³	7.9x10 ⁻⁵	8.5x10 ⁻⁶	+0.82	+1.90	+0.82	-0.41
Low Cl + High CO ₃ (c)	-0.96	-0.65	2.5x10 ⁻⁵	5.3x10 ⁻⁶	7.1x10 ⁻³	1.2x10 ⁻²	4.0x10 ⁻⁵	1.1x10 ⁻⁵	+0.78	+0.82	+0.78	+0.31
Low Cl + Low BO ₃ (c)	-0.68	-0.71	7.9x10 ⁻⁷	5.3x10 ⁻⁶	6.3x10 ⁻⁵	2.9x10 ⁻⁵	6.3x10 ⁻⁶	4.2x10 ⁻⁶	-0.41	-0.26	-0.75	-0.17
High Cl + Low BO ₃ (c)	-0.62	-0.80	1.6x10 ⁻⁷	1.9x10 ⁻⁶	3.4x10 ⁻⁵	3.0x10 ⁻⁵	-	2.2x10 ⁻⁵	-0.52	-0.84	-0.67	-0.89
High Cl + High BO ₃ (c)	-0.69	-0.74	1.0x10 ⁻⁵	1.9x10 ⁻⁶	6.0x10 ⁻⁵	3.0x10 ⁻⁵	1.6x10 ⁻⁵	1.2x10 ⁻⁵	-0.40	-0.83	-0.60	-0.78
Low Cl + High BO ₃ (c)	-0.52	-0.65	2.5x10 ⁻⁷	5.3x10 ⁻⁶	6.3x10 ⁻⁵	2.9x10 ⁻⁵	1.6x10 ⁻⁶	7.4x10 ⁻⁶	+0.17	+0.20	-0.58	+0.47
Low pH + Low Cl(d)	-0.78	-0.76	8.0x10 ⁻⁶	4.4x10 ⁻⁵	2.8x10 ⁻⁵	2.2x10 ⁻⁴	1.2x10 ⁻⁵	2.0x10 ⁻⁵	-0.40	-0.88	-0.78	-0.85
High pH + Low Cl(d)	-0.52	-0.67	6.3x10 ⁻⁸	9.1x10 ⁻⁷	2.5x10 ⁻⁵	5.6x10 ⁻⁶	2.8x10 ⁻⁷	1.1x10 ⁻⁶	-0.24	+0.25	-0.80	+0.38
High pH + High Cl(d)	-0.62	-0.76	5.6x10 ⁻⁸	3.3x10 ⁻⁷	2.5x10 ⁻⁵	4.9x10 ⁻⁶	-	6.0x10 ⁻⁶	-0.49	-0.69	-0.62	-0.74
Low pH + High Cl(d)	-0.75	-0.85	4.0x10 ⁻⁶	1.6x10 ⁻⁵	1.6x10 ⁻⁵	4.8x10 ⁻⁵	5.6x10 ⁻⁶	1.0x10 ⁻⁴	-0.61	-1.03	-0.70	-1.08
Low pH + Low BO ₃ (d)	-0.80	-0.76	8.3x10 ⁻⁶	4.4x10 ⁻⁵	5.0x10 ⁻⁵	2.2x10 ⁻⁴	8.3x10 ⁻⁶	2.0x10 ⁻⁵	-0.40	-0.88	-0.67	-0.85
High pH + Low BO ₃ (d)	-0.52	-0.67	5.0x10 ⁻⁸	9.1x10 ⁻⁷	6.3x10 ⁻⁶	5.6x10 ⁻⁶	5.0x10 ⁻⁷	1.1x10 ⁻⁶	-0.25	+0.25	-0.78	+0.38
High pH + High BO ₃ (d)	-0.65	-0.61	6.3x10 ⁻⁸	9.1x10 ⁻⁷	2.0x10 ⁻⁵	5.6x10 ⁻⁶	2.5x10 ⁻⁶	2.0x10 ⁻⁶	+0.67	+0.93	+0.67	+1.03
Low pH + High BO ₃ (d)	-0.73	-0.70	1.4x10 ⁻⁴	4.4x10 ⁻⁵	1.0x10 ⁻³	2.2x10 ⁻⁴	2.5x10 ⁻³	3.9x10 ⁻⁵	-0.43	-0.42	-0.57	-0.20
Low NO ₃ + Low O ₂ (c)	-0.78	-0.71	2.8x10 ⁻⁶	5.3x10 ⁻⁶	2.0x10 ⁻⁵	2.9x10 ⁻⁵	6.3x10 ⁻⁶	4.2x10 ⁻⁶	-0.50	-0.26	-0.75	-0.17
High NO ₃ + Low O ₂ (c)	-0.40	-0.58	2.3x10 ⁻⁷	4.3x10 ⁻⁷	2.0x10 ⁻⁵	2.9x10 ⁻⁵	1.0x10 ⁻⁶	1.2x10 ⁻⁶	+0.23	-0.05	-0.25	-0.36
High NO ₃ + High O ₂ (c)	-0.32	-0.42	1.8x10 ⁻⁷	2.0x10 ⁻⁶	3.2x10 ⁻⁵	2.9x10 ⁻⁵	7.1x10 ⁻⁷	3.0x10 ⁻⁶	+0.20	+0.20	-0.32	-0.35
Low NO ₃ + High O ₂ (c)	-0.62	-0.55	2.8x10 ⁻⁶	2.1x10 ⁻⁶	3.7x10 ⁻⁵	2.9x10 ⁻⁵	1.8x10 ⁻⁵	1.5x10 ⁻⁶	-0.40	-0.00	-0.70	-0.16

(a) Data from potentiodynamic experiments.

(b) Data predicted from model.

(c) For model predictions pH = 9.0 ($X_{pH}^* = -0.039$) and all other variables were assumed to be at their low values except as noted.

(d) For model predictions low pH = 6.0 ($X_{pH}^* = -0.82$) and high pH = 11.5 ($X_{pH}^* = +0.61$) and all other variables were assumed to be at their low values except as noted.

experimentally measured values and the predictions from the model were generally poor, but the trends in the data were fairly well predicted. For E_{cor} , trends were predicted with the exception of the chloride x carbonate conditions for high carbonate where the experiments showed very negative E_{cor} values and the predicted values did not indicate this behavior. For the i_{cor} values, the agreement was usually within an order of magnitude and trends were generally predicted. For i_{max} , trends were predicted and agreement was relatively good with the model clearly indicating an increase in i_{max} for the high-carbonate conditions. The predicted values of i_{pas} were typically within an order of magnitude of the measured values, with the exception of the low-pH plus high-borate and the low-pH plus high-chloride conditions. For the low pH-plus-borate condition, the predicted value was approximately two orders of magnitude low, and the predicted value for the low pH-plus-chloride condition was 1-1/2 orders of magnitude high. For the values of E_{pit} , quantitative agreement between the predicted and measured values were relatively poor, but trends in the data generally were predicted by the model. For E_{prot} , very poor agreement was observed and, for the most part, the trends in the data also were poorly predicted.

Although the predictive capability of the model was greatly diminished by the correlated terms, the model and the data obtained in the potentiodynamic polarization studies are extremely useful in understanding the ranges of expected behavior for carbon steel in repository environments. In addition, these data were used to select solution chemistries for the pit-propagation and SCC studies.

Effect of Thermodynamically Unstable Species. Two species included in the original matrix of potentiodynamic experiments were peroxide, H_2O_2 , and perchlorate, ClO_4^- . Both of these species are thermodynamically unstable in the solutions examined but may be generated at an overpack surface due to radiolysis. Because the effects of these species may have been overlooked as a result of the experimental procedure used during the statistical matrix of experiments, these species were examined in more detail. An experimental setup was devised such that these species could be continuously added to the electrochemical cell during the experiment. The initial experimental setup was similar to that used for performing standard potentiodynamic polarization tests. The steel specimen was placed in the deaerated basalt ground-water at 90 C where it remained overnight and obtained a steady-state E_{cor} value.

While the steel specimen remained at E_{cor} , additions of the desired species were initiated and the change in E_{cor} was recorded as a function of time. After E_{cor} again obtained a near-steady-state condition, the potentiodynamic polarization curve was performed at 0.6 V/hr with the species being continually added during the potentiodynamic polarization experiment.

- **Hydrogen Peroxide.** Figure 3.34 shows E_{cor} as a function of exposure time for carbon steel specimens with continuous H_2O_2 additions of 6.5 ppm/min. The two curves shown in Figure 3.34, which are for two separate runs, represent similar behavior with steady-state values of E_{cor} of approximately -0.6 V (SCE). In one experiment, a longer period between initiation of the H_2O_2 addition and the peak in potential was observed. It is

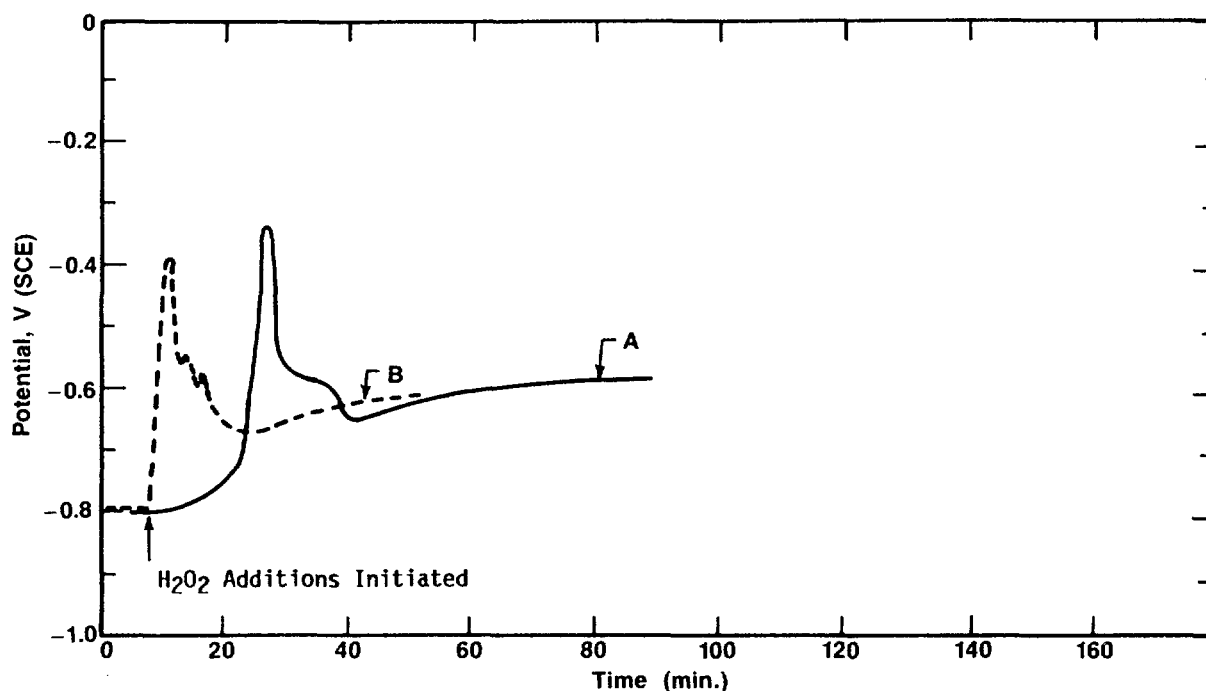


Figure 3.34. Free-corrosion potential as a function of exposure time for 1020 carbon steel specimens in deaerated basalt groundwater at 90 C with continuous H_2O_2 additions of 6.5 ppm/min.

A and B are data for replicate experiments.

believed that this is due to experimental procedure (that is, possible residual air in the injection system). Figure 3.35 shows a polarization curve produced at the end of the free-corrosion potential exposure (curve B in Figure 3.34). The polarization curve indicates a very high corrosion current of approximately $1 \times 10^{-3} \text{ A/cm}^2$ (11,700 $\mu\text{m}/\text{year}$) at the free-corrosion potential.

Figure 3.36 shows E_{COR} as a function of exposure time for carbon steel specimens with continuous H_2O_2 additions of 65 ppm/min. Discounting the leak problem experienced with Curve A, the two curves show very similar results with a final E_{COR} of approximately -0.1 V. Thus, the higher addition rate of H_2O_2 produced a much more positive E_{COR} than the lower addition rate seen in Figure 3.34. Figure 3.37 shows the polarization curves produced after the exposures shown in Figure 3.36. The behavior of the two curves is relatively similar with the exception that curve A shows a large anodic peak in the polarization curve.

The corrosion current densities measured in Figures 3.35 and 3.37 are between $1 \times 10^{-4} \text{ A/cm}^2$ and $1 \times 10^{-3} \text{ A/cm}^2$, which corresponds to an average corrosion rate of between 1,200 and 12,000 $\mu\text{m}/\text{yr}$ (47 and 470 mil/yr). The

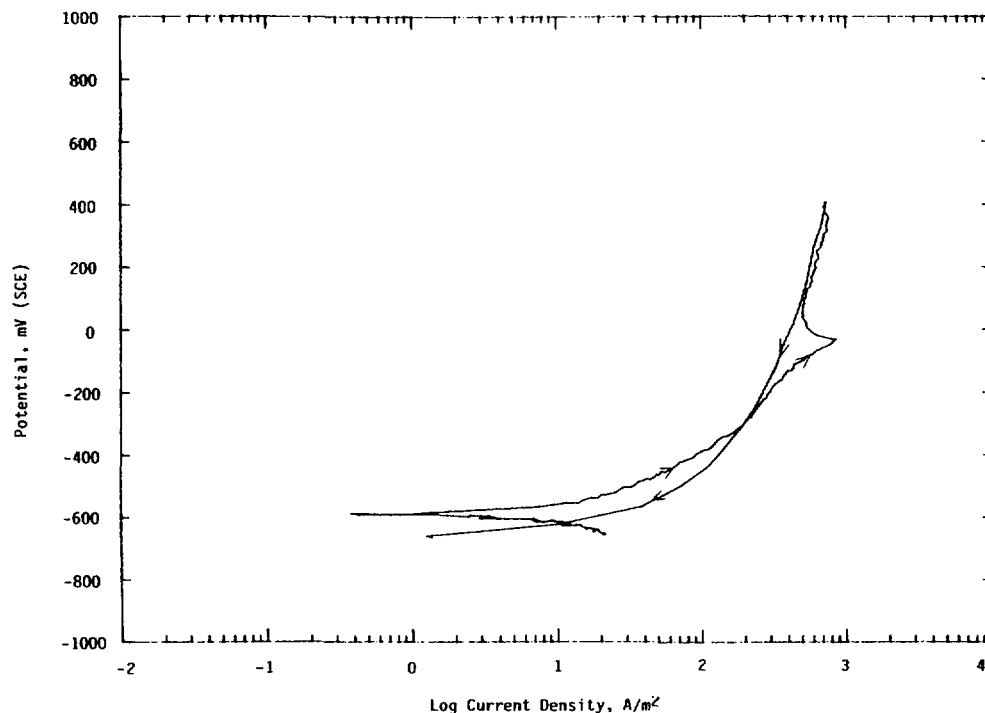


Figure 3.35. Potentiodynamic polarization curve for 1020 carbon steel under same conditions as for Figure 3.34.

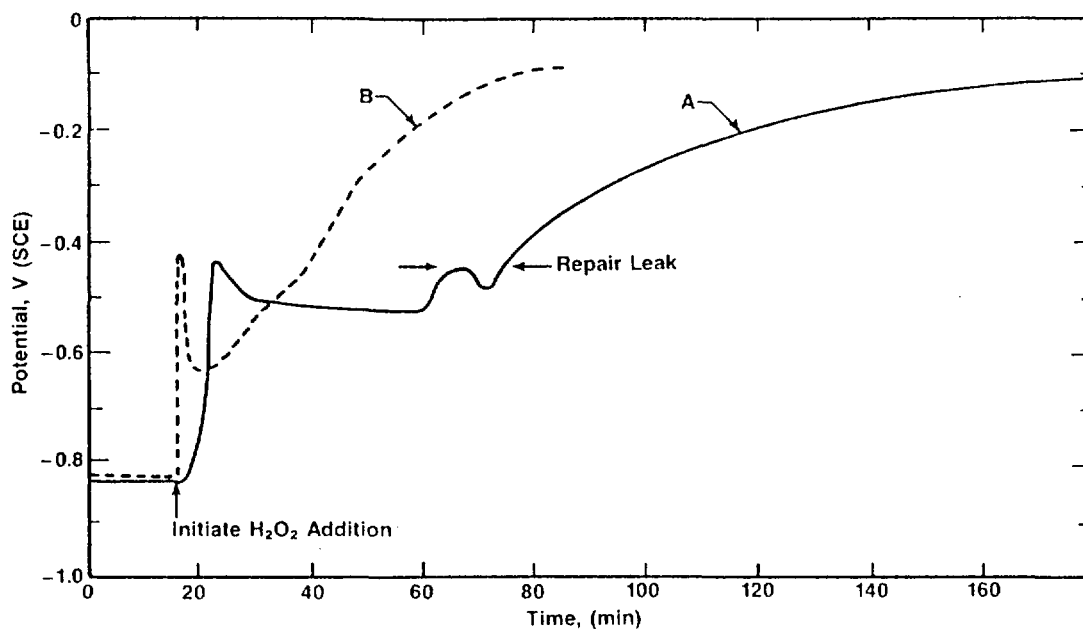


Figure 3.36. Free-corrosion potential as a function of exposure time for 1020 carbon steel specimens in deaerated basalt groundwater at 90 C with continuous H_2O_2 additions of 65 ppm/min. A and B are data for replicate experiments.

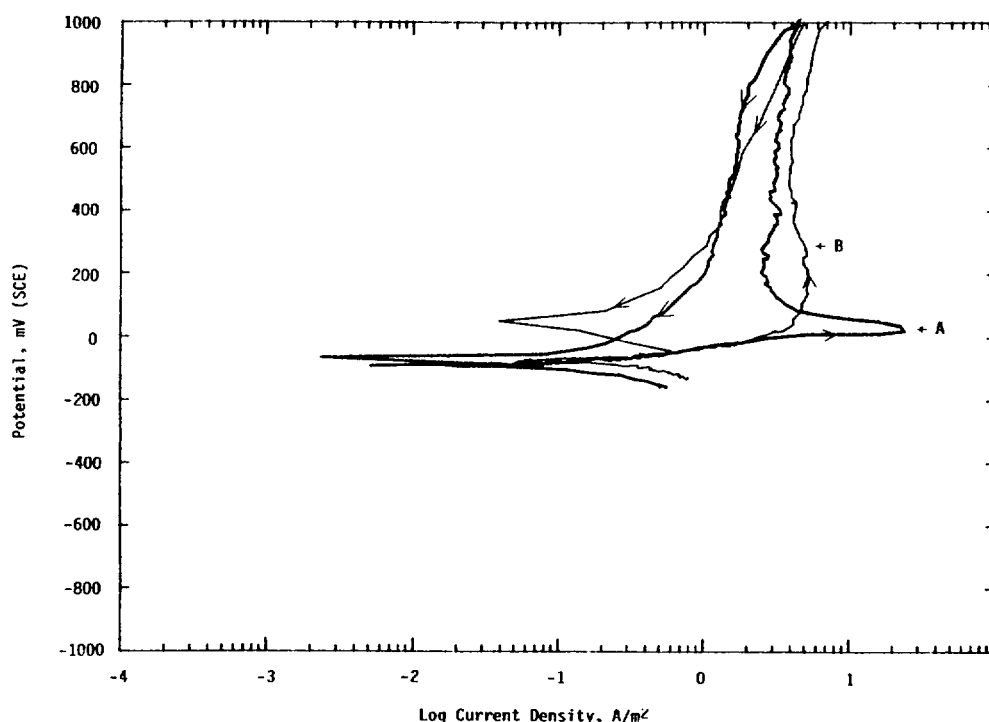


Figure 3.37. Potentiodynamic polarization curves for 1020 carbon steel under same conditions as for Figure 3.36.

fact that the higher value of i_{COR} was measured for the lower H_2O_2 concentration suggests that H_2O_2 , at the higher concentration, promoted film formation on the specimen. However, rates of attack for both H_2O_2 concentrations were excessive. The effects of H_2O_2 addition rates of less than 6.5 ppm/min were not examined in this task but merit examination based on these results.

- **Perchlorate.** Continuous perchlorate additions were made at a rate of 2.0 ppm/min. Figure 3.38 shows the free-corrosion potential as a function of exposure time for carbon steel specimens with continuous HClO_4 additions. As was observed for the H_2O_2 additions, there was a difference in the rate of change for E_{COR} for the two individual experiments with HClO_4 , but the steady-state potentials achieved were similar. The HClO_4 additions shifted the free-corrosion potential from -0.83 to approximately -0.7 V. Potentiodynamic polarization curves were then performed at the end of each free-corrosion exposure, and these are shown in Figure 3.39. The polarization curves for the two exposures are very similar, showing corrosion current densities of approximately $1 \times 10^{-3} \text{ A/cm}^2$. Both curves exhibit active behavior, and nonlinear behavior is observed which is likely due to IR drops resulting from the very high currents measured. In both cases, the pH of the solution measured prior to performing the experiments was approximately 4, which is significantly lower than the starting pH of 9.3. Therefore, the corrosion behavior observed is likely due, in part, to the decrease in pH.

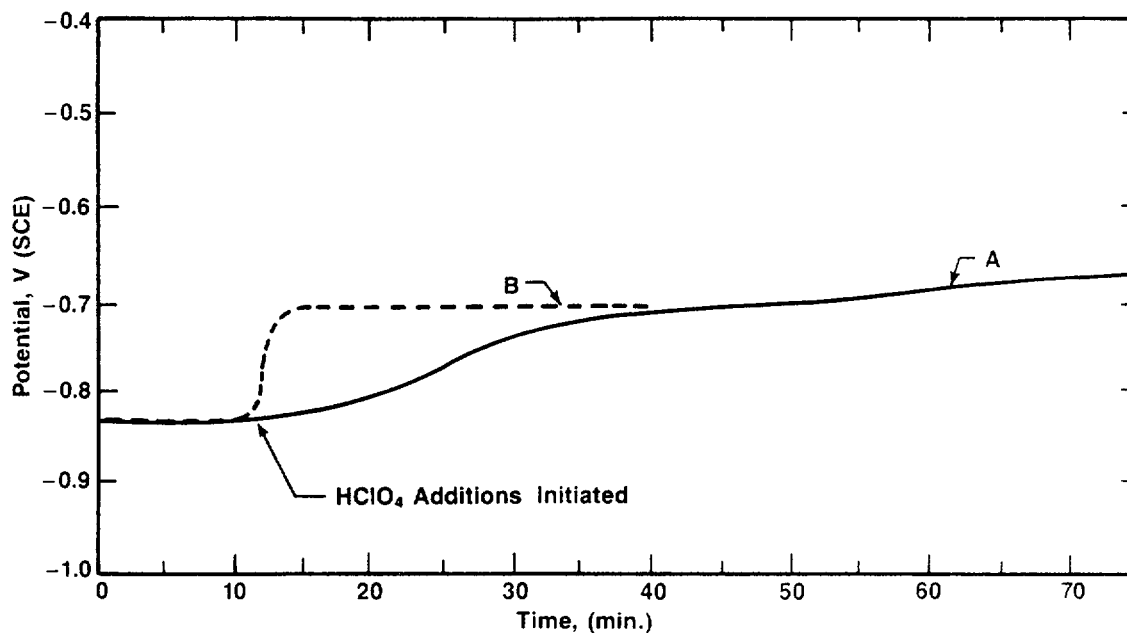


Figure 3.38. Free-corrosion potential as a function of exposure time for 1020 carbon steel specimen in deaerated basalt groundwater at 90 C with continuous HClO_4 additions of 2.0 ppm/min. A and B are data for replicate experiments.

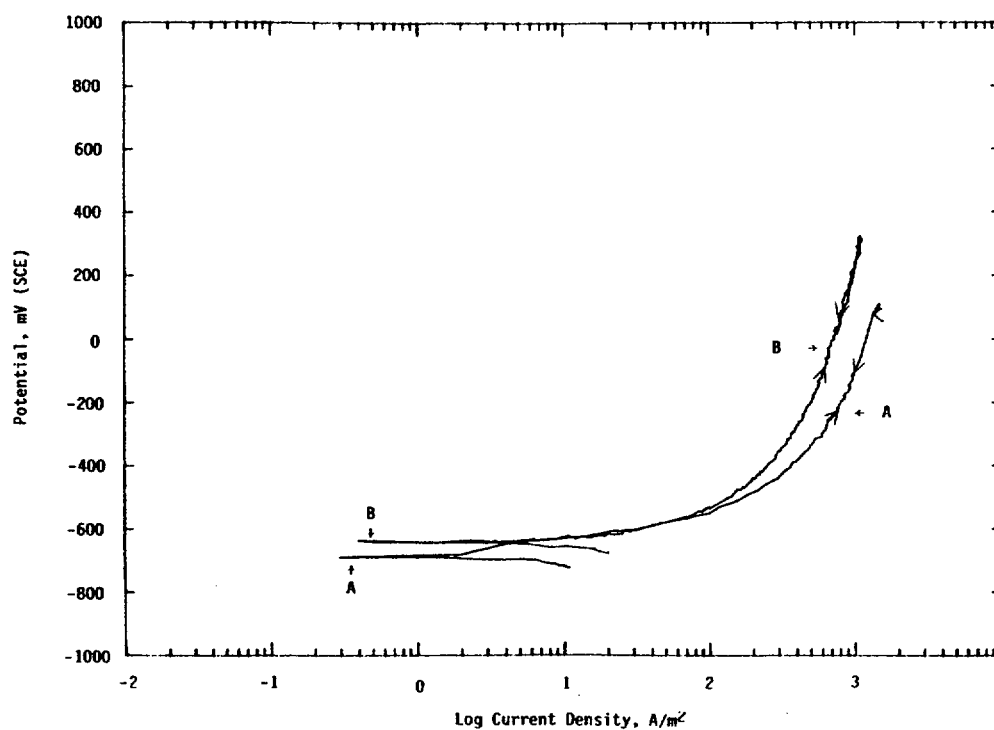


Figure 3.39. Potentiodynamic polarization curves for 1020 carbon steel under same conditions as for Figure 3.38.

These data indicate that, if significant amounts of ClO_4^- are produced during radiolysis, a significant pH decrease and corrosion rate increase will occur.

The data for both peroxide and perchlorate indicate that significant increases in corrosion rate could result from large quantities of these species being produced. Once estimates are made of the amounts of these species likely at an overpack surface and their rates of production, similar experiments could be repeated to establish the effect on corrosion. For peroxide, it was clearly shown that both the anodic and cathodic kinetics were affected since the higher corrosion rate occurred in the lower concentration.

3.2.1.6. Summary

The objective of this study was to evaluate the influence of metallurgical and environmental variables on the general corrosion, pitting, and SCC behavior of carbon steel in basalt repository environments. This was accomplished by using potentiodynamic polarization experiments to determine the effect of the metallurgical and environmental variables on a number of polarization parameters. The results of this task also were used in many of the other overpack corrosion tasks on this program to identify appropriate environments and steels for study.

Carbon steel was found to exhibit active-passive behavior in the simulated basalt groundwater, and the values for the polarization parameters indicated a high probability for pitting corrosion. On the other hand, the values for the parameters associated with SCC did not indicate a potent cracking environment.

The results of the metallurgical studies indicated that variation in the composition of the steels (from high-purity Ferrovac E to 1018 carbon steel) or thermomechanical treatments (cast versus wrought) did not have a marked effect on the electrochemical parameters associated with pit initiation or general corrosion in the simulated basalt repository environment. Thus, it appears that the use of high-purity iron for fabrication of the overpack would not greatly enhance the general or localized corrosion performance.

In the metallurgical studies, the electrochemical parameters associated with SCC also were not greatly affected by steel composition or microstructure. Thus, from an electrochemical standpoint, variation in the metallurgy of the steels over the range examined would not be expected to affect SCC. However, it must be cautioned that the influence of metallurgy on SCC susceptibility cannot be fully assessed by means of bulk electrochemical techniques since mechanical factors and grain boundary phenomena must also be considered.

Several tests were performed to study the effect of environmental variables on electrochemical behavior. In preliminary studies, it was found that equilibration of the simulated groundwater with basalt rock, or concentration of the groundwater by a factor of ten, did not have a marked effect on the polarization parameters. Similarly, increasing the temperature from 90

to 250 C did not markedly affect behavior, although a careful analysis of the data indicated a slightly higher likelihood of SCC at 250 C in comparison to the 90 C data.

A statistical experimental approach was used to evaluate the influence of 15 environmental variables on the electrochemical behavior of carbon steel. The species and ranges in concentration were selected for study based on a survey of the literature. Species considered included those present in the groundwater as well as those that may intrude the repository or be generated by radiolysis. A screening matrix of experiments was performed to reduced the number of variables from 15 to 11 for analysis in the main matrix. Twenty-one two-factor interactions were also considered in the main matrix.

From the statistical analyses, it was found that many of the environmental variables had important effects on the electrochemical parameters; this behavior was expected. Somewhat more surprising was the fact that many of the two-factor interactions also significantly affected the polarization parameters. These two-factor interactions are not normally considered in most corrosion studies.

The results of the statistical analyses were used to develop regression models that describe the influence of the main effects and two-factor interactions on the electrochemical parameters. These models were then tested for selected two-factor interactions. The quantitative agreement between the experimentally measured values and the predictions of the models were generally poor, but the trends in the data were fairly well predicted. This poor predictive capability of the models was attributed to correlation of the terms, which occurred because the design concentrations for the solutions could not be achieved in all instances as a result of precipitation in the solutions. Nevertheless, the studies were extremely useful in understanding the ranges of expected behavior for carbon steel in a repository environment. In addition, these data were used to select solution chemistries for the pit propagation and SCC studies.

A few species in the statistical matrix are thermodynamically unstable and the standard test procedure was not effective in studying their influence on corrosion behavior. Accordingly, the test procedure was modified to include continuous injection of these species. Two species, peroxide and perchlorate, were studied in greater detail. It was found that both species greatly increased the corrosion rate of carbon steel when present at reasonably high concentrations. Once estimates are made of the amounts of these species likely at an overpack surface, and of their rates of production, similar experiments can be repeated to establish the likely effect on corrosion. For peroxide, it was clearly shown that both the anodic and cathodic electrode kinetics were affected since, for carbon steel in simulated basalt solutions, the lower concentration of peroxide had the higher corrosion rate.

3.2.2 Pit-Propagation Studies

Results of the potentiodynamic polarization experiments and autoclave exposures suggest that pit initiation in low-carbon steel is likely in basalt

groundwater. The polarization curves exhibit considerable hysteresis on the reverse scans, and protection potentials are very near the corrosion potentials, even for deaerated solutions. In the autoclave exposures, pits actually were found on specimens exposed for approximately 1,000 hours in a deaerated simulated basalt groundwater at 250 C (see Section 3.2.3).

Accordingly, experiments were undertaken to characterize the pit-propagation behavior of carbon steel in simulated basalt-repository environments. Brine solutions were also briefly examined to characterize any differences in pit-propagation mechanisms. The compositions of these solutions are given in Table 3.9. Two types of experiments were performed: (1) long-term exposures and (2) electrochemical studies. The purpose of the long-term exposures was to examine the pit propagation as a function of time and to help verify the predictions made in the relatively short-term electrochemical studies. The electrochemical studies provided predictions of pit-propagation behavior within a relatively short time while providing fundamental mechanistic information on pit propagation.

3.2.2.1 Objectives

The overall objective of this study was to characterize the pit-propagation behavior of carbon steel and to develop a better understanding of the mechanism of pitting attack. The specific objectives were to:

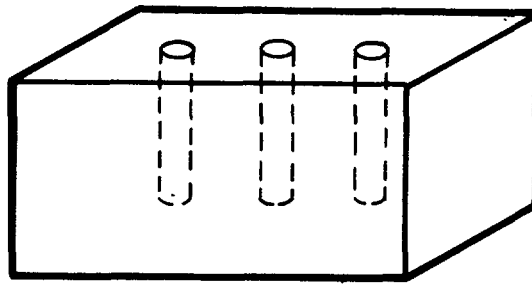
- establish the rate controlling process for pit propagation
- determine the effect of pit geometry
- examine the effect of environmental variables
- determine the effect of carbon steel surface finish.

3.2.2.2 Experimental Approach

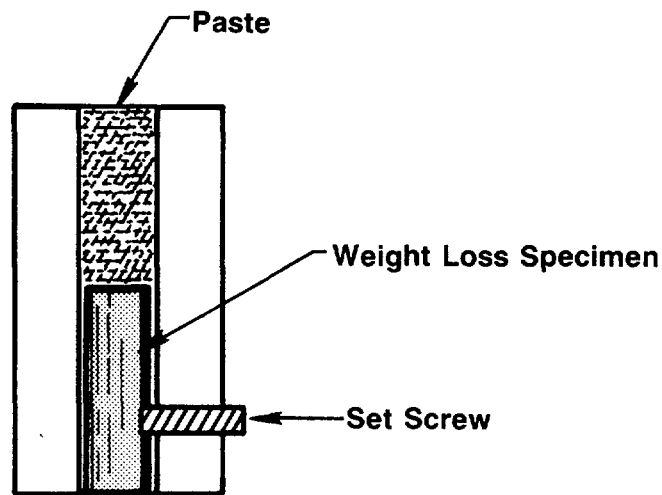
The following sections give details on the long-term exposure and electrochemical techniques that were used to study pit-propagation behavior.

Long-Term Exposures. Two types of long-term exposures were performed: exposures of mechanically drilled pits and weight-loss exposures of simulated pits. The pit geometries for the two types of experiments are given in Figure 3.40. In the first type of exposure, pits of various depths and aspect ratios (diameter/depth ratios) were drilled in specimens of hot-rolled 1018 carbon steel and exposed to deaerated and oxygenated basalt groundwater at 90 C. The steel used in this study was obtained commercially, and its composition is given in Table 3.8. Prior to exposure, the depths of the pits were measured with a micrometer having a thin needle point. After exposure, the specimens were metallographically sectioned so that the morphology and depth of attack could be studied.

Four different pit diameters were studied: 5.1 mm (0.2 inch), 2.54 mm (0.10 inch), 1.35 mm (0.05 inch), and 0.53 mm (0.021 inch). For each diameter, there were three diameter-to-depth ratios: 1:2, 1:5, and 1:10. Thus, for a 5.1-mm-diameter pit, the initial pit depths were 10 mm, 25 mm, and 50 mm. The overall specimen dimensions were approximately 40 mm long x 20 mm wide x 75 mm thick (in the dimension of the pit depth), and the specimens were machined from 7.6 cm (3 inches) x 15.2 cm (6 inches) strip steel.



a. Mechanically drilled pit.



b. Simulated pit for weight-loss tests.

Figure 3.40. Pit geometries used in long-term exposure tests.

Prior to exposure, the specimens were cleaned with acetone, each pit was filled with the simulated basalt groundwater using a syringe, and the specimens were placed in high-density polyethylene vessels containing one inch of crushed basalt. In each vessel, an electrical connection was attached to one specimen for subsequent potential measurements. The basalt-groundwater solution was added and the vessels were sealed. The vessels were then placed in oil baths, Luggin probes were connected, and the flow of nitrogen or oxygen was started (for deaerated or oxygenated solutions, respectively).

Aliquots of solution were collected periodically and the pH was analyzed. Also, during the experiments, the electrochemical potential of one specimen in each vessel was monitored. Specimens were removed from each solution

following a 4-month exposure and an 8-month exposure. The specimens were optically examined, metallographically sectioned, and reexamined to characterize the corrosion that had occurred.

Weight-loss tests were carried out on specimens having the same geometry as those used in the electrochemical pit-propagation experiments but shortened in the axial direction (see Figure 3.40). The experiments were conducted for 1,000 hours in three environments: a pitting environment, aerated basalt groundwater, and deaerated basalt groundwater, all at 75 C. The pitting environment was solution number 47 from the potentiodynamic polarization task (Section 3.2.1) and was selected on the basis of the results of those studies.

In addition to test solution composition and degree of aeration, other variables that were included in the experiments were the pit diameter-to-depth ratio (1:1 and 1:2), electrical coupling of the pit specimen to the boldly exposed surface (BES) specimen (coupled and uncoupled), and the pH of the Fe_3O_4 paste used to pack the pits (about pH = 1 [0.1M HCl] and about pH = 2 [0.01M HCl]). The experiments were conducted using a flow-through system with the solution being refreshed twice a week to maintain constant bulk-solution chemistry throughout the exposure period.

Electrochemical Studies. A schematic of the pit-propagation monitor is shown in Figure 3.41. The monitor was positioned vertically in a test cell containing an electrolyte, and the current flow between the pit and the BES specimen was monitored as a function of exposure time. Current measurements provide an estimate of the rate of pit propagation, where shifts in the electrochemical potential of the pit base, as a result of the couple, are greater than about 50 mV. For potential shifts less than this value, the rate measured may be somewhat nonconservative since the reduction reactions occurring on the pit base will contribute to pit propagation but will not be detected. The measured current does provide an indication of the increase in the rate of corrosion as a result of the couple.

A standard procedure was developed to initiate pitting with the monitor. This procedure consisted of (1) pre-packing the simulated pit with a modified paste prepared with 0.1N or 0.01N HCl and Fe_3O_4 ; (2) deaerating the test solution to fully deaerate the pit, during which time the simulated pit and boldly exposed surfaces were not coupled; and (3) aerating the test solution and coupling the simulated pit and boldly exposed surface through the zero-resistance ammeter (ZRA).

Double-walled Pyrex® cells were used in the experiments so that the temperature could be controlled by flowing a heat-transfer solution in the annular region between the inner and outer walls. The cells consisted of (1) a counter-electrode cell containing a platinum electrode for electrochemical measurements, (2) a reference-electrode cell containing a standard calomel electrode (SCE) for electrochemical potential measurements, (3) a platinum wire for Eh measurements, (4) a frit bubbler for deaeration or aeration of the solution. Prior to the test, the specimens were cleaned with acetone and assembled, and the simulated pits were packed with a paste as previously described. The specimens were then inserted in the cell, the

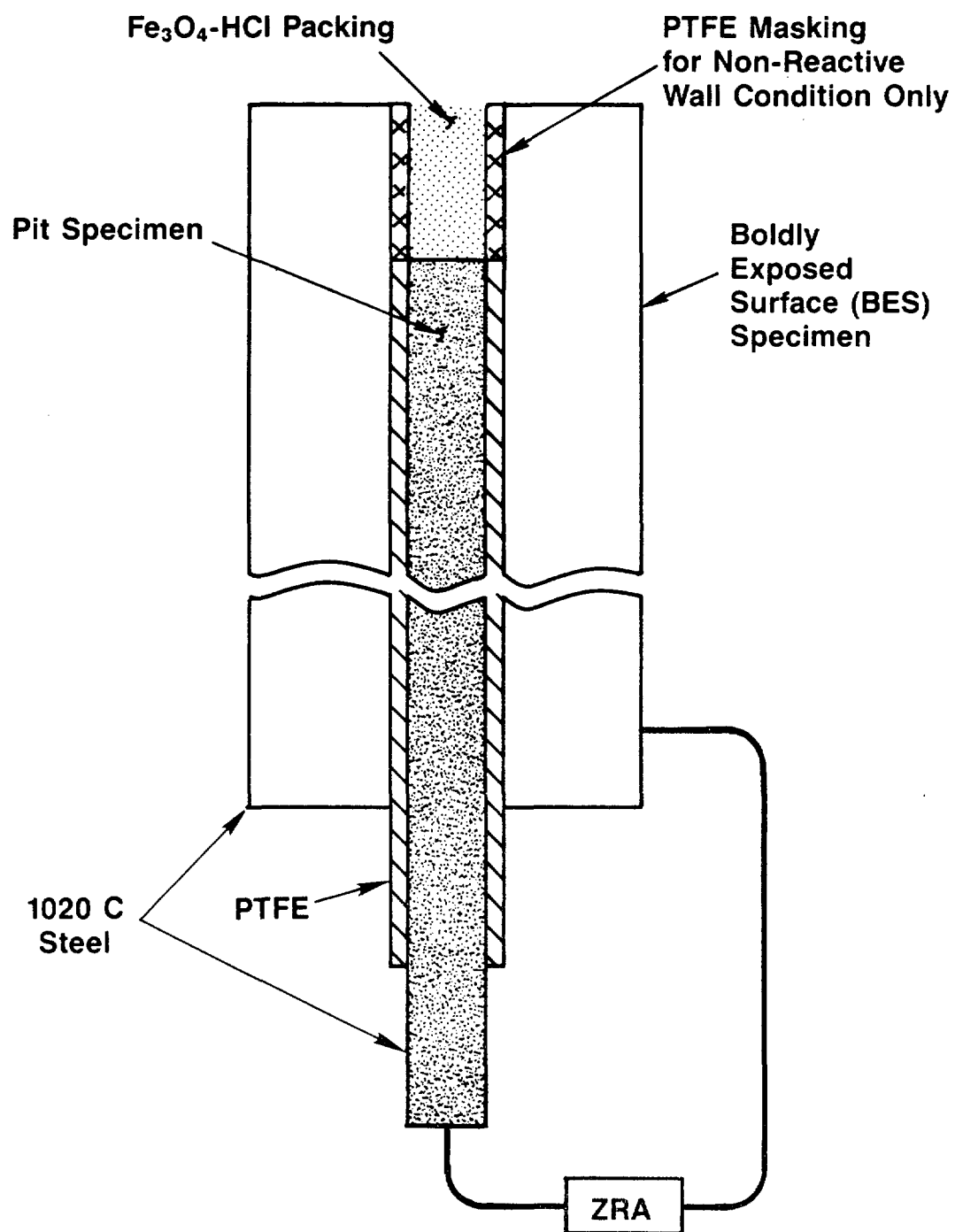


Figure 3.41. Schematic of pit-propagation monitor.

test solution was added, and the experiment was started. During the course of the experiment, couple potentials, E_h , temperature, and galvanic current flow were continuously monitored and recorded with a data acquisition system. In some experiments, the specimens were uncoupled and the specimen potentials also were measured. Solution and gas flow rates were continuously monitored and maintained at 40 cc/hour and 10 cc/min, respectively.

During these experiments, various secondary experiments were performed on the pit and BES specimens. In some of the initial experiments, potentiodynamic polarization curves were performed at the end of the exposures on these specimens. The potentiodynamic polarization experiments were performed in a similar fashion to that described in Section 3.2.1. In a majority of the later experiments, potential profiles were measured by moving a glass microcapillary Luggin probe down the pits. The measurements were taken at 1-mm intervals from approximately 10 mm above the pit down to the base of the pit specimens. For these measurements, the pit and BES specimens were coupled. However, in some instances the specimens were uncoupled prior to being measured.

3.2.2.3 Pit-Propagation Results

The results of the different pit-propagation experiments are presented below. These sections include a brief discussion of how the results of the long-term exposures, weight-loss exposures, and electrochemical studies relate to the overall pit-propagation studies. A detailed discussion on the pitting mechanism and how these pitting studies relate to the overall NRC goals are presented in the summary, Section 3.2.2.4.

Long-Term Exposures. As described in more detail in Section 3.2.2.2 (Experimental Approach), two types of long-term pit propagation tests were performed: exposures of mechanically drilled specimens and weight-loss experiments on simulated pits. Pit specimens of hot-rolled 1018 carbon steel containing mechanically drilled pits of various diameters (0.53 mm to 5.1 mm) and diameter-to-depth aspect ratios (1:2 to 1:10) were exposed to deaerated and oxygenated basalt groundwater for up to 8 months.

During the experiments, the electrochemical potential of one specimen in each vessel was monitored, and aliquots of solution were taken periodically for pH analyses. The results of the potential measurements are given in Figure 3.42. These data show that the potentials of the specimens in the deaerated vessels varied between -0.70 and -0.75 V(SCE) over the first 70 days of exposure, whereas the potentials of the specimens in the oxygenated vessels exhibited a marked increase after about 25 days of exposure and stabilized at about -0.22 V(SCE).

The results of the pH measurements are given in Table 3.23. The measurements were taken frequently over the first several weeks of exposure to establish the trends, but less frequently thereafter to conserve the solutions and minimize contamination of the deaerated solutions with oxygen. These data show some interesting trends. The pH of all the solutions decreased over the first 24 hours from about 9.8 to about 7.5, and the pH of the deaerated solutions continued to decrease somewhat over the first

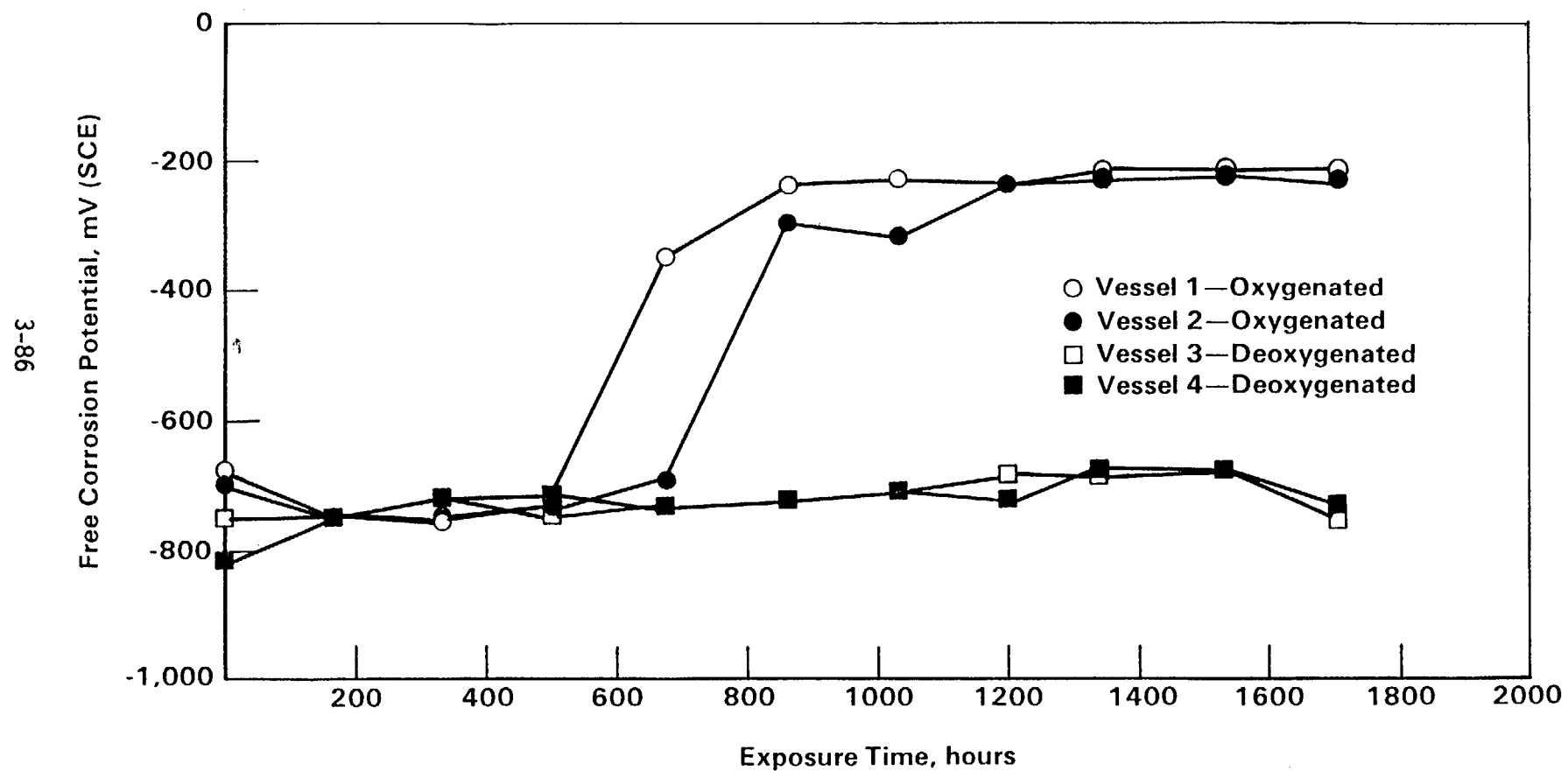


Figure 3.42. Electrochemical potential as a function of exposure time for mechanically prepitted 1018 carbon steel specimens in basalt groundwater containing crushed basalt at 90 C.

Table 3.23. pH as a function of exposure time for simulated basalt groundwater solutions in contact with basalt rock and 1018 carbon steel specimens at 90 C.

Exposure Time (hours)	Oxygenated		Deaerated	
	Vessel 1	Vessel 2	Vessel 3	Vessel 4
0	9.8	9.8	9.8	9.8
24	8.0	7.6	7.0	7.4
72	7.4	7.4	7.2	7.8
168	7.5	7.5	7.5	7.5
336	7.8	7.9	7.5	7.5
1080	11.2	11.5	7.5	7.5
2208	11.2	11.5	6.5	6.6

2 months of exposure. On the other hand, the pH of the oxygenated solutions increased over the 2-month period to values around 11.5. The mechanism for this pH increase is not fully understood.

Altogether, eight prepitted specimens were removed from the vessels and optically examined following 120 days of exposure. Specimens containing mechanically produced pits of each diameter were removed from both oxygenated and deaerated vessels. All specimens from the oxygenated vessels were covered with thick, red rust deposits, and the pits were all capped with corrosion products. On the other hand, specimens taken from the deaerated vessels were covered with thin black deposits, and the pits were not capped. Figure 3.43 illustrates some of these features as they appeared in specimens with 2.54-mm-diameter pits.

Following the optical examination, the specimens were metallographically sectioned, mounted, and polished, and the depths of the pits were measured with a microscope having a calibrated stage. No systematic trend in pit depth was evident from the data. The differences between the initial (pre-exposure) and the final pit depths varied by about ± 0.1 mm, which probably reflects the error in the measurement.

A close examination of the metallographic sections of the specimens exposed in the deaerated vessels did not indicate any evidence of appreciable attack. Similarly, the 5.1-mm, 2.45-mm, and 1.35-mm pits in the specimens exposed in the oxygenated vessels did not exhibit appreciable attack. On the other hand, the smallest-diameter pits exposed in the oxygenated vessels did show evidence of attack. The attack occurred over the entire pit for the lowest-aspect-ratio pit (1:2), whereas it occurred only near the mouth of the deeper pits. There is also evidence that the attack followed stringers in the walls of the pits (see Figures 3.44 to 3.45).



Oxygenated



Deaerated

Figure 3.43. Low-power photograph of prepitted hot-rolled 1018 carbon steel specimens following exposure in oxygenated and deaerated simulated basalt groundwater containing crushed basalt at 90 C.

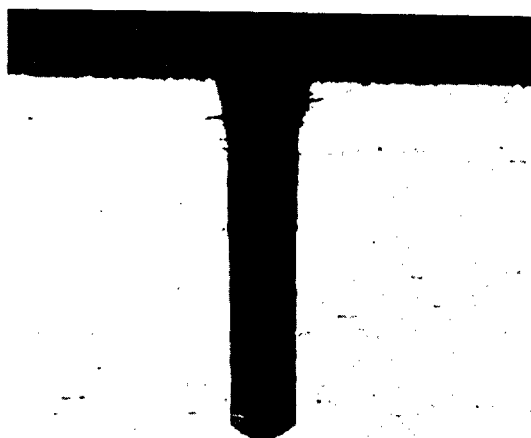
Note that the pits on the specimen in the oxygenated solution are capped with corrosion products.



20X

7L708

Figure 3.44. Optical photomicrograph of 1:2 aspect ratio 0.53-mm-diameter pit.



20X

7L707

Figure 3.45. Optical photomicrograph of 1:5 aspect ratio 0.53-mm-diameter pit.

ys of exposure, four prepitted specimens from the oxygenated re metallographically examined. There was considerably more corrosion on these specimens than on the oxygenated solution exposed after 120 days. Patches of localized attack were evident on exposed surfaces of the specimens, and these patches were associated with the presence of the thicker deposits. There was also evidence that this localized attack followed stringers or other microstructural features in the metal. An approximate corrosion rate for these areas ($245 \mu\text{m}/\text{yr}$) was calculated based on the change in surface profile. Actual rates were somewhat higher since some uniform attack on the free surface had occurred.

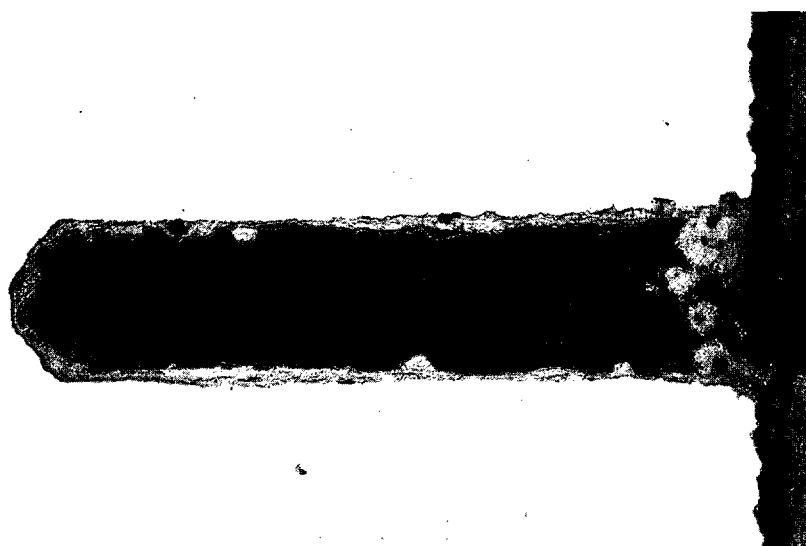
Results of the metallographic examination of the drilled pits from the 240-day exposure indicated that attack was generally greater for the shallow pits and near the mouth of the pits, as was reported for the 120-day exposures, as shown in Figure 3.46. However, the attack observed beneath deposits away from the pits was more severe in several instances than that observed near the pit mouths; thus, the drilled pits did not act as sites of initiation of severe attack.

Weight-Loss Experiments. Weight-loss tests of 1000 hours' duration were carried out on specimens having the same geometry as those used in the electrochemical pit-propagation experiments but shortened in the axial direction (see Figure 3.40). The experiments were carried out in three environments: a pitting environment, aerated basalt groundwater, and deaerated basalt groundwater at 75 C. The pitting environment was solution number 47 from the ~~potentiodynamic~~ polarization task (3.2.1) and was selected on the basis of the results of those studies. 41 days

Results of the weight-loss tests for the three environments are given in Figures 3.47 to 3.49. Figure 3.47, which contains data for the deaerated basalt groundwater, shows that the BES specimens had, in general, very low corrosion rates in this environment (25 to $50 \mu\text{m}/\text{yr}$) which were not affected by pit diameter-to-depth ratio or packing pH. The corrosion rates of the BES specimens appeared to be slightly lower for the coupled than for the uncoupled condition, as one might expect, but the differences were small.

The corrosion rates for the pits were generally higher than for the BES specimens ($200 \mu\text{m}/\text{yr}$ versus 25 to $50 \mu\text{m}/\text{yr}$) but, nevertheless, were moderate. There was no systematic effect of pH, coupling, or diameter-to-depth ratio on the corrosion rate of the pits. Thus, in the deaerated basalt groundwater, the corrosion rates of the pits were moderate and were probably controlled by the environment that developed within the pits.

Results of the weight-loss experiments performed in the aerated basalt groundwater are given in Figure 3.48, where it can be seen that the corrosion rates for the boldly exposed surfaces were quite high, about $500 \mu\text{m}/\text{yr}$, and that there was considerable scatter in the data. Optical examination of the BES specimens indicated that the high corrosion rates were the result of occluded cell corrosion occurring beneath deposits. The data in Figure 3.48 also show that uncoupled corrosion rates for the pits were comparable to or less than the corrosion rates for the BES specimens, whereas coupled



40X

2M063

a. 1:5-Aspect-Ratio Pit



40X

2M062

b. 1:2-Aspect-Ratio Pit

Figure 3.46. Optical photomicrographs of prepitted specimen (0.53-mm diameter pits) of hot-rolled 1018 carbon steel following exposure in oxygenated simulated basalt groundwater containing crushed basalt for 238 days (5712 hours).

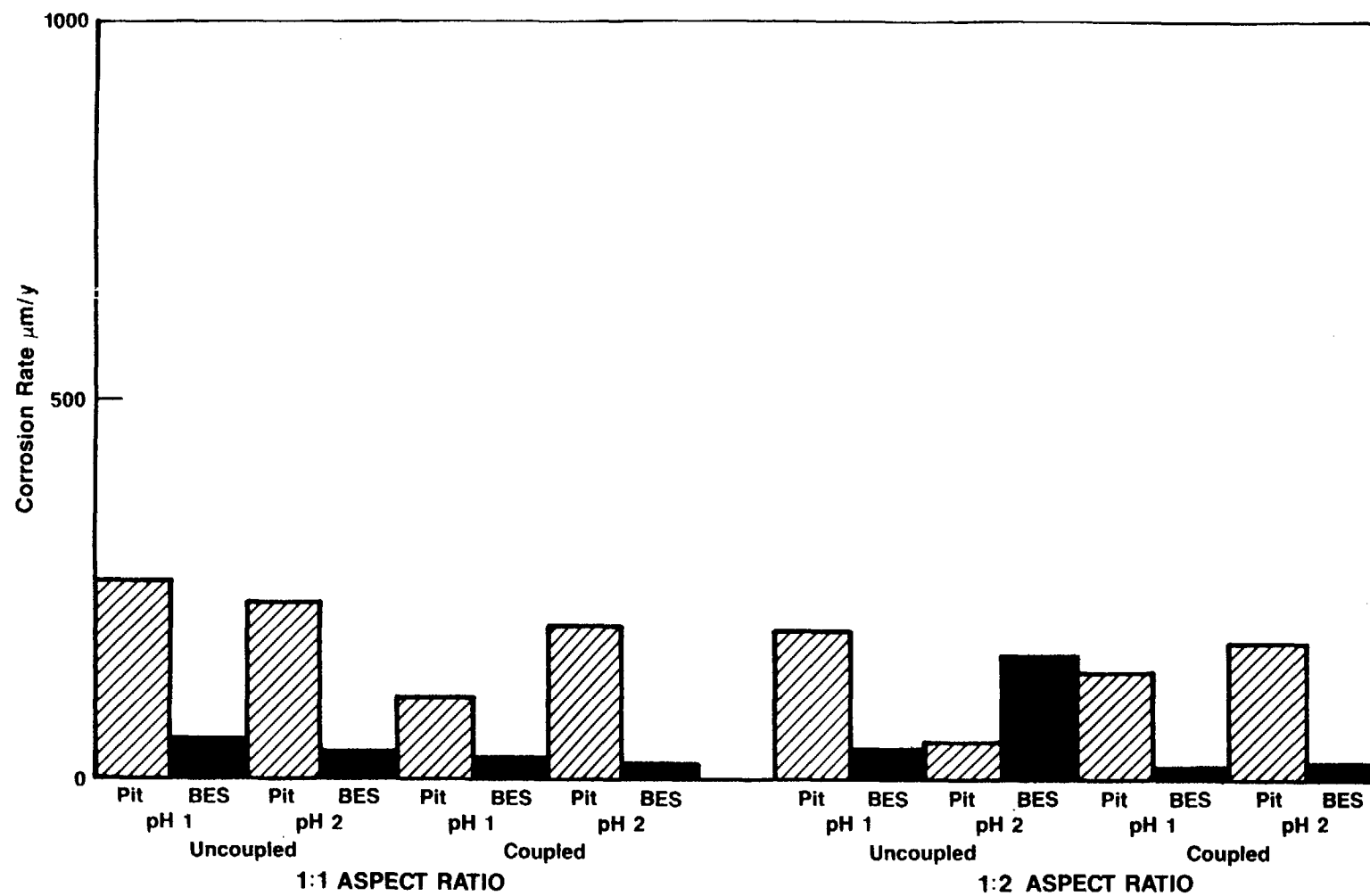


Figure 3.47. Results of 1000-hour weight-loss tests performed on simulated pits in deaerated basalt groundwater at 90 C.

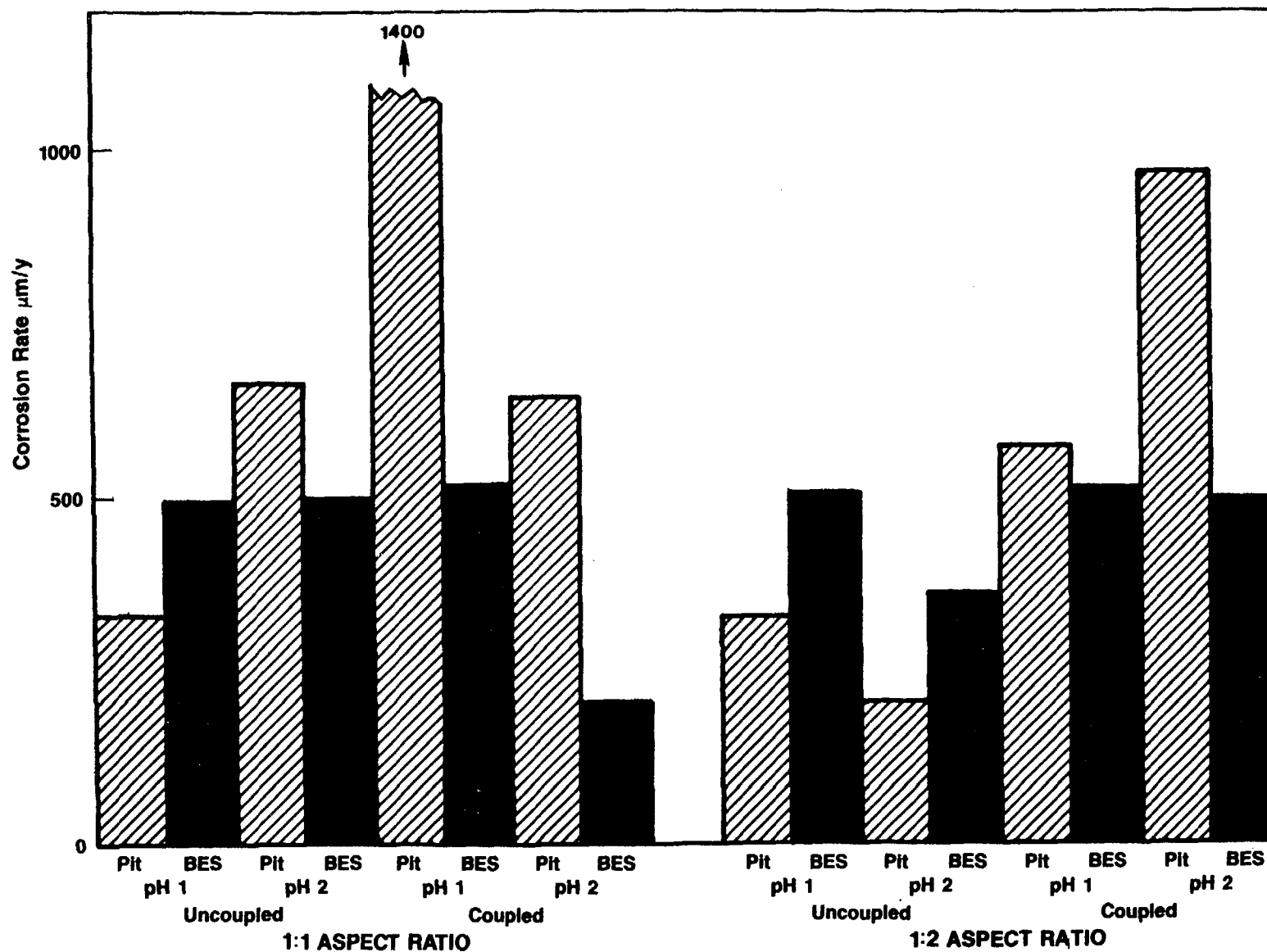


Figure 3.48. Results of 1000-hour weight-loss tests performed on simulated pits in aerated basalt groundwater at 90 C.

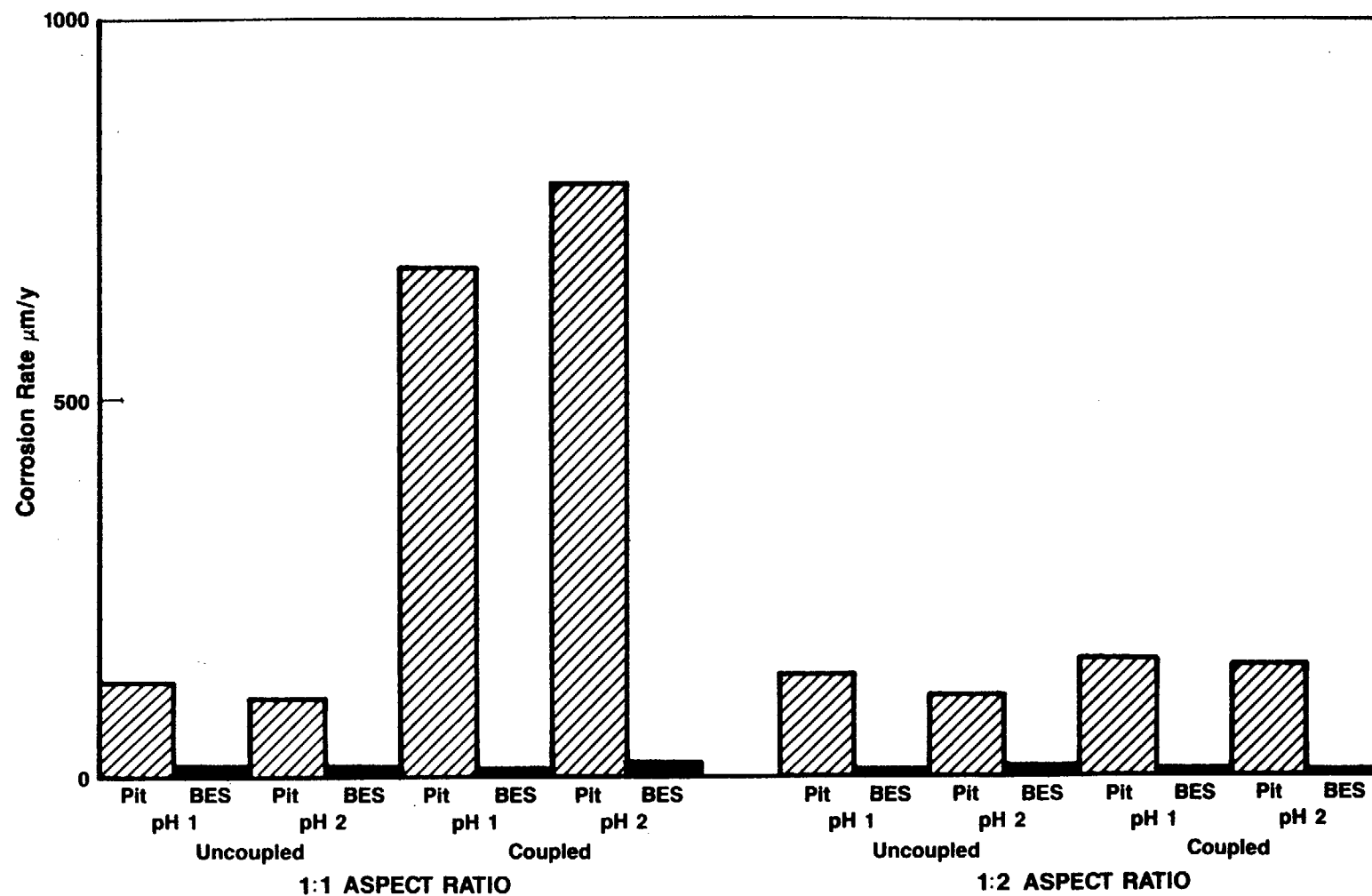


Figure 3.49. Results of 1000-hour weight-loss tests performed on simulated pits in an aerated pitting solution (Number 47 from potentiodynamic polarization studies) at 90 C.

corrosion rates for the pits were considerably higher than corrosion rates for the respective BES specimens at a diameter-to-depth ratio of 1:1. This coupling effect appeared to drop off rapidly with increasing pit depth; for the 1:2 diameter-to-depth ratio pit, the effect of coupling on the corrosion of the pits was much less pronounced.

The corrosion data for the aerated pitting solution are given in Figure 3.49. These data exhibited much less scatter than those observed for the aerated basalt groundwater but, nevertheless, the trends in the data were similar. Coupling clearly accelerated the rate of attack of the pit, and the effect of coupling dropped off rapidly with increasing diameter-to-depth ratio. Corrosion rates shown in Figure 3.49 for the BES specimens were extremely low, indicating that the pitting solution effectively passivated the surfaces of these specimens. The data in Figure 3.49 also indicate that the packing pH did not have an effect on the corrosion behavior of either the pit or the BES specimen.

To investigate the effect of the diameter-to-depth ratio of the pit and the relationship between pit-wall reactivity (inert versus reactive wall) on pitting rates, another matrix of 1000-hour exposures was performed. The previous tests did not indicate a large effect due to packing pH, and the data for the pitting solution exhibited much less scatter than the data for the aerated basalt groundwater. Therefore, these tests were performed with a single packing pH of 1 and in the aerated pitting solution. Four diameter-to-depth ratios were studied (1:0.5, 1:1, 1:2, and 1:5), and all specimens were coupled.

Results of the 1000-hour exposure are given in Figure 3.50. As was observed in the previous tests, the corrosion rates of the BES specimens all were quite low. On the other hand, the corrosion rates of the pits increased with decreasing diameter-to-depth ratio, from 300 to 500 $\mu\text{m}/\text{yr}$ at 1:0.5 to 1400 to 1700 $\mu\text{m}/\text{yr}$ at 1:2. Below that diameter-to-depth ratio, the corrosion rate for the reactive-wall pit dropped off rapidly, from 1700 $\mu\text{m}/\text{yr}$ at 1:2 to 250 $\mu\text{m}/\text{yr}$ at 1:5; whereas the corrosion rate for the nonreactive-wall pit dropped off more gradually with increasing depth, from 1400 $\mu\text{m}/\text{yr}$ at a diameter-to-depth ratio of 1:2 to 1050 $\mu\text{m}/\text{yr}$ at a diameter-to-depth ratio of 1:5.

The trend shown in Figure 3.50 in which the corrosion rate of the pit increases with a decrease in diameter-to-depth ratio is consistent with observations on the pit walls made during post-exposure investigations. These investigations indicated that the surfaces inside the pits were passivated about one pit diameter down the pit. The bulk electrolyte altered the environment within the pit and produced less aggressive coupling conditions for the more shallow pits. The opposite trend was seen upon going from the diameter-to-depth ratio of 1:2 to 1:5. This effect is likely due to the increasing importance of ohmic potential drop (down the pit) in controlling pit corrosion rates. The difference between the reactive-wall and the non-reactive-wall pits for the 1:5 diameter-to-depth ratio is interesting and is discussed further in the next section and Section 3.2.2.4 (Summary). ✓

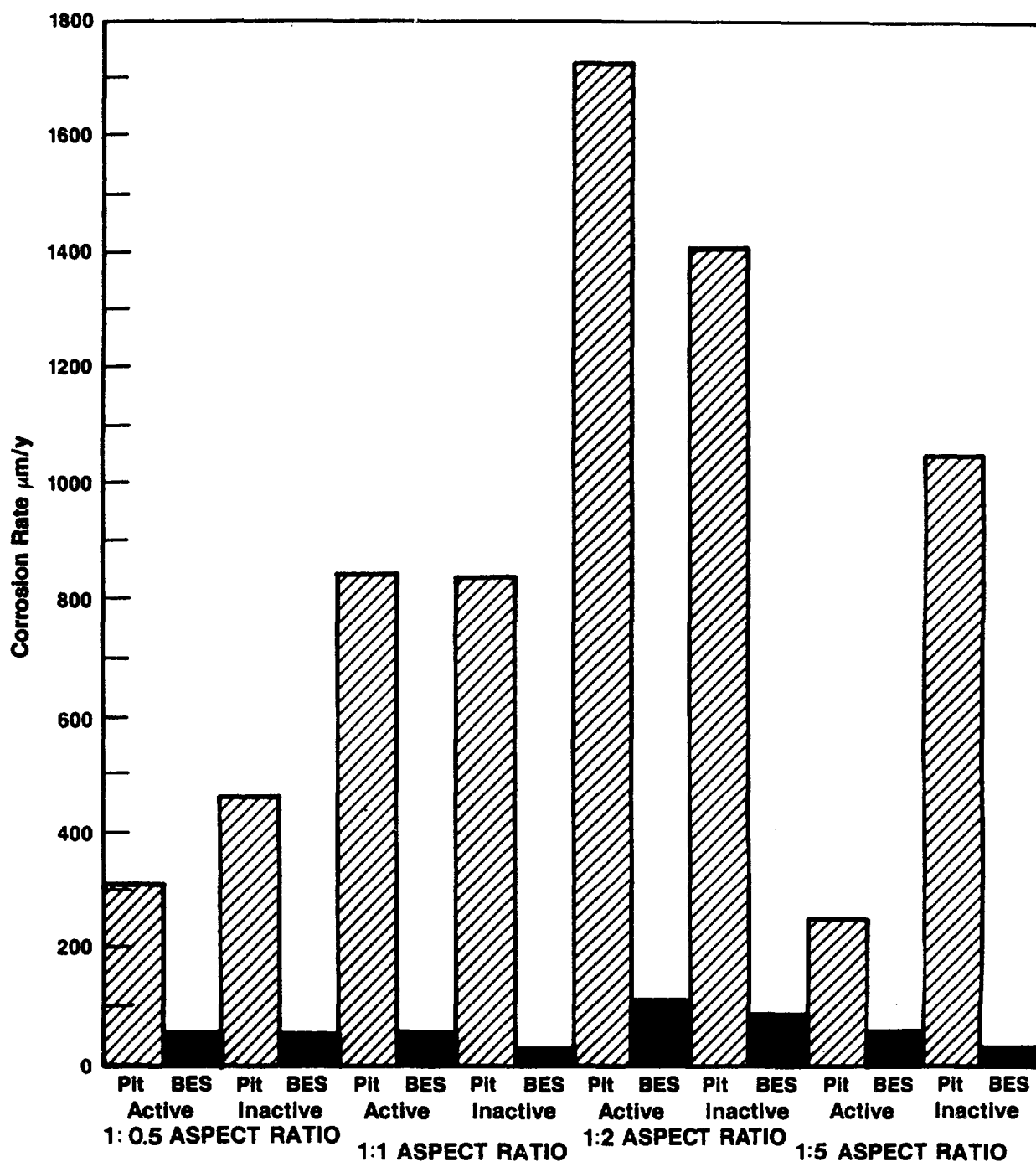


Figure 3.50. Effect of aspect ratio (diameter to depth) and pit-wall reactivity in the corrosion rate of pit and BES specimens in 1000-hour weight-loss tests.

Tests were conducted in aerated pitting solution (Number 47 from the potentiodynamic polarization studies) at 90 C with a packing pH of 1.

Electrochemical Studies. In this section, the results of experiments performed with the electrochemical pit-propagation monitor, previously shown in Figure 3.41, are presented. The majority of the work concentrated on examining the effects of pit geometry on pit propagation in the basalt groundwater. Also examined were the effect of the presence of milscale on the carbon steel surface and the effects of varying solution chemistry on pit propagation, including the examination of carbon steel in brine solutions. The results are described in the following subsections; Preliminary Experiments, Effect of Pit Geometry, Effect of Milscale, Active Versus Passive Solutions, and Brine Solutions.

● Preliminary Experiments. Several preliminary experiments were performed in oxygenated basalt groundwater at 75 C for the purpose of establishing test procedures and to determine the types of data that could be obtained using the pit specimen-barely exposed surface (BES) testing arrangement. No attempt was made in these preliminary experiments to mask-off the inside of the pit wall; thus, the experiments correspond to the reactive-wall condition. No packing material was used and the specimens were placed in the cells with deaerated solution added. Then, after an initial exposure period of a few hours, oxygen sparging was initiated. For diameter-to-depth ratios of 1:2 and 1:10, the coupled currents measured between the pit and BES specimens were negative after one week of exposure. This result indicated that the pit specimens were more positive (noble) than the BES specimens and that the current from the pit specimens was cathodic. In an attempt to activate the pits, the pit specimens were stimulated for approximately 24 hours by a 10 to 20 mA/cm² anodic current using a potentiostat and a platinum counter electrode. Following stimulation, both of the pits exhibited anodic coupled currents with the 1:2-aspect-ratio pit stabilizing at a current of approximately 50 μ A/cm² (23 mil/yr). On the other hand, the 1:10-aspect-ratio pit eventually exhibited a negative coupled current (cathodic current from the pit). Further experience indicated that it was difficult to activate the pits in a consistent manner.

Two artificial methods of occluding the pit were investigated: (1) packing the pit with an Fe₃O₄ slurry, and (2) plugging the pit mouth with a glass frit. The Fe₃O₄ slurry was selected based on results of X-ray diffraction analyses of deposits in pits on carbon steel. These deposits, which were in pits that developed on specimens from the long-term exposures, were composed primarily of Fe₃O₄ with some gamma-FeOOH and alpha-FeOOH. The simulated pits were set up with diameter-to-depth ratios of 1:3 using the basalt groundwater at 75 C. Again, the cells were initially deaerated with nitrogen for 24 hours followed by oxygen sparging at a flow rate of 10 cm³/min. For both conditions, anodic current from the pits were measured almost immediately upon introduction of oxygen, indicating that conditions for pit propagation had been established. The pitting currents were monitored during the course of the next 5 days.

For the Fe₃O₄-packed pits, the current fluctuated between 5 and 12 μ A/cm² (2.17 μ A/cm² is equal to 1 mil/yr). For the pits with the glass frit plugging the mouth, the coupled current varied between 0.5 and 1.2 μ A/cm². Because of the low coupled currents for both cases, stimulation of the pits by anodic polarization was performed using an anodic current of 15 mA/cm².

for 24 hours. After stimulation, the currents were found to be cathodic and remained cathodic over a period of 2 days, at which time the experiments were discontinued.

Further experiments to investigate the use of anodic stimulation of the pits met with only limited success. During these tests, it was found that temperature and oxygen fluctuations had a significant effect on the coupled currents measured. The experimental arrangement was adjusted to permit much better control of both the temperature and gas flow rate, and it was further decided to use the Fe_3O_4 packing with no anodic stimulation of the pits. With this new cell arrangement, one-week experiments were performed at three diameter-to-depth ratios (1:1, 1:5, 1:10) in basalt groundwater at 75 C. The oxygen flow rate was 10 cm^3/min and the pits were packed with an Fe_3O_4 slurry. The results of these experiments are shown in Figure 3.51. These data show that, for the initial 4,000 minutes of exposure, the current densities were highest for the higher diameter-to-depth ratio (that is, 1:1). However, the currents decreased with time and became similar for all three diameter-to-depth ratios.

Based on the results of these experiments, it was determined that stable pit-propagation behavior had not been achieved. Accordingly, a final adjustment was made to the packing procedure. It was decided to acidify the Fe_3O_4 paste using hydrochloric acid (HCl). This decision was based on results of pH analyses of deposits found within pits on specimens in the long-term experiments; pH values were between 2 and 3. Two experiments were conducted using a diameter-to-depth ratio of 1:5 in simulated basalt groundwater at 75 C. These and all subsequent experiments were performed with air sparging rather than oxygen sparging, at a rate of 10 cm^3/min . Pits were packed with a paste of 0.1 N HCl- Fe_3O_4 in one and 0.01 M HCl- Fe_3O_4 in the other. The results of the current-time measurements indicated that, as in the previous experiments, pitting currents were very low and fluctuated considerably during the exposure period. Coupled potentials for the two test cells were similar over the exposure period; prior to deaeration, the potentials were approximately -0.65 V(SCE) and a noble (positive) shift of 0.10 to 0.15 V occurred when air sparging was started. The potentials of the two cells tended to become more negative over the next few hours and fluctuated between -0.55 and -0.60 V (SCE) over the remainder of the test period.

Potential measurements were made for the pit specimen and BES specimen for the uncoupled condition. It was observed that these uncoupled potentials were within a few millivolts of each other, even when this low pH packing material was used for the pits. Although the reason for the similar potentials were not understood at that time, the coupled current would not be expected to give a true indication of the corrosion rate if the potentials of the two specimens being coupled were within approximately 50 millivolts of one another.

The above experiments were repeated with the addition of careful weight-loss measurements on the pit specimens. Results of the coupled-current and coupled-potential measurements for the two experiments were similar to those previously reported for the condition of the 0.1 N HCl and 0.01 N HCl packed pits. In these experiments, the potential measurements for the pit and BES

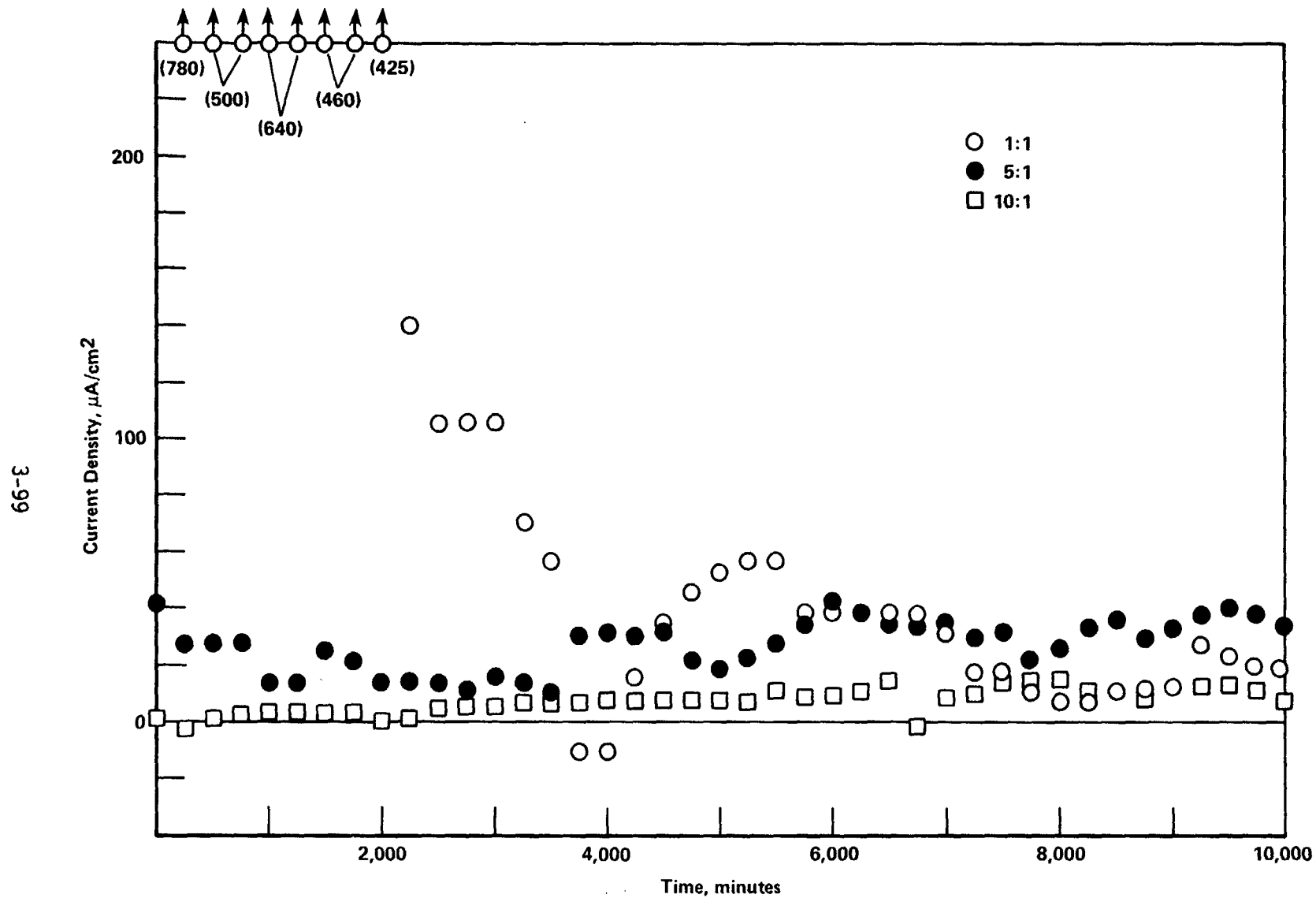


Figure 3.51. Current density as a function of exposure time for pit propagation experiments performed at diameter-to-depth ratios of 1:1, 1:5, and 1:10 in oxygenated basalt groundwater at 75 C.

specimen in the uncoupled condition were monitored periodically throughout the experiments. These data are summarized in Table 3.24. The data show that the BES specimens were a few millivolts more noble than the pit specimens during the experiments, and that the potential difference (ΔE) between the two decreased with exposure time. Although the measured potentials were slightly more positive for the 0.01 N HCl-packed pit, it is probable that the potential differences are experimental variations and not due to the acidity of the packed pit.

Table 3.24. Uncoupled potentials for pit and BES specimens as a function of exposure time and pH of packing paste for pit-propagation experiments in basalt groundwater at 75 C.

Time After Start of Air Purging (hours)	Potential (mV SCE)					
	0.1 N HCl-Packed Pit			0.01 N HCl-Packed Pit		
	Pit	BES	$\Delta\phi$	Pit	BES	$\Delta\phi$
8.0	-600	-595	5	-550	-546	4
8.1	-599	-594	5	-552	-548	4
8.4	-598	-593	5	-550	-547	3
73.3	-560	-559	1	-479	-476	3
73.5	-562	-560	2	-483	-480	3
73.7	-562	-560	2	-483	-480	3
122.1	-533	-531	2	-489	-488	1
122.3	-533	-532	1	-489	-488	1
122.5	-532	-531	1	-488	-487	1

Following termination of the exposures, careful weight-loss measurements were performed on the pit specimens. The specimens were alternately descaled in Clarke's solution* at room temperature and then weighed until there was no evidence of corrosion products on the specimens or of a change in the slope of the weight-time curve. The weight losses of the electrodes were converted to corrosion rates of 1,700 $\mu\text{m}/\text{yr}$ and 1,500 $\mu\text{m}/\text{yr}$ for the 0.1 N HCl-packed and 0.01 N HCl-packed pits, respectively. These corrosion rates are over 20 times greater than the values predicted from coupled current measurements, 5 $\mu\text{A}/\text{cm}^2$ or about 60 $\mu\text{m}/\text{yr}$. The similarities in the weight losses for the two pits suggest that, in these experiments, the

*This solution is composed of one liter HCl (specific gravity 1.19), 20 g Sb_2O_3 , and 50 g SnCl_2 .

environmental conditions that developed as a result of pit propagation dominated any effect that the initial packing pH may have had on corrosion. This agrees with the results of the long-term exposure with the simulated pit specimens shown in Figure 3.49.

The results of these preliminary tests indicated that the low coupled current did not provide a true measure of the pit-propagation rate for the case of reactive-wall pits. Additional miscellaneous experiments were performed with both reactive-wall and nonreactive- (inert) wall pits.* In these preliminary studies, ambient temperature conditions were used because more reproducible data were obtained at the lower temperature. This was possibly due to expansion and oozing of the packing paste from the pits at the higher test temperature. The nonreactive-wall geometry was examined because it is frequently selected for mathematical modeling studies to simplify the modeling. It is believed, however, that the reactive-wall geometry more closely simulates actual pits.

In the remaining studies discussed in the following paragraphs, the pitting experiments were performed with simulated pits packed with a 0.1 N HCl-Fe₃O₄ paste, maintained at room temperature (25 C), with a 10-cm³/min sparging of air. Complete details of the experimental procedures used are given in the Experimental Approach section (3.2.2.2).

● Effects of Pit Geometry. For this study, pit-propagation experiments were performed at varying diameter-to-depth ratios ranging from 1:0.5 to 1:10. The pit diameter was 0.41 cm, providing a pit area of 0.13 cm². The experiments were performed at 25 C with an air sparging rate of 10 cm³/min. The pits were packed using an Fe₃O₄ powder mixed with 0.1 N HCl to form a thick paste. The typical exposure period was 192 hours (8 days). Table 3.25 lists the experimental parameters for all the electrochemical pit-propagation experiments.

Table 3.26 summarizes the electrochemical pit-propagation data for the experiments involving carbon steel and basalt groundwater for several different diameter-to-depth ratios. There are several different measurements provided in Table 3.26. The corrosion rate of the pit is presented as the average corrosion rate in $\mu\text{m}/\text{yr}$ calculated from weight-loss measurements; the coupled current between the pit specimen and the BES specimen, as measured at the end of the experiment; and the coupled potential of the pit-BES couple measured at the end of the experiment. At intervals during the exposure period, the pit and BES specimens were uncoupled and allowed to freely corrode for approximately 15 min. At that time, the uncoupled potentials of both specimens were then measured prior to recoupling (Columns 5 and 6 in Table 3.26, respectively).

The last procedure performed in each of the pit-propagation experiments was the measurement of the potential profile down the pit using a microcapillary

*A Teflon® tube, which was sealed at the pit opening, was used to isolate the pit walls from the test solution.

Table 3.25. Experimental parameters for the electrochemical pit-propagation tests performed at 25 C; pit specimen area = 0.13 cm², BES specimen area = 24 cm².

Specimen No.	Diameter-to-Depth Ratio	Pit Packing Material	Exposure Time (hour)	Test Solution	Specimen Material
21-Inert	1:0.5	(a)	212	Basalt Groundwater	Carbon Steel
21-Reactive	1:0.5	(a)	212	"	"
30-Inert	1:1	(a)	214	"	"
29-Inert	1:2	(a)	172	"	"
29-Reactive	1:2	(a)	172	"	"
24-Inert	1:2.5	(a)	172	"	"
24-Reactive	1:2.5	(a)	172	"	"
17-Inert	1:5	(a)	142	"	"
17-Reactive	1:5	(a)	142	"	"
22-Inert	1:10	(a)	312	"	"
23-Reactive	1:10	(a)	192	"	"
20-Inert	1:5	(a)	158	"	Carbon Steel with Mill Scale
20-Inert	1:5	(a)	158	"	"
26-Inert	1:5	(b)	172	Solution 30	Carbon Steel
26-Reactive	1:5	(b)	172	"	"
31-Inert	1:5	(b)	165	Solution 47	"
31-Reactive	1:5	(b)	165	"	"
27-Inert	1:5	(b)	172	Brine A	"
27-Reactive	1:5	(b)	172	"	"
28-Inert	1:5	(b)	310	Brine B	"
28-Reactive	1:5	(b)	310	"	"

(a) Fe₃O₄ powder mixed with 1 N HCl.

(b) Fe₃O₄ powder mixed with test solution adjusted to pH 1 with HCl.

Table 3.26. Summary of electrochemical pit-propagation experiments for carbon steel in basalt groundwater at 25 C using simulated pits prepacked with 0.1 N HCl-Fe₃O₄ paste.

Specimen No.	1 Diameter- to-Depth Ratio	2 Corrosion Rate of Pit (Wt. Loss) μm/yr	3 Coupled(a) Current, μA/m ²	4 Coupled(a) Potential, V, SCE	5 Uncoupled(d) Potential of Pit, V, SCE	6 Uncoupled Potential of BES, V, SCE	7 Coupled(b) Potential at Pit Surface, V, SCE	8 Uncoupled(b) Potential at Pit Surface, V, SCE	9 Resistance Down Pit, ohm
21-Nonreactive	1:0.5	2,073	40	-0.640	-0.668	-0.639	-0.651	-0.671	1,600
21-Reactive	1:0.5	631	28	-0.584	-0.615	-0.588	-0.625	-0.635	180
30-Nonreactive	1:1	3,093	34	-0.564	-0.621	-0.556	-0.600	-0.641	1,200
30-Reactive	1:1 ₁	1,667	2	-0.627	-0.629	-0.629	-0.650	-0.652	270
29-Nonreactive	1:2	959	54	-0.566	-0.617	-0.562	-0.620	-0.659	5,340
29-Reactive	1:2	285	8	-0.607	-0.612	-0.609	-0.653	-0.655	180
24-Nonreactive	1:2.5	510	15(c)	-0.648	-0.690	-0.661	-0.668	-0.690	5,800
24-Reactive	1:2.5	596	3	-0.620	-0.610	-0.602	-0.672	-0.681	250
17-Nonreactive	1:5	--	41	-0.578	-0.646	-0.574	-0.631	-0.656	6,900
17-Reactive	1:5	--	0.5	-0.580	-0.591	-0.589	-0.648	-0.658	210
22-Nonreactive	1:10	380	38	-0.555	-0.646	-0.598	-0.620	-0.650	9,900
23-Reactive	1:10	311	1	-0.565	-0.608	-0.607	-0.667	--	175

(a) Values given in table represent end of exposure data.

(b) Measured using a microcapillary probe at the end of the experiment.

(c) Erratic current could indicate problems with high resistive contact between pit specimen and pit substrate (threaded connection).

(d) Measured at different time than coupled potential (Column 4). At any given time, the coupled potential equals the uncoupled potential of BES (Column 6).

reference probe. This was typically done with the pit specimen and BES specimen coupled; the potential at the bottom of the pit is given in Column 7. With the probe remaining at the bottom of the pit, the pit specimen and BES specimen were uncoupled and the pit surface was permitted to depolarize for approximately 5 min, at which time the uncoupled potential at the pit surface was measured (Column 8). Electrochemical impedance measurements were performed on the pit specimens for both the nonreactive and reactive-wall conditions. The primary purpose of the electrochemical impedance measurements was to determine the resistance down the pit, which was assumed to be equal to the solution resistance since the solution resistance between the Luggin probe and the BES specimen is always much less than that of the solution resistance down the pit (Column 9).

Before discussing the comparisons in Table 3.26 in more detail, some examples of the data are presented below. Figure 3.52 shows the coupled current as a function of exposure time for the nonreactive-wall and reactive-wall pits for the 1:5 diameter-to-depth ratio in basalt groundwater. The coupled current for the reactive-wall pit was very low and, for this experiment, remained positive, indicating anodic current from the pit. In other experiments, the current for the reactive-wall pit exhibited some periods of cathodic current from the pit specimen. The coupled current for the nonreactive-wall pit was approximately two orders of magnitude greater than the coupled current for the reactive-wall pit. This occurred in all other tests with basalt groundwater except for experiment 21, which had the most shallow pit geometry. In that experiment, the currents for both geometries was high.

The coupled potentials for the nonreactive- and reactive-wall conditions for Experiment 17 are given in Figure 3.53. Although some variations are seen during the initial exposure period, the coupled potentials are very similar for the nonreactive- and reactive-wall conditions. Because of the large surface area of the BES, it was expected that these potentials would be similar and that the presence of the nonreactive- or reactive-wall would not appreciably affect the coupled potential. Periodically, the pit and the BES specimens were uncoupled and the uncoupled potentials for each specimen were measured. Figure 3.54 shows the uncoupled potentials for the different specimens. Figure 3.54a shows the potentials of the pit and the BES for the nonreactive-wall condition. A 70 mV difference existed between the BES and the pit specimen, the latter being more negative. For this couple, a relatively high current was observed with the anodic current leaving the pit specimen. Figure 3.54b shows the uncoupled potentials for the pit and BES specimen for the reactive-wall condition. These potentials were always similar, with the potential of the pit specimen a few millivolts more negative than the potential of the BES specimen. In comparing Columns 5 and 6 in Table 3.26, the same trends existed for all the experiments performed. Experiment 21 was the only experiment in which a significant difference in the uncoupled potential (between the pit and BES specimen) was observed for the reactive-wall condition; it also had the most shallow pitting geometry examined. For Experiment 21, a high coupled current also was observed.

In Experiment 17, the pit specimen and the BES specimen were uncoupled and the potential profile down the pit was measured toward the end of the

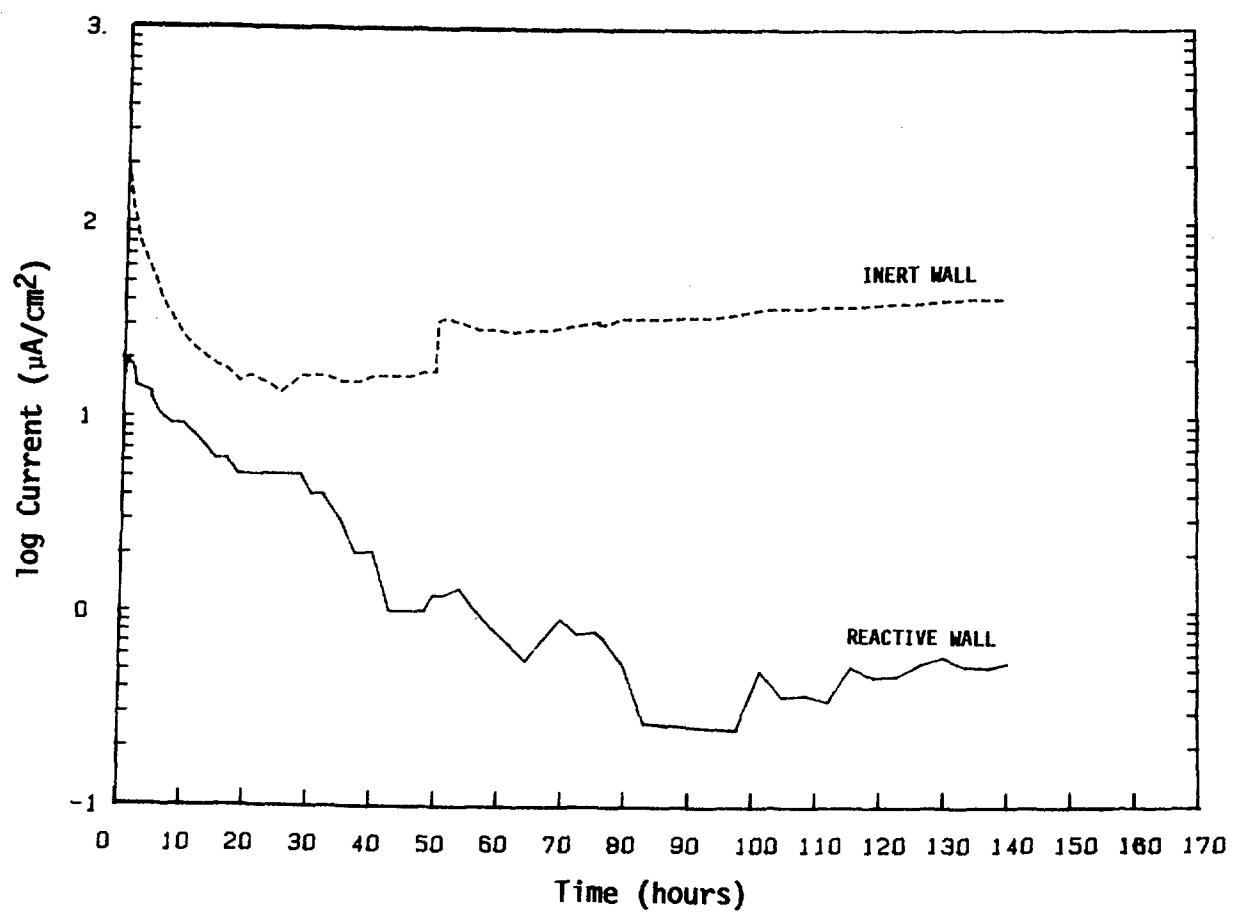
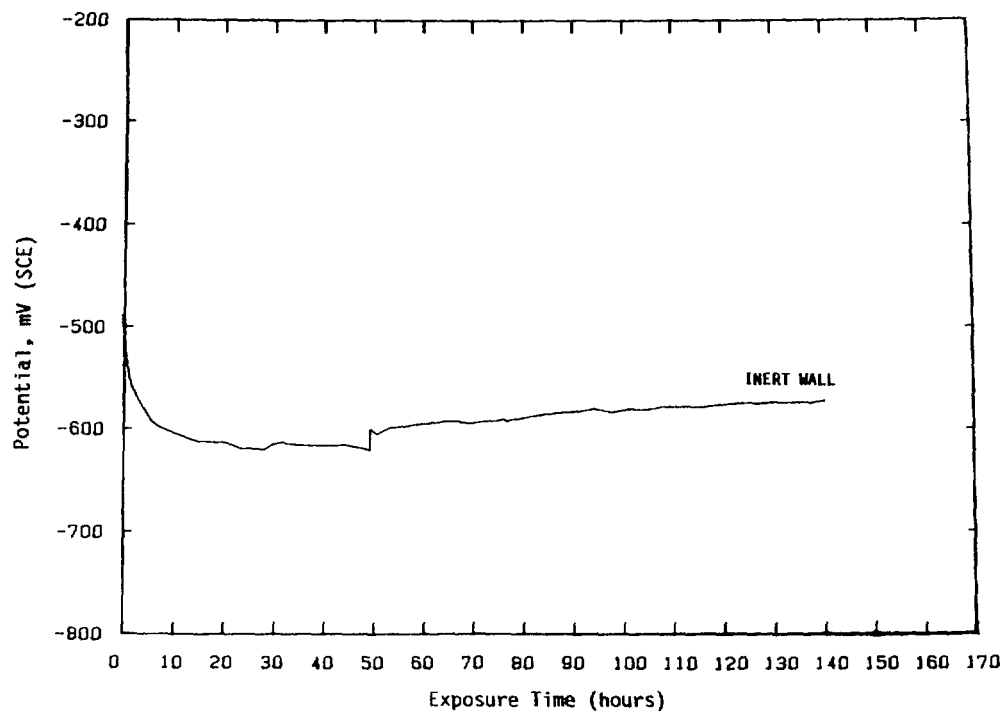
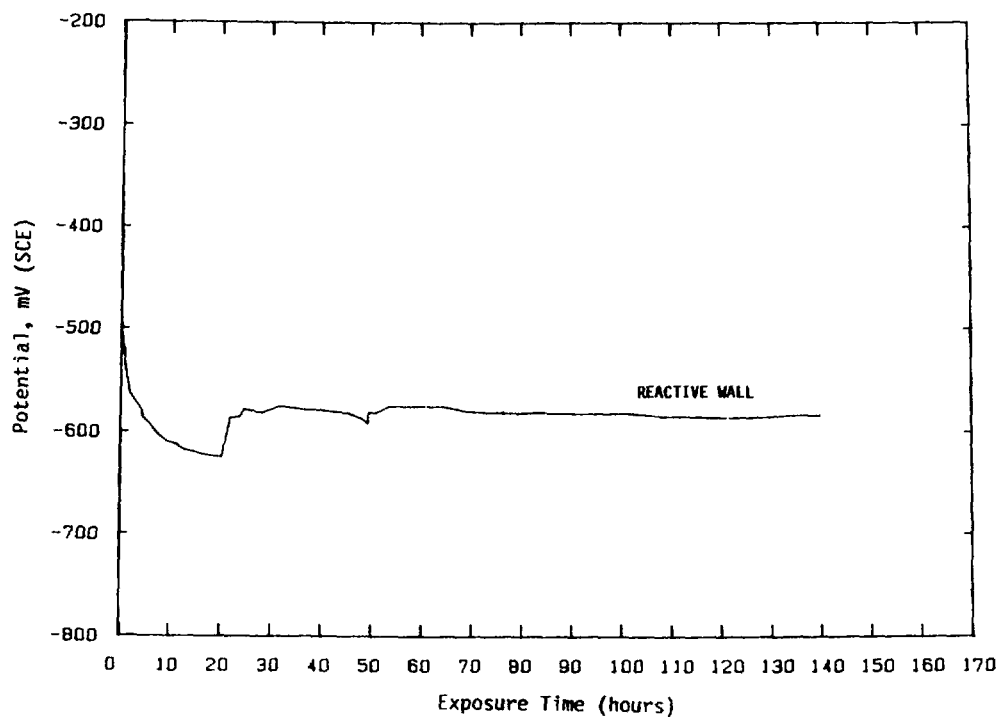


Figure 3.52. Coupled current density as a function of exposure time and pit-wall reactivity for pit-propagation Experiment 17 performed at a diameter-to-depth ratio of 1:5 in aerated basalt groundwater at 25 C.

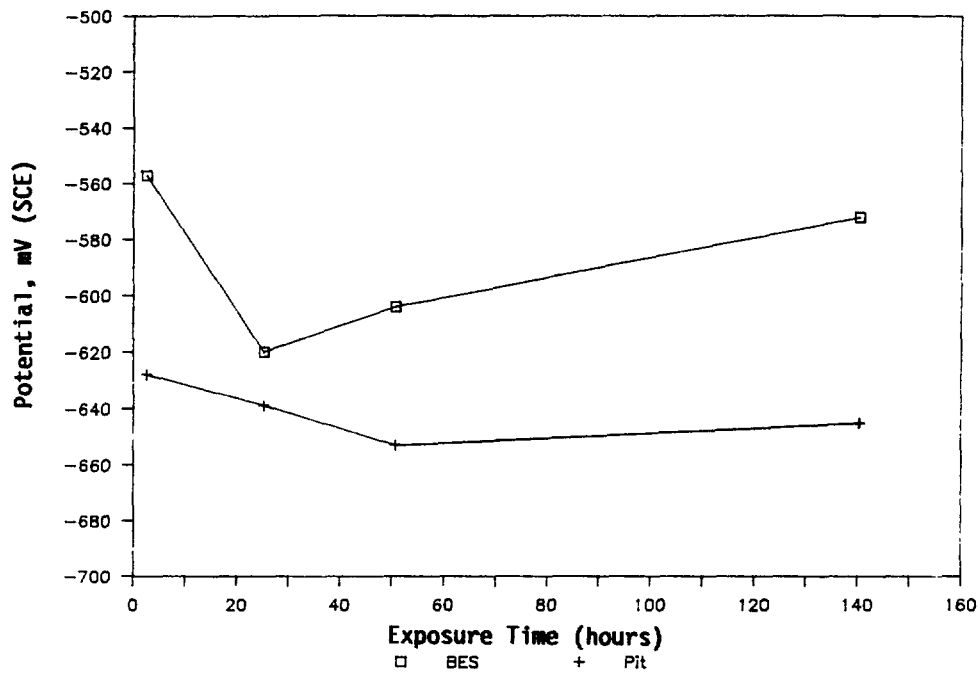


a. Inert Wall

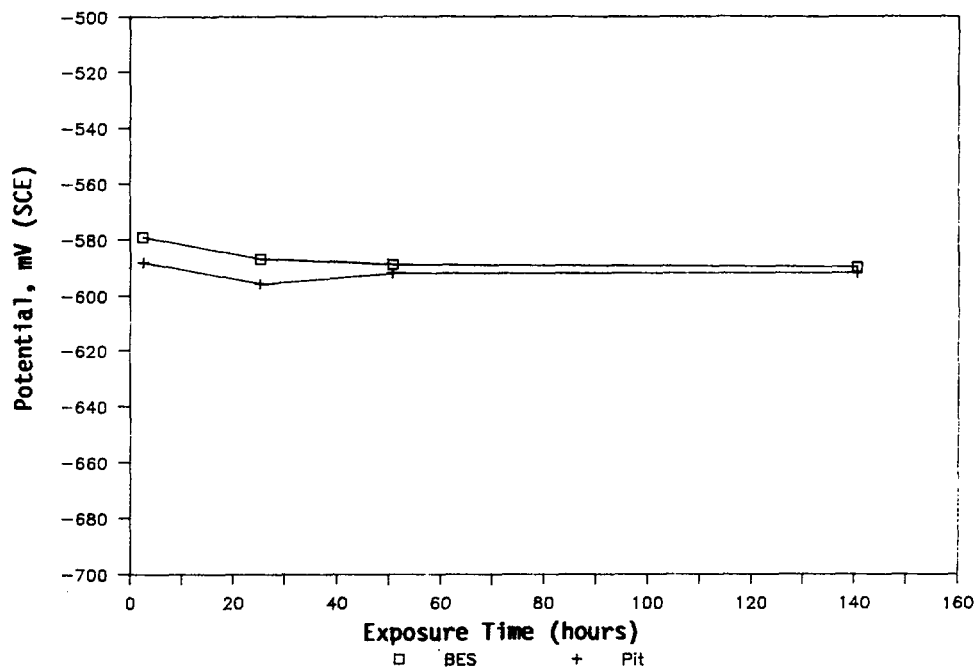


b. Reactive Wall

Figure 3.53. Coupled potential as a function of exposure time for pit-propagation Experiment 17 performed at a diameter-to-depth ratio of 1:5 in aerated basalt groundwater at 25 C.



a. Inert Wall



b. Reactive Wall

Figure 3.54. Uncoupled potential as a function of exposure time for pit-propagation Experiment 17 performed at a diameter-to-depth ratio of 1:5 in aerated basalt groundwater at 25 C.

exposure. Because the pit and BES specimen were uncoupled, there was no current flow. Figure 3.55 shows the uncoupled potential for the nonreactive- and the reactive-wall conditions as a function of microcapillary position down the pit. Except for a very small potential drop at the opening of the pit, the uncoupled potential of the pit for the nonreactive-wall condition shows no potential gradient down the pit. For the reactive-wall condition, a very large potential gradient existed as the probe was moved down the pit for the first 10 mm, and no further potential gradient existed further down the pit. This indicates that, for the reactive-wall condition, a significant amount of corrosion activity was taking place at the mouth of the pit with the reduction reactions occurring on the outside wall of the BES and the anodic reactions occurring on the inside pit wall of the BES.

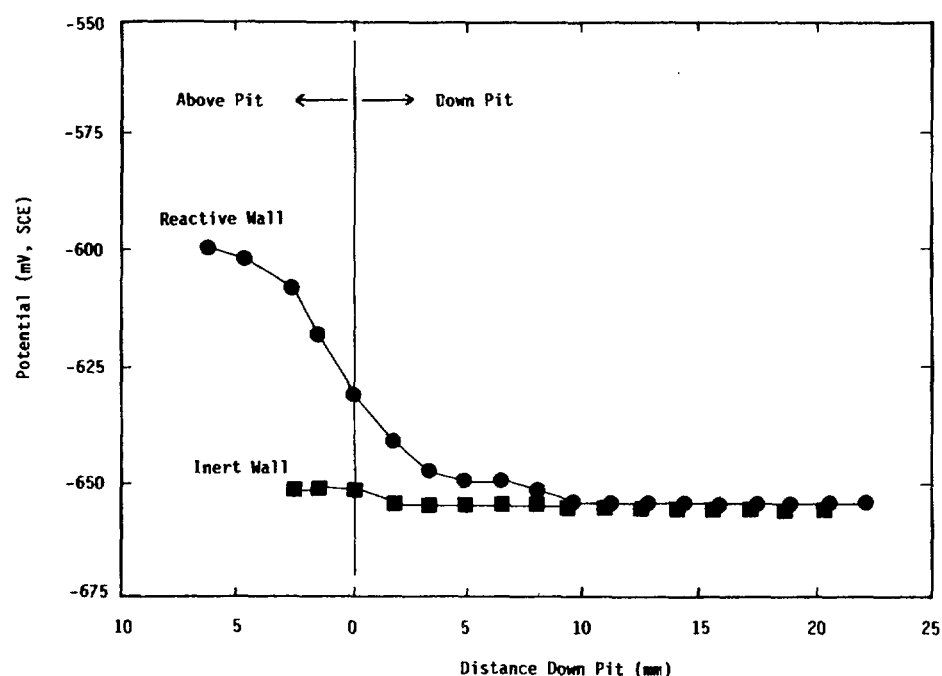


Figure 3.55. Potential for pit specimen as a function of microcapillary probe position down the pit when the pit specimen and BES were uncoupled; Experiment 17 in aerated basalt groundwater at 25 C.

Figure 3.56 shows the potentials of the pit for the nonreactive- and reactive-wall conditions as a function of microcapillary position down the pit when the pit specimen and the BES were coupled together. With the pit specimen and BES coupled, a near linear potential gradient existed in moving the capillary probe down the nonreactive-wall pit. The presence of this potential gradient indicates that there was current flow between the pit specimen and the outside surface of the BES specimen. For the reactive-wall

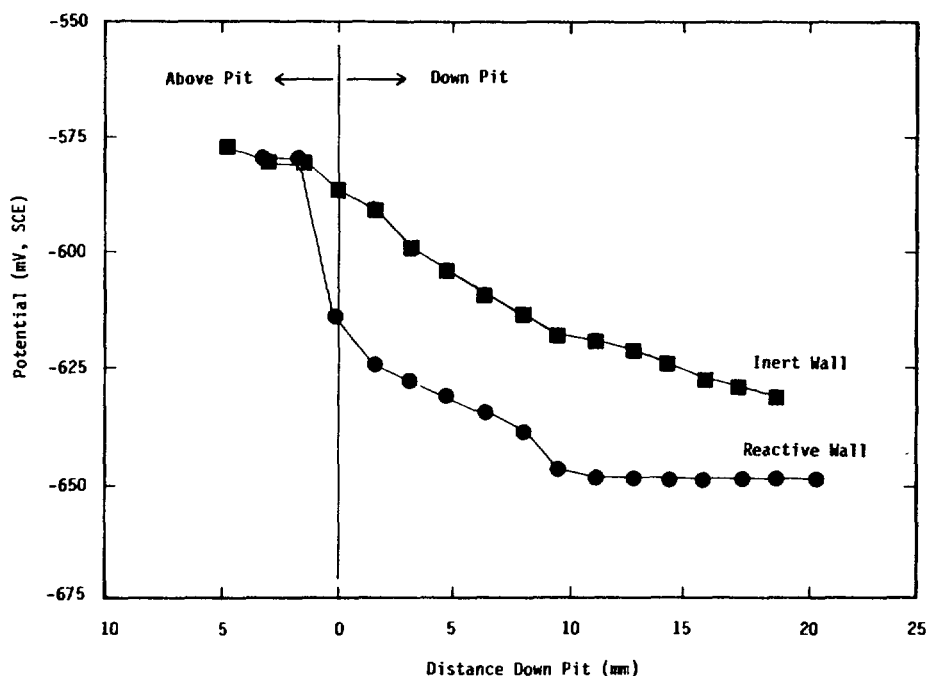


Figure 3.56. Potential for pit specimen as a function of microcapillary probe position down the pit where the pit specimen and BES specimen were coupled; Experiment 17 in aerated basalt groundwater at 25 C.

condition, a potential gradient similar to that observed for the uncoupled condition was again measured for the coupled condition. The presence of no gradient from 10 mm down the pit to the base of the pit (at 20 mm) suggests that the current flow between the pit specimen and BES was negligible. This is confirmed by the very low current measured for the reactive-wall condition with the pit specimen and BES coupled (shown in Figure 3.52). The level of polarization obtained due to the coupling can be examined by comparing Figures 3.55 and 3.56. Because the potential of the pit measured at the base was approximately the same for the coupled and uncoupled conditions for the reactive-wall, very little or no polarization of the pit occurred as a result of coupling. Again, this corresponds to the very low current measured for this condition. In the nonreactive-wall condition, however, there was approximately 25 millivolts difference in potential between the coupled and uncoupled condition. This potential difference is a measurement of the level of polarization provided to the pit surface due to coupling to the BES. These data are shown in Columns 7 and 8 of Table 3.26 for all of the experiments performed for carbon steel in basalt groundwater. In each case, it is seen that a much greater degree of polarization of the pit existed for the nonreactive-wall case when compared to the reactive-wall case.

Curves similar to those shown in Figure 3.52, 3.53, and 3.56 for the remaining experiments in Table 3.26 are given in Appendix B. The data show that there is very little coupling effect for reactive-wall pits except for the most shallow pit geometry (1:0.5). With a diameter-to-depth ratio of 1:1,

the coupled current and the potential profile data indicate that only a small amount of coupled current goes to increasing the pit-propagation rate. There does not appear to be a significant trend in the coupled current as a function of diameter-to-depth ratio. However, the corrosion rate, as measured by weight loss, tended to decrease upon going to smaller diameter-to-depth ratios (1:1 down to 1:10). The resistance down the pit for the non-reactive conditions did increase as the depth down the pit increased (see Column 9). This, of course, was expected. The values for the resistance down the pit in the reactive-wall condition are much lower than for the non-reactive-wall conditions and did not vary as a function of depth. This is due to the experimental arrangement that permits the BES specimen in the reactive-wall case to provide a low-resistance path for the measuring signal such that the path down the pit through the Fe_3O_4 paste is circumvented; that is, the high-frequency current path is on the outside of the BES, through the metallic path of the BES, off of the BES near the pit surface, and on to the pit specimen. Therefore, for the case of the reactive-wall pits, the resistance down the pit cannot be measured with the electrochemical impedance technique employed. One final observation from Table 3.26 is that the uncoupled potential at the pit surface (Column 8), for the nonreactive and reactive conditions for a given experiment (for example, Experiment 30), are within 10 mV of each other. This indicates that the environmental conditions within the pits for the nonreactive- and reactive-wall conditions are similar. This tells us that, although the environment within the pits may change from the preset condition, the environment established is not dependent upon the reactivity of the pit wall.

- Effect of Mill Scale. Because mill scale may or may not be present on the outside surface of the overpack, experiments were performed for the same pit geometries discussed above, except that the outside of the BES had mill scale present. The very top surface of the BES specimen was masked off such that the only bare steel exposed on the BES specimen was that of the pit specimen and the inside pit wall of the BES specimen. Table 3.27 summarizes the data for the experiments with the mill scale (Experiment 20) along with the results for Experiment 17 (previously presented). The actual data for Experiment 20 are given in Appendix B, Figures B-16 to B-18. The time dependence of the potential and current, and the potential profile as a function of distance down the pit, show similar trends to those discussed above for Experiment 17. A higher coupled current was measured in the presence of the mill scale, almost a factor of two greater for the mill scaled than for the bare carbon steel surface.

This higher current is likely due to the more positive potentials measured for the mill scaled surfaces. This more positive potential for the BES specimen provides a larger driving force for the couple. Although weight-loss measurements were not performed for these experiments, it would be expected that the pit specimen in the experiment with mill scale experienced greater weight loss as a result of the larger coupling effect, even for the reactive-wall condition. It should be noted that this larger coupling effect on currents due to mill scale for the reactive-wall condition (increase from 0.5 to 4.0 $\mu\text{A}/\text{cm}^2$) was still quite small in comparison to the coupled currents for the nonreactive-wall condition (41 to 92 $\mu\text{A}/\text{cm}^2$).

Table 3.27. Summary of electrochemical pit-propagation experiments for carbon steel with millscale in aerated basalt groundwater at 25 C using simulated pits prepaced with 0.1 N HCl-Fe₃O₄ paste.

Specimen No.	1 Diameter- to-Depth Ratio	2 Corrosion Rate of Pit (Wt. Loss) μm/yr	3 Coupled(a) Current, μA/cm ²	4 Coupled(a) Potential, V, SCE	5 Uncoupled(c) Potential of Pit, V, SCE	6 Uncoupled(c) Potential of BES, V, SCE	7 Coupled(b) Potential at Pit Surface, V, SCE	8 Uncoupled(b) Potential at Pit Surface, V, SCE	9 Resistance Down Pit, ohm
20-Nonreactive	1:5	-	92	-0.525	-0.630	-0.543	-0.611	-0.644	6,000
20-Reactive	1:5	-	4	-0.516	-0.486	-0.482	-0.637	--	690
17- Nonreactive(d)	1:5	-	41	-0.578	-0.646	-0.574	-0.631	-0.656	6,900
17-Reactive(d)	1:5	-	0.5	-0.580	-0.591	-0.589	-0-.648	-0.658	210

(a)Values given in table represent end of exposure data.

(b)Measured using a microcapillary probe at the end of the experiment.

(c)Measured at different time than coupled potential (Column 4). At any given time, the coupled potential equals the uncoupled potential of BES (Column 6).

Therefore, it is more critical to consider pit wall reactivity than to consider surface finish in predicting pit-propagation rates.

- Active Versus Passive Solutions. The solutions examined in this section were Solutions No. 30 and No. 47 from the statistical matrix of potentiodynamic polarization experiments. Solution No. 30 (Experiment No. 26 in Table 3.28) is a solution in which carbon steel exhibited active behavior. Solution No. 47 (Experiment No. 31 in Table 3.28) is a solution in which carbon steel exhibited active/passive behavior with the protection potential approximately 100 mV more positive than the free-corrosion potential. Therefore, in Solution No. 47, the outside surface of the BES should remain passive. This is in contrast to the basalt groundwater solution in which pitting and underdeposit corrosion initiated and propagated on the BES specimen throughout the exposures. This behavior was predicted electrochemically in that the protection potential was slightly more negative than the free-corrosion potential in basalt groundwater.

Table 3.28 summarizes the data for the electrochemical pit-propagation experiments on carbon steel in Solution 30 (Experiment 26) and Solution 47 (Experiment 31). In Experiment 26, very low coupled currents were measured for both the nonreactive- and reactive-wall conditions. In fact, it was observed that the coupled currents were initially negative (see Figure 3.57), that is, cathodic to the pit, during the initial stages for both wall conditions. Furthermore, in comparing Column 4 with Columns 7 and 8, it is seen that the potential changed very little upon coupling the pit and BES specimens for either the nonreactive- or reactive-wall condition. The potential profiles for the two conditions are shown in Figure 3.58. The data for the reactive wall condition indicate some coupling action near the base of the pit and, upon uncoupling, indicates that the pit specimen was cathodically polarized, which is consistent with the coupled current measurements. The data for the nonreactive- (inert) wall specimen show that the pit specimen was anodically polarized, which also corresponds to the measured coupled current. The first four data points for the nonreactive-wall condition are an apparent anomaly, and the 13 mV step near the pit mouth is not understood. The coupled potentials are not shown but remained steady throughout the experiment. These data indicate that, for Solution 30, in which carbon steel exhibited active corrosion behavior, pitting was not initiated even when the simulated pit was preconditioned with an acidic Fe_3O_4 paste. Because only slight coupled-current activity existed, it is not understood why the nonreactive-wall pit specimen exhibited such a high corrosion rate while no weight loss was observed for the reactive-wall pit specimen.

For carbon steel in Solution 47 (Experiment 31), large coupled currents were measured for both the nonreactive- and reactive-wall conditions. Figure 3.59 shows the coupled current as a function of time for the two conditions. For the nonreactive-wall condition, the current was initially very high and decreased as a function of time, while the current for the reactive-wall condition was relatively low and increased as a function of time. The increase in current for the reactive-wall condition can be explained, at least in part, by the profile of the potential down the pit. As seen in Figure 3.60, the profile did not show the large gradient until

Table 3.28. Summary of electrochemical pit-propagation experiments for carbon steel in aerated Solution No. 30 (#26) and aerated Solution No. 47 (#31) at 25 C using simulated pits prepacked with pH 1 Fe₃O₄ paste.

Specimen No.	1 Diameter- to-Depth Ratio	2 Corrosion Rate of Pit (Wt. Loss) μm/yr	3 Coupled(a) Current, μA/cm ²	4 Coupled(a) Potential, V, SCE	5 Uncoupled(c) Potential of Pit, V, SCE	6 Uncoupled(c) Potential of BES, V, SCE	7 Coupled(b) Potential at Pit Surface, V, SCE	8 Uncoupled(b) Potential at Pit Surface, V, SCE	9 Resistance Down Pit, ohm
26-Nonreactive	1:5	5,468	1.5	-0.710	-0.702	-0.694	-0.697	-0.705	650
26-Reactive	1:5	0	-0.3	-0.701	-0.696	-0.700	-0.699	-0.696	15
31-Nonreactive	1:5	3,594	48	-0.283	-0.402	-0.164	-0.360	-0.417	4,645
31-Reactive	1:5	1,805	36	-0.420	-0.427	-0.427	-0.583	-0.589	70

(a) Values given in table represent end of exposure data.

(b) Measured using a microcapillary probe at the end of the experiment.

(c) Measured at different time than coupled potential (Column 4). At any given time, the coupled potential equals the uncoupled potential of BES (Column 6).

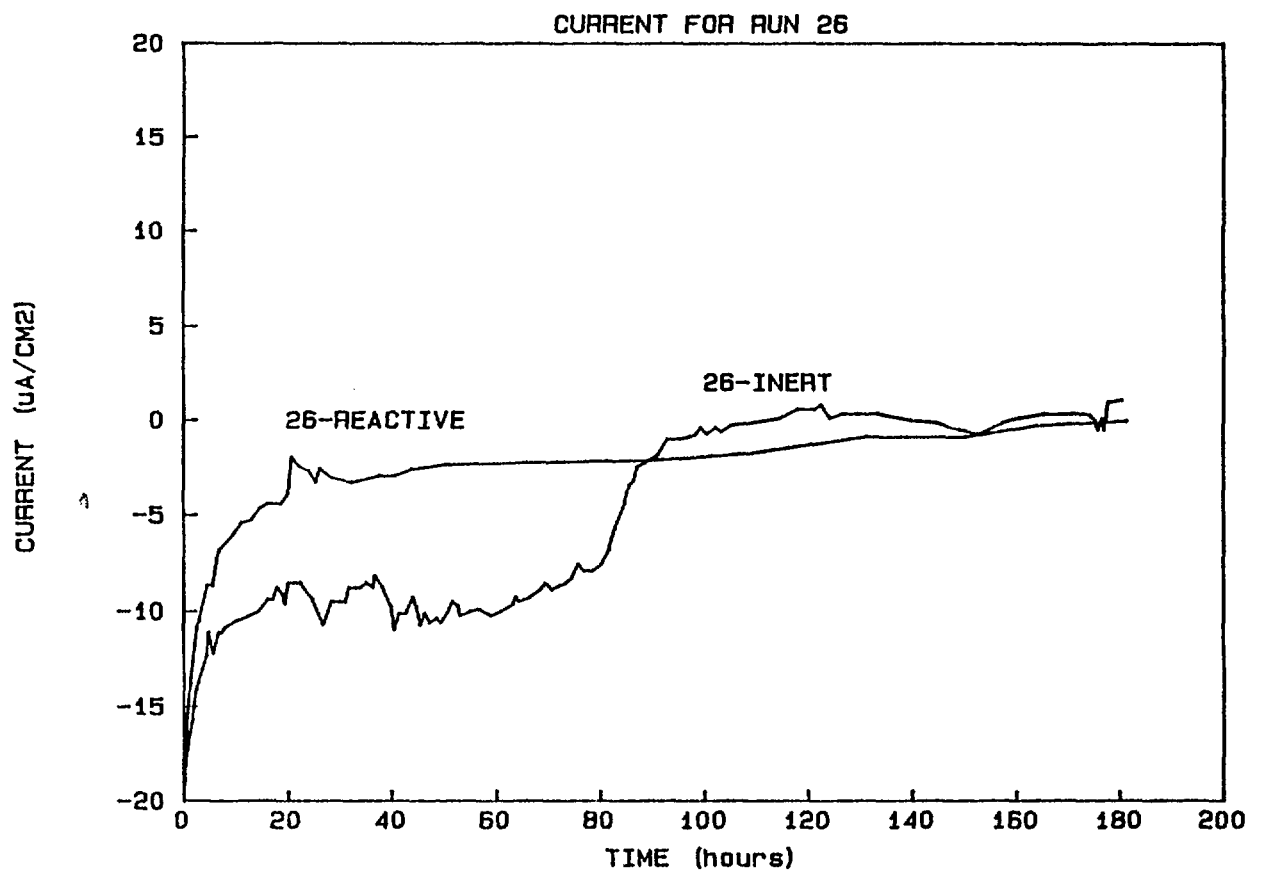


Figure 3.57. Coupled current density as a function of exposure time and pit-wall reactivity for Experiment 26 performed at a diameter-to-depth ratio of 1:5 in aerated solution No. 30 at 25 C.

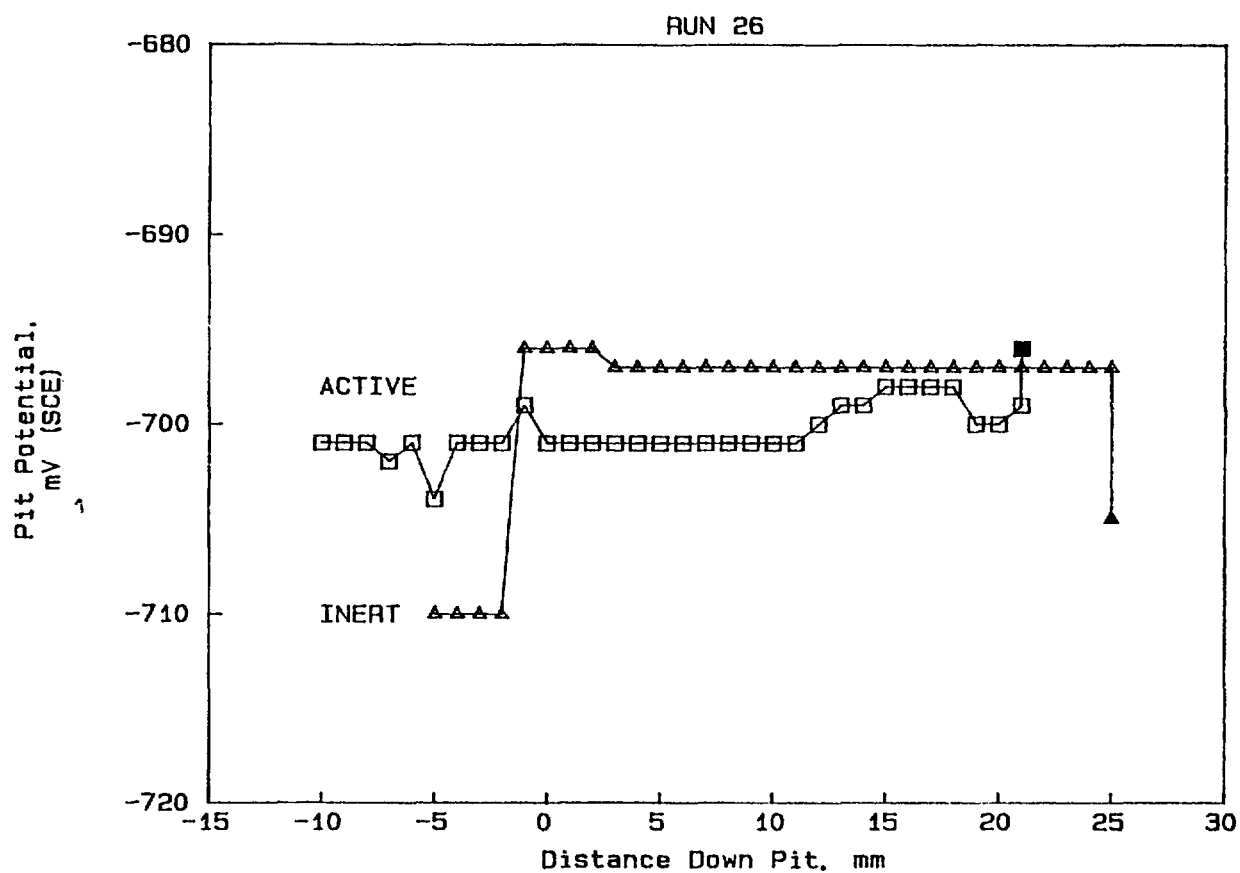


Figure 3.58. Potential for pit specimens as a function of microcapillary probe position down pit when the pit and BES specimens were coupled; carbon steel in aerated solution No. 30 (Experiment 26) at 25 C.

Open symbols (coupled), closed symbols indicate potentials when pit and BES specimens were uncoupled.

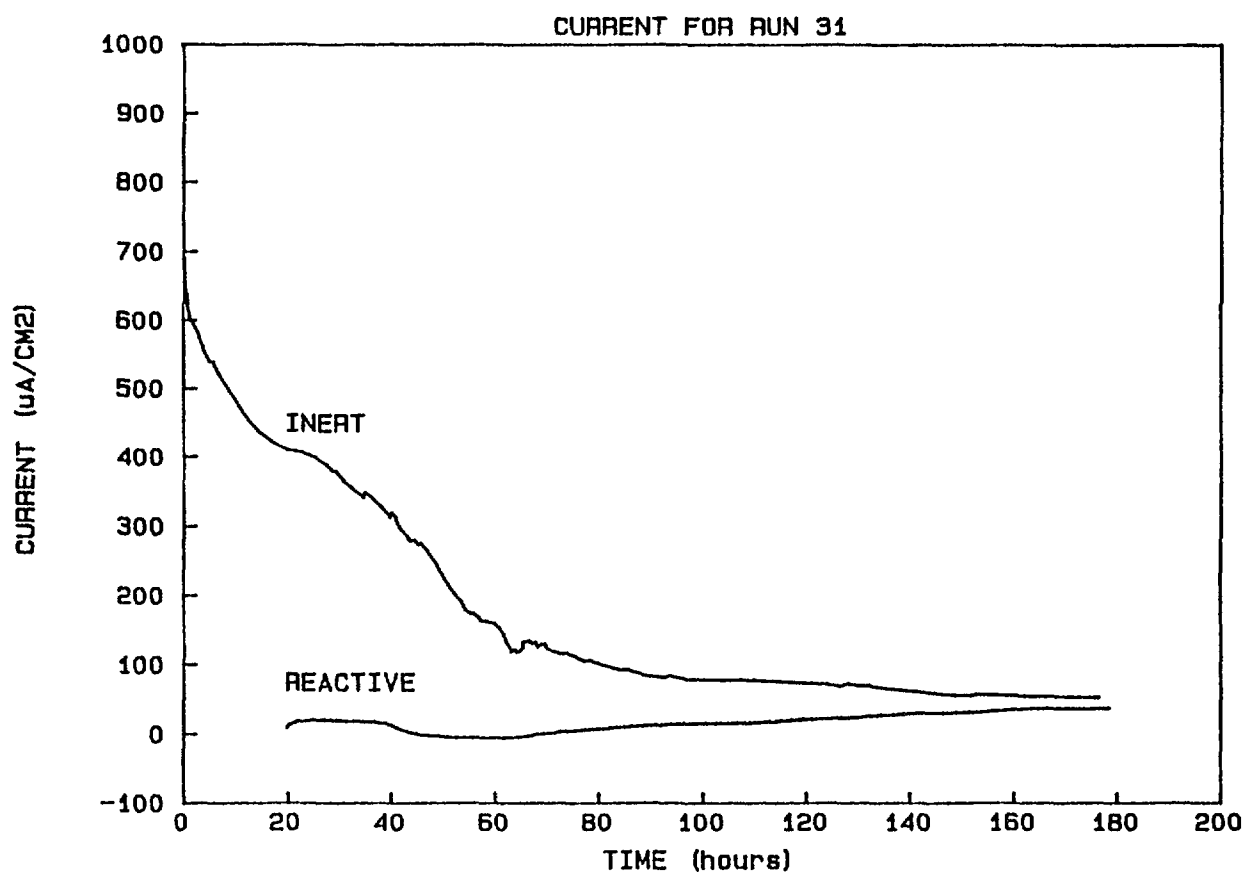


Figure 3.59. Coupled current density as a function of exposure time and pit wall reactivity for Experiment 31 performed at a diameter-to-depth ratio of 1:5 in aerated solution No. 47 (Experiment 31) at 25 C.

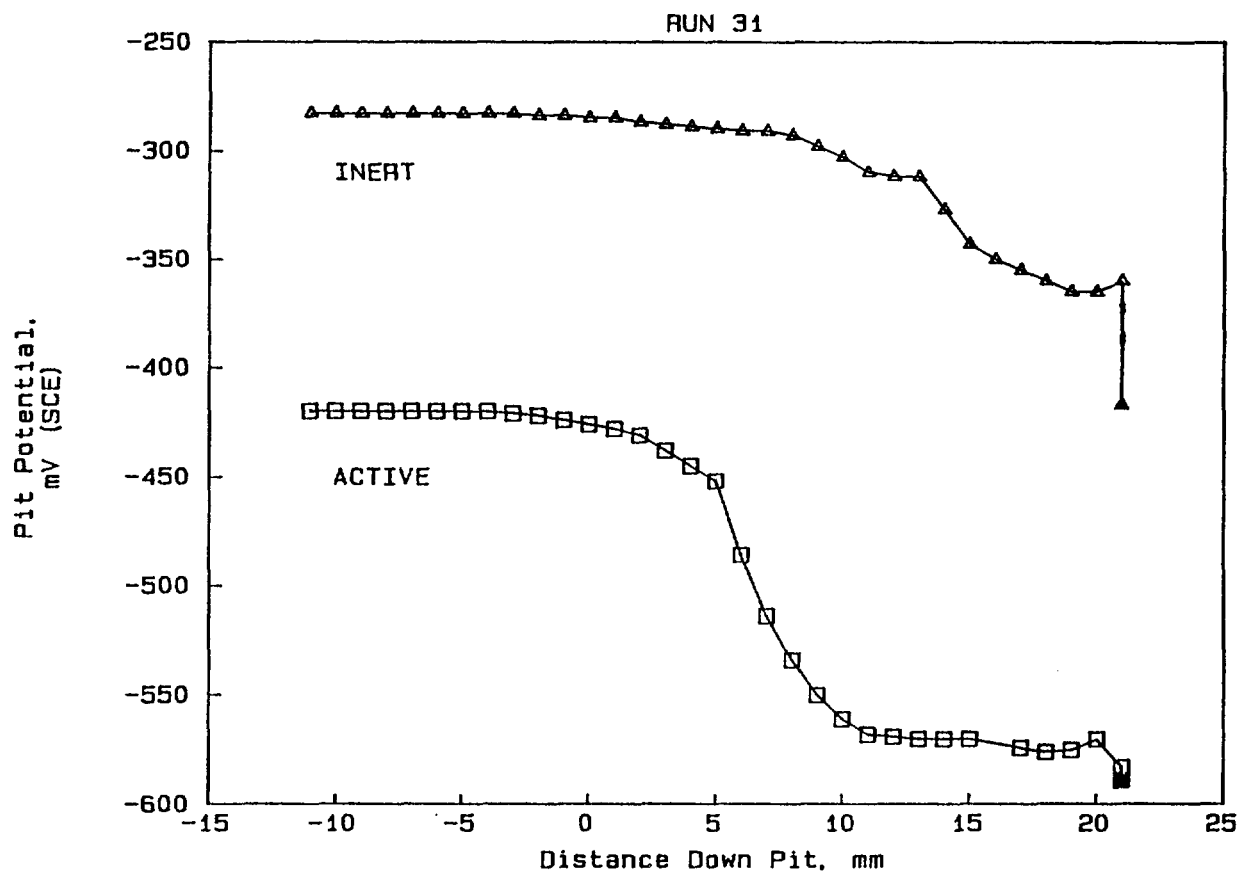


Figure 3.60. Potential for pit specimens as a function of microcapillary probe position down pit when the pit and BES specimens were coupled (open symbols); carbon steel in aerated solution No. 47 at 25 C (Experiment 31). Closed symbols indicate potentials when pit and BES specimens were uncoupled.

some depth within the pit. This suggests that the walls within the pit were passivated, thereby increasing the diameter-to-depth ratio. This would tend to make it easier to drive a coupled current. Also, the driving force for pit propagation was greater in Solution 47 than in the basalt groundwater, as indicated by the uncoupled potential measurements (Columns 5 and 6 in Table 3.28).

Figure 3.61 shows the coupled potentials as a function of exposure time for Experiment 31. Note that the coupled potential for the reactive-wall condition was much more negative than the coupled potential for the nonreactive-wall condition. For the nonreactive-wall condition, coupling of the pit specimen to the BES significantly affected the potential of the BES, as seen by the difference between the uncoupled potential of the BES (Column 6) and the coupled potential (Column 4). For the reactive-wall condition, there was a much larger surface area for the pit (the pit specimen surface area plus the surface area of the BES within the pit), which resulted in a much more negative coupled potential than for the nonreactive-wall condition. It is interesting to note that the coupled current obtained at the end of the exposure period ($48 \mu\text{A}/\text{cm}^2$) is similar to the currents obtained for the basalt groundwater solution. The initial average rate of pit propagation can be quite large and is comparable to those measured in basalt groundwater for a diameter-to-depth ratio of 1:1. It is not known, however, whether these high rates of pit propagation are maintained over long-term exposure periods.

- **Brine Solutions.** Electrochemical pit-propagation experiments were performed for carbon steel in Brine A and Brine B. These brines are used in much of the DOE Salt Repository research; their compositions are given in Table 3.9. Table 3.29 summarizes the data for the experiments in Brine A (Experiment 27) and Brine B (Experiment 28). With the exception that the initial coupled currents were positive (anodic with respect to the pit), the data for both brine solutions are very similar to the data obtained for Solution 30 in which carbon steel exhibited active polarization behavior. The coupled currents were very small and often were negative, or cathodic with respect to the pit. Very small or negligible potential gradients were observed upon moving the microcapillary probe down the pits. Thus, it appears that for either Brine A or Brine B pitting was not initiated after preconditioning the simulated pits with the acidic Fe_3O_4 paste. The curves showing the coupled current and coupled potential behavior as a function of time and the potential gradients down the pits for Brine A and Brine B are given in Appendix B.

3.2.2.4 Summary

Because of the time periods involved for the containment of nuclear waste, realistic mechanistic models that accurately predict the long-term pit-propagation behavior are imperative. Most of the mechanistic models for pit propagation are based on the assumption that the anodic reaction occurs only on the pit base and the cathodic reactions occur on the boldly exposed surfaces (Refs. 3.16-3.19). The pit walls are assumed to be nonreactive (inert) in order to simplify the models. The majority of these models are based on mass transport, where the rate of pit propagation is controlled by transport of corrosion products out of the pit.

Many of the experimental studies performed in conjunction with the modeling studies have utilized potentiostatic or galvanostatic control of the pit propagation using auxiliary electrodes. This approach may artificially accelerate pit propagation, affecting the rate-limiting step (for example, promoting mass transport control as opposed to activation control). In

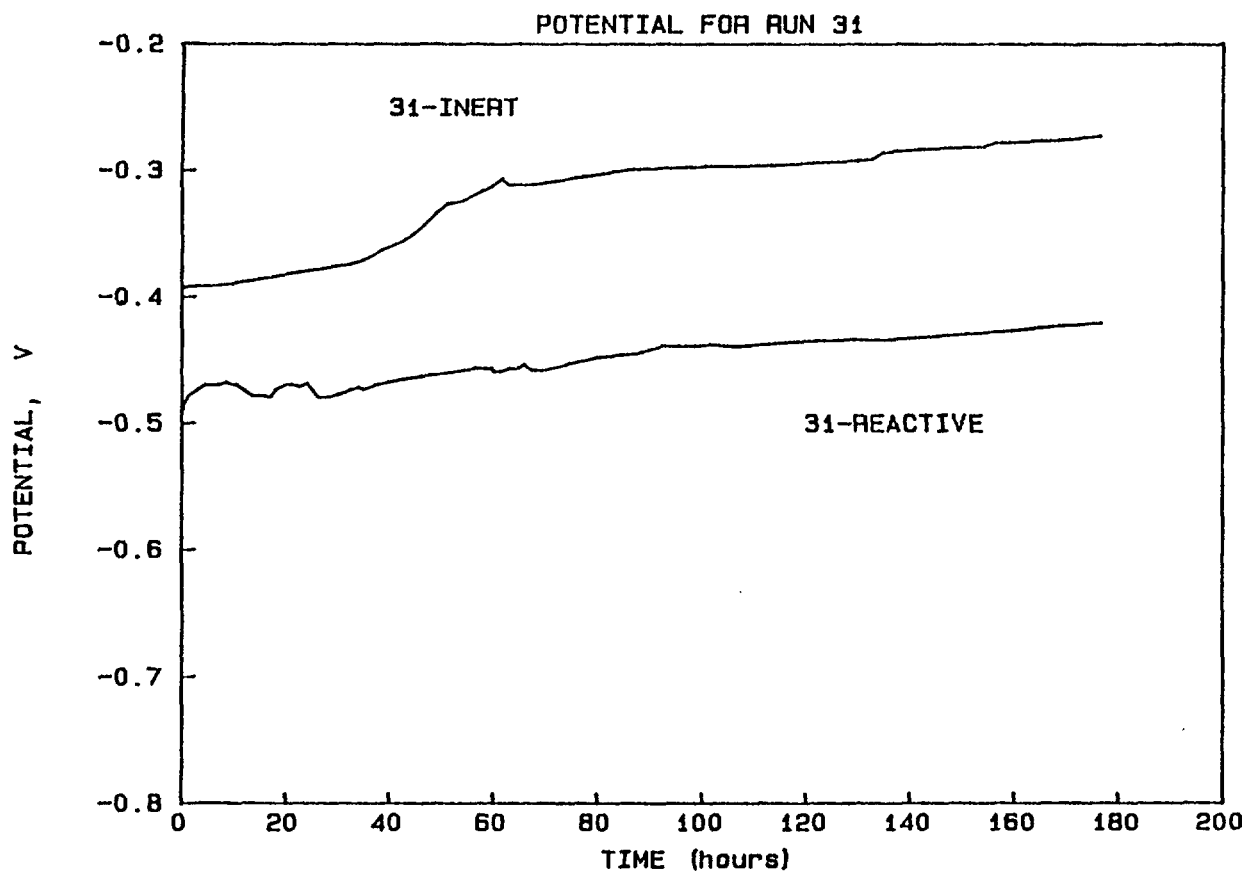


Figure 3.61. Coupled potential as a function of exposure time for experiment performed at a diameter-to-depth ratio of 1:5 in aerated Solution No. 47 (Experiment 31) at 25 C.

Table 3.29. Summary of electrochemical pit-propagation experiments for carbon steel in aerated Brine A (Experiment 27) and aerated Brine B (Experiment 28) at 25 C using simulated pits prepacked with pH 1 Fe_3O_4 paste.

Specimen No.	1 Diameter- to-Depth Ratio	2 Corrosion Rate of Pit (Wt. Loss) $\mu\text{m}/\text{yr}$	3 Coupled(a) Current, $\mu\text{A}/\text{cm}^2$	4 Coupled(a) Potential, V, SCE	5 Uncoupled(c) Potential of Pit, V, SCE	6 Uncoupled(c) Potential of BES, V, SCE	7 Coupled(b) Potential at Pit Surface, V, SCE	8 Uncoupled(b) Potential at Pit Surface, V, SCE	9 Resistance Down Pit, ohm
27-Nonreactive	1:5	147	0.5	-0.679	-0.671	-0.672	-0.680	-0.672	150
27-Reactive	1:5	0	-4	-0.684	-0.647	-0.680	-0.683	-0.679	34
28-Nonreactive	1:5	0	-7	-0.694	-0.642	-0.704	-0.693	-0.638(d)	190
28-Reactive	1:5	415	-0.5	-0.715	-0.705	-0.707	-0.713	-0.696(d)	16

(a) Values given in table represent end of exposure data.

(b) Measured using a microcapillary probe at the end of the experiment.

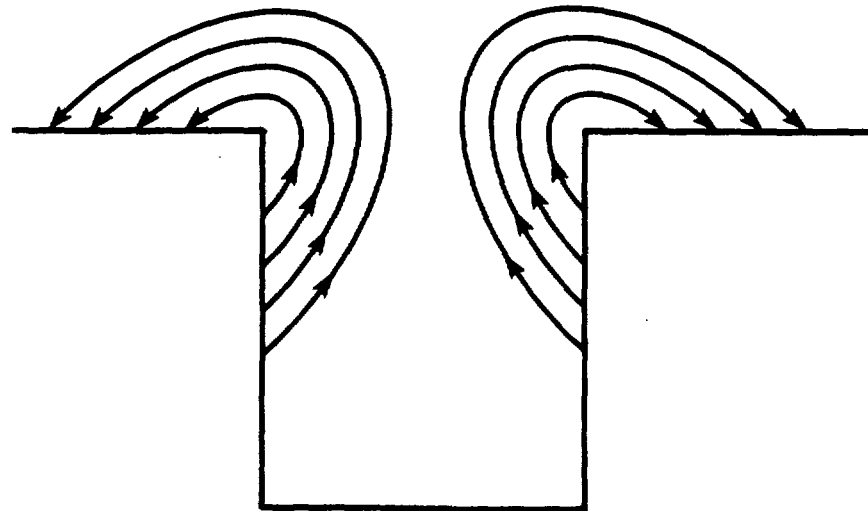
(c) Measured at different time than coupled potential (Column 4). At any given time, the coupled potential equals the uncoupled potential of BES (Column 6).

(d) The large noble potential shift was probably the result of microcapillary scraping of the pit specimen surface during the uncoupling.

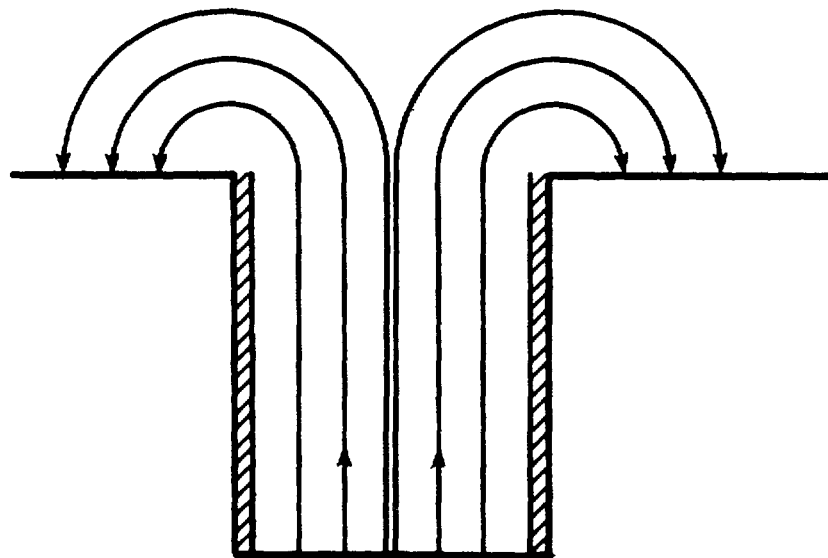
addition, this approach may not be realistic for systems where cathodic reactions occur within the pit during pit propagation (Ref. 3.20).

The results of the long-term exposures and electrochemical studies permit a better understanding of the process of pit propagation in carbon steel in basalt groundwater. Figure 3.62 shows a schematic of the current flow patterns for the reactive-wall and nonreactive (inert)-wall pits based on the measured potential gradients down the pits. For the reactive-wall condition, coupled currents were present but existed between the upper portions of the pit wall and BES. Significant current flow between the outside surface and base of the pit only occurred for the shallow pits. On the other hand, the current flow pattern for the nonreactive-wall condition was from the base of the pit to the boldly exposed outside surface. As a result of this behavior, the coupled current for the reactive-wall condition tends to widen the pit and does not promote pit propagation in the depth direction. Alternatively, for the nonreactive-wall condition, the coupled current tends to promote pit propagation. Therefore, for the nonreactive-wall geometry, relatively high propagation rates would occur for pits because of the coupling effects of the BES. For the reactive-wall pits, the high rates of attack are confined to the region near the pit mouth because the high voltage drop within the solution in this region effectively minimizes polarization of the deeper portions of the pit. This tends to produce a condition where the rate of the pit propagation for the reactive-wall condition is controlled by the electrode kinetics within the pits. This rate may be higher than corrosion rates on the BES because the presence of the anodic reactions near the pit mouth promotes the maintenance of a low-pH condition within the pit. However, the pit propagation rates for the reactive-wall geometry would be lower than those observed for the nonreactive-wall geometry because the rate for the latter is also driven due to the coupled currents with the BES.

Both the long-term exposure experiments and the electrochemical studies support the model presented for the reactive-wall condition as opposed to that for the nonreactive-wall condition. For example, in the studies using mechanically drilled pits, the more severe attack for the deeper pits was typically observed near the mouth of the pit. Similarly, for the weight-loss experiments, in which the simulated pits were exposed to Solution 47 at a diameter-to-depth ratio of 1:5, the nonreactive-wall condition had much greater corrosion than the reactive-wall condition. For larger diameter-to-depth ratios (shallower pits), the measured corrosion rates were similar for the reactive- and nonreactive-wall conditions, which is probably due to the presence of coupled currents down to the pit specimens even for the reactive-wall. The electrochemical studies show that, even at the diameter-to-depth ratio of 1:5 for Solution 47, relatively large coupled currents existed for the reactive-wall pit. The model for the reactive-wall condition shown in Figure 3.62 further explains why there is no difference in the uncoupled potential of the pit. Even with the pit and BES specimens uncoupled, the current flow is still present between the pit wall and the BES such that the potential measurement for the pit specimen includes the ohmic potential drop due to the coupled current. This makes the potential of the pit appear to be the same as that of the BES.



Reactive



Nonreactive

Figure 3.62. Schematic showing the postulated current behavior for nonreactive- and reactive-wall pits.

Direct of current flow is indicated by curved lines.

In light of these findings, pitting models based on nonreactive (inert)-wall geometries will predict higher pit propagation rates than models based on a reactive-wall geometry. In addition, the nonreactive-wall geometry model will predict a much lower diameter-to-depth ratio than is likely to occur in service. Because the models are attempting to predict extremely long-term pit-propagation behavior, they should be based on the more realistic conditions of reactive-wall geometries.

3.2.3 Autoclave Studies

3.2.3.1 Objective

The objectives of the autoclave studies on carbon steels were to selectively reproduce the corrosion data in basalt groundwater at elevated temperatures (250 C) and to evaluate the influence of steel composition and microstructure, as well as concentration of the groundwater, on the corrosion behavior.

3.2.3.2 Approach

Two carbon steel compositions were used in this study: one ("doped") approximating 1018 carbon steel, and one ("clean") with similar composition but with low phosphorus and sulfur. The compositions of these steels are given in Table 3.8. Both cast and wrought specimens were included in the experimental matrix. Cast specimens were machined directly from the billets, while wrought specimens were machined from billet sections that were hot-reduced approximately 87 percent. Four types of specimens were included in the autoclave exposures: gravimetric specimens, crevice specimens, 3-point bend specimens, and polarization-resistance (PR) specimens. The crevice-corrosion specimens had a boldly-exposed-surface-area to crevice-surface-area ratio of 10 and were made by attaching serrated PTFE washers to thin, rectangular specimens of the steels.

The autoclave exposures were performed in two simulated groundwaters at 250 C: one prepared according to a Rockwell-Hanford procedure (Ref. 3.6), referred to as basalt groundwater; and the other, a ten-times concentration of the basalt groundwater, referred to as 10X basalt groundwater. The nominal composition of the basalt groundwater is given in Table 3.9. Basalt rock, taken from an outcropping of the umtanum flow, was placed in the bottom of the autoclave during the exposures. The rock was prepared by first removing weathered surfaces and crushing in 7.6 to 2.5 cm jawcrushers. The crushed rock was then sieved on progressively finer screens with a rowtap shaker and the rock that passed through the number 4 screen, but was retained on the number 8 screen (-4+8), was used. Prior to placement in the autoclave, the rock was washed three times with deionized water.

3.2.3.3 Results and Discussion

One-thousand-hour autoclave exposures were completed on the carbon steel specimens in two simulated basalt groundwater compositions at 250 C under stagnant deaerated conditions.

Results of the gravimetric measurements performed on the specimens are given in Tables 3.30 through 3.33. These data show that general-corrosion rates were quite low in these environments under deaerated conditions and were similar for the two materials. These rates of general attack in the unconcentrated groundwater are comparable, in most instances, to those reported by Bradley et al. (Ref. 3.21) for ductile iron in a basalt groundwater. The O_2 concentration of the groundwater in the tests by Bradley et al. was not well controlled. A refreshed system was used with aerated makeup water, but the basalt rock in the autoclave rapidly consumed the oxygen. Surprisingly, general-corrosion rates were somewhat lower in the concentrated groundwater. The PR specimens tested in the concentrated groundwater did exhibit somewhat higher weight losses than the other specimens.

Tenacious black surface films were present on all the steel specimens following exposure to the basalt groundwater. The surface films on a cast specimen of the clean steel, which was exposed in the unconcentrated groundwater, were analyzed by energy dispersive X-ray (EDX) spectroscopy and X-ray diffraction (XRD). Results of these analyses are summarized in Table 3.34. These data indicate the films were primarily Fe_3O_4 . The presence of surface films on the specimen is consistent with the observed low rates of general attack and the occurrence of pitting (see discussion below); pitting corrosion is normally associated with the breakdown of passive films. The absence of any higher oxidation states for iron is good evidence that oxygen was successfully excluded from the autoclaves during the tests. In the presence of oxidants, generated by radiolysis of the groundwater, higher-oxidation-state oxides such as Fe_2O_3 or $FeOOH$ probably would be generated. Although Fe_2O_3 is much less soluble than Fe_3O_4 and thus potentially more protective, the corrosion performance of carbon steel in the presence of oxygen and chlorides is generally poor because of local breakdown of these oxide films.

The specimens also were optically examined following exposure for evidence of pitting, crevice corrosion, and stress-corrosion cracking. No evidence of stress-corrosion cracking was found on any of the 3-point bend specimens. The depths of pits were measured with a microscope having a calibrated stage. Results of the analyses are given in Tables 3.30 through 3.33, where it can be seen that shallow pits were detected on most specimens. Pitting was somewhat more severe in the concentrated groundwater and was similar for the two materials. The pits on the specimens exposed in the less concentrated groundwater appeared to be more prevalent in or near the crevices. A typical photograph of one such pit is given in Figure 3.63.

Deep pits were observed on one of the polarization-resistance specimens of the cast clean steel that had been exposed to the concentrated groundwater. This attack reached depths greater than 1000 μm and was localized in the region of the specimen exposed to the vapor space in the autoclave. All other specimens in the autoclave were fully submersed.

An additional autoclave exposure was performed to investigate further the vapor-phase corrosion behavior of the steels in the concentrated groundwater. Gravimetric and crevice specimens of cast and wrought clean and doped 1018 carbon steel were exposed for 1000 hours in the vapor and in the

Table 3.30. Corrosion rates calculated from weight loss and pit depths for cast specimens of clean 1018 steel exposed for 1000 hours to a deaerated simulated basalt groundwater at 250 C.

Specimen Type	Number of Specimens ^(a)	Corrosion Rate $\mu\text{m}/\text{y}$ ^(b)	Average ^(c) Pit Depth μm	Maximum Pit Depth μm
Gravimetric	3	15.64	6.0	9.0
Crevice	2	12.64	8.0	18 ^(d)
3-Point Bend	2	13.10	-	-
Polarization Resistance	2	7.42	-	-

(a) Some specimens were reserved for future analyses and thus the number of specimens of each type that were descaled and weighed varied.

(b) Weight losses were converted to depths of penetration assuming uniform attack and extrapolated linearly to give annual rates of penetration.

(c) For 5 deepest pits.

(d) In crevice region of specimen.

Table 3.31. Corrosion rates calculated from weight loss and pit depths for wrought specimens of 1018 steel exposed for 1000 hours to deaerated simulated basalt groundwater at 250 C.

Specimen Type	Number of Specimens ^(a)	Corrosion Rate $\mu\text{m}/\text{y}$ ^(b)	Average ^(c) Pit Depth, μm	Maximum Pit Depth, μm
Gravimetric	2	22.46	8.7	17
Crevice	2	22.49	8.3	15
3-Point Bend	1	15.35	-	-

(a) Some specimens were reserved for future analyses and thus the number of specimens of each type that were descaled and weighed varied.

(b) Weight losses were converted to depths of penetration assuming uniform attack and extrapolated linearly to give annual rates of penetration.

(c) For 5 deepest pits.

Table 3.32. Corrosion rates calculated from weight loss and pit depths for cast specimens of clean 1018 steel exposed for 1000 hours to deaerated simulated basalt groundwater at 250 C.

Specimen Type	Number of Specimens(a)	Corrosion Rate $\mu\text{m}/\text{y}$ (b)	Average(c) Pit Depth, μm	Maximum Pit Depth, μm
Gravimetric	3	5.59	18	30
Crevice	1	5.83	13	20
3-Point Bend	2	7.46	-	-
Polarization Resistance	2	18.1	12(d)	>1,000(e)

(a) Some specimens were reserved for future analyses and thus the number of specimens of each type that were descaled and weighed varied.

(b) Weight losses were converted to depth of penetration assuming uniform attack and extrapolated linearly to give annual rates of penetration.

(c) For 5 deepest pits.

(d) Average for PR specimen which did not contain the deep pits.

(e) It is likely that these very deep "pits" for the one specimen were metallurgical flaws and not corrosion pits.

Table 3.33. Corrosion rates calculated from weight loss and pit depths for wrought specimens of 1018 steel exposed for 1000 hours to deaerated simulated 10X basalt groundwater at 250 C.

Specimen Type	Number of Specimens(a)	Corrosion Rate $\mu\text{m}/\text{y}$ (b)	Average(c) Pit Depth, μm	Maximum Pit Depth, μm
Gravimetric	3	6.40	18	25
Crevice	1	3.92	21	25
3-Point Bend	2	6.78	-	-

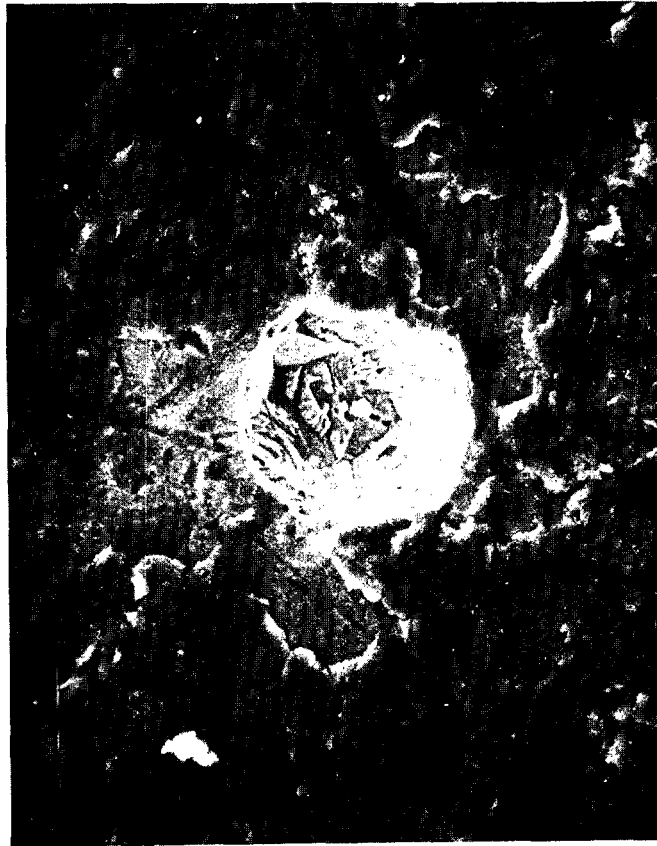
(a) Some specimens were reserved for future analyses and thus the number of specimens of each type that were descaled and weighed varied.

(b) Weight losses were converted to depths of penetration assuming uniform attack and extrapolated linearly to give annual rates of penetration.

(c) For 5 deepest pits.

Table 3.34. Results of EDX and XRD analyses of cast steel specimen exposed for 1000 hours in 250 C deaerated simulated basalt groundwater containing crushed basalt.

EDX Composition, weight percent					
Al	Si	S	K	Ca	Fe
8.97	26.0	7.58	1.71	1.31	54.43
XRD					
Compound				Powder Diffraction Number	
Fe ₃ O ₄				19-629	
Fe ₂ SiO ₄				29-720	



500X

42971

Figure 3.63. SEM photograph of pit found in the crevice region of a cast clean 1018 steel specimen exposed for 1000 hours in 250 C deaerated simulated basalt groundwater containing crushed basalt.

liquid at 250 C. Results given in Tables 3.35 through 3.38 do not indicate a significant or consistent effect of exposure to liquid, as compared to vapor, on general, pitting, or crevice corrosion for any of the four materials. Thus, the "pits" observed in the PR specimen from the previous autoclave exposure probably were simply metallurgical flaws in the specimen.

Electrochemical Measurements. Electrochemical measurements were performed during the autoclave test with the unconcentrated groundwater. The polarization resistance (PR) of the cast clean 1018 steel specimens was measured as a function of exposure time in the basalt groundwater using a two-electrode technique. Results given in Figure 3.64 show that the $1/PR$ value, which is proportional to the corrosion rate, increased over the first

Table 3.35. Corrosion rates calculated from weight loss and pit depths for duplicate specimens of clean cast 1018 steel exposed for 1000 hours to deaerated simulated 10X basalt groundwater at 250 C.

Specimen Type	Phase	Corrosion Rate(a) $\mu\text{m}/\text{y}$	Average Pit(b) Depth, μm	Maximum Pit Depth, μm
Gravimetric	V	9.47	10	14
Gravimetric	L	10.21	6.8	8
Crevice	V	12.16	10	13
Crevice	L	9.54	14	20

(a)Weight losses were converted to depths of penetration assuming uniform attack and extrapolated linearly to give annual rates of penetration.

(b)For 5 deepest pits.

Table 3.36. Corrosion rates calculated from weight loss and pit depths for duplicate specimens of clean wrought 1018 steel exposed for 1000 hours to deaerated simulated 10X basalt groundwater at 250 C.

Specimen Type	Phase	Corrosion Rate(a) $\mu\text{m}/\text{y}$	Average Pit(b) Depth, μm	Maximum Pit Depth, μm
Gravimetric	V	12.4	9.4	12
Gravimetric	L	9.49	11	14
Crevice	V	10.8	10	13
Crevice	L	8.14	14	18

(a)Weight losses were converted to depths of penetration assuming uniform attack and extrapolated linearly to give annual rates of penetration.

(b)For 5 deepest pits.

Table 3.37. Corrosion rates calculated from weight loss and pit depths for duplicate specimens of cast 1018 steel exposed for 1000 hours to deaerated simulated 10X basalt groundwater at 250 C.

Specimen Type	Phase	Corrosion Rate(a) $\mu\text{m}/\text{y}$	Average Pit(b) Depth, μm	Maximum Pit Depth, μm
Gravimetric	V	9.07	9.4	11
Gravimetric	L	8.52	12	16
Crevice	V	11.1	15	27
Crevice	L	9.44	16	22

(a)Weight losses were converted to depths of penetration assuming uniform attack and extrapolated linearly to give annual rates of penetration.

(b)For 5 deepest pits.

Table 3.38. Corrosion rates calculated from weight loss and pit depths for duplicate specimens of wrought 1018 steel exposed for 1000 hours to deaerated simulated 10X basalt groundwater at 250 C.

Specimen Type	Phase	Corrosion Rate(a) $\mu\text{m}/\text{y}$	Average Pit(b) Depth, μm	Maximum Pit Depth, μm
Gravimetric	V	8.36	5.6	10
Gravimetric	L	7.35	8.6	10
Crevice	V	11.9	12	15
Crevice	L	8.42	9.8	12

(a)Weight losses were converted to depths of penetration assuming uniform attack and extrapolated linearly to give annual rates of penetration.

(b)For 5 deepest pits.

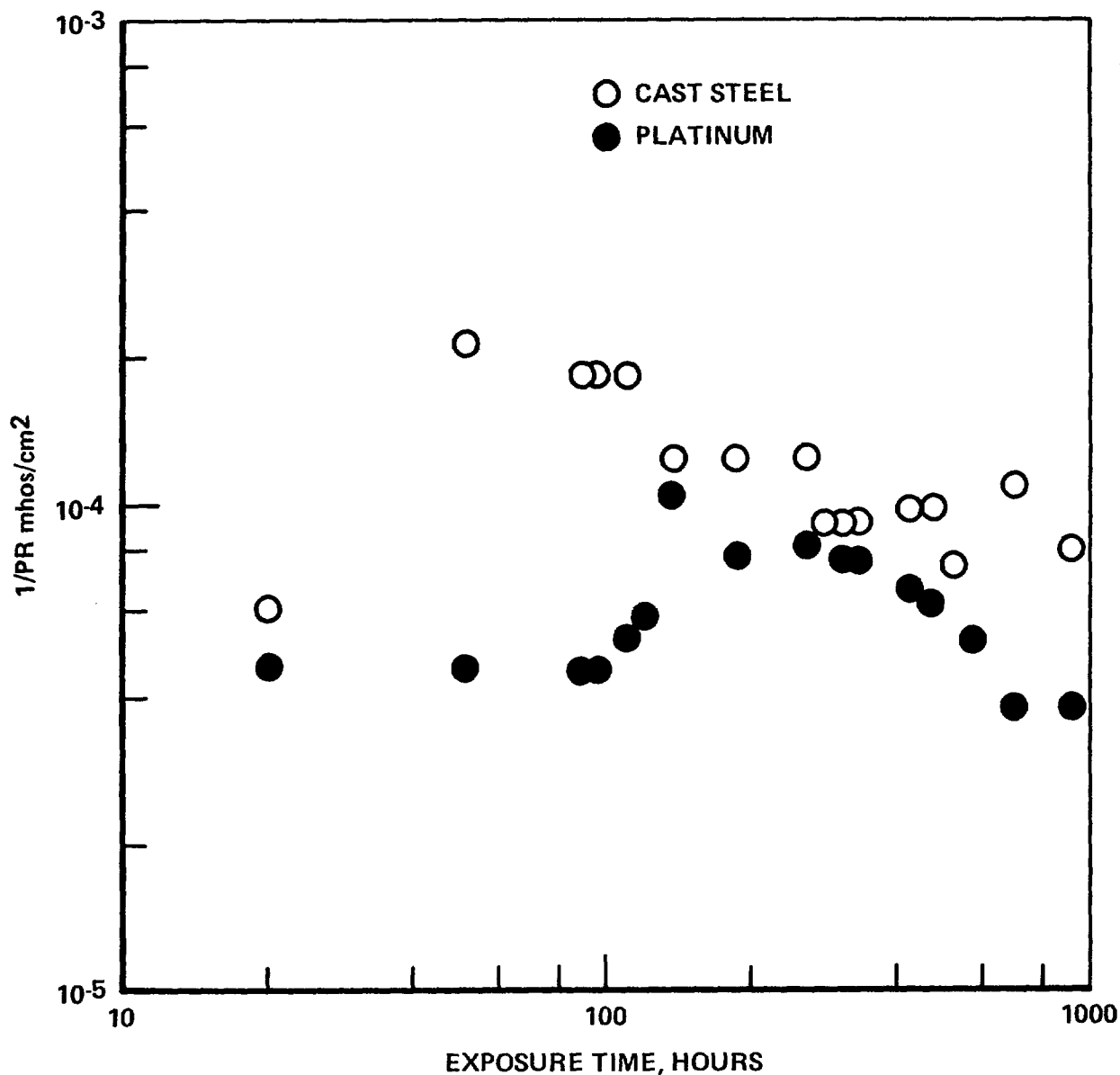


Figure 3.64. $1/PR$ as a function of exposure time for cast clean 1018 steel and platinum exposed in deaerated simulated basalt ground-water at 250 C containing crushed basalt.

50 hours of exposure and decreased over the remaining 950 hours. This decrease may be attributable to passivation of the carbon steel. The average value of 10^{-4} mhos/cm² corresponds to a corrosion rate of about 25 $\mu\text{m/y}$, assuming anodic and cathodic Tafel slopes of 100 mV/decade. This value is about two times higher than the corrosion rates measured by means of weight loss but is, nevertheless, in reasonable agreement. The polarization

resistance of platinum electrodes also was measured as a function of exposure time, and values of $1/PR$ were found to be lower than values for cast steel and appeared to achieve a maximum after about 250 hours of exposure.

Figure 3.65 shows a graphical representation of the electrode kinetics for a corroding metal; $m \rightarrow m^+ + e$ is the corrosion reaction and $Ox + ne^- \rightarrow Red$ is the reduction reaction. If $i_0 Red/Ox$ is greater than or equal to i_{corr} , then the polarization resistance value can be in error by an amount equal to $i_0 Red/Ox$. Although the $1/PR$ values for platinum estimate $i_0 Red/Ox$ for platinum, the $i_0 Red/Ox$ for the corroding metal may be somewhat less than the value for platinum. It is difficult to quantitatively estimate the value of $i_0 Red/Ox$ on the corroding metal, but it is possible, in view of the high value for platinum, that it produced at least a portion of the discrepancy between the corrosion rate prediction for the polarization resistance versus the weight-loss measurement. In this system, the primary reduction reaction under deaerated conditions is probably H_2O reduction, but in the presence of radiation many other reducible species may be generated.

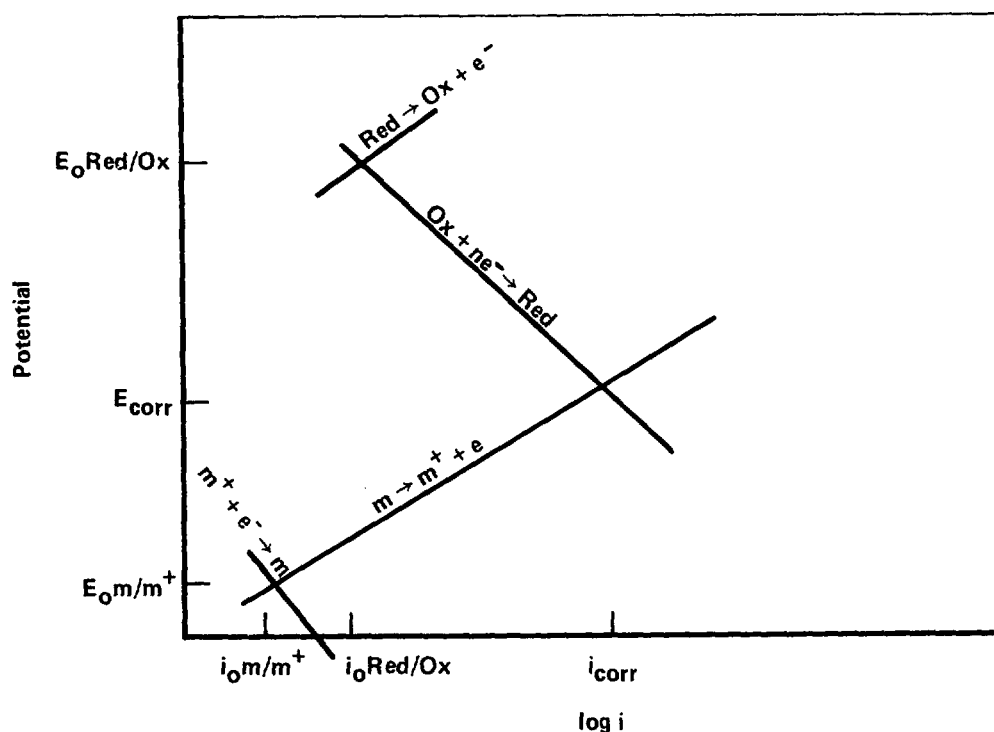


Figure 3.65. Graphical representation of electrode kinetics for a corroding metal where the oxidation and reduction reactions are under activation control.

Electrochemical potentials of the cast steel and platinum also were measured as a function of exposure time, with respect to an external (25 C) $Ag/AgCl$

(0.1 M KCl) reference electrode. The measurement performed on the steel specimen is referred to as the corrosion or open-circuit potential and is indicated graphically in Figure 3.65 as E_{corr} for a metal corroding under activation control. Activation control refers to a condition where the rate-limiting step for the reaction is charge transfer across the metal-solution interface. The measurement performed on the inert platinum electrode indicates the E_0 value, sometimes referred to as the solution E_h , for the dominant reduction reaction (see Figure 3.65). It must be cautioned that there are many problems associated with the use of a platinum electrode to measure solution E_h , such as filming of the electrode, but the measurement does provide an indication of the solution's oxidizing strength.

To convert the potential values to the standard hydrogen electrode (SHE), a correction must be made for the thermal junction potential and the standard potential difference between the two electrodes. These corrections nearly cancel each other out, and thus the Ag/AgCl (0.1 M KCl at 25 C) reference electrode is equal to +0.22 V (SHE) for the reference electrode at 25 C and the test solution at 250 C. Results of the measurements, given in Figure 3.66, show that the potentials for the platinum were consistently more noble than those of the cast steel, as anticipated, and the values for both materials exhibited a peak after about 250 hours of exposure. The increase in potential over the first few hundred hours of exposure is common in systems where film formation or passivation occurs. The range of potential from -0.8 to -0.4V (Ag/AgCl) is probably in the Fe_3O_4 domain of the E-pH diagram. It should be noted that deposits had formed on both the cast steel and platinum electrodes during the exposure.

It was thought that the drop in potential over the remainder of the exposure may have been the result of reference electrode degradation. Accordingly, the potential of the electrode was planned to be measured with respect to a saturated calomel electrode (SCE) at 25 C, following exposure, to determine whether or not degradation had occurred. Unfortunately, gas bubbles had formed in the electrode upon depressurization and cooling, and a final potential reading could not be made.

3.2.3.4 Summary

One-thousand-hour autoclave exposures were performed on carbon steel specimens in simulated basalt groundwater at 250 C under stagnant deaerated conditions. The objectives of the exposures were to selectively reproduce corrosion data for carbon steel in basalt groundwater at elevated temperature and to elevate the influence of steel composition and microstructure, as well as concentration of the groundwater on the corrosion behavior. General corrosion rates were found to be low in the basalt groundwater under the test conditions ($<25 \mu\text{m/y}$) and were not measurably different for the two materials evaluated: a clean (low P and S) cast 1018 composition and a wrought 1018 composition. Concentration of the groundwater by a factor of 10 decreased corrosion rates by about a factor of two.

Shallow pits ($<20 \mu\text{m}$) were found on most of the specimens in the exposures. These pits were associated with breakdown of magnalite film found on the specimen surfaces.

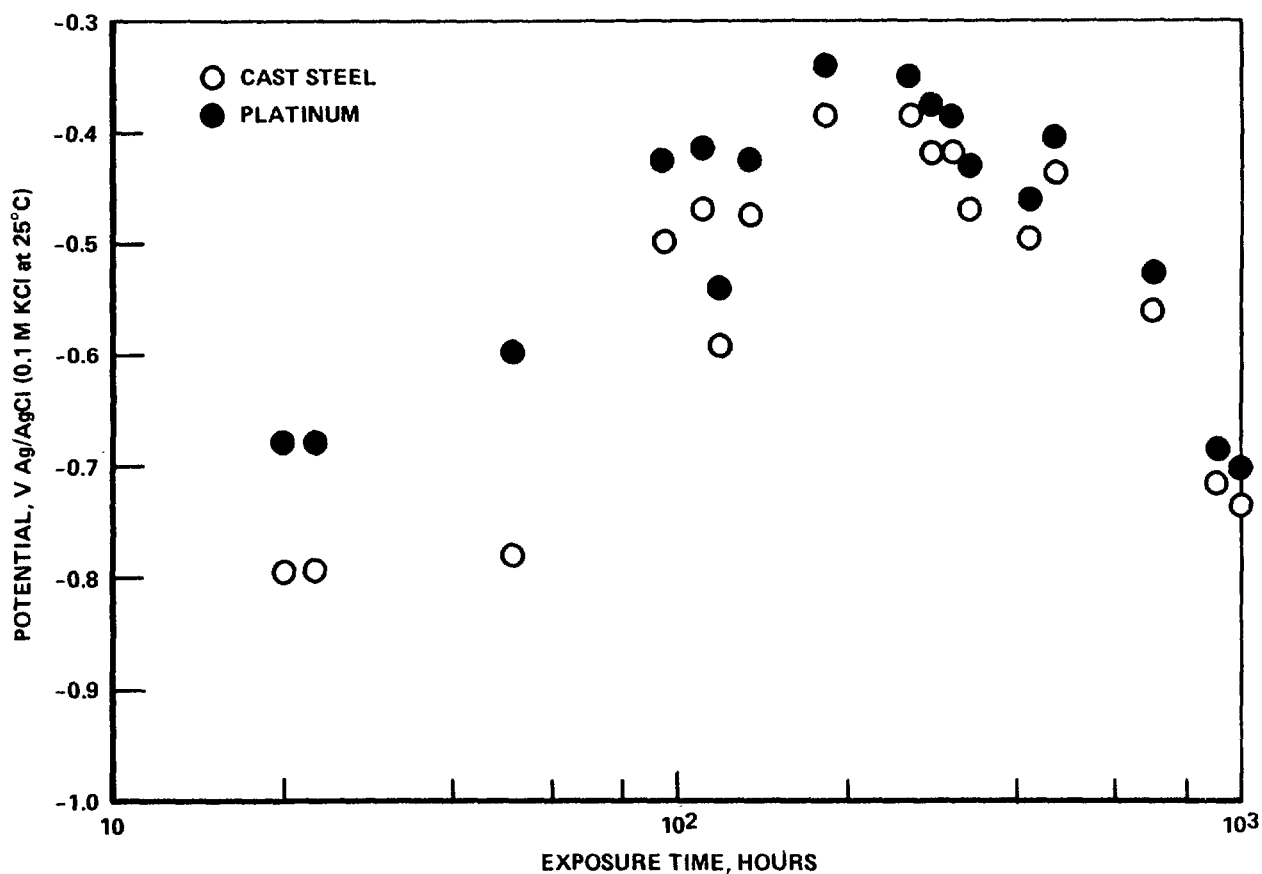


Figure 3.66. Potential as a function of exposure time for cast clean 1018 steel and platinum exposed at 250 C in deaerated simulated basalt groundwater containing crushed basalt.

Optical examination of 3-point bend specimens, which were included in the autoclaves, indicated no evidence of SCC for either material evaluated.

Polarization resistance (PR) and corrosion potential measurements were performed on specimens in the unconcentrated groundwater exposures. Reasonable agreement was found between corrosion rates predicted from the polarization resistance measurements and those obtained from weight-loss. PR values increased (1/PR values decreased) over most of the exposure period indicating a decreasing corrosion rate with time.

3.2.4 Literature Survey on Stress-Corrosion Cracking of Carbon Steels

A survey of the literature was performed on stress-corrosion cracking (SCC) of low-strength carbon steels in repository environments. This survey, submitted to NRC as a topical report (NUREG/CR-3861) (Ref. 3.5), is summarized below.

SCC of low-strength carbon steels has been observed in a number of environments. Some of the cracking agents identified for carbon and low-alloy steels are:

- NO_3^-
- OH^-
- $\text{CO}_3^{2-} - \text{HCO}_3^-$
- $\text{CO} - \text{CO}_2 - \text{H}_2\text{O}$
- PO_4^{3-}
- Water - O_2
- Water - Cl^- - Oxidant
- MgCl_2 (Ni Alloys)
- H_2SO_4 - KI
- Nonaqueous liquid NH_3 .

In all the environments in which electrochemical studies have been performed, stress-corrosion cracking occurs over an electrochemical potential range exhibiting a critical balance between active and passive behavior, which is reflected in the potentiodynamic-polarization curves. This relationship between passivation and stress-corrosion cracking is the basis for the dissolution mechanism for stress-corrosion cracking (Ref. 3.22). In this mechanism, the walls of the crack are passivated while plastic deformation continually bares unfilmed metal at the crack tip, which undergoes rapid dissolution. Environmental parameters play a role in cracking through their influence on the chemistry and electrochemistry of the system, whereas physical and metallurgical parameters affect the mechanical response at the crack tip as well as the electrochemical behavior of the material. A detailed discussion of this mechanism and additional supporting evidence are given by Parkins (Ref. 3.22).

The results of the mechanical-effects studies of SCC also are quite consistent with the dissolution mechanism. In most of the systems studied, stresses approaching the yield stress apparently are necessary for SCC to initiate. This behavior may simply reflect the necessity for significant plastic deformation to occur. Historically, use of this knowledge to limit SCC either by decreasing applied residual stresses or by increasing yield stress of the material has met with only limited success. One reason for this is the detrimental effect of cyclic loading on threshold stresses for cracking. Moreover, the presence of notches in a structure can cause local stresses to exceed the yield stress, even when static nominal stresses are considerably lower. Finally, altering an alloy's composition or microstructure to increase its yield stress may actually increase the probability that cracking will occur because of detrimental effects on the material's electrochemical behavior or the increased likelihood of hydrogen embrittlement.

One desirable feature of the dissolution model for stress-corrosion cracking is that it enables a rapid prediction of the potency of an environment on the basis of electrochemical measurements. Possible stress-corrosion cracking environments are those in which a pronounced active-to-passive transition is observed in the potentiodynamic-polarization curves or in current-time data. Actual cracking velocities also can be estimated on the basis of electrochemistry. Indeed, Parkins (Ref. 3.23) found a good correlation between the peak current densities measured on relatively bare metal surfaces with measured cracking velocities, as shown in Figure 3.67. The straight line in Figure 3.67 is calculated from Faraday's Law,

$$v = \frac{i_a M}{ZFd} \quad ,$$

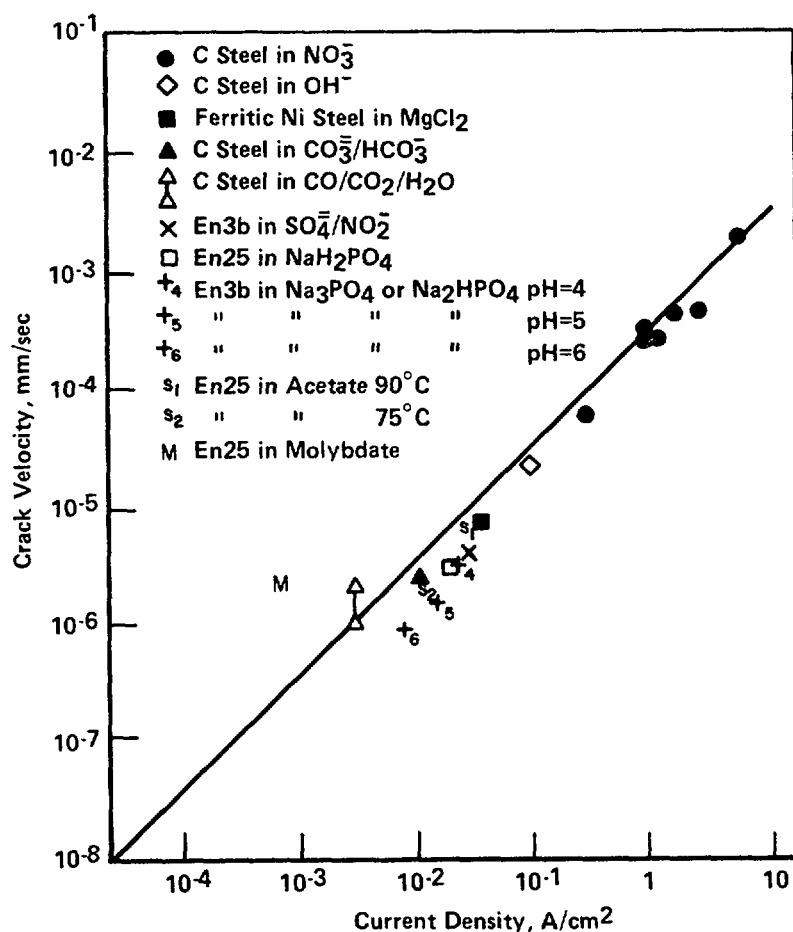


Figure 3.67. Measured stress corrosion crack velocities and current densities passed at a relatively bare surface for ferritic steel in a variety of solutions (Ref. 3.23).

where

i_a = anodic current density
M = atomic weight
Z = valency
F = Faraday's constant
d = alloy density

demonstrating the excellent correlation between the measured cracking velocities and those predicted on the basis of the proposed mechanism.

Results of the preliminary electrochemical studies performed on a 1018 carbon steel in a basalt groundwater suggest that some slight susceptibility to SCC may exist in the bulk environments. However, most stress-corrosion cracking problems of technological importance occur in systems where the bulk environment is relatively innocuous, but where potent cracking environments develop locally (for example, caustic cracking in boilers and carbonate/bicarbonate cracking of pipeline steels). Thus, one must examine the bulk environment to identify potential cracking agents and also examine possible mechanisms for concentration of these agents.

Unfortunately, a number of potential cracking agents are present at low concentrations in the candidate repository environments. These include carbonates, hydroxides, phosphates, nitrates, chlorides, and oxygen. Phosphates and nitrates may enter a repository by the intrusion of groundwater containing fertilizers, and it appears that cracking induced by phosphates is significant at low temperatures. Moreover, nitrate may be generated by radiolysis of N_2 . To complicate the problem further, species other than those currently identified also may promote cracking, because any species capable of promoting passivation also is a candidate stress-corrosion cracking agent. Along these lines, Koch and Thompson (Ref. 3.24) recently performed a literature survey of inorganic ionic species that affect corrosion of iron and iron-base alloys. Their findings, summarized in Table 3.39, show that the cracking agents NO_3^- , CO_3^{2-} , PO_4^{3-} , and I^- inhibit general corrosion of steels, as is well known. Additional general-corrosion inhibitors of steels which are present in repositories include Mg^{++} and Ca^{++} , silicates, and BO_3^{3-} .

A number of potential concentrating mechanisms for the cracking agents may operate in a waste repository. For example, during the thermal period but prior to pressure buildup, boiling and resulting concentration may occur at, or near, the waste package. Localized corrosion is likely, and anions will migrate into pits and crevices to maintain charge neutrality where hydrolysis occurs. Thermogalvanic corrosion, which can occur where there are gradients in the overpack skin temperature, separates the oxidation and reduction reactions, resulting in acidification at the anodic sites and hydroxide buildup at the cathodic sites.

One problem with relating concentration mechanisms to stress-corrosion cracking susceptibility is in identifying upper limits for concentration. Clearly, this would require extensive physical modeling of the transport of the species. On the other hand, the literature includes only limited data

Table 3.39. Summary of the effects of various ions on the corrosion of iron-base alloys (Ref. 3.24).

Anion	Effect	Cation	Effect
Cl ⁻	Accelerate	Cu ⁺²	Accelerate
Br ⁻	Accelerate	Cu ⁺²	Inhibit
I ⁻	Accelerate	Zn ⁺²	Accelerate
I ⁻	Inhibit	Ca ⁺²	Inhibit
F ⁻	Accelerate	Mg ⁺²	Inhibit
SO ₄ ⁻²	Accelerate	Fe ⁺²	Accelerate
SO ₃ ⁻²	Accelerate	Cr ⁺²	Accelerate
ClO ₃ ⁻	Accelerate		
ClO ₃ ⁻	Inhibit		
TcO ₄ ⁻	Inhibit		
CrO ₄ ⁻²	Inhibit		
Cr ₂ O ₇ ⁻²	Inhibit		
NO ₃ ⁻	Inhibit		
NO ₂ ⁻	Inhibit		
MnO ₄ ⁻	Inhibit		
IO ₃ ⁻	Inhibit		
AsO ₂ ⁻	Inhibit		
AsO ₄ ⁻³	Inhibit		
AsO ₄ ⁻³	Decrease Strength		
PO ₄ ⁻³	Inhibit		
HPO ₄ ⁻²	Inhibit		
H ₂ PO ₄ ⁻	Inhibit		
CO ₃ ⁻²	Inhibit		
B ₄ O ⁻²	Inhibit		
BO ₃ ⁻³	Inhibit		
MoO ₄ ⁻²	Inhibit		
WO ₄ ⁻²	Inhibit		
Silicate	Inhibit		

concerning lower limits in concentration for established cracking agents. Synergistic effects of the species present in the groundwater also must be considered.

Finally, the relationship between radiation and SCC warrants further amplification. In addition to the previously discussed effect of generating potential cracking agents, radiation also will move the Eh of the groundwater in the noble direction. Ford (Ref. 3.25) in a review of the stress-corrosion cracking of ferritic steels, overlaid the pH-potential domains for SCC of ferritic steels in a number of environments on a single Pourbaix diagram, as shown in Figure 3.68. These data show that the cracking domains for phosphates, carbonates, and caustic lie along the water or H^+ reduction line and the domains for the latter two systems correspond with the region of stability of Fe_3O_4 . Although data on Eh values in repositories are limited and of questionable accuracy, many repository environments are considered to be highly reducing, and thus the radiation fields may move the Eh values into these cracking domains. Furuya (Ref. 3.26) demonstrated a similar effect in SCC studies of sensitized Type 304 stainless steel.

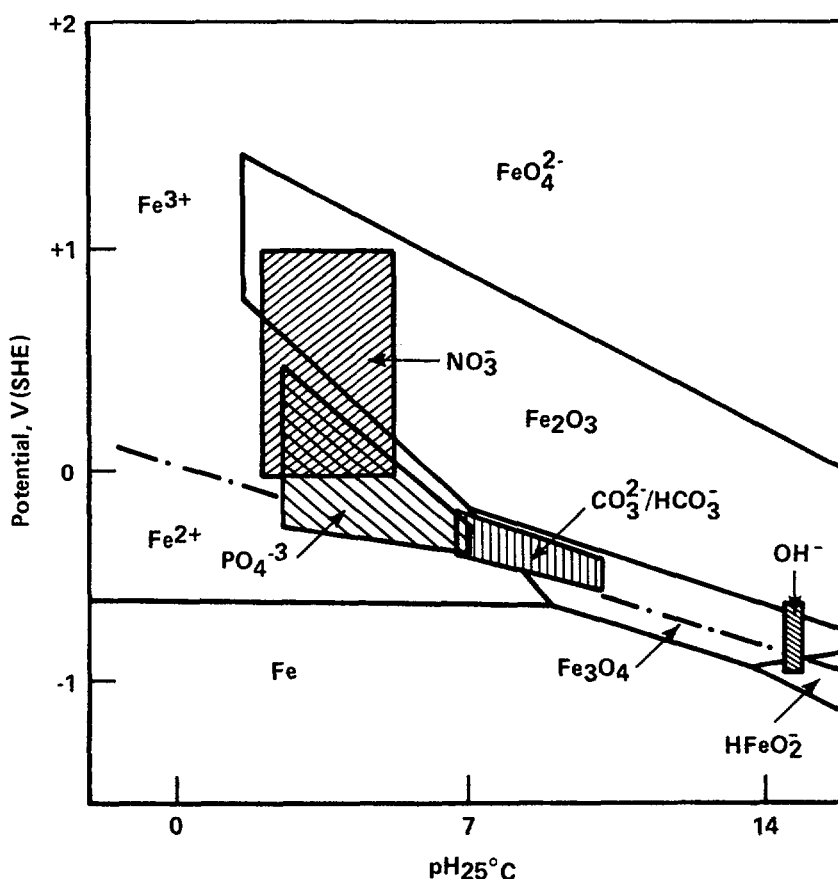


Figure 3.68. Potential-pH diagram for iron with cracking domains for some of the potent cracking agents (Ref. 3.25).

This literature survey leads to the following conclusions:

- A number of potential cracking agents are present at low concentrations in repository environments.
- Stress-corrosion cracking of mild steel is relatively unlikely in bulk repository environments because of low concentrations of the cracking species.
- The most serious threat to the integrity of a carbon-steel overpack with respect to stress-corrosion cracking is through concentration of the cracking species.
- Potential concentrating mechanisms include heat transfer, pitting, crevice corrosion, and thermogalvanic corrosion.
- The influence of radiation fields on stress-corrosion cracking is not fully understood, but limited experimental data suggest that one likely influence is in moving the free-corrosion potential in the noble direction, which may increase the probability of SCC.
- Another effect of radiation fields may be to generate cracking agents such as ferric ions or nitrates.
- Stresses approaching the yield stress generally are required for cracking to initiate, even where the cracking agents are present at high concentrations.

These conclusions suggest a number of data needs. First, experimental and modeling studies are needed to assess the likelihood of stress corrosion cracking of carbon steel in waste-repository environments. For the cracking agents identified in waste repositories, lower limits in concentration needed to promote cracking must be established. It is important to establish these data under realistic conditions where synergistic effects of other species in the waste repository are considered. These studies can be accomplished through electrochemical screening of the environments, followed by selected stress-corrosion tests. Because it is an accelerated test allowing rapid evaluation, the slow strain rate test for stress corrosion is probably the most promising. Where evidence of cracking susceptibility is observed, it may be desirable to perform fracture-mechanics tests to accurately measure cracking velocities.

In addition, physical modeling of possible concentrating mechanisms must be performed to more accurately assess the likelihood that these mechanisms operate and to bound the upper limits of concentration for each. Identifying and quantifying mechanisms where selective concentration of a single or of a few species occurs is especially important in relating the modeling to the laboratory studies. Finally, the model should be verified through experimentation.

3.2.5 Slow Strain Rate Studies

3.2.5.1 Objective

The objectives of the slow strain rate studies were (1) to evaluate the influence of environmental variables on the stress-corrosion cracking (SCC) susceptibility of carbon steels in simulated repository environments and, (2) evaluate the predictive capability of the potentiodynamic polarization technique in assessing SCC susceptibility.

3.2.5.2 Approach

In the slow strain rate (SSR) technique, a tensile specimen of metal is strained to failure at a very slow rate in the possible cracking environment. Typically, this rate is 10^{-6} to 10^{-7} sec^{-1} , which is 4 to 5 orders of magnitude slower than rates used in normal tensile tests. Stress-corrosion cracking susceptibility is indicated by a degradation in tensile properties over those observed in an inert environment, for example, a decrease in failure time, maximum load, strain to failure, or reduction in area. SCC susceptibility also can be measured by metallographically sectioning the specimen, following testing, and measuring the maximum depth of secondary cracking in the gauge length. This crack depth can be divided by the test time to obtain a cracking velocity. In these studies, the latter technique was used most extensively, although measurement of the mechanical parameters was made on all tests.

The majority of the SSR experiments were performed on hot-rolled 1020 carbon steel, although several early experiments were performed on cold-rolled 1018 carbon steel. The compositions of these steels are given in Table 3-8. The SSR specimens were 0.635 cm in diameter with a reduced gauge section 0.25 cm in diameter and 1.27 cm long. Prior to testing, the reduced section of each specimen was abraded with progressively finer SiC paper down to No. 600.

SSR experiments were performed at ambient pressure and temperatures up to 90 C, as well as at elevated pressures and temperatures up to 315 C. The tests were performed both under freely corroding conditions and under potentiostatic control. For the autoclave experiments, the techniques described in Autoclave Studies (Section 3.2.3) were used, with modification for the potentiostatic experiments. In the latter, an external pressure balanced Ag/AgCl electrode operating at 25 C was used for potential measurements, and the autoclave body was used as an auxiliary electrode. The ambient pressure tests were performed in PTFE* vessels sparged with N_2 to maintain deaerated conditions. A saturated calomel electrode (SCE), Luggin probe, platinum auxiliary electrode, and potentiostat were used to control the potential in the potentiostated tests.

The SSR experiments have been divided into three types: preliminary experiments in basalt groundwater, experiments in solutions from the matrix used

*Polytetrafluoroethylene.

in the potentiodynamic-polarization studies, and experiments in selected cracking environments. Results of these studies are described below.

3.2.5.3 Preliminary SSR Experiments in Basalt Groundwater

Slow strain rate tests were performed on cold-rolled 1018 carbon steel specimens (obtained from a commercial supplier) in the standard basalt groundwater at 90 C and a strain rate of $6 \times 10^{-7} \text{ sec}^{-1}$. The tests were performed over a potential range of -0.5 to -0.7 V (SCE), selected on the basis of the results of the potentiodynamic-polarization behavior. This potential range lies in the region of the active-passive transition in the anodic polarization curve; in this region, SCC of carbon steel is observed in all the cracking environments studied electrochemically. Results of the tests, given in Table 3.40, show that the materials' mechanical properties were similar in the basalt and inert environments. Moreover, optical examination of the specimens did not indicate any evidence of susceptibility to SCC. The small values of elongation to failure resulted from use of cold-worked, rather than hot-worked, material. Use of this material had the advantage of reasonably short failure times, even though the strain rate was quite low.

Table 3.40. Effect of electrochemical potential on the time to failure and the mechanical properties of cold-rolled 1018 carbon steel specimens in slow strain rate tests in basalt groundwater at 90 C and a strain rate of $6 \times 10^{-7} \text{ sec}^{-1}$.

Potential V(SCE)	Time to Failure, Hours	Percent Elongation
-0.50	26.2	4.21
-0.60	26.6	3.95
-0.70	28.5	5.29
Oil at 90 C	26.2	4.75
Air at 25 C	24.0	4.31

A single test also was performed in basalt groundwater at 250 C at -250 mV (saturated Ag/AgCl) and a strain rate of $6 \times 10^{-7} \text{ sec}^{-1}$. This potential was selected on the basis of the results of the potentiodynamic-polarization experiments performed at 250 C. No cracking was found in the gauge length of the specimen.

3.2.5.4 Slow Strain Rate Experiments in Solutions From the Statistical Design Matrix

Slow strain rate (SSR) experiments were performed on several solutions from the statistical design matrix of potentiodynamic polarization curves. The chemical compositions of these solutions are given in Table 3.41. Note that these solutions covered a broad range in concentration for most of the species evaluated in the potentiodynamic polarization studies. These solutions were selected for evaluation in the SSR experiments based on one of two criteria: (1) the maximum current in the fast scan of the potentiodynamic polarization experiment exceeded $1 \times 10^{-3} \text{ A/cm}^2$, or (2) there was an order-of-magnitude difference between current densities for the fast and slow scan potentiodynamic polarization experiments.

Table 3.41. Compositions of solutions from statistical design matrix that were used in the slow strain rate experiments.

Solution Number	Composition, mg/l								
	pH	NO ₃	CO ₃	HCO ₃	Cl	F	Fe	BO ₃	SiO ₃
5	6.2	2,000	0	4,980	100	2,950	1.8	2,000	112
8	9.2	0.2	52,000	18,100	100,000	3,000	3.0	50	50
21	9.3	0.2	60,000	24,000	112,500	10	23.4	52	60
23	9.7	0.2	168,000	21,000	100	10	10.7	1,943	15
31	9.6	2,000	53,000	37,500	100	10	6.6	26	35
57	7.2	2,000	0	4,540	100	5,425	2.8	1,920	340

Fast scan and slow scan polarization curves for the six solutions evaluated are given in Appendix C, and a summary of the potentiodynamic polarization parameters is given in Table 3.42. The potentiodynamic polarization curves for the high nitrate, low bicarbonate solutions (solutions 5 and 57) were the most difficult to interpret since they did not exhibit classical active/passive transitional behavior. On the other hand, the low nitrate solutions and solution 31, which contained high nitrate and carbonate/bicarbonate, exhibited active-passive behavior in most cases. For the nitrate solutions, the observed decreases in current with decreasing scan rate in the potentiodynamic polarization experiments is indicative of passivation of the electrode.

A summary of the results of the SSR experiments is given in Table 3.43. These data show that SCC occurred in all of the environments examined except

Table 3.42. Summary of potentiodynamic polarization parameters for 1020 carbon steel in the test solutions used in the SSR studies.

Solution Number	$I_{\max} \text{ A/cm}^2$		$\Delta I_{\max} \text{ (a)}$		$I_{\max} \text{ (b)}$ Ratio		Slow Scan		
	Slow	Fast	at $E_{\max} \text{ (c)}$ Fast	at E_{\max}	at E_{\max} Fast (c)	at (c) E_{\max}	I_{cor} A/cm ²	E_{cor} V (SIE)	I_{pas} A/cm ²
5	2.3×10^{-3}	-	$>4.4 \times 10^{-2}$	-	$>7 \times 10^2$	-	1.0×10^{-4}	-0.325	7.8×10^{-4}
8	4.4×10^{-4}	1.6×10^{-3}	1.1×10^{-3}	1.1×10^{-3}	2.54	2.54	4.2×10^{-5}	-0.891	2.3×10^{-5}
21	5.6×10^{-5}	6.2×10^{-3}	6.2×10^{-3}	6.1×10^{-3}	4.4×10^2	110	2.0×10^{-6}	-0.940	1.5×10^{-5}
23	8.6×10^{-3}	2.7×10^{-2}	2.7×10^{-2}	1.8×10^{-2}	4.1×10^2	3.1	3.3×10^{-5}	-0.876	6.5×10^{-5}
31	8.0×10^{-4}	3.4×10^{-3}	3.3×10^{-3}	2.6×10^{-3}	3.3×10^1	3.2	8.6×10^{-6}	-0.562	1.1×10^{-4}
57	-	8.7×10^{-3}	8.7×10^{-3}	-	2.1×10^3	-	3.7×10^{-5}	-0.325	1.0×10^{-4}

(a) $\Delta I_{\max} = I_{\max} \text{ (fast)} - I \text{ (slow)}$.

(b) $I_{\max} \text{ ratio} = I_{\max} \text{ fast} / I \text{ slow}$.

(c) ΔI_{\max} and I_{\max} ratio were measured two ways: at E_{\max} , the difference or ratio of currents was based on maximum currents; at E_{\max} fast; the difference or ratio of currents was measured at E_{\max} of fast scan.

Table 3.43. Summary of results of SSR experiments performed on solutions from potentiodynamic polarization matrix at 75 C and a strain rate of $2 \times 10^{-7} \text{ sec}^{-1}$.

Solution Number	Potential V (SCE)	Reduction in Area, percent	Time to Failure, hours	Cracking Velocity, mm/sec
8	-0.700	5.3	151	6.07×10^{-7}
8	-0.750	10.8	154	4.50×10^{-7}
8	-0.800	20	201	NC**
5*	-0.400	4.0	342	NC
5*	-0.500	7.0	216	NC
5	-0.800	22	187	NC
21	-0.700	25	190	NC
21	-0.800	20	161	4.58×10^{-7}
21	-0.900	21	213	NC
23*	-0.700	28	288	NC
23*	-0.800	10	290	1.98×10^{-7}
23*	-0.900	35	332	NC
31	-0.700	-	141	5.17×10^{-7}
31	-0.800	-	130	1.00×10^{-6}
31	-0.850	15	167	2.83×10^{-7}
57	-0.400	5.0	133	9.55×10^{-7}
57	-0.500	17	124	9.51×10^{-7}

*Strain rate = 1×10^{-7} .

**NC = no cracking.

solution 5. The absence of cracking in solution 5 is somewhat surprising considering the fact that cracking occurred in solution 57, which had a very similar composition. The major differences between the two solutions are the higher pH and higher fluoride composition of solution 57. Comparison of Table 3.41 and Table 3.43 indicates that a known SCC species was present in all of the experiments in the environments that produce cracking. Thus, no new cracking agents were identified in this study. Of course, it is conceivable that other environments in the test matrix, which did not contain a known cracking species, also could give rise to SCC. However, the potentiodynamic polarization studies did not indicate the presence of such an environment.

For the carbonate-containing environments, it is clear that the criteria for selecting cracking environments are effective. Although it is more difficult to apply the criteria in the nitrate solutions, these criteria also appear to be effective in nitrate solutions. Of course, non-cracking environments would need to be tested to assure that cracking is unlikely when the criteria are not met.

Several other conclusions can be made from the data in Tables 3.41 through 3.43. For example, the occurrence of SCC in solution 21 demonstrates that, in the presence of carbonates, high chloride concentrations will not completely inhibit SCC. This observation has significant implications for the salt repositories.

Attempts were made to correlate cracking susceptibility with the potentiodynamic polarization parameters, such as maximum current, maximum current ratio, and maximum current difference. The data, shown in Figures 3.69 through 3.71, do not indicate any apparent trend. Thus, while such correlations are frequently observed for simple cracking environments such as nitrates in distilled water, the complicated nature of the simulated groundwater solutions may preclude this type of analysis.

3.2.5.5 SSR Experiments in Ferric Chloride Solutions

In the literature survey (Ref. 3.5), several species that may be present in the repository were identified as potential stress-corrosion cracking (SCC) agents. Of these, FeCl_3 or chloride + ferric oxides or hydroxides are potentially problematic, since chlorides are present in the groundwater and overpack corrosion will generate ferrous ions that may be oxidized to ferric ions by radiolysis or oxygen ingress. Strauss and Bloom (Ref. 3.27) first reported on the SCC of low-carbon steels by ferric chloride solutions in 1961. They observed transgranular cracking in pressurized capsule tests at 316 C at very low concentrations of ferric chloride, 0.001 M, and in aqueous slurries of FeOOH or Fe_2O_3 and NaCl . However, $\text{NaCl} + \text{Fe}_3\text{O}_4$ did not produce cracking (see Table 3.44).

Although the SCC observed by Strauss and Bloom may be relevant to overpack performance, they did not establish whether SCC of carbon steel would occur at lower temperatures, more typical of waste repositories, or in more complicated aqueous solutions containing typical groundwater species. Moreover, it was not evident from the original reference whether cracking occurred in the vapor or liquid phase within the capsules. Accordingly, an experimental investigation was undertaken to reproduce the SCC observed in the original reference and to examine the influence of temperature and solution chemistry on SCC of low-carbon steels in these ferric-chloride solutions.

Initially, slow strain rate tests were performed on hot-rolled 1020 carbon steel in 0.001 M ferric chloride at 315 C over a range of strain rates to attempt to reproduce the SCC data and to establish the optimum strain rate for subsequent SCC testing. SCC was readily produced in the liquid phase. The cracking was transgranular, with some branching (see Figure 3.72), and was similar in morphology to that reported by Strauss and Bloom.

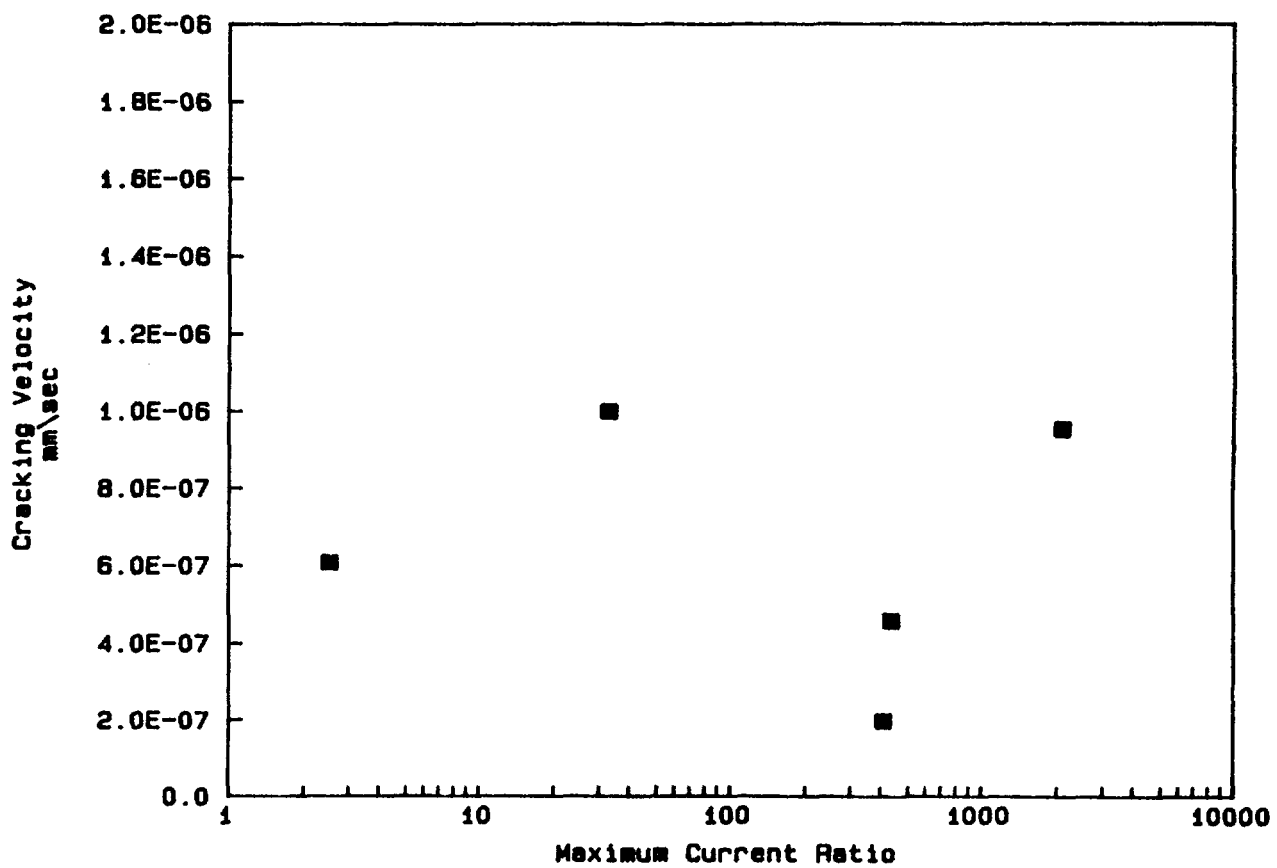


Figure 3.69. Cracking velocity as a function of maximum current ratio (between fast and slow scan polarization curves) for SSR experiments performed in solutions from the statistical design matrix.

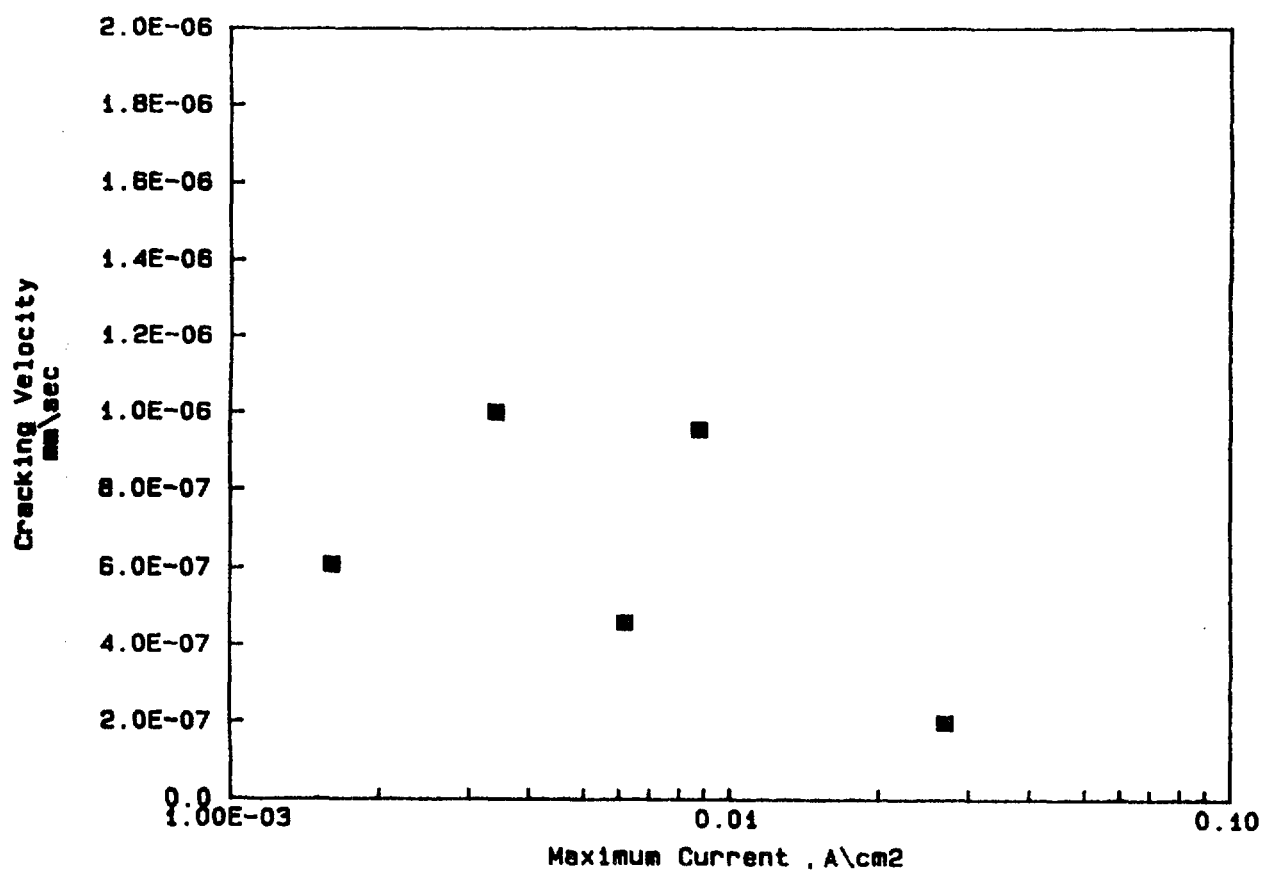


Figure 3.70. Cracking velocity as a function of maximum current from fast scan polarization curves for SSR experiments performed in solutions from the statistical design matrix.

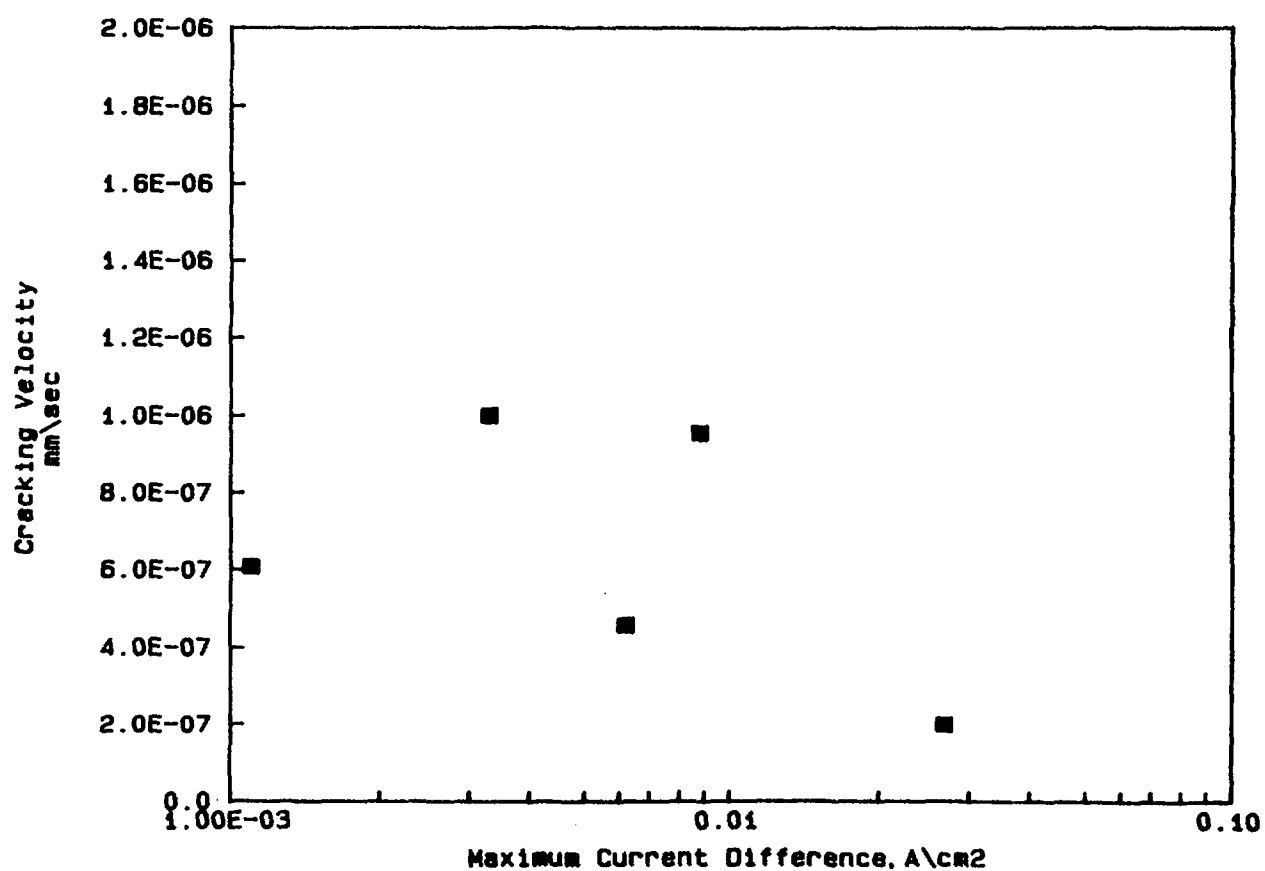


Figure 3.71. Cracking velocity as a function of maximum current difference (between fast and slow scan polarization curves) for SSR experiments performed in solutions from the statistical design matrix.

Table 3.44. Effect of various solutions and slurries containing Fe (III) and/or chloride on cracking at 316 C (Ref. 3.27).

Capsule Contents	Results of Treatment*
(1) 0.001 M FeCl ₃	Capsules cracked and leaked within 6 to 15 hours.
(2) 0.0001 M FeCl ₃	Very shallow cracks were produced within 1 week.
(3) 0.0005 M Fe ₂ (SO ₄) ₃	No cracking observed within 1 week.
(4) 0.001 M Fe(NO ₃) ₃	No cracking observed within 1 week.
(5) 0.003 M NaCl	No cracking observed within 1 week.
(6) 0.001 M NaCl	No cracking observed within 1 week.
(7) 0.1 M NaCl	Slight attack at weld junction within 1 week.
(8) 1 M NaCl	Localized corrosion in martensite penetrated welds within 20 hours.
(9) Aqueous slurry of γ-FeOOH containing 0.6% Cl ⁻	Capsules cracked and leaked within 6 hours.
(10) Aqueous slurry of γ-FeOOH generated by corrosion in 0.0005% Cl ⁻	Capsules cracked and leaked within 12 hours.
(11) Aqueous slurry of γ-FeOOH generated by corrosion in high-purity water	No cracking observed within 1 week.
(12) Slurry of γ-FeOOH in line 11 and 0.0001 M FeCl ₃	Capsules cracked and leaked within 16 to 18 hours.
(13) Aqueous slurry of α-FeOOH containing 0.01% Cl ⁻	Shallow cracks were produced within 1 week.
(14) Supernatant liquid γ-FeOOH slurry in line 9	No cracking observed within 1 week.
(15) Slurry of α-FeOOH in line 13 and liquid in line 14	Capsules cracked and leaked within 3 to 4 hours.
(16) Slurry of α-FeOOH containing 0.001% Cl ⁻ and 0.003 M NaCl	Moderately deep cracks were produced within 1 week.
(17) Slurry of γ-Fe ₂ O ₃ containing 0.01% Cl ⁻ and 0.003 M NaCl	Moderately deep cracks were produced within 1 week.
(18) Slurry of α-Fe ₂ O ₃ containing 0.02% Cl ⁻ and 0.003 M NaCl	Very deep cracks were produced within 1 week. One capsule cracked and leaked within 4 days.
(19) Slurry of Fe ₃ O ₄ containing <0.01% Cl ⁻ and 0.003 M NaCl	No cracking observed within 1 week.

*At least three and usually more capsules were given each treatment.



200X

7L773

Figure 3.72. Optical photograph of metallographic section of hot-rolled 1020 carbon steel specimen tested in 0.001 M FeCl_3 at 315 C and a strain rate of $1 \times 10^{-8}/\text{s}$.

Table 3.45. Summary of results of slow strain rate experiments performed on hot-rolled 1020 carbon steel in FeCl_3 solutions at 315 C and at various strain rates.

Strain Rate (s^{-1})	Solution Composition (M)	Maximum Crack Depth (mm)	Time to Failure (hours)	Crack Velocity (mm/s)
1×10^{-8}	1×10^{-3}	0.30	393	2.10×10^{-7}
6×10^{-8}	1×10^{-3}	0.11	146	2.09×10^{-7}
6×10^{-7}	1×10^{-3}	0.20	59.2	9.53×10^{-7}

A summary of the results of slow strain rate tests performed at various strain rates is given in Table 3.45. These data show that susceptibility, based on maximum depth of cracking, was highest at the lowest strain rate. This is unfortunate, experimentally, since a slow strain rate test at 1×10^{-8} /sec may last several weeks or more. For all subsequent work, an intermediate strain rate, 1×10^{-7} /sec, was selected.

Significant general attack occurred on the specimens exposed to the 1×10^{-3} M FeCl_3 solution at 315 C; accordingly, it was speculated that cracking would be at least as severe at lower FeCl_3 concentrations. Subsequent specimens tested in 5×10^{-4} M FeCl_3 solutions exhibited about the same susceptibility to cracking, but the morphology of the attack was altered by the change in solution concentration. Whereas the cracks in specimens tested in 1×10^{-3} M FeCl_3 were generally well defined, with sharp tips, those tested in 5×10^{-4} M FeCl_3 exhibited blunt crack tips (see Figure 3.73). Lower FeCl_3 concentrations were not studied since 5×10^{-4} M FeCl_3 corresponds to about 50 ppm chloride, which is well below the nominal chloride concentration of basalt groundwater.

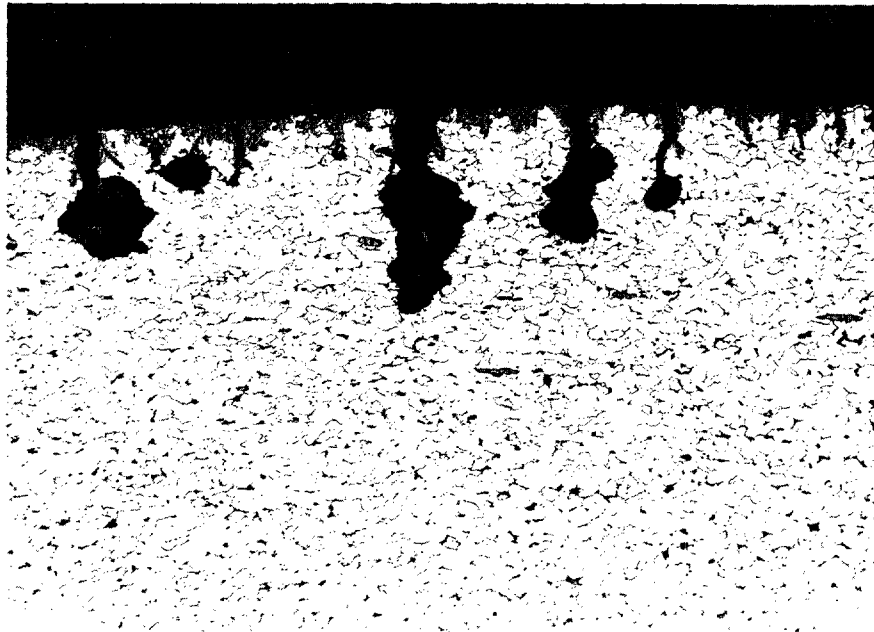
The effect of temperature on the stress-corrosion cracking of hot-rolled 1020 carbon steel was studied in 5×10^{-4} M FeCl_3 at a strain rate of 1×10^{-7} /sec. The results, summarized in Table 3.46 and Figure 3.74, show that susceptibility to SCC reached a maximum between 150 C and 200 C and decreased rapidly above or below this temperature range.

The morphology of the cracking was similar over the temperature range studied with blunt transgranular cracks. However, some temperature effects on morphology were evident. More corrosion products/oxides appeared to be present in the cracks at the lower temperatures. In addition, at 175 C, there was considerable pitting on the gauge section of the specimen and the cracks appeared to have nucleated at the base of the pits. At 125 C, the lowest temperature tested, only shallow groove like features were evident in the gauge length of the specimen (see Figure 3.75).

Studies were also performed on the effect of solution pH on SCC of carbon steel in 5×10^{-4} M FeCl_3 . SSR tests were run at a strain rate of 1×10^{-7} sec⁻¹ in FeCl_3 solutions in which the pH was adjusted with NaOH; the pH was about 3 for the 5×10^{-4} M FeCl_3 solution in which no NaOH was added. The tests were performed in static autoclaves at 175 C, and the pH of the solutions increased 1 to 3 units as a result of contact with carbon steel, as shown in Table 3.46.

Results of the SSR tests performed in the pH-adjusted solutions are also given in Table 3.46. These data show that SCC severity decreased with increasing pH and that negligible SCC occurred at an initial pH of 5.0.

Optical examination of metallographic sections of the specimens following testing indicated that the specimen tested in the pH-4.6 (initial value) solution experienced intergranular attack, in addition to transgranular SCC and pitting, as shown in Figure 3.76. As discussed above, the latter two forms of corrosion have been observed on specimens tested in the lower initial-pH solutions.



100X

8L343

Figure 3.73. Optical photograph of metallographic section of hot-rolled 1020 carbon steel specimen tested in 0.0005 M FeCl_3 at 315 C and a strain rate of 1×10^{-7} /sec.

Table 3.46. Summary of results of slow strain rate experiments performed on hot-rolled 1020 carbon steel in aqueous 5×10^{-4} M FeCl_3 at a strain rate of 1×10^{-7} sec $^{-1}$.

Temperature (C)	Maximum Crack Depth (mm)	Time to Failure (hours)	Crack Velocity (mm/sec)	Initial pH	Final pH
315	0.28	282	2.75×10^{-7}	3.00	3.00
275	0.12	165	2.05×10^{-7}	2.75	3.42
250	0.14	148	2.67×10^{-7}	2.60	5.60
225	0.52	164	8.80×10^{-7}	3.00	5.10
200	0.45	188	6.65×10^{-7}	3.30	4.80
175	0.59	211	9.37×10^{-7}	3.10	4.50
150	0.33	254	3.61×10^{-7}	3.00	5.25
125	0.07	366	5.30×10^{-8}	2.90	5.90
175	0.28	272	2.86×10^{-7}	4.00*	6.50*
175	0.44	208	5.88×10^{-7}	4.60*	5.60*
175	0.046	494	2.59×10^{-8}	5.00*	6.10*

*pH adjusted with NaOH prior to testing.

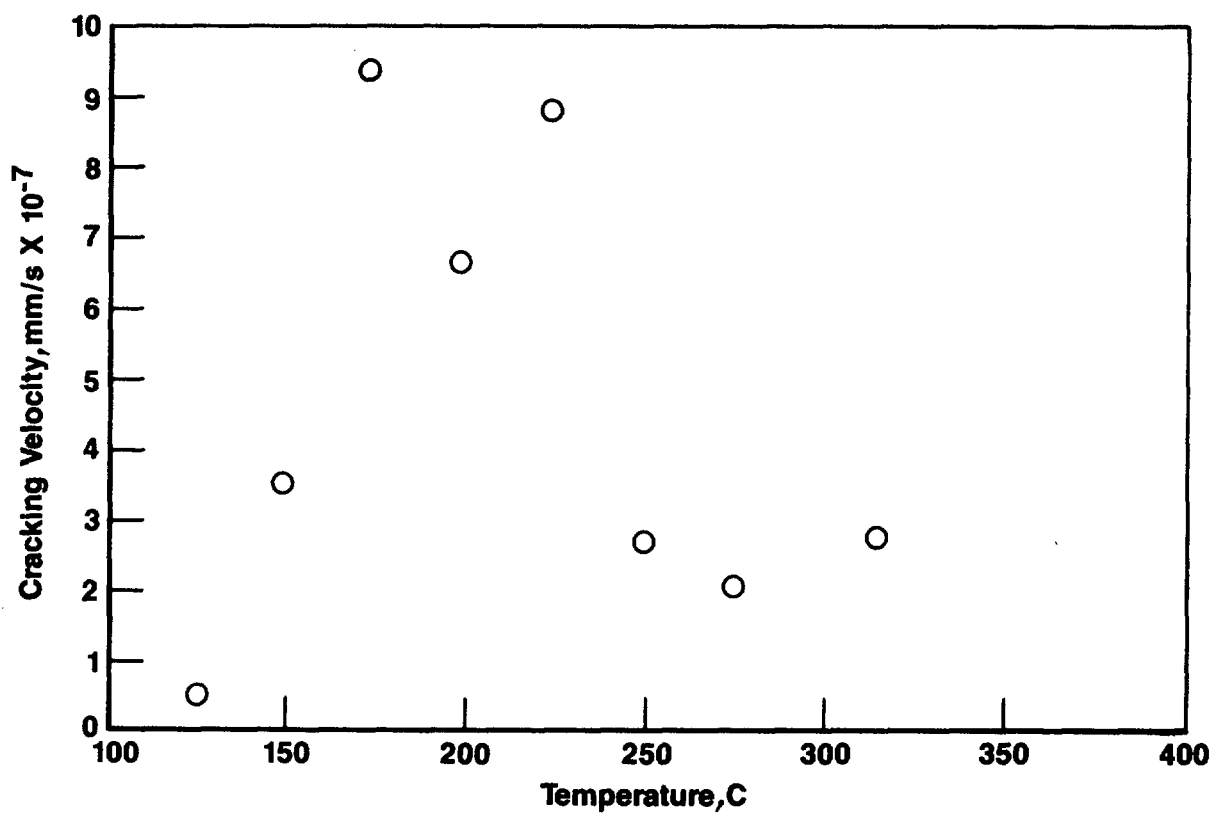


Figure 3.74. Crack velocity as a function of temperature for hot-rolled 1020 carbon steel tested in 5×10^{-4} M FeCl_3 at a strain rate of 1×10^{-7} /sec.



100X

OM911

a. Photomicrograph of gauge section

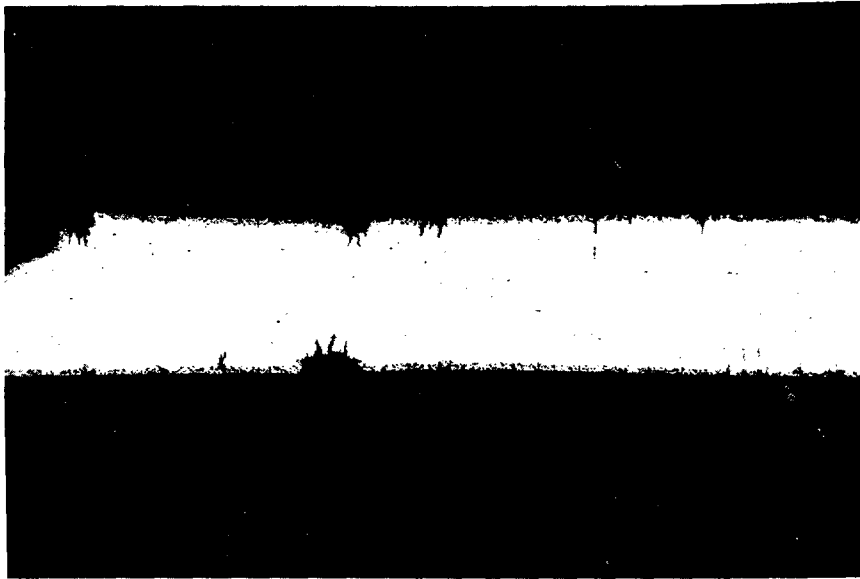


10X

OM908

b. Low-power photograph of gauge section of specimen.

Figure 3.75. Optical photographs of hot-rolled 1020 carbon steel specimen following slow strain rate testing at 125 C in aqueous 5×10^{-4} M FeCl_3 at a strain rate of $1 \times 10^{-7} \text{ sec}^{-1}$.



10X

2M889

a. Photomicrograph of gauge section.



100X

2M891

b. Photomicrograph of a crack shown in (a).

Figure 3.76. Optical photographs of hot-rolled 1020 carbon steel specimen following slow strain testing in aqueous 5×10^{-4} M FeCl_3 at a rate of 1×10^{-7} sec^{-1} with an initial pH of 4.6.

3.2.5.6 Slow Strain Rate Experiments in Nitrate Solutions

Nitrate is another potent cracking agent identified in the literature survey. Possible sources of nitrate include intrusion of the repository by nitrate containing surface waters or radiolysis. Although a considerable amount of research has been performed on SCC of carbon steels in nitrates, the effect of concentration on cracking susceptibility has not been studied, in detail, at low concentrations; nor has the effect of groundwater species on cracking been studied previously. The latter was addressed in the statistical experimental matrix, but those studies were performed at relatively high concentration. However, a strong nitrate effect on cracking was not apparent. This observation likely was the result of the difficulty encountered in interpreting the potentiodynamic polarization data for the nitrate containing solutions. The severity of nitrate cracking also may have been reduced somewhat by the presence of nitrites, added in equal molar quantities; nitrites are inhibitors of nitrate cracking. This approach allowed the effect of the redox potential on the $\text{NO}_3^-/\text{NO}_2^-$ ratio, and hence cracking, to be studied. Nevertheless, the absence of an indication of a strong nitrate effect on SCC warranted further study of this species.

Accordingly, SSR experiments were performed on hot-rolled 1018 carbon steel in NO_3^- solutions in which the effects on SCC of NO_3^- concentration, cation, and species present in basalt groundwater were studied. Prior to performing the SSR experiments, potentiodynamic-polarization curves were obtained, at a scan rate of 18 V/hr, to identify the optimum potential range for performing the SSR experiments.

Potentiodynamic-polarization curves for 1018 carbon steel in 0.1 M, 0.01 M, 0.005 M, and 0.001 M NaNO_3 , and NH_4NO_3 solutions are given in Appendix D. A summary of the parameters relevant to SCC, which were obtained from these curves, is given in Table 3.47. These curves show that the more concentrated NaNO_3 and NH_4NO_3 solutions exhibited passivation behavior; peaks were evident on several of the curves and the reverse scans were generally at lower currents than the forward scans. However, at the lowest concentration tested, 0.001 M, there was little evidence of passivation in either solution. Based on the polarization behavior, potentials of -300 mV (SCE) and -200 mV (SCE) were selected for subsequent SSR experiments with the NaNO_3 and NH_4NO_3 solutions, respectively.

A summary of the results of the SSR experiments with NaNO_3 and NH_4NO_3 solutions is given in Table 3.48 and Figure 3.77. These data show that the SCC severity was similar for the two cations and that SCC occurred in solutions as dilute as 5×10^{-3} M. Severe general attack of the specimen was evident in the most dilute nitrate solutions, an effect predicted from the potentiodynamic-polarization curves. In both solutions, the cracking was intergranular and branching. A typical metallographic section is given in Figure 3.78.

Included in Figure 3.77 are data for the cracking velocities predicted from Faraday's Law and calculated from the measured currents on the fast-scan polarization curves. Note that these predicted values are about an order of magnitude lower than actual measured cracking velocities. This discrepancy

Table 3.47. Summary of results of potentiodynamic-polarization experiments performed on 1020 carbon steel in deaerated nitrate solutions at 90 C and a scan rate of 18 V/hr.

Cation	Concentration M	E_{cor} V (SCE)	I_{cor} A/cm ²	E_{peak} V (SCE)	I_{peak} A/cm ²
Na	0.1	-0.675	4.2×10^{-5}	-	-
Na	0.01	-0.669	7.0×10^{-6}	-0.345	2.0×10^{-2}
Na	0.005	-0.695	7.7×10^{-5}	-	-
Na	0.001	-0.730	4.8×10^{-6}	-	-
NH ₄	0.1	-0.580	5.6×10^{-4}	-0.20	2.3×10^{-2}
NH ₄	0.01	-0.630	5.7×10^{-5}	-	-
NH ₄	0.005	-0.635	2.7×10^{-4}	-	-
NH ₄	0.001	-0.690	6.4×10^{-6}	-	-
Na*	0.1	-0.642	1.4×10^{-5}	-	-

*In basalt groundwater.

Table 3.48. Summary of results of slow strain experiments performed on hot-rolled 1020 carbon steel in nitrate solutions at 80 C and a strain rate of 2×10^{-7} sec⁻¹. Tests in Na solutions were performed at -0.3 V (SCE) while those in NH₄ solutions were performed at -0.2 V (SCE).

Cation	Concentration M	Reduction in Area, percent	Time to Failure, h	Cracking Velocity, mm/sec	Initial pH	Final pH
Na	0.1	1.5	41	4.5×10^{-6}	7.2	8.8
Na	0.01	3.2	97	1.7×10^{-6}	7.4	9.6
Na	0.005	3.3	69	1.6×10^{-6}	6.2	9.0
Na	0.001	16.1	152	-	6.5	9.7
NH ₄	0.1	2.6	41	7.2×10^{-6}	5.6	7.5
NH ₄	0.01	4.0	63	1.2×10^{-6}	6.7	6.2
NH ₄	0.005	3.7	84	1.3×10^{-6}	6.7	7.5
NH ₄	0.001	22.3	180	-	7.4	9.9
Na*	0.1	7.2	68	2.2×10^{-6}	9.5	10.2
Na*	0.05	12.0	103	9.6×10^{-7}	8.6	11.4

*In basalt groundwater.

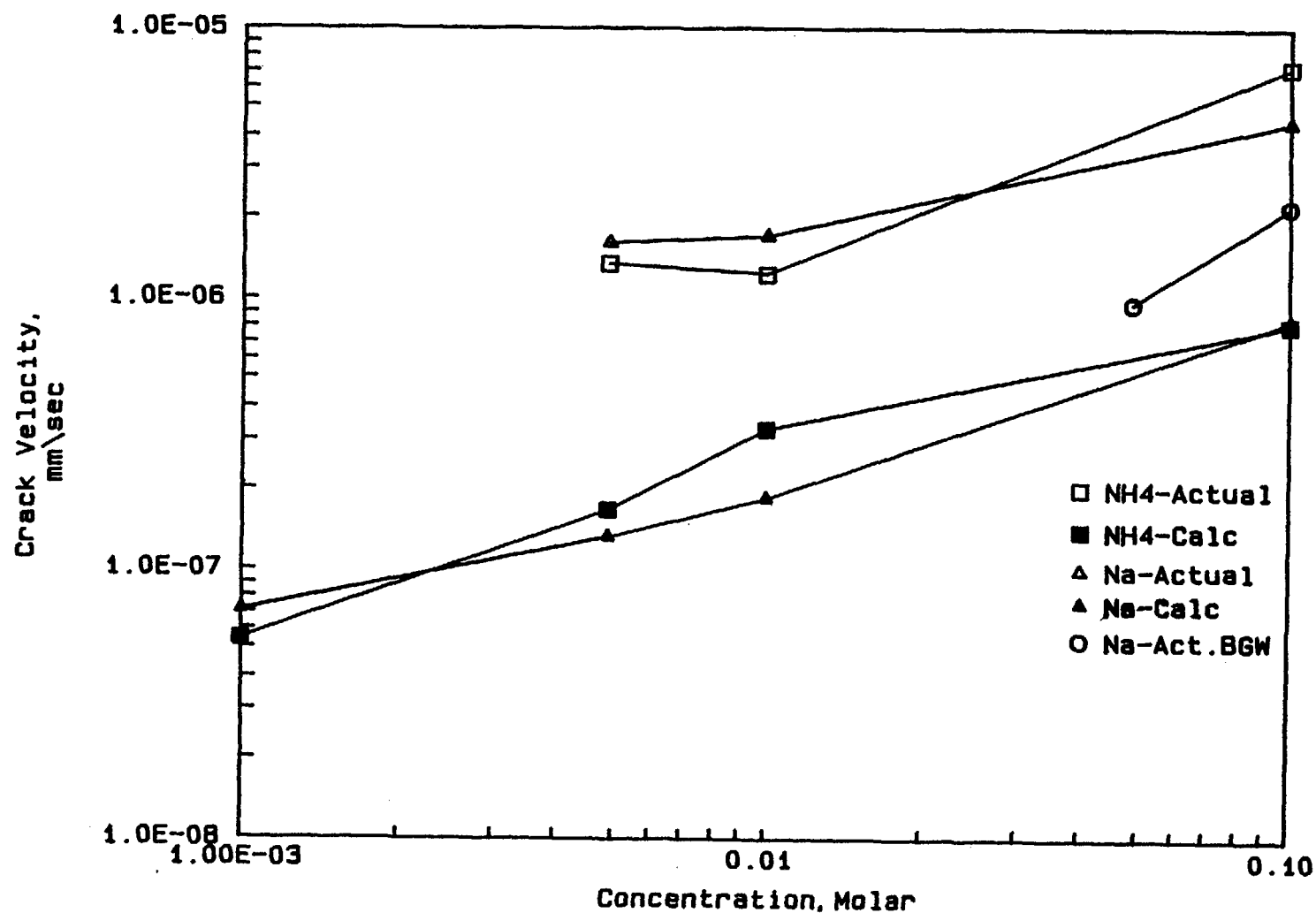


Figure 3.77. Crack velocity as a function of concentration for aqueous solutions of NH_4NO_3 and NaNO_3 . Cracking velocities from SSR experiments are in open symbols (actual) and cracking velocities estimated from potentiodynamic-polarization curves and Faraday's Law are in closed symbols (calculated). Experiments in basalt groundwater (BGW) doped with NaNO_3 also are included.

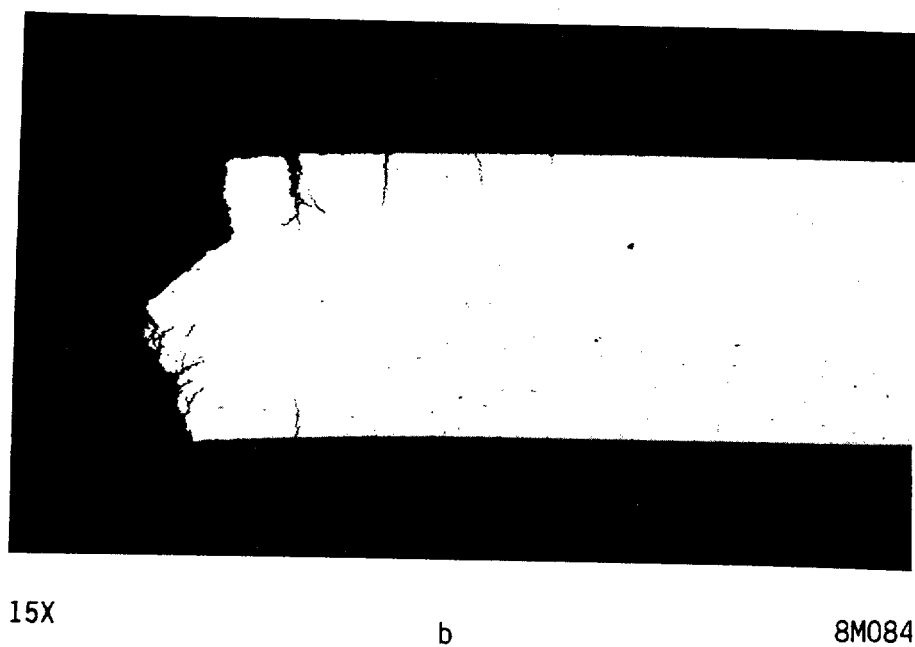
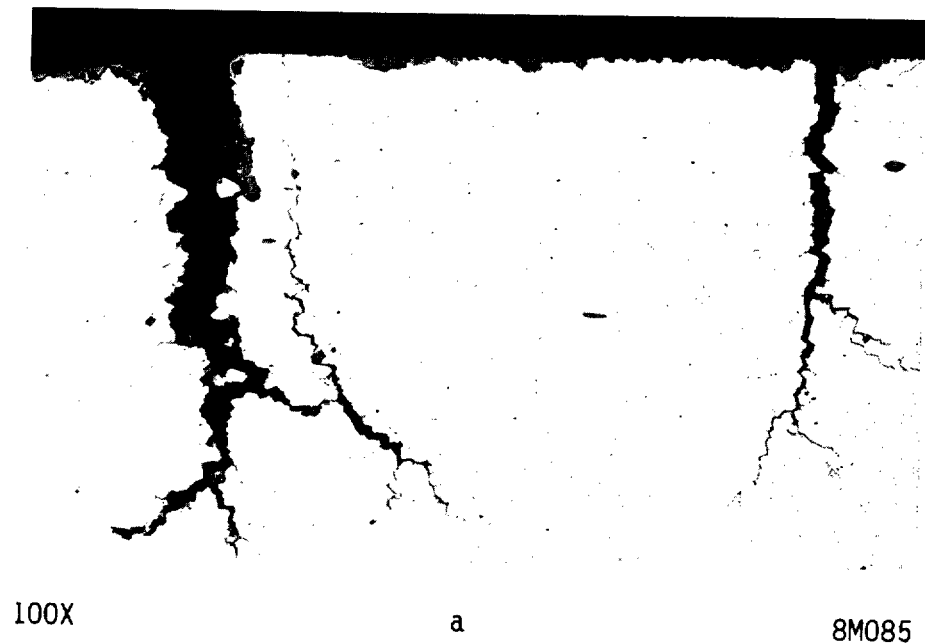


Figure 3.78. Optical photographs of metallographic section of SSR specimen following testing in 0.1 M NaNO_3 at 80 C.

probably reflects the fact that the maximum currents on a bare surface are potentially much higher than those measured by means of the fast-scan polarization technique. Nevertheless, the curve slopes for the actual and

calculated data were similar and, thus, the electrochemical data are capable of predicting the effect of NO_3^- concentration on cracking velocities.

To investigate the effect of groundwater species on SCC in the presence of NO_3^- , two SSR experiments were performed in basalt groundwater doped with NaNO_3 . Results of these experiments, given in Table 3.48 and Figure 3.77, show that susceptibility to SCC was somewhat lower in the presence of the species found in the basalt groundwater. This lower susceptibility may have been a consequence of the higher pHs of the basalt groundwater solutions.

3.2.5.7 Summary

Slow Strain Rate (SSR) experiments were performed on carbon steel in basalt groundwater, solutions from the statistical design matrix, and selected established cracking environments. The objectives of these experiments were (1) to evaluate the influence of environmental variables on SCC of carbon steel in simulated repository environments and, (2) evaluate the potentiodynamic-polarization technique in assessing SCC susceptibility. The experiments were performed under deaerated conditions with potential control. Potentials selected for testing were based on the potentiodynamic-polarization behavior.

In the basalt groundwater, no evidence of SCC was found at either 90 or 250 C at the optimum cracking potentials. On the other hand, a number of cracking environments were identified from the statistical design matrix, demonstrating the effectiveness of the potentiodynamic-polarization criteria used to select the cracking environments. Established cracking species were present in all of the environments that promoted SCC and, thus, no new SCC species were identified. It was observed that high Cl^- or F^- concentrations did not completely inhibit SCC in the presence of one established cracking species; HCO_3^- .

SSR experiments performed in FeCl_3 and HO_3^- solutions demonstrated that significant SCC could occur at very low concentrations (ppm range). The FeCl_3 cracking was found to be most severe at 175 C and pH values less than 5.

The pH and temperature dependency of the NO_3^- cracking was not investigated, but it was found that the cation (Na^+ or NH_4^+) did not greatly affect cracking. It also was shown that the effect of NO_3^- concentrations on SCC behavior could be predicted from simple potentiodynamic-polarization tests.

3.3 Stainless Steel-Tuff System

3.3.1 Introduction

The current reference design for the tuff repository waste package includes a thin stainless steel overpack. The reference horizon is located above the water table, and thus the overpack will only intermittently contact with groundwater. Under these conditions, it is likely that the groundwater will concentrate at the heated overpack surface. While stainless steels are resistant to general corrosion, they are susceptible to localized forms of corrosion, such as SCC, in the presence of halides. Since halide

concentrations sufficient to cause SCC could conceivably develop from relatively dilute groundwater, scoping experiments were conducted to investigate the performance of Type 304L stainless steel in the presence of concentrated tuff groundwater.

3.3.2 Approach and Results

Stress-corrosion cracking experiments were performed on Type 304L stainless steel in a simulated tuff groundwater. Two specimen geometries were used; U-bends and cylindrical slow strain rate (SSR) specimens. The U-bend specimens had dimensions of 12.5 cm by 1.91 cm by 0.159 cm, with 0.79-cm holes drilled 1.9 cm from each end, and they contained longitudinal welds. Prior to welding, surfaces were abraded through 120-grit silicon carbide. The U-bend specimens were bent and stressed as described in ASTM-G30; the U-bends were bent in a jig such that the legs were 25 degrees off parallel. A 0.63 cm-diameter Type 304L stainless steel bolt was then inserted into the drilled holes, and tightened such that the legs were parallel. The bolt was electrically isolated from the specimens with PTFE washers. The slow strain rate specimens were cylindrical and had dimensions of 0.635 cm diameter, by 18.4 cm long, with a centered reduced-gauge section 0.254 cm in diameter by 2.54 cm long. The specimen surfaces were abraded with 120-grit silicon carbide finish. Compositions and mechanical properties for the specimen materials are in Table 3.49. The composition of the test solution is in Table 3.50.

Three types of SCC experiments were performed with heated stainless steel specimens: slow strain rate experiments, drip experiments, and wick experiments. In the drip tests, U-bend specimens of Type 304L stainless steel were hung over a 1,000-watt bayonette type heater; the specimens were electrically isolated from the heater with PTFE sheathing. A thermocouple was attached to one of the specimens and the specimens were heated to 150 C. Tuff groundwater was dripped onto the highly stressed region of each specimen at a rate of 1 drop/80 seconds. The specimen remained wet for about 50 seconds after each drop.

Two drip tests were performed with duplicate specimens; one under fully aerated conditions and one under partially aerated conditions (two parts nitrogen and one part air). The latter test condition was used because austenitic stainless steels may be more susceptible to SCC under partially reducing conditions than under aerated conditions in some chloride-containing environments. Total test durations were 3,000 hours and 1,000 hours respectively, for the fully aerated and partially aerated tests. Although deposit build-up was evident on the specimens, no evidence of SCC or other forms of localized corrosion were found following the exposure periods.

A single wick test was performed on two U-bend specimens of Type 304L stainless steel in tuff repository groundwater at boiling temperature. A procedure was used in which the specimens were wrapped around a cylindrical 1000-watt heater and placed in contact with a glass wool wick, part of which was immersed in the tuff groundwater. The specimens were electrically isolated from the heater with PTFE sheathing. In 403 hours of exposure, no SCC or

Table 3.49. Compositions and mechanical properties for Type 304L stainless steel stock used in the SCC tests.

Specimen Type	Composition, Weight Percent														Heat	Tensile Strength, ksi	Yield Point	Reduction in Area	Elong., %
	C	Mn	P	S	Si	Cr	Ni	Mo	Cu	N	Co	Cb	Ti	Fe					
SSR	0.022	1.55	0.024	0.025	0.63	18.31	9.26	0.36	0.46	0.072	0.16	0.01	0.002	Bal.	D343	114.0	97.0	68.3	39.0
U-Bend	0.020	1.39	0.022	0.015	0.54	18.27	9.44	0.10	0.47	0.023	0.18	--	--	Bal.	D489	81.9	38.9	--	59.0

Table 3.50. Nominal composition of simulated tuff groundwater.

Ion	Concentration (ppm)
Na	46
K	5.5
Mg	1.7
Ca	12
Cl	6.4
SO ₄	19.2
HCO ₃	121
CO ₃	0
Br	--
F	1.9
NO ₃	12.4
SiO ₂	64.2
pH	7.0

localized corrosion was evident on the specimens, although significant deposit formation had occurred.

Finally, a single SSR test was performed on a heated Type 304L stainless steel specimen in a tuff groundwater at a strain rate of $1 \times 10^{-7} \text{ sec}^{-1}$ and at a temperature of 175 C. The tuff groundwater was ultrasonically atomized under partially aerated conditions (two parts nitrogen and one part air). The specimen, which was electrically isolated from the heater with PTFE sheathing, was heated by contacting the gauge section with a small bayonette heater. No evidence of SCC was found on the specimen. The specimen failed ductally after 684 hours with 53.6 percent reduction in area.

In summary, three types of stress-corrosion tests were performed on Type 304L stainless steel in simulated tuff groundwater that dried and deposited onto the specimens. These tests were performed under two conditions; fully aerated and partially aerated. No evidence of SCC was found in any of the tests performed.

3.4 References for Chapter 3

- (3.1) J. W. Braithwaite, N. J. Magnani, and J. W. Mumford, "Titanium Alloy Corrosion in Nuclear Waste Environments," Corrosion/80, Paper No. 213, National Association of Corrosion Engineers, Houston, TX.
- (3.2) T. M. Ahn, and P. Soo, "Container Assessment-Corrosion Study of HLW Container Materials," NUREG/CR-2317, BNL-NUREG 51449, 1981.
- (3.3) A. Harris and M. A. Finan, "A Theory of the Formation of Magnesium Scales in Seawater Distillation Plants, and Means of Their Prevention," Desalination 14, 325 (1974).
- (3.4) R. A. Wood, D. H. Williams, H. R. Ogden, and R. I. Jaffe, "Porosity in Formed Titanium," TML Report No. 72, BMI, May 17, 1957.
- (3.5) J. A. Beavers, N. G. Thompson, and R. N. Parkins, "Stress-Corrosion Cracking of Low-Strength Steels in Candidate High Level Waste Repository Environments," Topical Report, NUREG/CR-3861, February 1987.
- (3.6) T. E. Jones, "Reference Material Chemistry--Synthetic Groundwater Composition," RHO-BW-St-37 P (April 1982).
- (3.7) "Long-Term Performance of Materials Used for High-Level Waste Packaging," D. Stahl and N. E. Miller (Compilers), NUREG/CR-3427, Vol. 1, June 1984.
- (3.8) "Appendix D: Range of Environmental Parameters," Draft NUREG-1076, ORNL, 1984.
- (3.9) T. E. Jones, Personal Communication to J. Means, Battelle Columbus Division, 1983.
- (3.10) W. J. Gray, "Gamma Radiolysis Effects on Grande Ronde Basalt Groundwater," RHO-BW-SA-315 P (presented at the Materials Research Society Symposium-Scientific Basis for Nuclear Waste Management, Boston, MA, November 14-17, 1983).
- (3.11) S. A. Simonson and W. L. Kuhn, "Predicting Amounts of Radiolytically Produced Species in Brine Solution," PNL-SA-11426 (presented at the Materials Research Society Symposium-Scientific Basis for Nuclear Waste Management, Boston, MA, November 14-17, 1983).
- (3.12) E. P. Grause, C. Brewster, and P. Soo, "Determination of the Waste Package Environments for a Basalt Repository: Phase 1--Gamma Irradiation Conditions in the Absence of Methane," BNL-NUREG-24297, Draft Report (February 1984).
- (3.13) NRC Nuclear Waste Geochemistry '83, Proceedings of the U.S. Nuclear Regulatory Commission, Reston, VA, August 1983, p. 245.

- (3.14) "Long-Term Performance of Materials Used for High-Level Waste Packaging," D. Stahl and N. E. Miller (Compilers), NUREG/CR-3900, Vol. 4 (July 1985).
- (3.15) "Long-Term Performance of Materials Used for High-Level Waste Packaging," D. Stahl and N. E. Miller (Compilers), NUREG/CR-4329, Vol. 2 (January 1986).
- (3.21) P. J. Bradley et al., "Nuclear Waste Package Materials Testing Report: Basaltic and Tuffaceous Environments," PNL-4452 (March 1983).
- (3.22) R. N. Parkins, "Environmental Aspects of Stress-Corrosion Cracking in Low Strength Ferritic Steels," Stress-Corrosion Cracking and Hydrogen Embrittlement of Iron Base Alloys, R. W. Staehle, et al. (ed.), NACE, p. 601, 1977.
- (3.23) R. N. Parkins, "Predictive Approaches to Stress Corrosion Cracking Failure," Corrosion Science 20, 2, 147 (1980).
- (3.24) G. H. Koch, N. G. Thompson, and J. L. Means, "Trace Elements in Flue Gas Desulfurization Environments and Their Effect on Corrosion of Alloys," EPRI Research Project RP1871-6, to be published December, 1984.
- (3.25) F. P. Ford, "Stress Corrosion Cracking," Corrosion Processes, R. N. Parkins (ed.), Applied Science Publisher (1982).
- (3.26) T. Furuya et al., "Study of X-Ray Radiation Effects on Corrosion Resistance of Alloys for Storage of High-Level Waste Packages," JAERI-M 82-061, May 1982.
- (3.27) M. B. Strauss and Bloom, M. C., "Cracking of Low Carbon Steel by Ferric Chloride Solutions," Corrosion 16, 11, 553t (1960).

4. INTERNAL CANISTER CORROSION

The amount of corrosion that will occur in the inside wall of a canister containing high-level radioactive waste is difficult to predict for two reasons: (1) there are few experimental data applicable to the long-term intermediate temperature conditions to which the interior of the canister will be subjected, and (2) a simple extrapolation of high-temperature results may give misleading information at lower temperatures because different corrosion mechanisms may be involved.

During the filling process, the canister will be in contact for a short time with the molten glass containing the high-level waste at high temperatures. To the extent that corrosive agents are present at the metal-glass interface during the solidification period, attack of the container may be initiated during filling and cool-down of the canister. The initiation of pits in the metal surface at the start of exposure could have a significant effect on the lifetime of a canister, particularly if the material responsible for initiating the pits is readily available in the waste glass. Thus, the general approach to the problem of internal corrosion was to investigate metal surface attack under accelerated conditions and utilize these data to develop a model to predict canister life.

In the course of studies focused on the high-level waste storage problem at DOE sites for several years, Type 304L stainless steel emerged as the prime candidate material for the canister. This choice resulted from considering the alloy properties required for the canister and the relative costs of the candidate materials. Consequently, research was directed toward investigating Type 304L stainless steel.

4.1 Background

Some experiments have been conducted with simulated waste glasses to investigate the performance of various alloys that have been suggested as canister materials. This research was performed primarily at the Savannah River Laboratory and the Pacific Northwest Laboratory, where the technology for radioactive waste storage is being developed. These experiments have included Type 304L stainless steel, so experimental data on this alloy are available for a number of exposure conditions.

In addition to this information on waste glass exposures, data are also available in the literature on high-temperature corrosion of Type 304 stainless steel by various compounds. These data can be used to determine which constituents of a waste form can be particularly corrosive to the canister interior.

4.1.1 Savannah River Laboratory (SRL) Data

Several alloys, including Type 304L stainless steel, were investigated as candidate canister materials at the Savannah River Laboratory (SRL) (Ref. 4.1). Oxidation of Type 304L stainless steel by air entrapped during the canister-filling process was evaluated from literature data. The authors at SRL calculated that an oxide layer from 0.25 to 0.64 mm (10 to

25 mils) in thickness would be formed on the stainless steel during the filling of a canister by the continuous melting of the waste glass.

Exposure tests in which a waste glass was heated in stainless steel capsules at 100 C and 350 C for periods up to 10,000 hours resulted only in formation of a thin corrosion layer, on the order of 13 μm (0.5 mil). However, tests of the in-can melting approach by heating at 1150 C for 3 hours showed that wall thinning amounting to 25 to 50 μm (1 to 2 mils) would occur in Type 304L stainless steel during the process.

Follow-on investigations at SRL to determine the long-term effects of both actual and simulated waste glasses on Type 304L stainless steel and two low-carbon steels also were conducted (Ref. 4.2). These tests were designed to provide information pertinent to the continuous melting process.

Short-term tests at high temperature also were performed at SRL to compare the corrosive effect of pure glass frits with that of a combination of frit and simulated waste (Ref. 4.3). Four frits, whose compositions are shown in Table 4.1, were used in the tests. Type 304L stainless steel was exposed to each of the frits for 24 hours at 1050 C. The depth of penetration of the steel that resulted from the exposures ranged from 0.33 to 0.67 mm (13.5 to 26.7 mils). The extent of penetration was found to be approximately proportional to the Na_2O content of the frit.

Table 4.1. Composition of glass frits used at Savannah River Laboratory.

Metal Oxide	Amount in Frit (Weight Percent)			
	No. 18	No. 211	No. 21	No. 411
SiO_2	52.5	58.3	52.5	58.3
Na_2O	22.5	20.6	18.5	12.5
B_2O_3	10.0	11.1	10.0	11.1
TiO_2	10.0	--	10.0	--
CaO	5.0	5.6	5.0	5.6
Li_2O	--	4.4	4.0	12.5

The effect of exposure time at 1050 C also was observed during this work at SRL. The penetration of the stainless steel as a function of time is shown in Figure 4.1. Although there was a good deal of scatter in the data, the general pattern for the four frits indicates that the slope is about the same for all of them. Protective oxide layers apparently were not developed in the 24-hour period because there was no indication that the rate of penetration was decreasing as time progressed.

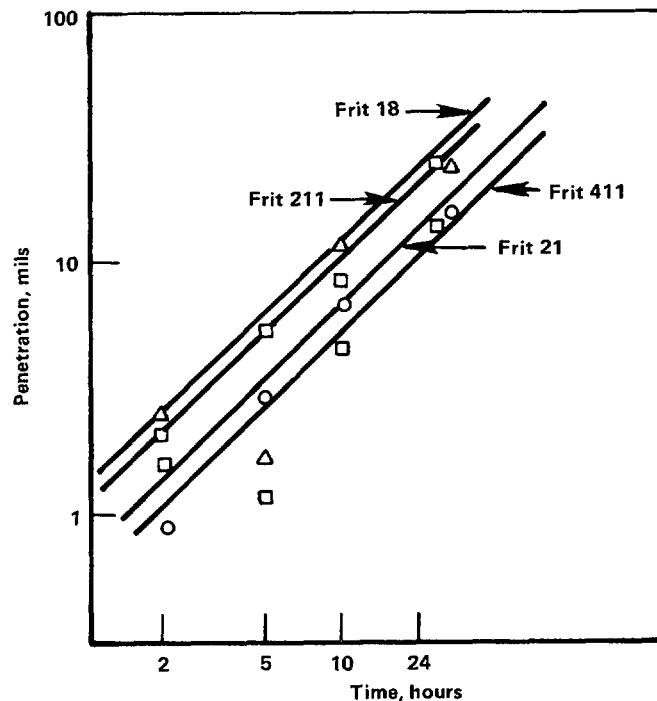


Figure 4.1. Penetration of Type 304 stainless steel as a function of exposure time at 1050 C.

When simulated waste was incorporated into Frit 411 to form a waste glass, the penetration of the stainless steel was reduced significantly. Whereas the pure frit caused a 0.33-mm (13.5-mil) penetration in 24 hours at 1050 C, the combination of 75 weight percent frit and 25 weight percent waste resulted in only a 0.04-mm (1.7-mil) penetration. The reason for this reduction in corrosiveness was not determined, but because the main components of the simulated waste were iron, aluminum, manganese, calcium, and nickel, it is possible that the iron and aluminum combined with the sodium oxide to form ferrite and aluminate, thereby reducing attack by the alkali.

The Type 304L stainless steel also was exposed to Frit 211 at 1150 C. This frit has the highest Na_2O content of those under consideration and thus is potentially the most corrosive. After 24 hours, the penetration of the alloy amounted to 0.44 mm (17.6 mils), as compared to the 0.65 mm (25.9 mils) found at 1050 C for this frit. Differences such as this illustrate the difficulty in obtaining accurate measurements of corrosive attack where penetration by pitting rather than general surface corrosion is the mode of attack.

4.1.2 Pacific Northwest Laboratory Data

The work at Pacific Northwest Laboratory (PNL) has focused on the in-can melting process, where the container would be subjected to the molten glass temperature for about 24 hours. Both surface oxidation by air and attack by the molten glass were considered in their program.

Type 304L stainless steel was found to corrode at rates up to 35 mm/yr (1400 mils/yr) on exterior surfaces of engineering-scale canisters heated to 1075 C in air (Ref. 4.4). This rate amounts to 0.1 mm (4 mils) of metal wastage during the 24-hour exposure which would occur during the in-can melting process.

The effect of 72-68 waste glass on the Type 304L stainless steel at temperatures from 950 to 1150 C was also studied at PNL. As shown in Figure 4.2, the metal wastage rate increased rapidly with temperature in this range. Slightly higher rates occurred in areas exposed to the melt than in areas exposed to the vapor above the glass. The values for the melt exposure, converted to the amount of wastage in a 24-hour period, are shown in Table 4.2.

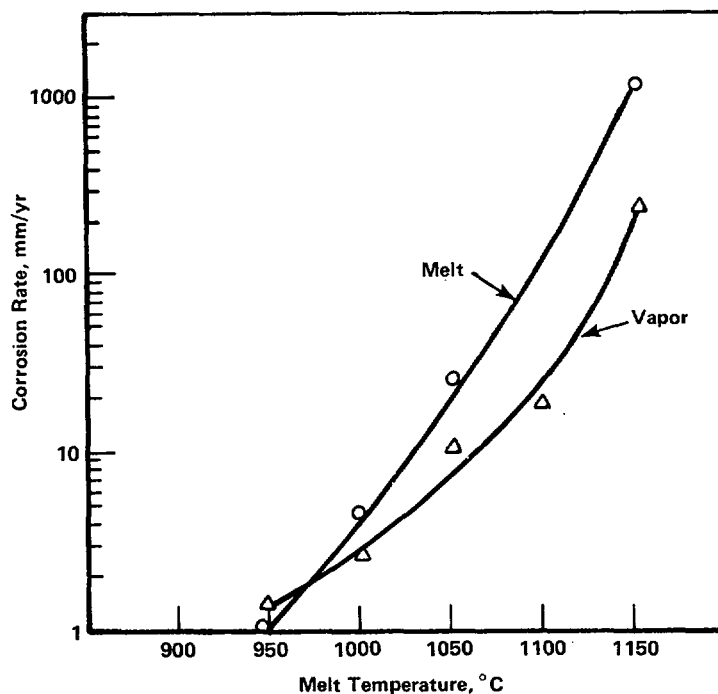


Figure 4.2. Corrosion rate of Type 304 stainless steel in 72-68 waste glass as a function of temperature.

Table 4.2. Wastage of Type 304 stainless steel in 72-68 waste glass over a 24-hour period.

Temperature (C)	Wastage	
	mm	mils
950	0.003	0.1
1000	0.013	0.5
1050	0.074	2.9
1100	0.30	12.1
1150	3.15	126.0

These data indicate that there would be a significant initiation of attack on the stainless steel during the melting process, particularly if the melt temperature was not well controlled. Exposures of the stainless steel to two other waste glass compositions at 700 C for 1 month resulted in corrosion rates of 10 and 15 $\mu\text{m}/\text{yr}$ (0.4 and 0.6 mils/yr).

The corrosiveness of cesium-bearing glass also was investigated at PNL. A melt of zinc-containing frit (1 part) and cesium carbonate (0.95 part) was held at 900 C for 300 hours in contact with specimens of Type 304L stainless steel. The melt and vapor phase attack amounted to 0.06 and 0.5 mm/yr (2.4 and 20 mils/yr), respectively. Intergranular penetration was 0.13 mm (5.2 mils) as well. However, when the temperature of exposure was reduced to 400 C, the corrosion rate in the melt dropped to $<2.5 \mu\text{m}/\text{yr}$ (0.1 mil/yr). Although the attack by cesium vapor would be less at the canister storage temperature than was found in these experiments, it could still be important in very long exposure times.

Other experiments conducted at PNL with additions made to a waste glass to test the effects of specific components on the stainless steel gave the following results:

- (1) One percent NaCl at 1000 C gave a corrosion rate of 0.64 mm/yr (25.6 mils/yr) as compared to 0.73 mm/yr (29.2 mils/yr) for the waste glass without additive. There was evidence that a volatile chloride escaped from the melt, probably as a molybdenum or zirconium compound, thus reducing the effect of the chloride and making the validity of the test questionable.
- (2) One percent NaF at 1000 C gave a corrosion rate of 5.3 mm/yr (212 mils/yr) and caused intergranular attack.
- (3) Silicon (1.5 weight percent) and Zircaloy-4 (20 weight percent) caused intergranular attack on stainless steel when exposed for

48 hours at 1050 C. The depth of penetration was 50 to 75 μm (2 to 3 mils).

The NaF was by far the most aggressive of the added materials which were tried, and its presence in a waste glass may be a significant cause of corrosion, even at the low temperatures of long-term storage.

4.1.3 Oak Ridge National Laboratory Data

The compatibility of candidate canister metals with several different waste forms was investigated at the Oak Ridge National Laboratory (Refs. 4.5,4.6). Experiments were conducted by placing metal specimens in contact with disks of the waste forms in spring-loaded capsules. The test exposures were made at temperatures of 100 C and 300 C for 6888 or 8821 hours. A one-half hour test at 800 C was made to simulate exposure to an accidental fire.

The results of these exposures showed that the effects of a simulated waste glass on Type 304L stainless steel under such exposure conditions were very slight. In the test at 100 C, a weight gain of less of 1 mg was attributed to oxide formation, although it was not enough to change the metallic luster of the samples. Similar results were obtained in the tests of 300 C, which had a duration of 6888 hours. Scanning electron microscopy (SEM) and energy-dispersive analysis by X-ray (EDAX) showed that the appearance of the specimens and the chemical composition of the surface were the same as observed for the original material.

In the test at 800 C for 0.5 hour, the glass melted and adhered to the metal, so the post-test examination was limited to microscopic examination of a mounted section. No evidence was found of any reaction between the glass and the stainless steel as a result of this exposure.

4.1.4 Miscellaneous Data

There are data in the literature on the attack of various chemical compounds on Type 304 or 304L stainless steel under different conditions of time and temperature. In most cases, the results have been expressed as corrosion rates of the alloy. These data are presented in Table 4.3. All of the materials listed showed rates of attack on the stainless steel that would be significant over long-term exposure.

4.2 Experimental Approach

The experimental investigation of internal canister corrosion was carried out by exposing metal coupons to a reference waste glass under a range of temperature conditions. The corrosive effects of the waste glass on the coupons were determined by measurement of pit depths. The mechanism of the corrosive attack was studied by analyzing the corrosion products using EDAX-SEM.

Table 4.3. Corrosion rates of Type 304 or 304L stainless steel exposed to various corrosive agents.

Corrosive Agent	Temperature (C)	Time (hr)	Corrosion Rate	Reference
NaCl-KCl-MgCl ₂ (eutectic)	450-500	1000	10 $\mu\text{m}/\text{yr}$	4.7,4.8
NaCl	700	10	1.5 $\mu\text{m}/\text{hr}$	4.9
KCl	700	10	1.0 $\mu\text{m}/\text{hr}$	4.9
MgCl ₂	700	10	3.5 $\mu\text{m}/\text{hr}$	4.9
Sodium hexametaphosphate	700	120	3.8 $\text{mg}/\text{cm}^2\text{-hr}$	4.10
Sodium polyphosphate	700	120	1.5 $\text{mg}/\text{cm}^2\text{-day}$	4.10
NaOH	400	680	78.4 $\text{mg}/\text{dm}^2\text{-day}$	4.11
NaOH	600	170	>1000 $\text{mg}/\text{dm}^2\text{-day}$	4.11
Sodium metal	816	1000	0.05 $\mu\text{m}/\text{hr}$	4.12
Potassium metal	850	--	2.5-15 $\mu\text{m}/\text{hr}$	4.13,4.14
Fluoride mixture	668-688	10000	38 $\mu\text{m}/\text{yr}$	4.15
Fluoride mixture	668-688	30000	25 $\mu\text{m}/\text{yr}$	4.15
Na ₂ SO ₄ + 1% NaCl	538	250	1.1 mm/yr	4.16
CaO	843	1000	0.8 mm/yr	4.17

4.2.1 Materials

Coupons of Type 304L stainless steel having the nominal dimensions 3.81 cm x 2.54 cm x 0.238 cm were used for the experiments. The specimens were polished to a 600-grit finish before use. Crucibles of Type 304L stainless steel were fabricated by welding bases on short lengths of tubing. The certified analysis for the stainless steel sheet and tubing that were used for the specimens and the crucibles are shown in Table 4.4.

A few specimens also were prepared from CF8 alloy, which is the cast equivalent of Type 304L stainless steel. Some consideration has been given to casting high-level waste canisters from the large supply of contaminated Type 304 stainless steel. Thus, some evaluation of CF8 alloy was made in this study. The composition of the CF8 alloy is shown in Table 4.5. This alloy contained substantially more chromium and slightly less nickel than the Type 304L stainless steel.

A supply of PNL 76-68 reference simulated waste glass, obtained from PNL, was used for the coupon exposures. This glass is composed of two parts Frit

Table 4.4. Certified analyses of Type 304L stainless steel.

Component	Weight Percent	
	Sheet	Tubing
Carbon	0.017	0.016
Manganese	1.44	1.72
Phosphorus	0.026	0.024
Sulfur	0.010	0.013
Silicon	0.58	0.43
Chromium	18.29	18.64
Nickel	8.63	8.66
Molybdenum	0.29	--

Table 4.5. Certified analysis of CF8 alloy.

Component	Weight Percent
Carbon	0.052
Manganese	0.069
Phosphorus	0.119
Sulfur	0.017
Silicon	0.93
Chromium	20.59
Nickel	8.48
Molybdenum	0.11

76-101 and one part Waste Type PW-8a. The chemical composition of the particular lot of glass from which the supply was obtained is shown in Table 4.6.

4.2.2 Test Planning

A baseline experiment for the program was developed. The responses were the extent of pitting corrosion and chemical species present in pitted areas. The primary experimental variables were exposure temperature and time. For each temperature, the extent of corrosion was studied at multiple times. The maximum test temperature was 900 C. Based on data reported in the literature, a tentative average trend curve of general corrosion versus time was derived for planning purposes. Tentative exposure times at 900 C were established based on this curve. These exposure times proved to be adequate.

4.2.3 Laboratory Procedure

The metal coupons were exposed to the waste glass by heating in muffle furnaces at temperatures of 900, 700, 500, and 300 C. Approximately 120 g of the glass was melted in each crucible at 1000 C, and two metal specimens were then immersed in each crucible. The exposure times for the different temperatures were based on the assumption of an Arrhenius relationship for temperature effects and were as follows:

<u>900 C</u>	<u>700 C</u>	<u>500 C</u>	<u>300 C</u>
400 hrs	470 hrs	620 hrs	974 hrs
750	890	1172	1826
1330	2664	2065	3273
1930			

The third set of specimens at 700 C was inadvertently exposed longer than the planned 1580 hours.

Six specimens were removed from exposure at each of the times indicated and were taken from different regions of the furnace. When the specimens were removed from the crucibles, the glass adhered to the surfaces in different amounts for the various specimens. Most of this glass could be broken away, but enough remained so that weight change measurements could not be used as a measure of the metal corrosion. Consequently, pit-depth measurements were made to determine the extent of corrosive attack on the specimens.

Each specimen was sectioned across the width at the center line and one of the cut surfaces was mounted and polished. The edges which had been in contact with the glass were then examined for pitting attack using an optical microscope. The measurements were made at a magnification of 200X using a microscope equipped with a calibrated eyepiece.

Table 4.6. Composition of PNL 76-68 glass.

Oxide	Average Analysis of 3 Bars (percent)	Standard Deviation (percent)
Al ₂ O ₃	0.84	0.03
B ₂ O ₃	8.65	0.06
BaO	0.62	0.01
CaO	2.29	0.04
CdO	0.05	0.01
Cr ₂ O ₃	0.50	0.02
Cs ₂ O	1.21	0.08
Dy ₂ O ₃	0.01	0.00
Eu ₂ O ₃	0.01	0.00
Fe ₂ O ₃	9.08	0.12
Gd ₂ O ₃	0.03	0.01
K ₂ O	0.09	0.03
La ₂ O ₃	4.89	0.06
MgO	0.18	0.01
MnO ₂	0.06	0.00
MoO ₃	2.17	0.01
Na ₂ O	11.60	0.95
Nd ₂ O ₃	1.65	0.01
NiO	0.25	0.03
P ₂ O ₅	0.56	0.08
SiO ₂	40.33	0.81
SrO	0.49	0.01
TiO ₂	2.86	0.04
ZnO	4.75	0.08
ZrO ₂	<u>2.33</u>	0.04
Total	95.50	

4.3 Results and Discussion

4.3.1 Pit-Depth Measurements

In all specimens, a relatively large number of small pits having depths of 5-10 μm were observed. The numbers of such pits increased with exposure time at each temperature, as would be expected. The effect of exposure time on pit development at 900 C is shown in Figure 4.3, where the pit distribution along the center line of the two worst specimens is plotted for each of the four exposure times. There was a reasonably uniform increase in the number of pits less than 20 μm depth as the time increased from 400 to 1930 hours. However, for deeper pits the growth pattern was erratic. There was a large increment in the moderate-depth pitting between 400 and 750 hours, after which the numbers stayed about the same. The deeper pits (60-150 μm) were relatively few, and the increase with time was small. Nevertheless, the deep pits are the most important in determining the rate at which the stainless steel will be penetrated by the corrosive attack of the waste glass.

The results at 700 C are shown in Figure 4.4. More small pits were observed at this temperature than at 900 C, but there were very few pits deeper than 10 μm in the 700 C specimens. This rapid drop in pit-depth growth at the lower temperature indicates that, although pit initiation occurs readily at 700 C, there is little driving force to increase the pit depth. As Figure 4.4 illustrates, there were very few pits deeper than 20 μm , with a single pit that reached a depth of 100 μm .

At 500 C, the number of 5-10 μm pits was approximately proportional to exposure time, as shown in Figure 4.5. As at the other temperatures, there was a sharp drop in the number of larger pits, and in spite of the long exposure time, only one was detected that grew as deep as 40 μm .

The pit development at 300 C is presented in Figure 4.6. As at the other temperatures, there was a significant increase in the number of small pits as the exposure time was lengthened. However, in this case, no pits greater than 20 μm depth were observed, and there were relatively few pits in the 15-20 μm range.

When the maximum pit depths for each time-temperature combination are converted to penetration rates in micrometers/year, the resulting data produce the curves shown in Figure 4.7. The maximum penetration rates plotted as a function of exposure time at the four temperatures make a family of curves that illustrate the rapid decrease in corrosive attack on the stainless steel as the temperature is lowered. From the trend of these curves it could be estimated that, at a canister wall temperature of 100-150 C, the long-term rate of attack would be of the order of 10-15 $\mu\text{m}/\text{year}$.

The maximum penetration rates for the longest exposure times at each of the four temperatures are plotted as a function of temperature in Figure 4.8. These data result in a curve which indicates that a penetration rate of 15-20 $\mu\text{m}/\text{year}$ would occur at a temperature of 200 C.

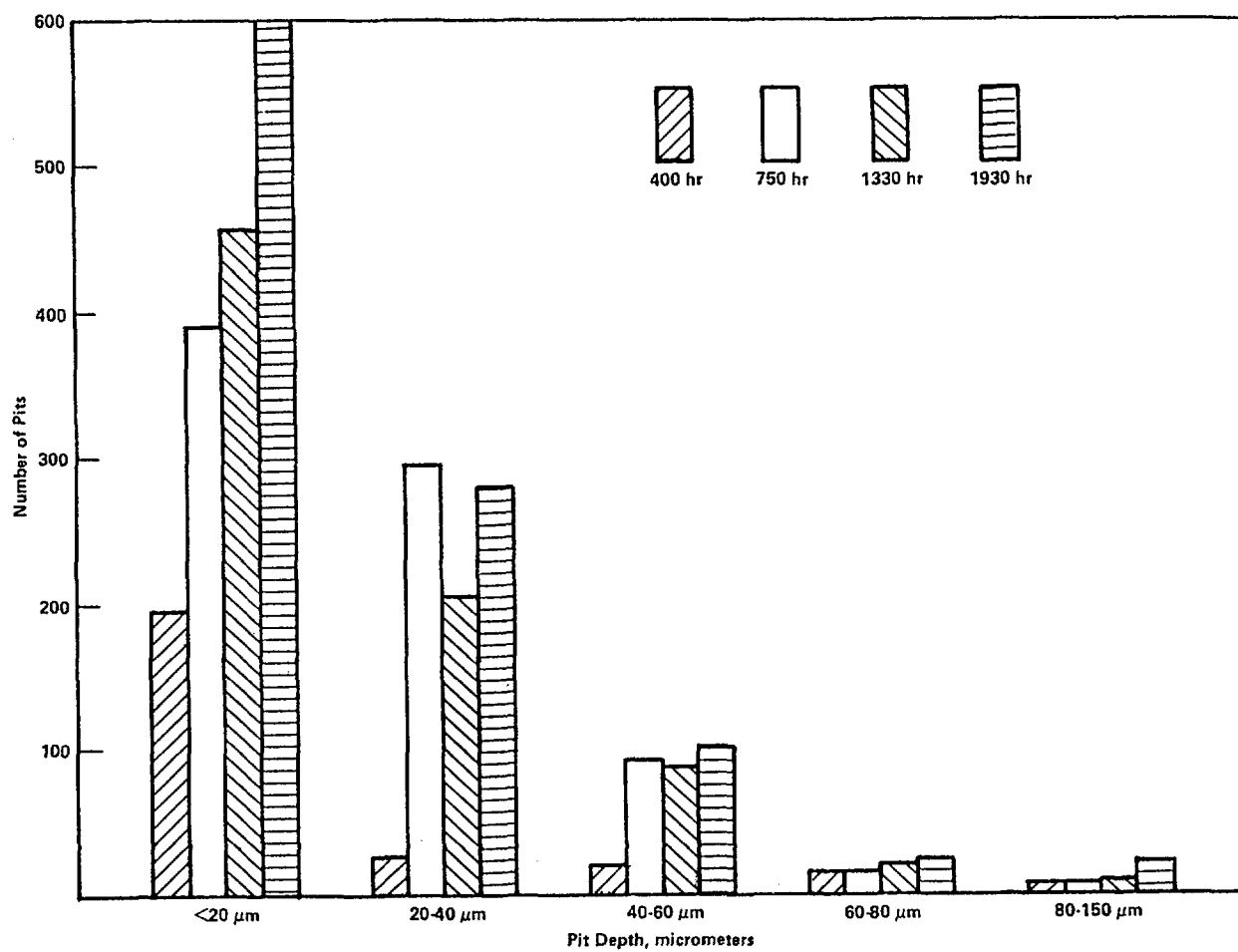


Figure 4.3. Effect of exposure time on pit development at 900 C.

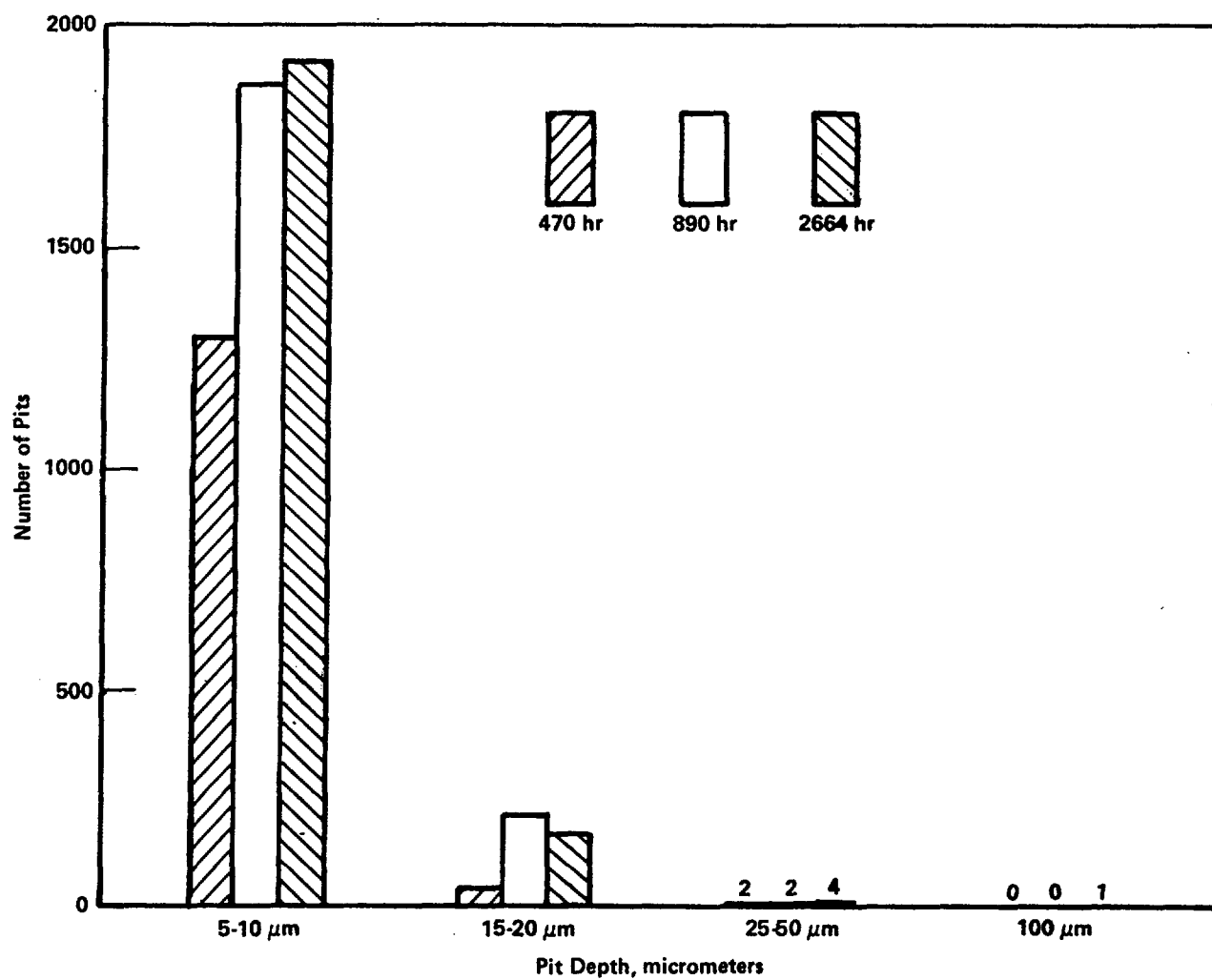


Figure 4.4. Effect of exposure time on pit development at 700 C.

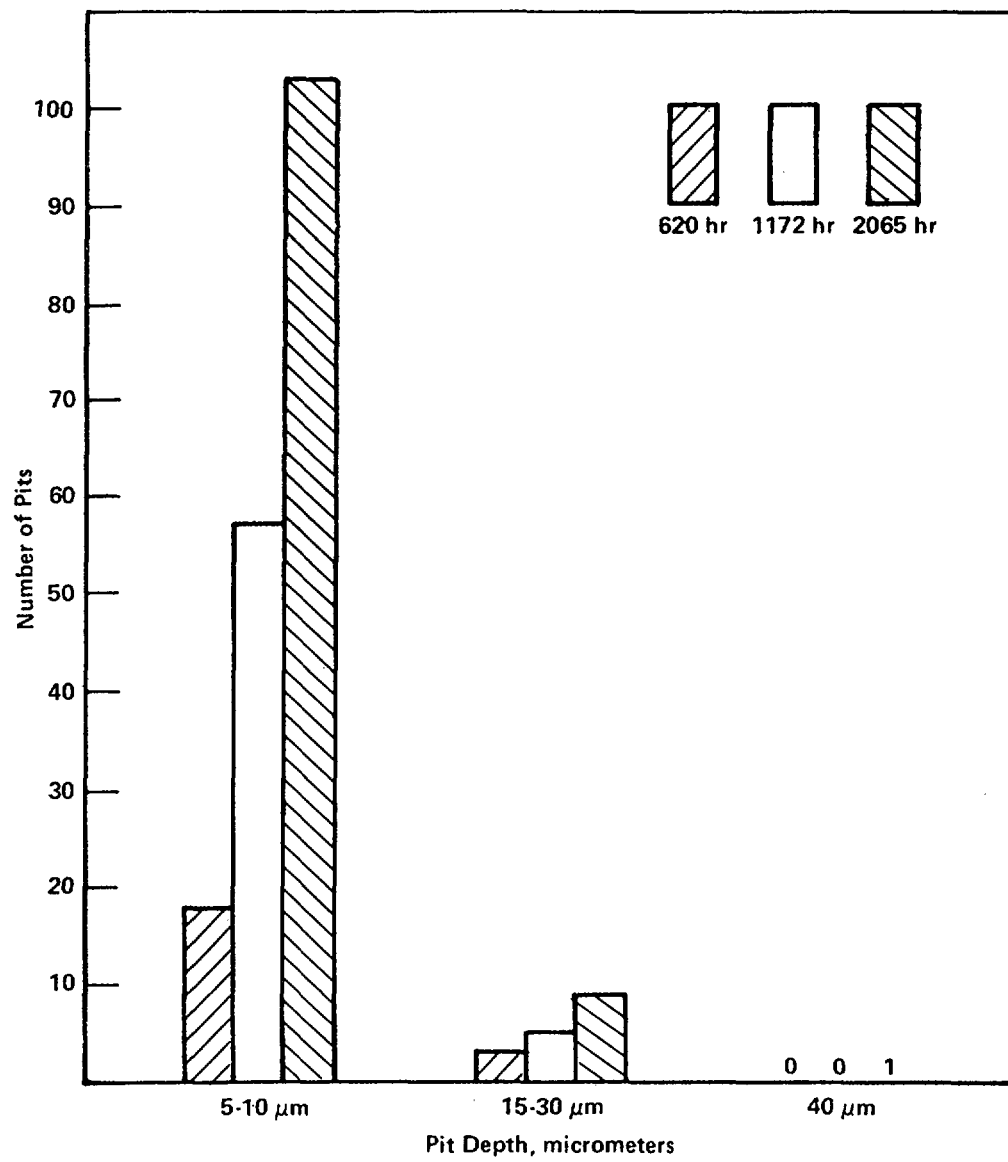


Figure 4.5. Effect of exposure time on pit development at 500 C.

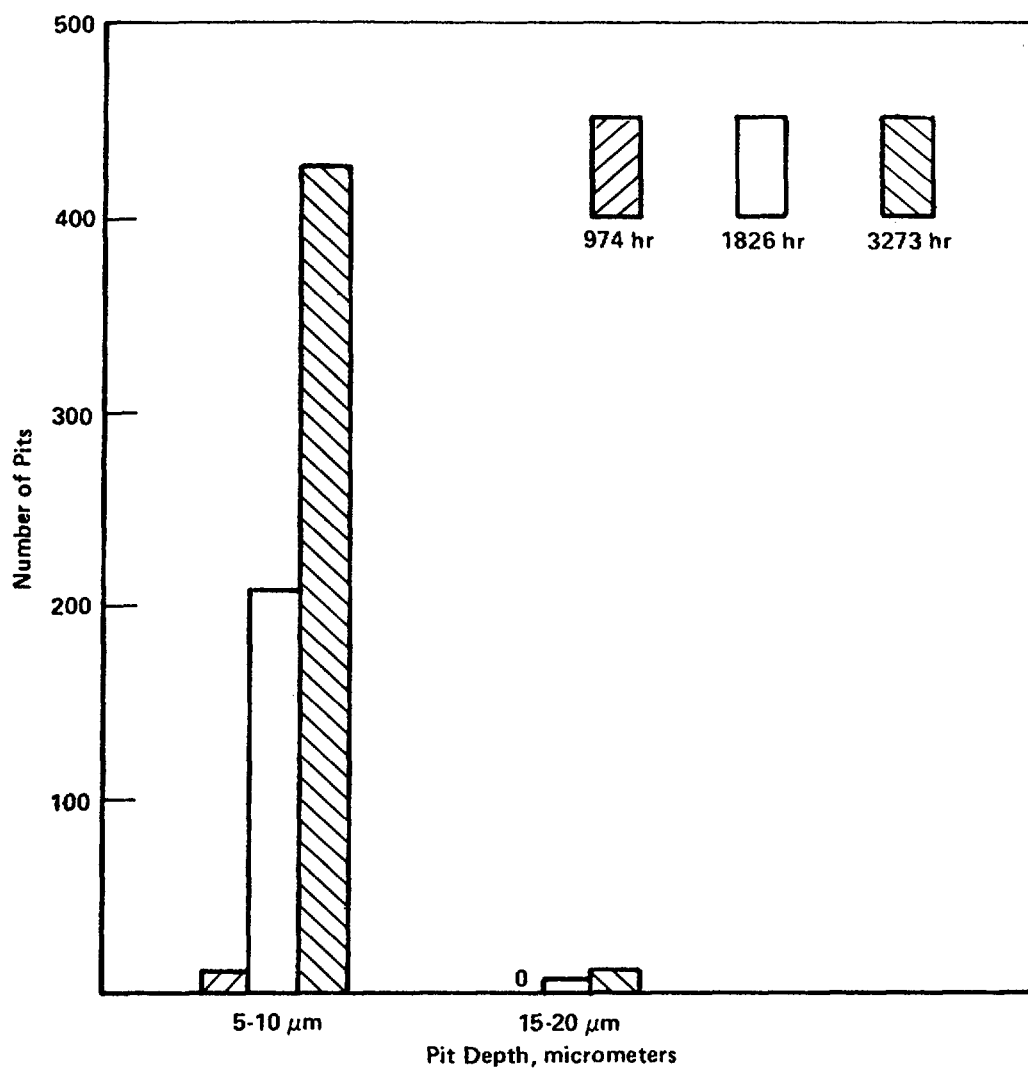


Figure 4.6. Effect of exposure time on pit development at 300 C.

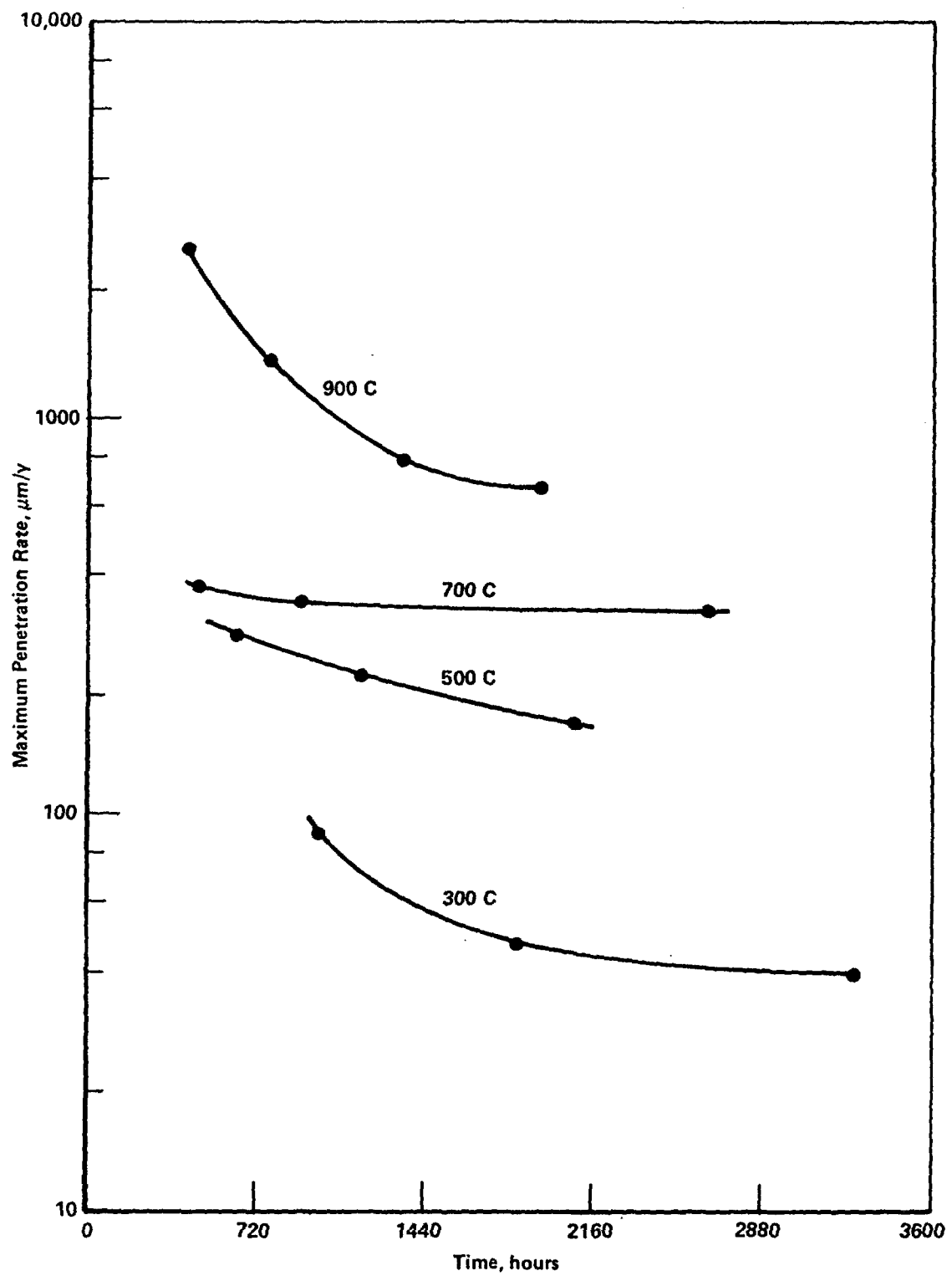


Figure 4.7. Pitting penetration rates as a function of time.

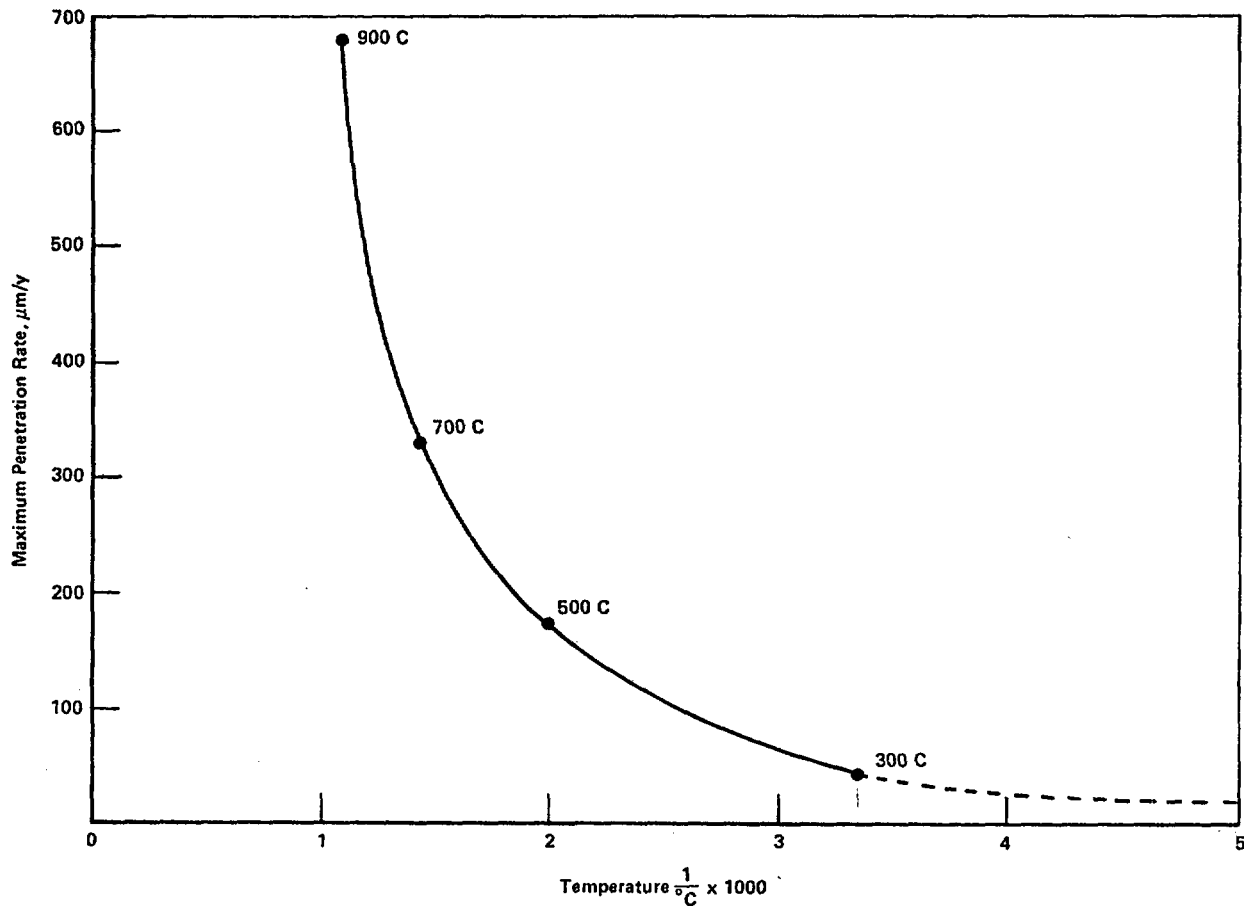


Figure 4.8. Pitting penetration rates for longest exposure times as a function of temperature.

When a curve was fitted to these four points, the best fit proved to be an exponential having the following rate equation:

$$\mu\text{m/yr} = 878.734 \left(\frac{1000}{T} \right)^{-2.535}$$

Calculation of the penetration rate at 200 C from this equation gives a value of 14.8 $\mu\text{m}/\text{yr}$. At 150 C, the rate would drop to 7.2 $\mu\text{m}/\text{yr}$ from this calculation. This latter value is somewhat lower than that estimated in Figure 4.7. The result obtained from the curve fitting is probably more valid than that obtained by estimating the temperature trends shown in Figure 4.7.

It has been suggested that a 3/8-inch (9525 μm) wall thickness of the stainless steel be used for the canister. If there were to be a constant pit penetration rate as high as 14.8 $\mu\text{m}/\text{year}$, such a wall thickness would be penetrated in 643 years. If the rate were only 7.2 $\mu\text{m}/\text{year}$, it would take 1330 years for penetration. These times may be conservatively short, because they assume a constant diffusion of corrosive agents to the glass-metal interface.

It should be emphasized that the maximum rates used to obtain the plots in Figures 4.7 and 4.8 occurred for only a few pits at each temperature. Consequently, if such attack rates were achieved at the canister wall for the long term, there would still only be relatively few points of penetration.

4.3.2 Corrosion-Product Analysis

One of the mounted and polished specimens from each time-temperature combination was examined in the scanning electron microscope. Typical pits were selected, and the composition of the corrosion products in these pits was determined by EDAX analysis.

All specimens were examined by SEM, and the elemental analyses of the corrosion products were determined. A typical pit in a specimen exposed for 400 hours at 900 C, as shown in Figure 4.9, contained the iron, chromium, and nickel of the base metal, plus silicon and zinc from the glass. Two distinct phases were observed in the glass which adhered to the specimen. The light-colored phase A was largely silicon, titanium, praseodymium, and iron. The dark-colored phase B was mostly silicon and iron, with moderate amounts of zinc and lead. Neither of these compositions is typical of the bulk glass, and it is likely that other phases exist in the waste glass. Another pit in the same specimen contained a large amount (21.36 percent) of zinc in addition to the base metal components. This concentration of zinc is 5.6 times that present in the waste glass.

Pit growth increased with an exposure of 750 hours as compared to 400 hours. The longer exposure also resulted in a higher concentration of zinc in the pit. A small amount of sulfur also was present in the 750-hour specimen.

Extending the exposure to 1330 hours resulted in a typical pit having a greater volume but not greater depth than that at 750 hours. The zinc concentration was about the same in both cases, but the longer exposure resulted in more silicon in the corrosion products. Titanium appeared instead of sulfur.

After 1930 hours (Figure 4.10), the pit depth was substantially greater. Note that the magnification is 200X rather than 1000X. The amounts of

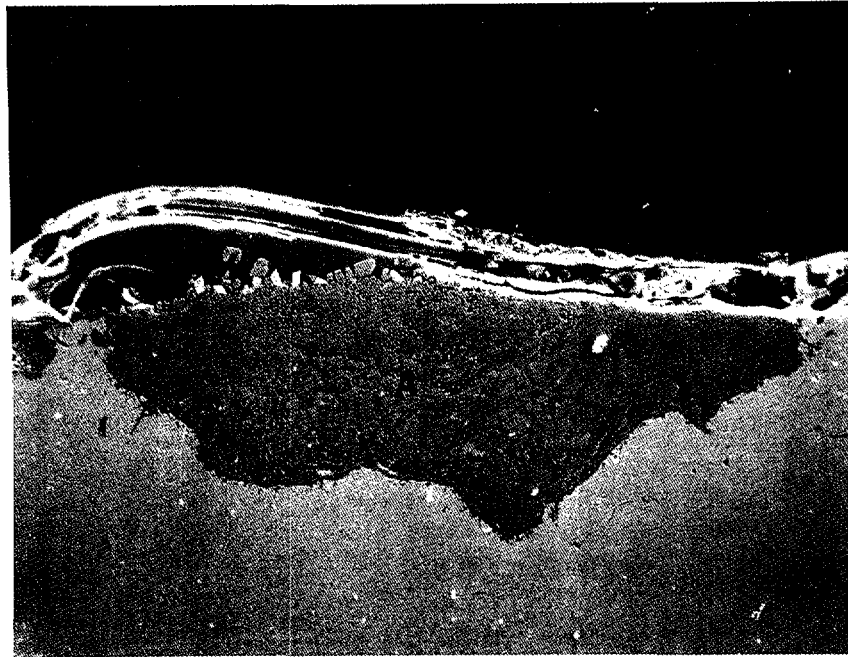


42004

1000X

Component	Composition (weight percent)			
	Base Metal (Area 1)	Corrosion Pit (Area 2)	Glass (Phase A)	Glass (Phase B)
Fe	71.69	8.23	12.10	17.17
Cr	18.48	62.76	5.18	--
Ni	9.83	10.54	2.49	0.71
Si	--	17.23	20.18	50.74
Zn	--	1.24	--	8.71
Pb	--	--	--	8.18
Ti	--	--	25.51	--
Ca	--	--	4.29	3.73
Pr	--	--	24.49	4.01
Gd	--	--	2.68	--
P	--	--	3.08	4.61
Cs	--	--	--	1.87
K	--	--	--	0.27

Figure 4.9. Energy dispersive X-ray analysis of 900 C specimen.
(400-hour exposure)



45756

200X

<u>Component</u>	<u>Composition (Area A) (weight percent)</u>
Cr	34.11
Fe	33.16
Ni	14.91
Si	10.61
Zn	7.09
Ti	0.13

Figure 4.10. Energy dispersive X-ray analysis of 900 C specimen.
(1930-hour exposure)

silicon, zinc, and titanium in the pit were very close to those found in the previous analysis. The distribution of base metal elements was quite different, however.

Pits developed at 700 C were similar to those developed at 900 C. At 470 hours the pit was small, but there was grain boundary penetration to 7 μ m. In addition to the elements found in the pits at 900 C, sodium and vanadium were detected in small amounts. Pit development was greater after 890 hours at 700 C. The levels of silicon, zinc, titanium, and sulfur all were higher in this case, with phosphorus and calcium appearing as well. The analysis for pitting after 2664 hours is the first that did not show the presence of zinc, although silicon, titanium, and sulfur were present in small amounts, along with aluminum.

Pits developed at 500 C were shallow compared to many of those formed at higher temperatures, but the zinc content of the corrosion product layer was high. After 1172 hours at 500 C, the pit depth was slightly greater, and more elements were detected in the pit. However, the only one not previously detected in corrosion products was potassium. The pits were still rather shallow after 2065 hours at 500 C. In this case a large amount of zinc was found, together with the usual silicon and titanium. Molybdenum was observed for the first time in a corrosion-product layer.

Although pits developed on the 300 C specimens during the 974-hour exposure, most of them were in the early stages of growth, and the corrosion layer contained a variety of elements. None of these were new, but the high silicon and sodium contents were unusual. A large amount of zinc was found in the products on the 1826-hour specimen at 300 C. The other elements present were typical of those found for other specimens that were analyzed. Only a thin corrosion-product layer was found on the specimen exposed at 300 C for 3273 hours. However, there was grain boundary penetration as deep as 10 μm . Only small concentrations of silicon and zinc were found in this case.

These analyses demonstrated that silicon, zinc, and titanium were almost always present in the corrosion products, sometimes in large amounts. Although a few other elements were detected in addition to these three, the silicon, zinc, and titanium must play a major role in the pitting attack on the stainless steel.

4.3.3 CF8 Alloy Exposure

Enough material was available to prepare six specimens of the CF8 alloy for comparison with the Type 304L stainless steel. These specimens were exposed at 900 C for 750 hours, thus providing data under the same exposure conditions as those for one set of the Type 304L specimens. On completion of the exposure, it was found that very little glass adhered to the CF8 alloy, in contrast to the strong bonding of the waste glass to the Type 304L alloy. Pit-depth measurements for the two worst specimens are shown below with comparable data for the corresponding exposure of the Type 304L stainless steel:

<u>Pit depth (μm)</u>	<u>Number of Pits</u>	
	<u>CF8</u>	<u>304L</u>
20	644	390
20-40	68	295
40-60	15	90
60-80	2	15
80-150	--	10

Many more small pits were initiated in the CF8 alloy, but few of these pits increased in depth during the exposure, as compared to the Type 304L stainless steel. Apparently the inability of the waste glass to bond to the CF8

alloy resulted in superficial pitting, with little penetration into the metal surface.

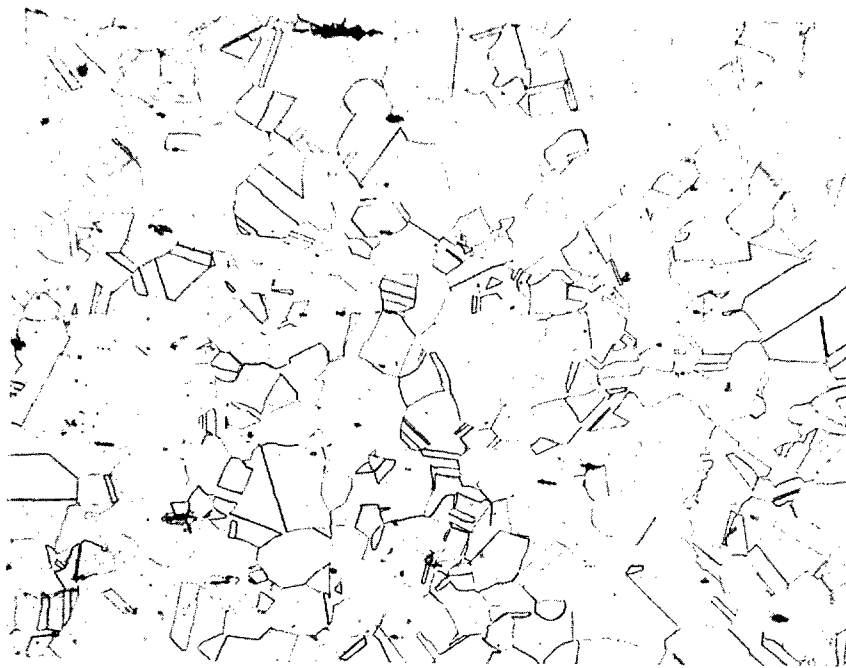
Metallographic examination of the CF8 alloy showed that its microstructure was distinctly different from that of the Type 304L stainless steel. The photomicrographs shown in Figure 4.11 illustrate this difference. The Type 304L had a typical austenitic structure, with small equiaxed grains and annealing twins. On the other hand, the CF8 alloy had large grains, with ferrite islands (dark) in a matrix of austenite. This structural difference would provide a surface on the Type 304L alloy with more grains per unit area, and this could account for greater bonding of the glass to the metal. The small difference in chemical composition of the two alloys (Tables 4.4 and 4.5) would not be expected to influence the bonding to any great extent, and it is more likely that surface effects are responsible for the lack of adherence of the glass to the CF8 alloy.

4.4 Conclusions

From the results of the exposures of the Type 304L stainless steel to the waste glass over a range of temperatures, the following conclusions can be reached:

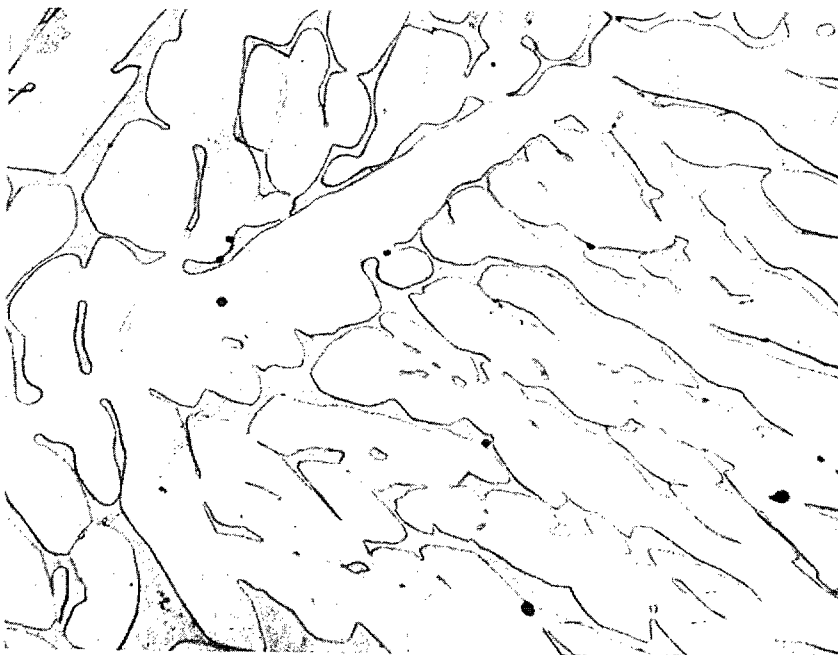
- (1) Pits initiate rapidly on the metal surface at the exposure temperatures of 300-900 C, with more pits forming as the temperature is increased.
- (2) The increase in pit depth with time of exposure is slow, so that few deep pits are formed even at higher temperatures.
- (3) The pitting attack results in maximum penetration rates of the order of 10-20 $\mu\text{m}/\text{year}$. A 3/8-inch stainless steel canister would be penetrated in about 500 years at the higher rate and 1000 years at the lower rate.
- (4) Silicon, zinc, and titanium from the waste glass were found in the corrosion products at all temperatures, indicating that these elements play a role in the attack on the metal.
- (5) The presence of the same elements in the corrosion products at all temperatures suggests that the corrosion mechanism does not change with temperature.
- (6) Limited experiments indicate that the glass does not attack CF8 cast stainless steel as much as it does the Type 304L stainless steel; CF8 may be preferable for canister use.

Thus, it appears likely that Type 304L stainless steel will contain high-level waste glass for the retrieval period and probably the thermal period. The cast version (CF8) may yield superior behavior. Since these tests utilized simulated waste glass, it is recommended that confirmatory tests with more prototypic glass be performed if credit for containment is to be taken.



304L

200X



CF8

200X

Figure 4.11. Photomicrographs of Type 304L and CF8 stainless steels.

4.5 References for Chapter 4

- (4.1) C. L. Angerman and W. N. Rankin, "Durability of Containers for Storing Solidified Radioactive Wastes," Materials Performance 17(4), 9-18 (April 1978).
- (4.2) W. N. Rankin, "Compatibility Testing of Vitrified Waste Forms," Paper No. 117, Corrosion/78, Houston, TX (March 1978).
- (4.3) W. N. Rankin, "Attack of High-Strength, Oxidation Resistant Alloys During In-Can Melting of Simulated Waste Glasses," Paper No. 215, Corrosion/80, Chicago, IL (March 1980).
- (4.4) S. C. Slate and R. F. Maness, "Corrosion Experience in Nuclear Waste Processing at Battelle-Northwest," Mater. Perf. 17(6), 13-21 (June 1978).
- (4.5) H. E. McCoy and J. E. Mack, "Characterization of Materials for Waste-Canister Compatibility Studies," Oak Ridge National Laboratories, Report No. ORNL/TM-7917, October 1981.
- (4.6) H. E. McCoy, "Studies of Waste-Canister Compatibility," Oak Ridge National Laboratory Report No. ORNL/TM-8491, January 1983.
- (4.7) H. Susskind, F. B. Hill, L. Green, S. Kalish, L. Kukacka, W. E. McNulty, and E. Wirsing, Jr., "Corrosion Studies for a Fused Salt-Liquid Metal Extraction Process for the Liquid Metal Fuel Reactor," USAEC Rept: BNL-585, 1960.
- (4.8) H. Susskind, F. B. Hill, L. Green, S. Kalish, L. Kukacka, W. E. McNulty, and E. Wirsing, Jr., "Combating Corrosion in Molten Extraction Processes," Chem. Eng. Prog. 56, 57-63 (1960).
- (4.9) S. I. Stepanov, E. B. Kachina-Pullo, V. N. Devyatkin, and E. A. Ukshe, "Investigation of Corrosion Processes in Molten Chlorides," in A. I. Belyaev (ed.), Surface Phenomena in Metallurgical Processes (Consultant Bureau, New York, 1965, translation) 203-210.
- (4.10) M. A. Hiller, T. L. Young, L. F. Grantham, and W. S. Ginell, "Molten Phosphate Reactor Fuels. II-Corrosion of Metals in Molten Sodium Polyphosphate," USAEC Rept. NAA-SR-5926, 1961.
- (4.11) J. N. Gregory and P. F. Wave, Preliminary Work on Corrosion in Caustic Soda, RCTC/P-33, 1954.
- (4.12) A. S. Brasunas and E. E. Stansbury, Symposium on Corrosion Fundamentals, pp. 65-83, The University of Tennessee Press, 1956.
- (4.13) J. H. DeVan, "Compatibility of Structural Materials with Boiling Potassium," USAEC Rept. ORNL-TM-1361, 1966.

- (4.14) W. O. Harms and A. P. Litman, "Compatibility of Materials for Advanced Space Nuclear Power Systems," USAEC Rept. ORNL-TM-1964 (1967).
- (4.15) J. W. Koger, "Alloy Compatibility with LiF-BeF₂ Salts Containing ThF₄ and UF₄," USAEC Rept. ORNL-TM-4286 (1972).
- (4.16) P. D. Miller and H. H. Krause, "Corrosion Studies in Municipal Incinerators," U.S. EPA Report No. SW-72-3-3, 70 (1972).
- (4.17) H. H. Krause and V. Nagarajan, "Corrosion of High Chromium Alloys in AFBC Boilers," p. 4, Battelle-Columbus Report No. TV-36914A, March 12, 1982.

5. CORROSION MODELING STUDIES

The objective of the corrosion-modeling effort is to develop a set of comprehensive mathematical models for use in understanding the corrosion processes associated with waste-container materials. Results of this modeling work are used to relate experimental data to the physical mechanisms of these processes and to direct further experiment work. Studies in this effort have focused on pitting-corrosion modeling and general-corrosion modeling.

5.1 Pitting-Corrosion Modeling

The development of pits on a container surface is considered to be an important mechanism for the ultimate loss of container integrity. Modeling studies of pitting corrosion at Battelle have centered on three different aspects of the overall process: pit-initiation kinetics, pit-growth kinetics, and the evolution of the pit-depth distribution. Actually, as is described below in more detail, the last aspect is just a combination of the first two; that is, if both the rate of pit generation on a container surface and the rate of pit growth, once pits are generated, are known, then the time-dependence of the pit-depth distribution follows directly. Of course, additional considerations such as the "deactivation" or cessation of growth of certain pits must also be considered. Nevertheless, it is possible to make some generalizations regarding the pit-depth distribution without having full knowledge regarding either pit generation or growth. Battelle's modeling efforts in these areas are summarized below.

5.1.1 Pit-Generation Kinetics

Battelle's analysis of pit-generation kinetics has been limited to general observations and a review of some existing work in this area. Effects that are characteristic of a repository environment, such as the ambient gamma-radiation field, the transfer of heat across the container surface, and the presence of chemical species that are unique to this environment, are not treated and must be the subject of other studies.

5.1.1.1 Literature Review

A number of investigators have considered the problem of pit-generation kinetics. For example, Sato et al. (Ref. 5.1), in their studies of chloride pitting associated with a rotating stainless-steel electrode in acid solution, found the pit-generation rate to be approximately constant in time. On the other hand, Janik-Czachor and Ives (Ref. 5.2) have suggested that, for their pitting-kinetics experiments, the function which describes the pit-generation rate is of a "peaked" type, which they interpreted as probably being representative of a statistical distribution of pitting susceptibilities existing on the metal surface, centered at a "mean" susceptibility which is represented by a characteristic time of incubation. They found no evidence for a time-independent pit-generation rate. Interestingly, in their modeling studies of the evolution of the pit-depth distribution, they used a simple, $\sin^2(0.2 t)$ function to represent the "peaked" function describing the rate of pit nucleation.

Probably the most comprehensive physically based model currently available to describe pit-generation kinetics is one that was recently reported (Refs. 5.3-5.5), consisting of a deterministic treatment of the statistical nature of passive-film breakdown on metal surfaces. This model, which is based on an earlier point-defect model for passive-film breakdown (Refs. 5.6-5.8), has been used to obtain good (even quantitative) agreement with existing experimental data.

5.1.1.2 Relationship Between Pit-Generation Rate and Other Quantities

As pointed out above, the major aspects of pit behavior under consideration (pit generation and growth and evolution of the pit-depth distribution) are interrelated. Neglecting other aspects (such as deactivation of growing pits), this relationship can be expressed quantitatively, as follows: Let us assume that the rate of growth (or deepening), v , of a given pit is an explicit function only of its instantaneous depth, h ; that is, $v = v(h)$. It is also assumed that pits grow only by deepening. No account is taken of growth in a lateral direction, which could eventually result in overlap of adjacent pits.

Next, let $G(t)$ be the rate per unit area at which pits are generated on the metal surface at time t and let $f(h,t)$ be the pit-depth frequency distribution, defined such that $f(h,t)dh$ is the number of pits per unit area of surface, at time t , having depth within the range h to $h + dh$. (No account is taken of any dependence that the pit-depth distribution may have on spatial coordinates.) Individual pits can be regarded as "points" in a one-dimensional "pit-depth" space. As a given pit deepens, its characteristic "point" moves along the one-dimensional space in the direction of increasing h . The "flux", then, of such points crossing a given fixed value of h at time t must be equal to the rate at which those particular pits were generated at the time they actually were generated. This statement can be expressed mathematically as

$$v(h)f(h,t) = G\left(t - \int_0^h \frac{dh}{v(h)}\right) \quad (5-1)$$

If pitting is assumed to begin at time $t = 0$, then Eq. 5-1 is valid only for those values of h for which the argument of the G function is greater than zero. For larger h values, $f(h,t) = 0$ since no pits have yet grown to these larger sizes. Thus, if $v(h)$ is known (for example, by direct measurement of pit-growth kinetics for individual pits) and if $f(h,t)$ is measured at a given time t , then $G(t)$, for times up to the given value, t , can be estimated by applying Eq. 5-1.

Deducing nucleation (or generation) rates from other measured properties of a system is actually a common technique. Moreover, the subject has been of interest for many years and is still under investigation. For example, more

than four decades ago Hull et al. (Ref. 5.9) described a method analogous to Eq. 5-1 for calculating the nucleation rate of pearlite from austenite using size-distribution data. They considered the special case for which the growth rate of the pearlite species is independent of size.

These same authors also reviewed another method which involved calculating the nucleation rate from measurements of the total concentration of pearlite species as a function of time (Ref. 5.9). Indeed, an approach analogous to the latter has been suggested by Janik-Czachor and Ives (Ref. 5.2) for determining pit-generation rates. With this method, the instantaneous pit concentration on a surface, $n(t)$, is measured experimentally and related to $G(t)$ through the expression

$$G(t) = dn(t)/dt \quad (5-2)$$

Eq. 5-2 would have to be modified as the area fraction of the container surface covered by pits becomes appreciable. An analogous modification that was included in the treatment of Hull et al. (Ref. 5.9) applied to pearlite.

The general problem of estimating nucleation and species growth rates from measurements of more "global" properties continues to be a problem of interest. This is shown, for example, in the recent work of Gokhale and DeHoff (Ref. 5.10). It appears that information relative to pit-generation kinetics can be obtained from measurements of related quantities.

Finally, an analysis of crystal-size-distribution kinetics for glass crystallization has been reported by Markworth (Ref. 5.11) using an approach analogous to that leading to Eq. 5-1. That particular analysis, which can also be applied to pit generation/growth kinetics, was conducted under this project and serves to further illustrate the more general applicability of the relationship summarized in Eq. 5-1.

5.1.2 Pit-Growth Kinetics

Modeling studies of pit-growth kinetics were carried out in successive stages. First, a rather simple model was constructed in which ionic transport within the solution inside the pit was considered. Then, effects of electrode kinetics at the pit base were included. Finally, effects of chemically active pit walls were studied. The results are summarized below in this sequence following a brief review of existing research on pit-growth kinetics.

5.1.2.1 Background and Review

The rate at which a pit on a metal surface, once initiated, penetrates into the metal is a subject that has long been of interest. The following general relationship describes many types of pit growth:

$$h = a(t - t_0)^b \quad (5-3)$$

where h is the depth, at time t , of a pit that had been generated at time $t_0 \leq t$, and where a and b are parameters that characterize the particular pit-growth process. It has been found experimentally that, in a wide variety of cases, the parameter b lies within the range $0.3 \leq b \leq 1$.

A few examples can be cited. A relationship similar to Eq. 5-3 was used many years ago (Ref. 5.12) to describe the variation with time of the maximum pit depth for ferrous specimens in a soil environment. Somewhat more recently (Ref. 5.13), it was pointed out that the special case for which $b = 1/3$ has been found to apply to a number of situations, including the maximum pit depth in laboratory tests in almost 200 fresh waters, a 2,000-foot industrial water-carrying pipeline for an interval of more than 13 years, and the pitting of aluminum in seawater. A time dependence for pit growth similar to that in Eq. 5-3 has also been discussed by Sato and coworkers (Ref. 5.1). Finally, in an experimental study of the pitting corrosion of carbon steel, Marsh et al. (Ref. 5.14) reported that the variation with time t , in years, of the maximum pit depth, h_{\max} , in mm, was as follows:

$$h_{\max} = 8.35 t^{0.46} \quad . \quad (5-4)$$

Clearly, the value of b in Eq. 5-4 (0.46) lies within the indicated range.

Of course, the exact nature of the parameters a and b is determined by a number of factors, such as pit geometry and the mass-transport processes that contribute to pit growth. Also, since these factors, as well as the experimental conditions (for example, temperature), in general vary with time, the parameters a and b are likely themselves to be time-dependent, particularly when pitting kinetics is considered as occurring over extended periods of time.

A few very simple examples serve to illustrate the validity of Eq. 5-3 for various pit geometries and rate-controlling kinetic processes. Without presenting the details, it can be shown that:

- For dissolution-controlled growth of a hemispherical pit of radius h , with time-independent total current to the pit and with the current density across the pit surface being everywhere the same,

$$h \sim (t - t_0)^{1/3} \quad .$$

- For dissolution-controlled growth of a hemispherical pit, with time-independent and spatially independent current density across the pit surface,

$$h \sim (t - t_0)^1 \quad .$$

The same relation holds for a cylindrical pit having constant cross-sectional area perpendicular to the growth direction and time-independent current supplied to its bottom, dissolving surface. Of course, the constant of proportionality is different for the two cases, and h represents pit depth for the case of a cylindrical pit.

- For a cylindrical pit of depth h , again having constant cross-sectional area perpendicular to the growth direction, but growing by chemical-diffusion-controlled migration of the metal-containing species from the pit bottom to the upper surface,

$$h \sim (t - t_0)^{1/2}$$

assuming time-independent values for the concentration of that species in the solution at the upper and lower pit surfaces.

It is clear that, in each of the above cases, pit growth is indeed described by a specific form of Eq. 5-3, despite the fact that the assumed pit geometries and rate-controlling processes do vary from one case to another. This may help explain why Eq. 5-3, in some form, is so often found to describe pit-growth data.

It is, of course, desirable to place our understanding of pit-growth kinetics on a firm, quantitative basis in terms of physical models, particularly if one is to predict, with some degree of confidence, the long-term pitting behavior of a metal surface. Indeed, a number of models for pitting corrosion, based essentially on the application of mass-transport kinetics to simple pit geometries, have been developed over the years. Examples of these can be found in the literature (Refs. 5.1, 5.15-5.23). In addition, several detailed mathematical treatments of pitting corrosion have been reported, for example, References 5.24-5.26. A related area, in which a considerable amount of modeling has been carried out, is stress-corrosion cracking of metals. A review of this topic has recently been presented elsewhere (Ref. 5.27).

5.1.2.2 Binary-Electrolyte Pit-Growth Model for an Inert-Wall Pit, With No Consideration of Electrode Kinetics at Pit Base

As an initial step in developing a model for pitting corrosion of a waste-package container, a simple model was initially developed based on the well-known transport theory characterizing a "binary electrolyte", which is a solution containing one type of cation and one type of anion. A detailed discussion of the general theory of binary electrolytes has been presented by Newman (Ref. 5.28). For our purposes, the cation represents the

dissolving metal and the anion represents an "average" of all the anions that may exist within the solution inside the pit.

The following assumptions are included in this model:

- The pit geometry, as illustrated in Figure 5.1, has two-dimensional, rectangular symmetry (which could be easily generalized to a cylindrical configuration).

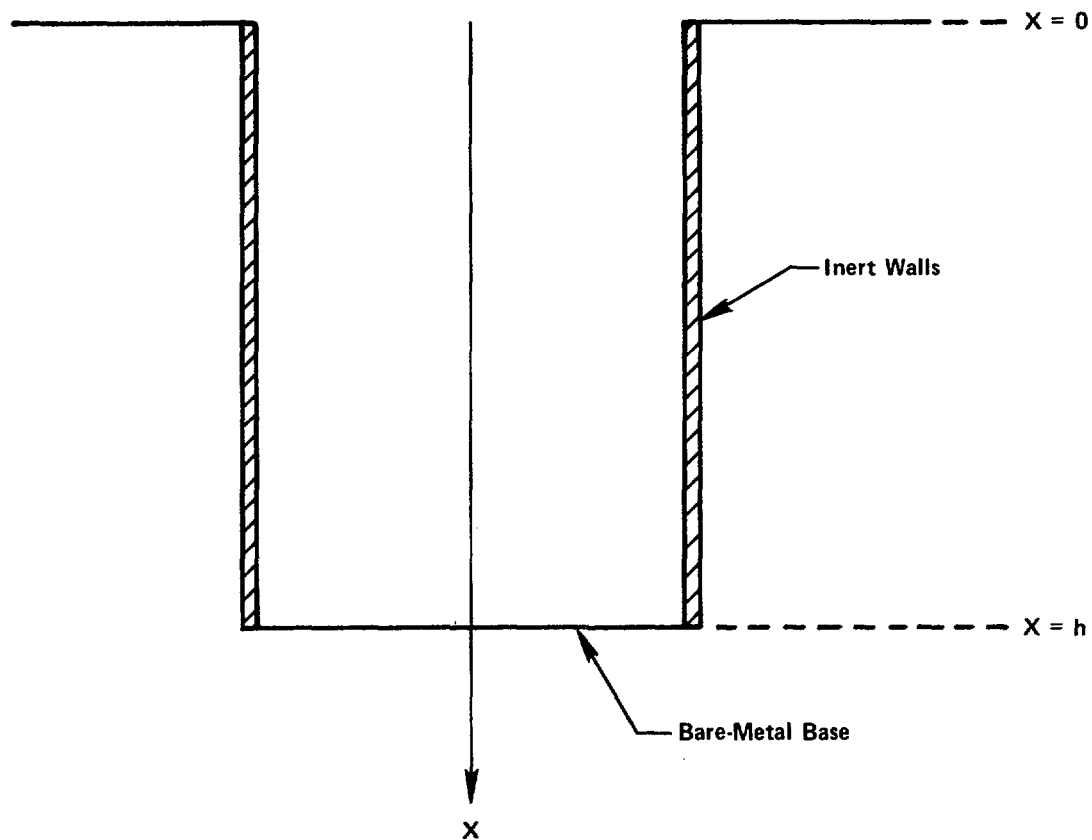


Figure 5.1. Illustration of pit configuration used with binary-electrolyte model.

- The pit walls are chemically inert, so that growth can occur only along the pit length, which is taken to be parallel to the x-axis, with growth occurring as a result of anodic dissolution of the bare metal that is assumed to exist at the pit base located at $x = h$. Current flow within the pit is likewise one-dimensional, since the walls are chemically inert.

- No chemical reactions occur within the solution.
- No convective flow of solution takes place.
- Ionic transport occurs under steady-state conditions and according to dilute-solution theory.
- The mobility of each of the ionic species is given by the Nernst-Einstein relation (Ref. 5.28).

Given these assumptions, it can be shown (using, for example, Equation 69-1 of Newman (Ref. 5.28)) that the flux, $N_+(x)$ and $N_-(x)$, of cations and anions, respectively, within the solution inside the pit is given by

$$N_+(x) = -D_+ \left[\frac{F}{RT} z_+ c_+(x) \frac{d}{dx} \phi(x) + \frac{d}{dx} c_+(x) \right] \quad (5-5a)$$

$$N_-(x) = -D_- \left[\frac{F}{RT} z_- c_-(x) \frac{d}{dx} \phi(x) + \frac{d}{dx} c_-(x) \right] = 0 \quad (5-5b)$$

where D_{\pm} , z_{\pm} and $c_{\pm}(x)$ are, respectively, the diffusivity, number of proton charges, and x -dependent concentration of the cation (+) and anion (-), F the Faraday constant, R the gas constant, T the absolute temperature, and $\phi(x)$ the electrostatic potential. Clearly, the first term within brackets in Eq. 5-5 represents a contribution due to electromigration, whereas the second term is a contribution due to chemical diffusion. The fact that N_- is zero everywhere follows from the fact that the anions are not generated or lost, in this model, due to any type of chemical reaction.

Since no chemical reactions occur within the solution, the expression for cation material balance becomes as follows (see Equation 69-3 of Newman (Ref. 5.28)).

$$\frac{d}{dx} N_+(x) = 0 \quad . \quad (5-6)$$

Moreover, since the solution must be electrically neutral at all points,

$$z_+ c_+(x) + z_- c_-(x) = 0 \quad . \quad (5-7)$$

Eqs. 5-5, 5-6, and 5-7 can be solved simultaneously (see Reference 5.29 for details) to yield the following major results:

$$c_+(x) = c_+(0) + c_+(h) - c_+(0) (x/h) \quad . \quad (5-8)$$

$$\phi(x) = \phi(0) - \frac{RT}{z_- F} \ln \frac{c_+(x)}{c_+(0)} \quad . \quad (5-9)$$

The cation flux is of particular interest, because it is this quantity that is directly related to the rate of pit growth. It is now a simple matter to calculate this flux simply by using Eqs. 5-8 and 5-9 in conjunction with Eq. 5-5a, from which we obtain

$$N_+ = D_+ \left(\frac{z_+}{z_-} - 1 \right) [c_+(h) - c_+(0)] \frac{1}{h} \quad . \quad (5-10)$$

Clearly, the rate of pit growth is given by

$$\frac{dh}{dt} = - \frac{m}{\rho} N_+ \quad (5-11)$$

where m is the molar mass of the dissolving metal and ρ is its mass density. The minus sign on the right-hand side of Eq. 5-11 is included because $N_+ < 0$ (cation flux in the direction of the crevice mouth) implies that $dh/dt > 0$ (crevice growth). Combining Eqs. 5-10 and 5-11, and recalling that $z_+ > 0$ and $z_- < 0$, we obtain, taking $h = 0$ at $t = 0$,

$$h^2 = \frac{mD_+}{\rho} \left(\left| \frac{z_+}{z_-} \right| + 1 \right) [c_+(h) - c_+(0)] t \quad . \quad (5-12)$$

Hence, for this model the parameter b is exactly 0.5. Again, the first term inside parentheses on the right-hand side of Eq. 5-12 is a contribution to pit growth due to electromigration, whereas the second term is a contribution due to chemical diffusion. Thus, for example, for $z_+ = +2$ and $z_- = -1$, electromigration contributes twice as much to pit growth as does chemical diffusion.

Current-Density Calculation. One can also calculate the current density, i , flowing along the pit length, based on the present model. Clearly, this current density is due entirely to the flow of cations, since $N_-(x) = 0$. It has been shown (Ref. 5.30) that this current density is equal to $z_+ F N_+$ which, in turn, can be expressed as

$$i = Fz_+D_+ \left(\left| \frac{z_+}{z_-} \right| + 1 \right) \frac{c_+(0)}{h} \left\{ 1 - \exp \left(\frac{z_- F}{RT} [\phi(0) - \phi(h)] \right) \right\} \quad (5-13)$$

Clearly, Eq. 5-13 constitutes a relationship between the pitting current and the potential difference across the pit length. One limiting case of particular interest is that for which $c_+(h) \gg c_+(0)$. This corresponds to the assumption that the concentration of dissolved metal in the solution immediately adjacent to the base of the pit far exceeds that at the pit mouth, which is adjacent to the bulk solution. For this special case, Eq. 5-13 becomes (see Reference 5.30 for details)

$$i \approx -Fz_+D_+ \left(\left| \frac{z_+}{z_-} \right| + 1 \right) \frac{c_+(0)}{h} \exp \left(\frac{z_- F}{RT} [\phi(0) - \phi(h)] \right) \quad (5-14)$$

Eq. 5-14 can be equivalently expressed in the alternative and somewhat more familiar form

$$\phi(0) = \phi(h) - \frac{RT}{|z_-|F} \ln \left(\frac{i}{i_0} \right) \quad (5-15)$$

where the minus sign on the right-hand side of Eq. 5-14 has been dropped, and where

$$i_0 \equiv Fz_+D_+ \left(\left| \frac{z_+}{z_-} \right| + 1 \right) \frac{c_+(0)}{h} \quad (5-16)$$

It is clear from either Eq. 5-14 or 5-15 that the pitting current is indeed sensitive to a number of parameters. For instance, assuming the h^{-1} factor on the right-hand side of Eq. 5-14 is the only factor therein that actually varies with h , it follows that i varies as h^{-1} and that the pitting current therefore decreases as the pit becomes deeper. Likewise, if experimental conditions cause a variation of the potential at the crevice mouth, $\phi(0)$, the relative effect on i would be substantially greater because of the exponential dependence of i upon $\phi(0)$.

Spatial Variation of Electrostatic Potential. It is also of interest to make some observations regarding the spatial dependence of the electrostatic potential within the pit. This potential, as described by Eqs. 5-8 and 5-9, is plotted in Figure 5.2 for selected values of the ratio c_h^+/c_0^+ . In this figure, the potential $\phi(0)$ is arbitrarily set equal to zero, and the

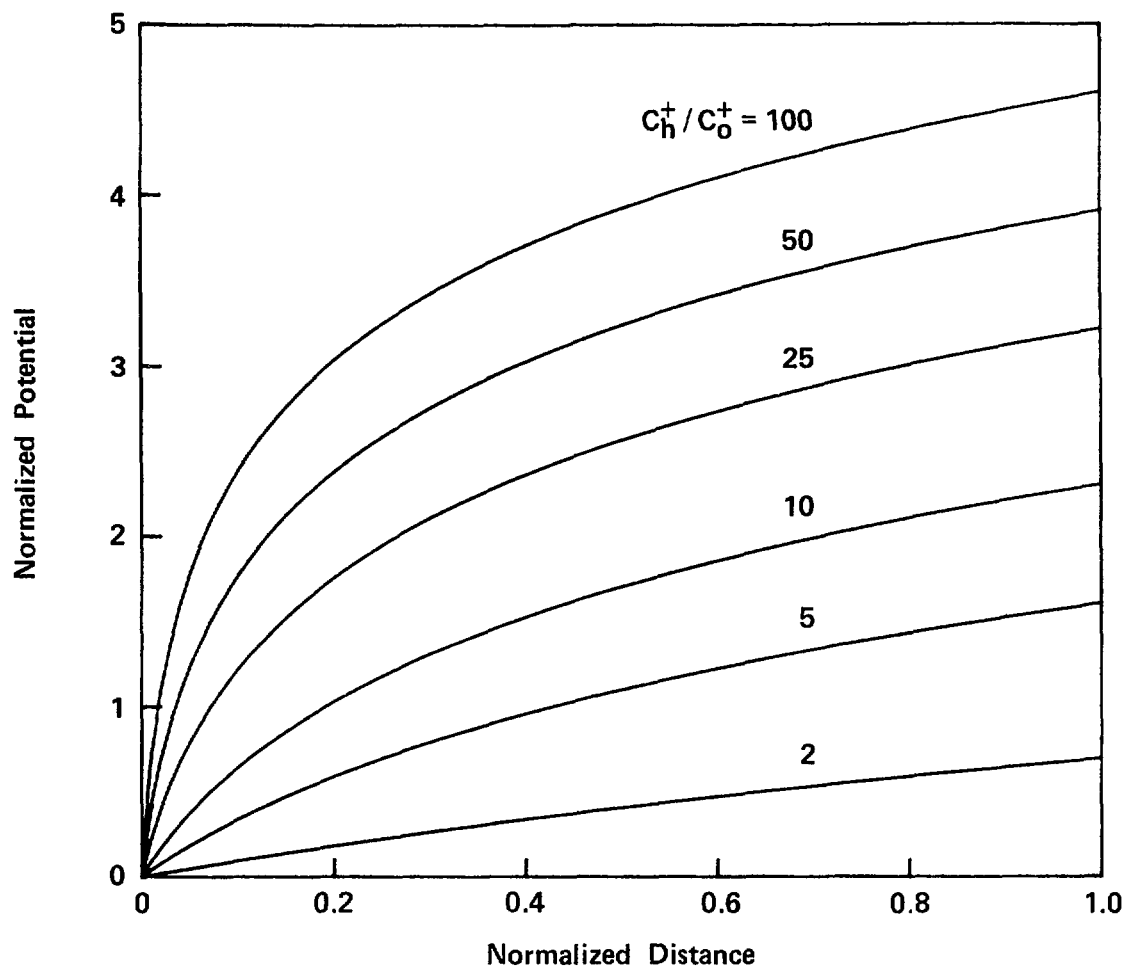


Figure 5.2. Variation of potential with distance for inert-wall pit-growth model for selected values of c_h^+ / c_0^+ , where $c_h^+ \equiv c_+(h)$ and $c_0^+ \equiv c_+(0)$.

"normalized potential" and "normalized distance" are dimensionless quantities defined as follows:

$$\text{Normalized Potential} \equiv \frac{|z_-|F}{RT} \phi(x)$$

$$\text{Normalized Distance} \equiv \frac{x}{h} \quad .$$

An important feature in Figure 5.2 is the behavior of the potential in the vicinity of the pit mouth (that is, around $x = 0$). Clearly, as the ratio c_h^+/c_o^+ is increased, the potential rises more quickly with increasing x around the position $x = 0$. Indeed, for the larger values of this ratio illustrated in the figure, most of the change in potential down the entire pit length takes place within the region near the pit mouth. This behavior is readily seen to follow from the general form of Eqs. 5-8 and 5-9.

The reason that the potential does not vary linearly with x is that the model includes both chemical diffusion and electromigration of the cation and anion species. For the limiting case in which electromigration contributes to the net flux of cations and anions to a much greater extent than chemical diffusion, the electrostatic potential satisfies the Laplace equation to a good approximation, in which case the potential would vary in an approximately linear fashion with x .

Comparison with Data of Marsh et al. (Ref. 5.14). While being careful not to claim detailed physical validity of the pit-growth model just derived, it is interesting nevertheless to compare predictions obtained using the model with results reported by Marsh et al. (Ref. 5.14), as presented above in Eq. 5-4. This is a particularly attractive comparison to make in view of the fact that Marsh reported a b -value of 0.46, which is very close to the value of 0.5 obtained in our analysis.

Toward this end, let us take $z_+ = +2$, $z_- = -1$, $m = 55.847$ g/mol (for iron), $\rho = 7.86$ gm/cm³ (also for iron), and $D_+ = 1 \times 10^{-5}$ cm²/sec. Then, taking Marsh's b -value to be 0.5, one can directly compare Equations 3.21 and 3.27 to obtain a value for the difference in cation concentration along the crevice length. One thus obtains

$$c_+(h) - c_+(0) = 0.05 \text{ mol/L} \quad .$$

This value is indeed within "reasonable" limits. For example, Ateya and Pickering (Ref. 5.31) estimated the concentration of Fe^{2+} ions at the base of a crack-like slot to be < 0.1 M.

5.1.2.3 Inclusion of Electrode Kinetics at Pit Base

One extension of the model discussed in Section 5.1.2.2 involved consideration of the kinetics of metal-atom transport across the metal/solution interface at the pit base. This transport process was coupled with the ionic-transport process in solution that was described above in order to obtain a more general description of pit-growth kinetics.

The general type of pit under consideration here has the form illustrated in Figure 5.3, which is the same as that used above. Electrode-reaction kinetics at the pit base was included in the model during the past quarter using the general approach summarized by Smyrl (Ref. 5.32). This approach is characterized by a dissolution (anodic) reaction of the metal together with

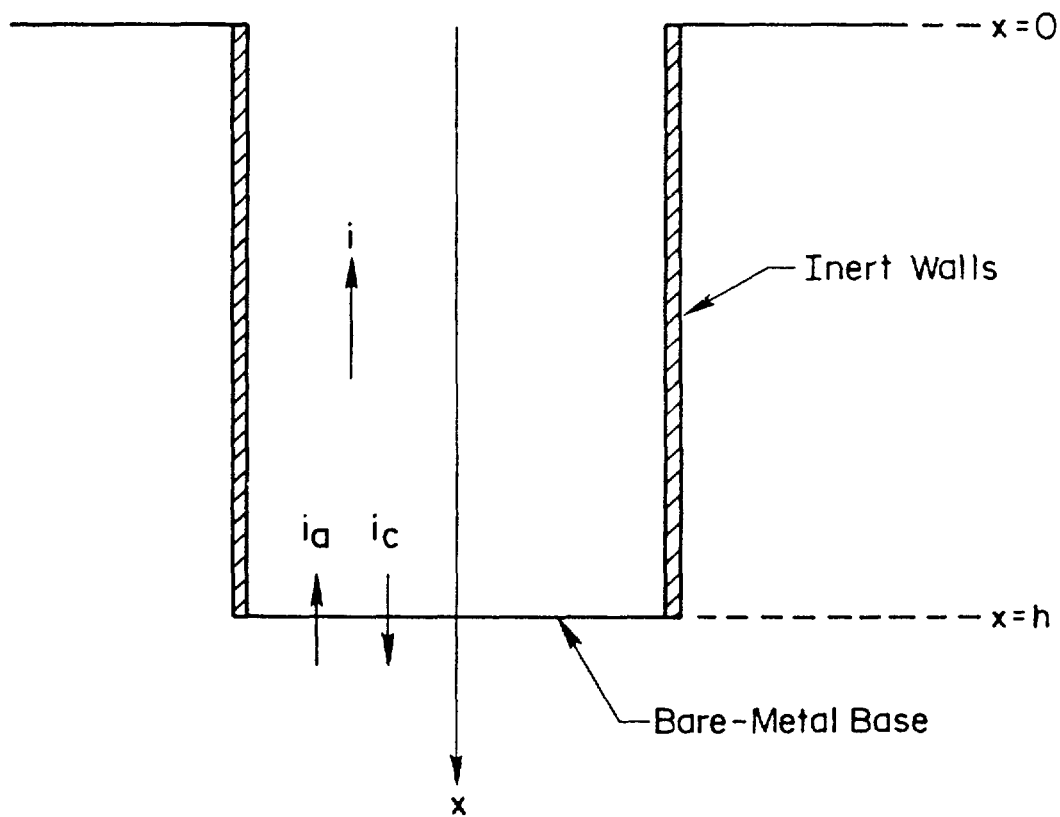


Figure 5.3. Schematic illustration of pit configuration used with binary-electrolyte model, showing the current densities associated with cation transport.

a backward (cathodic) reaction for the dissolved metal cation, the current density associated with each being designated as i_a and i_c , respectively, as also illustrated in Figure 5.3. Following Smyrl (Ref. 5.32), these currents are expressed (using notation specific to the present problem) as

$$i_a = - Fk_a \exp\left(\frac{\alpha_a F}{RT} \phi_h\right) \quad (5-17)$$

$$i_c = Fk_c c_h^+ \exp\left(-\frac{\alpha_c F}{RT} \phi_h\right) \quad (5-18)$$

where k_a and k_c are heterogeneous-reaction-rate constants (which are independent of potential but which do depend upon which reference potential is arbitrarily selected). Also, α_a and α_c are intrinsic kinetic parameters, ϕ_h

is the electrostatic potential at the pit base measured on the metal surface, and the other symbols are as defined above, with $c_h^+ \equiv c_+(h)$. The minus sign used on the right-hand side of Eq. 5-17, together with the plus sign implied for the right-hand side of Eq. 5-18, is selected to conform with the sign convention illustrated in Figure 5.3, that is, the positive x-direction being directed from the pit opening toward the pit base.

It is important to note that ϕ_h is not the same as ϕ_h , the latter being equal to $\phi(h)$ as would be given by setting $x = h$ in Eq. 5-9. Both quantities are measured at the pit base; however, the former is measured on the metal surface whereas the latter is measured in the solution.

The total current density, i , flowing in the solution (see Figure 5.3) must, by conservation of charge, be equal to that crossing the pit base, that is,

$$i = i_a + i_c \quad . \quad (5-19)$$

Combining Eqs. 5-17 to 5-19,

$$\frac{i}{F} = -k_a \exp\left(\frac{\alpha_a F}{RT} \phi_h\right) + k_c c_h^+ \exp\left(-\frac{\alpha_c F}{RT} \phi_h\right) \quad . \quad (5-20)$$

As shown by Smyrl (Ref. 5.32), Eq. 5-20 can be expressed in the form of the familiar Butler-Volmer relationship.

As has been shown elsewhere (Ref. 5.30), one can use a procedure similar to that used by Hine (Ref. 5.34) to obtain the following relationship:

$$\frac{i}{F} = \frac{-k_a \exp\left(\frac{\alpha_a F}{RT} \phi_h\right) + k_c c_o^+ \exp\left(-\frac{\alpha_c F}{RT} \phi_h\right)}{1 + \frac{k_c h}{\lambda} \exp\left(-\frac{\alpha_c F}{RT} \phi_h\right)} \quad . \quad (5-21)$$

where $c_o^+ \equiv c_+(0)$. Eq. 5-21 represents a general expression for the current density, i , that involves the anodic and cathodic reactions undergone by the cation at the electrode (that is, the pit base) as well as ionic transport in the solution via electromigration and chemical diffusion. Moreover, one can also show (Ref. 5.33) that

$$\frac{c_h^+}{c_o^+} = \frac{1 + \frac{k_a h}{c_o^+ \lambda} \exp\left(\frac{\alpha_a F}{RT} \phi_h\right)}{1 + \frac{k_c h}{\lambda} \exp\left(-\frac{\alpha_c F}{RT} \phi_h\right)} \quad (5-22)$$

Clearly, Eq. 5-22 represents a general relationship between the cation concentration at the pit base and that at the pit opening including both electrode-reaction and solution-transport effects. Of course, the quantities c_h^+ , c_o^+ , and $\phi_h - \phi_o$ are also interrelated such that Eq. 5-9 is satisfied at $x = h$; this consideration is not pursued further here.

Again, following the general approach of Hine (Ref. 5.34), we shall examine some characteristics of two important limiting cases: solution-transport-limited kinetics and electrode-reaction-limited kinetics.

Solution-Transport-Limited Kinetics. For this limiting case, ionic transport within the solution occurs very slowly compared to the electrode-reaction kinetics at the pit base. From Eq. 5-21, we see that this corresponds to the condition

$$\frac{k_c h}{\lambda} \exp\left(-\frac{\alpha_c F}{RT} \phi_h\right) \gg 1 \quad (5-23)$$

in which case, Eq. 5-21 becomes

$$\frac{i}{F} \approx \frac{\lambda}{h} \left\{ -\left(\frac{k_a}{k_c}\right) \exp\left[\frac{(\alpha_a + \alpha_c)F}{RT} \phi_h\right] + c_o^+ \right\} \quad (5-24)$$

and Eq. 5-22 becomes

$$\frac{c_h^+}{c_o^+} \approx \frac{\lambda}{k_c h} \exp\left(\frac{\alpha_c F}{RT} \phi_h\right) + \frac{1}{c_o^+} \left(\frac{k_a}{k_c}\right) \exp\left[\frac{(\alpha_a + \alpha_c)F}{RT} \phi_h\right] \quad (5-25)$$

As expected, the current density, i , depends upon both λ and h for this limiting case.

If, in addition, the first term on the right-hand side of Eq. 5-25 is small compared to the second, that is, if

$$\frac{k_a h}{c_o^+ \lambda} \exp \left(\frac{\alpha_a F}{RT} \phi_h \right) \gg 1 \quad (5-26)$$

then Eq. 5-25 becomes

$$c_h^+ = \left(\frac{k_a}{k_c} \right) \exp \left[\frac{(\alpha_a + \alpha_c) F}{RT} \phi_h \right] \quad (5-27)$$

As seen from Eqs. 5-17 and 5-18, Eq. 5-27 corresponds to the anodic and cathodic cation current densities at the pit base being approximately equal in magnitude. This is an expected result if the rates at which the cathodic and anodic reactions occur are large compared to the rate at which ions can be transported away up the length of the pit.

Electrode-Reaction-Limited Kinetics. For this limiting case, ionic transport within the solution occurs very rapidly compared to the electrode-reaction kinetics at the pit base. Again, using Eq. 5-21, we see that this corresponds to the condition

$$\frac{k_c h}{\lambda} \exp \left(- \frac{\alpha_c F}{RT} \phi_h \right) \ll 1 \quad (5-28)$$

in which case Eq. 5-21 becomes

$$\frac{i}{F} = -k_a \exp \left(\frac{\alpha_a F}{RT} \phi_h \right) + k_c c_o^+ \exp \left(- \frac{\alpha_c F}{RT} \phi_h \right) \quad (5-29)$$

with i now being independent of λ and h . Also, Eq. 5-22 becomes

$$c_h^+ = c_o^+ + \frac{k_a h}{\lambda} \exp \left(\frac{\alpha_a F}{RT} \phi_h \right) \quad (5-30)$$

As noted previously, a relationship also exists between c_h^+ , c_o^+ , and $\phi_h - \phi_o$, obtained by setting $x = h$ in Eq. 5-9.

If, in addition,

$$\frac{k_a h}{c_o^+} \exp\left(\frac{\alpha_a F}{RT} \phi_h\right) \ll 1 \quad (5-31)$$

then Eq. 5-30 becomes

$$c_h^+ \approx c_o^+ \quad . \quad (5-32)$$

As a result, the gradient of cation concentration along the pit length is relatively small for this case. Correspondingly, the difference in electrostatic potential between the pit opening and base is relatively small (as seen by combining Eqs. 5-9 and 5-32).

5.1.2.4 Inclusion of Chemically Active Pit Walls

Experimental results obtained under this program, including some which have recently been reported in the literature (Ref. 5.35), have indicated that chemically active pit walls may play a major role in affecting electrochemical characteristics of a pit. Because of these results, the decision was made to extend the pit-growth modeling studies to include chemically active walls.

Of the various pitting-corrosion models and models of related phenomena that have been reported, some (for example, Pickering and Frankenthal (Ref. 5.17), and Galvele (Ref. 5.20)) are based on chemically inert walls. However, others (for example, Alkire and Siitari (Ref. 5.22), and Markworth and Kahn (Refs. 5.27, 5.36)) are based on chemically active walls.

The approach that we used to describe active-wall effects was to generalize the binary-electrolyte pit-growth model summarized in Section 5.1.2.2. It was assumed that only cations can react chemically with the pit walls. Moreover, no effects of electrode kinetics at the pit base were included in this analysis.

Although active walls result in ionic flow in a direction perpendicular to the pit length as well as parallel to its length, we have used an approximation that essentially reduces the problem to one involving only one dimension (that being along the pit length). This approximation, which applies best to long, narrow, crevice-like pits, is equivalent to the lowest-order contribution in the "hierarchical ionic-transport" model developed by Markworth and Kahn (Refs. 5.27, 5.36). Within this approximation, the active walls can be regarded as being essentially position-dependent (that is, x -dependent) "sources" or "sinks" for ionic species in the pertinent mass-balance equations. This fact has been pointed out by Turnbull and Thomas (Ref. 5.37) in their related modeling study of crack electrochemistry.

Applying Eq. 36 of Reference 5.36 (or Eq. 3-36 of Reference 5.27) to the present case, we obtain the following mass-balance equation, in which variation of the flux N_+ in a direction perpendicular to x is not included:

$$\frac{d}{dx} N_+(x) = \frac{2}{w} n_+(x) \quad . \quad (5-33)$$

This expression is a generalization of Eq. 5-6. Here, N_+ is given by Eq. 5-5a, w is the width of the rectangular crevice, and n_+ is the x -dependent flux of cations at, and normal to, a crevice wall. The flux n_+ is positive for anodic currents at a wall and negative for cathodic currents. Eq. 5-33 could also be easily derived by applying a simple conservation-of-charge argument to a small segment (of incremental length dx) of the pit.

Clearly, the right-hand side of Eq. 5-33 does act effectively as a source term for cations if n_+ is positive and as a sink term if n_+ is negative. Of course, $N_-(x)$ (given by Eq. 5-5b) is still zero since the anion does not undergo any type of chemical reaction. One can easily show that Eq. 5-9 is still valid. However, Eq. 5-8 is not valid for this case.

To carry the problem further, we must make some assumption regarding $n_+(x)$. Toward this end, we note that the current density, $j(x)$, associated with the flux $n_+(x)$, is given by

$$j(x) = z_+ F n_+(x) \quad . \quad (5-34)$$

In turn, we assume that $j(x)$ can be described using a type of Butler-Volmer kinetics (see, for example, Bockris and Reddy (Ref. 5.38)), that is,

$$j(x) = 2J \sinh \left\{ \frac{F}{2RT} [\phi_C - \phi(x)] \right\} \quad (5-35)$$

where J is a constant (having units of current density) and ϕ_C , taken to be independent of x , is the value of ϕ for which $j(x)$ is zero. It must be emphasized that ϕ , as defined here, is the electrostatic potential measured in the solution adjacent to the crevice wall at position x (which is consistent with our previous usage of ϕ being a potential measured within the solution). The quantity $\phi_C - \phi(x)$ is an overpotential that exists at position x .

The problem is now sufficiently defined such that only some elementary manipulation, involving Eqs. 5-5a, 5-5b, 5-7, 5-9, and 5-33 to 5-35, is required to obtain the following expression in which all quantities are dimensionless:

$$\frac{d^2\theta}{dy^2} = \alpha^{-1} \theta^{-\eta} - \alpha \theta^{\eta} \quad (5-36)$$

where

$$\theta \equiv c_+(x)/c_0^+ \quad (5-37)$$

$$y \equiv \left[\frac{2J}{wz_+FD_+} \left(1 - \frac{z_+}{z_-} \right)^{-1} \frac{1}{c_0^+} \right]^{1/2} x \quad (5-38)$$

$$\alpha \equiv \exp \left\{ \frac{F}{2RT} [\phi_c - \phi(0)] \right\} \quad (5-39)$$

$$\eta \equiv (2z_-)^{-1} . \quad (5-40)$$

Thus, Eq. 5-36 is a nonlinear differential equation, the integration of which yields the explicit dependence of $c_+(x)$ upon x . The boundary conditions are (recalling that we are now neglecting electrode kinetics at the pit base) the same as those used in Section 5.1.2.2, namely, that $c_+(0) \equiv c_0^+$ and $c_+(h) \equiv c_h^+$ have arbitrarily specified values.

Of course, once $c_+(x)$ is known, then the electrostatic-potential distribution can be calculated using Eq. 5-9. Also, $j(x)$ can be determined using its relationship to the electrostatic potential as expressed in Eq. 5-35.

Application to Special Case. As an example, we consider the following special case: $\alpha = 10$, $\eta = -0.5$ (that is, $z_- = -1$), $\theta(x = h) = 100$, $y(x = h) = 80$. One can readily show that, for this case, $j(h)$ is exactly zero. In addition, for $T = 300$ K, the overpotential, $\phi_c - \phi(0)$, is equal to 0.119 V for this value of α .

To determine whether the value of $y(h)$ that was selected is physically reasonable, we calculate the value that c_0^+ would have using the following numerical values: $h = 0.5$ cm, $w = 0.1$ cm, $z_+ = +2$, $z_- = -1$, $D_+ = 1 \times 10^{-5}$ cm²/sec, and $J = 1$ mA/cm². Then, for $y(h) = 80$, we obtain $c_0^+ \approx 1 \times 10^{-4}$ mol/L, which is a reasonable value given the order-of-magnitude estimates made for some of these parameters.

Equation 5-36 was integrated numerically, for this example, using a fourth-order Runge-Kutta procedure, from which $c_+(x)$ was obtained as an explicit function of x and from which $\phi(x)$ and $j(x)$ were also determined. The

results are plotted in Figures 5.4 to 5.6 and compared with corresponding results for an inert-wall pit having the same value of c_H^+/c_0^+ ($= 100$).

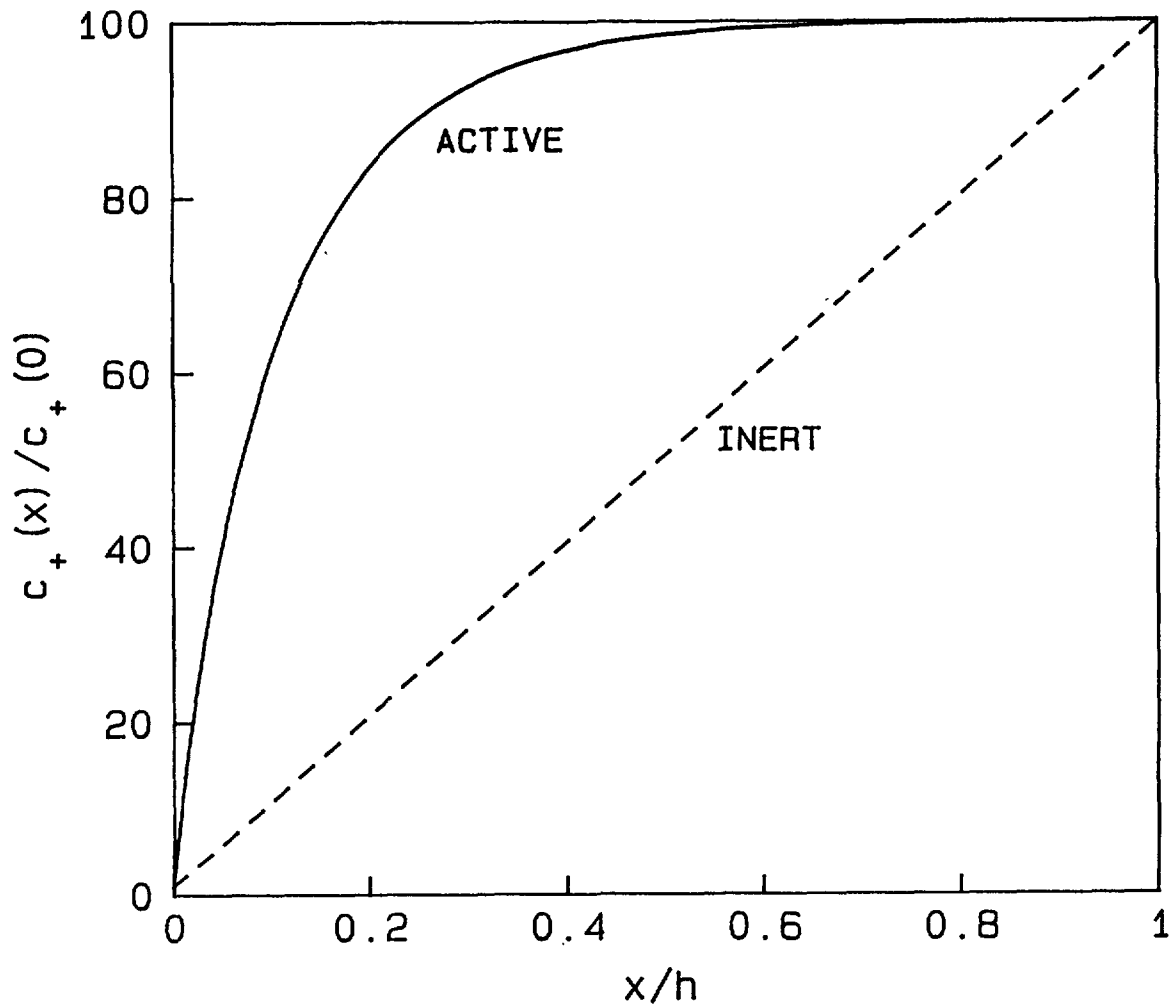


Figure 5.4. Variation of cation concentration with distance along pit length for example of active-wall and inert-wall pits discussed in text.

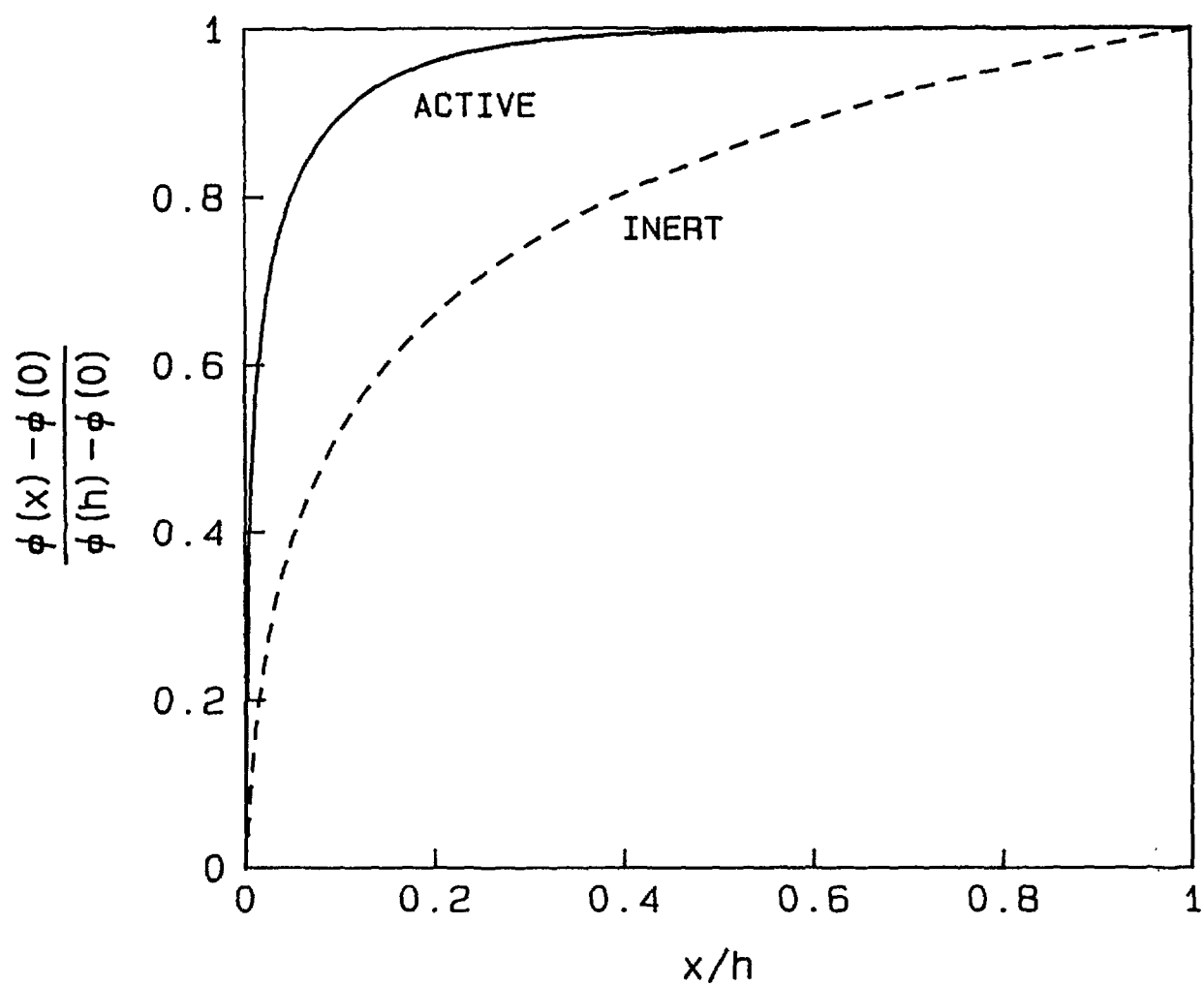


Figure 5.5. Variation of electrostatic potential with distance along pit length for example of active-wall and inert-wall pits discussed in text.

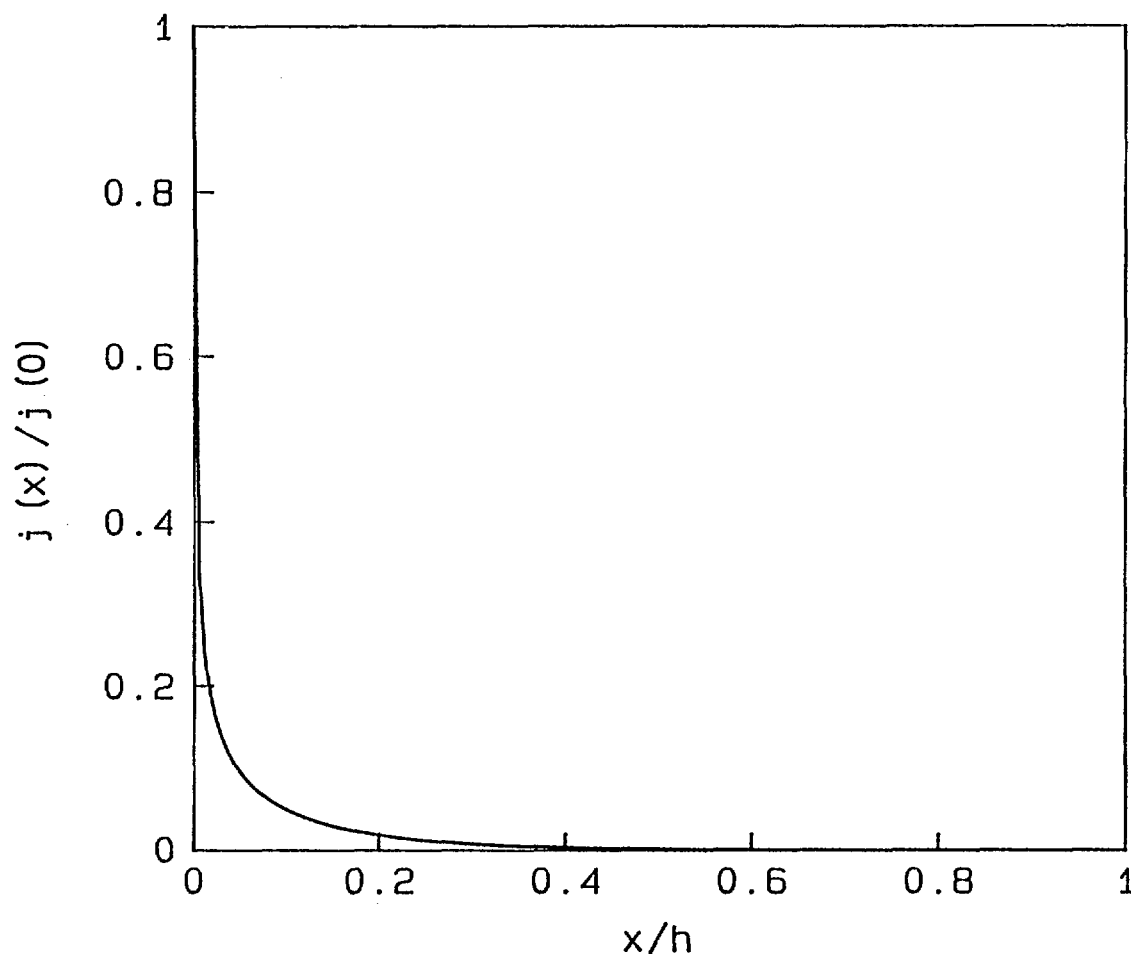


Figure 5.6. Variation of current density at and normal to pit wall with distance along pit length for example of active-wall pit discussed in text.

As seen in Figure 5.4, a large difference exists between the two cases as far as the variation of $c_+(x)$ with x is concerned. For the inert-wall pit, this variation is linear (after Eq. 5-8), whereas for the active-wall pit, most of the change of c_+ toward its final value of $100 c_0^+$ takes place at positions along the pit length that are relatively close to the mouth. This also has a large effect on the rate of metal dissolution at the pit base, which, for both cases, is proportional to dc_+/dx measured at $x = h$. Clearly, this quantity is much larger for the inert-wall pit than for the active-wall pit.

Figure 5.5 shows that, for both cases, the electrostatic potential increases most quickly, toward its final value at $x = h$, at positions near the pit mouth. However, this initially rapid rate of increase is much more pronounced for the active-wall pit than for the inert-wall pit.

Finally, the current density, $j(x)$, is plotted in Figure 5.6 for the active-wall pit. Of course, this quantity is identically zero for the inert-wall

pit. Clearly, this current density is substantially non-zero only at positions near the pit mouth.

In summary, this example demonstrates that active pit walls can have pronounced effects on electrochemical conditions within the pit. The results are consistent, at least in a qualitative sense, with experimental measurements of pit behavior obtained under this program and described elsewhere in this report (Chapter 3) and in the literature (Ref. 5.35). Another discussion of experimental and modeling studies of this type is presented in Reference 5.39.

5.1.3 Evolution of the Pit-Depth Distribution

Knowledge of the pit-depth distribution at any given time provides a description of the overall extent of pitting damage at that time. This is the main reason for focusing attention on this distribution.

Some comments have already been made, in Section 5.1.1.2, of the relationship between the frequency distribution for pit depths, $f(h,t)$, the rate of pit generation, $G(t)$, and the rate of pit growth, $v(h)$; these are summarized in Eq. 5-1.

Examples of pit-depth distributions calculated at various times, for various assumed functional forms for $G(t)$ and $v(h)$, have been presented in other reports on this project (Refs. 5.40-5.42) and are not repeated here. In addition, and as already pointed out, a similar approach has been used under this project to describe the evolution in time of the crystal-size distribution in a crystallizing glass (Ref. 5.11).

It would be a relatively straightforward matter to apply this approach using, say, a more deterministic model for $G(t)$ (for example, as described in References 5.3-5.5) and an experimentally determined function for $v(h)$ (for example, as in Reference 5.14). In addition, other aspects of pit growth, such as deactivation of growing pits, could be included as well. Another extension that could be treated would be that for which v exhibits more complex behavior than that considered here, such as depending explicitly upon both h and t (that is, $v = v(h,t)$) or involving effects on v of electrode kinetics at the pit base or of chemically active pit walls.

5.1.4 Conclusions

The pitting-kinetics modeling studies presented here have concentrated on a number of important aspects of the overall pitting process. Moreover, the frequent reference to related experimental work that was made throughout these modeling studies indicates the importance of maintaining a close relationship between experiment and theory.

Extensions of the modeling effort could be useful in a number of areas. These would include inclusion of effects of radiolytically produced chemical species on pit-growth kinetics, coupling of realistic models of pit generation and pit growth, and prediction of pitting behavior over very long time

intervals. Application of the models to specific repository conditions would also be very important.

5.2 General Corrosion Modeling

The general subject of effects of irradiation on metallic corrosion has long been of interest (Refs. 5.43, 5.44). Additional activity in this area has recently been spurred by concern regarding the long-term performance of container materials for high-level nuclear waste buried in an underground repository. Both general and localized corrosion can potentially occur and can ultimately lead to a breached container, thus exposing to the environment either the next level of containment or finally the waste form itself. Along these lines, a number of experimental studies of irradiation effects on corrosion, relating specifically to waste-package containment materials, have been reported (Refs. 5.45-5.47). Another approach to evaluating effects of irradiation on corrosion is through the application of predictive models. Indeed, several models for the corrosion of waste-package container materials have been developed with varying degrees of complexity (Refs. 5.49-5.52).

The following sections describe a model for the general corrosion of a metal surface in contact with an aqueous environment. The model is physically based in the sense that it includes the major kinetic processes contributing to such corrosion: transport of molecular species through the surrounding water by chemical diffusion and film-growth kinetics on the metal surface. The model is applied to three simple hypothetical examples illustrating how variation of certain input parameters and assumptions ultimately affects the overall time-dependent extent of general corrosion.

Attention is on effects of gamma-radiation-induced production of chemical species on the overall corrosion kinetics, although chemical-reaction-induced annihilation of species is considered as well. Finally, the application of this formalism to predicting the behavior of actual materials is discussed, including approaches to some of the problems associated with the description of complex systems.

5.2.1. General Description of Model

5.2.1.1 Assumptions

The major assumptions inherent in the corrosion model developed in this section are the following:

- The chemical species that contribute to general corrosion are electrically neutral. This assumption is introduced purely for the sake of simplicity. It precludes the possibility of describing electromigration of charged species along a gradient of electrostatic potential within the water, but eliminates the need to impose the point-by-point constraint of charge neutrality or to calculate the ambient potential distribution.
- No convective flow of the aqueous environment takes place.

- Film-growth kinetics at the metal surface is described using the point-defect model of Chao, Lin, and Macdonald (Ref. 5.53).
- The spatial geometry has radial cylindrical symmetry.
- The aqueous environment is isothermal, an assumption which could easily be relaxed, but which is imposed here for the sake of simplicity.

5.2.1.2 Mass-Transport Formalism

Since we are considering radial cylindrical symmetry, we take the metal surface to be defined by $r = r_0$, where r is the radial position coordinate. The aqueous environment exists within the region $r > r_0$, and the gamma-radiation field is assumed to emanate from the region $r < r_0$.

Under the present assumptions, a mass-balance expression for the i th chemical species within the region $r > r_0$ has the following form:

$$\frac{\partial C_i}{\partial t} = \nabla \cdot \left(\frac{D_i}{\xi} \nabla C_i \right) + G_i - A_i \quad (5-41)$$

where $C_i(r,t)$ is the concentration of the species at radial position r and time t ; $D_i(r,t)$ is its diffusivity within the aqueous medium; $\xi(r,t)$ is a tortuosity factor (which, for a high-level waste-package container, would account for the porous nature of the backfill or host rock); $G_i(r,t)$ accounts for the generation of the i th species (for example, by radiolysis or chemical reaction); and $A_i(r,t)$ accounts for the annihilation (for example, by chemical reaction). Of course, the ∇ operator is that appropriate to radial cylindrical symmetry. Clearly, the first term on the right-hand side of Eq. 5-41 accounts for chemical diffusion, which, under present assumptions, is the only means by which the i th species can be transported through the solution to the metal surface.

5.2.1.3 Generation and Annihilation of Chemical Species

Of the variety of possibilities by which chemical species can be generated and annihilated, we consider just two. These are used in the examples presented below.

Species production by gamma radiolysis is described as follows:

$$G_i = g_i I(t) (r_0/f) \exp [-\epsilon(r-r_0)] . \quad (5-42)$$

Here g_i is a "g-factor" characteristic of the i th species and, as used in Eq. 5-42, a measure of the volumetric rate of generation of the species per unit intensity of the radiation field. $I(t)$ is the gamma-radiation

intensity at $r = r_0$; the factor r_0/r represents geometric "spreading" of the radiation at distances beyond r_0 ; and ϵ is the linear absorption coefficient for the radiation in the surrounding medium.

In our calculations, the tortuosity factor is equated to unity, which is equivalent to ignoring effects of backfill or host rock outside the metal surface. Also, $I(t)$ is treated as exhibiting simple exponential decay, that is,

$$I(t) = I_0 \exp(-\lambda t) \quad (5-43)$$

where λ is an effective radioactive decay constant for the source of the gamma radiation. Finally, the quantity ϵ is treated as a constant.

We treat the annihilation rate, A_i , as resulting from a homogeneous, second-order chemical reaction within the water; its form is

$$A_i = C_i \sum_j \eta_{ij} C_j. \quad (5-44)$$

In Eq. 5-44, η_{ij} is the rate constant for the reaction between species i and species j , and the summation is taken over all the species that can react with species i . In general, $\eta_{ij} \neq \eta_{ji}$, unless species i and j are annihilated in equal amounts when the reaction occurs.

5.2.1.4 Film-Growth Kinetics

The model for film-growth kinetics used in this analysis was developed by Chao, Lin, and Macdonald (Ref. 5.53) based on concepts of point-defect migration within a passive film resulting from the presence of an electrostatic field. This model is summarized as follows (Eq. 49 of Reference 5.52):

$$\frac{dL}{dt} = \frac{A (B - 1)}{\exp(2KL) - 1} \quad (5-45)$$

Here

$$A \equiv A_0 \exp\left(\frac{-2\alpha F}{RT} V_{\text{ext}}\right) \quad (5-46)$$

$$B \equiv B_0 \exp\left(\frac{2F}{RT} V_{\text{ext}}\right) \quad (5-47)$$

$$K \equiv \frac{FE}{RT} . \quad (5-48)$$

In these expressions, L is the film thickness at time t ; A_0 and B_0 are parameters that are treated here as constants (although, in reality, they vary with the pH of the aqueous medium [Ref. 5.52]); α is a dimensionless parameter that typically is less than but on the order of unity; F , R , and T are the Faraday constant, the gas constant, and the absolute temperature, respectively, with T regarded as being constant; V_{ext} is an "external potential"; and E is the electric field strength within the film (assumed constant).

Application of the film-growth model is complicated by the fact that V_{ext} generally is a function of the solution composition at the film/solution interface. For example, if the solution contains only one oxidizing species and one reducing species, whose concentrations are denoted C_1 and C_2 , respectively, then this functional dependence is taken to be of the general form

$$V_{\text{ext}} = V_{\text{ext}}^0 + \frac{RT}{F} \ln \left(\frac{C_1(r_0)}{C_2(r_0)} \right) \quad (5-49)$$

where V_{ext}^0 is a constant. Equation 5-49 is based on the assumption that the Nernst equation can be applied, which is valid only for a single process (one oxidizing species and one reducing species). For more general cases, which are not considered here, the concept of a "mixed potential" must be used (as discussed, for example, by Macdonald et al. [Ref. 5.54]).

5.2.1.5 Initial Conditions and Boundary Conditions

A number of initial and boundary conditions must be imposed in order to completely define a given corrosion problem. The conditions used here are defined in this section.

At large distances from the metal surface, we take all C_i values to be fixed, that is,

$$C_i(r \rightarrow \infty, t \geq 0) = C_i^0 \quad (5-50)$$

where C_i^0 is a constant and the corrosion process is assumed to begin at time $t = 0$. This is the "far-field" boundary condition. For computational purposes, it is convenient to express Eq. 5-50 in the somewhat different form

$$C_i(N \equiv r/r_0 \rightarrow \infty, t \geq 0) = C_i^0 . \quad (5-51)$$

If one selects a finite value for the ratio N , then Eqs. 5-50 and 5-51 are not exactly equivalent, although they become more so as N is increased. For the examples presented below, the value $N = 5$ is selected, which is adequate for present illustrative purposes.

The film/solution interface is taken to be $r = r_0$ for all times in our calculations. In other words, the slight time-dependent shift of this interface, which takes place as metal oxidation occurs, is ignored. The boundary condition for a reducing chemical species in the solution at the metal surface is

$$\frac{\partial C_i}{\partial r} (r_0, t) = 0 \quad (5-52)$$

which constitutes an expression of the fact that a reducing species does not undergo any chemical reaction at the metal surface.

For oxidizing species in the solution at the metal surface, the boundary condition is generally determined by requiring that the rate of supply of these species is exactly accounted for by a commensurate rate of film growth, that is,

$$\frac{dL}{dt} = \sum_i k_i \frac{\partial C_i}{\partial r} (r_0, t) \quad (5-53)$$

where k_i is a constant that is characteristic of both the metal and the i th oxidizing species, and the summation is carried out over all the oxidizing species. The actual boundary condition is obtained by equating the right-hand side of Eq. 5-45 to the right-hand side of Eq. 5-53, where we take $L(t = 0) = 0$.

An interesting limiting case is that in which film-growth kinetics occurs very rapidly in comparison with the rate at which oxidizing species can be transported through the solution to the metal surface. For this case, denoted as "maximum-rate kinetics", the appropriate boundary condition for the i th oxidizing species (indeed, for all such species) is

$$C_i(r_0, t) > 0) = 0 \quad (5-54)$$

The initial condition is just an extension of Eq. 5-50, that is,

$$C_i(r_0 < r < \infty, t = 0) = C_i^0 \quad (5-55)$$

In other words, it is assumed that, initially, the concentration of the i th species is spatially uniform and equal to its "far-field" value. In terms of the notation of Eq. 5-51, Eq. 5-55 is re-expressed as

$$C_i(r_0 < r < Nr_0, t = 0) = C_i^0 \quad (5-56)$$

where, as noted above, N is taken to be equal to 5 in the calculations discussed here.

5.2.2 Numerical-Integration Technique

The approach used to numerically integrate the coupled partial differential equations that describe the diffusion process in the aqueous medium, although clearly an important part of the problem's overall treatment, is merely summarized here. In particular, three aspects of this approach are discussed: integration of the mass-transport equations; coupling of mass transport in solution at the film/solution boundary with the model used for film-growth kinetics; and calculation of concentration gradients in solution at the container surface.

The coupled mass-transport equations for the region $r > r_0$ are solved by reducing the partial differential equation for $C_i(r, t)$ to a system of ordinary differential equations for $C_i(t)$ using a finite-difference method. These ordinary differential equations are then integrated using a third-order Runge-Kutta method.

Imposition of boundary conditions is relatively straightforward except for that at $r = r_0$ for the case in which film-growth kinetics is included, as outlined in Sections 2.4 and 2.5. Clearly, this boundary condition consists of a complex relationship between concentration gradients and concentrations measured at $r = r_0$. In general, its imposition can be accomplished only through the application of a numerical, iterative procedure. Briefly, this was accomplished by taking the difference between the right-hand side of Eq. 5-45 and that of Eq. 5-53, at each time step of the calculation, and applying a secant method to determine conditions for which that difference is equal to zero.

Calculation of concentration gradients in solution must be treated differently at the container surface than at positions further away from the surface. For $r > r_0$, a central-difference approximation is used to calculate gradients. However, this approach cannot be used at $r = r_0$ because concentrations are not defined. Therefore, a one-sided difference approximation is used at $r = r_0$, resulting in about twice the error associated with the usual central-difference approximation.

5.2.3 Application to Specific Examples

In this section, the corrosion model is applied to three specific examples and the behavior of a highly simplified physical system is described for

each. From a computational standpoint, the first example is the simplest, and the last is the most complex. The primary reason for examining simplified physical systems such as these is that one can generally make an unambiguous assessment of gross features of the corrosion process in terms of the various contributing phenomena. This would likely be more difficult for complex physical models due to coupling between the various factors that contribute to the overall corrosion process; such coupling can complicate and obscure the features of interest. In addition, simplified examples are useful for checking the accuracy of the numerical procedure and for determining if boundary conditions are being appropriately imposed.

The calculations described below were carried out with the value of unity assigned to certain parameters, namely, r_0 , I_0 , λ , D_i , and certain others as indicated below. Values for C_i (the species concentration at $r \rightarrow \infty$ or, in this case, $N = 5$) were selected as either zero or unity, as appropriate in each example. Moreover, radial distance was normalized with respect to r_0 ; species concentration in solution was taken in units of (that is, was normalized with respect to) C_i , and time was measured in units of (again, normalized with respect to) r_0^2/D_i , with D_i being taken as unity for all species that may be present. Also, ϵ was normalized with respect to $r_0 - 1$. Wherever specific values for these quantities are used and reported as being dimensionless, this normalization is understood to exist.

5.2.3.1 One Chemical Species (Oxidizing) With Maximum-Rate Kinetics

The first example provides a simple yet effective means for demonstrating possible effects of gamma radiation on the kinetics of general corrosion. Just one chemical species is considered; an oxidizing species which is radiolytically produced in the solution outside the container and having a concentration of unity everywhere within the solution at $t = 0$. In addition, maximum-rate kinetics is assumed for the interface at $r = 1$ (at the container surface), as described by Eq. 5-54.

Shown in Figures 5.7 to 5.10 are concentration profiles calculated for this one-species model for selected times and for the following four different sets of values for g and ϵ :

- $g = 0$
- $g = 1, \epsilon = 1$
- $g = 10, \epsilon = 1$
- $g = 10, \epsilon = 2$

the case $g = 0$ clearly corresponding to a radiation-free environment. In all these figures, the maximum-rate-kinetics boundary condition is illustrated by the species concentration being maintained at zero at the container surface. In addition, the far-field boundary condition, in which the concentration is maintained at unity at $r = 5$, also applies in all cases.

The tendency of the slope of the concentration profile at $r = 1$ to decrease with increasing time results from continuing loss of the chemical species from the solution, which is due to the heterogeneous reaction the species

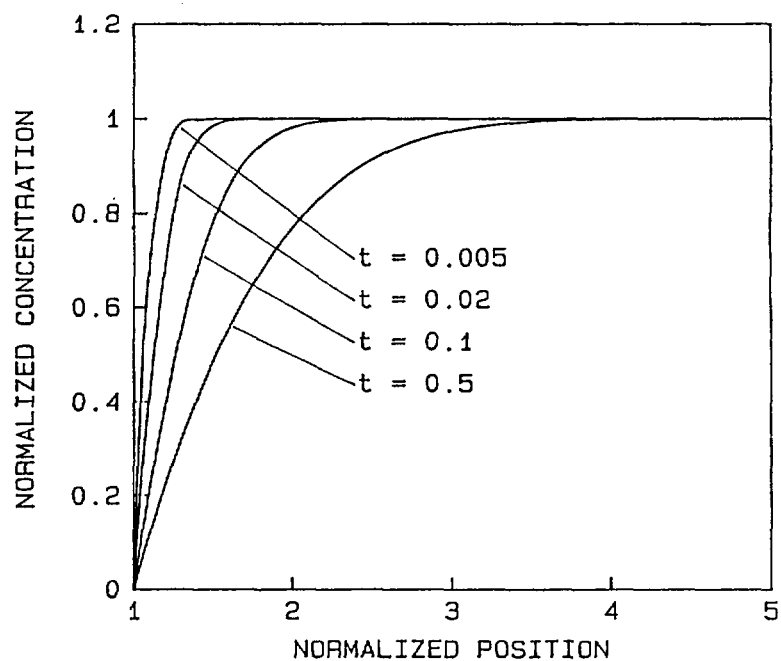


Figure 5.7. Selected concentration profiles calculated using one-species model with maximum-rate kinetics and $g = 0$.

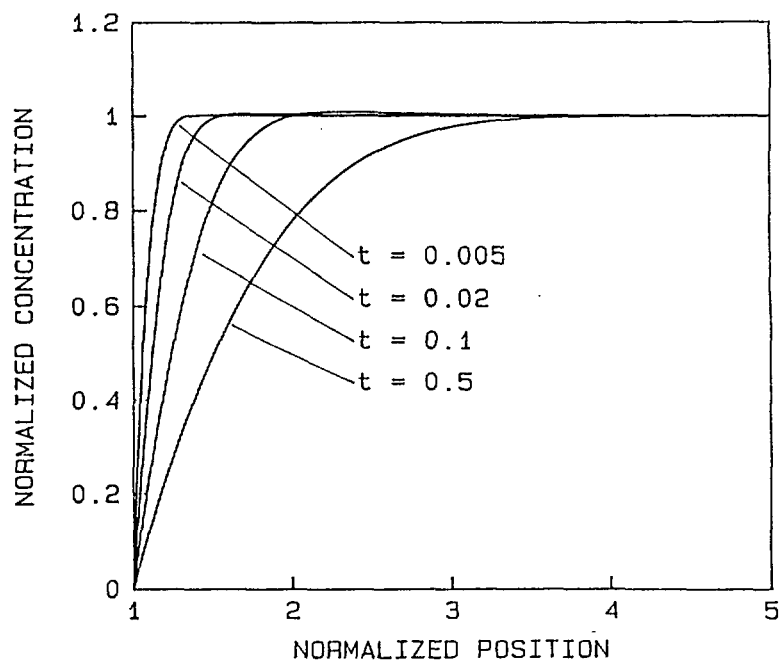


Figure 5.8. Selected concentration profiles calculated using one-species model with maximum-rate kinetics and $g = 1$, $\epsilon = 1$.

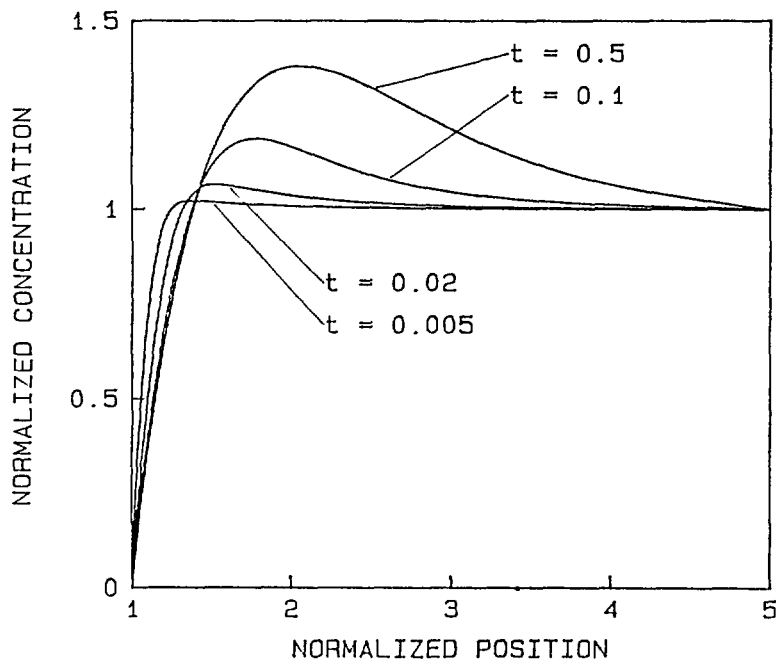


Figure 5.9. Selected concentration profiles calculated using one-species model with maximum-rate kinetics and $g = 10$, $\varepsilon = 1$.

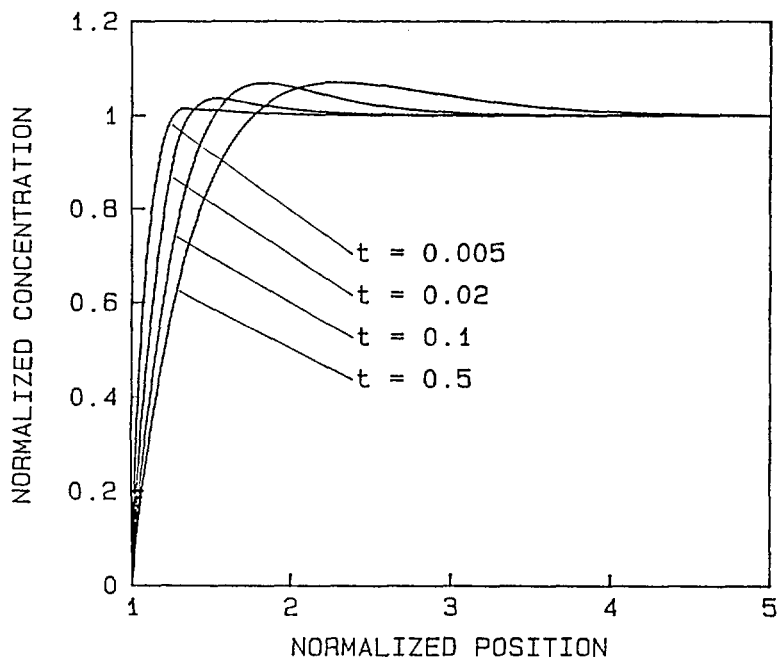


Figure 5.10. Selected concentration profiles calculated using one-species model with maximum-rate kinetics and $g = 10$, $\varepsilon = 2$.

undergoes at this position. Moreover, radiolytic production of the species causes a maximum to occur in the concentration profile at a given time. This maximum results from the decreasing intensity of the radiation field (and hence the species' rate of production) with increasing distance from the container surface, coupled with the existence of maximum-rate kinetics at the container surface. Effects of varying the values of g and ϵ on the concentration profiles are clearly illustrated in Figures 5.7 to 5.10 and require no additional discussion.

The rates of corrosion and the corrosion depth are shown, for these four cases, in Figures 5.11 and 5.12, respectively. The corrosion rate is proportional to the concentration gradient of the oxidizing species at $r = 1$ and, indeed, in Figure 5.11 is presented in normalized fashion as being equal to this gradient using units for concentration and distance consistent with those in Figures 5.7 to 5.10. The overall corrosion depth is equal to the integral over time of the corrosion rate and is presented in normalized form in Figure 5.12 in terms of units consistent with those in Figure 5.12.

As expected, the effect of increasing g at fixed t is to increase the corrosion rate and depth, and the effect of increasing ϵ , at fixed g , is to reduce these quantities. Clearly, the net effect of irradiation is to enhance the corrosion rate and depth. This enhancement can be considerable, depending upon values used for g and ϵ . Other than that, the general manner in which corrosion rate and depth vary with time is similar for radiation and radiation-free environments (except that the case $g = 10$, $\epsilon = 1$ exhibits a slight minimum followed by a slight maximum in corrosion rate). This observation is consistent with that made by Byalobzheskii (Ref. 5.55) for the corrosion of steel in NaCl and H₂SO₄ solutions in a gamma-environment; he reported no change in the general form of the corrosion-time relationships due to irradiation, but a marked increase in the corrosion rate.

5.2.3.2 Two Chemical Species (One Oxidizing and One Reducing) With Maximum-Rate Kinetics

The second example is identical to the first except for the added feature of a reducing chemical species that can undergo homogeneous chemical reaction with the oxidizing species within the solution. The oxidizing species is taken to be subject to the same initial and boundary conditions as in the previous example. The reducing species, on the other hand, must satisfy Eq. 5-52 at $r = 1$; in addition, its concentration is assumed to be zero for $r > 1$, $t = 0$, and for $r = 5$, $t > 0$. The value $g = 10$ was assigned to each species and, as indicated above, the diffusivity for each was taken as unity. In addition, the homogeneous chemical reaction kinetics in solution was taken to be of the second-order type shown in Eq. 5-44 (obviously with no summation sign required for this example), with the rate constant being the same for both species and equal to unity in units of (normalized concentration \times normalized time)⁻¹. Finally, the value $\epsilon = 2$ was selected for the linear absorption coefficient.

From the statement of the problem presented above, it is clear that the reducing species exists purely as a result of radiolytic production. Consequently, if one were to set $g = 0$ just for the reducing species, the

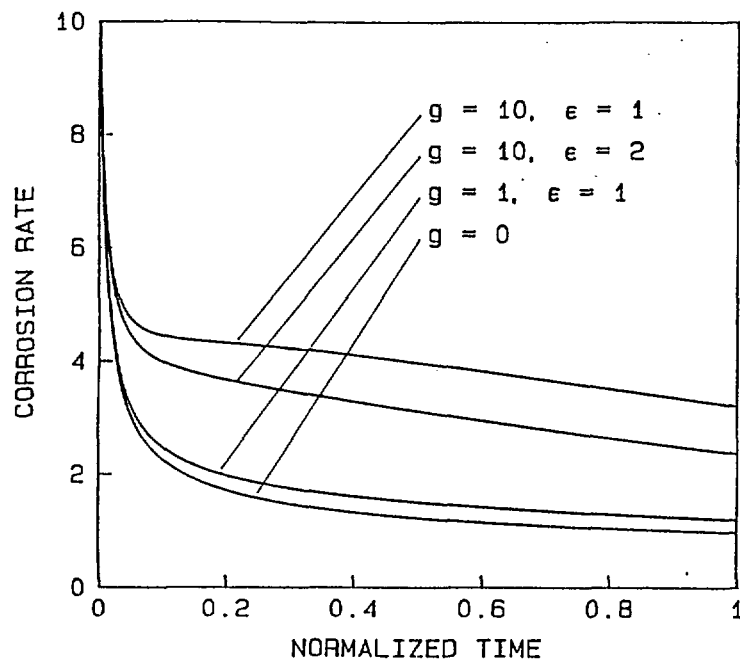


Figure 5.11. Corrosion rate calculated as a function of time for one-species model with maximum-rate kinetics.

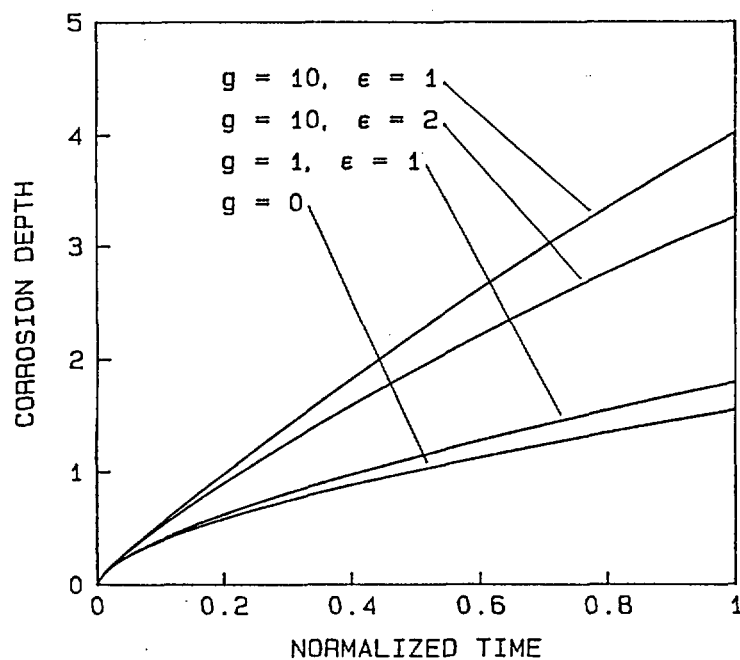


Figure 5.12. Corrosion depth calculated as a function of time for one species model with maximum-rate kinetics.

resultant system would be equivalent to the one-species model discussed previously.

Selected concentration profiles, calculated for the oxidizing and reducing species, are shown in Figures 5.13 and 5.14, respectively. The radiolytically induced generation of the reducing species is seen, in Figure 5.14, to be most pronounced in the vicinity of the container surface, due to the higher intensity of the radiation field within this region.

Figure 5.15 illustrates the effect of the reducing species on the concentration profiles, and several observations can be made. First, the overall effect of the reducing species in the solution is to lower the concentration of the oxidizing species, at a given position and time. This is due to the fact that the two species annihilate each other when they interact via the second-order chemical reaction in solution. Second, this lowering of oxidizing-species concentration is most pronounced at positions nearer to the container surface, where the intensity of the radiation field, and hence the rate of radiolytic production of the reducing species, is highest. Third, the difference between oxidizing-species concentration profiles for the one-species and two-species models becomes greater as time progresses. This results from the fact that, initially, none of the reducing species is present in the solution; its concentration, thus also its rate of reaction, increases with time until effects of radiation field decay finally would begin to predominate (such effects are not shown in these figures).

The corrosion rate and corrosion depth are shown as functions of time in Figures 5.16 and 5.17, respectively. These were calculated in the same manner as the corresponding quantities for the first example (Figures 5.11 and 5.12). As expected, the presence of the reducing species results in a lowering of the corrosion rate (and consequently the corrosion depth) at a given time. Again, this results from loss of the oxidizing species, via chemical reaction in solution, which leaves less of this species available for the corrosion reaction at $r = 1$. The radiolytic-production-free case ($g = 0$) for both species is shown for purpose of comparison. As discussed above, this is the same as the $g = 0$ case for the one-species model.

5.2.3.3 One Chemical Species (Oxidizing) With Film-Growth Kinetics

The final example considered here is identical to the first in every respect except one: Instead of maximum-rate kinetics at $r = 1$, the film-growth model discussed in Section 2.4 is used. Imposition of this boundary condition is carried out as described in Section 3.

One might question how Eq. 5-49 in Section 3 can be applied if no reducing species is included in the analysis. This problem can be avoided by simply assuming that a reducing species actually is present, but that $C_2(r = 1)$ is a constant, and that its contribution to V_{ext} is "absorbed" into V_{ext}^0 .

The magnitude selected for parameters A_0 , α , and k_1 (with no summation over i needed in Eq. 5-53) was unity in terms of the normalized units used here. In addition, values of $B_0 = 10$, $T_i = 300^\circ\text{K}$, $FV_{\text{ext}}^0/R = 1^\circ\text{K}$, and $2FE/R = 10^5$

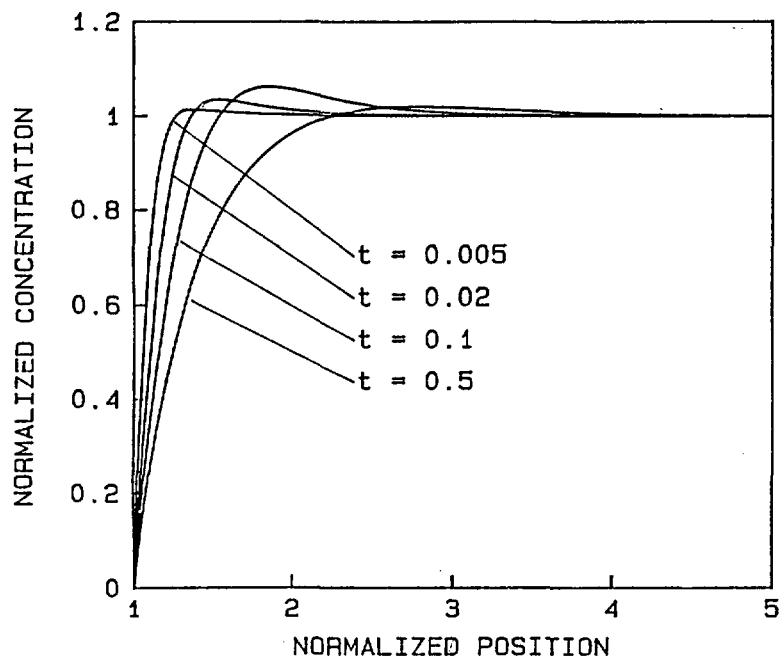


Figure 5.13. Selected concentration profiles calculated for oxidizing species using a two-species model with maximum-rate kinetics, and $g = 10$, $\epsilon = 2$.

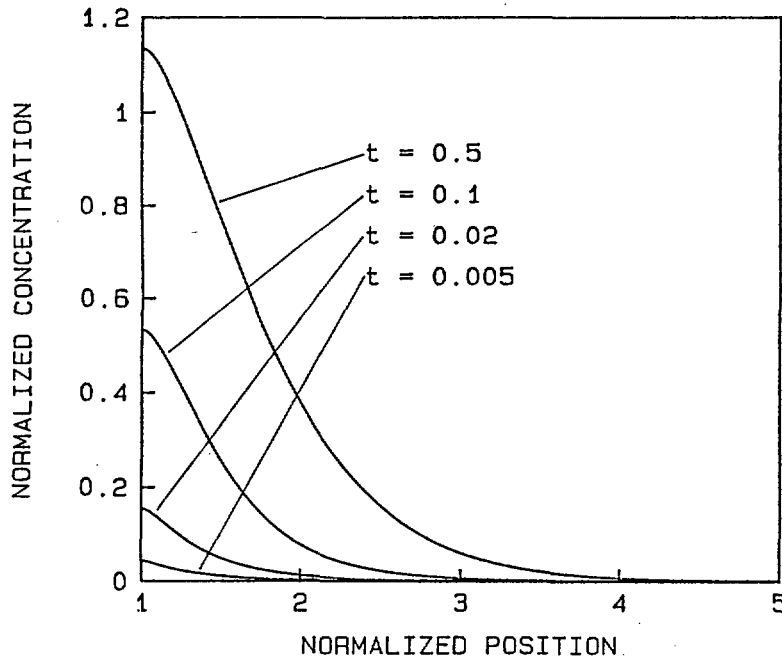


Figure 5.14. Selected profiles calculated for reducing species using the same model as in Figure 5.13.

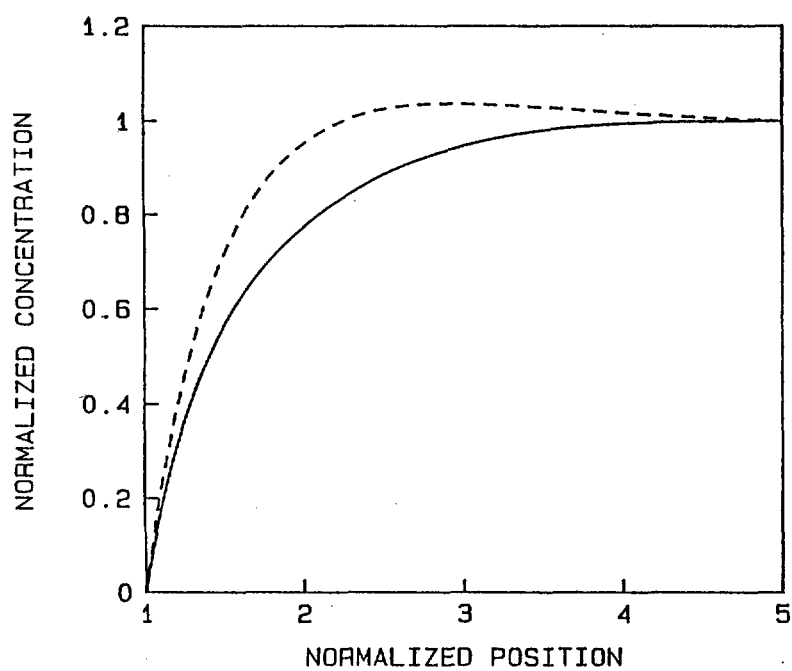
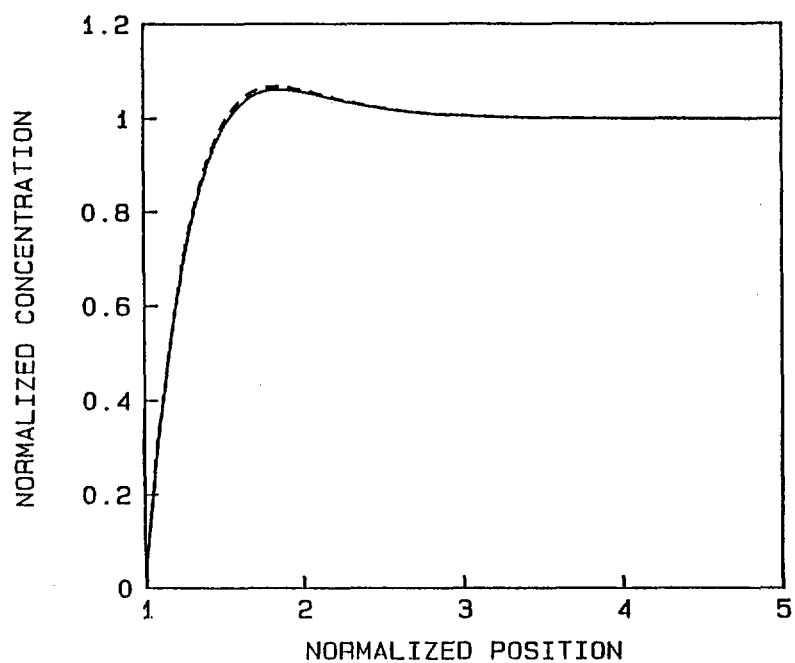


Figure 5.15. Comparison of concentration profiles calculated for oxidizing species using one-species and two-species models (dashed and solid curves, respectively) with maximum-rate kinetics at normalized time, 0.1 and 1 (a and b, respectively), with $g = 10$, $\epsilon = 2$ for both models.

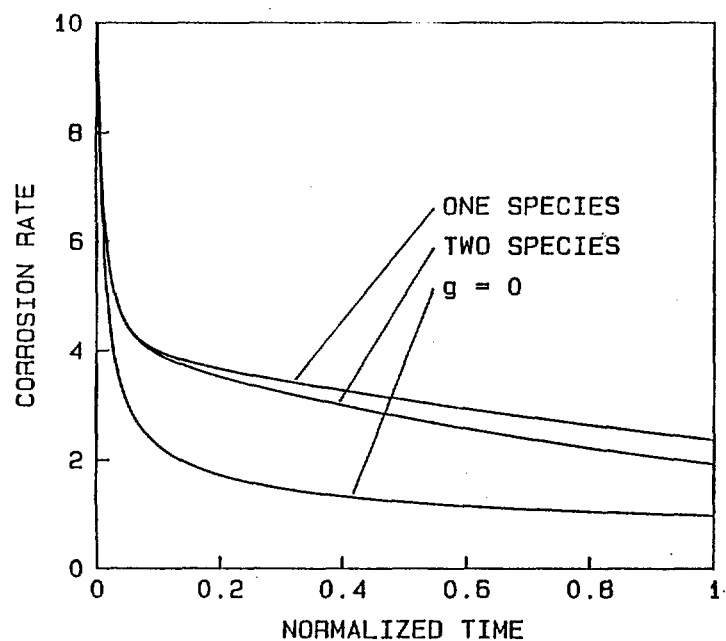


Figure 5.16. Corrosion rate calculated as a function of time for two-species model, with maximum-rate kinetics and $g = 10$, $\epsilon = 2$.

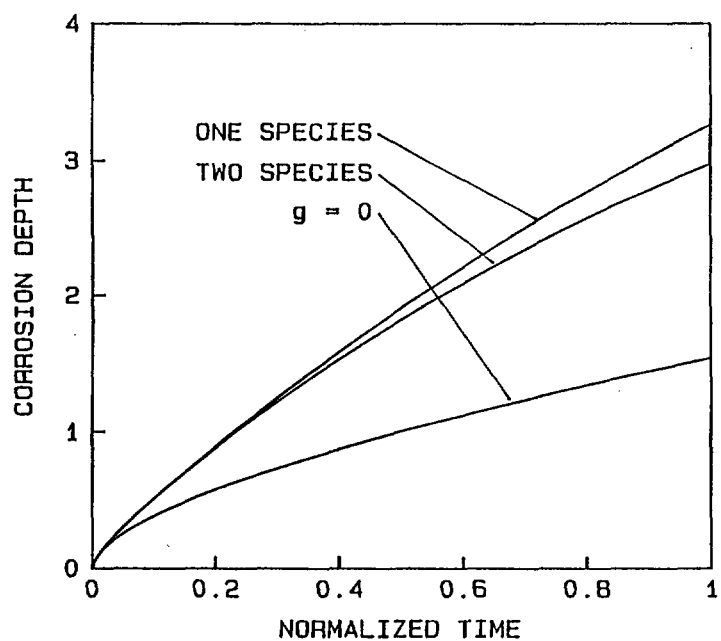


Figure 5.17. Corrosion depth calculated as a function of time for two-species model with maximum-rate kinetics and $g = 10$, $\epsilon = 2$.

were selected, the units of the last quantity being @K per unit of length being used. A g-value of 10 was used to describe radiolytic production of the oxidizing species, and ϵ was taken as 2.

The singularity in dL/dt at $L = 0$, predicted by Eq. 5-45, was avoided by selecting an initial value of $L = 10^{-4}$. One can show that, at this non-zero initial value for L , and for the numerical values selected for FE/R and T , the exponential function in Eq. 5-45 still has a value close to unity (about 1.03).

Some concentration profiles calculated for the oxidizing species are shown in Figure 5.18 for the radiation-free case ($g = 0$). At very early times, the oxidizing species concentration drops to very low values near the container surface. This results from the fact that the oxide-layer thickness is quite small at these times, so that film-growth kinetics has not yet become an important factor; hence, the kinetics of mass transport in the solution at the film surface still resembles that for maximum-rate kinetics (see Figure 5.7). However, as time progresses and the film becomes thicker, film-growth kinetics becomes more important as the oxidizing species cannot be transported across the interface as quickly as for maximum-rate kinetics. Hence, its concentration at the interface increases and the magnitude of the concentration gradient at that position decreases.

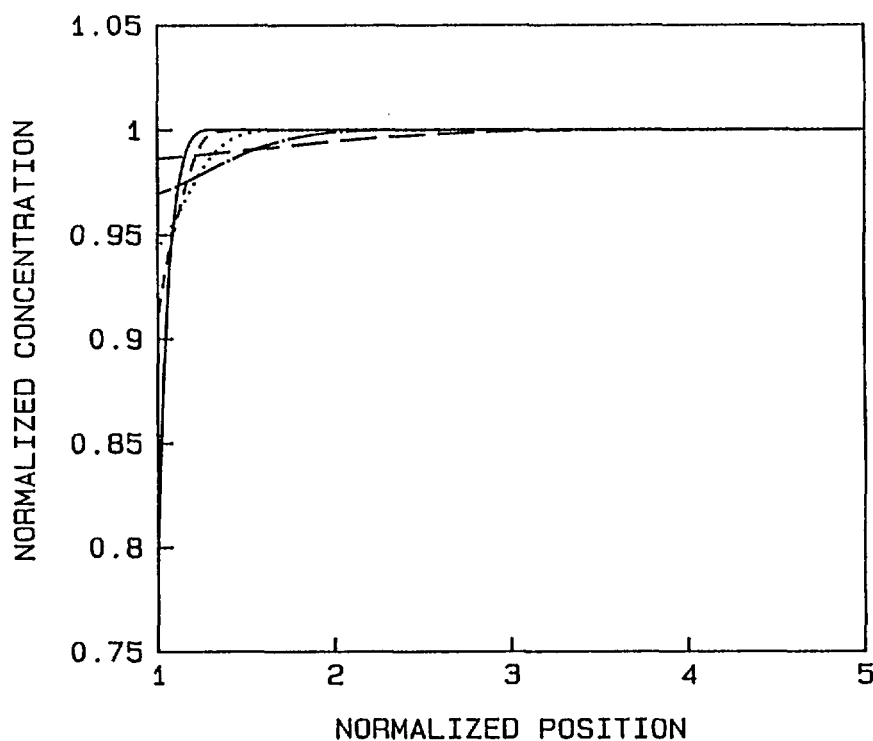


Figure 5.18. Selected concentration profiles calculated using one-species model with film-growth kinetics and $g = 0$. Solid, short-dashed, dotted, dot-dash, and long-dashed curves represent times 0.001, 0.005, 0.02, 0.1, and 0.5, respectively.

Similar concentration profiles are shown in Figure 5.19, except that the oxidizing species is now being radiolytically produced, with $g = 10$, $\epsilon = 2$. (Otherwise, the two examples are identical). In this case, the concentration increases rapidly near the interface because the species is being generated within the solution, but its transport across to the film is being inhibited by slower film-growth kinetics. Figure 5.19 can be compared with Figure 5.20, the latter representing the same problem except with maximum-rate kinetics. Clearly, far less radiation-induced buildup of the concentration field occurs within the solution in the vicinity of the metal surface when maximum-rate kinetics is imposed at the interface.

In Figure 5.20 the corrosion rate is plotted as a function of time for the two cases illustrated in Figures 5.18 and 5.19. It can be seen that, despite the fact that the concentration profiles of the oxidizing species near the metal surface are quite different for the two cases, the time dependent corrosion rates are virtually the same. Several characteristics of the overall kinetics result in this behavior. The kinetics tends toward film-growth control, as opposed to solution transport control, as evidenced by the concentration profiles in Figures 5.18 and 5.19. For film-growth-controlled kinetics, the overall corrosion rate is governed by Eq. 5-45. However, from Eqs. 5-45 to 5-47 and Eq. 5-49, the instantaneous corrosion rate does depend upon the concentration of the oxidizing species in the solution at the film surface. This dependence does become small, as seen from Eqs. 5-45 to 5-47, for $B \gg 1$. As an example, we find that for the set of numerical parameters used here, and for the special case $V_0^{\text{ext}} = V_{\text{ext}}$ (that is, $C_1(r = 1) = 1$ in our normalized units, where C_1 , as defined for Eq. 5-49, is the concentration of the oxidizing species), we obtain $B \approx 10.1$, so that the dependence of dL/dt on V_{ext} is not expected to be large.

The time-dependent corrosion depth is plotted for these same two examples in Figure 5.21. Again, these were obtained simply by integrating the corrosion rates as in the previous examples. Clearly, the radiation field causes only a very slight enhancement of the corrosion depth; in contrast, the results based on maximum-rate kinetics (Figure 5.12) indicate a corrosion depth strongly enhanced by radiation-field effects.

Thus, when film-growth kinetics, instead of solution-transport kinetics, dominates the corrosion process, the effect of the radiation field on the overall rate and extent of metal corrosion can be substantially suppressed, as has been illustrated with this example. Other cases, such as those involving film-growth-controlled kinetics in which the right-hand side of Eq. 5-45 has stronger dependence on $C_1(r = 1)$, would exhibit a greater relative enhancement of corrosion as a result of the radiation field.

Moreover, as can be seen by comparing Figure 5.20 with corresponding curves for maximum-rate kinetics in Figure 5.11, as well as comparing Figure 5.21 again with corresponding curves for maximum-rate kinetics in Figure 5.12, inclusion of film-growth kinetics has resulted in an extremely large reduction in the overall extent of general corrosion at a given time. This is not altogether surprising in view of the large changes brought about in the concentration profiles due to inclusion of film-growth kinetics, as seen by comparing Figure 5.7 with Figure 5.18 and Figure 5.10 with Figure 5.19.

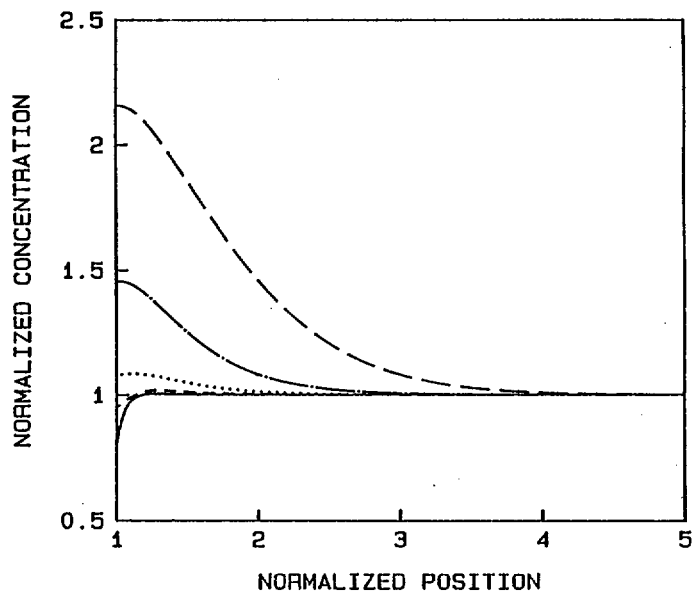


Figure 5.19. Selected concentration profiles calculated using one-species model with film-growth kinetics and $g = 10$, $\epsilon = 2$. Nomenclature associated with curves is the same as that used in Figure 5.18.

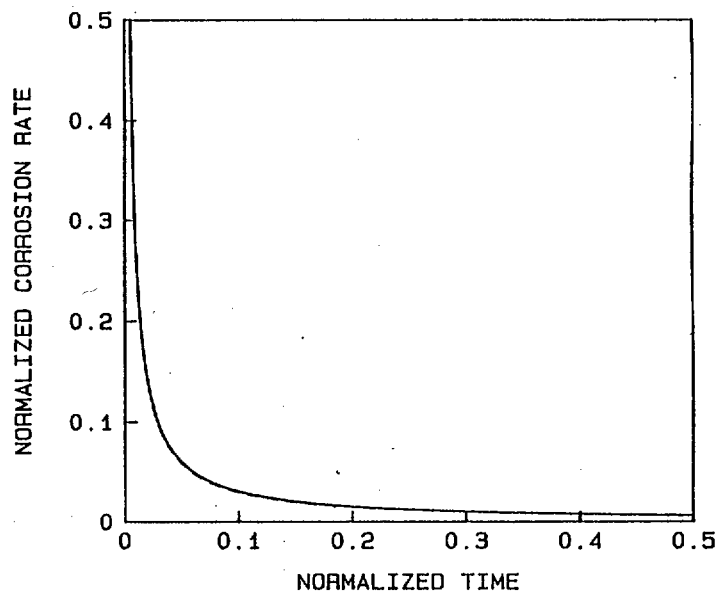


Figure 5.20. Corrosion rate calculated as a function of time for one-species model with film-growth kinetics. The dashed and solid curves represent $g = 0$ and $g = 10$, $\epsilon = 2$, respectively.

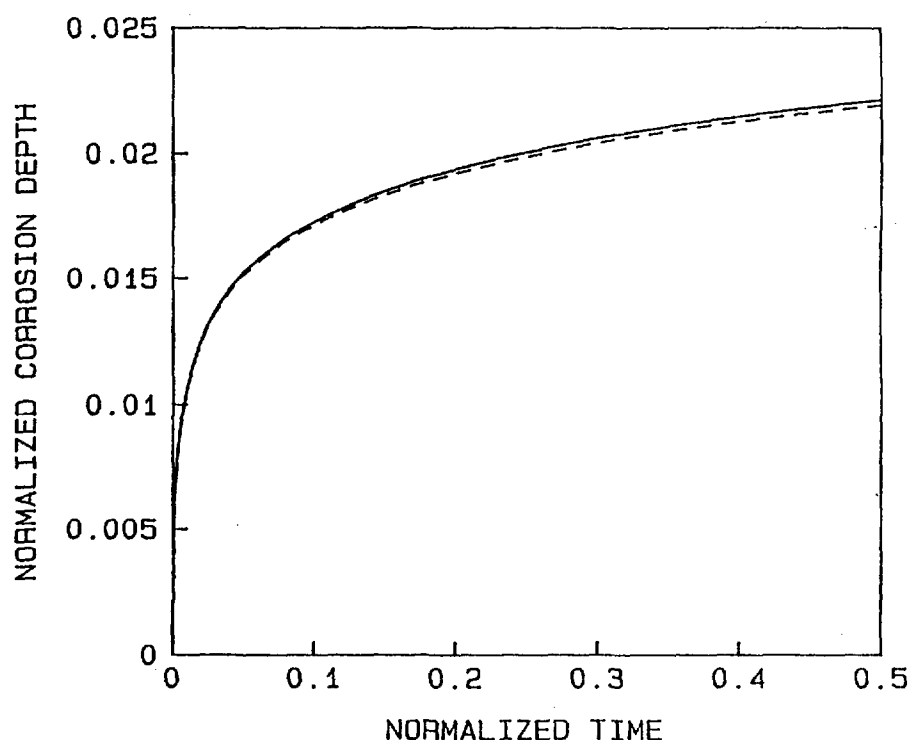


Figure 5.21. Corrosion depth calculated as a function of time for one-species model with film-growth kinetics. The dashed and solid curves represent $g = 0$ and $g = 10$, $\epsilon = 2$, respectively.

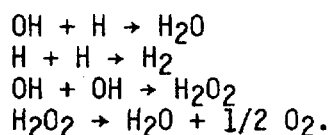
5.2.4 Conclusions

In summary, it is clear that the kinetics of aqueous general corrosion in a gamma-radiation environment can be extremely complex. In addition to the coupled kinetic processes of mass transport in solution and film growth on the metal surface, there are also the radiolytic production of chemical species (which itself varies with both time and position) and the loss or production of species in solution due to homogeneous chemical reactions. The hypothetical examples presented above have served to illustrate the general manner in which such effects can influence the overall time-dependent extent of corrosion.

Some additional problems would have to be addressed in applying this procedure to "real" systems. These are associated with establishment of an adequate physical description and then the numerical integration of the resultant model.

The former problem results from the fact that many chemical species are generally present in actual aqueous systems. These include the naturally occurring groundwater species and, for a package that contains nuclear waste, species characteristic of the repository. Moreover, radiolytic production can involve literally dozens of chemical reactions, although many of the pertinent rate constants have been measured (Refs. 5.56-5.58). Some

substantial reduction in complexity, relative to the overall composition of the aqueous solution, would likely have to be made. Despite this fact, the physical reasonableness of the model can be preserved if such reductions are made with care. For example, as far as radiolysis is concerned, one simplified set of reactions, associated with radiolytically produced H and OH, is the following:



The last of these reactions is clearly not elementary, and would have to be represented using an effective rate constant.

In addition, as pointed out in the discussion associated with Eq. 5-49, the presence of multiple chemical species alters the manner in which the film-growth model is applied. Moreover, if some of the chemical species are charged, then one must include an electromigration contribution in the mass-transport expressions for the solution as well as impose a charge-neutrality condition (Ref. 5.59).

Effects of heat flux could be included in the formalism by regarding the region $r < 1$ as a heat source and treating the region $r > 1$ as consequently having a temperature field that varies both spatially and temporally. The heat-conduction equation would then have to be solved simultaneously with the mass-transport equations which, in general, contain some temperature-dependent factors. (We have seen, for example, in Eqs. 5-45 to 5-49, that even the boundary conditions may include some temperature dependence.) Another temperature-dependent effect that may be important is related to the fact that a certain characteristic potential of some electrolytes is temperature-dependent (Ref. 5.60), so that a temperature gradient in solution could, in this manner, contribute to a gradient in electrostatic potential.

The problem associated with numerical integration results largely from the fact that rates of simultaneously occurring chemical reactions may cover a wide range of values, resulting in what is known as a set of "stiff" partial differential equations. However, systems of equations of this type are not uncommon; their treatment has received considerable attention in the literature.

5.3 References for Chapter 5

- (5.1) N. Sato, T. Nakagawa, K. Kudo, and M. Sakashita, in Localized Corrosion, R. W. Staehle, B. F. Brown, J. Kruger, and A. Agrawal (eds.), NACE-3, Nat. Assoc. of Corrosion Engrs., Houston, TX, p. 447 (1974).
- (5.2) M. Janik-Czachor and M. B. Ives, in Passivity of Metals, R. P. Frankenthal and J. Kruger (eds.) (Electrochem. Soc., Princeton, NJ, 1978), p. 369.

- (5.3) D. D. Macdonald and M. Urquidi-Macdonald, Indian J. Technol. 24, 485 (1986).
- (5.4) D. D. Macdonald and M. Urquidi-Macdonald, Electrochim. Acta 31, 1079 (1986).
- (5.5) M. Urquidi-Macdonald and D. D. Macdonald, J. Electrochem. Soc. 134, 41 (1987).
- (5.6) C. Y. Chao, L. F. Lin, and D. D. Macdonald, J. Electrochem. Soc. 128, 1187 (1981).
- (5.7) L. F. Lin, C. Y. Chao, and D. D. Macdonald, J. Electrochem. Soc. 128, 1194 (1981).
- (5.8) D. D. Macdonald, M. Urquidi, and B. G. Pound, in Proc. Conf. 24, Australasian Corr. Assoc., Rotorua, NZ (Nov. 1984), p. 1.
- (5.9) F. C. Hull, R. A. Colton, and R. F. Mehl, Trans. Am. Inst. Mining Metall. Engrs. 150, 185 (1942).
- (5.10) A. M. Gokhale and R. T. DeHoff, Metall. Trans. A. 16A, 559 (1985).
- (5.11) A. J. Markworth, J. Mater. Sci. Lett. 5, 161 (1986).
- (5.12) M. Romanoff, Underground Corrosion, National Bureau of Standards Circular 579 (April 1957), pp. 38, 47, 64, 72.
- (5.13) H. P. Godard, W. B. Jepson, M. R. Bothwell, and R. L. Kane, The Corrosion of Light Metals (John Wiley & Sons, Inc., New York, 1967), pp. 60, 61.
- (5.14) G. P. Marsh, K. J. Taylor, I. D. Bland, C. Westcott, P. W. Tasker, and S. M. Sharland, in Scientific Basis for Nuclear Waste Management IX, L. O. Werme (ed.) (Mater. Res. Soc., Pittsburgh, 1986), MRS, Vol. 50, p. 421.
- (5.15) H. J. Engell and N. D. Stolice, Zeit. Physik-Chemie Neue Folge 20, 113 (1959).
- (5.16) K. J. Vetter and H. H. Strehblew, Ber. Bunsen. Gesell. Physik. Chemie 74, 1024 (1970).
- (5.17) H. W. Pickering and R. P. Frankenthal, J. Electrochem. Soc. 119, 1297 (1972).
- (5.18) H. S. Isaacs, J. Electrochem. Soc. 120, 1456 (1973).
- (5.19) J. W. Tester and H. S. Isaacs, J. Electrochem. Soc. 122, 1438 (1975).
- (5.20) J. R. Galvele, J. Electrochem. Soc. 123, 464 (1976).

- (5.21) K. Nisancioglu and H. Holtan, Electrochim. Acta 23, 251 (1978).
- (5.22) R. Alkire and D. Siitari, J. Electrochem. Soc. 126, 15 (1979).
- (5.23) T. R. Beck and R. C. Alkire, J. Electrochem. Soc. 126, 1662 (1979).
- (5.24) J. Newman, in Localized Corrosion, op. cit. (Ref. 5.1), p. 45.
- (5.25) G. P. Cherepanov, in Comprehensive Treatise of Electrochemistry, Vol. 4: Electrochemical Materials Science, J. O'M. Bockris, B. E. Conway, E. Yeager, and R. E. White (eds.) (Plenum Press, New York, 1981), p. 333.
- (5.26) Ya. M. Kolotyrkin, Yu. A. Popov, and Yu. V. Alekseev, in Advances in Physical Chemistry - Current Developments in Electrochemistry and Corrosion, Ya. M. Kolotyrkin (ed.) (MIR Publishers, Moscow, 1982), p. 11.
- (5.27) A. J. Markworth and L. R. Kahn, EPRI RD-4877, Final Report from Battelle Columbus Division on Project 2258-2 to Electric Power Research Institute, Palo Alto, CA (Nov. 1986).
- (5.28) J. S. Newman, Electrochemical Systems (Prentice-Hall, Inc., Englewood Cliffs, NJ, 1973), pp. 223 ff. and elsewhere within volume.
- (5.29) "Long-Term Performance of Materials Used for High-Level Waste Packaging", D. Stahl and N. E. Miller (compilers), NUREG/CR-3427, BMI-2113, Vol. 4 (June 1984), pp. 3-126 ff.
- (5.30) "Long-Term Performance of Materials Used for High-Level Waste Packaging", D. Stahl and N. E. Miller (compilers), NUREG/CR-3900, BMI-2127, Vol. 4 (July 1985), pp. 3-97 ff.
- (5.31) B. G. Ateya and H. W. Pickering, J. Electrochem. Soc. 122, 1018 (1975).
- (5.32) W. H. Smyrl, in Comprehensive Treatise of Electrochemistry, Vol. 4: Electrochemical Materials Science, op. cit. (Ref. 5.25), p. 97.
- (5.33) "Long-Term Performance of Materials Used for High-Level Waste Packaging", D. Stahl and N. E. Miller (compilers), NUREG/CR-4379, BMI-2128, Vol. 4 (June 1986), pp. 3-83 ff.
- (5.34) F. Hine, Electrode Processes and Electrochemical Engineering (Plenum Press, New York, 1985), pp. 59 ff.
- (5.35) J. A. Beavers and N. G. Thompson, Corrosion - NACE 43, 185 (1987).
- (5.36) A. J. Markworth and L. R. Kahn, in Predictive Capabilities in Environmentally Assisted Cracking, R. Rungta (ed.), PVP - Vol. 99 (The Am. Soc. Mech. Engrs., New York, 1985), p. 143.

- (5.37) A. Turnbull and J.G.N. Thomas, J. Electrochem. Soc. 129, 1412 (1982).
- (5.38) J. O'M. Bockris and A.K.N. Reddy, Mod. Electrochem., Vol. 2 (Plenum Press, New York, 1970), pp. 883 ff.
- (5.39) J. A. Beavers, A. J. Markworth, and N. G. Thompson, to be published in Proc. NACE Int. Conf. on Localized Corrosion (1987).
- (5.40) "Long-Term Performance of Materials Used for High-Level Waste Packaging", D. Stahl and N. E. Miller (compilers), NUREG/CR-3405, BMI-2105, Vol. 1 (July 1983), pp. 6-18 ff.
- (5.41) Reference 5-29, pp. 3-132 ff.
- (5.42) Reference 5-30, pp. 3-95 ff.
- (5.43) J. J. Stobbs and A. J. Swallow, Metall. Rev. 7, 25, 95 (1962).
- (5.44) A. V. Byalobzheskii, "Radiation Corrosion" (Israel for Scientific Translations, Jerusalem, 1970). English translations of: Radiatsionnaya Korroziya (Nauka, Moscow, 1967).
- (5.45) J. L. Nelson, R. E. Westerman, and F. S. Gerber, in Scientific Basis for Nuclear Waste Management VII, G. L. McVay (ed.), Elsevier Sci. Publ. Co., Inc. (New York, 1984), Mater. Res. Sci. Symp. Proc. 26, 121.
- (5.46) R. S. Glass, E. E. Overturf, R. A. Van Konynenburg, and R. D. McCright, Corrosion Sci. 26, 577 (1986).
- (5.47) Y. J. Kim and R. A. Oriani, Corrosion--NACE 43, 85 (1987).
- (5.48) Y. J. Kim and R. A. Oriani, Corrosion--NACE 43, 92 (1987).
- (5.49) D. H. Lester, in Proc. Workshop (in Seattle, WA) on Near-Field Phenomena in Geologic Repositories for Radioactive Waste, Nucl. Energy Agency, Org. for Economic Co-Operation and Devel., 361 (Paris, 1981).
- (5.50) ONWI Report No. 452 (Office of Nuclear Waste Isolation, April 1983).
- (5.51) K. J. Taylor, I. D. Bland, A. H. Harker, C. Westcott, and G. P. Marsh, AERE Report No. G2856 (Dec. 1983).
- (5.52) J. C. Walton and B. Sagar, in Scientific Basis for Nuclear Waste Management X, Mater. Res. Soc. Symp. Proc. 84, in press.
- (5.53) C. Y. Chao, L. F. Lin, and D. D. Macdonald, J. Electrochem. Soc. 128, 1187 (1981).

- (5.54) D. D. Macdonald, A. C. Scott, and P. Wentrcek, J. Electrochem. Soc. 128, 250 (1981).
- (5.55) A. V. Byalobzheskii, op. cit., 128.
- (5.56) I. G. Draganic and F. G. Draganic, "The Radiation Chemistry of Water" (Academic Press, New York, 1981).
- (5.57) A. W. Boyd, M. B. Carver, and R. S. Dison, Radiat. Phys. Chem. 15, 177 (1980).
- (5.58) S. L. Nicolosi, in Scientific Basis for Nuclear Waste Management VIII, C. M. Jantzen, J. A. Stone, and R. C. Ewing (eds.), Mater. Res. Soc. (Pittsburgh, 1985), Mater. Res. Soc. Symp. Proc. 44, 631.
- (5.59) J. S. Newman, "Electrochemical Systems" (Prentice-Hall, Inc., Englewood Cliffs, NJ, 1983), 217 ff.
- (5.60) D. D. Macdonald, A. C. Scott, and P. Wentrcek, J. Electrochem. Soc. 126, 1618 (1979).

6. CONCLUSIONS

This chapter presents a discussion of conclusions for the experimental and modeling studies conducted in the container materials task. Experimental studies focused on hydrogen embrittlement, overpack corrosion, and internal canister corrosion. Modeling studies focused on pitting corrosion and general corrosion.

6.1 Hydrogen Embrittlement

The objective of the hydrogen embrittlement studies was to obtain an improved understanding of potential degradation mechanisms associated with hydrogen entry into cast waste container steels. Because hydrogen will likely be generated in a repository, arising either from radiolytic reactions or from corrosion reactions, the possibility that hydrogen-induced damage could compromise the structural integrity of waste containers is an important concern. The scenario under consideration was rather complex, with the initial temperature in the repository set at approximately 260 C (500 F) and gradually reducing to room temperature over a very long time period. Under such conditions, the two major mechanisms of failure anticipated were hydrogen embrittlement and hydrogen attack. Accordingly, studies were undertaken to obtain initial estimates of hydrogen-induced damage.

Additional complexities were included by the requirement to assess microstructural influence on hydrogen effects. To determine whether commercial levels of purity would be adequate for the cast steel containers, effects of metal purity level on hydrogen embrittlement needed to be determined. The use of pure iron or wrought welded plates as alternate materials needed to be assessed. Also, since container integrity is required over a very long time period, there was a need to assess both short-term and long-term effects of hydrogen on strength and fracture resistance of the material.

To investigate these effects, the approach used was to subdivide the effort into three subtasks. These are illustrated in Figure 2.2. In the first two subtasks, hydrogen embrittlement was evaluated by testing tensile and fracture toughness specimens in 6.9 MPa (1000 psi) hydrogen or inert (nitrogen or helium) environments at room temperature. The primary consideration was to evaluate the roles of composition, processing, and heat treatment on hydrogen-induced degradation. Emphasis was on evaluating fracture parameters, namely J_{IC} and dJ/da , for two important reasons. First, these parameters provide design data to evaluate container integrity under a worst-case scenario--one in which the structure is assumed to contain a crack that could rapidly propagate under imposed mechanical-thermal-environmental conditions. Second, data analyses showed that fracture parameters were much more sensitive to the influence of hydrogen than were tensile properties.

In the third subtask, both short-term and long-term effects of hydrogen were determined for a clean cast steel in elevated-temperature, high-pressure hydrogen. In the short-term the temperature in the repository would be close to 260 C (500 F). Accordingly, fracture properties were evaluated at 260 C (500 F) in hydrogen and compared with those in helium. Long-term effects were determined under the scenario that long periods of exposure in

the vicinity of 260 C (500 F) would degrade the material. Since the temperature in the repository would decrease with time, the residual fracture resistance at room temperature could provide realistic estimates of long-term damage. Accelerated tests were conducted by pre-exposing specimens at temperatures above 260 C (500 F), the rationale being that short-term exposure at higher temperatures could simulate long-term service damage at temperatures of 260 C (500 F) and below.

The results indicate that over a long time period hydrogen could significantly reduce fracture resistance. Room-temperature tests on unexposed specimens indicate that hydrogen embrittlement was the primary mode of failure. While this result was expected, a result of greater concern is the fact that there was continued decrease in room-temperature fracture toughness properties with increased times of pre-exposure at 260 C (500 F). Selection of steels for structural members to be used in high-pressure, elevated-temperature hydrogen environments are usually based on Nelson curves. These curves are plots of temperature versus hydrogen partial pressure, and the curves separate regions of failure and no-failure. The curves are based on service experience and are generally relied on in the petrochemical industry for selecting materials for components used in hydrogen service. The curves indicate that at 260 C (500 F) and 6.9 MPa (1000 psi), no hydrogen-attack failures have been reported for service exposures as long as 10,000 hours. On the other hand, the present investigation indicated significant reductions in J_{IC} and dJ/da over a period as short as 250 hours. Consequently, a significant conclusion is that the use of Nelson curves to select hydrogen-resistant materials may not be adequate to assure integrity of cast steel containers over a period as long as 1000 years.

As previously mentioned, accelerated tests using pre-exposure temperatures of up to 593 C (1100 F) were conducted to predict degradation over very long time periods. Based on the limited number of tests on a rather inhomogeneous cast microstructure, it is premature to provide quantitative and reliable estimates of long-term damage. Competing mechanisms, such as hydrogen embrittlement and hydrogen attack, made determination of damage rates at long times difficult. For example, pre-exposures at various temperatures indicated that damage, measured in terms of loss in fracture properties at room temperature, was a maximum for temperatures ranging from 399 to 454 C (750 to 850 F). Thus, further tests involving temperatures closer to 260 C (500 F) and longer times of pre-exposures are necessary to quantitatively predict damage over a long time period. Alternately, threshold experiments could be conducted to estimate the threshold J , below which crack propagation would not occur at 260 C (500 F) in hydrogen. These experiments are recommended for future research.

Qualitatively, the J -integral results, fracture surfaces, and estimates of activation energy indicated that hydrogen embrittlement and possibly incipient hydrogen attack accompanied pre-exposure or testing at 260 C (500 F). Even though no voids were optically resolvable, tests on unexposed specimens at 260 C (500 F) showed large reductions in dJ/da . The corresponding fracture mode was microvoid coalescence, so that the primary effect of hydrogen was to enhance void initiation and/or growth at lower stresses and strains. These results are consistent with the hydrogen-embrittlement mechanism,

where as suggested by Beachem, hydrogen enhances whatever mode of fracture is dominant under a particular set of temperature and pressure conditions. In the case of the long-term tests, the continued decrease of room temperature fracture properties with time of pre-exposure at 260 C (500 F), together with the measured activation energy, indicate that damage was caused by a combination of hydrogen embrittlement and incipient attack. Further microstructural analyses, involving transmission electron microscopy, are necessary to pinpoint the mechanism of incipient attack. This work may provide valuable insight regarding the rate controlling process for degradation in the neighborhood of 260 C (500 F), and thus provide better means of predicting rate of damage at long times.

The other important conclusions of the work are as follows:

- (1) Room-temperature tests of unexposed specimens show that fracture toughness properties were much more sensitive to the presence of hydrogen than were tensile properties. For the different microstructures, J_{IC} values were lowest for the higher tensile strength levels. This result is consistent with the well-known behavior that hydrogen damage increases with increased strength levels. On the other hand, the tensile test results indicate a much weaker relationship between elongation or reduction in area and tensile strengths.
- (2) Annealed cast steels were much more sensitive to hydrogen degradation than as-cast steel. Redistribution of impurities could be a reason for this behavior in the doped steels. The results indicate that thermal history and heat treatment of cast steels and weld heat-affected zones are important parameters and need to be carefully considered in assessing container integrity.
- (3) For the as-cast steels, hydrogen embrittlement is not significantly influenced by commercial steel impurity levels. This result would suggest that commercial-purity steel might be used for the containers. However, considering that only few room-temperature tests of unexposed specimens were conducted, further tests are essential to check whether the initial findings are valid for long-term exposures to high-pressure, elevated-temperature hydrogen.
- (4) Tests conducted in hydrogen at 260 C (500 F) with specimens that were not pre-exposed to hydrogen indicate that hydrogen primarily reduced dJ/da , leaving J_{IC} relatively less affected. These results were in contrast to the room-temperature results, which indicate that the major effect of hydrogen was on J_{IC} . The behavior was consistent with a hydrogen-embrittlement mechanism, since quasi-cleavage occurred in hydrogen at room temperature, while at 260 C (500 F) the failure mode was microvoid coalescence. Since J_{IC} is primarily stress driven, while dJ/da is largely controlled by the total strain to failure, the relative extents by which J_{IC} and dJ/da were affected at the two temperatures can be rationalized. Additionally, the composite parameter, J_G , indicated that

the steel was much more sensitive to hydrogen at 260 C (500 F) than it was at room temperature.

6.2 Overpack Corrosion

Overpack corrosion studies were performed on three candidate alloy-repository environment systems; Titanium Grade 12 - salt, carbon steel - basalt, and stainless steel - tuff. Significant findings for these three systems are described below.

6.2.1 Titanium Grade 12-Salt System

Autoclave exposures were performed on Titanium Grade 12 in a high-magnesium brine (Brine A) at 250 C. The objectives of this work were to selectively reproduce the data found in the literature and evaluate the influence of crevices, surface condition, heat transfer, and temperature gradients on corrosion behavior.

The most significant finding of the research was the observation of acidification within the autoclave--a result of hydrolysis of the magnesium chloride found in the brine. While the Titanium Grade 12 performed well in this acidified brine environment, the Hastelloy alloy C-276 autoclave underwent severe general and pitting attack in the vapor phase. Considering the aggressive nature of the environment generated, it is considered unlikely that Titanium Grade 12 could survive 1000 years. Thus, the issue of hydrolysis of magnesium chloride within a salt repository appears to be important with regard to performance of any material. The rate of HCl generation by hydrolysis needs to be established for credible repository conditions.

In other work, evidence of accelerated attack also was observed, in the absence of heat transfer, beneath crevices in the brine at 250 C. This observation is consistent with findings elsewhere. Similarly, moderate acceleration of attack of the Titanium Grade 12 was observed as a result of embedding iron in the surface of the specimens.

6.2.2 Carbon Steel-Basalt System

In the carbon steel basalt system, four types of overpack corrosion experiments were performed: potentiodynamic polarization, pit propagation, autoclave exposures, and slow strain rate tests.

6.2.2.1 Potentiodynamic Polarization

The objective of the potentiodynamic polarization task was to evaluate the influence of metallurgical and environmental variables on the general corrosion, pitting, and SCC behavior of carbon steel in basalt repository environments. This was accomplished by using potentiodynamic polarization experiments to determine the effect of metallurgical and environmental variables on a number of polarization parameters. The results of this task also were used in many of the other overpack corrosion tasks in this program to identify appropriate environments and steels for study.

Carbon steel was found to exhibit active-passive behavior in the simulated basalt groundwater, and the values for the polarization parameters indicated a high probability for pitting corrosion. On the other hand, the values for the parameters associated with SCC did not indicate a potent cracking environment.

The results of the metallurgical studies indicate that variation in steel composition (from high-purity Ferrovac E to 1018 carbon steel) or thermo-mechanical treatments (cast versus wrought) did not have a marked effect on the electrochemical parameters associated with pit initiation or general corrosion in the simulated basalt repository environment. Thus, it appears that the use of high-purity iron for fabrication of the overpack would not greatly enhance general or localized corrosion performance.

In the metallurgical studies, the electrochemical parameters associated with SCC also were not greatly affected by steel composition or microstructure. Thus, from an electrochemical standpoint, variation in the metallurgy of the steels over the range examined would not be expected to affect SCC. However, it must be cautioned that the influence of metallurgy on SCC susceptibility cannot be fully assessed by means of bulk electrochemical techniques since mechanical factors and grain-boundary phenomena must also be considered.

Several tests were performed to study the effect of environmental variables on electrochemical behavior. In preliminary studies, it was found that equilibration of the simulated groundwater with basalt rock, or concentration of the groundwater by a factor of ten, did not have a marked effect on the polarization parameters. Similarly, increasing the temperature from 90 to 250 C did not markedly affect behavior, although a careful analysis of the data indicated a slightly higher likelihood of SCC at 250 C than at 90 C.

A statistical experimental approach was used to evaluate the influence of 15 environmental variables on the electrochemical behavior of carbon steel. The species and ranges in concentration were selected to study based on a survey of the literature. Species considered included those present in the groundwater as well as those that may intrude the repository or be generated by radiolysis. A screening matrix of experiments was performed to reduce the number of variables from 15 to 11 for analysis in the main matrix. Twenty-one two-factor interactions were also considered in the main matrix.

Statistical analyses showed that many of the environmental variables had important effects on the electrochemical parameters; this behavior was expected. Somewhat more surprising was the fact that many of the two-factor interactions also significantly affected the polarization parameters. These two-factor interactions are not normally considered in most corrosion studies.

The results of the statistical analyses were used to develop regression models describing the influence of the main effects and two-factor interactions on the electrochemical parameters. These models were tested for selected two-factor interactions. The quantitative agreement between the

experimentally measured values and the predictions of the models were generally poor, but the trends in the data were fairly well predicted. The models' poor predictive capability was attributed to correlation of the terms, which occurred because the design concentrations for the solutions could not be achieved in all instances due to precipitation in the solutions. Nevertheless, the studies were extremely useful in understanding the ranges of expected behavior for carbon steel in a repository environment. In addition, these data were used to select solution chemistries for the pit propagation and SCC studies.

A few species in the statistical matrix are thermodynamically unstable and the standard test procedure was not effective in studying their influence on corrosion behavior. Accordingly, the test procedure was modified to include continuous injection of these species. Two species, peroxide and perchlorate, were studied in greater detail. It was found that both species greatly increased the corrosion rate of carbon steel when present at reasonably high concentrations. Once estimates are made of the amounts of these species likely at an overpack surface, and of their rates of production, similar experiments can be repeated to establish the likely effect on corrosion. For peroxide, it was clearly shown that both the anodic and cathodic electrode kinetics were affected since, for carbon steel in simulated basalt solutions, the lower concentration of peroxide had the higher corrosion rate.

6.2.2.2 Pit Propagation

As previously described in this chapter, the results of the potentiodynamic polarization and autoclave studies suggest that pit initiation in low-carbon steels is likely in basalt groundwater. Accordingly, rates of pit-propagation must be estimated to assess the performance of the overpack. With this in mind, the overall objective of the pit-propagation task was to characterize the pit-propagation behavior of carbon steel and to develop a better understanding of the mechanism of attack.

Two types of pit-propagation experiments were performed; long-term exposures and electrochemical experiments with simulated pits. The electrochemical experiments were performed with simulated pits having electrically isolated pit bottoms (bases) and either reactive or nonreactive (inert) walls. With this design, a gun-drilled rod of carbon steel was used to contain the pit. The pit cavity was packed with an acidified paste whose composition was based on analyses of pits found in long-term exposures. A variety of measurements were performed on the pits, including coupled currents between the pit base and the bold exposed surfaces (BES), corrosion potentials for the pit base and BES, and potential profiles down the pits.

For the long-term exposures, two types of simulated pit geometries were used; one similar to that used in the above electrochemical experiments, and mechanically drilled pits in thick plates of carbon steel.

A major focus of the pit-propagation work was a comparison of the behavior of reactive and nonreactive wall pits. This work has considerable significance since most models use nonreactive walls to simplify the mathematics,

while actual pits have reactive walls. Both the long-term exposures and the electrochemical studies demonstrated that reactive and nonreactive wall pits behave quite differently. In general, propagation rates for nonreactive wall pits are several orders of magnitude higher than those for reactive wall pits. The implication of these findings is that prediction of overpack performance, based on nonreactive wall pits, may be highly conservative. While it is desirable to obtain conservative estimates of overpack performance, predictions based on models utilizing nonreactive walls may lead to rejection of carbon steel as a viable overpack material when, on the basis of pitting performance, it may perform adequately. Accordingly, it is recommended that any predictive models for pit propagation incorporate active walls.

6.2.2.3 Autoclave Studies

Autoclave exposures were performed on carbon steel specimens at 250 C in simulated basalt groundwater under stagnant deaerated conditions. The objectives of the exposures were to selectively reproduce corrosion data for carbon steel in basalt groundwater at elevated temperatures, and to evaluate the influence of steel composition and microstructure, as well as concentration of the groundwater, on the corrosion behavior.

The most significant finding of these experiments was evidence for pitting of carbon steel in basalt groundwater. Shallow pits (less than 20 μm) were found on most of the specimens in the exposures. These pits were associated with breakdown of magnetite films found on the specimen surfaces. This observation is consistent with the results of the potentiodynamic polarization studies. Thus, the protection potential was found to be close to the free-corrosion potential, even under deaerated conditions, indicating a high probability of pit initiation.

On the other hand, general corrosion rates were found to be low in the basalt groundwater under the test conditions (less than 25 $\mu\text{m}/\text{year}$), and were not measurably affected by the composition or microstructure of the steel. Surprisingly, concentration of the groundwater by a factor of ten actually decreased corrosion rates by about a factor of two.

Optical examination of three-point bend specimens, which were included in the autoclaves, indicated no evidence of SCC. This observation is consistent with the low-temperature, slow strain rate results.

Polarization resistance and corrosion potential measurements were performed on specimens in the unconcentrated groundwater exposures. Reasonable agreement was found between corrosion rates predicted from the polarization resistance measurements and those obtained from weight loss. Polarization resistance values increased over most of the exposure period, indicating a decreasing corrosion rate with time. Thus, the corrosion rates obtained from weight loss are probably conservative.

6.2.2.4 Slow Strain Rate Studies

Slow strain rate (SSR) experiments were performed on carbon steel in basalt groundwater solutions from the statistical design matrix and selected established cracking environments. The objectives of these experiments were to (1) evaluate the influence of environmental variables on SCC of carbon steel in simulated repository environments, and (2) evaluate the predictive capability of the potentiodynamic polarization technique in assessing SCC susceptibility.

Prior to performing these SSR experiments, a survey of the literature was performed to identify potential cracking species for carbon steel in the basalt repository. The survey results indicated that a number of potential cracking agents are present at low concentrations in the repository environment. However, SCC of carbon steel is relatively unlikely in the bulk repository environment because of low concentration of the cracking species. The most serious threat to the integrity of a carbon steel overpack with respect to SCC is through concentration of the cracking species. Potential concentrating mechanisms include heat transfer, pitting, crevice corrosion, and thermogalvanic corrosion.

The influence of radiation fields on SCC is not fully understood, but limited experimental data suggest that one likely influence is in moving the free-corrosion potential in the noble direction, which may increase the likelihood of SCC. Another effect of radiation fields may be to generate cracking agents such as ferric ions or nitrates.

The SSR experiments were performed under deaerated conditions with potentiostatic control; potentials were selected for testing based on the results of the potentiodynamic polarization studies. In the basalt groundwater, no evidence of SCC was found at either 90 or 250 C, which is consistent with the conclusions from the literature survey. On the other hand, a number of cracking environments were identified from the statistical design matrix, demonstrating the effectiveness of the potentiodynamic polarization criteria used to select the cracking environments. Established cracking species were present in all of the environments that promoted SCC; thus, no new cracking species were identified. It was also found that high chloride or fluoride concentrations did not completely inhibit SCC in the presence of one established cracking species, bicarbonate.

Slow strain rate experiments performed in ferric chloride solutions and nitrate solutions demonstrated that significant SCC could occur at very low concentrations. The ferric chloride cracking was found to be most severe at 175 C and pH values of less than 5.

The pH and temperature dependence of the nitrate cracking were not investigated, but it was found that the cation (Na^+ or NH_4^+) did not greatly effect cracking. It also was shown that the effect of nitrate concentration on SCC behavior could be predicted from the potentiodynamic polarization experiments.

These SSR studies demonstrated the usefulness of this technique, in combination with the potentiodynamic polarization technique, in evaluating possible cracking environments. While no new cracking species were identified in the study, it is somewhat disconcerting that very low levels of some species, such as nitrates or ferric chloride, can promote cracking. The finding of significant cracking in bicarbonate, containing high concentrations of chlorides or fluorides, also is significant since it suggests that cracking is a potential problem even in brine repositories. The most severe limitation in applying the SCC data to the actual repository is in identifying the ranges of possible environmental variables.

6.2.3 Stainless Steel-Tuff System

A limited number of SCC experiments was performed on Type 304L stainless steel in simulated tuff groundwater. The objective of these experiments was to evaluate the influence of concentration of the groundwater on SCC behavior. Three types of experiments were performed with heated Type 304L stainless steel specimens: slow strain rate experiments with a groundwater mist condensing on the specimens; welded U-bend exposures with groundwater dripping on the specimens; and welded U-bend exposures with the specimens in contact with a wick submerged in the groundwater. Experiments were performed under fully aerated and partially aerated conditions at metal temperatures above boiling.

No cracking was observed under any of the above exposure conditions. While the nominal Cl^- content of the groundwater is low, less than 10 ppm, concentration of the water to dryness should have produced chloride concentrations sufficient to cause SCC. Thus, other species in the groundwater must have inhibited the cracking. Future studies should focus on the identification of those species and their role in cracking behavior.

6.3 Internal Canister Corrosion

Long-term exposure experiments were performed to evaluate the kinetics of pit propagation on the referenced canister material, Type 304L stainless steel, in the presence of a simulated reference waste glass. Specimens of Type 304L stainless steel and the cast equivalent (CF8) were exposed to PNL 76-68 reference simulated glass at temperatures between 300 and 900 C for periods up to 3270 hours. Following exposure, the specimens were metallographically examined, and the number and depths of pits were measured.

It was found that, over the temperature range studied, pits initiated rapidly on the metal surfaces, but the propagation rates decreased with time. The propagation rates also decreased with temperature; the maximum penetration rates for the longest exposure time followed a rate law of the form

$$\text{Rate } (\mu\text{m/yr}) = 879 (1000/T)^{-2.54} .$$

This rate law predicts a maximum penetration rate of about 10 to 20 $\mu\text{m}/\text{yr}$ at temperatures of 150 and 200 C, respectively. Thus, a 3-inch-thick canister would be penetrated in about 500 years at the higher temperature and about 1000 years at the lower temperature.

Silicon, zinc, and titanium from the waste glass were found in the corrosion products in the pits at all temperatures, suggesting that these elements played a role in the attack on the metal. The fact that similar corrosion products were present at all test temperatures also suggests that the mechanism of attack does not change over this temperature range. Nevertheless, it is conceivable that at lower temperatures a corrosion mechanism change does occur, thus invalidating the data extrapolation. Comparison of the data for the two steels suggests that the cast stainless steel (CF8) is somewhat more resistant to pitting than the wrought Type 304L stainless steel.

Based on the above findings, it appears likely that the Type 304L stainless steel or its cast equivalent will contain high-level wastes for the retrieval period and probably the thermal period. Since these predictions were based on tests with simulated glass and involved data extrapolation, it is recommended that confirmatory, long-term tests with more prototypic glass and lower temperatures be performed if credit for containment is to be given.

6.4 Corrosion Modeling Studies

6.4.1 Pitting Corrosion

Pitting of the container surface is considered to be an important mechanism for the ultimate loss of container integrity. Modeling studies of pitting centered on three aspects of the overall process: pit-initiation kinetics, pit-growth kinetics, and evolution of pit-depth distribution, with emphasis placed upon pit-growth kinetics.

These modeling studies were conducted primarily to support experimental work on pitting in this program. Useful extensions to the model, to characterize actual repository conditions, would include accounting for the effects of radiolytically produced species on pit-growth kinetics and coupling of pit generation and pit growth models. Finally, the model should be extended to predict pitting behavior over long time intervals.

6.4.2 General Corrosion

Both general and localized corrosion can lead to breach of containment. Studies were conducted on the effects of irradiation on the general corrosion of waste-package materials, and a model describing the general corrosion of a metal surface in an aqueous environment was developed. These studies show that the kinetics of aqueous general corrosion in a gamma-radiation environment can be very complex. The model was applied to some simplified, hypothetical examples to demonstrate relative effects of radiolytic production and chemical-reaction-induced annihilation of chemical species, as well as effects of film-growth kinetics, on the overall rate at

which corrosion proceeds. It was found, for example, that the relative extent to which radiolytic production of chemical species enhances the rate of corrosion can depend strongly on the nature of the chemical kinetics at the interface between the solution and the metal surface.

APPENDIX A

POTENTIODYNAMIC POLARIZATION
DATA AND ANALYSES

APPENDIX A

POTENTIODYNAMIC POLARIZATION DATA AND ANALYSES

This appendix provides a detailed listing of data from the potentiodynamic polarization studies described in Section 3.2.1.

Table A.1 gives the concentrations used in the experimental matrix, which was designed to determine the effects of varying chemical variables on the polarization parameters.

Table A.2 gives the results of statistical analyses for the main-effect terms, and Table A.3 gives the results of statistical analyses for the interaction terms. As explained in Section 3.2.1, the data used in these tables were normalized.

Table A.1. Concentrations for the solutions used in the final statistical model.

Experiment No.	Concentration, mg/L												
	pH	Cl	F	Fe	CO ₃	HCO ₃	NO ₃	BO ₃	SiO ₃	H ₂ O ₂	O ₂	CO	CO ₃ /HCO ₃
1	6.0	100	10	3.0	0	1,600	2,000.0	2,000	90	0	0	0.0	1,600
2	9.3	100	10	0.1	5,800	0	0.2	2,008	55	100	2	0.0	5,800
3	8.4	100,000	10	3.0	0	5,690	2,000.0	50	90	100	0	1.0	5,690
4	8.7	114,465	10	2.1	0	600	0.2	41	15	0	2	1.0	600
5	6.2	100	2,950	1.8	0	4,980	2,000.0	2,000	112	100	2	1.0	4,980
6	9.3	100	3,450	11.4	60,000	44,000	0.2	1,843	325	0	0	1.0	104,000
7	6.0	100,000	3,000	2.4	0	2,460	2,000.0	140	100	0	2	0.0	2,460
8	9.2	100,000	3,000	3.0	52,000	18,100	0.2	50	50	100	0	0.0	70,100
9	6.0	100	10	1.5	0	900	0.2	46	15	0	2	1.0	900
10	9.3	100	10	1.2	1,100	1,100	2,000.0	30	70	100	0	1.0	2,200
11	6.0	103,968	10	10.9	0	19,000	0.2	1,848	35	100	2	0.0	19,000
12	9.2	100,000	10	3.0	1,940	4,275	2,000.0	2,000	50	0	0	0.0	6,215
13	6.0	100	3,000	3.0	0	1,630	0.2	50	60	100	0	0.0	1,630
14	9.0	100	3,575	2.4	25,000	29,000	2,000.0	80	960	0	2	0.0	54,000
15	6.4	100,000	3,000	3.0	0	1,630	0.2	2,000	90	0	0	1.0	1,630
16	9.2	79,975	1,420	8.6	73,000	21,500	2,000.0	2,079	160	100	2	1.0	94,500
17	9.3	107,967	3,000	2.0	240	1,510	0.2	157	425	100	2	1.0	1,750
18	6.3	104,468	1,750	2.5	0	1,800	2,000.0	63	70	0	0	1.0	1,800
19	9.3	100	5,150	8.5	1,000	8,500	0.2	2,038	70	0	0	0.0	9,500
20	6.0	100	5,100	5.4	0	1,460	2,000.0	1,984	165	100	0	0.0	1,460
21	9.3	112,465	10	23.4	60,000	24,000	0.2	52	60	0	0	0.0	84,000
22	5.3	107,467	10	2.0	0	200	2,000.0	30	55	100	2	0.0	200
23	9.7	100	10	10.7	168,000	21,000	0.2	1,943	15	100	0	1.0	189,000
24	6.2	100	10	5.7	0	480	2,000.0	1,949	15	0	2	1.0	480
25	9.0	110,466	2,275	2.0	4,000	7,000	2,000.0	1,951	105	100	0	0.0	11,000
26	7.5	108,966	1,875	2.2	0	3,260	0.02	1,872	30	0	2	0.0	3,260
27	9.3	100	4,125	0.5	320	6,680	2,000.0	187	110	0	0	1.0	7,000
28	6.3	100	4,200	6.0	0	1,740	0.2	88	290	100	2	1.0	1,740
29	9.3	113,465	10	17.8	73,000	29,500	2,000.0	2,000	65	0	2	1.0	102,500
30	5.9	107,967	10	1.1	0	60	0.2	1,698	15	100	0	1.0	60
31	9.6	100	10	6.6	53,000	37,500	2,000.0	26	35	100	2	0.0	90,500
32	8.0	100	10	0.7	0	80	0.2	1	70	0	0	0.0	80
33	7.6	55,483	2,020	9.0	0	26,500	1,000.0	861	50	50	1	0.5	26,500
34	7.6	55,483	2,020	9.0	0	26,500	1,000.0	861	50	50	1	0.5	26,500

Table A.1. Continued

Experiment No.	Concentration, mg/L												
	pH	Cl	F	Fe	CO ₃	HCO ₃	NO ₃	BO ₃	SiO ₃	H ₂ O ₂	O ₂	CO	CO ₃ /HCO ₃
35	8.7	55,483	2,020	9.0	8,000	18,500	1,000.0	861	50	50	1	0.5	26,500
36	8.8	55,483	2,020	9.0	8,000	18,500	1,000.0	861	50	50	1	0.5	26,500
37	11.5	95,970	10	4.0	182,000	0	2,000.0	83	45	0	0	1.0	182,000
38	12.0	100	5,750	1.0	156,330	0	2,000.0	120	174	100	0	0.0	156,330
39	10.3	106,967	10	1.2	2,520	2,480	2,000.0	19	50	100	2	0.0	5,000
41	11.2	100	10	1.3	11,000	3,000	2,000.0	1,861	90	100	2	1.0	14,000
42	9.1	100	10	0.8	618	522	2,000.0	22	26	0	0	1.0	1,140
43	7.7	104,967	10	4.4	0	3,550	2,000.0	1,635	30	100	0	1.0	3,550
44	11.1	100	3,000	0.4	18,335	6,365	2,000.0	2,000	162	0	0	1.0	24,600
45	6.0	102,968	10	0.9	0	200	0.2	1,674	35	100	2	1.0	200
46	11.7	100	10	1.3	196,860	14,140	2,000.0	2,000	162	0	0	1.0	211,000
47	11.7	100	10	3.0	3,755	0	2,000.0	50	50	0	2	0.0	3,755
48	11.2	100,000	5,100	1.7	2,826	0	2,000.0	127	88	100	0	1.0	2,826
49	11.2	100	70	1.5	2,000	0	0.2	21	25	0	2	0.0	2,000
50	11.1	100	5,350	0.7	1,500	500	0.2	252	300	100	2	1.0	2,000
51	11.9	100	10	2.2	142,000	97,000	2,000.0	1,669	50	0	2	1.0	239,000
52	11.0	100	10	8.2	795	0	0.2	20	14	100	0	0.0	795
53	11.2	105,967	10	1.8	10,000	3,000	0.2	1,883	890	0	2	1.0	13,000
54	13.0	100,000	10	1.3	449	0	0.2	35	132	0	0	0.0	419
55	12.1	95,970	2,025	3.3	200,000	0	0.2	1,716	105	100	2	0.0	200,000
56	11.3	100	10	1.4	3,464	0	0.2	2,000	140	100	0	0.0	3,464
57	7.2	100	5,425	2.8	0	4,540	2,000.0	1,920	340	100	0	0.0	4,540
58	11.2	100	10	3.4	20,600	191,300	0.2	79	348	0	0	1.0	211,900
59	9.4	100	8,250	13.0	200	1,250	2,000.0	127	435	100	2	1.0	1,450
60	11.0	100,000	10	2.7	103,800	0	2,000.0	2,000	284	0	0	0.0	103,800
61	6.2	100	10	5.5	0	80	0.2	1,677	65	0	2	1.0	80
62	11.5	105,967	2,175	4.4	146,000	68,000	0.2	1,614	165	0	0	0.0	214,000
63	11.0	100,000	3,850	2.5	193,400	0	0.2	2,000	112	100	0	1.0	193,400
64	10.5	108,966	3,550	2.1	16,000	0	2,000.0	1,761	120	100	2	0.0	16,000
65	11.3	99,970	10	3.8	210,000	1,000	2,000.0	115	1,360	0	2	1.0	211,000
66	11.3	100	10	2.7	208,000	7,000	0.2	99	900	100	2	1.0	215,000

Table A.2. Results of statistical analyses for main-effect terms showing coefficients, intercept, significance level, and explained variability for each polarization parameter in final model.

Main Effect	E_{cor} V (SCE) RC (OSL)(a)	$\log i_{cor}$ (A/cm ²) RC (OSL)	$\log i_{max}$ (A/cm ²) RC (OSL)	$\log i_{pas}$ (A/cm ²) RC (OSL)	E_{pit} V (SCE) RC (OSL)	E_{prot} V (SCE) RC (OSL)
pH	-	-1.456 (0.000)	-2.149 (0.000)	-1.436 (0.000)	-0.659 (0.004)	-
Cl	-0.072 (0.000)	-	-0.306 (0.002)	-	-	-0.418 (0.000)
F	-	+0.402 (0.037)	+0.298 (0.029)	+0.272 (0.032)	-	-
Fe	-0.112 (0.010)	-	+0.605 (0.008)	-	-	-
CO ₃	-	-	+1.044 (0.000)	-	+0.923 (0.000)	+0.234 (0.001)
NO ₃	+0.060 (0.000)	-0.637 (0.005)	-	-	-	-
BO ₃	-	-	-	-	-	-
SiO ₃	-	-	-	-	-	-
H ₂ O ₂	-	-	-	-	-	-
O ₂	-	-	-	-	+0.065 (0.090)	-
CO	-	-	-	-	-	-
Intercept	-0.664	-5.329	-2.605	-4.844	+0.736	-0.094
R ² (b)	54%	62%	72%	73%	78%	71%

(a) RC = regression coefficient; OSL = observed significance level. RC > 0 indicates that the parameter increases with increasing concentration; RC < 0 indicates that the parameter decreases with increasing concentration. A small OSL indicates that the term is significant.

(b) R²: coefficient of determination for the final model. The "R²" term is the percentage of total variability explained by the model.

Table A.3. Results of statistical analyses for interaction terms showing coefficients and significance level for each polarization parameter in final model.

Interaction Term	E_{cor} V (SCE) RC (OSL)*	$\log i_{cor}$ (A/cm ²) RC (OSL)	$\log i_{max}$ (A/cm ²) RC (OSL)	$\log i_{pas}$ (A/cm ²) RC (OSL)	E_{pit} V (SCE) RC (OSL)	E_{prot} V (SCE) RC (OSL)
pH x Cl	-	-	+0.422 (0.005)	-	-0.279 (0.002)	-0.315 (0.002)
pH x CO ₃	-	-	-1.460 (0.002)	-	-0.852 (0.000)	-0.227 (0.033)
pH x NO ₃	-0.059 (0.040)	-	-	-0.191 (0.111)	-	-
pH x BO ₃	-	-	-	-	-	-
pH x SiO ₃	-	-	-	-0.610 (0.088)	-	-
pH x H ₂ O ₂	-	-	-	-	-	-
pH x O ₂	-	-	-	+0.232 (0.054)	-0.165 (0.027)	-0.173 (0.048)
pH x CO	-	-0.275 (0.115)	-	-	-0.157 (0.039)	-0.147 (0.098)
pH x CO ₃	-	-	-0.196 (0.111)	-0.208 (0.019)	+0.416 (0.000)	-
pH x NO ₃	-	+0.219 (0.037)	-	+0.221 (0.003)	-	+0.092 (0.067)
pH x BO ₃	-	-	-	-0.122 (0.120)	-0.113 (0.020)	-0.138 (0.017)
pH x H ₂ O ₂	-0.026 (0.139)	-	-0.128 (0.058)	-0.249 (0.001)	-	-
CO ₃ x H ₂ O ₂	-0.032 (0.088)	-	-	-	-	-
CO ₃ x O ₂	-	-	-	-	-	-
NO ₃ x BO ₃	-	-	-	-	-	-
NO ₃ x SiO ₃	-	-0.647 (0.013)	-	-0.148 (0.062)	-0.104 (0.027)	-
NO ₃ x O ₂	-	-0.201 (0.038)	-	+0.216 (0.001)	-	-
BO ₃ x SiO ₃	-0.030 (0.146)	-	-	-	-0.119 (0.023)	-0.186 (0.003)
BO ₃ x H ₂ O ₂	-	-	-	-	-	-
SiO ₃ x O ₂	-0.043 (0.023)	-	-	-	-	-
H ₂ O ₂ x O ₂	-0.37 (0.022)	-	-	-	-0.058 (0.122)	-

*RC = regression coefficient; OSL = observed significance level. RC > 0 indicates that the parameter increases with increasing concentration; RC < 0 indicates that the parameter decreases with increasing concentration. A small OSL indicates that the term is significant.

APPENDIX B

POTENTIAL AND CURRENT DATA
FOR ELECTROCHEMICAL PIT-PROPAGATION
EXPERIMENTS

APPENDIX B

POTENTIAL AND CURRENT DATA FOR ELECTROCHEMICAL PIT-PROPAGATION EXPERIMENTS

Potential and current data for electrochemical pit-propagation experiments are summarized in Tables 3.26 and 3.29.

Appendix B contains graphs detailing results of the potential and current data for electrochemical pit-propagation Experiments 20, 21, 22, 23, 24, 27, 28, 29, and 30.

The experiments were conducted in aerated basalt groundwater, except for Experiment 27, which was conducted in aerated Brine A, and Experiment 28, which was conducted in aerated Brine B. Temperature was 25 C for all experiments.

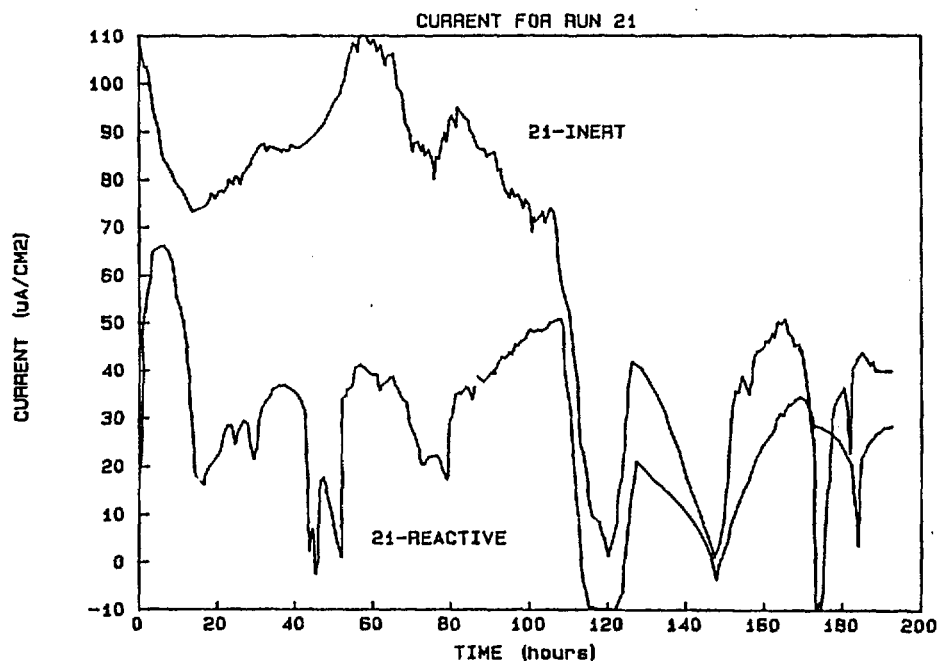


Figure B.1. Coupled current density as a function of exposure time and pit-wall reactivity for pit-propagation Experiment 21 performed at a diameter-to-depth ratio of 1:0.5 in aerated basalt groundwater at 25 C.

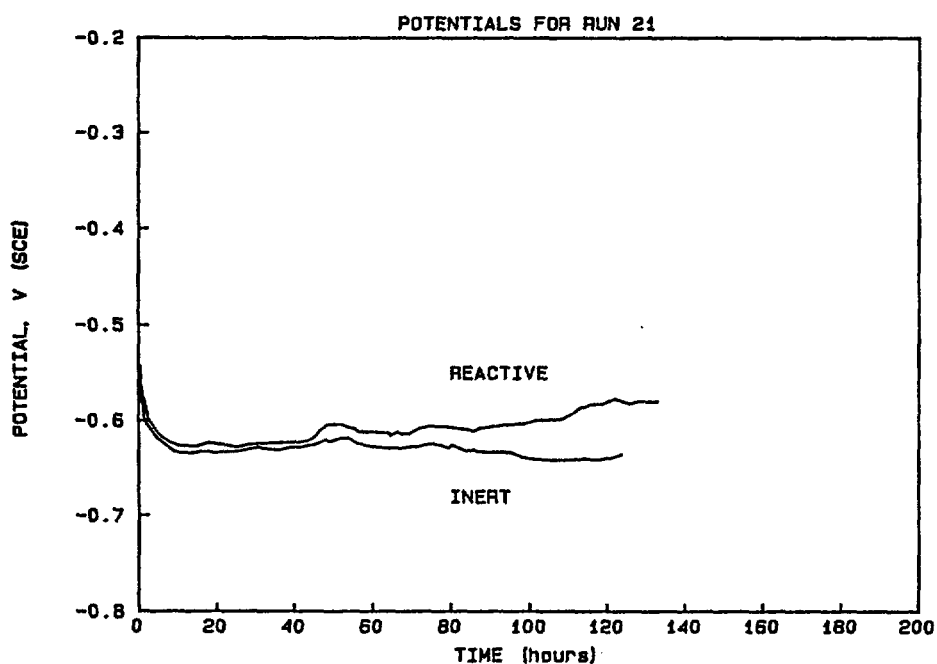


Figure B.2. Coupled potential as a function of exposure time for pit-propagation Experiment 21 performed at a diameter-to-depth ratio of 1:0.5 in aerated basalt groundwater at 25 C.

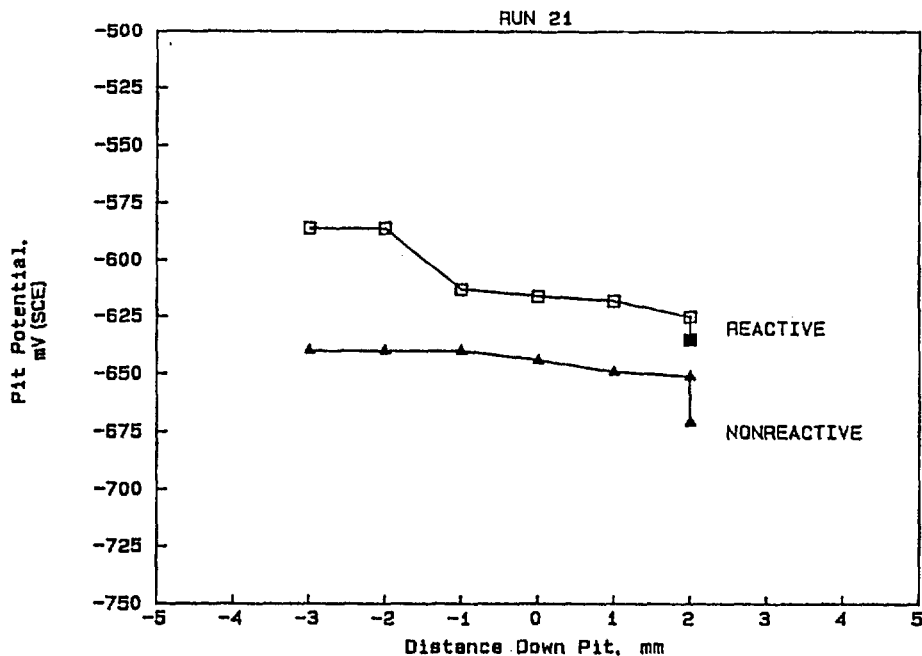


Figure B.3. Potential for pit specimen as a function of microcapillary probe position down the pit where the pit specimen and BES specimen were coupled (open symbols). Closed symbols indicate potentials when pit and BES specimens were uncoupled; Experiment 21 in aerated basalt groundwater at 25 C.

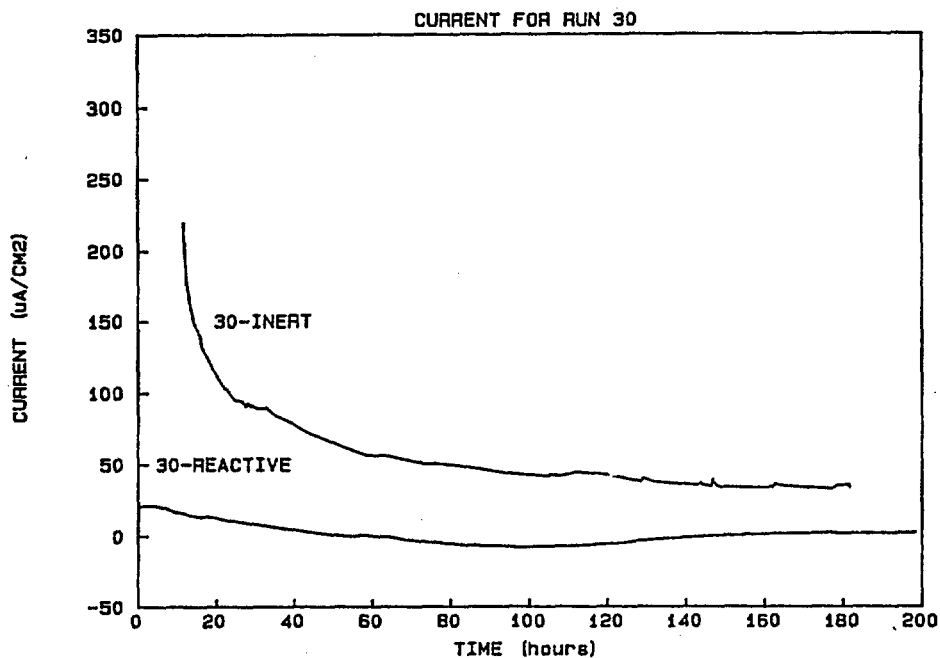


Figure B.4. Coupled current density as a function of exposure time and pit-wall reactivity for pit-propagation Experiment 30 performed at a diameter-to-depth ratio of 1:1 in aerated basalt groundwater at 25 C.

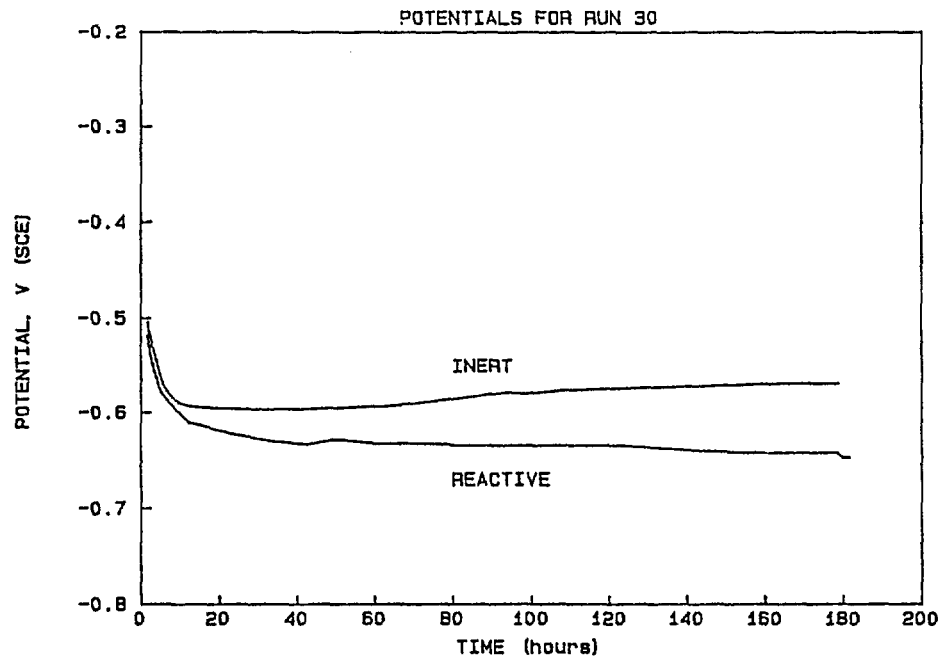


Figure B.5. Coupled potential as a function of exposure time for pit-propagation Experiment 30 performed at a diameter-to-depth ratio of 1:1 in aerated basalt groundwater at 25 C.

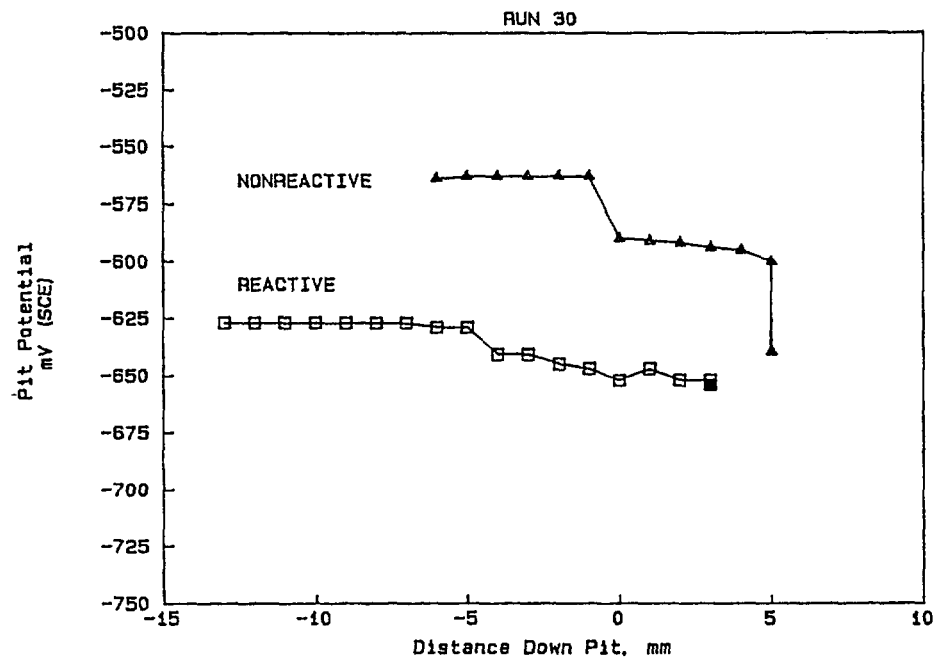


Figure B.6. Potential for pit specimen as a function of microcapillary probe position down the pit where the pit specimen and BES specimen were coupled (open symbols). Closed symbols indicate potentials when pit and BES specimens were uncoupled; Experiment 30 in aerated basalt groundwater at 25 C.

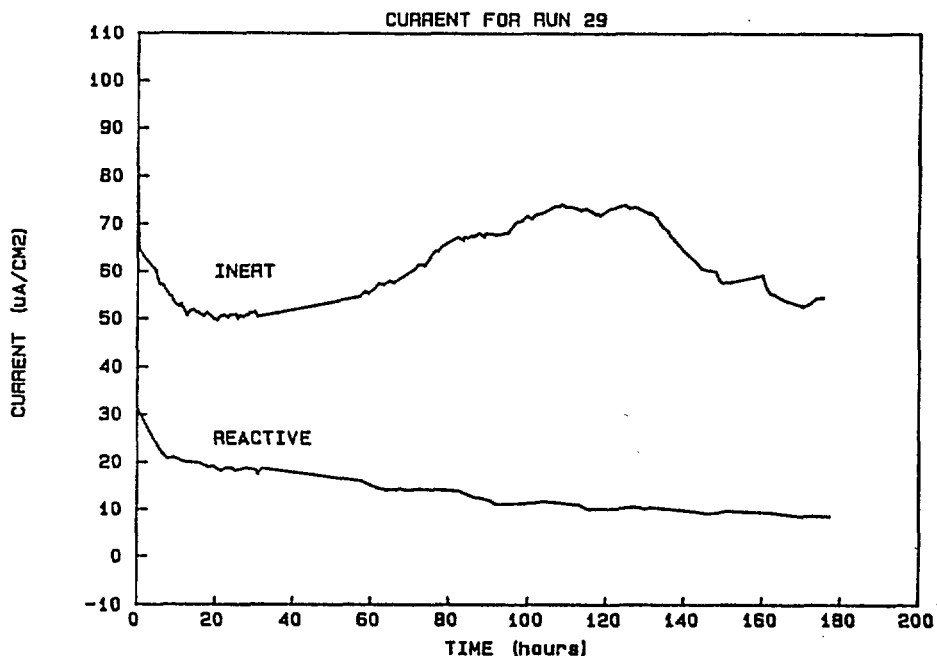


Figure B.7. Coupled current density as a function of exposure time and pit-wall reactivity for pit-propagation Experiment 29 performed at a diameter-to-depth ratio of 1:2 in aerated basalt groundwater at 25 C.

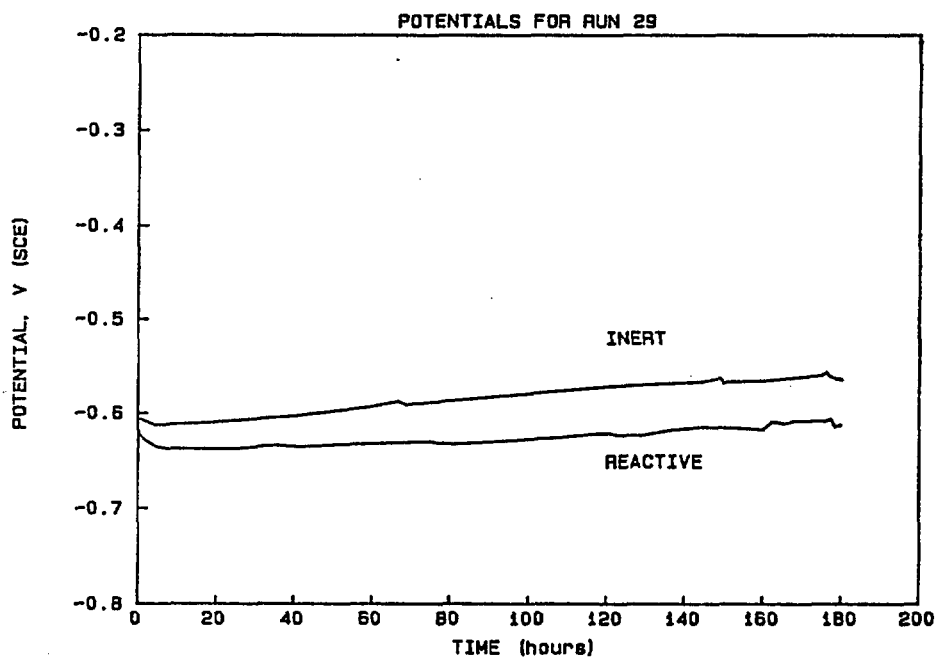


Figure B.8. Coupled potential as a function of exposure time for pit-propagation Experiment 29 performed at a diameter-to-depth ratio of 1:2 in aerated basalt groundwater at 25 C.

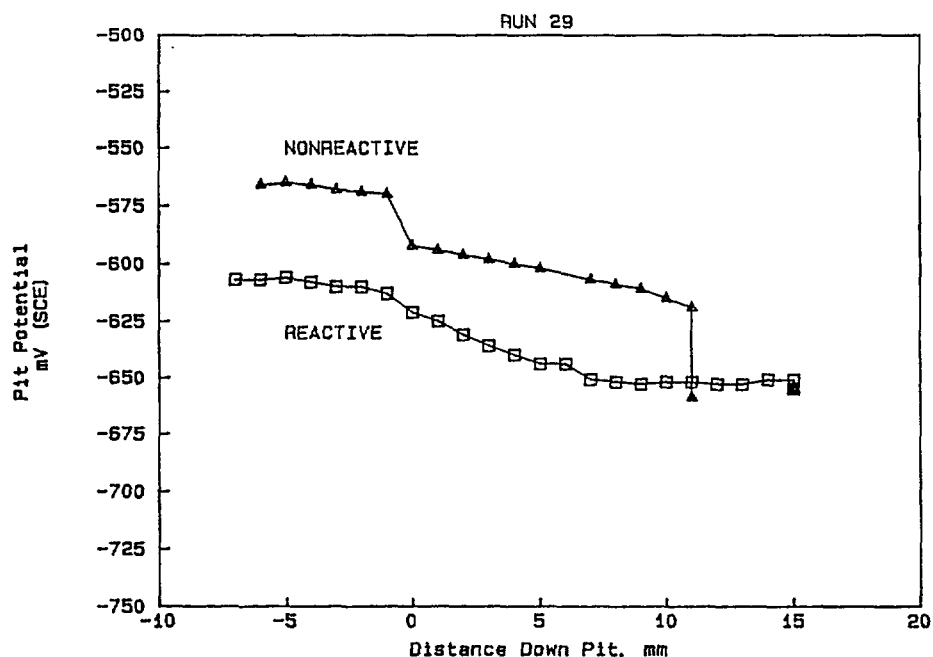


Figure B.9. Potential for pit specimen as a function of microcapillary probe position down the pit where the pit specimen and BES specimen were coupled (open symbols). Closed symbols indicate potentials when pit and BES specimens were uncoupled; Experiment 29 in aerated basalt groundwater at 25 C.

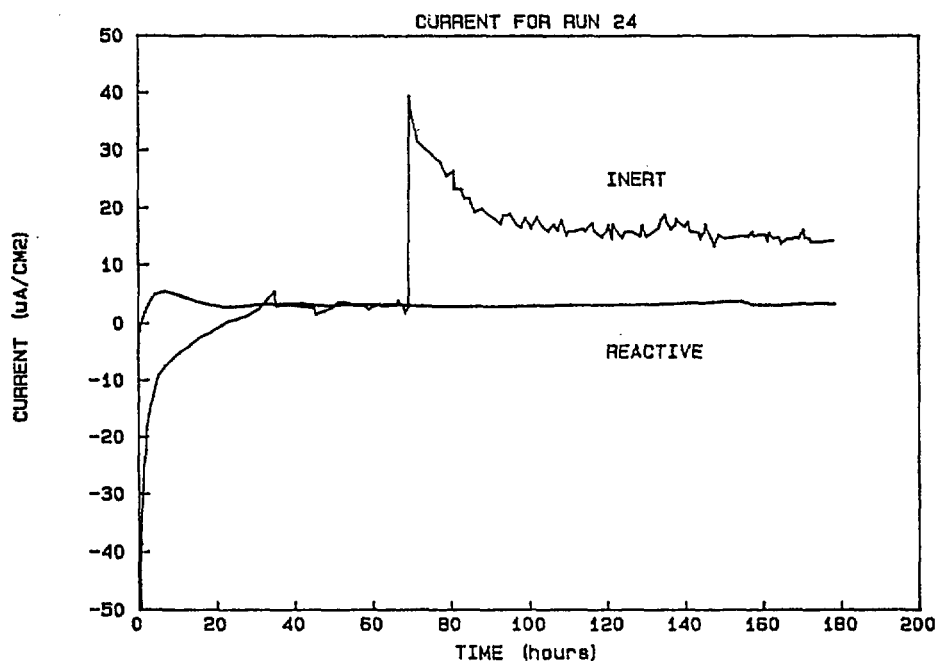


Figure B.10. Coupled current density as a function of exposure time and pit-wall reactivity for pit-propagation Experiment 24 performed at a diameter-to-depth ratio of 1:2.5 in aerated basalt groundwater at 25 C.

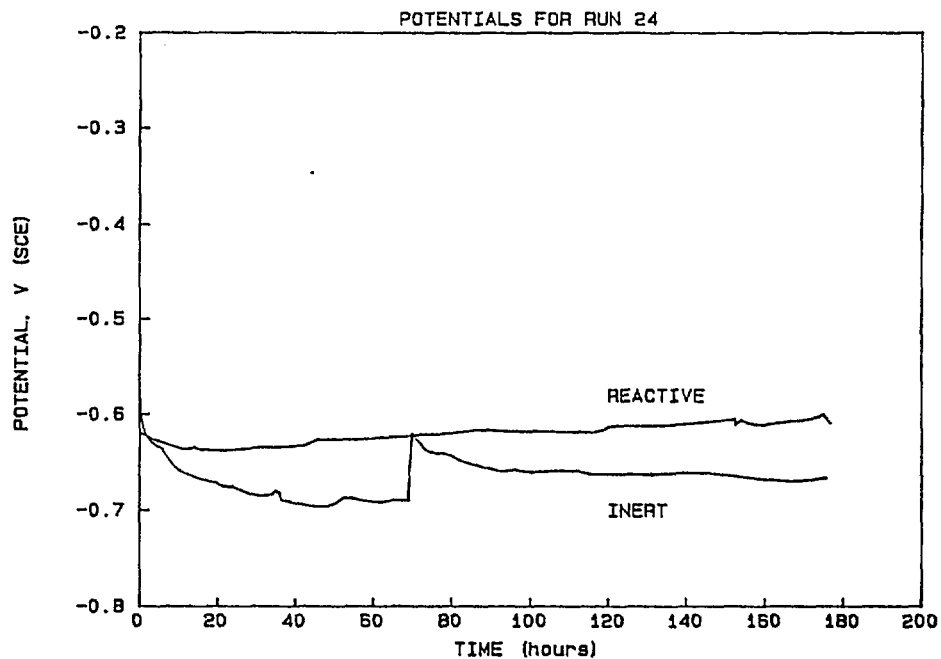


Figure B.11. Coupled potential as a function of exposure time for pit-propagation Experiment 24 performed at a diameter-to-depth ratio of 1:2.5 in aerated basalt groundwater at 25 C.

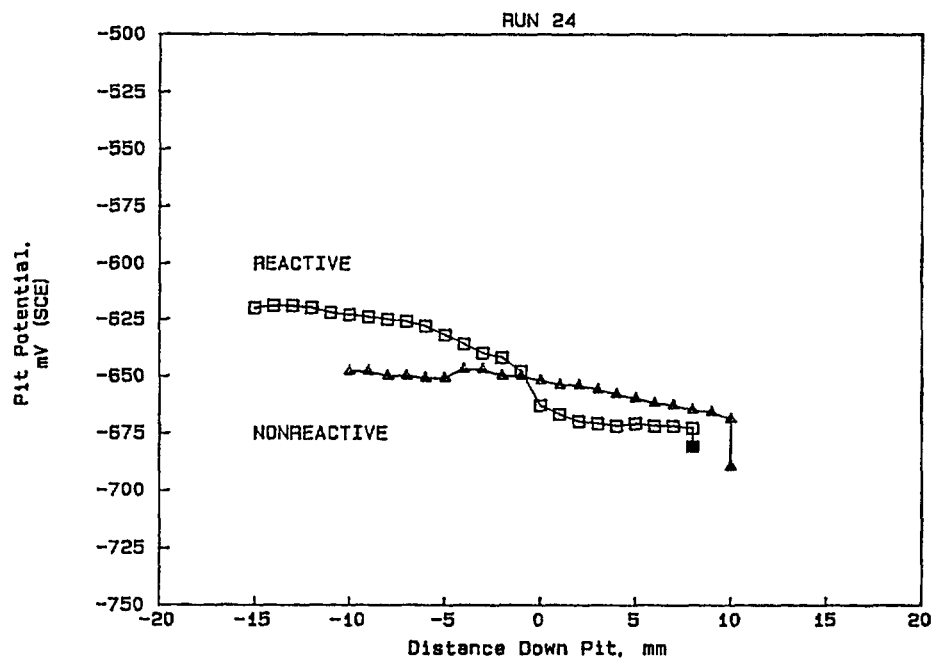


Figure B.12. Potential for pit specimen as a function of microcapillary probe position down the pit where the pit specimen and BES specimen were coupled (open symbols). Closed symbols indicate potential when pit and BES specimens were uncoupled; Experiment 24 in aerated basalt groundwater at 25 C.

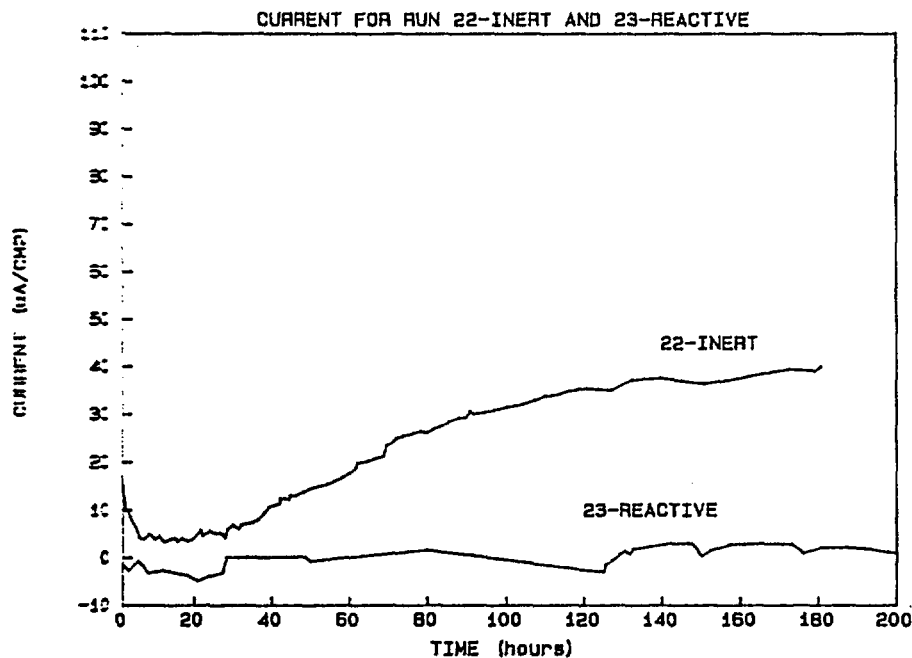


Figure B.13. Coupled current density as a function of exposure time and pit-wall reactivity for pit-propagation Experiments 22 and 23 performed at a diameter-to-depth ratio of 1:10 in aerated basalt groundwater at 25 C.

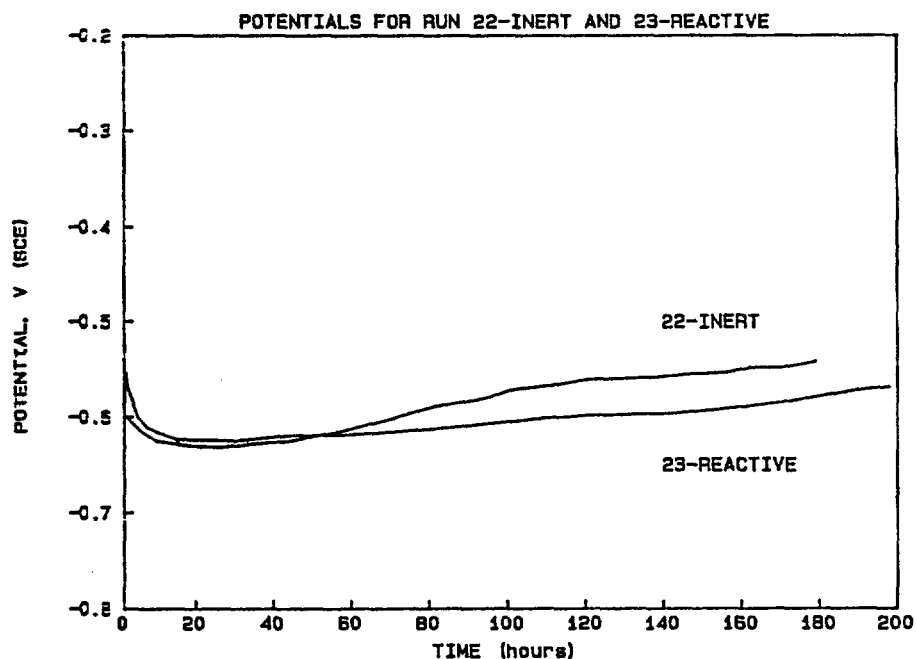


Figure B.14. Coupled potential as a function of exposure time for pit-propagation Experiments 22 and 23 performed at a diameter-to-depth ratio of 1:10 in aerated basalt groundwater at 25 C.

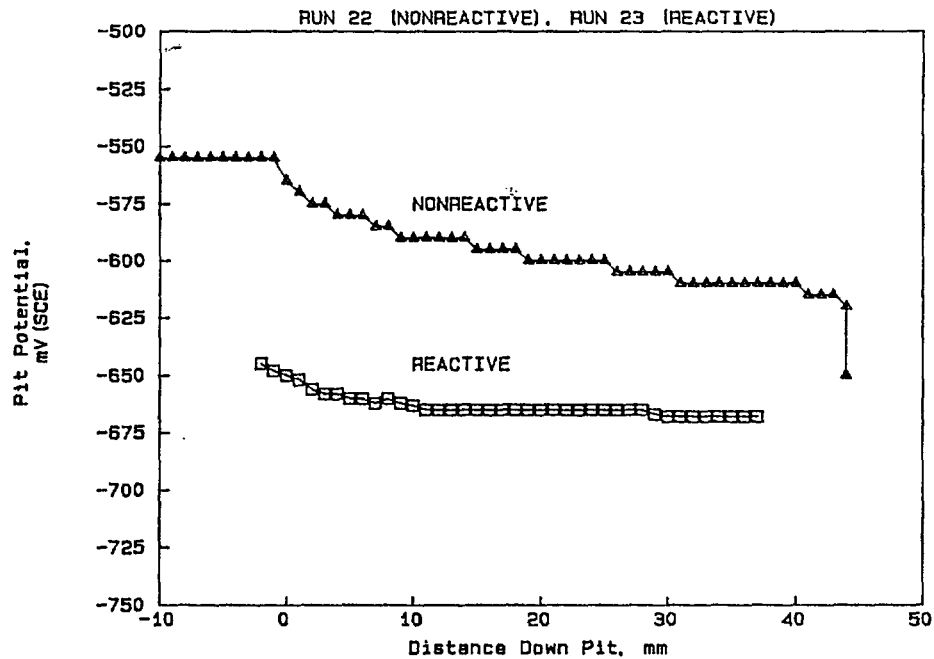


Figure B.15. Potential for pit specimen as a function of microcapillary probe position down the pit where the pit specimen and BES specimen were coupled (open symbols). Closed symbols indicate potential when pit and BES specimens were uncoupled; Experiments 22 and 23 in aerated basalt groundwater at 25 C.

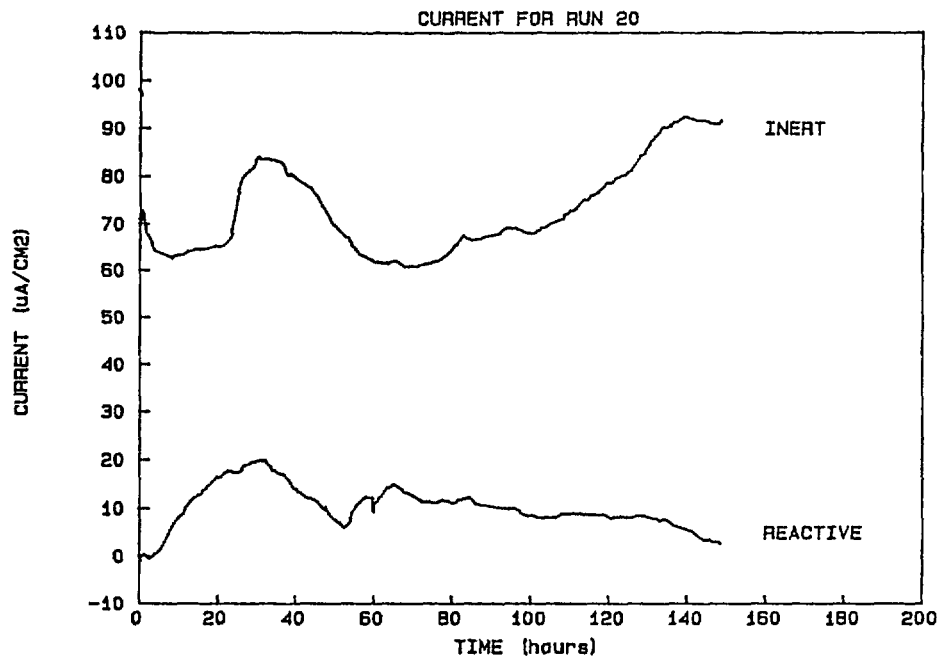


Figure B.16. Coupled current density as a function of exposure time and pit-wall reactivity for pit-propagation Experiment 20 performed at a diameter-to-depth ratio of 1:5 in aerated basalt groundwater at 25 C.

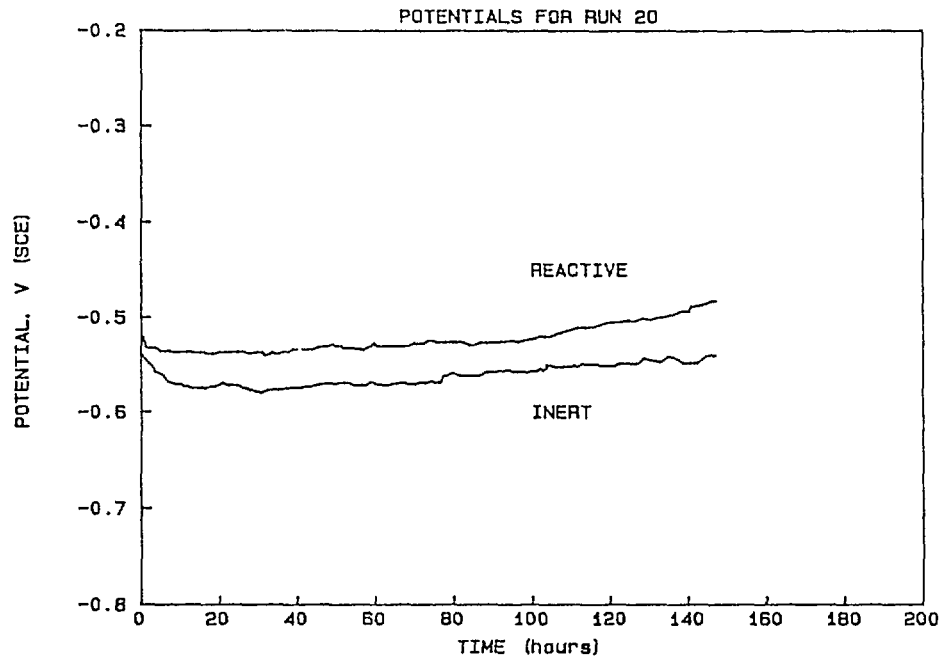


Figure B.17. Coupled potential as a function of exposure time for pit-propagation Experiment 20 performed at a diameter-to-depth ratio of 1:5 in aerated basalt groundwater at 25 C.

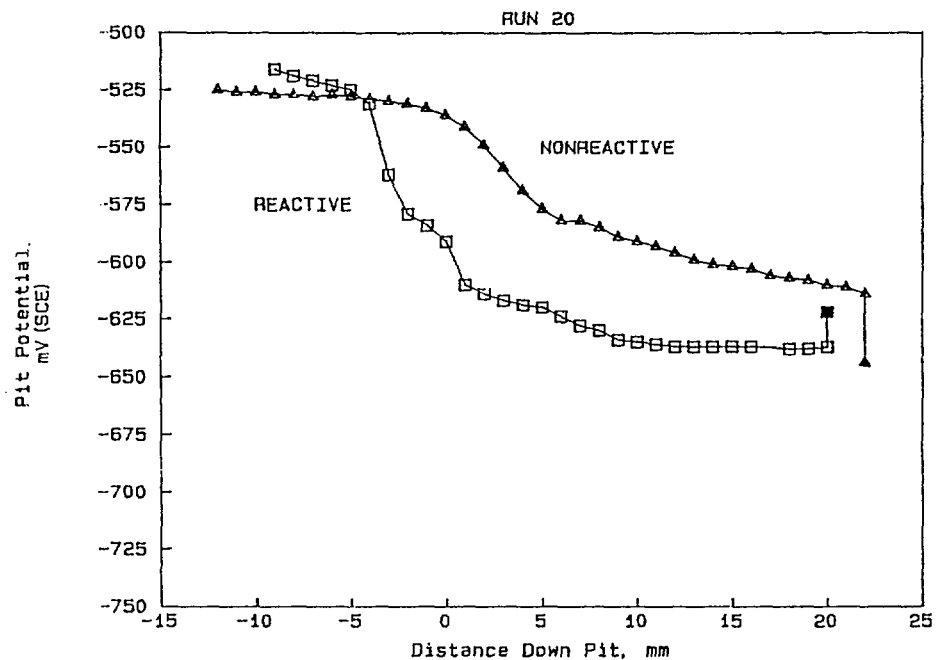


Figure B.18. Potential for pit specimen as a function of microcapillary probe position down the pit where the pit specimen and BES specimen were coupled (open symbols). Closed symbols indicate potentials when pit and BES specimens were uncoupled; Experiment 20 in aerated basalt groundwater at 25 C.

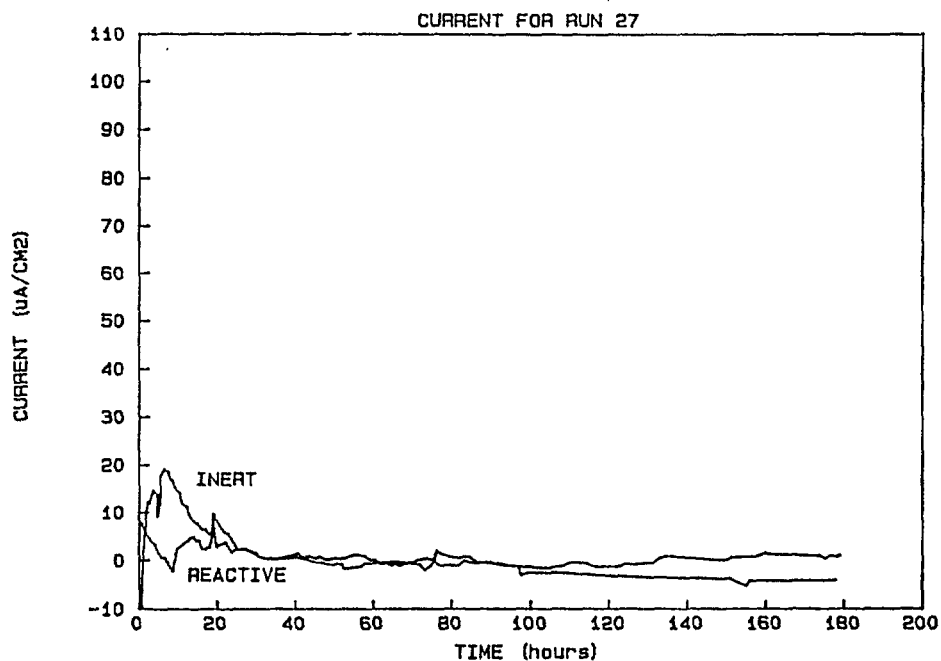


Figure B.19. Coupled current density as a function of exposure time and pit-wall reactivity for pit-propagation Experiment 27 performed at a diameter-to-depth ratio of 1:5 in aerated Brine A at 25 C.

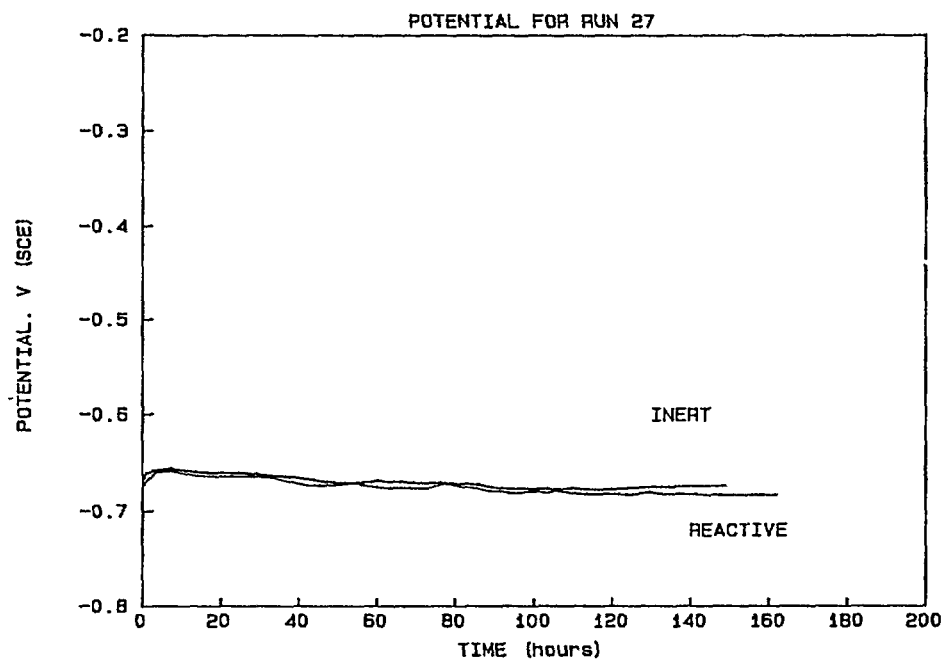


Figure B.20. Coupled potential as a function of exposure time for pit-propagation Experiment 27 performed at a diameter-to-depth ratio of 1:5 in aerated Brine A at 25 C.

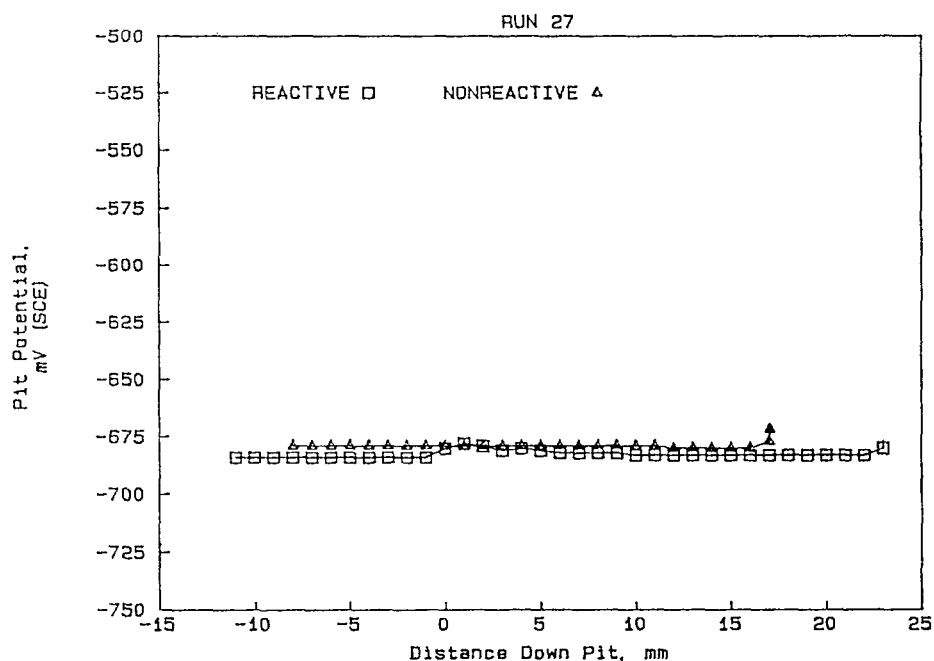


Figure B.21. Potential for pit specimen as a function of microcapillary probe position down the pit where the pit specimen and BES specimen were coupled (open symbols). Closed symbols indicate potential when pit and BES specimens were uncoupled; Experiment 27 in aerated Brine A at 25 C.

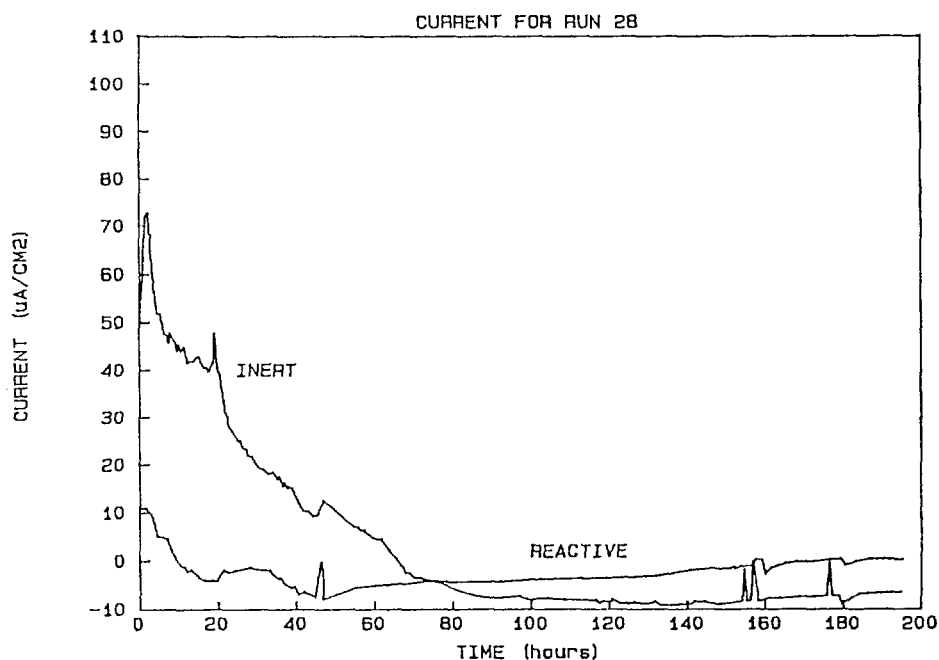


Figure B.22. Coupled current density as a function of exposure time and pit-wall reactivity for pit-propagation Experiment 28 performed at a diameter-to-depth ratio of 1:5 in aerated Brine B at 25 C.

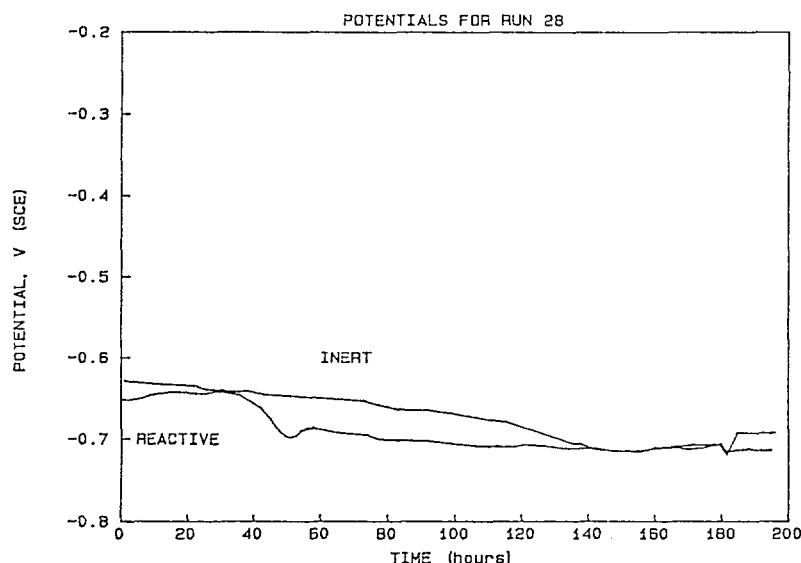


Figure B.23. Coupled potential as a function of exposure time for pit-propagation Experiment 28 performed at a diameter-to-depth ratio of 1:5 in aerated Brine B at 25 C.

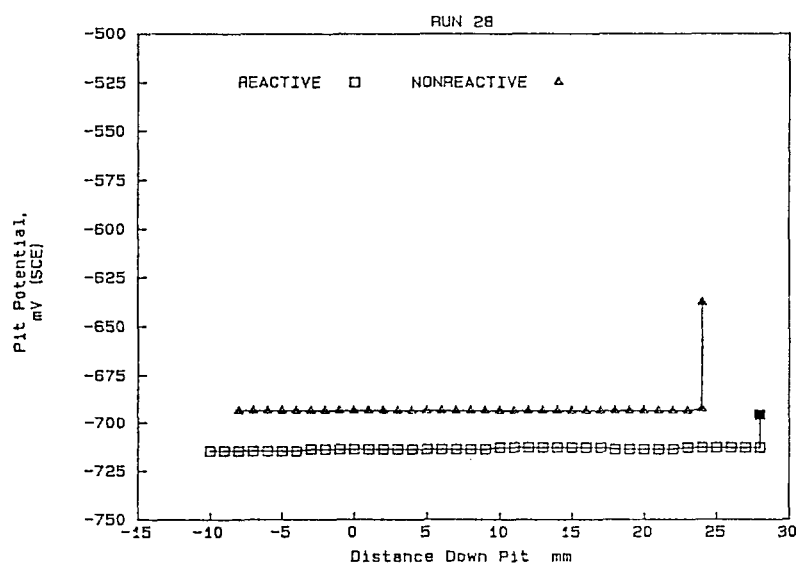


Figure B.24. Potential for pit specimen as a function of microcapillary probe position down the pit where the pit specimen and BES specimen were coupled (open symbols). Closed symbols indicate potential when the pit and BES specimens were uncoupled; Experiment 28 in aerated Brine B at 25 C.

*The large noble shifts observed for the uncoupled potentials were probably the result of the microcapillary scraping the surface of the pit specimen.

APPENDIX C

POTENTIODYNAMIC POLARIZATION CURVES
FOR SELECTED SOLUTIONS FROM STATISTICAL MATRIX

APPENDIX C

POTENTIODYNAMIC POLARIZATION CURVES FOR SELECTED SOLUTIONS FROM STATISTICAL MATRIX

This appendix presents the potentiodynamic polarization curves for hot-rolled 1020 carbon steel in solutions (from statistical experimental matrix) that were used in SSR studies.

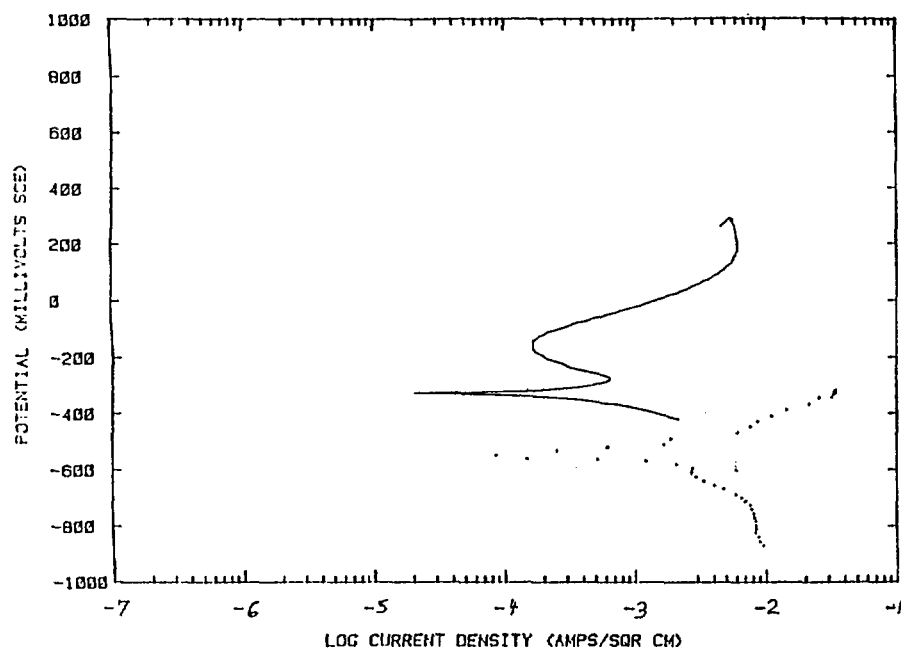


Figure C.1. Fast scan (18 V/hour) and slow scan (0.6 V/hour) potentiodynamic polarization curves for hot-rolled 1020 carbon steel in deaerated solution 5 from statistical experimental matrix.

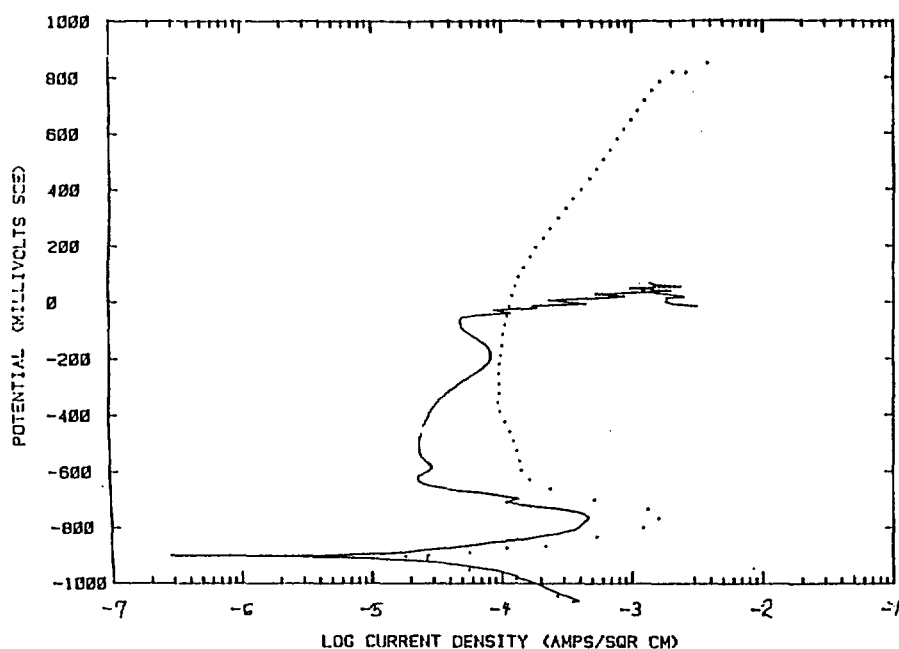


Figure C.2. Fast scan (18 V/hour) and slow scan (0.6 V/hour) potentiodynamic polarization curves for hot-rolled 1020 carbon steel in deaerated solution 8 from statistical experimental matrix.

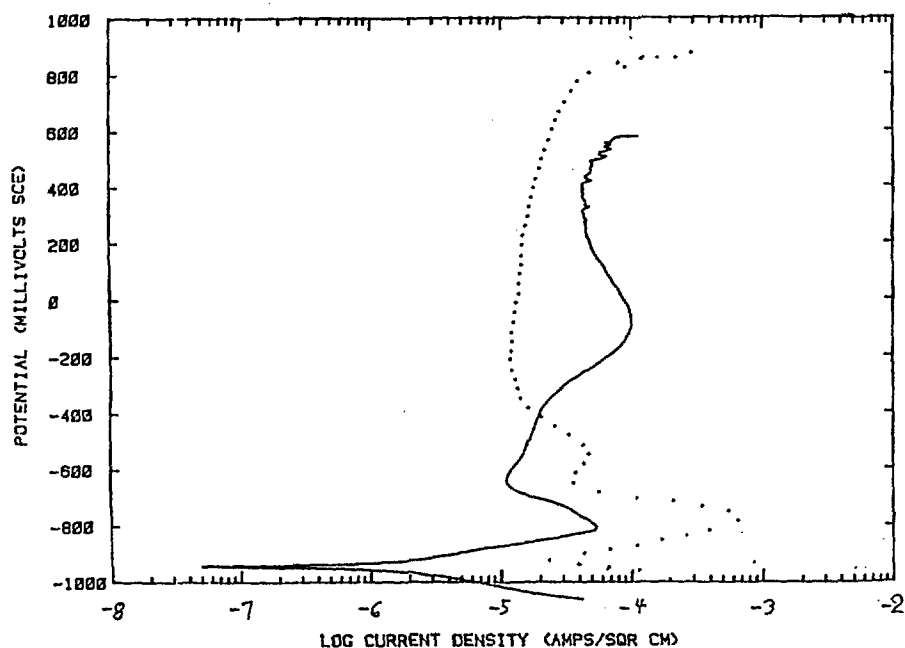


Figure C.3. Fast scan (18 V/hour) and slow scan (0.6 V/hour) potentiodynamic polarization curves for hot-rolled 1020 carbon steel in deaerated solution 21 from statistical experimental matrix.

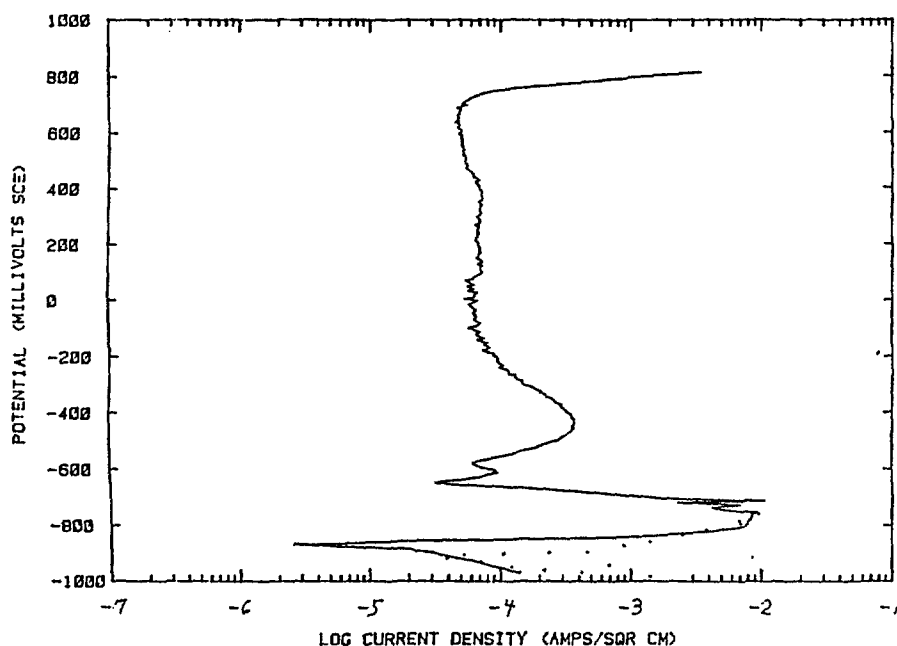


Figure C.4. Fast scan (18 V/hour) and slow scan (0.6 V/hour) potentiodynamic polarization curves for hot-rolled 1020 carbon steel in deaerated solution 23 from statistical experimental matrix.

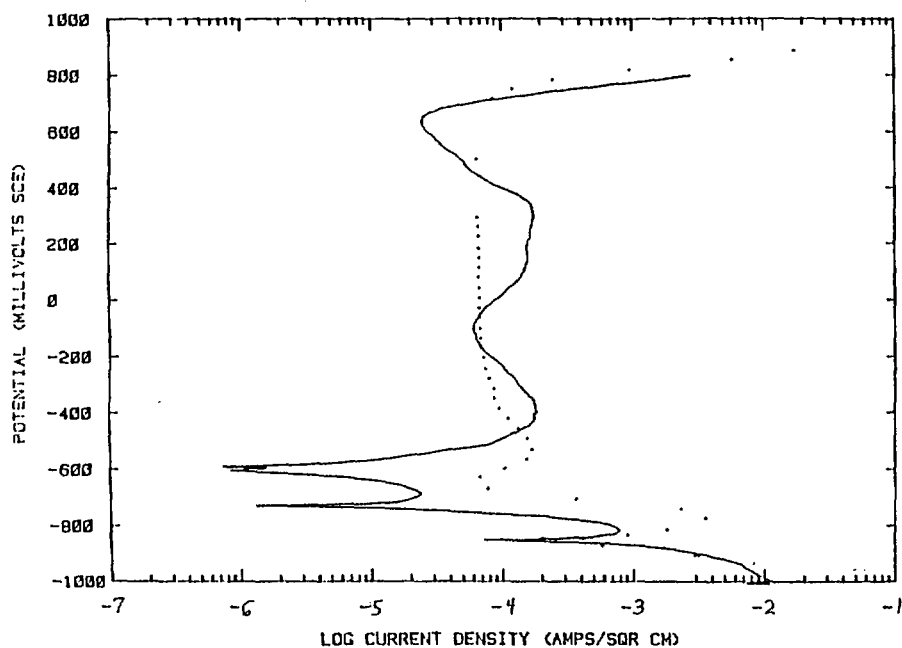


Figure C.5. Fast scan (18 V/hour) and slow scan (0.6 V/hour) potentiodynamic polarization curves for hot-rolled 1020 carbon steel in deaerated solution 31 from statistical experimental matrix.

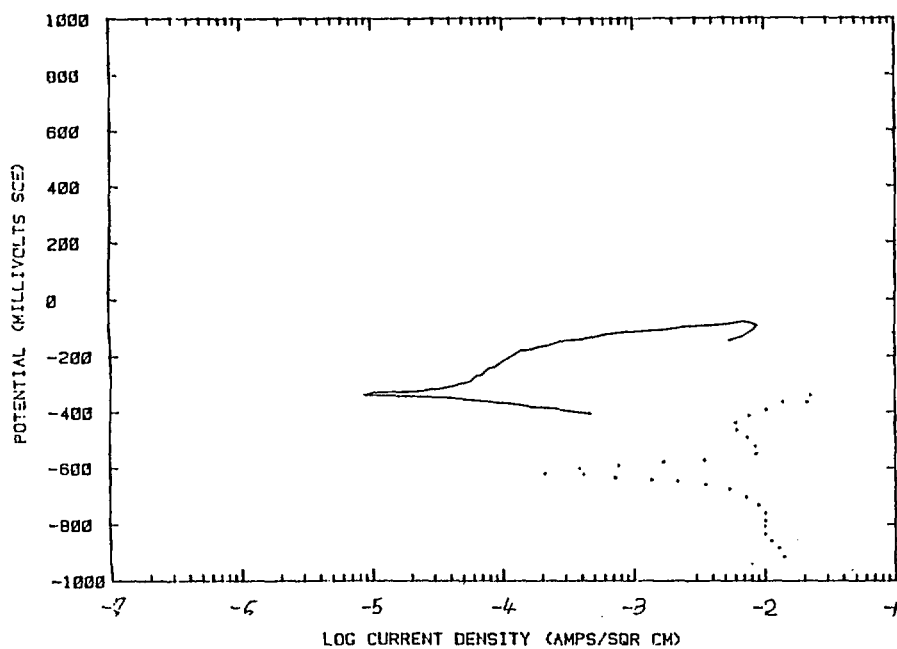


Figure C.6. Fast scan (18 V/hour) and slow scan (0.6 V/hour) potentiodynamic polarization curves for hot-rolled 1020 carbon steel in deaerated solution 57 from statistical experimental matrix.

APPENDIX D

POTENTIODYNAMIC POLARIZATION CURVES
FOR NITRATE SOLUTIONS

APPENDIX D

POTENTIODYNAMIC POLARIZATION CURVES FOR NITRATE SOLUTIONS

The eight graphs in Appendix D show the potentiodynamic polarization curves for hot-rolled 1020 carbon steel in various solutions of sodium and ammonium nitrate at 90 C and a scan rate of 18 V/hr.

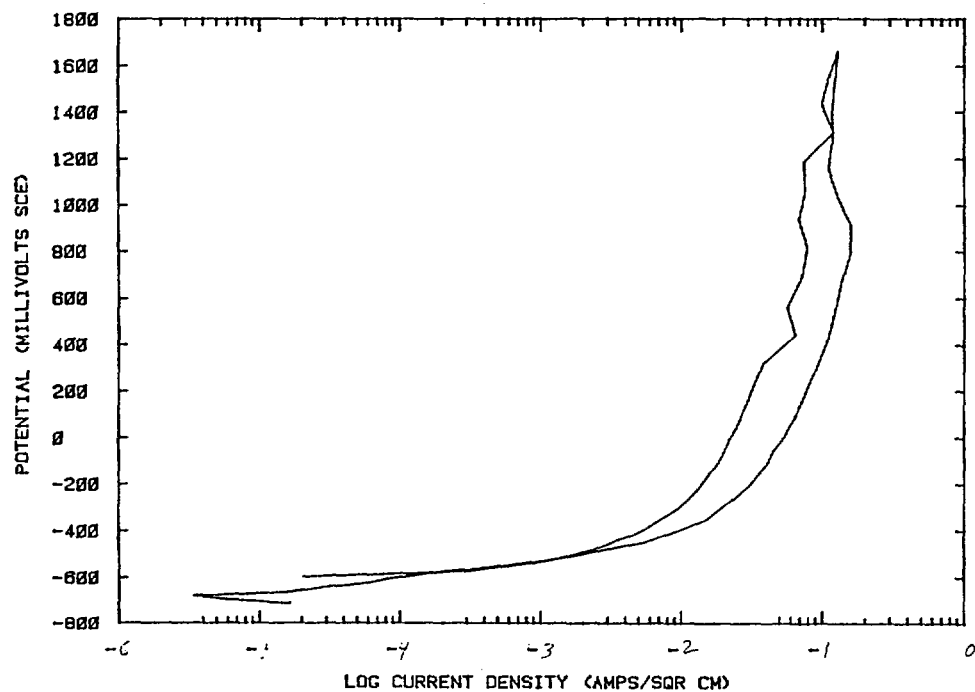


Figure D.1. Potentiodynamic polarization curve for 1020 carbon steel in 0.1 M NaNO_3 at 90 C and a scan rate of 18 V/hr.

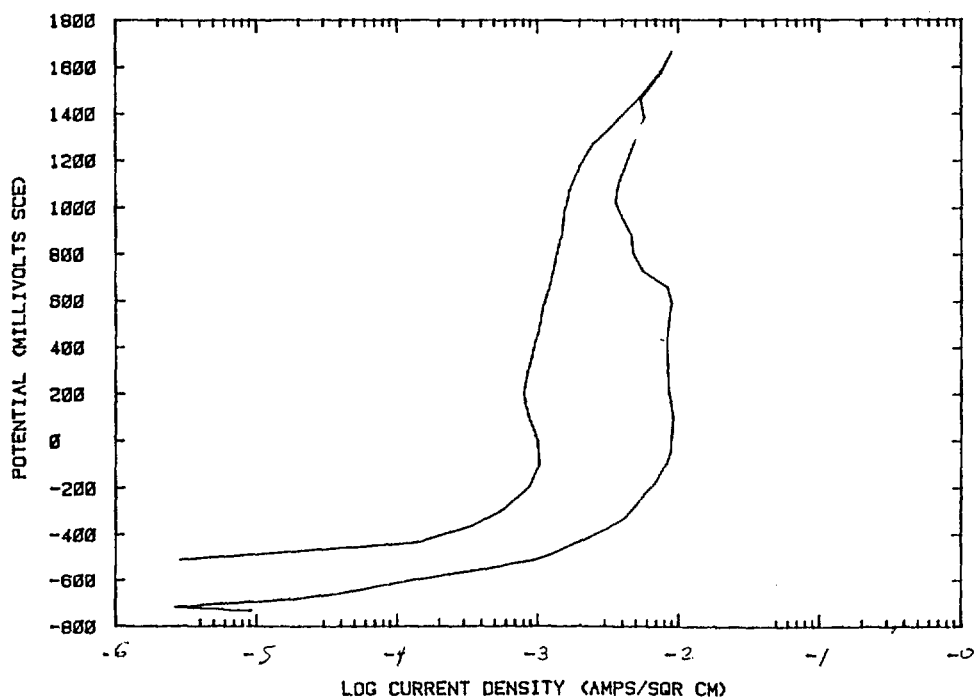


Figure D.2. Potentiodynamic polarization curve for 1020 carbon steel in 0.01 M NaNO_3 at 90 C and a scan rate of 18 V/hr.

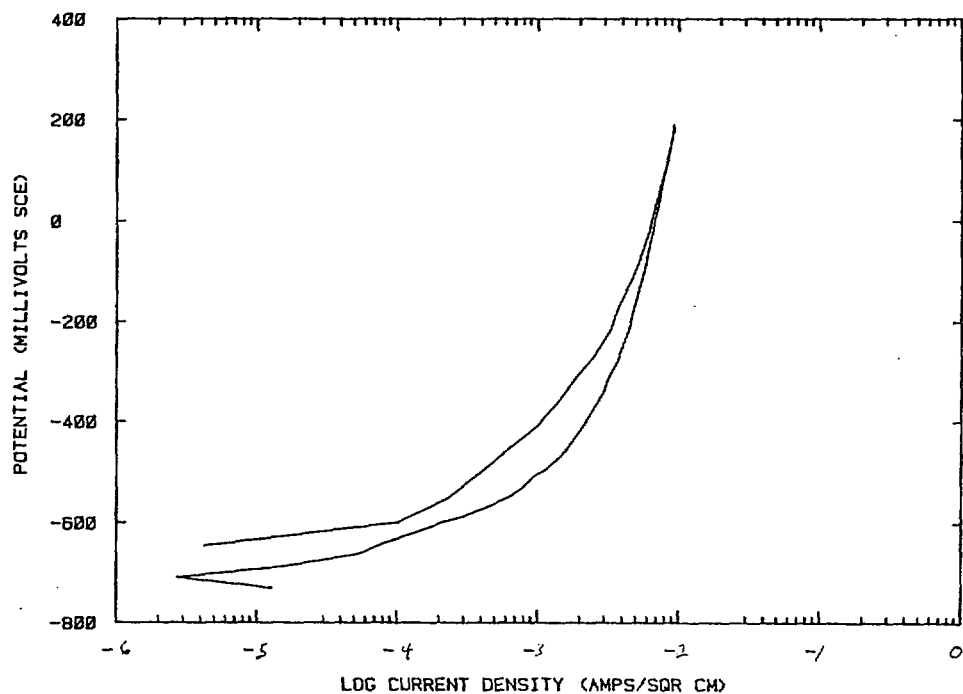


Figure D.3. Potentiodynamic polarization curve for 1020 carbon steel in 0.005 M NaNO₃ at 90 C and a scan rate of 18 V/hr.

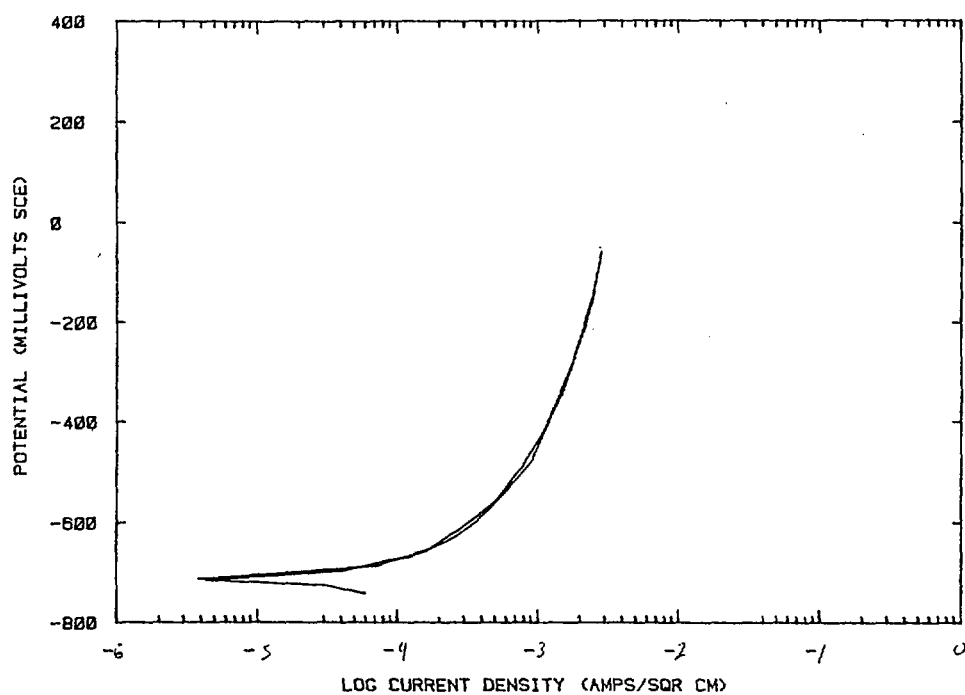


Figure D.4. Potentiodynamic polarization curve for 1020 carbon steel in 0.001 M NaNO₃ at 90 C and a scan rate of 18 V/hr.

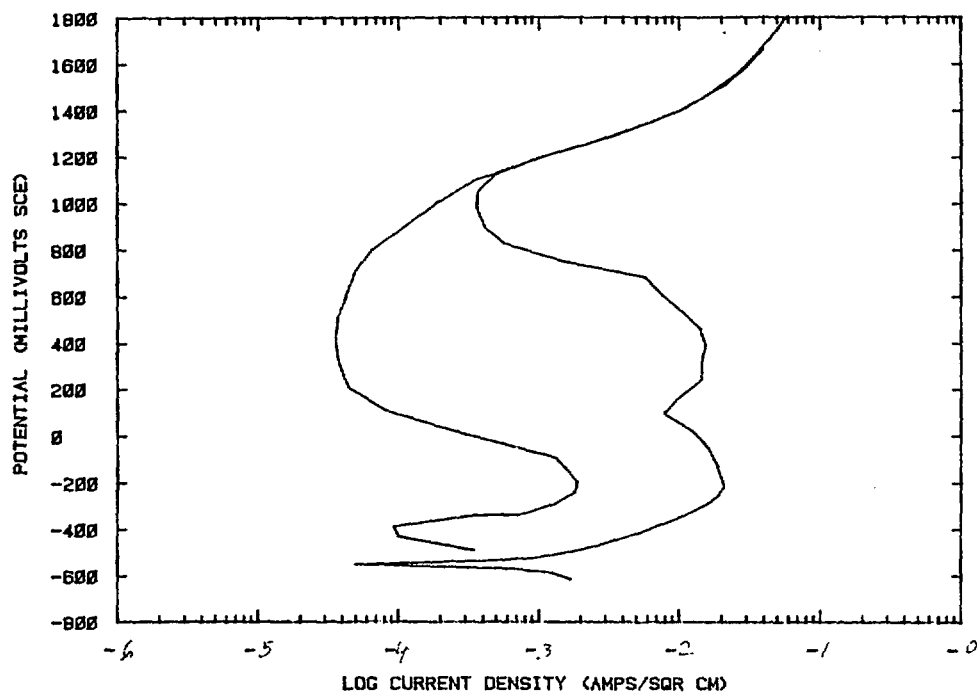


Figure D.5. Potentiodynamic polarization curve for 1020 carbon steel in 0.1 M NH_4NO_3 at 90 C and a scan rate of 18 V/hr.

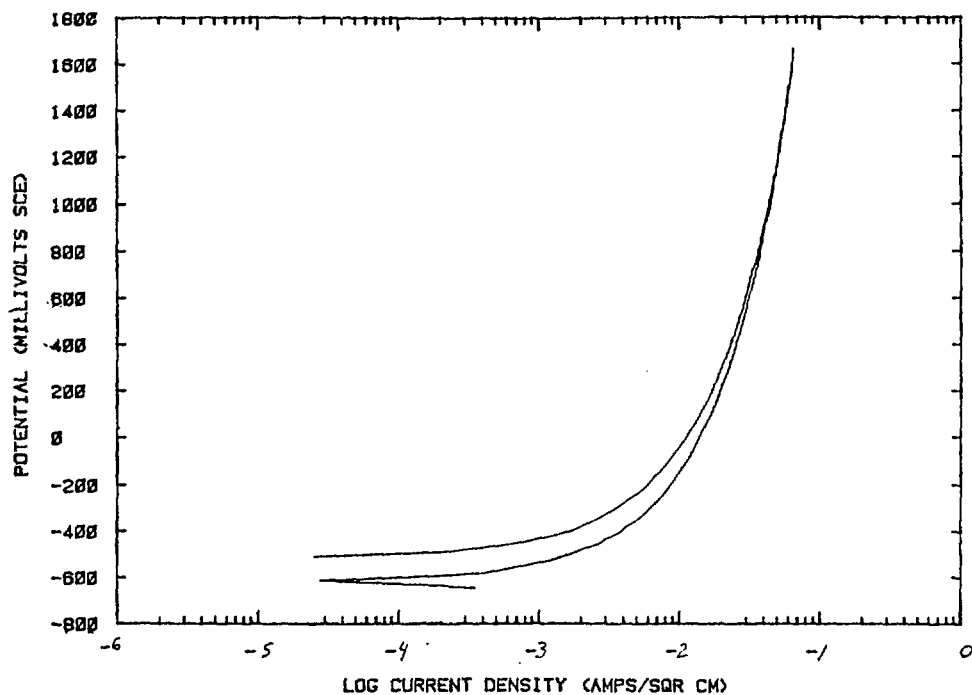


Figure D.6. Potentiodynamic polarization curve for 1020 carbon steel in 0.01 M NH_4NO_3 at 90 C and a scan rate of 18 V/hr.

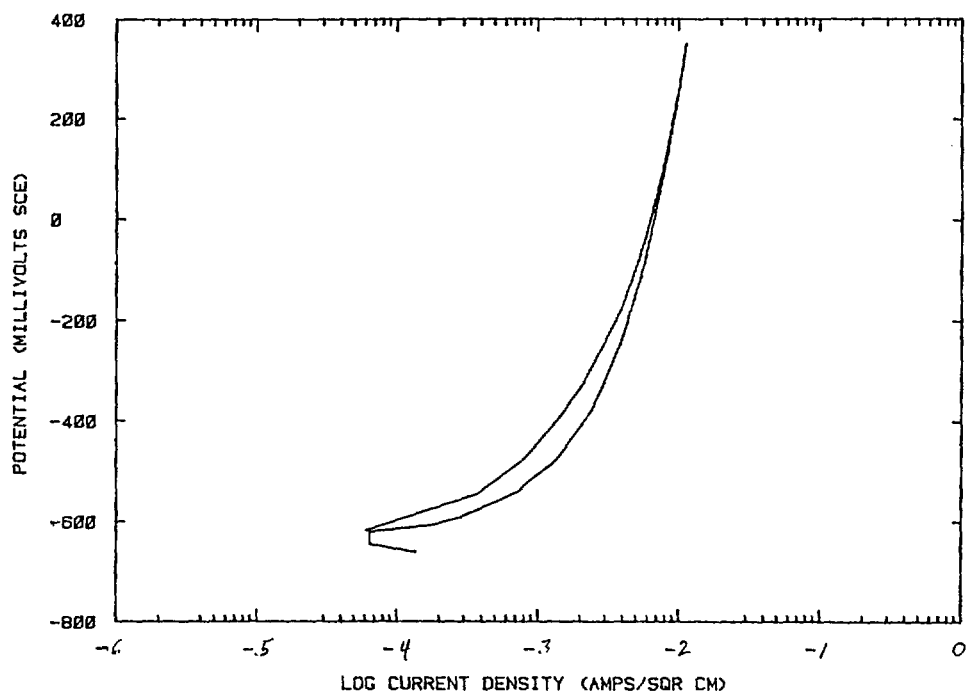


Figure D.7. Potentiodynamic polarization curve for 1020 carbon steel in 0.005 M NH_4NO_3 at 90 C and a scan rate of 18 V/hr.

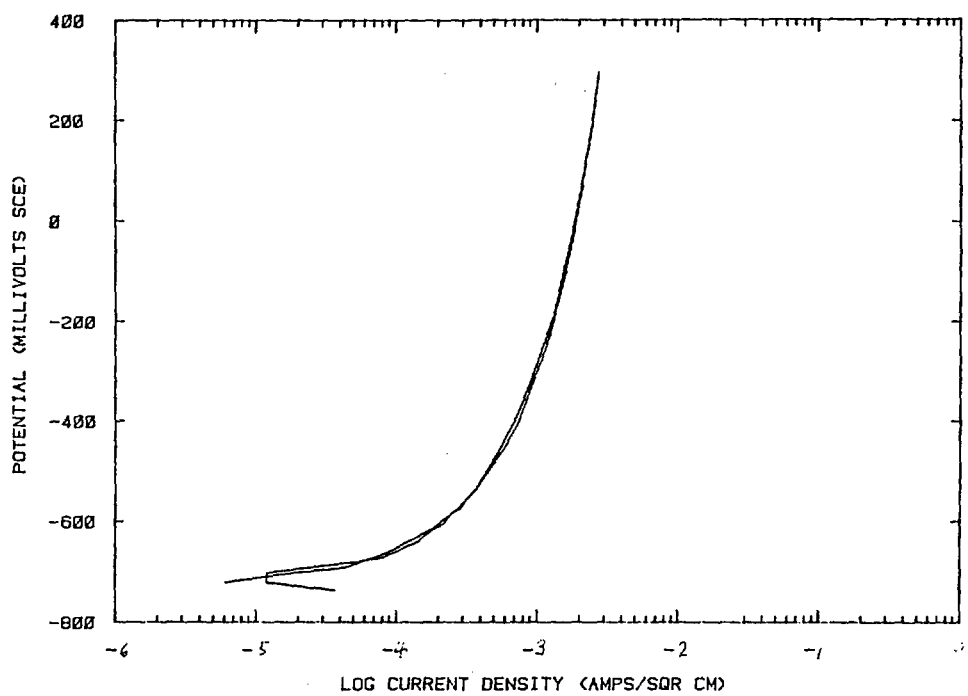


Figure D.8. Potentiodynamic polarization curve for 1020 carbon steel in 0.001 M NH_4NO_3 at 90 C and a scan rate of 18 V/hr.

APPENDIX E

CORROSION MODEL
CODE DOCUMENTATION

FEDERAL INFORMATION PROCESSING STANDARD SOFTWARE SUMMARY

01. Summary date Yr. Mo. Day 87 06 30		02. Summary prepared by (Name and Phone) J. Kevin McCoy 614-424-4050		03. Summary action New <input checked="" type="checkbox"/> Replacement <input type="checkbox"/> Deletion <input type="checkbox"/> Previous Internal Software ID	
04. Software date Yr. Mo. Day 87 06 30		05. Software title Models for general corrosion of waste containers			
06. Short title Models for general corrosion of waste containers					
08. Software type <input type="checkbox"/> Automated Data System <input checked="" type="checkbox"/> Computer Program <input type="checkbox"/> Subroutine/Module		09. Processing mode <input type="checkbox"/> Interactive <input checked="" type="checkbox"/> Batch <input type="checkbox"/> Combination		10. Application area <u>General</u> <input type="checkbox"/> Computer Systems Support/Utility <input checked="" type="checkbox"/> Scientific/Engineering <input type="checkbox"/> Bibliographic/Textual <u>Specific</u> corrosion modeling	
11. Submitting organization and address Battelle Memorial Institute 505 King Avenue Columbus, Ohio 43201-2693				12. Technical contact(s) and phone J. Kevin McCoy 614-424-4050	
13. Narrative These programs model general corrosion of waste containers at various levels of detail. Aqueous radiolytic species are assumed to diffuse to and oxidize the waste container. The models differ in the boundary conditions at the waste container and in the complexity of the treatment of radiolysis.					
14. Keywords corrosion, general corrosion, waste container, models					
15. Computer manufacturer and model IBM PC		16. Computer operating system DOS		17. Programming language(s) C	
18. Number of source program statements 1328		19. Computer memory requirements 640 KB		20. Tape drives 0	
21. Disk/Drum units 1 360 KB floppy		22. Terminals 0		23. Other operational requirements	
24. Software availability Available <input checked="" type="checkbox"/> Limited <input type="checkbox"/> In-house only <input type="checkbox"/>			25. Documentation availability Available <input checked="" type="checkbox"/> Inadequate <input type="checkbox"/> In-house only <input type="checkbox"/>		
26. FOR SUBMITTING ORGANIZATION USE					

APPENDIX E

CORROSION MODEL CODE DOCUMENTATION

E.1 Mathematical Models and Numerical Methods

In this report, we document four models of general corrosion, named corrode1, corrode2, corrode3, and corrode4. The mathematical models and numerical methods underlying the general corrosion models are documented in previous reports. corrode1 is a one-species maximum-rate model, described in Reference E.1. corrode2 is a two-species maximum-rate model, described in Reference E.2. corrode3 is a one-species film-growth model, described in Reference E.3. corrode4 is a five-species film-growth model, described in Reference E.4.

E.2. User's Manual

E.2.1 Program Considerations

E.2.1.1 Overview

The attached 5.25-in floppy disk contains programs and sample data for four models of general corrosion developed at Battelle. The disk is written in the standard 360-kilobyte format used by IBM personal computers.

The disk is organized into six directories: /corrode1, /corrode2, /corrode3, /corrode4, /corrlib, and /mathlib. The directories /corrlib and /mathlib contain functions used by several programs. The directories /corrode1, /corrode2, /corrode3, and /corrode4 contain the source code, object, and executable files for the four corrosion models. In the discussion below, the name of a corrosion model will be taken to be the same as the name of the directory in which it appears, minus the backslash.

E.2.1.2 Program Paths

The programs are composed of several functions. Source code for functions /newln and /scanrqn is found in directory /corrlib, that for /vadd, /vcpy, /vsc1, /nonlin, and /rkstep is found in directory /mathlib, and all other functions appear in the /corrode# directories for the model to which they pertain. The purposes of the functions are as follows.

- corrode: This is the main program. It invokes a function to initialize parameters and a function to initialize the state of the system. It prints the initial state. It loops once per time step, invoking the differential equation solver to calculate the new state, incrementing the time, and printing the new state.
- initpar: This function reads the input data except for the initial state of the system. It is invoked by corrode.

initstate: This function reads the initial state of the system. It is invoked by corrode.

statediff: This function calculates the time derivative of the state of the system. It is invoked by rkstep.

rkstep: This function is the differential equation solver. It uses a fourth-order Runge-Kutta method. It is invoked by corrode. Two versions exist. In one, the user is required to provide a work area; this version is used for models corrodel, corrode2, and corrode3. In the other version, the work area is obtained by invoking the memory allocator; this version is used for model corrode4. The second version will print an error message and abort the program if memory allocation fails.

tcan: In models corrodel, corrode2, and corrode3, this function returns the current temperature of the surface of the container. It is invoked by statediff. In model corrode4, this boundary condition is handled directly by statediff.

conc0: In models corrode3 and corrode4, this function is used to determine the concentration of oxidizing species at the surface of the container according to the point defect model of general corrosion. It returns a value of zero when the concentration is correct. It is invoked by nonlin. In models corrodel and corrode2, the concentration of oxidizing species at the surface of the container is assumed to be zero, so conc0 is unnecessary.

bound: In model corrode4, this function is used before printing to ensure that the state of the system is consistent with the point defect model of general corrosion. It is invoked by corrode.

nonlin: This function returns the value of a root to a nonlinear equation. It uses a modified secant method. This function is not used in models corrodel and corrode2, as it is unnecessary. nonlin accepts two tolerances. A root is considered to be found if two successive approximants to the root differ by less than tolx, or if the absolute value of function value at the current approximant is less than toly. If both tolx and toly are negative, nonlin will print an error message and abort the program. If the two initial approximants differ by less than tolx, nonlin will print an error message and return the second approximant.

scanrgn: This function reads data from standard input and initializes an array. It reads a pair of numbers, first one of type int, then one of type double. The int specifies the number of locations in the array that are to be initialized to the double value. The function continues to read until

the array is full. If the int specifies more locations than remain in the array, the excess is ignored. If either the int or the double is illegal in form scanrgn prints an error message and aborts the program. Number pairs with non-positive ints are silently ignored.

- newln: This function discards all data from standard input up to a new line character, ASCII character code 012 octal.
- vadd: This function adds the elements of two arrays.
- vcpy: This function copies all elements of an array into a second array.
- vscl: This function multiplies all elements of an array by a scalar.

E.2.1.3 Data Structures

The three primary data structures in corrode are state, kpar, and time. The structures kpar and time contain kinetic parameters and time parameters, respectively. kpar is of type struct kpars, while time is of type struct times. The contents of these two types of structures are described in the file structs.

In contrast, state is a simple array. It contains the entire state of the system and may be thought of as a series of vectors: one vector for each concentration profile, followed by a vector for the temperature profile, followed by a single element containing the corrosion wastage. The number of elements in each vector in state is equal to the number of nodes at which the partial differential equations are to be solved. corrode also contains a structure, statenew, which is identical to state, except it describes the state of the system at the end of a time step rather than at the beginning. A similar structure, stateder, also appears in statediff; it contains the time derivatives of the state of the system.

Dimensioning of state is controlled through the contents of file defs. defs defines a manifest constant, MAXSTEP, which is the maximum number of radius steps which may be used. This is one less than the maximum number of nodes. In the case of corrode4, defs also defines NSPEC, the number of species under consideration. MAXSPEC may be changed as desired; NSPEC must not be changed.

E.2.2 Data Files

All models read their standard input and write to their standard output. No other files are used.

E.2.3 Input Data

All quantities, both for input and output, are assumed to be in a consistent set of units. These may be different from standard engineering units.

Since we have no way of knowing what units will be used with the program, we will treat all quantities as dimensionless.

Following the usual C practice, data are read by scanf. No field width specifications are used. In the discussions below, we will use the term "scanrgn format" to refer to a series of pairs of int values followed by a double value, as described in the description of scanrgn above. Unless specified as type int below, all data are type double and are read under "%lf" control. ints are read under "%d" control.

For easier editing of data files, we provide for annotations at the end of groups of data. The annotation must be on the same line as the last datum of the group and separated from the datum by at least one space or horizontal tab character. Annotations are terminated by a newline character, ASCII character code 012 octal.

In model corrode4, the rate constants for the four homogeneous reactions involving the radiolytic species are specified in the code for statediff.

E.2.3.1 Data for corrode1

The first three values read are the initial model time, the time step, and the maximum (ending) model time. These are read into time.mdl, time.step, and time.max, respectively. This group may be followed by an annotation.

The next three values read are the container radius, the radial step length, and the (int) number of steps. These are read into kpar.radius.can, kpar.radius.step, and kpar.radius.steps, respectively. This group may be followed by an annotation.

The next three values read are the initial container temperature, the far-field temperature, and the time constant for decay of the temperature of the container. These are read into kpar.therm.can0, kpar.therm.bkgd, and kpar.therm.decay, respectively. This group may be followed by an annotation.

The next group contains the profile of the thermal diffusivity the matrix in scanrgn format. This is read into kpar.therm.th-diff. kpar.radius.steps + 1 values must be specified. This group may be followed by an annotation.

The next two values read are the initial γ -field intensity at the container surface, and the time constant for decay of the γ intensity. These are read into kpar.radio.intens0, and kpar.radio.decay, respectively. This group may be followed by an annotation.

The next group contains the profile of the total linear absorption coefficient of the matrix in scanrgn format. This is read into a temporary array in initpar and used to initialize kpar.radio.intens. kpar.radius.steps + 1 values must be specified. This group may be followed by an annotation.

The next two values read are the g-value at infinite temperature for the oxidizing species and the activation temperature for the g-value of the

oxidizing species. These are read into kpar.radio.ginf, and kpar.radio.gactv, respectively. This group may be followed by an annotation.

The next value read is the total linear absorption coefficient of water. This is read into kpar.radio.absh20. This group may be followed by an annotation.

The next two values read are the diffusivity at infinite temperature for the oxidizing species and the activation temperature for the diffusivity of the oxidizing species. These are read into kpar.diff.inf, and kpar.diff.actv, respectively. This group may be followed by an annotation.

The next group contains the profile of the porosity of the matrix in scanrgn format. This is read into kpar.diff.porosity. rpar.radius.steps + 1 values must be specified. This group may be followed by an annotation.

The next group contains the profile of tortuosity of the matrix in scanrgn format. This is read into kpar.diff.tortuosity. kpar.radius.steps + 1 values must be specified. This group may be followed by an annotation.

The next value read is the rate constant for decay of the oxidizing species. This is read into kpar.recom.mult. This group may be followed by an annotation.

The next group contains the profile of the concentration of the oxidizing species in scanrgn format. This is read into a portion of state. kpar.radius.steps + 1 values must be specified. This group may be followed by an annotation.

The next group contains the profile of the temperature of the matrix in scanrgn format. This is read into a portion of state. kpar.radius.steps + 1 values must be specified. This group may be followed by an annotation.

The last group contains the initial corrosion wastage. This is read into a portion of state. This group may be followed by an annotation.

E.2.3.2 Data for corrode2

The first three values read are the initial model time, the time step, and the maximum (ending) model time. These are read into time.mdl, time.step, and time.max, respectively. This group may be followed by an annotation.

The next three values read are the container radius, the radial step length, and the (int) number of steps. These are read into kpar.radius.can, kpar.radius.step, and kpar.radius.steps, respectively. This group may be followed by an annotation.

The next three values read are the initial container temperature, the far-field temperature, and the time constant for decay of the temperature of the container. These are read into kpar.therm.can0, kpar.therm.bkqd, and

kpar.therm.decay, respectively. This group may be followed by an annotation.

The next group contains the profile of the thermal diffusivity the matrix in scanrgn format. This is read into kpar.therm.th-diff. kpar.radius.steps + 1 values must be specified. This group may be followed by an annotation.

The next two values read are the initial γ -field intensity at the container surface, and the time constant for decay of the γ intensity. These are read into kpar.radio.intens0, and kpar.radio.decay, respectively. This group may be followed by an annotation.

The next group contains the profile of the total linear absorption coefficient of the matrix in scanrgn format. This is read into a temporary array in initpar and used to initialize kpar.radio.intens. kpar.radius.steps + 1 values must be specified. This group may be followed by an annotation.

The next two values read are the g-value at infinite temperature for the oxidizing species and the activation temperature for the g-value of the oxidizing species. These are read into kpar.radio.ginf[0], and kpar.radio.gactv[0], respectively. This group may be followed by an annotation.

The next two values read are the g-value at infinite temperature for the reducing species and the activation temperature for the g-value of the reducing species. These are read into kpar.radio.ginf[1], and kpar.radio.gactv[1], respectively. This group may be followed by an annotation.

The next value read is the total linear absorption coefficient of water. This is read into kpar.radio.absh20. This group may be followed by an annotation.

The next two values read are the diffusivity at infinite temperature for the oxidizing species and the activation temperature for the diffusivity of the oxidizing species. These are read into kpar.diff.inf[0], and kpar.diff.actv[0], respectively. This group may be followed by an annotation.

The next two values read are the diffusivity at infinite temperature for the reducing species and the activation temperature for the diffusivity of the reducing species. These are read into kpar.diff.inf[1], and kpar.diff.actv[1], respectively. This group may be followed by an annotation.

The next group contains the profile of the porosity of the matrix in scanrgn format. This is read into kpar.diff.porosity. kpar.radius.steps + 1 values must be specified. This group may be followed by an annotation.

The next group contains the profile of tortuosity of the matrix in scanrgn format. This is read into kpar.diff.tortuosity. kpar.radius.steps + 1 values must be specified. This group may be followed by an annotation.

The next two values read are the rate constant for decay of the oxidizing species and the rate constant for reaction of the oxidizing species with the reducing species. These are read into kpar.recom.mono[0], and kpar.recom.mono[0], respectively. This group may be followed by an annotation.

The next two values read are the rate constant for decay of the reducing species and the rate constant for reaction of the reducing species with the oxidizing species. These are read into kpar.recom.mono[1], and kpar.recom.mono[1], respectively. This group may be followed by an annotation.

The next group contains the profile of the concentration of the oxidizing species in scanrgn format. This is read into a portion of state. kpar.radius.steps + 1 values must be specified. This group may be followed by an annotation.

The next group contains the profile of the concentration of the reducing species in scanrgn format. This is read into a portion of state. kpar.radius.steps + 1 values must be specified. This group may be followed by an annotation.

The next group contains the profile of the temperature of the matrix in scanrgn format. This is read into a portion of state. kpar.radius.steps + 1 values must be specified. This group may be followed by an annotation.

The last group contains the initial corrosion wastage. This is read into a portion of state. This group may be followed by an annotation.

E.2.3.3 Data for corrode3

The first three values read are the initial model time, the time step, and the maximum (ending) model time. These are read into time.mdl, time.step, and time.max, respectively. This group may be followed by an annotation.

The next three values read are the container radius, the radial step length, and the (int) number of steps. These are read into kpar.radius.can, kpar.radius.step, and kpar.radius.steps, respectively. This group may be followed by an annotation.

The next three values read are the initial container temperature, the far-field temperature, and the time constant for decay of the temperature of the container. These are read into kpar.therm.can0, kpar.therm.bkgd, and kpar.therm.decay, respectively. This group may be followed by an annotation.

The next group contains the profile of the thermal diffusivity the matrix in scanrgn format. This is read into kpar.therm.th-diff. kpar.radius.steps + 1 values must be specified. This group may be followed by an annotation.

The next two values read are the initial γ -field intensity at the container surface, and the time constant for decay of the γ intensity. These are read

into kpar.radio.intens0, and kpar.radio.decay, respectively. This group may be followed by an annotation.

The next group contains the profile of the total linear absorption coefficient of the matrix in scanrgn format. This is read into a temporary array in initpar and used to initialize kpar.radio.intens. kpar.radius.steps + 1 values must be specified. This group may be followed by an annotation.

The next two values read are the g-value at infinite temperature for the oxidizing species and the activation temperature for the g-value of the oxidizing species. These are read into kpar.radio.ginf, and kpar.radio.gactv, respectively. This group may be followed by an annotation.

The next value read is the total linear absorption coefficient of water. This is read into kpar.radio.absh20. This group may be followed by an annotation.

The next two values read are the diffusivity at infinite temperature for the oxidizing species and the activation temperature for the diffusivity of the oxidizing species. These are read into kpar.diff.inf, and kpar.diff.actv, respectively. This group may be followed by an annotation.

The next group contains the profile of the porosity of the matrix in scanrgn format. This is read into kpar.diff.porosity. kpar.radius.steps + 1 values must be specified. This group may be followed by an annotation.

The next group contains the profile of tortuosity of the matrix in scanrgn format. This is read into kpar.diff.tortuosity. kpar.radius.steps + 1 values must be specified. This group may be followed by an annotation.

The next value read is the rate constant for decay of the oxidizing species. This is read into kpar.recom.mult. This group may be followed by an annotation.

The next six values read are A_1 , B_1 , α , FV_{ext}^0/R , FE/R , and the volume of a unit of corrosion product. These quantities are all defined in Reference E.1. These are read into kpar.corr.a1, kpar.corr.b1, kpar.corr.alpha, kpar.corr.pot1, kpar.corr.field, and kpar.corr.volume, respectively. This group may be followed by an annotation.

The next group contains the profile of the concentration of the oxidizing species in scanrgn format. This is read into a portion of state. kpar.radius.steps + 1 values must be specified. This group may be followed by an annotation.

The next group contains the profile of the temperature of the matrix in scanrgn format. This is read into a portion of state. kpar.radius.steps + 1 values must be specified. This group may be followed by an annotation.

The last group contains the initial corrosion wastage. This is read into a portion of state. This group may be followed by an annotation.

E.2.3.4 Data for corrode4

The first three values read are the initial model time, the time step, and the maximum (ending) model time. These are read into time.mdl, time.step, and time.max, respectively. This group may be followed by an annotation.

The next three values read are the container radius, the radial step length, and the (int) number of steps. These are read into kpar.radius.can, kpar.radius.step, and kpar.radius.steps, respectively. This group may be followed by an annotation.

The next four values read are the far-field temperature, initial heat output of the container, the time constant for decay of the heat output of the container, and the thermal conductivity at the surface of the container. These are read into kpar.therm.can0, kpar.therm.bkgd, and kpar.therm.decay, respectively. This group may be followed by an annotation.

The next group contains the profile of the thermal diffusivity the matrix in scanrgn format. This is read into kpar.therm.th-diff. kpar.radius.steps + 1 values must be specified. This group may be followed by an annotation.

The next two values read are the initial γ -field intensity at the container surface, and the time constant for decay of the γ intensity. These are read into kpar.radio.intens0, and kpar.radio.decay, respectively. This group may be followed by an annotation.

The next group contains the profile of the total linear absorption coefficient of the matrix in scanrgn format. This is read into a temporary array in initpar and used to initialize kpar.radio.intens. kpar.radius.steps + 1 values must be specified. This group may be followed by an annotation.

The next five groups are composed of two values each, the g-value at infinite temperature for the oxidizing species and the activation temperature for the g-value of the oxidizing species. These are read into kpar.radio.ginf[0], and kpar.radio.gactv[0], through kpar.radio.ginf[4], and kpar.radio.gactv[4], respectively. Each group may be followed by an annotation.

The next value read is the total linear absorption coefficient of water. This is read into kpar.radio.absh20. This group may be followed by an annotation.

The next five groups are composed of two values each, the diffusivity at infinite temperature for the oxidizing species and the activation temperature for the diffusivity of the oxidizing species. These are read into kpar.diff.inf[0], and kpar.diff.actv[0], through kpar.diff.inf[4], and kpar.diff.actv[4], respectively. Each group may be followed by an annotation.

The next group contains the profile of the porosity of the matrix in scanrgn format. This is read into kpar.diff.porosity. kpar.radius.steps + 1 values must be specified. This group may be followed by an annotation.

The next group contains the profile of tortuosity of the matrix in scanrgn format. This is read into kpar.diff.tortuosity. kpar.radius.steps + 1 values must be specified. This group may be followed by an annotation.

The next six values read are A_1 , B_1 , α , FV_{ext}^0/R , FE/R , and the volume of a unit of corrosion product, and the concentration of OH^- ions in the groundwater. These quantities are all defined in Reference E.1. These are read into kpar.corr.a1, kpar.corr.b1, kpar.corr.alpha, kpar.corr.pot1, kpar.corr.field, and kpar.corr.volume, respectively. This group may be followed by an annotation.

The next group contains the profile of the concentration of the oxidizing species in scanrgn format. This is read into a portion of state. kpar.radius.steps + 1 values must be specified. This group may be followed by an annotation.

The next group contains the profile of the temperature of the matrix in scanrgn format. This is read into a portion of state. kpar.radius.steps + 1 values must be specified. This group may be followed by an annotation.

The last group contains the initial corrosion wastage. This is read into a portion of state. This group may be followed by an annotation.

E.2.4 System Interface

E.2.4.1 System-Dependent Features

It is expected that this C code will be readily portable. The only system call used by the programs is exit, which terminates a process. All other invocations are of functions in the standard C input/output and mathematical libraries.

E.2.4.2 Compiler Requirements

The programs as delivered have been successfully compiled by the Masscomp "cc" C compiler on an MC-5500 running Real-Time UNIX version 2.2A and by the Microsoft C compiler version 4.0 on an IBM personal computer running MS-DOS version 3.11. On the personal computer, a stack space of 10,000 bytes was found to be sufficient for all four models. It was not assumed that an 8087 co-processor was present.

E.2.4.3 Invocation of Programs

The directories /corrode1, /corrode2, /corrode3, and /corrode4 each contain an executable program for a corrosion model named corrode.exe. As an example, with the disk in the B drive, type

```
b:
cd /corrode2
corrode < dfile
```

to run the second corrosion model with data from file dfile.

E.3 Output

The output will be of the form

```
time = 0.000000e+000 wastage = 1.000000e-004
0.000000e+000 3.000000e+002
1.000000e+000 3.000000e+002
1.000000e+000 3.000000e+002
```

The model time and corrosion wastage are given in the first line. This line is followed by a series of lines with one or more concentrations and, in the last field, a temperature. There will be one line of this type for each node at which the temperature and concentration are determined. Finally, there will be a blank line. The pattern above will be repeated for each time step.

E.3.1 Sample Problems

In each of the directories /corrode1, /corrode2, /corrode3, and /corrode4, we have included files zdata and zoutput. zdata is a sample input file, and zoutput is the output resulting from the command

```
corrode < zdata > zoutput.
```

Presentation of the results in graphic form logically belongs outside the program. Since the available software and hardware will vary from environment to environment, we have left the details of postprocessing and plotting to the user.

E.4 Directory Listings

Volume in drive B has no label
Directory of B:/

CORRLIB	<DIR>	11-14-86	11:27a
MATHLIB	<DIR>	11-14-86	11:29a
CORRODE2	<DIR>	11-14-86	12:11p
CORRODE3	<DIR>	11-14-86	12:11p
CORRODE4	<DIR>	11-14-86	12:11p
CORRODE1	<DIR>	3-20-87	5:20p
6 File(s)		82944 bytes free	

Volume in drive B has no label
Directory of B:/CORRODE1

.	<DIR>	3-20-87	5:20p
..	<DIR>	3-20-87	5:20p
CORRODE C		1710	12-04-86 12:30p
INITPAR C		1815	12-04-86 11:42a
INITSTAT C		842	12-04-86 11:43a

STATEDIF	C	2843	11-14-86	2:59p
TCAN	C	266	11-14-86	2:59p
STRUCTS		1768	11-14-86	2:59p
DEFS		20	11-14-86	2:54p
ZDATA		404	11-14-86	2:59p
README		154	11-14-86	2:59p
CORRODE	OBJ	1124	12-04-86	3:41p
STATEDIF	OBJ	1872	12-03-86	4:36p
INITPAR	OBJ	1350	12-04-86	11:46a
TCAN	OBJ	467	12-03-86	4:40p
INITSTAT	OBJ	547	12-04-86	11:44a
LD		166	12-04-86	3:39p
CORRODE	EXE	26800	12-04-86	3:43p
LINKEM	BAT	20	12-04-86	2:55p
19 File(s)		82944 bytes free		

Volume in drive B has no label
Directory of B:/CORRODE2

.	<DIR>		11-14-85	12:11p
..	<DIR>		11-14-86	12:11p
README		154	11-14-86	3:02p
CORRODE	C	1527	11-14-86	3:01p
DEFS		20	11-14-86	3:01p
INITPAR	C	2093	12-04-85	3:52p
INITSTAT	C	1071	12-04-86	3:53p
STATEDIF	C	3820	12-04-86	4:13p
STRUCTS		1817	11-14-86	3:02p
TACN	C	266	11-14-86	3:02p
ZDATA		610	11-14-86	3:18p
LD		166	12-04-86	3:39p
CORRODE	OBJ	1090	12-04-86	3:54p
INITPAR	OBJ	1499	12-04-86	4:00p
INITSTAT	OBJ	498	12-04-86	4:01p
TCAN	OBJ	467	12-04-86	4:04p
STATEDIF	OBJ	2516	12-04-86	4:15p
LINKEM	BAT	20	12-04-86	2:55p
CORRODE	EXE	27354	12-04-86	4:18p
19 File(s)		82944 bytes free		

Volume in drive B has no label
Directory of B:/CORRODE3

.	<DIR>		11-14-86	12:11p
..	<DIR>		11-14-86	12:11p
README		156	11-14-86	3:05p
CONCO	C	1477	11-14-86	3:04p
CORRODE	C	1794	11-14-86	3:04p
DEFS		76	11-14-86	3:04p
INITPAR	C	2058	12-04-86	4:35p
INITSTAT	C	1094	12-04-86	4:35p
STATEDIF	C	3126	11-14-86	3:20p

STRUCTS		2142	11-14-86	3:06p
TCAN	C	266	11-14-86	3:06p
LD		190	12-04-86	4:59p
ZDATA		467	11-14-86	3:06p
ZDATA2		958	11-14-86	3:07p
LINKEM	BAT	20	12-04-86	2:55p
CONCO	OBJ	1208	12-04-86	4:30p
CORRODE	OBJ	1257	12-04-86	4:31p
INITPAR	OBJ	1525	12-04-86	4:37p
INITSTAT	OBJ	725	12-04-86	4:38p
STATEDIF	OBJ	2052	12-04-86	4:39p
TCAN	OBJ	467	12-04-86	4:40p
CORRODE	EXE	28490	12-04-86	5:00p
22 File(s)			82944 bytes free	

Volume in drive B has no label
Directory of B:/CORRODE4

.	<DIR>		11-14-86	12:11p
..	<DIR>		11-14-86	12:11p
README		158	11-14-86	3:09p
BOUND	C	573	12-09-86	12:36p
CONCO	C	1794	12-09-86	12:37p
DEFS		106	11-14-86	3:22p
CORRODE	C	1702	12-09-86	12:37p
INITPAR	C	2164	12-09-86	12:37p
INITSTAT	C	934	12-09-86	12:37p
STATEDIF	C	4256	12-09-86	12:37p
STRUCTS		2116	11-14-85	3:09p
BOUND	OBJ	593	12-09-86	12:38p
LINKEM	BAT	20	12-04-86	2:55p
LD		189	12-09-86	12:47p
CONCO	OBJ	1410	12-09-86	12:39p
CORRODE	OBJ	1186	12-09-86	12:40p
INITPAR	OBJ	1595	12-09-86	12:41p
INITSTAT	OBJ	816	12-09-86	12:42p
STATEDIF	OBJ	3118	12-09-85	12:46p
CORRODE	EXE	29806	12-09-86	12:48p
ZDATA		594	12-09-86	12:51p
21 File(s)			82944 bytes free	

Volume in drive B has no label
Directory of B:/CORRLIB

.	<DIR>		11-14-86	11:27a
..	<DIR>		11-14-75	11:27a
NEWLN	C	96	12-03-85	5:49p
SCANRGN	C	497	12-04-86	11:41a
NEWLN	OBJ	351	12-03-86	5:50p
SCABRGN	OBJ	581	12-04-86	11:48a
6 File(s)			82944 bytes free	

Volume in drive B has no label
Directory of B:/MATHLIB

.	<DIR>		11-14-86	11:29a
..	<DIR>		11-14-86	11:29a
OLDRKSTP	C	1873	12-03-86	5:05p
VADD	C	208	11-14-86	3:12p
VCPY	C	164	11-14-86	3:12p
VDOT	C	232	11-14-86	3:12p
VEXCH	C	220	11-14-86	3:12p
VMUL	C	208	11-14-86	3:13p
VSCL	C	200	11-14-86	3:13p
VSET	C	149	11-14-86	3:13p
VSUB	C	208	11-14-86	3:13p
XPRINTF	C	148	11-14-86	3:13p
NONLIN	C	1621	12-08-86	1:40p
RKSTEP	C	1982	12-03-86	5:04p
VADD	OBJ	389	12-03-86	4:42p
VCPY	OBJ	367	12-03-86	4:44p
VDOT	OBJ	458	12-03-86	4:45p
VEXCH	OBJ	393	12-03-86	4:45p
VMUL	OBJ	389	12-03-86	4:46p
VSCL	OBJ	383	12-03-86	4:47p
VSET	OBJ	361	12-03-86	4:47p
VSUB	OBJ	389	12-03-86	4:48p
XPRINTF	OBJ	358	12-03-86	4:51p
NONLIN	OBJ	1467	12-08-86	1:41p
OLDRKSTP	OBJ	1176	12-03-86	5:06p
RKSTEP	OBJ	1294	12-03-86	5:07p
VI	BAT	51	12-04-86	11:09a
27 File(s)		82944 bytes free		

E.5 References

- (E.1) "Long-Term Performance of Materials Used for High-Level Waste Packaging," D. Stahl and N. E. Miller (compilers), NUREG/CR-3427, Vol. 4, BMI-2113 (June 1984), pp. 3-106 ff.
- (E.2) "Long-Term Performance of Materials Used for High-Level Waste Packaging," D. Stahl and N. E. Miller (compilers), NUREG/CR-3900, Vol. 4, BMI-2127 (July 1985), pp. 3-84 ff.
- (E.3) "Long-Term Performance of Materials Used for High-Level Waste Packaging," D. Stahl and N. E. Miller (compilers), NUREG/CR-3900, Vol. 4, BMI-2127 (July 1985), pp. 3-89 ff.
- (E.4) "Long-Term Performance of Materials Used for High-Level Waste Packaging," D. Stahl and N. E. Miller (compilers), NUREG/CR-4379, Vol. 4, BMI-2128 (June 1986), pp. 3-77 ff.

APPENDIX F

QUALITY ASSURANCE PROCEDURES

APPENDIX F

QUALITY ASSURANCE PROCEDURES

Quality assurance (QA) procedures were established for all experimental activities. Procedures were revised and new ones prepared as necessary to meet program requirements. Thirty-one approved procedures are applicable to this task.

A summary of these QA procedures is given in Table F.1, which lists each procedure number, the current revision number, the title, and the procedure status.

Table F.1. NRC waste package program QA procedures.

Procedure No.	Title	Status
WF-PP-20 Revision 0	Procedure for Determining the Corrosion Rates of Alloys at High Temperatures	Approved
WF-PP-25 Revision 0	Procedure for Preparation of Carbon-Steel Casting	Approved
WF-PP-26 Revision 0	Procedure for Preparation of Steel Hydrogen-Embrittlement Test Specimens	Approved
WF-PP-26.1 Revision 1	Procedure for Preparation of Hydrogen-Embrittlement Test Specimens from Steel or Iron Samples	Approved
WF-PP-27 Revision 4	Procedure for J-Testing Compact Tension Specimens	Approved
WF-PP-27.1 Revision 0	Procedures for Performing Subcritical-Crack-Growth Tests with Compact Tension Specimens	Approved
WF-PP-28 Revision 1	Procedure for Performing Tension Tests of Steel Specimens	Approved
WF-PP-29 Revision 0	Procedure for Conducting Hydrogen-Absorption Experiments	Approved
WF-PP-30 Revision 0	Laboratory Procedure for Preparation, Cleaning, and Evaluation of Titanium Grade-12 Specimens for Corrosion Studies of the Overpack Performance for the NRC Waste Packaging Program	Approved

Table F.1. Continued.

Procedure No.	Title	Status
WF-PP-31 Revision 0	Laboratory Procedure for Preparation, Cleaning, and Evaluation of Cast and Wrought Carbon Steel Specimens for Corrosion Studies of the Overpack Performance for the NRC Waste Packaging Program	Approved
WF-PP-32 Revision 1	Laboratory Procedure for Preparation of Simulated WIPP Brine A	Approved
WF-PP-33 Revision 0	Procedure for Preparation of Simulated Basalt Groundwater Solution	Approved
WF-PP-33.1 Revision 0	Procedure for Preparation of Basalt Rock for Use in Corrosion Studies for the NRC Waste Packaging Program	Approved
WF-PP-34 Revision 0	Laboratory Procedure for Preparation of Simulated Tuff Groundwater Solutions	Approved
WF-PP-35 Revision 1	Procedure for Performing Autoclave Exposures for Corrosion Tests in Simulated Brines	Approved
WF-PP-35.1 Revision 0	Procedure for Performing Autoclave Exposures for Corrosion Tests in Simulated Brines Using Sealed Internal Canister	Approved
WF-PP-36 Revision 0	Procedure for Performing Stagnant Autoclave Exposures for Corrosion Tests in Simulated Basalt or Tuff Groundwaters	Approved
WF-PP-37 Revision 0	Laboratory Procedure for Preparing Polarization Resistance Specimens, Performing Polarization Resistance Measurements and Evaluating Polarization Resistance Data	Approved

Table F.1. Continued.

Procedure No.	Title	Status
WF-PP-37.1 Revision 0	Laboratory Procedure for Performing Eh and Corrosion Potential Measurements in Autoclave Exposures in Simulated Basalt and Tuff Groundwater	Approved
WF-PP-37.2 Revision 0	Laboratory Procedure for Determination of the Polarization Behavior of Metal Specimens at Ambient Pressure	Approved
WF-PP-38 Revision 0	Procedure for Preparing and Evaluation of U-Bend Specimens for Stress Corrosion Studies of Overpack Materials for the NRC Waste Packaging Project	Approved
WF-PP-38.1 Revision 0	Procedure for Performing and Evaluating 3 Point Bend Beam Specimens for Stress Corrosion Studies of Overpack Materials for NRC Waste Package Program	Approved
WF-PP-39 Revision 0	Procedure for Preparing, Testing and Evaluating Crevice Corrosion Specimens of Titanium Grade-12 and Cast Steel	Approved
WF-PP-40 Revision 0	Laboratory Procedures for Preparation, Cleaning, and Evaluation of Thermogalvanic and Heat-Transfer Specimens	Approved
WF-PP-41 Revision 0	Laboratory Procedures for Determination of Corrosion Rates Under Heat-Transfer Conditions	Approved
WF-PP-42 Revision 0	Laboratory Procedure for Determination of Thermogalvanic Corrosion Rates	Approved
WF-PP-43 Revision 0	Procedure for Welding Titanium Grade-12 Plate for Use in Corrosion Studies of Overpack Materials for NRC Waste Isolation Project	Approved

Table F.1. Continued.

Procedure No.	Title	Status
WF-PP-45 Revision 0	Laboratory Procedure for Preparing and Evaluating Slow Strain-Rate Specimens and for Performing Slow Strain-Rate Tests	Approved
WF-PP-45.1 Revision 0	Laboratory Procedures for Performing Slow Strain-Rate Tests Under Potentiostated Conditions	Approved
WF-PP-46 Revision 0	Procedure for Preparation of Titanium Grade-12 Corrosion Specimens with Metallic Iron Embedded in the Surface	Approved
WF-PP-47 Revision 0	Procedure for Preparing Specimens and Performing Electrochemical Pit Propagation Experiments on Carbon Steel	Approved

NRC FORM 335 (2-84) NRCM 1102, 3201, 3202		U.S. NUCLEAR REGULATORY COMMISSION		1. REPORT NUMBER (Assigned by TIDC, add Vol. No., if any) NUREG/CR-4955 BMI-2155					
BIBLIOGRAPHIC DATA SHEET SEE INSTRUCTIONS ON THE REVERSE									
2. TITLE AND SUBTITLE Long-Term Performance of Container Materials for High-Level Waste				3. LEAVE BLANK					
5. AUTHOR(S) J.A. Beavers*, N.G. Thompson*, A.J. Markworth, H.J. Cialone, B.S. Majumdar, and J.K. McCoy				4. DATE REPORT COMPLETED <table border="1"> <tr> <td>MONTH</td> <td>YEAR</td> </tr> <tr> <td>September</td> <td>1987</td> </tr> </table>		MONTH	YEAR	September	1987
MONTH	YEAR								
September	1987								
7. PERFORMING ORGANIZATION NAME AND MAILING ADDRESS (Include Zip Code) Battelle Columbus Division 505 King Avenue Columbus, Ohio 43201-2693 *Cortest Columbus, Inc.				6. DATE REPORT ISSUED <table border="1"> <tr> <td>MONTH</td> <td>YEAR</td> </tr> <tr> <td>November</td> <td>1987</td> </tr> </table>		MONTH	YEAR	November	1987
MONTH	YEAR								
November	1987								
10. SPONSORING ORGANIZATION NAME AND MAILING ADDRESS (Include Zip Code) Division of Engineering Office of Nuclear Regulatory Research U.S. Nuclear Regulatory Commission Washington, DC 20555				8. PROJECT/TASK/WORK UNIT NUMBER 9. FIN OR GRANT NUMBER B6764					
11a. TYPE OF REPORT Technical				b. PERIOD COVERED (Inclusive dates) April 1982--August 1987					
12. SUPPLEMENTARY NOTES									
13. ABSTRACT (200 words or less) <p>This report describes the results of experimental and analytical studies of high-level waste container degradation. Corrosion and hydrogen embrittlement tests were conducted on selected materials to identify environmental and metallurgical factors that promote material degradation, especially stress-corrosion cracking. A major emphasis on overpack materials focused on cast and wrought low-carbon steels.</p> <p>Results of the corrosion work show that, to more completely identify potential failure modes, exposure environments must be further defined. Predictions of pitting rates based on models utilizing nonreactive walls may lead to rejection of carbon steel as a viable overpack material when, on the basis of performance, it may perform satisfactorily. Hydrogen embrittlement was shown to be promoted in regions of microstructural change such as the weld heat-affected zone. These findings show that hydrogen embrittlement is important to container integrity.</p> <p>A small portion of this task was devoted to studying the possible internal corrosion of the canister. It was found that Type 304L stainless steel will likely contain high-level waste glass for the retrieval period and probably the thermal period. Modeling studies focused on general corrosion and pitting corrosion, with the models being extended to account for more realistic conditions. Results show that pit wall reactivity is an important consideration in predicting corrosion rates.</p>									
14. DOCUMENT ANALYSIS - a. KEYWORDS/DESCRIPTORS High-level waste Waste package materials Waste package performance Overpack b. IDENTIFIERS/OPEN-ENDED TERMS				15. AVAILABILITY STATEMENT Unlimited					
				16. SECURITY CLASSIFICATION (This page) Unclassified (This report) Unclassified					
				17. NUMBER OF PAGES					
				18. PRICE					

**UNITED STATES
NUCLEAR REGULATORY COMMISSION
WASHINGTON, D.C. 20555**

**OFFICIAL BUSINESS
PENALTY FOR PRIVATE USE, \$300**

**SPECIAL FOURTH-CLASS RATE
POSTAGE & FEES PAID
USNRC
PERMIT No. G-67**